NOTES ON NUMERICAL FLUID MECHANICS AND MULTIDISCIPLINARY DESIGN · VOLUME 106

Imaging Measurement Methods for Flow Analysis

Results of the DFG Priority Programme 1147 "Imaging Measurement Methods for Flow Analysis" 2003–2009

Wolfgang Nitsche
Christoph Dobriloff (Eds.)

Springer

Imaging Measurement Methods for Flow Analysis

Results of the DFG Priority Programme 1147 "Imaging Measurement Methods for Flow Analysis" 2003–2009

Wolfgang Nitsche
Christoph Dobriloff
(Editors)

Springer

Prof. Dr.-Ing. Wolfgang Nitsche
Berlin Institute of Technology
Department of Aeronautics and Astronautics
Chair of Aerodynamics
Marchstraße 12–14
10587 Berlin
Germany
E-mail: wolfgang.nitsche@tu-berlin.de

Dipl.-Ing. Christoph Dobriloff
Berlin Institute of Technology
Department of Aeronautics
and Astronautics
Chair of Aerodynamics
Marchstraße 12–14
10587 Berlin
Germany
E-mail: christoph.dobriloff@tu-berlin.de

ISBN 978-3-642-01105-4 e-ISBN 978-3-642-01106-1

DOI 10.1007/978-3-642-01106-1

Notes on Numerical Fluid Mechanics
and Multidisciplinary Design ISSN 1612-2909

Library of Congress Control Number: applied for

Typeset & Cover Design: Scientific Publishing Services Pvt. Ltd., Chennai, India.

Printed in acid-free paper
5 4 3 2 1 0
springer.com

NNFM Editor Addresses

Prof. Dr. Wolfgang Schröder
(General Editor)
RWTH Aachen
Lehrstuhl für Strömungslehre und
Aerodynamisches Institut
Wüllnerstr. zw. 5 u. 7
52062 Aachen
Germany
E-mail: office@aia.rwth-aachen.de

Prof. Dr. Kozo Fujii
Space Transportation Research Division
The Institute of Space
and Astronautical Science
3-1-1, Yoshinodai, Sagamihara
Kanagawa, 229-8510
Japan
E-mail: fujii@flab.eng.isas.jaxa.jp

Dr. Werner Haase
Höhenkirchener Str. 19d
D-85662 Hohenbrunn
Germany
E-mail: office@haa.se

Prof. Dr. Ernst Heinrich Hirschel
(Former General Editor)
Herzog-Heinrich-Weg 6
D-85604 Zorneding
Germany
E-mail: e.h.hirschel@t-online.de

Prof. Dr. Bram van Leer
Department of Aerospace Engineering
The University of Michigan
Ann Arbor, MI 48109-2140
USA
E-mail: bram@engin.umich.edu

Prof. Dr. Michael A. Leschziner
Imperial College of Science
Technology and Medicine
Aeronautics Department
Prince Consort Road
London SW7 2BY
U.K.
E-mail: mike.leschziner@ic.ac.uk

Prof. Dr. Maurizio Pandolfi
Politecnico di Torino
Dipartimento di Ingegneria
Aeronautica e Spaziale
Corso Duca degli Abruzzi, 24
I-10129 Torino
Italy
E-mail: pandolfi@polito.it

Prof. Dr. Jacques Periaux
38, Boulevard de Reuilly
F-75012 Paris
France
E-mail: jperiaux@free.fr

Prof. Dr. Arthur Rizzi
Department of Aeronautics
KTH Royal Institute of Technology
Teknikringen 8
S-10044 Stockholm
Sweden
E-mail: rizzi@aero.kth.se

Dr. Bernard Roux
L3M – IMT La Jetée
Technopole de Chateau-Gombert
F-13451 Marseille Cedex 20
France
E-mail: broux@l3m.univ-mrs.fr

Prof. Dr. Yurii I. Shokin
Siberian Branch of the
Russian Academy of Sciences
Institute of Computational
Technologies
Ac. Lavrentyeva Ave. 6
630090 Novosibirsk
Russia
E-mail: shokin@ict.nsc.ru

Preface

In 2003 the German Research Foundation established a new priority programme on the subject of "Imaging Measurement Methods for Flow Analysis" (SPP 1147). This research programme was based on the fact that experimental flow analysis, in addition to theory and numerics, has always played a predominant part both in flow research and in other areas of industrial practice. At the time, however, comparisons with numerical tools (such as Computational Fluid Dynamics), which were increasingly used in research and practical applications, soon made it clear that there are relatively few experimental procedures which can keep up with state-of-the-art numerical methods in respect of their informative value, e.g. with regard to visual-spatial analysis or the dynamics of flow fields. The priority programme "Imaging Measurement Methods for Flow Analysis" was to help close this development gap. Hence the project was to focus on the investigation of efficient measurement methods to analyse complex spatial flow fields. Specific cooperations with computer sciences and especially measurement physics were to advance flow measurement techniques to a widely renowned key technology, exceeding the classical fields of fluid mechanics by a long chalk.

The SSP-Research Programme, which was funded over a period of six years, was roughly divided into the subject areas of field measurement methods, surface measurement methods as well as flow measurement techniques based on micro electromechanical sensors (MEMS). These sub-areas were investigated by interdisciplinary research groups from the fields of flow mechanics (including users from applied engineering sciences), measurement physics and computer sciences (in the latter case involving methods for digital imaging and analysis). The objective of the individual tasks was to arrive at a meaningful "image" of the flow field, making it possible, for instance, to recognize coherencies in the physical flow and to assess model representations.

The articles on the individual projects combined in this book aim to provide a comprehensive overview of the research activities in the years 2003 to 2009. All papers submitted were thoroughly screened at first and subsequently presented to the Editor General of the NNFM series of publications. The editors wish to express

their gratitude to all authors concerned, the reviewers listed below as well as Prof. W. Schröder, the NNFM-Editor responsible, for their great and congenial collaboration.

Last but not least everyone involved would like to thank the German Research Foundation for funding the SPP1147 joint research project. Special thanks go to the respective staff of the German Research Foundation, particularly Dr. Lachenmeier, Dr. Meier as well as to Dr. Hillenherms (Ms) for the final phase of the project.

Berlin,
January 2009

Prof. Dr.-Ing. Wolfgang Nitsche
Coordinator of the SPP1147

List of Reviewers (in alpabetical order)

Prof. Dr.-Ing. Andreas Dillmann
Dr. Werner Hentschel
Prof. Dr.-Ing. Rudolf Mester
Prof. Dr.-Ing. Herbert Olivier
Dr. Klaus Reymann
Prof. Dr.-Ing. Christoph Egbers
Prof. Dr.-Ing. Johannes Janicka
Prof. Dr.-Ing. Heinrich Niemann
Prof. Dr.-Ing. Dieter Petrak
Prof. Dr.-Ing. Wolfgang Schröder

Contents

List of Contributors

Klaus Affeld
Biofluid Mechanics Laboratory,
Charité - Universitätsmedizin
Berlin, Thielallee 73, 14195 Berlin,
Germany,
klaus.affeld@charite.de

Olga Alhaj
Institute of Turbomachinery and Fluid Dynamics,
Leibniz University Hannover,
Appelstraße 9, 30167 Hannover,
Germany,
alhaj@tfd.uni-hannover.de

Bradley Atcheson
Department of Computer Science,
University of British Columbia,
2366 Main Mall,
Vancouver, BC, V6T 1Z4,
Canada,
atcheson@cs.ubc.ca

Kudret Baysal
Institut für Aerodynamik und Gasdynamik,
Universität Stuttgart,
Pfaffenwaldring 21, 70569 Stuttgart,
Germany,
Kudret.Baysal@
iag.uni-stuttgart.de

Christian Bendicks
"Otto-von-Guericke" Universität Magdeburg,
IESK, Universitätsplatz 2,
39106 Magdeburg, Germany,
Christian.Bendicks@ovgu.de

Kai Berger
Department of Computer Science,
Computer Graphics Lab,
TU Braunschweig,
Mühlenpfordtstraße 23,
38106 Braunschweig,
Germany,
berger@cg.cs.tu-bs.de

Andreas Berns
Microsensor & Actuator Technology Center (MAT),
Berlin University of Technology,
Gustav-Meyer-Allee 25,
13355 Berlin, Germany,
berns@mat.ee.tu-berlin.de

André Berthe
Biofluid Mechanics Laboratory,
Charité - Universitätsmedizin Berlin,
Thielallee 73, 14195 Berlin,
Germany,
andre.berthe@charite.de

Volker Beushausen
Department of Photonic Sensor Technology,
Laser-Laboratorium Göttingen e.V.,
Hans-Adolf-Krebs-Weg 1,
37077 Göttingen,
Germany,
Volker.Beushausen@llg-ev.de

Robert Bordás
"Otto-von-Guericke"
Universität Magdeburg,
ISUT/ LSS, Universitätsplatz 2,
39106 Magdeburg,
Germany,
robert.bordas@ovgu.de

Emanuela Botello-Payro
Institute of Fluid Mechanics,
Technical Faculty,
Friedrich-Alexander University
Erlangen-Nuremberg,
Cauerstraße 4,
91058 Erlangen,
Germany,
ebotello@lstm.uni-erlangen.de

Andreas Bräuer
Lehrstuhl für Technische Thermodynamik and Erlangen Graduate School in Advanced Optical Technologies (SAOT),
Friedrich-Alexander-Universität Erlangen-Nürnberg,
Paul-Gordan-Straße 6,
91052 Erlangen,
Germany,
ab@ltt.uni-erlangen.de

Martin Brede
Chair of Fluid Mechanics,
University of Rostock,
Albert-Einstein-Straße 2,
18051 Rostock,
Germany,
martin.brede@uni-rostock.de

Christoph Brücker
TU Bergakademie Freiberg,
Institut für Mechanik und Fluiddynamik,
Lampadiusstraße 4,
09596 Freiberg,
Germany,
Christoph.Bruecker@imfd.tu-freiberg.de

Kai Bürger
Technische Universität München,
Informatik 15 (Computer Graphik & Visualisierung),
Boltzmannstraße 3,
85748 Garching bei München,
Germany,
buergerk@in.tum.de

Sebastian Burgmann
Institute of Aerodynamics,
RWTH Aachen University,
Wuellnerstraße 5a, 52062 Aachen,
Germany,
s.burgmann@aia.rwth-aachen.de

Lars Büttner
Technische Universität Dresden,
Department of Electrical Engineering and Information Technology, Laboratory of Measurement and Test Techniques, Helmholtzstraße 18,
01062 Dresden, Germany,
lars.buettner@tu-dresden.de

Jürgen Czarske
Technische Universität Dresden,
Department of Electrical Engineering and Information Technology, Laboratory of Measurement and Test Techniques,

Helmholtzstraße 18, 01062
Dresden, Germany,
juergen.czarske@
tu-dresden.de

Antonio Delgado
Institute of Fluid Mechanics,
Technical Faculty,
Friedrich-Alexander University
Erlangen-Nuremberg,
Cauerstraße 4, 91058
Erlangen, Germany,
antonio.delgado@
lstm.uni-erlangen.de

Cornelia Denz
University of Münster,
Institute of Applied Physics,
Corrensstraße 2/4,
48149 Münster,
Germany,
denz@uni-muenster.de

Christoph Dobriloff
Institute of Aeronautics and Astronautics, Berlin
University of Technology,
Marchstraße 12-14,
10587 Berlin,
Germany,
christoph.dobriloff@
tu-berlin.de

Jan Domhardt
Institute of Aeronautics
and Astronautics, Berlin
University of Technology,
Marchstraße 12-14,
10587 Berlin,
Germany,
jan.domhardt@
ilr.tu-berlin.de

Michael Eggert
Physikalisch-Technische
Bundesanstalt, Department of
Gas Flow, Bundesallee 100,
38116 Braunschweig,
Germany,
michael.eggert@ptb.de

Gerrit E. Elsinga
Department of Aerospace
Engineering, Delft University of
Technology, P.O. Box 5058,
2600 GB Delft, The Netherlands

Thomas Ertl
Institut für Visualisierung und Interaktive Systeme,
Universität Stuttgart,
Universitätsstraße 38,
70569 Stuttgart,
Germany,
Thomas.Ertl@
vis.uni-stuttgart.de

Andreas Fischer
Technische Universität Dresden,
Department of Electrical
Engineering and Information
Technology, Laboratory of
Measurement and Test Techniques,
Helmholtzstraße 18, 01062 Dresden,
Germany,
andreas.fischer2@
tu-dresden.de

Octavian Frederich
Berlin Institute of Technology, Institute
of Fluid Mechanics and Engineering
Acoustics, Sekr. MB1,
Müller-Breslau-Straße 12, 10623 Berlin,
Germany,
octavian.frederich@
tu-berlin.de

Christoph S. Garbe
Heidelberg Collaboratory for Image
Processing (HCI),
Interdisciplinary Center for
Scientific Computing (IWR),
University of Heidelberg,
Speyerer Straße 4, 69115

Heidelberg, Germany,
Christoph.Garbe@
iwr.uni-heidelberg.de

Reinhard Geisler
Institut für Aerodynamik und Strömungstechnik, Deutsches Zentrum für Luft- und Raumfahrt e.V. (DLR), Bunsenstraße 10, 37073 Göttingen, Germany,
Reinhard.Geisler@dlr.de

Joachim Georgii
Technische Universität München, Informatik 15 (Computer Graphik & Visualisierung), Boltzmannstraße 3, 85748 Garching bei München, Germany,
georgii@in.tum.de

Erik Goldhahn
Institute of Turbomachinery and Fluid Dynamics, Leibniz University Hannover, Appelstraße 9, 30167 Hannover, Germany,
goldhahn@
tfd.uni-hannover.de

Rainer Hain
Universität der Bundeswehr München, Institut für Strömungsmechanik und Aerodynamik LRT-7, Werner-Heisenberg-Weg 39, 85577 Neubiberg,
rainer.hain@unibw.de

Wolfgang Heidrich
Department of Computer Science, University of British Columbia, 2366 Main Mall, Vancouver, BC, V6T 1Z4, Canada,
heidrich@cs.ubc.ca

Florian Herbst
Institute of Turbomachinery and Fluid Dynamics, Leibniz University Hannover, Appelstraße 9, 30167 Hannover, Germany,
herbst@tfd.uni-hannover.de

Frank Holtmann
University of Münster, Institute of Applied Physics, Corrensstraße 2/4, 48149 Münster, Germany,
frank.holtmann@
uni-muenster.de

Markus Holzner
Institute of Environmental Engineering, Swiss Federal Institute of Technology, Wolfgang-Pauli-Strasse 15, 8093 Zürich, Switzerland

Frank Hüttmann
Chair of Fluid Mechanics, University of Rostock, Albert-Einstein-Straße 2, 18051 Rostock, Germany,
frank.huettmann@
uni-rostock.de

Ivo Ihrke
Department of Computer Science, University of British Columbia, 2366 Main Mall, Vancouver, BC, V6T 1Z4, Canada,
ivoihrke@cs.ubc.ca

Bernd Jähne
Heidelberg Collaboratory for Image Processing (HCI), Interdisciplinary Center for Scientific Computing (IWR),

University of Heidelberg,
Speyerer Straße 4, 69115
Heidelberg, Germany,
Bernd.Jaehne@
iwr.uni-heidelberg.de

Markus Jehle
Heidelberg Collaboratory for
Image Processing (HCI),
Interdisciplinary Center for
Scientific Computing (IWR),
University of Heidelberg,
Speyerer Straße 4, 69115 Heidelberg,
Germany,
Markus.Jehle@
iwr.uni-heidelberg.de

Mario Jensch
Chair of Fluid Mechanics,
University of Rostock,
Albert-Einstein-Straße 2,
18051 Rostock, Germany,
mario.jensch@
uni-rostock.de

Christian J. Kähler
Universität der Bundeswehr München,
Institut für Strömungsmechanik und
Aerodynamik LRT-7,
Werner-Heisenberg-Weg 39,
85577 Neubiberg,
christian.kaehler@
unibw.de

Ulrich Kertzscher
Biofluid Mechanics Laboratory,
Charité - Universitätsmedizin
Berlin, Thielallee 73, 14195
Berlin, Germany,
ulrich.kertzscher@
charite.de

Matthias Kinzel
Institute of Fluid Mechanics
and Aerodynamics, Technische
Universität of Darmstadt,
64287 Darmstadt, Germany

Wolfgang Kinzelbach
Institute of Environmental
Engineering, Swiss Federal
Institute of Technology,
Wolfgang-Pauli-Strasse 15,
8093 Zürich, Switzerland

Clemens Kirmse
TU Bergakademie Freiberg, Institut für
Mechanik und Fluiddynamik,
Lampadiusstraße 4,
09596 Freiberg, Germany,
Clemens.Kirmse@
imfd.tu-freiberg.de

Jens Kitzhofer
TU Bergakademie Freiberg,
Institut für Mechanik und
Fluiddynamik, Lampadiusstraße 4,
09596 Freiberg, Germany,
Jens.Kitzhofer@
imfd.tu-freiberg.de

Jürgen Kompenhans
Institut für Aerodynamik und
Strömungstechnik, Deutsches
Zentrum für Luft- und
Raumfahrt e.V. (DLR),
Bunsenstraße 10,
37073 Göttingen, Germany

Daniel Kondermann
Heidelberg Collaboratory for
Image Processing (HCI),
Interdisciplinary Center for
Scientific Computing (IWR),
University of Heidelberg,
Speyerer Straße 4, 69115
Heidelberg, Germany,
Daniel.Kondermann@
iwr.uni-heidelberg.de

Polina Kondratieva
RTT AG, Rosenheimer Straße 145,
81671 München, Germany,
kondrati@in.tum.de

Jörg König
Technische Universität
Dresden, Department of
Electrical Engineering and
Information Technology,
Laboratory of Measurement
and Test Techniques,
Helmholtzstraße 18, 01062
Dresden, Germany,
Joerg.Koenig@tu-dresden.de

Alfred Leder
Chair of Fluid Mechanics,
University of Rostock,
Albert-Einstein-Straße 2,
18051 Rostock, Germany,
alfred.leder@uni-rostock.de

Alfred Leipertz
Lehrstuhl für Technische
Thermodynamik and Erlangen
Graduate School in Advanced
Optical Technologies (SAOT),
Friedrich-Alexander-Universität
Erlangen-Nürnberg,
Am Weichselgarten 8,
91058 Erlangen, Germany,
sek@ltt.uni-erlangen.de

Alexander Liberzon
School of Mechanical Engineering, Tel
Aviv University, 69978 Ramat Aviv,
Israel

Elka Lobutova
Faculty of Mechanical
Engineering, Ilmenau University
of Technology, P.O. Box
100565, 98684 Ilmenau,
Germany,
elka.lobutova@
tu-ilmenau.de

Dirk Martin Luchtenburg
Berlin Institute of
Technology, Institute of Fluid
Mechanics and Engineering
Acoustics, Sekr. MB1,
Müller-Breslau-Straße 12,
10623 Berlin, Germany,
dirk.m.luchtenburg@
tu-berlin.de

Beat Lüthi
Institute of Environmental
Engineering, Swiss Federal
Institute of Technology,
Wolfgang-Pauli-Strasse 15,
8093 Zürich, Switzerland

Hans-Gerd Maas
Institute of Photogrammetry
and Remote Sensing,
Technische Universität Dresden,
Helmholtzstraße 10,
01069 Dresden,
Germany,
hans-gerd.maas@tu-dresden.de

Marcus Magnor
Department of Computer Science,
Computer Graphics Lab,
TU Braunschweig,
Mühlenpfordtstraße 23,
38106 Braunschweig,
Germany,
magnor@cg.cs.tu-bs.de

Anna Malarski
Lehrstuhl für Technische
Thermodynamik and Erlangen Graduate
School in Advanced Optical Technolo-
gies (SAOT), Friedrich-Alexander-
Universität Erlangen-Nürnberg, Am
Weichselgarten 8, 91058
Erlangen, Germany,
sek@ltt.uni-erlangen.de

Bernd Michaelis
“Otto-von-Guericke”
Universität Magdeburg, IESK,
Universitätsplatz 2, 39106
Magdeburg, Germany,
bernd.michaelis@ovgu.de

Dirk Michaelis
La Vision GmbH,
Anna-Vandenhoeck-Ring 19,
37081 Göttingen, Germany

Dirk Müller
E.ON Energy Research
Center, RWTH Aachen
University, Jägerstraße 17–19,
52066 Aachen, Germany

Harald Müller
Physikalisch-Technische
Bundesanstalt, Department of
Gas Flow, Bundesallee 100,
38116 Braunschweig,
Germany,
harald.mueller@ptb.de

Jens Müller
Department of Photonic Sensor
Technology, Laser-Laboratorium
Göttingen e.V.,
Hans-Adolf-Krebs-Weg 1,
37077 Göttingen, Germany

Wolfgang Nitsche
Institute of Aeronautics
and Astronautics, Berlin
University of Technology,
Marchstraße 12-14,
10587 Berlin, Germany,
wolfgang.nitsche@
tu-berlin.de

Ernst Obermeier
Microsensor & Actuator
Technology Center (MAT),
Berlin University of Technology,
Gustav-Meyer-Allee 25,
13355 Berlin, Germany,
obermeier@
mat.ee.tu-berlin.de

Inken Peltzer
Institute of Aeronautics
and Astronautics, Berlin
University of Technology,
Marchstraße 12-14,
10587 Berlin, Germany,
inken.peltzer@tu-berlin.de

Stefania Petra
University of Heidelberg,
Department of Mathematics
and Computer Science, Image
and Pattern Analysis Group,
Speyerer Straße 4–6, 69115
Heidelberg, Germany,
petra@
math.uni-heidelberg.de

Christian Poelma
Laboratory for Aero &
Hydrodynamics, Delft University
of Technology, Leeghwaterstraat
21, 2628 CA Delft,
The Netherlands

Torsten Putze
Institute of Photogrammetry and
Remote Sensing, Technische
Universität Dresden,
Helmholtzstraße 10,
01069 Dresden, Germany,
torsten.putze@
tu-dresden.de

Rolf Radespiel
Technische Universität Braunschweig,
Institut für Strömungsmechanik,
Bienroder Weg 3,
38106 Braunschweig,
r.radespiel@
tu-braunschweig.de

Robert Rank
E.ON Energy Research
Center, RWTH Aachen
University, Jägerstraße
17–19, 52066 Aachen,
Germany,
Robert.Rank@
eonerc.rwth-aachen.de

Christian Resagk
Faculty of Mechanical Engineering,
Ilmenau University of Technology,
P.O. Box 100565, 98684 Ilmenau,
Germany

Matthias Reyer
Institute of Aeronautics
and Astronautics, Berlin
University of Technology,
Marchstraße 12–14, 10587 Berlin,
Germany,
matthias.reyer@
ilr.tu-berlin.de

Ulrich Rist
Institut für Aerodynamik und
Gasdynamik, Universität Stuttgart,
Pfaffenwaldring 21, 70569 Stuttgart,
Germany,
Ulrich.Rist@
iag.uni-stuttgart.de

Markus Röhl
Department of Photonic Sensor Technology, Laser-Laboratorium Göttingen e.V.,
Hans-Adolf-Krebs-Weg 1,
37077 Göttingen, Germany

Karsten Roetmann
Department of Photonic
Sensor Technology,
Laser-Laboratorium
Göttingen e.V.,
Hans-Adolf-Krebs-Weg 1,
37077 Göttingen, Germany,
Karsten.Roetmann@llg-ev.de

Frank Rotter
Department of Photonic
Sensor Technology,
Laser-Laboratorium
Göttingen e.V.,
Hans-Adolf-Krebs-Weg 1,
37077 Göttingen, Germany,
frank.rotter@llg-ev.de

Ilka Rudolph
Institute of Aeronautics
and Astronautics, Berlin
University of Technology,
Marchstraße 12-14,
10587 Berlin, Germany,
ilka.rudolph@
ilr.tu-berlin.de

Paul Ruhnau
Computer Vision, Graphics
and Pattern Recognition
Group, University of Mannheim,
68131 Mannheim, Germany

Fulvio Scarano
Department of Aerospace
Engineering, Delft University
of Technology, P.O. Box 5058,
2600 GB Delft, The Netherlands

Tobias Schafhitzel
Institut für Visualisierung und Interaktive Systeme,
Universität Stuttgart,
Universitätsstraße 38,
70569 Stuttgart, Germany,
Tobias.Schafhitzel@
vis.uni-stuttgart.de

Waldemar Schmunk
Department of Photonic Sensor
Technology, Laser-Laboratorium
Göttingen e.V.,
Hans-Adolf-Krebs-Weg 1,
37077 Göttingen, Germany,
waldemar.schmunk@
llg-ev.de

Christoph Schnörr
University of Heidelberg,
Department of Mathematics and
Computer Science, Image and Pattern
Analysis Group, Speyerer Straße 4-6,

69115 Heidelberg,
Germany,
schnoerr@
math.uni-heidelberg.de

Jochen Scholz
Department of Photonic Sensor Technology, Laser-Laboratorium Göttingen e.V.,
Hans-Adolf-Krebs-Weg 1,
37077 Göttingen, Germany

Andreas Schröder
German Aerospace Center (DLR),
Institute of Aerodynamics and Flow Technology,
Bunsenstraße 10, 37073 Göttingen, Germany,
andreas.schroeder@dlr.de

Wolfgang Schröder
Institute of Aerodynamics,
RWTH Aachen University,
Wuellnerstraße 5a, 52062 Aachen, Germany,
office@aia.rwth-aachen.de

Jon Scouten
Berlin Institute of Technology, Institute of Fluid Mechanics and Engineering Acoustics, Sekr. MB1,
Müller-Breslau-Straße 12, 10623 Berlin, Germany,
jon.scouten@
cfd.tu-berlin.de

Jörg Seume
Institute of Turbomachinery and Fluid Dynamics,
Leibniz University Hannover,
Appelstraße 9, 30167 Hannover, Germany,
seume@tfd.uni-hannover.de

Katsuaki Shirai
Technische Universität Dresden, Department of Electrical Engineering and Information Technology,
Laboratory of Measurement and Test Techniques,
Helmholtzstraße 18,
01062 Dresden, Germany,
Katsuaki.Shirai@
tu-dresden.de

Christoph Skupsch
Technische Universität Dresden, Department of Electrical Engineering and Information Technology, Laboratory of Measurement and Test Techniques,
Helmholtzstraße 18, 01062 Dresden, Germany

Karsten Staack
Institut für Aerodynamik und Strömungstechnik, Deutsches Zentrum für Luft- und Raumfahrt e.V. (DLR),
Bunsenstraße 10,
37073 Göttingen, Germany

Dominique Tarlet
"Otto-von-Guericke" Universität Magdeburg, ISUT/ LSS,
Universitätsplatz 2, 39106 Magdeburg, Germany,
dominique.tarlet@ovgu.de

Dominique Thévenin
"Otto-von-Guericke" Universität Magdeburg, ISUT/ LSS,
Universitätsplatz 2, 39106 Magdeburg, Germany,
thevenin@ovgu.de

Frank Thiele
Berlin Institute of Technology, Institute of Fluid Mechanics and Engineering Acoustics, Sekr. MB1,
Müller-Breslau-Straße 12, 10623 Berlin, Germany,
frank.thiele@tu-berlin.de

Cameron Tropea
Institute of Fluid Mechanics and Aerodynamics, Technische Universität of Darmstadt, 64287 Darmstadt, Germany

Andrey Vlasenko
University of Heidelberg, Department of Mathematics and Computer Science, Image and Pattern Analysis Group, Speyerer Straße 4-6, 69115 Heidelberg, Germany, vlasenko@math.uni-heidelberg.de

Andreas Voigt
Technische Universität Dresden, Department of Electrical Engineering and Information Technology, Laboratory of Measurement and Test Techniques, Helmholtzstraße 18, 01062 Dresden, Germany, Andreas.Voigt@tu-dresden.de

Mike Wellhausen
Department of Photonic Sensor Technology, Laser-Laboratorium Göttingen e.V., Hans-Adolf-Krebs-Weg 1, 37077 Göttingen, Germany, mike.wellhausen@llg-ev.de

Rüdiger Westermann
Technische Universität München, Informatik 15 (Computer Graphik& Visualisierung), Boltzmannstraße 3, 85748 Garching bei München, Germany, westermann@in.tum.de

Jerry Westerweel
Laboratory for Aero & Hydrodynamics, Delft University of Technology, Leeghwaterstraat 21, 2628 CA Delft, The Netherlands

Patrick Westfeld
Institute of Photogrammetry and Remote Sensing, Technische Universität Dresden, Helmholtzstraße 10, 01069 Dresden, Germany, patrick.westfeld@tu-dresden.de

Bernhard Wieneke
La Vision GmbH, Anna-Vandenhoeck-Ring 19, 37081 Göttingen, Germany

Tim Wiersbinski
Department of Photonic Sensor Technology, Laser-Laboratorium Göttingen e.V., Hans-Adolf-Krebs-Weg 1, 37077 Göttingen, Germany

Mike Woerdemann
University of Münster, Institute of Applied Physics, Corrensstraße 2/4, 48149 Münster, Germany, woerde@uni-muenster.de

Bernd Wunderlich
"Otto-von-Guericke" Universität Magdeburg, ISUT/ LSS, Universitätsplatz 2, 39106 Magdeburg, Germany, bernd.wunderlich@ovgu.de

Bogumila Ewelina Zima-Kulisiewicz
Institute of Fluid Mechanics, Technical Faculty, Friedrich-Alexander University Erlangen-Nuremberg, Cauerstraße 4, 91058 Erlangen, Germany, ezima@lstm.uni-erlangen.de

Principles of a Volumetric Velocity Measurement Technique Based on Optical Aberrations

Rainer Hain, Christian J. Kähler, and Rolf Radespiel

Abstract. In this contribution, a simple and robust three dimensional measurement technique for the determination of all velocity components is presented. As opposed to other techniques, only a single camera is required in order to calculate the particle positions in physical space. This is possible because the depth position of the particles is encoded using an optical aberration or wavefront distortion, called astigmatism. The astigmatism causes the particle images to have ellipse-like shapes. The length of the semi-major axis and the semi-minor axis depends on the depth wise position of the particle. It will be shown that this effect is well suited for extracting the particle positions. In the first section, an introduction is given and the measurement principle is shown in detail. Subsequently, the validation of the technique is illustrated by means of synthetically generated images. Finally, experimental results are presented and a conclusion is drawn.

1 Introduction

The measurement of the three velocity components in a volume is of interest for many fluid mechanics investigations. Therefore, different techniques with different advantages and drawbacks have been developed in recent years. One of these

Rainer Hain
Universität der Bundeswehr München, Institut für Strömungsmechanik und Aerodynamik LRT-7, Werner-Heisenberg-Weg 39, 85577 Neubiberg
rainer.hain@unibw.de

Christian J. Kähler
Universität der Bundeswehr München, Institut für Strömungsmechanik und Aerodynamik LRT-7, Werner-Heisenberg-Weg 39, 85577 Neubiberg
christian.kaehler@unibw.de

Rolf Radespiel
Technische Universität Braunschweig, Institut für Strömungsmechanik, Bienroder Weg 3, 38106 Braunschweig
r.radespiel@tu-braunschweig.de

W. Nitsche and C. Dobriloff (Eds.): Imaging Measurement Methods, NNFM 106, pp. 1–10.
springerlink.com

methods is the particle tracking velocimetry, which allows the determination of the velocities of single particles [14]. A drawback of this method is the large number of cameras which is required to determine the particle positions in physical space unambiguously and the limited depth of focus which restricts the measurement volume depth. Another technique is the scanning particle image velocimetry [4, 9], where the volume is scanned with thin light sheets in order to determine the velocities in these sheets. Occasionally the in-plane velocities are measured and the third velocity component is calculated by means of mass conservation. Due to the recording of many planes, the temporal sampling of the volume is reduced, which is why this method is only applicable to flows with large time scales (10 scanning sheets reduce the temporal resolution for the volume at least by a factor of 10). A benefit of this approach is the use of a light sheet as opposed to the other three dimensional methods which require volume illumination. Another method for the determination of the three velocity components in a volume is holographic PIV [2, 8, 11]. This method requires a record carrier with high capacity. Using an analog medium leads to the problem of a complicated recording and evaluation process. The application of a digital camera chip restricts the measurement volume size significantly because of the limiting pixel number. A relatively new approach is tomographic PIV [5, 6], where a reconstruction of the measurement volume by means of tomographic algorithms is done. Similar to PTV, 4 cameras are usually required to acquire the positions of the particles in space reliable and with sufficient accuracy. However, multiple camera systems are expensive and frequently not applicable due to limited optical access or problems associated with the calibration. Willert and Gharib [15] proposed a concept which solved most of the drawbacks of the discussed methods. Their approach is based on a single camera with a modified three hole-aperture which makes it possible to obtain three particle images from a single particle. The depth position of the particle can thus be gathered from the distances between the three images. Unfortunately, the modification of the aperture and the required laser power are drawbacks of this technique. In order to overcome these problems, the so called V3V system was developed by TSI, see [13]. Instead of an aperture with three holes, three separate cameras are used.

The 3D3C time-resolved measurement technique presented here requires a single camera as well, but no modification of the aperture is necessary [7]. A similar approach was applied to microfluidics in the past by [10, 12]. They put a cylindrical lens in the optical path which leads to a distortion of the particle images in dependence on their position in depth direction. This principle was also used by [1] to measure flow velocities in larger volumes. The effect caused by a cylindrical lens is similar to an optical aberration called astigmatism [3]. In Fig. 1(a) the principle path of rays is shown under the consideration of this effect. If a point light source P is not placed on the optical axis of a lens, there is no focal point in the image plane. Instead of one focal point, two focal lines with orthogonal orientations appear. Between these focal lines, the point light source produces an ellipse-like image. The size and shape of the particle image can be used to determine the three dimensional position of the particle in physical space.

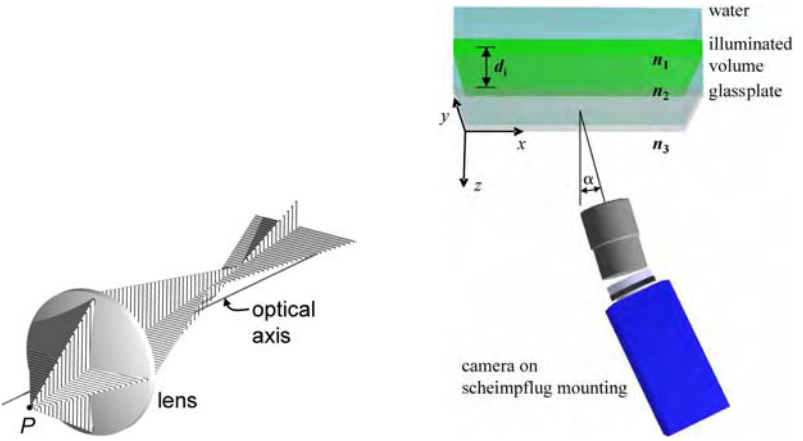

(a) Astigmatism

(b) Principle of the experimental setup

Fig. 1 Astigmatism using a single lens and applied experimental setup

2 Measurement Principle

The astigmatism mentioned earlier hardly occurs if objectives are used because optical aberrations are corrected for in such a way that the aberrations are below the resolution limit of the CCD / CMOS sensors. The larger the distance of the light rays from the optical axis, the larger the optical aberrations. In order to obtain a well defined astigmatism, the specific setup shown in Fig. 1(b) is applied. A single camera mounted on a Scheimpflug adapter is aligned to the measurement volume at angle α. This angle leads in a combination with the refraction indices n_1, n_2 and n_3 to astigmatism. Three exemplary images are shown in Fig. 2 to illustrate the effect. Only a thin light sheet was used to illuminate the particles in this case. The light sheet was traversed about 6 mm towards the camera from image 1 to image 3. In the first recording, the particle images have an ellipse like shape with a small width and a large height. In the second image the width and height of the particle images are nearly equal and at the third position, the width of the particle images is much larger than their height. When the whole volume is illuminated, the positions of the particles in depth-direction can be determined by means of their orientation and shape.

Fig. 2 Dependence of the particle image shape on the position in the measurement volume (only a thin sheet in the measurement volume is illuminated)

To estimate the positions of the particles in physical space, the following steps are required:

1. Calibration of the measurement volume by means of a traversed grid (similar to stereo PIV or other 3D3C Techniques)
2. Calibration by means of thin light sheets to determine the particle shape dependence on the position of the particle in the light sheet
3. Reconstruction of the particle position in physical space by means of the particle position on the chip, the particle shape, and the calibrations mentioned above.

2.1 Measurement Volume Size

The measurement volume size in the $x-$ and $y-$directions (defined in Fig. 1(b)) is mainly specified by the focal length of the objective and the distance of the objective from the measurement volume. The depth of the measurement volume depends on the angle α, the refraction indices n_1, n_2 and n_3, and the thickness of the glass plate. Furthermore, the distance d_i from the center of the measurement volume to the glass plate influences the measurement volume depth. If the glass plate is neglected ($n_1 = n_2$), the measurement volume depth assumes the size which is shown in Fig. 3. The calculation of this depth is done in the following way: A ray starts in the $x-z-$plane with angle α_0 from an arbitrarily positioned point light source near the measurement volume. Because intersections of rays must be calculated later, four additional rays are generated. Two rays (A_1 and A_2) are generated by rotating the initial ray around $\pm \mathrm{d}\alpha_0$ in the $x-z-$plane. Two additional rays (B_1 and B_2) are generated by rotating the initial ray around $\pm \mathrm{d}\alpha_0$ in the plane which is produced by the $y-$axis and the initial ray. The four rays are refracted at the intersection plane of water-air. Now the intersection points of the refracted rays A_1, A_2 and B_1, B_2 are determined for $\mathrm{d}\alpha_0 \to 0$. By means of this method, two virtual particle positions whose distance in the $z-$direction is assumed to be the measurement volume depth are calculated. The mid-point between the virtual particle positions in the $z-$direction is d_i.

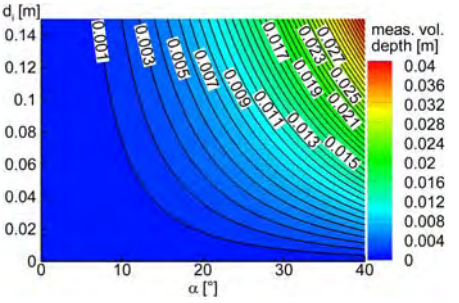

Fig. 3 The dependence of the measurement volume depth on the angle α and the distance d_i of the center of the measurement volume to the boundary ($n_1 = 1.33$, $n_2 = n_3 = 1.0$)

2.2 Calibration of the Measurement Volume

The measurement volume is viewed at the angle α leading to the distortion of the grid which is aligned parallel to the light sheet. In addition, the distortion depends on the position in the measurement volume. For this reason it is necessary to make a 3D calibration to convert the coordinates in the image plane to coordinates in physical space:

$$\begin{aligned} f(x[\mathrm{m}]) &= f(x[\mathrm{px}], y[\mathrm{px}], z[\mathrm{m}]) \\ f(y[\mathrm{m}]) &= f(x[\mathrm{px}], y[\mathrm{px}], z[\mathrm{m}]) \\ f(z[\mathrm{m}]) &= f(x[\mathrm{px}], y[\mathrm{px}], z[\mathrm{m}]) \end{aligned} \tag{1}$$

A grid is placed in the measurement volume and recorded at several positions. The intersections of the grid lines are determined by means of cross correlation of the calibration images with an artificially generated cross. The line thickness of the cross in the $x-$ and $y-$directions is entered manually for each calibration position because the astigmatism causes a different line width and height for each position of calibration target in $z-$position.

2.3 Particle Image Fitting

The fitting of the particle images is essential for the presented measurement technique because the particle position is directly associated with the particle image shape. In Fig. 4 the measurement uncertainty in the $z-$direction is shown as a function of the particle $z-$position and the uncertainty in determining the particle image width and height. The measurement volume depth is assumed to be 1 and the uncertainty is the standard deviation given in percent of the measurements volume depth. The calculation was done for particle images with width and height between 1 px and 20 px depending on the $z-$position of the particle. Applying a larger range, the measurement error is reduced.

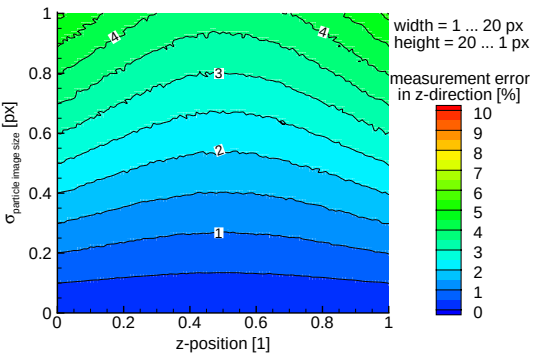

Fig. 4 Dependence of the measurement uncertainty in the $z-$direction in percent of the measurement volume depth on the $z-$position and the uncertainty in determining the particle image width and height (particle image width and height vary between 1 px and 20 px in dependence on the $z-$position)

The setup causes a wave front deformation which results in the distorted particle images. The size of the particle images in the $x-$ and $y-$directions depends on the light intensity which is scattered by a particle. However, if the particle image intensity distribution is assumed to be 2D Gaussian, the particle image width and height defined by the e^{-2} intensity do not depend on the intensity of a particle in physical space. The scattered light intensity of a particle depends strongly on the particle size, the index of defraction, the stability of the laser, and the position of the particle in the light sheet. Due to the fact that the particle image intensity distribution is not a 2D Gauss function and the particle image width and height therefore depend on the particle intensity, the particle shape is defined here by the ratio of the particle image width to the particle image height. This ratio is nearly independent from the intensity of the scattered light of a particle.

The determination of the particle image width and height is performed in the following way: First, the pixels which might belong to a particle image are determined by means of a median filter. Then, the segmentation takes place (see Fig. 6) where neighboring pixels are assigned to particle images. In the next step, the pixels of a particle image in a rectangular area around the particle image are applied to fit a 2D Gauss function:

$$f(x,y) = a_1 \cdot \exp\left(-8.0 \cdot \frac{(a_2 - x)^2}{a_3} - 8.0 \cdot \frac{(a_4 - y)^2}{a_5}\right) + a_6 \tag{2}$$

The fitting is done by means of a Gauss-Newton method. In order to get a result for the fitting coefficients which does not depend on the initially-chosen rectangular pixel area, 4 iterations are done. In each iteration the width and height of the area are chosen at twice the width and height of the particle image (width = $\sqrt{a_3}$, height = $\sqrt{a_5}$). A reconstructed particle image is shown in Fig. 6. Actually, the particle images do not have a gaussian intensity distribution which often leads to the problem that the fitting does not work very well (lock in of the fitting-function to the pixels with a high intensity), see Fig. 5 on the left hand side. Therefore, the autocorrelation of the particle image with the rectangle determined earlier is performed. Again, four iterations for the adaption of the rectangle are done. The correlation peak is much smoother than the intensity distribution of the particle image that makes the estimation of the particle image width and height easier, see Fig. 5 on the right hand side. So far, the particle image width is assumed to be the width of the normalized correlation peak at a correlation amplitude of 0.5. The particle image height is determined in a similar way.

A drawback of the autocorrelation method is that one gets only the particle image width and height so that the particle position is given by the parameters a_2 and a_4 from the Gaussian fit. The reconstructed particle image is shown in Fig. 6. The $z-$positions of the two particles are similar because only a thin light-sheet was used for the illumination. The Gaussian fit leads to a ratio of the particle image width to the particle image height of 3.55 for the upper, and 2.95 for the lower particle image. By applying the approach with the autocorrelation, one gets ratios of 3.35 and 2.92, which is in much better agreement. The ratio 3.35 leads to a z-position of 14.527 mm and the ratio 2.92 leads to a z-position of 14.145 mm.

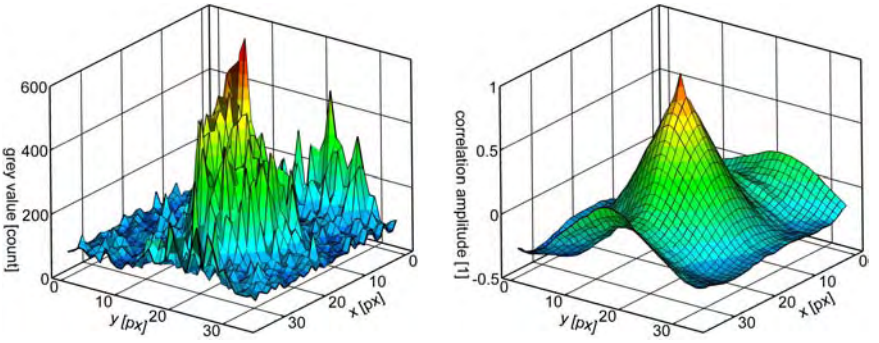

Fig. 5 Original particle image (left hand side) and autocorrelation plane (right hand side)

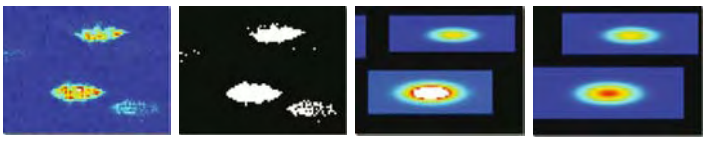

Fig. 6 Original particle image, segmented particle image, reconstructed particle image with parameters from a Gaussian fit (width/height upper particle = 3.55; width/height lower particle = 2.95) and reconstructed particle image with parameters from autocorrelation (width/height upper particle = 3.35; width/height lower particle = 2.92)

2.4 Calibration with Particle Images

Due to the astigmatism, the particle image shape depends on the positions of the particles in the depth direction (z), as pointed out before. In addition, the particle image shape varies in the $x-$ and $y-$directions. For this reason, a calibration

$$f(x[\text{px}], y[\text{px}], shape) = z[\text{m}] \tag{3}$$

is necessary which maps the particle position and shape unambiguously. Therefore, the measurement volume is scanned with light sheets which are as thin as possible and many images are recorded at every light sheet position. The particle images are extracted and fitted as mentioned in section 2.3, and for each particle image the shape parameter is calculated. This is done for the whole volume. With these extracted particle images the coefficients of the 4th order rational calibration function are determined by means of the Levenberg-Marquardt method.

3 Validation

In order to validate the presented measurement technique, a simulation software for the generation of synthetic images was developed. Due to the implementation of the ray tracing technique, the software allows the simulation of astigmatism. The

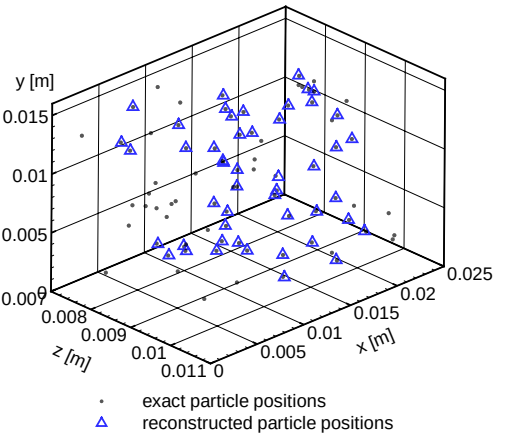

Fig. 7 Comparison of the exact and the reconstructed particle positions

generation of calibration grids is also possible so that the whole measurement procedure can be emulated. In Fig. 7 a result of the synthetic simulation is shown. The black points indicate the exact particle positions which are known due to the simulation. The blue triangles are the particle positions which have been calculated by means of the method presented. It can be seen that the agreement between these positions is quite good. Presently, the error (RMS) of the particle locations is $2.6 \cdot 10^{-5}$ m. In the experimental setup the particle positions are not known. However, examinations on the accuracy can still be done. The calibration with particle images mentioned in section 2.4 is applied to experimentally recorded images in the following. In this experiment the angle α was 30° and the measurement volume depth $\delta z = 15$ mm. In Fig. 8 on the left-hand side the particle images extracted from the calibration recordings are shown. The $x-$ and $y-$positions in the image coordinate system and the exact $z-$position in physical space are known. The contour color

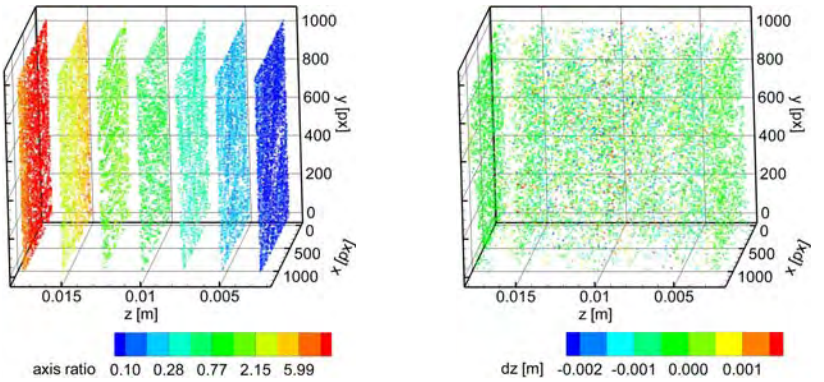

Fig. 8 The dependence of the axis ratio on the particle position (left-hand side) and the deviation of the calculated z-positions to the exact z-positions (right-hand side)

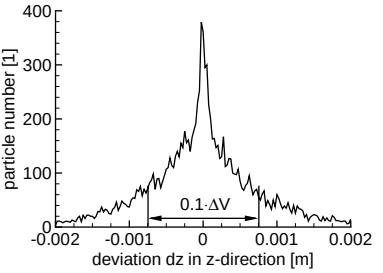

Fig. 9 PDF of the deviations in z-direction shown in Fig. 8 on the right-hand side

indicates the axis ratio (particle image width / particle image height). This data is used to calculate the coefficients of the calibration function for the particle images. The $z-$position can now be reconstructed by means of the positions $x\,[\mathrm{px}]$, $y\,[\mathrm{px}]$ and the axis ratio. This is given in Fig. 8 on the right-hand side where the contour color indicates the deviation of the calculated $z-$position to the exact $z-$position. The PDF of this field is shown in Fig. 9. Without any postprocessing, the standard deviation in the $z-$direction is 0.81 mm (5.4 % of the measurement volume depth). It can be seen that there is a clear peak at the position of 0 mm deviation in the $z-$direction which means that the presented method is free of systematic errors.

4 Determination of the Flow Velocity

In the last sections the determination of the particle positions in physical space by means of astigmatism has been explained. However, the goal of the presented technique is the determination of the three velocity components in a volume. There are mainly two possibilities to do this. One possibility is a three dimensional correlation, similar to the PIV interrogation. Similar to tomographic PIV, interrogation volumes must be applied for the evaluation. Another possibility for the determination of the particle displacements is the application of a particle tracking algorithm. The uncertainty in the displacement determination will be larger than for the correlation approach but the spatial resolution will be much better. Further investigations will show the advantages and drawbacks of each method.

5 Conclusion and Outlook

The principle of a measurement technique for the determination of all three velocity components in a three dimensional volume with only a single camera was shown. This is of interest for many applications with limited optical access like 3D-μ-PIV or the internal flow of a motor. μ-PIV requires a different calibration approach than the one with thin light-sheets described here, because the minimum thickness of light-sheets is limited. Therefore, particles aligned on a target will be moved by means of a micro-positioning system.

Further benefits of the measurement technique are the alignment and the calibration which are very easy with a single camera. The measurement uncertainty of the particle position in depth direction is approximately 5.4% of the measurement volume depth so far. In the future, more suitable functions for fitting the particle images will be examined to increase the accuracy. It is assumed that this leads to an uncertainty in the $z-$direction of approximately 2%. In addition, a postprocessing will be applied once the displacement of the particles is determined. It is assumed that this will eliminate particles whose $z-$positions have been found to be inaccurate.

Acknowledgements. The authors greatly acknowledge the support from the German Research Foundation (DFG) in the priority program 1147.

References

1. Angarita-Jaimes, N., McGhee, E., Chennaoui, M., Campbell, H.I., Zhang, S., Towers, C.E., Greenaway, A.H., Towers, D.P.: Wavefront sensing for single view three-component three-dimensional flow velocimetry. Exp. Fluids 41, 881–891 (2006)
2. Barnhart, D.H., Adrian, R.J., Papen, G.C.: Phase conjugate holographic system for high resolution particle image velocimetry. Appl. Opt. 33, 7159–7170 (1994)
3. Born, M., Wolf, E.: Principles of Optics. Pergamon Press, Oxford (1980)
4. Brücker, C.: Digital-Particle-lmage-Velocimetry (DPIV) in a scanning light-sheet: 3D starting flow around a short cylinder. Exp. Fluids 19, 255–263 (1995)
5. Elsinga, G.E., Scarano, F., Wieneke, B., van Oudheusden, B.W.: Tomographic particle image velocimetry. Exp. Fluids 41, 933–947 (2006)
6. Hain, R., Kähler, C.J., Michaelis, D.: Tomographic and time resolved PIV measurements on a finite cylinder mounted on a flat plate. Exp. Fluids 45, 715–724 (2008)
7. Hain, R., Kähler, C.J.: Single camera volumetric velocity measurements using optical aberrations. In: 12th International Symposium on Flow Visualization, Göttingen, Germany, Septermber 10-14 (2006)
8. Hinsch, K.D.: Holographic particle image velocimetry. Meas. Sci. Technol. 13, R61–R72 (2002)
9. Hori, T., Sakakibara, J.: High-speed scanning stereoscopic PIV for 3D vorticity measurement in liquids. Meas. Sci. Technol. 15, 1067–1078 (2004)
10. Pin Kao, H., Verkman, A.S.: Tracking of Single Fluorescent Particles in Three Dimensions: Use of Cylindrical Optics to Encode Particle Position. Biophys. J. 67, 1291–1300 (1994)
11. Pu, Y., Meng, H.: An advanced off-axis holographic particle image velocimetry (HPIV) system. Exp. Fluids 29, 184–197 (2000)
12. Ragan, T., Huang, H., So, P., Gratton, E.: 3D Particle Tracking on a Two-Photon Microscope. J. Fluorescence 16, 325–336 (2006)
13. TSI Incorporated. V3V Volumetric 3-Component Velocimetry System, September 13th (2008), http://www.tsi.com/en-1033/products/2350/v3v.aspx
14. Virant, M., Dracos, T.: 3D PTV and its application on Lagrangian motion. Meas. Sci. Technol. 8, 1539–1552 (1997)
15. Willert, C.E., Gharib, M.: Three-dimensional particle imaging with a single camera. Exp. Fluids 12, 353–358 (1992)

The Wall-PIV Measurement Technique for Near Wall Flow Fields in Biofluid Mechanics

André Berthe, Daniel Kondermann, Christoph Garbe, Klaus Affeld, Bernd Jähne, and Ulrich Kertzscher

Abstract. This chapter describes the development of a new time resolved 3D PIV technique for near wall flow field measurements. This measurement technique, called wall-PIV, is based on Beer-Lambert's law. It substitutes the classical PIV laser sheet by a diffuse, monochromatic full-field illumination that is limited to the near wall region by an absorbing molecular dye in the fluid. Aimed range of applications is the investigation of flow fields next to one- or two dimensionally curved, possibly flexing surfaces. The three dimensional three component flow estimation uses a new optical flow algorithm, based on particle trajectories. Results of the measurement technique's application on a displacement pediatric blood pump are presented.

1 Introduction

The time resolved measurement of three dimensional flow fields next to non-plane surfaces is of great interest in biofluid mechanics. Many medical issues, such as thrombotic events and atherosclerosis, depend on shear stresses and shear rates near vaulted walls [18]. Hereby we define a vaulted wall as a wall with two main non-zero curvatures. The investigation of flow fields and shear stresses near vaulted walls is non-trivial. Moreover, biological surfaces and some parts of artificial organs are often moving. Among others, the development of the wall-PIV technique aims for the full-field investigation of shear stresses at membranes of displacement pumps. The movement of the membranes with up to 2 Hz requires the application of a measurement technique that can capture instantaneously and non-contacting the flow field

André Berthe · Klaus Affeld · Ulrich Kertzscher
Biofluid Mechanics Laboratory, Charité - Universitätsmedizin Berlin,
Thielallee 73, D-14195 Berlin
andre.berthe@charite.de

Daniel Kondermann · Christoph Garbe · Bernd Jähne
Digital Image Processing Research Group, Heidelberg Collaboratory for Image Processing,
University of Heidelberg, Speyerer Straße 4, D-69115 Heidelberg
daniel.kondermann@iwr.uni-heidelberg.de

W. Nitsche and C. Dobriloff (Eds.): Imaging Measurement Methods, NNFM 106, pp. 11–20.
springerlink.com

in the near wall region. Thereby many well established point and field measurement techniques are of limited use. Today, there are several 3D measurement techniques and shear stress measurement techniques. A brief overview of them is given in section 2. Then, in section 3 the measurement technique including the used algorithm of flow estimation is described. Following, section 4 shows an error estimation for this approach. To distinguish between aberrations of measurements and aberrations of the flow estimation, artificial data sets and experiments with known analytical solution and known particle position, called "single particle experiments" were established (see section 5). Concluding, section 6 shows results of an experiment on a pediatric blood pump.

2 Flow and Shear Stress Measurement Techniques

Some medical measurement techniques as magnetic resonance imaging (MRI) and echocardiography allow the three dimensional measurement of flow fields. However, their spatial and temporal resolutions are not yet sufficient for the investigation of near wall flow fields. First tests to access near wall flows and wall shear stresses using MRI showed clearly the current limitations of this technique [19].

In the following we will only consider field methods, that can measure instantaneously a whole flow field. Most of these techniques are reviewed in [6, 17]. However, only few of them have the potential to be used at vaulted walls. The most promising techniques for the instantaneous, time resolved measurement of three dimensional flow fields are based on PIV.

Holographic PIV seems to provide a high potential for the assessment of near wall flows. This technique is based on a hologram, storing particle positions obtained from the interference pattern of a reference light beam and reflected light of the recorded particles. Reference beam and scattered light have to be recorded at a small angle, so that numerical aperture and depth resolution are limited [11]. Furthermore, until now high resolutions urge the use of holographic films what leads to huge processing times. The development of measurement and computer hardware might enhance the potential and solve the limitations of this technique in the future.

Defocusing digital PIV (DDPIV) and 3D PTV are based on particle identification on recordings of multiple directions. Limitations of these techniques are given by the alignment of the optical axes and the particle density. According to Hill et al. (2008) the seeding density of DDPIV can be higher than in PTV [10]. Inherent limitation of the setup, sold by TSI Inc. (Shoreview, USA) as "Volumetric 3-component velocimetry", is the direct transfer of the camera's alignment to the particle's alignment. This requires a plane flow phantom surface, aligned normal to the camera-setups center-line. Providing these conditions, the technique should be tested for a part of the described applications in biofluid mechanics.

Tomographic PIV uses the same camera setup with an expanded laser sheet and typically four cameras. According to Elsinga et al. (2006) the technique allows approximately 10 times higher particle densities than 3D PTV. This results from the fact, that the technique does not identify single particles. Instead, a three dimensional

light intensity distribution is reconstructed by a tomography algorithm and a 3D cross-correlation is applied on the voxels of the reconstructed volume [6]. A new challenge of this approach is the appearance of so called “ghost-particles”. This kind of errors depends strongly on the number of cameras and the particle diameter (see [22] for details). A further problem of this technique are high processing times of about thirty minutes to one hour for one volume (see [24, 1]).

3 Wall-PIV

The measurement principle of wall-PIV is similar to that of PIV: The displacement of tracer particles in an illuminated thin region of the fluid is recorded. Subsequently the velocity of the fluid is estimated by, depending on the flow estimation algorithm, the displacement of particles (particle tracking), the displacement of speckles (cross-correlation) or the displacement of image gray values (optical flow). In PIV the classical algorithm is cross-correlation, allowing higher particle densities than PTV. The application of optical flow algorithms is relatively new to PIV. For wall-PIV all three kinds of algorithms have been tested (see subsection 3.2).

3.1 Wall-PIV Setup

The major difference between PIV and wall-PIV is the kind of illumination: In most PIV setups (ignoring e.g. micro-PIV), the flow is illuminated by a laser sheet. The thickness of this light sheet for applications with cross-sections of several tenths of millimeters is approximately 0.5 to 1.0 mm. As a light sheet can not be aligned to a vaulted surface, the transparent flow phantom is fully illuminated from the outside with a diffuse monochromatic light placed next to the camera. To limit the depth of view of particles to approximately 0.3 mm, a molecular dye with a high absorbance for the immited wavelength of light is added to the fluid, a further key difference from PIV. The depth of light penetration and thereby the depth of view can be adjusted by varying either the incoming light intensity or the concentration of the dye.

When monochromatic light with the light intensity I_0 penetrates a fluid, the intensity will be decreased by absorption on the way through the fluid (see sketch of Fig. 1). Assuming an incidence of light at a particle at a distance R from the surface of the wall, the reduced light intensity is given by I_p, which can be calculated with the Beer-Lambert’s law (1).

$$I_p = I_0 \cdot \exp(-\varepsilon \cdot c \cdot R) \tag{1}$$

In equation 1, ε is the molar absorption coefficient of the dyed fluid and c is the concentration of the dye.

Assuming total reflection of the light on the particle, the reflected light passes the same distance R through the fluid again. The intensity is reduced to the intensity I, given by equation (2).

$$I = I_p \cdot \exp(-\varepsilon \cdot c \cdot R) = I_0 \cdot \exp(-2 \cdot \varepsilon \cdot c \cdot R) \tag{2}$$

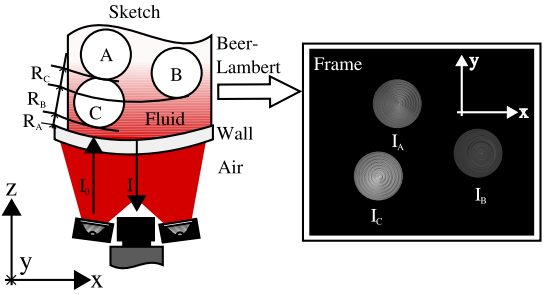

Fig. 1 Illustration of the method used in wall-PIV: On the left a sketch of part of the fluid flow and the apparatus used. It shows the illuminated region of the fluid and three tracer particles *A*, *B* and *C* with the corresponding distances *R*. On the right a representation of an image recorded by the camera with the corresponding particle intensities I_A, I_B, and I_C

Neglecting the absorption of light by the transparent flow phantom and the exterior air, the gray value, recorded by the camera is proportional to the light intensity *I*. Thereby, it is possible to use the recorded gray value of the particle as depth information. Including the gray values and the displacement of a recorded particle, we obtain principally all three components and all three coordinates. In section 4 the causes of variations between theoretical and recorded values, as well as the resulting calibration techniques are discussed.

3.2 Flow Estimation Algorithm

A straightforward approach to obtain a 3D near wall flow field by the gray values of recorded particles is their separation in several layers. Following, a 3D-2C flow field can be calculated by a cross-correlation for every layer [4]. However, the image data contains enough information to calculate the whole 3D-3C flow field.

In the field of optical flow (OF) estimation, techniques based on the Brightness Constancy Constrained Equation (BCCE) assume that a pixel intensity remains constant along its trajectory of motion:

$$(I(x,y,t) - I(x,y,t+1))^2 = 0 \tag{3}$$

This quadratic penalization of the discrepancy of this model is then linearized by first order Taylor Expansion, yielding the traditional BCCE:

$$\mathbf{d}^\top \mathbf{p} = [I_x, I_y, I_t] \cdot [u_1, u_2, 1]^\top = 0. \tag{4}$$

Partial derivatives are denoted by subscripts, I is the image and (u_1, u_2) the flow to be estimated. Basic methods using this constraint have been proposed in local [21] and global [12] optimization frameworks. A more recent application of OF in the PIV community is e.g. [23]. Whenever particles are large and slow and/or dense

enough, such BCCE-based flow estimation techniques can be applied (for details see e.g. [23]).

To adapt the standard BCCE to our needs, we made use of its extension proposed in [9], which incorporates models of brightness changes to obtain the so-called Brightness Change Constrained Equation for exponential decay:

$$\mathbf{d}^\top \mathbf{p} = [\kappa, I_x, I_y, I_t] \cdot [I, u_1, u_2, 1]^\top = 0. \tag{5}$$

The additional unknown κ is the constant of exponential decay and thus directly related to the depth of the particle image through Beer-Lambert's law. As described above, the flows measured by our method are two dimensional projections of inherently three dimensional flows. Hence, spatial motion models can not assist in the finding of correct motion estimates. Global techniques make assumption of spatial motion models by means of regularization, rendering these approaches infeasible for our needs. Therefore we limited ourselves to the study of local approaches.

To this end, we developed a method to deal with our new BCCE [14, 15]. Together with advanced preprocessing techniques [14] this method can be used to directly measure wall shear rates from wall-PIV images.

The faster the motion of particles, the more difficult the estimation of the flow of the particle images by OF algorithms becomes and conventional OF techniques fail. Furthermore, the computation of image derivative approximations can not easily be estimated for small particle images. Therefore, we firstly did not linearize the BCCE as in equation 4. Secondly, instead of formulating a spatial motion model, we formulated a purely temporal motion model based on trajectories by means of unsupervised learning techniques as detailed in [20]. As the used trajectories are only of limited length (between 5 and 19 time steps), the trained model is on the one hand sufficient to represent a large number of flows, which have not yet been observed but on the other hand captures important properties of the training data. Hence, the trajectory motion model alleviates the nonlinear optimization by limiting the search space to a statistically meaningful subset of all possible motions.

4 Error Estimation

First of all, the particles ability to follow the flow has to be investigated. One practicable approach is the calculation of the Stokes number, that should be much smaller than 1. Calculations based on the definition of Subramanian and Brady (2006) complied with this criterion for investigated flows [25].

In wall-PIV the depth position of a tracer particle, moving with its center of mass, is obtained from the reflection on its surface. This has to be included by adding the particle's radius to the distance of its surface to the wall. Consequently, variations of the particle's diameter lead to falsified shear rates. The relative error of shear rate calculations is given in [2].

In section 3.1 a total reflection of light at the tracer particle was assumed. For the used wavelength silver has a reflectance r of about 0.9. Introducing this into the calculation of the particle distance R from equation 2, we obtain equation 6:

$$R = \frac{-1}{2 \cdot \varepsilon \cdot c} \cdot \ln(r \cdot \frac{I}{I_0}) = \frac{-1}{2 \cdot \varepsilon \cdot c} \cdot (\ln(\frac{I}{I_0}) + \ln(r)) \tag{6}$$

We can conclude, that the partial reflectance would lead to a fix offset for all depth estimates. The same would result from a faulty value for the incoming light intensity I_0. Calibrating the measurement technique with a particle at depth zero and compensating light fluctuations based on a calibration target incorporated in the image sequences can cancel out this source of aberrations. In cases where the intensity I_0 can not be assumed constant over the whole ROI or can not be accessed in the flow phantom, two monochromatic wavelength λ_1 and λ_2 can be used instead of one. This bi-chromatic approach allows the reference to the ratio $\frac{I_{0,1}}{I_{0,2}}$ instead of a reference to the absolute values [15]. When using flow phantoms from materials with non-selective absorbance, the ratio, and thereby the used reference value, is not changed by different material thickness.

Uncertainties in particle depth caused by sensor noise are proportional to the uncertainty of the recorded gray value. The resulting resolution of depth of wall-PIV can be estimated with 60 layers for a 8 bit camera with 5 % signal to noise ratio [15].

5 Experimental Validation

Experimental validation of a flow measurement technique requires the exact knowledge of a flow under investigation. Exact analytical solutions of the Navier Stokes equations are rare [13]. The wall-PIV technique was first validated on a rectangular duct [4], showing a good agreement between theoretical and experimental data. Another validation was realized on a falling film, providing reliable depth estimations for the near wall region as well [15]. However, both investigated flows did not provide a proof for the ability to measure all three components of the flow. Exact analytical solutions for a fully 3D-3C flow exist, but are unfortunately not applicable experimentally [7]. Therefore no such solutions can be used to gain insight in the quality of wall-PIV as 3D-3C measurement technique. Experiments on a u-shaped duct with backward facing step compared wall-PIV results to classical PIV and computational fluid dynamics [4, 16]. However, aberrations between the resulting flow fields can not be easily assigned to a source of aberration. To overcome this limitation, artificial traversals of particles have been used. The basic idea of a particle traversal is to realize a known particle movement under realistic measurement conditions. The depth traversal of several particles on a glass support showed good results for the wall-PIV technique's depth measurement abilities under two different hardware configurations [4, 15]. The depth resolution of this approach is limited due to its mechanical accuracy (the support has to stay exactly plane-parallel to the wall) and adhesive forces can occur between the supporting media and the wall. Therefore the technique was developed to "single particle setups" for further calibrations and multi-directional movements [3]. In a single particle setup, one particle is attached to a glass capillary. The diameter of the capillary is inferior to that of the particle,

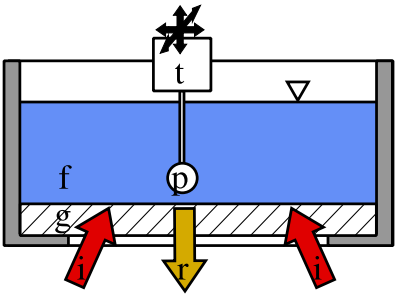

Fig. 2 Detail of the single particle setup: The particle *p* is connected by the capillary at the milling cutter, representing a three dimensional traversal system *t*. Immited light *i* enters the reservoir filled by the bottom through a glass window *g*. After transversal of the fluid *f* the reflected light *r* is captured by a camera

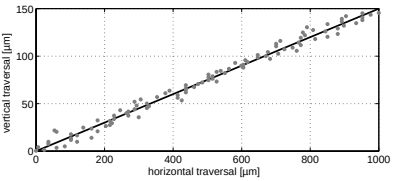

Fig. 3 Flow estimation on a horizontally and vertically traversed particle. Markers show the estimated flow, the solid line shows the particle traversal.

so that the support is hidden from the bottom. Attaching the capillary at a traverse system, the particle can be moved three dimensionally with the given accuracy of the system. For the presented experiments we used a high precision milling cutter (at the Fachgebiet Micro- und Feingerätetechnik, TU Berlin), allowing a traversal accuracy up to 100 nm in all three directions. A systematic sketch of the setup is shown in Fig. 2. Further details of the setup are given in [3]. Figure 3 shows a flow estimation on a horizontally and vertically traversed particle. As flow estimation algorithm we used the trajectory approach of section 3.2. The horizontal traversal was of 1000 μm, the vertical traversal was of 150 μm. The average error for the horizontal movement was 0.0453 px with a standard deviation of 0.0359 px.

6 Experiments

The flow at the back of a pediatric displacement blood pump model with a stroke volume of 10 ml was investigated. Optical diffractions at the inner surface of the pump were avoided by a replacement of the polyurethane pump wall by a silicone block with identical refractive index as the used test fluid. The inner shape of the silicone block was identical to that of the original wall, the outer wall of the transparent silicone was plane. To avoid mechanical deformation, the silicon was surrounded by a glass housing.

The inflow of the pump was connected to a reservoir of a size of 250 mm x 250 mm, so that the change in the fluid level during the pumping caused a negligible pressure variation of less than 1 %. The outflow was connected to a windkessel (see Fig. 4), allowing the adjustment of the pressure curve to biological conditions.

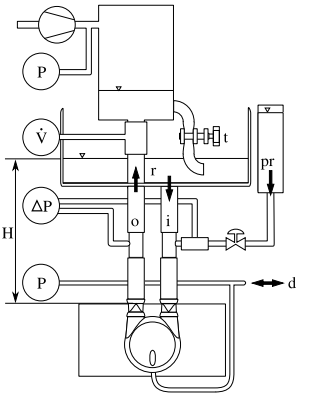

Fig. 4 Mock circulation used during the investigation of a displacement pump. Pressure variations at the inflow *i* were below 1 % because of the size of the reservoir *r*. Pressure measurements between inflow and outflow *o*, at the windkessel and at the drive line *d* as well as the flow rate at the outflow were registered by a data acquisition board. The windkessel was adjusted by the air pressure and a throttle *t*. Addition of particles can be effected by a particle reservoir *pr*

Pressure measurements at the windkessel were realized with a pressure sensor capable of measuring 0–300 mbar (SensorTechnics, Puchheim, Germany). The flow rate was measured using a ultrasonic flow meter T106 (Transonic Systems Inc., Ithaca, USA). A differential pressure sensor 24PC (Honeywell Inc., Minnesota, USA) was mounted between inflow and outflow duct. The displacement pump was actuated by a Linmot (NTI AG, Spreitenbach, Switzerland) driven pneumatic system. The systole (pump ejection phase) was set to 200 ms and the diastole (pump filling phase) to 300 ms.

Images were taken with 2080 frames per second (fps) with an image size of 1280x1048 pixels with a Redlake MotionPro X-3 (Imaging Solutions GmbH, Eningen, Deutschland). A fixed focal lens of 50 mm, 1:0.95 was used at f 2.8.

Illumination was realized with two light panels. Each of them assembling 104 3 W Luxeon LED (Philips Lumileds, San Jose, USA); 48 with a wavelength of $\lambda_1 = 617$ nm and 56 with a wavelength of $\lambda_2 = 627$ nm. By a trigger impulse the illumination changed between both wavelengths.

Camera, light sources, pneumatic system and sampling rate of the sensors (10 data points per image) were triggered by a PCI 1200 data acquisition board (National Instruments, Austin, USA). The same board was used to acquire the sensor data sets. LabView 8.0 (National Instruments, Austin, USA) was used for system control and data acquisition.

We used silver coated hollow ceramic spheres with a diameter of 71 to 75 μm (Potters Industries Inc., Carlstadt, USA).

The used fluid was a mixture of distilled water and glycerin with 37.5 vol-% glycerin (CVH, Hannover, Germany) with a viscosity of 3.5 mm^2/s . The viscosity corresponds to that of blood with determined viscosities between 2.5 mm^2/s to 5.6 mm^2/s (see [5, 8] for the viscosity of blood).

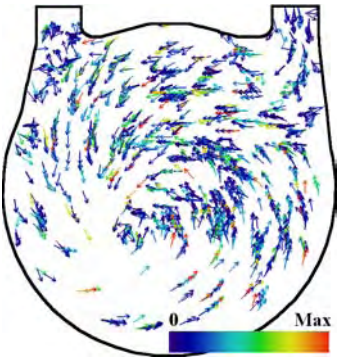

Fig. 5 Velocity field estimate for the pediatric blood pump with a stroke volume of 10 ml. The motion vectors indicated direction of the flow, whereas color denotes vector magnitude. Please note that the mixture of long and short vectors is due to particle images moving in different depths of the projected real volume, showing that spatial regularization techniques of standard OF algorithms would fail in this context

The fluid was dyed with the food coloring dye patent blue V with a concentration of 0.3 mg/l. A phase averaged flow field over four pump cycles is shown in Fig. 5. The flow corresponds to the flow phase 0.025 s before start of the systole (ejection phase). We can see, that a vortex fills the whole pump body, providing a good wash out of the pump. Colors of the vectors indicate different vector magnitudes, coupled to different particle depth. The presented data provides a starting point for the calculation of wall shear stresses.

Acknowledgements. We gratefully acknowledge the support of the Deutsche Forschungsgemeinschaft DFG within the research program SPP 1147. We also thank the MFG, TU Berlin for their support.

References

1. Atkinson, C.H., Dillon-Gibbons, C.J., Herpin, S., Soria, J.: Reconstruction techniques for tomographic piv (tomo-piv) of a turbulent boundary layer. In: Proceedings of the 14th International Symposium on Applications of Laser Techniques to Fluid Mechanics, Lisbon, Portugal (2008)
2. Berthe, A., Christensen, C., Debaene, P., Goubergrits, L., Kertzscher, U., Affeld, K.: Further development of an image-based optical measurement technique for complex near-wall flows. In: The 12th International Symposium on Flow Visualization, Goettingen, Germany (2006)
3. Berthe, A., Kondermann, D., Christensen, C., Goubergrits, L., Kertzscher, U.: Using single particles for the validation of a 3d-3c near wall measurement technique. In: The 7th International Symposium Particle Image Velocimetry, Rome, Italy (2007)
4. Debaene, P., Kertzscher, U., Goubergrits, L., Affeld, K.: Visualization of a wall shear flow: Development of a new particle image interrogation method. J. Visual-Japan 8, 285–364 (2005)
5. Dintenfass, L.: Blood Microrheology – Viscosity Factors in Blood Flow, Ischaemia and Thrombosis. Butterworths, London (1971)

6. Elsinga, G., Scarano, F., Wieneke, B., van Oudheusden, B.: Tomographic particle image velocimetry. Experiments in Fluids 41(6), 933–947 (2006)
7. Ethier, C.R., Steinman, D.A.: Exact fully 3D navier-stokes solutions for benchmarking. International Journal for Numerical Methods in Fluids 19(5), 369–375 (1994)
8. Geigy, J. (ed.): Documenta Geigy, Wissenschaftliche Tabellen, 6th edn. Geigy (1960)
9. Haussecker, H., Fleet, D.: Computing optical flow with physical models of brightness variation. IEEE Transactions on Pattern Analysis and Machine Intelligence (PAMI) 23(6), 661–673 (2001)
10. Hill, D., Troolin, D., Walters, G., Lai, W., Sharp, K.: Volumetric 3-component velocimetry (v3v) measurements of the turbulent flow in stirred tank reactors. In: Proceedings of the 14th International Symposium on Applications of Laser Techniques to Fluid Mechanics, Lisbon, Portugal (2008)
11. Hinsch, K.D.: Holographic particle image velocimetry. Measurement Science and Technology 13(7), R61–R72 (2002)
12. Horn, B., Schunck, B.: Determining optical flow. Artificial Intelligence 17, 185–204 (1981)
13. Hui, W.H.: Exact solutions of the unsteady two-dimensional navier-stokes equations. Zeitschrift für Angewandte Mathematik und Physik (ZAMP) 38(5), 689–702 (1987)
14. Jehle, M.: Spatio-temporal analysis of flows close to free water surfaces. PhD thesis, University of Heidelberg (2006)
15. Jehle, M., Jähne, B.: A novel method for three-dimensional three-component analysis of flows close to free water surfaces. Experiments in Fluids 44(3), 469–480 (2008)
16. Jehle, M., Jähne, B., Kertzscher, U.: Direct estimation of the wall shear rate using parametric motion models in 3D. Pattern Recognition, 434–443 (2006)
17. Kertzscher, U., Debaene, P., Goubergrits, L., Affeld, K.: Experimental assessment of wall shear flow. In: Kowalewski, T. (ed.) Abiomed Lecture Notes: Blood Flow, Modelling and Diagnostics, 6, Abiomed, Warschau, pp. 109–134 (2005)
18. Kertzscher, U., Berthe, A., Goubergrits, L., Affeld, K.: Particle image velocimetry of a flow at a vaulted wall. Proceedings of the Institution of Mechanical Engineers, Part H: Journal of Engineering in Medicine 222(4), 465–473 (2008)
19. Köhler, U., Marshall, I., Robertson, M.B., Long, Q., Xu, X.Y., Hoskins, P.R.: Mri measurement of wall shear stress vectors in bifurcation models and comparison with cfd predictions. Journal of Magnetic Resonance Imaging 14(5), 563–573 (2001)
20. Kondermann, D., Kondermann, C., Berthe, A., Kertzscher, U., Garbe, C.: Motion estimation based on a temporal model of fluid flows. In: The 13th International Symposium on Flow Visualization, Nice, France (2008)
21. Lucas, B., Kanade, T.: An iterative image registration technique with an application to stereo vision (darpa). In: Proceedings of the 1981 DARPA Image Understanding Workshop, pp. 121–130 (1981)
22. Michaelis, D., Wieneke, B.: Comparison between tomographic piv and stereo piv. In: Proceedings of the 14th International Symposium on Applications of Laser Techniques to Fluid Mechanics, Lisbon, Portugal (2008)
23. Ruhnau, P., Schnörr, C.: Optical stokes flow estimation: an imaging-based control approach. Experiments in Fluids 42(1), 61–78 (2007)
24. Schroeder, A., Geisler, R., Elsinga, G., Scarano, F., Dierksheide, U.: Investigation of a turbulent spot and a tripped turbulent boundary layer flow using time-resolved tomographic piv. Experiments in Fluids 44(2), 305–316 (2008)
25. Subramanian, G., Brady, J.F.: Trajectory analysis for non-brownian inertial suspensions in simple shear flow. Journal Of Fluid Mechanics 559, 151–203 (2006)

Laser Doppler Field Sensor for Two Dimensional Flow Measurements in Three Velocity Components

Andreas Voigt, Christoph Skupsch, Jörg König, Katsuaki Shirai, Lars Büttner, and Jürgen Czarske

Abstract. The laser Doppler field sensor presented in this paper is suited for high resolution flow velocity field imaging on the micro scale without use of a camera. The field sensor is constructed by the superposition of two laser Doppler velocity profile sensors. The profile sensor is based on the principle of Laser Doppler Anemometry (LDA). However, instead of one parallel fringe system one divergent and one convergent fringe system are employed. Utilizing a total number of four fringe systems the field sensor can determine the tracer particle position two-dimensionally in the measurement volume. The spatial resolution and velocity accuracy are increased compared to conventional LDA by more than one order of magnitude. Since no camera is used, the resolution of the sensor is not influenced by pixel size effects. Two-dimensional velocity field measurements of an injection nozzle flow and of a micro channel flow with quadratic cross section are presented.

1 Introduction

The evaluation of small scale flows is of vital importance both for fundamental and applied fluid mechanics. An example of fundamental research is the resolution of free shear flows which exhibit no dominant flow direction. One example of applied research is the measurement of nozzle flows, especially of injection nozzles or micro nozzles used for the positioning of satellites. The vast field of microfluidics includes the in-vivo measurements of blood flows and the associated determination of wall shear stress for the research on arteriosclerosis. Lab-on-a-chip technologies offer flow dimensions in the 10 µm range and are especially promi-sing when it comes to the analysis of biochemical substances (micro total analysis system, µTAS). Mixing processes on the microscale have to be analyzed in detail since, on

Andreas Voigt · Christoph Skupsch · Jörg König · Katsuaki Shirai · Lars Büttner · Jürgen Czarske
Department of Electrical Engineering and Information Technology, Laboratory for Measuring and Testing Techniques, Technische Universität Dresden, Helmholtzstrasse 18, 01069 Dresden, Germany
Andreas.Voigt@tu-dresden.de

W. Nitsche and C. Dobriloff (Eds.): Imaging Measurement Methods, NNFM 106, pp. 21–30.
springerlink.com

the microscale, undisturbed flow behavior is always laminar, and mixing can hence only be achieved by flow perturbation. A special challenge for microflow sensors is the measurement of flow rates. Precise flow rate measurement is especially important for applications such as high-performance liquid chromatography and medical dosing. All the flow structures mentioned require analysis with high spatial resolution, high velocity accuracy and, in most cases, in more than one spatial dimension and velocity component.

Laser Doppler Anemometry (LDA) is a quasi point-wise technique and suffers from the limitation of the spatial resolution given by the size of the measurement volume. In addition the velocity accuracy is limited by the non-parallelity of the fringe system stemming from the divergence of the utilized Gaussian beams which becomes higher by stronger focusing. For small sizes of the measurement volume needed for microfluidics the velocity uncertainty exceeds 2 % [1]. Micro particle image velocity (µPIV) facilitates two dimensional two velocity component flow measurements with sub-micrometer spatial resolution. However the velocity accuracy is only around 3 % [2] and the resolution is limited by diffraction effects and pixel size. In addition a short working distance is needed. Conventional µPIV provides only limited information in the direction of the optical access.

Doppler Fourier domain optical coherence tomography (OCT) can be applied to microflow measurements. It has been used to measure the velocity profile in a microchannel of 340 µm width [3]. However, the proposed OCT method has two drawbacks. Firstly, only the velocity in the direction of the optical axis can be measured. Furthermore the maximum measurable velocity is limited to a value of about 2.5 mm/s due to the uncorrelated phase relation of signals stemming from different depths.

Various approaches have been proposed to overcome the limitations posed by LDA to reduce the size of the measurement volume without deteriorating velocity accuracy. One approach developed in the course of this project is based on the use of quasi divergence free Bessel beams instead of the conventionally used Gaussian beams achieving an increase of the spatial resolution by a factor of ten compared to a conventional LDA with the same fringe curvature [5].

The laser Doppler velocity profile sensor is an enhanced LDA method which is based on the use of two fringe systems and provides flow resolution with spatial resolution in the µm-range in the axial dimension and velocity accuracy in the order of 10^{-4} in the lateral component. In the course of this project the profile sensor was used for the precise determination of the natural gas flow rate at the German national gas standard (Chapter 2). An advanced burst signal processing scheme based on frequency-time analysis was developed, which allows for the determination of the axial velocity component and lateral accelerations (Chapter 3). The laser Doppler velocity field sensor for two dimensional flow field imaging in three velocity components consists of two combined profile sensors. So far it has been applied for the measurement of an injection nozzle flow at velocities of up to 25 m/s and for the analysis of a microflow in a channel with quadratic cross section of 80 µm x 80 µm (Chapter 4) where velocities smaller than 1 mm/s were obtained.

2 Velocity Profile Sensor

The laser Doppler velocity profile sensor is based on the principle of laser Doppler anemometry. However instead of one parallel fringe system two fringe systems – one diverging, one converging – are utilized [4]. To distinguish the two fringe systems, frequency division multiplexing (FDM) or wavelength division multiplexing (WDM) can be applied. A particle passing the measurement volume emits two burst signals from which the lateral velocity v_x and the axial particle position z in the measurement can be obtained by frequency evaluation. In order to determine the spatial resolution in real flow conditions a WDM profile sensor was applied to measure the velocity profile of a quasi one-dimensional microchannel water flow with channel dimensions 100 µm x 2 mm along the short dimension [15]. By a parabolic fit, according to the expected behavior due to the laminar flow characteristic, the spatial resolution in this measurement could be determined as 3.5 µm.

A frequency multiplexing based laser Doppler velocity profile sensor with a fiber coupled passive measurement head was specially developed for the measurement of the flow rate of high pressure (50 bar) natural gas [6-10]. The results of the measurement at the flow rate test facility which is operated by the E.ON Ruhrgas AG in collaboration with the PTB (Physikalisch-Technische Bundesanstalt) are shown in Figures 1a and 1b. As can be seen the measured degree of turbulence in the inner part of the flow is a factor of 20 lower for the profile sensor compared to the measurement with a conventional LDA. The higher value of the conventional LDA arises from the measurement uncertainty due to the fringe spacing variation (see Introduction) and does not correspond to real flow turbulence. The measurement is a significant progress, since the turbulence profile is directly used to calculate the flow rate uncertainty. The volume flow rate was determined from the measured data by a fitting algorithm corresponding to the theoretically expected tanh behavior. This yielded a value of Q=(153.80±1.00) m^3/s compared to a value of Q=(154.32±0.42) m^3/s determined by a critical nozzle scale which was calibrated by the piston prover primary flow rate standard.

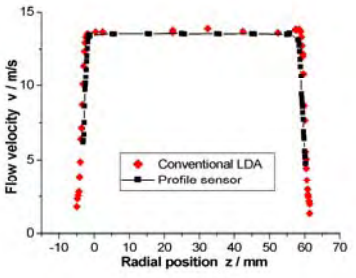

Fig. 1a Velocity profile of the natural gas flow

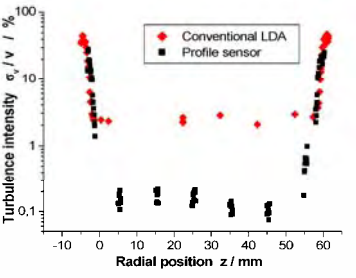

Fig. 1b Turbulence profile of the natural gas flow

3 Measurement of Inclined Trajectories and Accelerated Particles

The divergent fringes of the profile sensor entail a chirped burst signal for a particle that passes the measurement volume at an inclined angle. By evaluation of the chirp of the two burst signals both acceleration and axial velocity of a particle can be determined. Therefore a signal processing scheme had to be found to obtain the instantaneous burst frequency f(t) [11-14]. A combined fast Fourier transform (FFT)/quadrature demodulation technique (QDT) was developed which is especially suited for signals of low SNR. Firstly the Fourier transformed burst signal is filtered by an adaptive bandpass corresponding to the signal bandwidth. The inverse transform of the single-sided spectrum yields a low-noise analytic signal from which the instantaneous phase is determined. The time-resolved frequency is then obtained by differentiation. From the instantaneous frequencies of the burst signals corresponding to the two fringe systems the particle position z_0 in the center of the measurement volume, the lateral velocity v_x, the axial velocity v_z and the acceleration a_x of the particle can be determined.

The efficiency of the signal processing scheme was evaluated by simulated noisy model bursts under variation of the burst parameters z_0, v_x, v_z, a_x with different SNR values. The processing proved to operate close to the minimally achievable uncertainty, deviating by less than a factor of 2 from the Cramer Rao lower bound. For typical conditions of 20 fringes with a spacing of 3 µm, a slope of the calibration curve of 0.67 mm^{-1} and an SNR of 10 dB the signal processing permits a spatial resolution of 0.9 µm, a lateral velocity uncertainty of $3 \cdot 10^{-4}$, an axial velocity uncertainty of 4 % (relative to the total particle velocity) and an acceleration uncertainty of $3 \cdot 10^{-3}$ m/s^2 (at a particle velocity of 1 cm/s).

To test the measurement of lateral acceleration and the lateral velocity component a test stand was developed consisting of a pinhole with a diameter of 2 µm mounted to an electro-dynamically driven harmonic oscillator (loudspeaker). A reference triangulation sensor with a resolution of 0.5 µm was used to monitor the time-dependent position of the moving object. Figure 2a shows the results of the experiment for a tilt angle of 42°. The angle determined by measurement amounted to 45° with a standard deviation of 1.5°, a value that is in the range one would expect from theory. The profile sensor measurement uncertainty of 0.11 m/s^2 was consistent with the value determined by simulation and the results were within the uncertainty band of the triangulation sensor.

As an application a stagnation flow in front of a cylinder of 80 µm diameter was measured (Figure 2b), where a considerable variation of the lateral acceleration and the axial velocity was exhibited. These experiments imply the feasibility of the sensor for turbulent flows with acceleration as in transport and mixing processes. The signal processing algorithm is necessary for the extension of the laser Doppler velocity field sensor for three velocity component measurements.

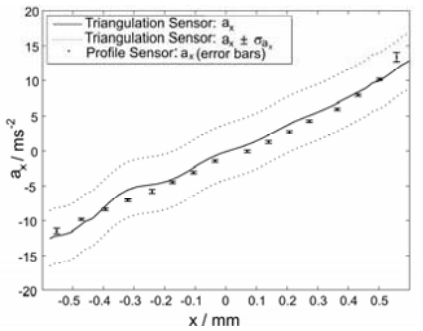

Fig. 2a Acceleration measurement of the harmonic oscillator

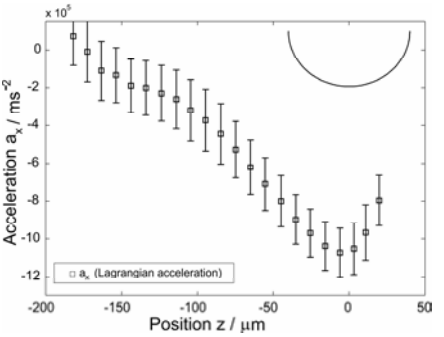

Fig. 2b Acceleration measurement of the stagnation flow

4 Velocity Field Sensor

The laser Doppler velocity field sensor [15-25] is an extension of the profile sensor principle and is constructed by combining two profile sensors, such that their optical axes are orthogonal and their measurement volumes overlap (Figure 3).

The intersection region of the two ellipsoidal profile sensor measurement volumes yields a quasi-rectangular measurement volume where the size is determined by the widths of profile sensor measurement areas. The light detection unit(s) can be freely positioned depending on optical access and the optimization of the detected scattered light. Each particle passing the measurement volume emits four burst signals from which the positions x and y and the velocity v_z are determined. The enhanced signal processing scheme allows for the determination of the lateral velocities v_x and v_y and the acceleration a_z as well.

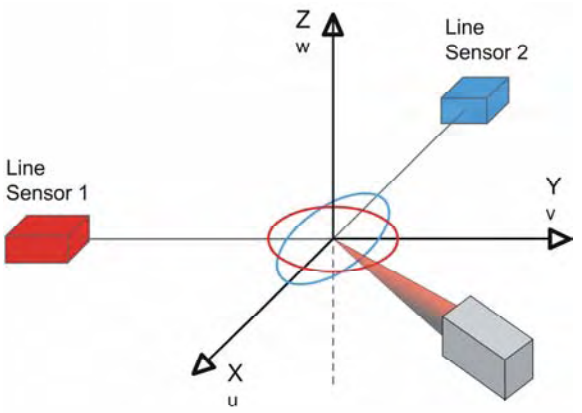

Fig. 3 Set-up of the field sensor

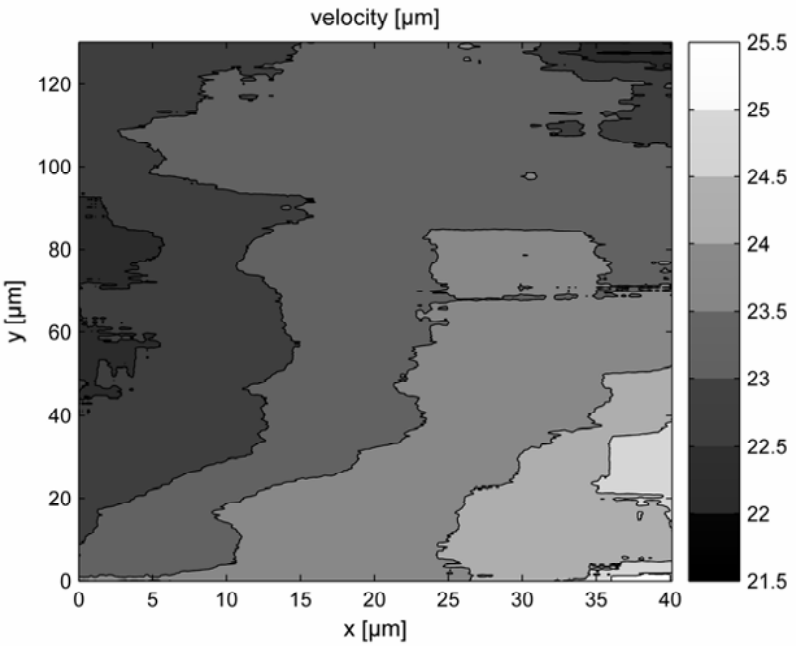

Fig. 4 Mean velocity profile of the injection nozzle flow

As a first complex application the velocity flow field of an injection nozzle driven by air pressure was analyzed with a field sensor based on combined FDM and WDM [15]. To enhance the resolution of the sensor a 2-dimensional calibration is necessary in order to correct for wave front aberration effects. So far a spatial resolution of 4 µm (x-direction) and 16 µm (y-direction) and a velocity accuracy of 10^{-3} have been shown in the calibration process; however, these values can be improved by an improved calibration method. The spatially resolved mean velocity profile is shown in Figure 4 with the middle of the nozzle being in the lower right corner. The maximum velocity amounted to 25 m/s with a velocity decline of about 3 m/s over the measured area. This experiment shows the feasibility of the field sensor for turbulent high velocity flows.

Due to the high spatial resolution, velocity accuracy and the information about the direction of optical access the laser Doppler field sensor is expected to be highly suitable for investigations of microchannel flows. Because of the high velocity accuracy one possible area of application is the precise determination of flow rates. Therefore a field sensor based on the WDM technique was developed to fit the requirements of microfluidics. WDM was chosen for channel separation since it facilitates the use of photodetectors with small bandwidth and hence high sensitivity with low noise equivalent power. Two profile sensors were constructed with an average fringe spacing of 1.82 µm and 2.28 µm respectively. One sensor used laser diodes at 654 nm and 784 nm with a power of 100 mW, the other one a frequency doubled Nd:YAG laser at 532 nm with a power of 150 mW and a laser

diode at 830 nm with a power of 120 mW. The working distance amounted to 5 cm. Thus a measurement field of 50 µm x 150 µm was obtained, corresponding to typical microchannel dimensions. Two demultiplexing units, incorporating a total of 2 dichroic mirrors, 2 optical shortpasses, one longpass and one bandpass filter, were built to separate the scattering light of the four wavelengths onto four separate detectors with optical cross-coupling below 3 %.

A microchannel with a nominal cross section of 80 µm x 80 µm was manufactured from polydimethylsiloxane (PDMS). The applied bonding technique yielded a channel in solid PDMS without glue at interfaces. The channel was stabilized by a polycarbonate carrier. In order to minimize reflexes from interfaces and unwanted refraction effects a 54.3:45.7 water-glycerin mixture was used as a fluid to achieve the matching condition with the refractive index of PDMS (n=1.41). This yielded a fluid viscosity of about 5 mPas. The flow was driven by hydrostatic pressure with a height difference of 890 mm, corresponding to a maximum flow velocity of 10.5 cm/s in the channel center. Due to the low Reynolds number of $Re \approx 10^{-3}$ the flow was perfectly laminar. Monodisperse polystyrene particles with a density of 1.05 g/cm^3 and a diameter of 1.3 µm were used as tracers. Figure 5a shows the measured mean velocity profile for the channel with the center of the channel being on the upper side. Figure 5b depicts the curve fitted by a quadratic order fit. According to the figures about half of the flow profile was acquired. By integration the flow rate through the measurement area was determined as (163 ± 1.3) nl (statistical error) while the total flow rate through the channel was determined as 347 nl/s by precise weighing after a long time measurement.

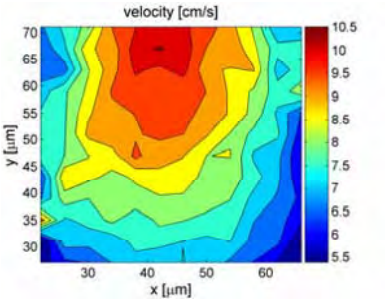

Fig. 5a Measured velocity profile of the microchannel

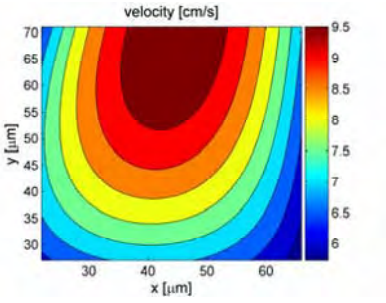

Fig. 5b Quadratic order fit of the velocity profile

5 Conclusion and Outlook

In this paper we proposed a laser Doppler velocity profile sensor for two dimensional flow velocity field measurements in three velocity components which consists of two laser Doppler profile sensors whose measurement volumes overlap. To determine the particle velocity components along the axes of the profile sensors a signal processing scheme was developed operating near the Cramer Rao lower bound. The field sensor facilitates measurements with a spatial resolution in

the µm-range and a velocity accuracy in the order of $10^{-4}…10^{-3}$ for the main velocity component. The high-speed turbulent velocity flow field of an air pressure driven injection nozzle was measured. The field sensor was further applied for the measurement of the velocity field of an 80 µm x 80 µm microchannel flow.

In contrast to the OCT method proposed in [3] the velocities the field sensor can measure are only limited by the bandwidth of the detector where values above 25 m/s have been achieved, while only values below 2.5 mm/s were achieved by OCT. Furthermore the OCT system measures only the velocity component along the optical axis while the field sensor can measure in all three velocity components.

The field sensor offers velocity resolution more than one order of magnitude higher than µPIV and is not limited by diffraction effects and pixel size. The working distance in the cm range is high compared to µPIV, where typical values are in the mm range and lower. The dynamic range of the field sensor is only limited by the bandwidth of the detectors and can hence span several orders of magnitude whereas PIV measurements are typically limited to a dynamic range of about one or two orders of magnitude. The computational effort is much lower for the field sensor since signal processing only involves the determination of the frequencies of four burst signals, whereas the correlation of multiple image segments is necessary for PIV methods. Since the measurement area spanned by the field sensor can be aligned in the cross section of the flow channel the field sensor has high potential for flow rate measurements.

Microchannels with different geometries are under preparation which will exhibit flow structures with non-zero components of the lateral velocity components of the field sensor and acceleration. Another challenge is the analysis of the microflow of non-Newtonian fluids, especially the determination of the wall shear stress behavior compared to Newtonian fluids. The field sensor will also provide helpful information for two-dimensional spatial and temporal correlation measurements. Set-ups of the field sensor with an up-scaled measurement field can provide flow rate measurements of injection nozzle flows without traversing.

Acknowledgments. We thank Dr. H. Müller of the Physikalisch-Technische Bundesanstalt (PTB) and the staff of E.ON Ruhrgas AG at pigsar™ for their contribution to the gas flow rate measurement. The funding of the Deutsche Forschungsgemeinschaft (funding code Cz 55/18-1 and Cz 55/18-2) is gratefully acknowledged.

References

1. Lo, Y.L., Chuang, C.H.: Fluid velocity measurements in a microchannel performed with two new optical heterodyne microscopes. Appl. Optics 41, 6666–6675 (2002)
2. Westerweel, J.: Fundamentals of digital particle image velocimetry. Meas. Sci. Technol. 8, 1379–1392 (1997)
3. Walther, J., Mueller, G., Cuevas, M., Morawietz, H., Koch, E.: Flow velocity analysis with phase-resolved Doppler Fourier Domain Optical Coherence Tomography. In: 22nd international Eurosensors conference, Dresden, September 7-10, 2008, book of abstracts, p. 236, 4 pages (2008)

4. Czarske, J., Büttner, L., Razik, T., Müller, H.: Boundary layer velocity measurements by a laser Doppler profile sensor with micrometer spatial resolution. Meas. Sci. Technol. 13, 1979–1989 (2002)
5. Voigt, A., Heitkam, S., Büttner, L., Czarske, J.: A Bessel Beam Laser Doppler Velocimeter. Opt. Commun. (2009) (accepted for publication)
6. Büttner, L., Bayer, C., Voigt, A., Czarske, J., Müller, H., Pape, N., Strunck, V.: Precise Flow Rate Measurements of Natural Gas under high Pressure with a laser Doppler Velocity Profile Sensor. Exp. Fluids 45, 1103–1115 (2008)
7. Büttner, L., Voigt, A., Czarske, J., Müller, H.: Neue Entwicklungen in der optischen Strömungsmesstechnik. In: Odin, A., Schwartz, R. (eds.) Optische Methoden in der Mengen- und Durchflussmessung - PTB-Report PTB-MA-84, Braunschweig, April 2008, pp. 17–28 (2008)
8. Voigt, A., Büttner, L., Czarske, J., Müller, H.: Hochauflösender Laser-Doppler-Profilsensor zur Durchflussmessung von Hochdruck-Erdgas. In: Czarske, J. (ed.) XXII. Messtechnisches Symposium des Arbeitskreises der Hochschullehrer für Messtechnik e.V., Dresden, pp. 251–263. Shaker Verlag (2008)
9. Voigt, A., Büttner, L., Czarske, J., Müller, H.: Hochauflösender Laser-Doppler-Profilsensor zur Durchflussmessung von Hochdruck-Erdgas. In: 109. Jahrestagung der Deutschen Gesellschaft für angewandte Optik (DGaO), Esslingen, 13. - 17. May 2008, number A2, 2 pages (2008),
`http://www.dgao-proceedings.de/download/109/109_a2.pdf`
10. Büttner, L., Voigt, A., Bayer, C., Shirai, K., Czarske, J., Pape, N., Strunck, V., Müller, H.: Optisches Durchflussnormal für HD-Erdgas: Präzise Durchflußmessung mit dem Laser-Doppler-Profilsensor. In: Leder, A., Brede, M., Hüttmann, F., Ruck, B., Dopheide, D. (eds.) Lasermethoden in der Strömungsmesstechnik – 15. Fachtagung, Rostock, Deutsche Gesellschaft für Laser-Anemometrie GALA e.V., number 43, pp. 43.1–43.9 (2007)
11. Bayer, C., Shirai, K., Büttner, L., Czarske, J.: Measurement of acceleration und multiple velocity components using a laser Doppler velocity profile sensor. Meas. Sci. Technol. 19, 055401 (11 pp.) (2008)
12. Büttner, L., Czarske, J.: Determination of the axial velocity component by a laser Doppler velocity profile sensor. J. Opt. Soc. Am. A 23, 444–454 (2006)
13. Bayer, C., Shirai, K., Büttner, L., Czarske, J.: Messunsicherheitsbetrachtungen für den Laser-Doppler Profilsensor zur ortsaufgelösten Messung beschleunigter Partikel mit schräger Trajektorie. In: Leder, A., Brede, M., Hüttmann, F., Ruck, B., Dopheide, D. (eds.) Lasermethoden in der Strömungsmesstechnik – 15. Fachtagung, Rostock, 2007, Deutsche Gesellschaft für Laser-Anemometrie GALA e.V., number 2, pp. 2.1–2.9 (2007)
14. Büttner, L., Czarske, J.: Vermessung schräger Teilchentrajektorien mit dem LDA-Geschwindigkeitsprofilsensor. In: Egbers, C., Jehring, L., von Larcher, T., Ruck, B., Leder, A., Dopheide, D. (eds.) Lasermethoden in der Strömungsmesstechnik – 13. Fachtagung, Cottbus, 2005, Deutsche Gesellschaft für Laser-Anemometrie GALA e.V., number 5, pp. 5.1–5.8 (2005)
15. Voigt, A., Bayer, C., Shirai, K., Büttner, L., Czarske, J.: Laser Doppler field sensor for high resolution flow velocity imaging without camera. Appl. Optics 47, 5028–5040 (2008); selected by the editor-in-chief, Gregory Faris, for publication in the Virtual Journal for Biomedical Optics (VJBO) 3(11)(2008),
`http://vjbo.osa.org/virtual_issue.cfm`

16. Bayer, C., Voigt, A., Shirai, K., Büttner, L., Czarske, J.: Interferometrischer Laser-Doppler-Feldsensor zur Messung der Geschwindigkeitsverteilung von komplexen Strömungen. TM-Tech. Mess 74, 224–234 (2007)
17. Czarske, J., Büttner, L.: Micro Laser Doppler Velocimetry μ-LDV. In: Encyclopedia of Microfluidics and Nanofluidics. Springer, Heidelberg (2008)
18. Skupsch, C., Voigt, A., Shirai, K., Büttner, L., Czarske, J.: The laser Doppler field sensor - a new technique for flow research. In: 22nd international Eurosensors conference, Dresden, September 7-10, 2008, book of abstracts, p. 238, 4 pages (2008)
19. Büttner, L., Voigt, A., Bayer, C., Czarske, J.: Three Component Flow Imaging by an Extended Laser Doppler Sensor. In: XVIII IMEKO World Congress, Rio de Janeiro, Brazil, September 17-22, 2006, number TC9-7, pp. 1–6 (2006)
20. Büttner, L., Voigt, A., Bayer, C., Czarske, J.: 2D3C-Laser Doppler Sensor for highly spatially resolved flow field investigations. In: 13th Internationl Symposium on Applications of Laser Techniques to Fluid Mechanics, Lissabon, July 26-29, 2006, number 31.2, pp. 1–10 (2006)
21. Skupsch, C., Voigt, A., Büttner, L., Czarske, J.: Der Laser-Doppler-Geschwindigkeitsfeldsensor – eine neue Technik für die Strömungsforschung. In: 109. Jahrestagung der Deutschen Gesellschaft für angewandte Optik (DGaO), Esslingen, 13-17 May 2008, number P14, 1 page, poster (2008),
http://www.dgao-proceedings.de/download/109/109_p14.pdf
22. Voigt, A., Bayer, C., Shirai, K., Büttner, L., Czarske, J.: Hochauflösender Laser-Doppler-Feldsensor zur dreikomponentigen ortsverteilten Strömungsgeschwindigkeitsmessung. In: Leder, A., Brede, M., Hüttmann, F., Ruck, B., Dopheide, D. (eds.) Lasermethoden in der Strömungsmesstechnik – 15. Fachtagung, Rostock, 2007, Deutsche Gesellschaft für Laser-Anemometrie GALA e.V., number 1, pages 1.1–1.9 (2007)
23. Bayer, C., Voigt, A., Shirai, K., Büttner, L., Czarske, J.: Interferometrischer Laser-Doppler-Feldsensor zur flächenhaften Messung der Geschwindigkeitsverteilung von komplexen Strömungen. In: Fischerauer, G. (ed.) XX. Messtechnisches Symposium des Arbeitskreises der Hochschullehrer für Messtechnik e.V., Bayreuth, pp. 141–155. Shaker Verlag (2006)
24. Shirai, K., Bayer, C., Voigt, A., Pfister, T., Büttner, L., Czarske, J., Müller, H., Petrak, D.: Application of Laser-Doppler Velocity-Field Sensor to Highly Resolved Shear Flow Measurements. In: Dopheide, D., Müller, H., Strunck, V., Ruck, B., Leder, A. (eds.) Lasermethoden in der Strömungsmesstechnik – 14. Fachtagung, Braunschweig, Deutsche Gesellschaft für Laser-Anemometrie GALA e.V., number 11, pp. 11.1–11.10 (2006)
25. Voigt, A., Bayer, C., Büttner, L., Czarske, J.: Hochauflösender Laser-Doppler-Sensor zur dreikomponentigen ortsverteilten Geschwindigkeitsmessung in Strömungsfeldern. In: 107. Jahrestagung der Deutschen Gesellschaft für angewandte Optik (DGaO), Weingarten, 6. - 10. June 2006, number P47, 2 pages (2006),
http://www.dgao-proceedings.de/download/107/107_p47.pdf

Array Doppler Global Velocimeter with Laser Frequency Modulation for Turbulent Flow Analysis – Sensor Investigation and Application

Andreas Fischer, Lars Büttner, Jürgen Czarske, Michael Eggert, and Harald Müller

Abstract. Velocity field measurement results of a Doppler global velocimeter (DGV) using sinusoidal laser frequency modulation are presented. Contrary to conventional DGV systems, which suffer from low temporal resolutions of several seconds, the novel DGV system allows measurement rates up to 100 kHz. The high temporal resolution is afforded by using a fibre-coupled detector array, which has a higher bandwidth than conventionally applied cameras. Additionally, low uncertainties can be achieved in contrast to conventional DGV since no second reference

Andreas Fischer
Technische Universität Dresden, Department of Electrical Engineering and Information Technology, Laboratory of Measurement and Test Techniques, Helmholtzstr. 18, D-01062 Dresden, Germany
andreas.fischer2@tu-dresden.de

Lars Büttner
Technische Universität Dresden, Department of Electrical Engineering and Information Technology, Laboratory of Measurement and Test Techniques, Helmholtzstr. 18, D-01062 Dresden, Germany
lars.buettner@tu-dresden.de

Jürgen Czarske
Technische Universität Dresden, Department of Electrical Engineering and Information Technology, Laboratory of Measurement and Test Techniques, Helmholtzstr. 18, D-01062 Dresden, Germany
juergen.czarske@tu-dresden.de

Michael Eggert
Physikalisch-Technische Bundesanstalt, Department of Gas Flow, Bundesallee 100, D-38116 Braunschweig, Germany
michael.eggert@ptb.de

Harald Müller
Physikalisch-Technische Bundesanstalt, Department of Gas Flow, Bundesallee 100, D-38116 Braunschweig, Germany
harald.mueller@ptb.de

W. Nitsche and C. Dobriloff (Eds.): Imaging Measurement Methods, NNFM 106, pp. 31–41.
springerlink.com

detector unit is necessary. The optimised set-up is capable of acquiring turbulence spectra simultaneously at multiple points. The measurement data from the wake of a cylinder agrees well with comparison measurements using hot-wire anemometry and correctly yields the Kármán vortex frequency. With the novel DGV, turbulence spectra up to about 10 kHz were resolved. Further measurement results illustrate the high potential of the described technique for non-invasive, temporally resolved, imaging flow inspection e.g. in turbomachines.

1 Introduction

Velocity field measurements are challenging, if low uncertainty and high temporal and spatial resolution are required. For this purpose, we describe, characterise and apply a novel Doppler global velocimeter using a sinusoidal frequency modulation (FM-DGV), which is capable of acquiring two-dimensionally and synchronously turbulence spectra for e.g. turbulence analysis or correlation studies. Contrary to hot-wire anemometry, where also high measurement rates up to a few 100 kHz can be achieved, it is non-invasive and an imaging measurement technique. In comparison with laser Doppler anemometry, the statistical particle arrival does not complicate spectra calculations, since multiple particle scattering allows temporal equidistant acquisition of flow velocities. On the other hand, high seeding concentrations are necessary for Doppler global techniques in order to achieve strong scattering signals and consequently low measurement uncertainty. The article begins with a description of the measurement principle and its advantages compared to conventional DGV. Subsequently, the measurement capabilities of the system are characterised. Selected measurement results are presented in the next section, which finally demonstrate the potential of the designed FM-DGV system for turbulent flow analysis.

2 Measurement Principle

The schematic arrangement of a DGV system using sinusoidal laser frequency modulation (FM-DGV) is illustrated in figure 1 for 2d1c-measurements. The beam of a narrow band laser with the sinusoidally modulated frequency

$$f_L(t) = f_c + f_h \cos(2\pi f_m t), \tag{1}$$

is expanded to a light sheet, which illuminates the measurement region in the flow. The modulation frequency is f_m, the stabilised laser centre frequency is f_c and the modulation amplitude is f_h. Due to the flow velocity and the occurring Doppler effect, the scattering on seeding particles causes a shift in frequency of the scattered light. The average Doppler shift frequency f_D indicates the velocity component along the direction $(\mathbf{o} - \mathbf{i})$, with $\mathbf{o}$ as observation direction and $\mathbf{i}$ as light incident direction (see fig. 1). For 2d3c-measurements, e.g. two further observation directions are required. An additional scanning of the light sheet plane would provide 3d3c-measurements, but is not considered here further.

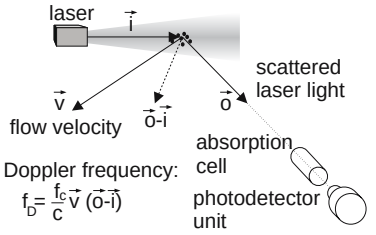

Fig. 1 Schematic set-up of the FM-DGV technique and average Doppler shift frequency formula (c denotes the light velocity.)

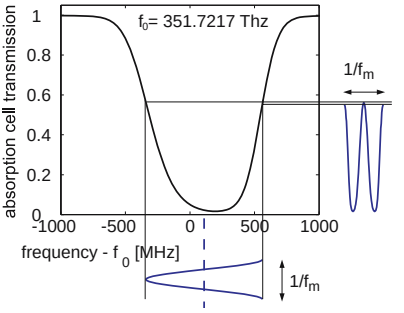

Fig. 2 Measurement principle of the FM-DGV technique showing one frequency modulation period ($f_h = 450$ MHz, $f_c + f_D - f_0 = 131.5$ MHz))

Measuring the scattered light through a molecular absorption cell, here with a photodetector array, allows to determine the Doppler shift in a plane as follows: Because of the laser frequency modulation, each photodetector element will receive a power modulated signal as illustrated in fig. 2, which varies with respect to the Doppler shifted laser centre frequency. The given transmission curve was measured at a 5 cm long cell filled with caesium gas. The non-symmetry of it corresponds to the weighted superposition of three absorption lines [5]. The output signal of one detector element can be described by the relation

$$s(t) = g \cdot \tau(f_L(t) + f_D) \cdot P_s(t), \tag{2}$$

with g as detector sensitivity [V/W], τ as spectral transmission of the absorption cell and $P_s(t)$ as scattered light power [W] falling onto the active area of the photodetector. In order to describe the measurement principle, the scattered light power is initially assumed to be constant during one measurement cycle: $P_s(t) = P_0$. The first and second order harmonic amplitudes A_1, A_2 of the sampled output signal of each detector can be estimated according the discrete Fourier transform by

$$A_k = \frac{2}{N} \sum_{n=0}^{N-1} s(n/f_a) \cdot \cos(2\pi k n f_m / f_a), \quad k = 1,2, \tag{3}$$

with f_a as sampling rate and N as number of samples. For additive white Gaussian noise, these estimations are efficient [5]. The temporal resolution $T = N/f_a$ is always set to integer multiples of the modulation period $T_m = 1/f_m$, so that no leakage effect of the discrete Fourier transform occurs [10].

As can be seen from fig. 3a, both amplitudes are sensitive to velocity dependent changes in the laser centre frequency. In order to eliminate the additional sensitivity concerning the scattered light power P_0, both harmonic amplitudes are divided:

$$q = A_1/A_2. \tag{4}$$

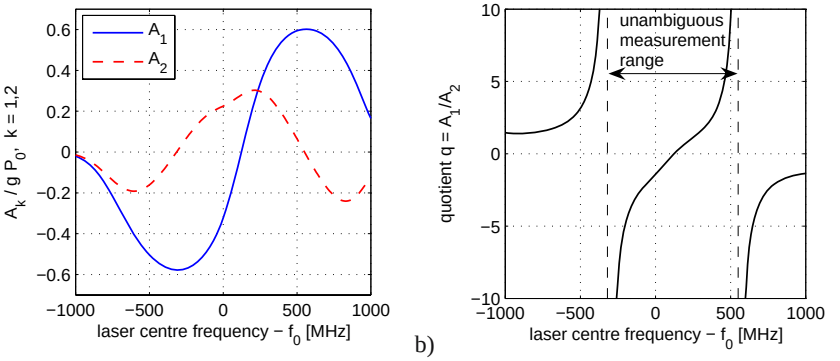

Fig. 3 a) Calculated first and second order harmonic amplitudes A_1 and A_2 normalised by gP_0 using the measured caesium absorption cell transmission curve (see fig. 2) and b) their quotient q ($f_0 = 351.7217$ THz)

The quotient q, which is shown in fig. 3b w.r.t. the laser centre frequency, finally serves as measurement quantity. As a rule of thumb, the unambiguous measurement range approximately equals the Full-Width-Half-Maximum (FWHM) of the transmission curve and amounts here ± 420 MHz [3]. This corresponds e.g. to ± 250 m/s for a laser wavelength of $c/f_c = 852.1$ nm (in air) and $\mathbf{i} \perp \mathbf{o}$. The measurement range can be enhanced, e.g. by choosing a different observation direction.

In comparison with conventional DGV, the laser frequency modulation allows to omit the beam splitter and so-called reference detector unit for measuring the scattered light intensity [4]. Hence, image misalignment errors and beam splitting errors do not occur, which can amount up to 5 m/s and 7 m/s, respectively [2]. Furthermore, the principle inherent use of a frequency modulation enables self calibration procedures.

3 Measurement System

In this section, the set-up of our measurement system is described and calibration results are presented. In order to understand the system capabilities for turbulent flow analysis, its spatial and the temporal resolution as well as the achievable uncertainty is discussed subsequently.

3.1 General Set-Up and Calibration

Adapted to the molecular resonance of caesium gas, we use a DFB diode laser emitting at 852.1 nm wavelength, which can be fast modulated in frequency up to several GHz by altering the diode current. The modulation frequency is chosen to $f_m = 100$ kHz as a trade-off between high temporal resolution and negligible

disturbance by fluctuations of the scattered light [10]. The diode laser has a narrow line width of <3 MHz, and thus can resolve the spectral transmission of the used caesium cell well. The laser centre frequency is on the one hand stabilised according [6] and on the other hand monitored by evaluating the amplitude ratio q_r of the reference photo detector signal. This signal results from a small portion of the unshifted laser light, that is passed though a reference absorption cell and is evaluated analogue to the general signal processing scheme. By subtracting q_r from the measured amplitude ratios of the Doppler shifted detector signals, the statistical uncertainty of the laser centre frequency corresponds to about 0.02 m/s.

The caesium absorption cell is filled with caesium gas, about 5 cm long and 2.5 cm in diameter. The cell body and the cold finger are temperature stabilised separately at 45 °C and 25 °C, respectively, which stabilises the cell transmission behaviour. The separate temperature control allows precise and stable settings of the transmission curve. It further guarantees, that no caesium condenses at the windows, which would create unpredictable disturbances. A model, which describes and explains the spectral transmission is derived in [5]. The estimated velocity uncertainty due to the remaining temperature fluctuations is about 0.1 m/s.

The detector unit consists of 25 fibre-coupled avalanche photo diodes (APD) with optimum band width and low noise. The application of fibres provides flexible alignment of the measurement points in the light sheet plane. As an example, a fibre holder for 2D (5×5) or 1D (25×1) was built. The detector output signals are captured with a multi-channel data acquisition system. With the current memory, measurements up to 8 s can be performed at once yielding a sufficient maximum frequency resolution of 0.125 Hz for turbulence analysis.

For system calibration, a rotating glass disc is usually applied as calibration object. With known position and known rotation frequency, a velocity value can be assigned to the measured harmonic amplitude ratios for each channel. The calibration results of all 25 channels are shown in fig. 4 together with a calculated calibration curve from the signal model. Both coincide and show nonlinear behaviour. The possibility of extrapolating the calibration curve by model based predictions is useful e.g. for measuring high flow velocities in turbomachines, for which a calibration might be difficult to achieve. Low calibration uncertainty is achieved, e.g. by a using separate polynomial fit curves with the order of three for each channel. The deviation between the measured values is lower than 0.09 m/s and thus lower than the errors due to the absorption cell stability.

3.2 Spatial Resolution

The lateral resolution is set by the fibres' aperture (400 μm) and the optical image magnification (0.43) to ≈ 930 μm. Since the depth of focus is currently 1.3 cm, the longitudinal resolution is given by the smaller light sheet width. It was adjusted to about 1 mm, which equals the lateral resolution.

3.3 Temporal Resolution

Since at least one period of the frequency modulation is necessary for determining the harmonic amplitudes, the current maximum temporal resolution T follows from the choice of the modulation frequency according

$$T \geq 1/f_m \tag{5}$$

and is currently 10 μs [10]. Hence, turbulence spectra can be acquired up to 50 kHz. However, in many applications lower temporal resolutions are sufficient, which lowers the amount of data being processed. Using e.g. seeding particles consisting of DEHS with 1 μm diameter, a possibly required slip smaller than 1% is estimated to occur up to 6.7 kHz [1].

In order to measure continuously up to 8 s long, the signal processing is accomplished afterwards off-line. If real-time conditions have to be fulfilled, the harmonic amplitudes can alternatively be determined using lock-in techniques by a signal preprocessing before the sampling. This approach was already successfully tested and applied [9], but is not considered here.

3.4 Velocity Uncertainty

The measurement uncertainty has been widely studied. A comparison between the capabilities of FM-DGV and conventional DGV is contained in [3, 5, 7, 8, 12]. Regarding thermal, dark current and shot noise, the achievable measurement uncertainty of FM-DGV and conventional DGV was shown to be approximately equal. However, the elimination of image misalignment errors, beam splitting errors and ambient light influence provides lower uncertainties with FM-DGV as already mentioned. The publications above also contain the calculation of the minimum achievable measurement uncertainty for all DGV systems using laser frequency modulation by deriving a general signal model and applying the theory of Cramér and Rao. This allows e.g. uncertainty predictions for challenging measurement tasks, comparisons between the different DGV approaches and system optimisations concerning the hardware, system parameters or the signal processing. For instance, the optimum laser centre frequency $f_c + f_D$ was found to be close to the transmission minimum of the absorption cell for FM-DGV. The optimum amplitude of the frequency modulation f_h is approximately half the FWHM of the transmission curve.

Furthermore, the disturbing effect of scattered light fluctuations due to the the particle scattering behaviour and the imaging process was intensively investigated in [10]. Since this disturbance can be lowered by decreasing the spatial resolution or by increasing the modulation frequency, a tradeoff is necessary. For our experiments, the chosen spatial resolution and modulation frequency enables negligibly small errors due to scattered light fluctuations in comparison with that of thermal noise from the detectors. Simultaneously, the chosen modulation frequency enable high temporal resolution and the resultant detector signals do not exceed the detector

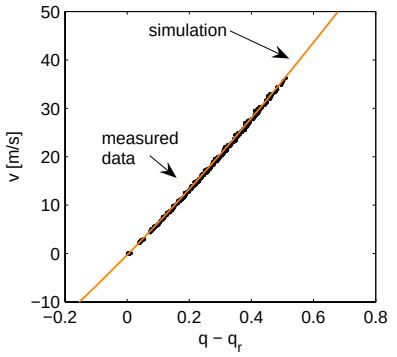

Fig. 4 Calibration of all 25 channels compared with signal model ($f_h = 450$ MHz, $f_c = 133.5$ MHz, $q_r = 0.1$, $v = f_D/1.66$ MHz/(m/s), due to detector transfer function: $q = 0.9 \cdot q_{\text{nominal}}$)

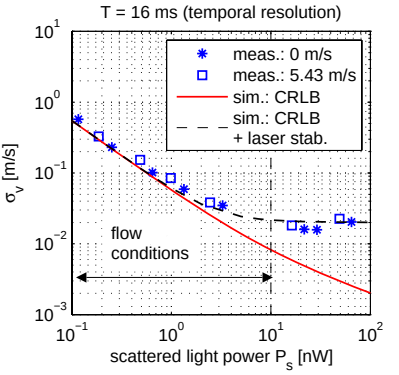

Fig. 5 Measured and estimated velocity standard deviation σ_v w.r.t. the scattered light power P_s

bandwidth and the sampling theorem. Laser induced fluctuations of the scattered light are negligibly small, so that a correction procedure, although possible, is not necessary.

The dependency of the statistical measurement uncertainty w.r.t. the scattered light power is given in fig. 5. Since the measurement results for a resting and a rotating glass disc coincide, scattered light fluctuations are shown to have no effect. For scattered light powers $P_s < 10$ nW, which is typical for flow measurements, the velocity standard deviation σ_v is indirect proportional to P_s. This agrees well with the calculated Cramér-Rao lower bound (CRLB) resulting from the thermal noise of the detectors. Although shot noise becomes dominant for higher scattered light powers, the corresponding CRLB illustrates, that its contribution to the measured uncertainty is negligible. For $P_s > 10$ nW, the laser centre frequency stabilisation has to be taken into account additionally, which finally yields an excellent agreement between measurement and simulation results. However, the focus of interest is for $P_s < 10$ nW, where according experiments the velocity uncertainty satisfies approximately [6]

$$\sigma_v \approx (0.007 \ldots 0.012)\ \text{m/s} \times \left(P_s/\text{nW} \cdot \sqrt{T/\text{s}} \right)^{-1}. \tag{6}$$

Typically, the achieved scattered light power is about a few nW. An experimental and analytic investigation of the dependency $\sigma_v \sim T^{-0.5}$ can be extracted e.g. from [5]. For high temporal resolutions greater than 1 ms, the statistical uncertainty due to noise from the detector is larger than the systematic errors from the absorption cell stability. Assuming band limited white noise, the corresponding noise power spectral density reads

$$S_v = (0.49 \ldots 1.44) \cdot 10^{-4} \frac{(\mathrm{m/s})^2}{\mathrm{Hz}} \times (P_s/\mathrm{nW})^{-2}, \tag{7}$$

which is relevant for turbulence spectra measurements [10].

4 Measurement Results

Validation measurements of a laminar boundary layer profile and the nozzle free jet velocity fields have already been reported in [3]. Furthermore, non-steady flow phenomena have been measured and validated successfully according [10, 6]. Recently, the wake of an infinite and a truncated cylinder as well as so-called grid turbulence has been measured. The most recent results are shown below. Generally, the velocity component along the main flow direction was measured, and the linear arrangement of the 25 fibres was initially chosen for maximising the available scattered light power by decreasing the light sheet height. The measurement took 2 s, that means 200000 velocity values with a temporal resolution of 10 μs were captured per channel.

The measured flow field of a cylinder wake at a low Reynolds number of 139 is shown in figure 6 and clearly indicates the reduction of the mean velocity due to flow obstacle: the (infinite) cylinder. The field was captured by traversing the linearly arranged 25 measurement points in stream-wise direction, which are represented by the diagonals. The undisturbed flow should have a constant velocity, but the data indicates that different flow velocities have occurred during the acquisitions of the velocity profiles (diagonals). It is assumed, that the flow was not stationary due to strong seeding and the poor stabilisation of the low wind tunnel motor frequency. As an example, the velocity time series of one channel is analysed in frequency domain and compared with hot-wire anemometry (HWA) measurements. Both measured

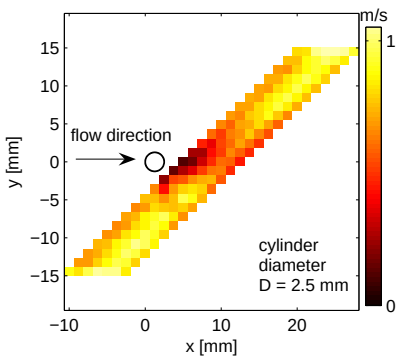

Fig. 6 Measured velocity field in the wake of a cylinder (Re = 139, flow along x-direction with ≈ 0.8 m/s)

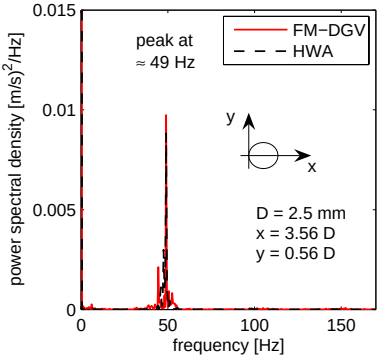

Fig. 7 Turbulence spectrum of one channel from the cylinder wake measurement (see fig. 6) compared with HWA measurement

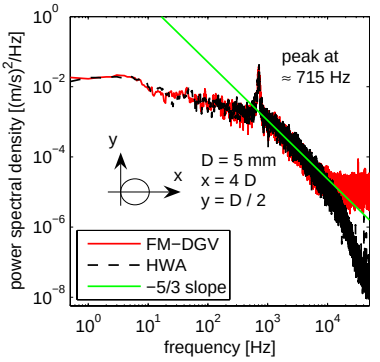

Fig. 8 Turbulence spectrum measured with FM-DGV (one channel out of 25) and HWA behind infinite cylinder with diameter D (Re = 6785, flow along x-direction with 19.6 m/s)

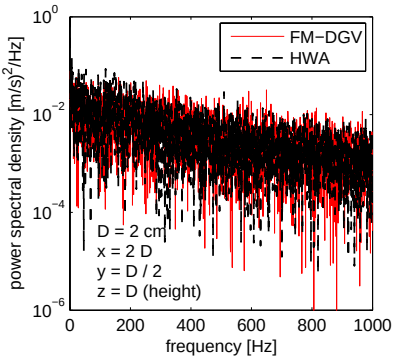

Fig. 9 Turbulence spectrum measured with FM-DGV and HWA behind the truncated cylinder with diameter D (Re = 40000, flow along x-direction with 28.9 m/s)

power spectral densities (PSD), which are given in fig. 7, coincide well. The containing fundamental frequency at about 49 Hz corresponds to a Strouhal number of 0.15, which is also consistent with other measurements reported in literature [14].

A selected turbulence spectra, measured at a higher Reynolds number of 6785, is shown and compared to a HWA measurement in fig. 8 as an example. For better visibility, the spectra were averaged over 10 adjacent points. The vortex shedding frequency, measured with FM-DGV and HWA, coincide and corresponds to a Strouhal number of 0.18. This is consistent with measurements from [14]. Furthermore, a decay with a slope of -5/3 is correctly measured between 1 kHz and 10 kHz, which represents according Kolmogorov's theory isotropic turbulence [13]. Over 10 kHz, the spectrum of the FM-DGV measurement converges asymptotically to about $2 \cdot 10^{-5}\mathrm{m/s^2/Hz}$ in contrast to the HWA data. This behaviour is due to the measurement uncertainty and has already been explained in section 3.4. Inserting the present scattered light power of 1.3 nW into equation (7) yields a predicted noise PSD of about $3 \cdot 10^{-5}\mathrm{m/s^2/Hz}$, which is close to the measured value. As a result, turbulence spectra up to 10 kHz were resolved.

Finally, we measured in the wake of a truncated cylinder according the set-up from [11], but with a lower cylinder diameter of 2 cm (instead of 12 cm) and a lower Reynolds number of 40000 (instead of 200000). An acquired turbulence spectrum is shown in fig. 9. According [11], a dominant frequency corresponding to the Kármán vortex street of an infinite cylinder is not present. However, the measurement data from HWA and FM-DGV coincide qualitatively, although great care should be taken by comparing both results. FM-DGV measures a velocity component in a fix direction and HWA measures the velocity component in the plane perpendicular to the wire. Since the flow around a truncated cylinder is three dimensional, different results might occur.

5 Conclusions

A Doppler global velocimeter for velocity field measurements with high temporal resolution has been described. A reference detector unit for measuring the scattered light power is not required, thus image misalignment and beam splitting errors of conventional systems are overcome. Due to the applied laser frequency modulation and the signal evaluation in frequency domain, the measurement principle is not sensitive to ambient light and the detector offset in addition. The application of an fibre-coupled avalanche photodiode array provides simultaneous measurements in a plane of a flow with rates up to 100 kHz. In contrast to usually applied slow cameras, this allows to acquire turbulence spectra, as is demonstrated for the first time, or to accomplish correlation studies in turbulent flows.

The current system set-up has a lateral and axial spatial resolution of about 1 mm. It was successfully calibrated, characterised and then applied in wind tunnel experiments. Minimum velocity standard deviations down to 0.02 m/s have been achieved for a temporal resolution of 16 ms at the calibration object. According to an uncertainty analysis, the velocity standard deviation is indirectly proportional to the scattered light power and the square root of the temporal resolution for flow measurements. This explains the demand for high scattered light powers, which can be achieved e.g. by high seeding concentrations, if measurements with high temporal resolution and low uncertainty are desired. The typically achieved noise power spectral density is $(1 \ldots 10) \cdot 10^{-5}$ $(\mathrm{m/s})^2/\mathrm{Hz}$, which allows to resolve turbulence spectra up to 10 kHz. The measured turbulence spectra in the wake of an infinite cylinder agree well with hot-wire comparison measurements and contain the correct vortex shedding frequency according to Kármán. Furthermore, a -5/3 slope in the turbulence spectra was measured for high Reynolds numbers, which were again validated by hot-wire measurements and agree with Kolmogorov's theory regarding isotropic turbulence. Furthermore, measurements in the wake of a truncated cylinder, which was mounted on a plate, as well as measurements behind a grid have been accomplished and successfully compared with hot-wire measurements. The achieved results demonstrate the promising contributions of FM-DGV for the analysis or inspection of turbulent flow phenomena, e.g. in turbomachines.

Acknowledgements. We would like to thank Prof. Dr. Roger Grundmann, Dr. Veit Hildebrand and Jürgen Frey (Institute of Aerospace Engineering, TU Dresden) for their excellent support during the wind tunnel experiments. The financial support of the Deutsche Forschungsgemeinschaft (DFG) is gratefully acknowledged (CZ 55/16-3 and MU 1252/2-3).

References

1. Albrecht, H.: Laser-Doppler-Strömungsmessung. Akademie-Verlag, Berlin (1986)
2. Charrett, T.O.H., Tatam, R.P.: Single camera three component planar velocity measurements using two-frequency planar Doppler velocimetry (2ν-PDV). Measurement Science and Technology 17, 1194–1206 (2006)

3. Fischer, A., Büttner, L., Czarske, J., Eggert, M., Grosche, G., Müller, H.: Investigation of time-resolved single detector Doppler global velocimetry using sinusoidal laser frequency modulation. Measurement Science and Technology 18, 2529–2545 (2007)
4. Fischer, A., Büttner, L., Czarske, J., Eggert, M., Müller, H.: Doppler-Global-Velozimter mit sinusförmiger Laserfrequenzmodulation zur präzisen Messung von Geschwindigkeitsprofilen. tm - Technisches Messen 73(4), 237–244 (2006)
5. Fischer, A., Büttner, L., Czarske, J., Eggert, M., Müller, H.: Measurement uncertainty and temporal resolution of Doppler global velocimetry using laser frequency modulation. Applied Optics 47(21), 3941–3953 (2008)
6. Fischer, A., Büttner, L., Czarske, J., Eggert, M., Müller, H.: Measurements of velocity spectra using time-resolving Doppler global velocimetry with laser frequency modulation and a detector array. Experiments in Fluids (2009) (submitted for publication)
7. Fischer, A., König, J., Büttner, L., Czarske, J., Eggert, M., Müller, H.: Messunsicherheitsschranke der Doppler-Global-Velozimetrie mit Laserfrequenzmodulation. tm - Technisches Messen 75(12), 631–640 (2008)
8. Fischer, A., Czarske, J.: Signal Processing Efficiency of Doppler Global Velocimetry with Laser Frequency Modulation. Signal Processing (2009) (submitted for publication)
9. Fischer, A., König, J., Büttner, L., Czarske, J., Eggert, M., Müller, H.: Messung von Geschwindigkeitsspektren mit einem 2d3k-Doppler-Global-Array-Velozimeter mit Laserfrequenzmodulation. In: Ruck, B., Leder, A., Dopheide, D. (eds.) Lasermethoden in der Strömungsmesstechnik - 16. Fachtagung, Deutsche Gesellschaft für Laser-Anemometrie GALA e.V., Karlsruhe (2008)
10. Fischer, A., König, J., Czarske, J.: Speckle noise influence on measuring turbulence spectra using time-resolved Doppler global velocimetry with laser frequency modulation. Measurement Science and Technology 19, 125402 (15pp.) (2008)
11. Jensch, M., Brede, M., Hüttmann, F., Leder, A., Frederich, O., Wassen, E., Thiele, F.: Time-Resolved Stereo-PIV Messungen im Kopfbereich und Nachlauf eines Kreiszylinderstumpfes. In: Leder, A., Brede, M., Hüttmann, F., Ruck, B., Dopheide, D. (eds.) Lasermethoden in der Strömungsmesstechnik - 15. Fachtagung, Deutsche Gesellschaft für Laser-Anemometrie GALA e.V., Rostock (2007)
12. Müller, H., Eggert, M., Czarske, J., Büttner, L., Fischer, A.: Single-camera Doppler global velocimetry based on frequency modulation techniques. Experiments in Fluids 43, 223–232 (2007)
13. Pope, S.B.: Turbulent Flows. Cambridge University Press, Cambridge (2000)
14. White, F.M.: Viscous Fluid Flow. McGraw-Hill, New York (1991)

Self-calibrating Single Camera Doppler Global Velocimetry Based on Frequency Shift Keying

Michael Eggert, Harald Müller, Jürgen Czarske, Lars Büttner,
and Andreas Fischer

Abstract. By applying frequency shift keying (FSK) to the Doppler Global Velocimetry (DGV) and analyzing image sequences, it is possible to omit the reference camera which usually is required in conventionally used DGV systems. Additionally frequency shift keying realized by well defined frequency steps of the laser used for the light sheet generation in the measuring plane allows an absolute online calibration of the Doppler shift evaluation in the over-all DGV set-up for the velocity field analysis. Thus the uncertainty of velocity field measurements can be reduced and the absolute velocity measurement accuracy increased. Analyzing temporally resolved data without pixel binning, standard deviations of approximately 0.12 m/s and absolute deviations below 0.5 m/s were achieved on a spinning disc. Flow field measurements in a 20 cm diameter pipe have shown a standard deviation of 0.5 m/s for single pixels in single measurement cycles with 100 ms exposure time per image, while structures down to 0.1 m/s could be resolved in temporally binned measurements.

1 Introduction

Doppler Global Velocimetry (DGV) has been successfully applied especially for the investigation of high speed flow fields. The increasing interest to apply this technique for manifold applications in the whole field of engineering enforced the efforts to decrease the measurement uncertainty of DGV as flow diagnostic tool, outlined in

Michael Eggert · Harald Müller
Physikalisch-Technische Bundesanstalt, Bundesallee 100, D-38116
Braunschweig, Germany
michael.eggert@ptb.de, harald.mueller@ptb.de

Jürgen Czarske · Lars Büttner · Andreas Fischer
Technische Universität Dresden, Department of Electrical Engineering and Information
Technology, Laboratory Measurement and Test Techniques, Helmholtzstr. 18, D-01062
Dresden, Germany
andreas.fischer2@tu-dresden.de, lars.buettner@tu-dresden.de,
juergen.czarske@tu-dresden.de

W. Nitsche and C. Dobriloff (Eds.): Imaging Measurement Methods, NNFM 106, pp. 43–52.
springerlink.com

a review given by Ainsworth et al. [1]. Theoretical and experimental investigations were done by Meyers et al. to find out methods to increase measurement accuracy and repeatability, to improve the system calibration and to eliminate influences caused by instabilities of the laser frequency output, variations in the optical transmissivity and optical distortions in the data images. Measuring the velocity profile of a rotating wheel, an error of 1.75 % in the mean with a standard deviation of 0.5 m/s was achieved [2]. Röhle and Schodl found the uncertainty to be about 2.5 m/s [3] and Morrison et al. investigated the effects of light intensity gradients and pixel location accuracy upon the DGV measurement accuracy and estimated the overall uncertainty of the DGV system to be approximately 4 m/s [4]. An approach to avoid pixel alignment errors was presented by Ford et al. [5], who described a single-camera planar Doppler velocimeter based on acousto-optic frequency switching. Using a spinning disc they achieved a velocity resolution of +/- 1 m/s. Müller et al. presented a similar approach for saving the reference camera based upon the frequency modulation of a tunable high power DBR laser diode at 852 nm. By evaluating the first und second harmonic of the resulting amplitude modulation of the scattered light transmitted through the absorption cell this technique allowed to save the reference detector unit and to increase the accuracy of the velocity measurement compared to conventional systems [6]. Based upon this technique a simplified DGV flow profile sensor was realized [7] and velocity field measurements were demonstrated [8, 9]. Fischer et al. presented time-resolved measurements of flow profiles using sinusoidal modulation and an APD array [10]. This paper describes the further development of the FSK based DGV technique using a camera, especially regarding online calibration for measuring Doppler frequency shifts absolutely.

2 Principle of DGV

The Doppler global technique is based on the application of a frequency stabilized laser and an absorption cell to analyze the Doppler shift of the laser light, scattered by tracer particles. Using the slope of an absorption line filter for the frequency to intensity conversion, the intensity of the scattered light imaged through the absorption cell onto a detector gives the measuring information.

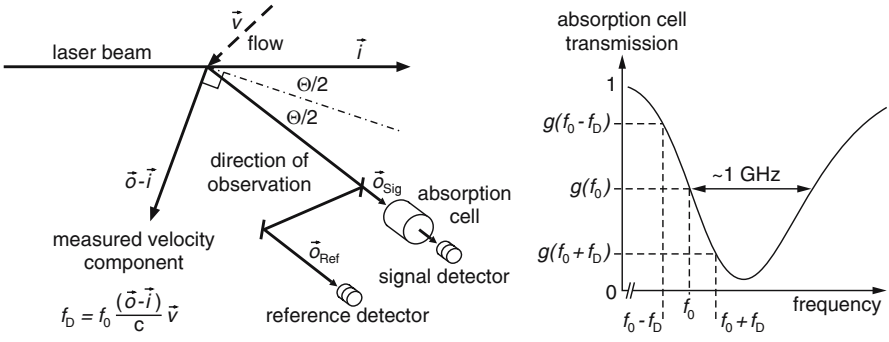

Fig. 1 Principle of Doppler Global Velocimetry

The component of the velocity which can be measured is given by the geometry of the set-up and depends on the angle between the incident direction of the laser light sheet and the observation direction. As the intensity of the light transmitted through the absorption cell directly gives the measuring information, small intensity variations caused by parasitic intensity fluctuations in the observed light sheet have serious effects on the accuracy of the velocity measurement. Thus in conventional systems, the influence of intensity fluctuations of the scattered light is eliminated by employing a signal and an additional reference detector unit (see figure 1), where the image alignment of both detectors on each other is of particular importance.

When applying frequency modulation techniques such as continuous sinusoidal modulation (FM-DGV) as well as frequency shift keying (FSK-DGV) to the Doppler Global Velocimetry it is possible to omit the reference detector unit and to reduce the uncertainty of the velocity measurement.

3 Self-calibrating DGV Based on FSK-Techniques

In contrast to conventional DGV systems requiring an additional reference camera and a laser for the light sheet generation which is frequency stabilized at a single working point on a preliminary calibrated absorption line edge, the described FSK technique is able to omit the reference camera by evaluating a sequence of the images taken for two working points with a well defined frequency difference at both edges of the absorption line allowing an additional on-line calibration.

As shown in figure 2, the laser frequency is alternately stabilized to both edges of the absorption line. Consequently, the intensity of each pixel will change according to the Doppler shift f_D and the slopes $(dg/df)_F$ and $(dg/df)_R$ at the falling and rising edges. Taking two images per absorption line edge, while the laser is stabilized to frequencies with a well defined difference Δf, the slopes dg/df can be determined simultaneously.

Presuming

$$\left[\, g(0) + g(1) \,\right]_{f_D=0} \;=\; \left[\, g(2) + g(3) \,\right]_{f_D=0} \tag{1}$$

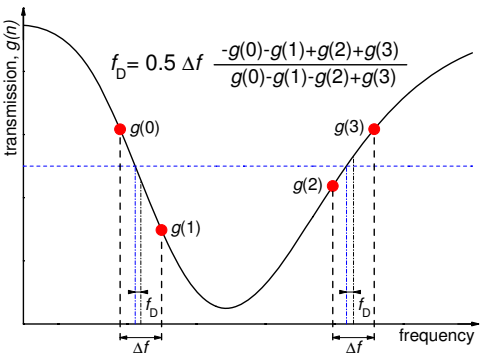

Fig. 2 Principle of self-calibration

for non shifted laser light, a Doppler shift will result in the intensity difference

$$[g(2)+g(3)]-[g(0)+g(1)] = 2\, f_D\, [(dg/df)_R-(dg/df)_F]. \quad (2)$$

As the slopes on falling and rising edge are given by

$$(dg/df)_F = \frac{g(1)-g(0)}{\Delta f} \quad \text{and} \quad (dg/df)_R = \frac{g(3)-g(2)}{\Delta f}, \quad (3)$$

the Doppler frequency can be calculated by

$$f_D = 0.5\,\Delta f \; \frac{-g(0)-g(1)+g(2)+g(3)}{g(0)-g(1)-g(2)+g(3)} \quad (4)$$

as far as the absorption line edges can be assumed as linear.

This method gives the possibility to trace back the measured velocities directly to a well defined laser frequency step Δf, while the scattered light intensity, absorption line slope and camera sensitivity are automatically included for each pixel. Also extraneous light and dark image intensities of the camera will have no influence on the evaluation, as only differences in intensities of the same pixels in consecutive images are considered. Additionally erroneous effects of small laser frequency offsets or fluctuations of the absorption cell can be monitored by superimposing a spot of non Doppler shifted laser light into the camera image, also measured through the absorption cell. This spot can be achieved by either placing some scattering material into the lightsheet, or coupling light into the absorption cell optics by an optical fiber. In evaluation, it is accounted as “velocity zero” reference value in the Doppler shift evaluation algorithm.

4 System Setup

The FSK-DGV system has been realized by using a fiber coupled DFB-MOPA laser system that allows fast frequency switching while keeping the output power of about 160 mW (measured at the lightsheet heads) constant. According to the wavelength of 852 nm a caesium absorption cell (50 mm diameter, 50 mm length) is used for frequency-to-intensity conversion. In order to generate well defined, reproducible frequency steps, the lightsheet laser is locked to a second, frequency stabilized reference laser.

As shown in figure 3, the prescaled beat signal derived from reference and lightsheet generating laser is compared to a set frequencies generated by direct digital synthesis (DDS) using a phase locked loop (PLL) circuit, adjusting the laser current. The frequency control settling time is reduced by additionally applying fast current steps to the laser when switching the frequency (feed forward). In order to avoid changes of the laser system output power P_{Laser} when modulating the laser diode current, the output power is controlled adjusting the optical amplifier current. Also changing the laser current will directly bias the amplifier current in order to reduce the power control settling time. The laser diode temperature is controlled digitally to match the laser frequency within a desired laser current range. A microcontroller is used to generate the frequency sequences by internal or external

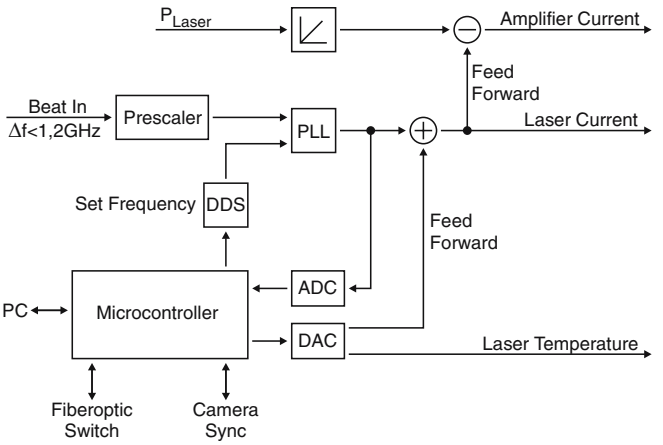

Fig. 3 System electronics

synchronization with different cameras and may also drive a fiberoptic switch to toggle the three lightsheets needed for three-componential measurements.

5 Measurements

5.1 Spinning Disc

The described FSK-DGV system has been verified by measuring the well defined velocity field on a 12 cm diameter rotating scattering disc, including self-calibration and automatic offset-correction by monitoring a reference point of scattering light directly from the lightsheet laser without Doppler shift. The measurements were made under ambient light.

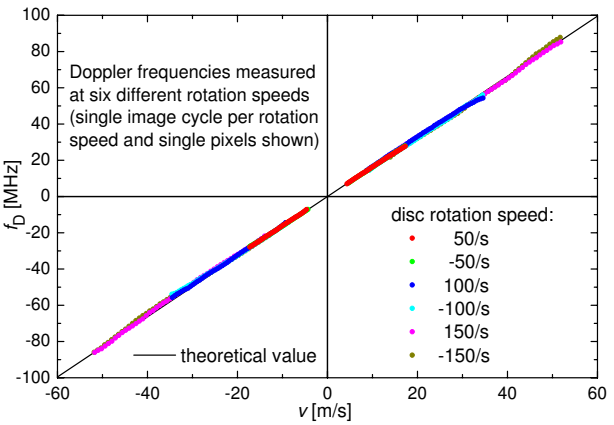

Fig. 4 Measured Doppler frequencies after automatic nonlinearity correction

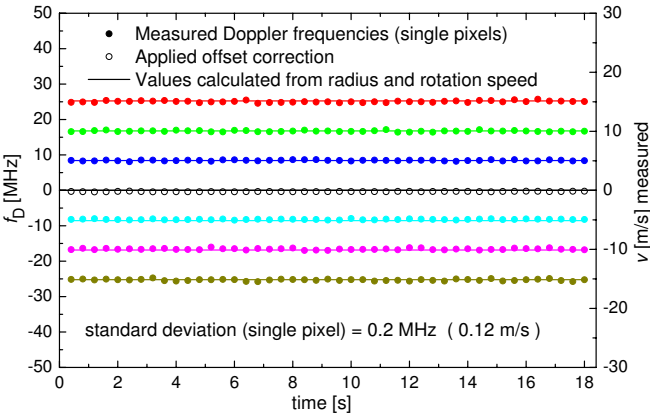

Fig. 5 Time-resolved measurement of single pixels at six radial positions on the rotating disc

Single measurements of a single pixel column for different rotation speeds have shown that the premise of linear absorption line edges can be used for low velocities only. Nevertheless, the nonlinearity of the measurements can be reduced by a correction function derived by automatically starting each measurement series with sampling the absorption line analyzing the intensity of the the superimposed reference spot. Figure 4 shows the linearized Doppler frequencies measured at several rotation speeds compared to the expected velocity calculated from radius and actual rotation speed. For single measurements of single pixels we found an absolute, total deviation of less than 0.5 m/s for velocities below 15 m/s and about 3 % for higher velocities, while some linearization using a more sophisticated correction function might give even better results.

Time resolved measurements, accomplished with our camera's image rate of 10 Hz leading to a measurement cycle rate of 2.5 Hz, show a standard deviation of about 0.12 m/s (figure 5).

5.2 Flow Field

Using the self-calibrating DGV with nonlinearity correction implemented, and a frame-transfer CCD camera with 384 by 286 pixels and 14 Bit dynamics, the flow field in a 20 cm diameter pipe 4 m behind a double elbow has been measured at different flow rates. After recording patterns for image restitution and determination of the lightsheet directions needed for the vector evaluations, 300 measurement cycles comprising 12 images (4 frequencies, 3 lightsheets), 100 ms exposure time each, have been taken.

The figures 7a,b and 8a,b show the position of the swirl center and the asymmetrical axial velocity profile caused by the double elbow changing with the flow rate, while velocities down to 0.1 m/s are resolved, as shown in the close-up look to the swirl center (figure 8c).

The axial component, calculated for single pixels without binning, show a standard deviation of about 0.5 m/s calculated from single measurement cycles, while the standard deviation in 100 temporal binned cycles is reduced down to about

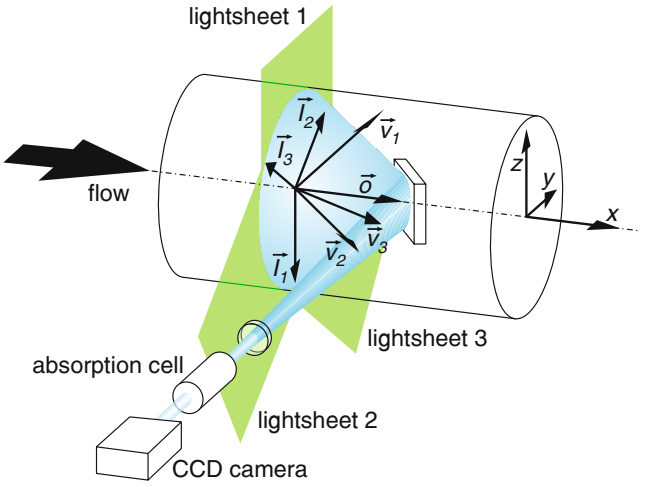

Fig. 6 Principle of 3 component single camera FSK-DGV velocity field measurement in a pipe

0.05 m/s (figure 9). This continuity implies that there is only uncorrelated noise affecting the measurements, easily to be averaged out in numerous cycles, so the velocity resolution is directly linked to the temporal resolution.

As there is no significant difference between the standard deviation derived from single pixels and 10 by 10 binned pixels, the uncertainty is obviously not dominated by pixel noise, as might be expected from the laser power of only 160 mW, but from influences affecting regions of pixels the same way. Considering that the deviation caused by laser frequency variation is also remarkably lower (measured using the reference spot), the standard deviation of this flow measurement seems to be dominated by seeding variations or the flow itself.

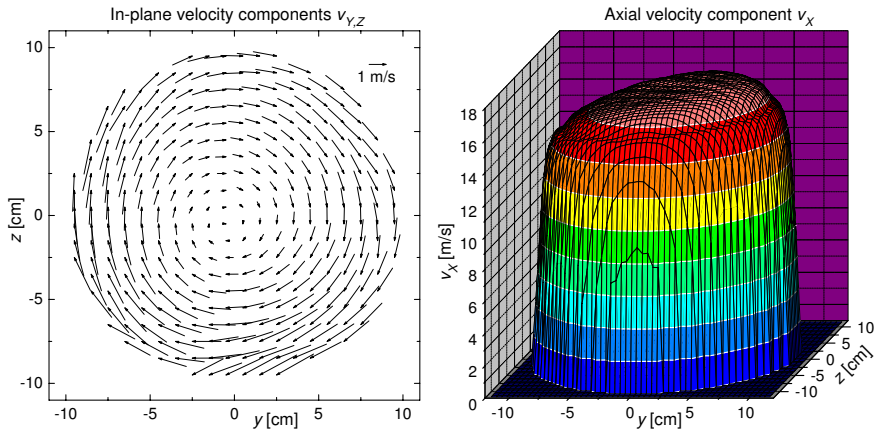

Fig. 7 (a,b) Velocity components at a flow rate of about 2000 m³/h

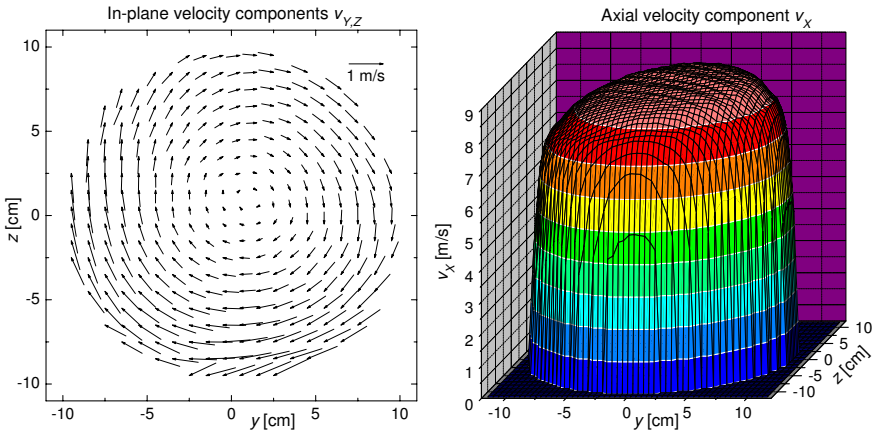

Fig. 8 (a,b) Velocity components at a flow rate of about 1000 m³/h

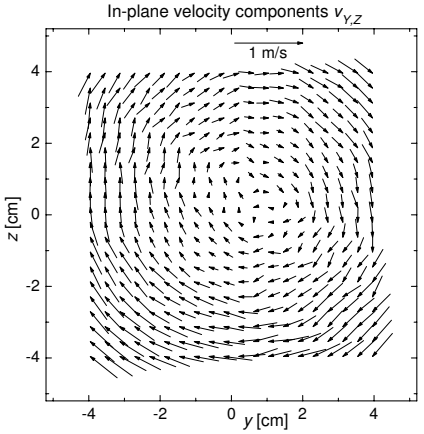

Fig. 8 (c) Zoom (1000 m³/h flow rate)

Fig. 9 Velocity standard deviation w. r. t. temporal resolution

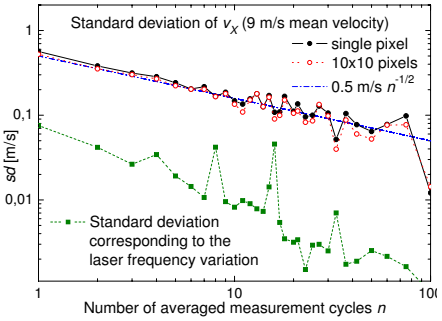

6 Phase-Averaged Measurements

As the evaluation of integrated images has shown good results for the pipe flow measurement, phase averaging measurements should also be possible by taking interleaved images: As long as an unsteady flow incorporates periodical elements, the acquisition can be synchronized to take one or more images at dedicated flow phase steps, followed by a frequency step after every flow period and a lightsheet changeover after every frequency cycle. After acquisition of multiple cycles, the single images can be integrated to sum images, each consisting of numerous images from one lightsheet, frequency and flow phase slice. The more images are taken, the less will the sums be affected by arbitrary velocity and scattered light intensity changes. Only flow processes occurring with integer multiples of the cycles affecting images of the same laser frequency step in the same way, could distort the results - but the image acquisition cycles could also be expanded to even measure these flow elements instead of getting distorted. So assuming enough images per sum image, and only changes in velocity and scattered light intensity that are uncorrelated with the frequency step cycles, the velocity evaluation will just result in the constant and periodical elements of the flow.

To verify this theory, a transportable system with camera and lightsheet optics fixed on a plate as a module to be placed in wind tunnels has been developed. The system is currently under test in the Kármán vortex street experiment at the University of Rostock.

7 Conclusions

The application of frequency shift keying allowed to build a DGV system without reference camera, which is independent from ambient light, camera pixel sensitivity, scattered light intensity and absorption line slopes. Self calibrated measurements on the rotating disc have shown a standard deviation of about 0.12 m/s and an absolute total deviation of less than 0.5 m/s for time resolved velocity measurements considering single pixels and low Doppler shifts. For higher velocities, as the Doppler shifted light frequency exceeds the linear range of the absorption line edges, the absolute deviation has been reduced to about 3 %. Three-componential measurements of a pipe flow have shown a standard deviation of about 0.5 m/s for the axial component in single pixels and single measurement cycles with 100 ms exposure time. With temporal binned images, a standard deviation of about 0.05 m/s for the axial component was achieved and in-plane component structures down to 0.1 m/s have been resolved.

Further investigations will be made about phase-averaged measurements, including a verification at the Kármán vortex street.

Acknowledgments. We would like to thank the Deutsche Forschungsgemeinschaft (DFG) for the support of the projects MU 1252/2-3 and CZ 55/16-3 within the framework of the SPP 1147 and the chair in fluid mechanics, University of Rostock, for kindly providing their wind tunnel and helpful assistance.

References

1. Ainsworth, R.W., Thorpe, S.J., Manners, R.J.: A new approach to flow-field measurement - A view of Doppler global velocimetry techniques. Int. J. Heat and Fluid Flow 18 (1997)
2. Meyers, J. F., Lee, J.W., Schwartz, R.J.: Characterization of measurement error sources in Doppler global velocimetry. Meas. Sci. Technol. 12, 357–368 (2001)
3. Röhle, I., Schodl, R.: Evaluation of the accuracy of the Doppler global technique. In: Proc. Optical Methods and Data Processing in Heat and Fluid Flow, London, pp. 155–161 (1994)
4. Morrison, G.L., Gaharan Jr., C.A.: Uncertainty estimates in DGV systems due to pixel location and velocity gradients. Meas. Sci. Technol. 12, 369–377 (2001)
5. Ford, H.D., Nobes, D.S., Tatam, R.P.: Acousto-optic frequency switching for single-camera planar Doppler velocimetry. In: Proc. SPIE, vol. 4448 (2001)
6. Müller, H., Lehmacher, T., Grosche, G.: Profile sensor based on Doppler Global Velocimetry. In: 8th International Conference Laser Anemometry Advances and Applications, Rome, pp. 475–482 (1999)
7. Müller, H., Pape, N., Grosche, G., Strunck, V., Dopheide, D.: Simplified DGV on-line profile sensor. In: 11th Int. Symp. On Applications of Laser Techniques to Fluid Mechanics, paper 9.3, Lisbon (2002)
8. Müller, H., Eggert, M., Pape, N., Dopheide, D., Czarske, J., Büttner, L., Razik, T.: Time resolved DGV based on laser frequency modulation. In: 12th International Symposium on Applications of Laser Techniques to Fluid Mechanics, paper 25.2, Lisbon (2004)
9. Müller, H., Eggert, M., Czarske, J., Büttner, L., Fischer, A.: Single-camera Doppler global velocimetry based on frequency modulation techniques. Exp. Fluids 43, 223–232 (2007)
10. Fischer, A., Büttner, L., Czarske, J., Eggert, M., Müller, H.: Investigation of time-resolved single detector Doppler-Global-Velocimetry using sinusoidal laser frequency modulation. Meas. Sci. Technol. 18, 2529–2545 (2007)

Recent Developments in 3D-PTV and Tomo-PIV

Hans-Gerd Maas, Torsten Putze, and Patrick Westfeld

Abstract. The article gives an overview on recent developments to 3D flow measurement techniques, focusing on photogrammetric aspects of 3D geometric modelling and multi-camera system configuration. A geometric model for a virtual four-camera system, which is realized by a single camera and a four-fold mirror system, is presented. The 3D-PTV model is extended by a ray tracing technique to strictly handle the spatial intersection of manifold broken optical beams when determining coordinates of particles in a liquid from images from multiple viewpoints taken by cameras observing the flow through multiple curved interfaces. Transferring these geometric models to PIV, we present some algorithmic improvements to tomographic PIV, which have the potential to achieve a significant reduction of the computational effort.

1 Introduction

In many fluid mechanics applications there is a special interest for non-contact time-resolved fully 3C3D (= determination of 3 components of velocity in 3-D space) measurement techniques. Most methods base on seeding particles, which visualize

Hans-Gerd Maas
Institute of Photogrammetry and Remote Sensing, Technische Universität Dresden,
Helmholtzstraße 10, 01062 Dresden, Germany
hans-gerd.maas@tu-dresden.de

Torsten Putze
Institute of Photogrammetry and Remote Sensing, Technische Universität Dresden,
Helmholtzstraße 10, 01062 Dresden, Germany
torsten.putze@tu-dresden.de

Patrick Westfeld
Institute of Photogrammetry and Remote Sensing, Technische Universität Dresden,
Helmholtzstraße 10, 01062 Dresden, Germany
patrick.westfeld@tu-dresden.de

W. Nitsche and C. Dobriloff (Eds.): Imaging Measurement Methods, NNFM 106, pp. 53–62.
springerlink.com

the flow and can be recorded by an imaging system. 3D particle tracking velocimetry (3D-PTV) is an established method to determine 3D trajectories of a large number of particles in a flow from multiple camera image sequences. It is based on the detection of discrete particles in the images, the establishment of multi-image correspondences, the determination of 3D particle coordinates and a subsequent discrete particle tracking in 3D object space. 3D-PTV requires a system consisting of at least two, but rather three or four synchronized cameras [6]. Especially when observing high speed flows, the configuration of a multi-camera system may pose financial and technical challenges. In these cases, an interesting alternative may be given by a single camera, which is extended to multiple virtual cameras by a mirror system in front of the optics. The configuration and performance of such a system is shown in section 2.

In liquid flow measurement applications, where particles in a liquid are observed by outside cameras through glass interfaces, multimedia photogrammetry techniques (e.g. [5]) can be employed to handle the spatial intersection of beams, which are broken according to Snell's Law. Section 3 describes a strict ray tracing procedure to handle beams from multiple cameras broken at multiple planar or non-planar parametrized interfaces.

The spatial resolution potential of 3D-PTV is limited by ambiguities occurring in the processes of particle detection and multi-image correspondence establishment [6]. Recently, Elsinga et al. [1] have proposed a Tomo-PIV approach, which is based on a tomographic reconstruction of the observation volume. In section 4, this approach is compared to 3D-PTV, and some algorithmic modifications are shown in order to reduce the computational effort of the technique.

2 Virtual Four Camera System

3D-PTV is based on processing stereoscopic particle image sequences. The minimum requirement of stereoscopy is the observation of particle constellations from two viewpoints. If the relative orientation between the cameras is known from a calibration procedure, the computation of epipolar lines facilitates the establishment of correspondences between the views. The length of the baseline between the two cameras, related to the distance to the observation volume (base-to-height ratio), determines the depth resolution of the system. While a base-to-height ratio in the order of 1:1 would be desirable to achieve homogeneous precision in the XYZ coordinates of particles, spatial restrictions as well as limitations given by depth-of-focus and the necessity of achieving a common field of view will often compromise to a base-to-height ratio in the order of 1:3. As a consequence, the depth coordinate will usually be worse than the lateral coordinates in 3D-PTV systems.

3D-PTV data processing is based on identifying discrete particles in all images, establishing stereo correspondences, calculating 3D particle coordinates and tracking particles between consecutive time instances. Maas et al. [6] realize the spatio-temporal matching process by first establishing stereo correspondences and then tracking particles in 3D space. Netzsch&Jähne [8] reverse the processing step order

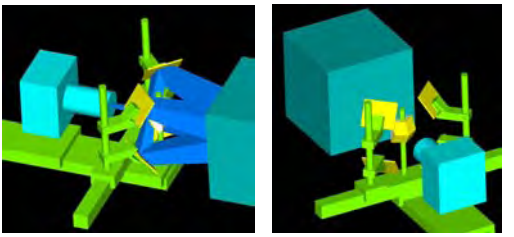

Fig. 1 Four-fold mirror system [14]

by first tracking particles in 2-D image space and then establishing stereo correspondences between image space trajectories. A step towards integrated spatio-temporal matching is shown by Willneff&Grün [18], who combine the two approaches by a back-projection search of missing trajectory links. Generally, the step of establishing stereoscopic correspondences is prone to ambiguities at high seeding densities. These ambiguities can only be solved reliably when using a multi-camera system consisting of three or four synchronized cameras, with the ideal camera arrangement in a triangle or square [4].

The configuration of a multi-camera system may come with a considerable instrumental, technical and financial effort. An elegant solution to this may be given by the combination of a single camera and a mirror system. Two-fold mirror systems are commercially available for amateur cameras; they have also been designed for high speed cameras in car crash test analysis [16]. For the high speed camera based 3D-PTV system described here, a more sophisticated four-fold mirror system has been developed [10]. The system consists of a static central prism mirror placed in front of the camera optics and four adjustable outer mirrors (fig. 1). It generates four viewing directions for the four quadrants of the sensor. In the geometric modelling of the system, the four quadrants can be considered virtual cameras with their projection centers behind the outer mirrors of the system. The base-to-height ratio and the common field of view of the four virtual cameras can be adapted by shifts and rotations of the outer mirrors.

Using photogrammetric spatial resection or bundle adjustment techniques, the system can be calibrated automatically from images of a reference body. The calibration includes the relative orientation between the virtual cameras as well as the camera interior geometry, including lens distortion. The accuracy potential can be described by a standard deviation of unit weight of 0.1 pixel in image space and a 3D coordinate precision of 0.13/0.12/0.39 mm (related to an observation volume of $25 \times 25 \times 30\,\mathrm{cm}^3$ [10]. Note that in multi-camera 3D motion analysis systems, the precision of the motion vector components is usually significantly better than the precision of 3D coordinates [11].

Fig. 2 shows the results of an application of the system in the measurement of particle trajectories in an air flow around a finite cylinder ($\varnothing = 11\,\mathrm{cm}$, $\mathrm{H} = 22\,\mathrm{cm}$) in a wind tunnel. The mean velocity in the tunnel was $7\,\mathrm{m/s}$, the Reynolds number was $4 \cdot 10^4$. In a $25 \times 25 \times 30\,\mathrm{cm}^3$ observation volume, a total of 3787 particles could be tracked. On average, particles could be tracked over 12 time steps with a

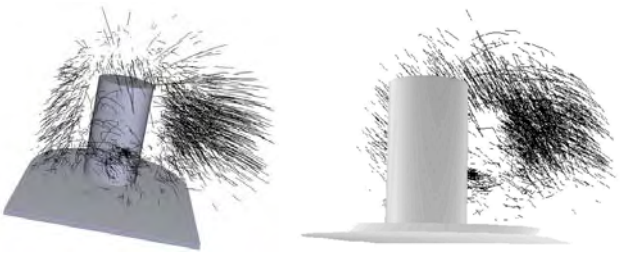

Fig. 2 Resulting trajectories behind the cylinder

maximum of 51 time steps. While an average particle can be expected to stay in the observation volume for 17 time step.

3 Multimedia Geometry

Applications of photogrammetry, where the beam from an object to the sensor passes several optical media with different refractive indices, are called multimedia photogrammetry. In flow measurement applications, where particles in a liquid are observed by cameras from outside through a plane glass interface, multimedia photogrammetry techniques can be employed to strictly handle the spatial intersection of twice-broken beams from multiple (real or virtual) viewpoints in 3D-PTV. Maas [5] describes a versatile technique for geometric modelling in multimedia photogrammetry, which can easily be implemented as a module into photogrammetric standard procedures such as spatial resection for camera calibration, epipolar line computation and spatial intersection for 3D particle coordinate determination. The solution is restricted to the standard case of multimedia photogrammetry, where the object is situated in a liquid, the sensor is positioned in air, and a plane-parallel glass plate divides these two media.

If the object is observed through non-planar interfaces, the modelling becomes more complex. In the following, a strict approach to handle multimedia geometry by ray tracing based on [3] will be shown. In a first step, the approach requires the determination of the geometry parameters of all relevant interfaces in a model coordinate system. We assume, that the refractive indices of the optical media are

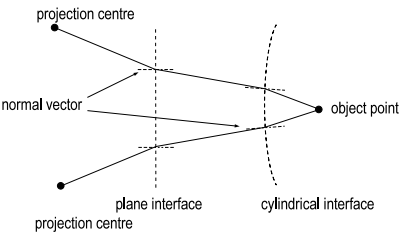

Fig. 3 Twice broken beams from two cameras

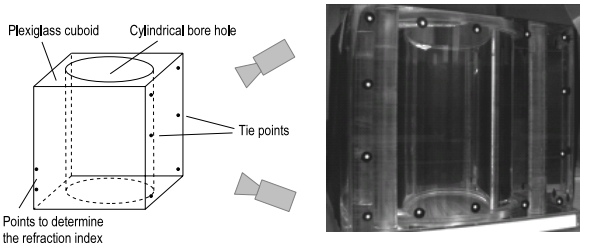

Fig. 4 3D-PTV observation volume in a water analogon of an engine

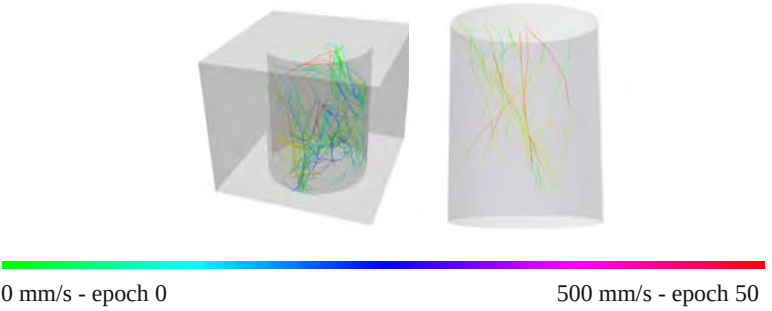

Fig. 5 3D-PTV trajectories, colour coded in time (left) and in velocity (right)

known, and that the camera system is calibrated. Then, a ray tracing is performed for each particle detected in the images. The rays are projected into object space using the camera orientation parameters. At each interface, the new direction is calculated on the basis of the local normal vector and Snell's Law. Finally, 3D particle coordinates are determined by the spatial intersection of multiple rays originating from corresponding particles in the images from all viewpoints (fig. 3). For camera calibration purposes, the ray tracing can also be performed backward from a particle to the image. This backward approach requires an iterative procedure. The technique is described in more detail in [12].

The multimedia photogrammetry module has been used for 3D-PTV measurements in a plexiglass car engine analogon (fig. 4). The dimension of the cuboid is $11.5 \times 11.5 \times 10\,\mathrm{cm}^3$, with a cylindrical bore hole with a diameter of $7.5\,\mathrm{cm}$. The used flow medium was water with a flow rate of $8.4\,\mathrm{l/min}$. The flow was observed with a convergent four camera arrangement. The used tracers are Vestosint particles with a diameter of $30\,\mu m$. The flow inside the analogon was imaged by a four camera system.

In the experiment, a total of 651 particles could be tracked. An extended four frame approach [9] was used for 3D tracking. Trajectories with a length of up to 14 epochs could be determined. Fig. 5 shows some trajectories inside the cylinder. The velocity vector component precision was estimated in the order of $0.1\,\mathrm{mm}$.

4 Tomographic PIV

3D-PTV has a spatial resolution limit, which is set by ambiguities occurring at high seeding densities in the processing steps of detecting particles in the images, establishing multi-view correspondences and tracking. The Tomo-PIV approach as suggested by Elsinga et al. [1] has the potential to expand this resolution limit, because it is based on tracking cuboids in voxel data rather than identifying, matching and tracking individual particles. The obvious draw-back is in the fact, that Tomo-PIV is best suited to determine velocity fields on a regular grid, while 3D-PTV has the potential to determine long 3D trajectories by tracking individual particles.

Tomo-PIV generates a tomographic reconstruction of a 3D particle constellation from a limited number of camera views in an approach similar to shape-from-silhouette. A reconstruction of the 3D observation space can for instance be performed by the MART (multiplicative algebraic reconstruction technique) algorithm [2]. The basic idea of the technique is to represent the observation volume by a 3D voxel structure with a resolution adapted to the camera resolution by the following procedure:

- Every pixel of the first image is projected into the voxel space through the projection centre of its camera. Every voxel, which is hit by the projected ray, gets a greyvalue obtained by interpolation from the originating pixel (fig. 6a)
- Then, every pixel of the second image is projected into the voxel space. In every voxel, which is hit by the projected ray, the existing voxel greyvalue (obtained from the first image) is multiplied by the greyvalue of the originating pixel (fig. 6b)
- Likewise, the content of all other camera views is projected into the voxel space (fig. 6c)

As a result, the voxel space will contain multiplicatively accumulated image intensity information of the instantaneous particle constellation. It is obvious, that only voxels at valid particle positions will show high values (as they have high values in all factors of the grey value multiplication), while all remaining voxels will show rather low values. Repeating the procedure for each time step, a time-resolved 3D

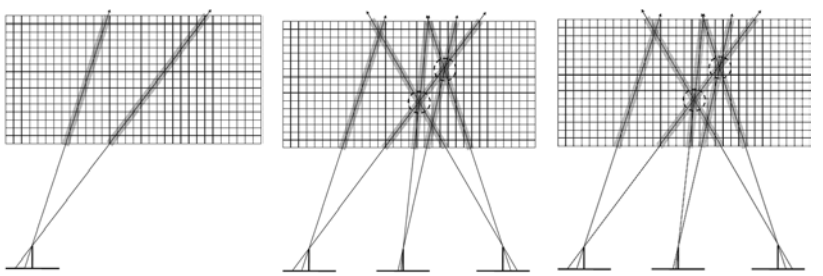

Fig. 6 Tomographic reconstruction principle

voxel space representation is obtained. In this voxel data sequence, 3D flow velocity vectors can be obtained by 3D cross correlation or similar techniques. Elsinga et al. [1] show, that four camera views will usually be sufficient for the reconstruction. The requirements to the geometric camera configuration are identical with those for conventional 3D-PTV [6].

The advantage of Tomo-PIV over 3D-PTV is in the fact that it avoids the ambiguity-prone processing steps of discrete particle detection and establishment of multi-view correspondences, thus allowing for a higher seeding density and delivering denser flow velocity field information. A disadvantage of early implementations is in the high computational effort. In the following, we will show some enhancements to Tomo-PTV to improve the speed of the tomographic reconstruction process.

The pixel-wise projection method as described above is straightforward, but computationally rather inefficient and time consuming. The core of our new tomographic reconstruction technique, which is presented in detail in [13], is a multiple projective transformation based approach. The object space voxel structure is initialized by setting the value of every voxel value to 255. The reconstruction of the object space light intensity field is performed by transforming the content of each camera image into each depth layer of the voxel space. Using homogeneous coordinates, a simple and fast computation can be performed. The relationship between the image coordinates x' and the voxel coordinates of a depth layer D_i in object space is:

$$x' = H_i \cdot D_i \tag{1}$$

H_i contains the 8 parameters of a projective transformation. For a layer D_0, the elements of H_0 can be determined from the parameters of the exterior and interior orientation of the camera (projection center X0,Y0,Z0, 3x3 rotation matrix r, focal length c):

$$H_0 = \begin{bmatrix} -c \cdot r_{11} & -c \cdot r_{12} & c \cdot (r_{11} \cdot X_0 + r_{21} \cdot Y_0 + r_{31} \cdot Z_{03}) \\ -c \cdot r_{11} & -c \cdot r_{12} & c \cdot (r_{11} \cdot X_0 + r_{21} \cdot Y_0 + r_{31} \cdot Z_0) \\ -c \cdot r_{11} & -c \cdot r_{12} & c \cdot (r_{11} \cdot X_0 + r_{21} \cdot Y_0 + r_{31} \cdot Z_0) \end{bmatrix} \tag{2}$$

The transformation matrices H_i of all further depth slices can be simplified by adding an increment h_i to H_0. Due to the parallelism of the depth layers, the determination h_i of is simplified:

$$h_i = \begin{bmatrix} 0 & 0 & -c \cdot r_{31} \cdot Z_i \\ 0 & 0 & -c \cdot r_{31} \cdot Z_i \\ 0 & 0 & -c \cdot r_{31} \cdot Z_i \end{bmatrix} \tag{3}$$

$$H_i = H_0 + h_i' \tag{4}$$

In homogeneous coordinates, it is sufficient to go through the transformation for the corner pixels of a layer. All other grey values can be obtained by a bilinear interpolation.

The layer-wise rectification procedure is repeated for each camera view. Obviously, each object space voxel will obtain different grey values from different views. The voxel space particle reconstruction is based on a very simple rule: A voxel belonging to a valid particle must have a high grey value in every image. This rule has been realized by a multiplication of the grey values from each projection in the implementation of Elsinga et al. (2005). This way, only those voxels, which get a high grey value from every view, will 'survive'. The rule can be implemented even more efficiently by a minimum operator, where the grey value of a voxel GV is the minimum of its grey values in all views gv_j:

$$GV = \min\left\{\mathrm{gv_j}\right\} \;\ldots\; \mathrm{gv_j} \in \{0\ldots255\} \tag{5}$$

This way, only those voxels will survive, which correspond to particles in all participating camera views. The rest of the voxel space will be filled with dark values. A background image obtained from spatio-temporal histogram analysis can be subtracted from each image be-forehand to eliminate the effect of background reflections. Multimedia geometry (i.e. the handling of a broken optical path when observing particles in liquids through a glass interface, see section 3) can be incorporated into the rectification process by ray tracing from the camera through the air-glass interface to the glass-water interface and consecutive linear depth layer mapping using a matrix h_i with direction vector components obtained from the ray tracing process using Snell's Law.

The tomographic reconstruction facilitates the implementation of volume-based particle tracking techniques without the necessity of detecting individual particles. This could for instance be 3D cross correlation like in [1] or 3D least squares matching [7]. 3D cross correlation depicts a rather simple technique to determine 3D displacement vectors between cuboids of the dimension $(2K+1)\times(2L+1)\times(2M+1)$ in the voxel space of two consecutive epochs A,B:

$$\rho = \frac{\sum_M \sum_N \sum_N \left(A_{MNO} - \bar{A}\right)\cdot\left(B_{MNO} - \bar{B}\right)}{\sqrt{\sum_M \sum_N \sum_N \left(A_{MNO} - \bar{A}\right)^2 \cdot \sum_M \sum_N \sum_N \left(B_{MNO} - \bar{B}\right)^2}} \tag{6}$$

Subvoxel precision can be obtained by fitting a Gaussian function into the cross correlation coefficient field.

$$\rho\,(x,y,z) = \frac{1}{\sigma_x \cdot \sigma_y \cdot \sigma_z \cdot \sqrt[3]{2\pi}} \cdot e^{-\frac{1}{2}\left(\frac{(x-x_0)^2}{\sigma_x^2} + \frac{(y-y_0)^2}{\sigma_y^2} + \frac{(z-z_0)^2}{\sigma_z^2}\right)} \tag{7}$$

Cross correlation offers the advantage of a simple implementation. Elsinga et al. [1] implemented it in a hierarchical manner (multigrid correlation) to improve the convergence behaviour. It is, however, limited to the determination of three cuboid shift parameters. Cuboids with significant deformations will not be tracked well, as shown by Putze&Maas [15]. This may be partially compensated by iterative window deformation techniques, which have been presented for 2D-PIV [17], but at a much larger computational effort.

As an alternative, 3D least-squares-tracking (3D-LST) is a volume-based tracking technique, which is adaptive to linear cuboid deformation and rotation. 3D-LST minimizes the sum of the squares of voxel value differences between cuboids from consecutive time steps by determining the coefficients of a 3D affine transformation [7]. In addition to the three displacement vector components, the 12 parameters of the 3D affine transformation in 3D-LST contain scale, rotation and shear information. This allows for a higher precision in case of velocity gradients in the interrogation volume. Moreover, these parameters enable to determine a deformation tensor for each interrogation cube. The result of 3D-LST applied to sequences of tomographically reconstructed voxel structures is a dense 3D velocity vector field with inherent additional shear tensor information.

5 Conclusion

Mirror-based optical systems in combination with a single camera may depict a valuable tool in generating multi-view stereoscopic imaging systems for 3D flow measurement applications. Herein, the introduction of virtual cameras facilitates geometric modelling and calibration of a 3D-PTV system by photogrammetric standard techniques. 3D-PTV can be extended by ray tracing procedures to strictly handle manifold broken beams when observing particles in liquids by multiple cameras through planar or non-planar glass interfaces.

Other than 3D-PTV, Tomo-PIV is based on applying volume-based matching techniques to tomographic reconstructions of the observation volume at consecutive time instances, thus avoiding ambiguities in the establishment of spatio-temporal particle correspondences and potentially increasing the processable seeding density. A sequential projective transformation based approach, combined with resampling and a minimum voxel grey value search, depicts a strict technique which may significantly reduce the large computational effort connected with the tomographic reconstruction.

Acknowledgements. The work presented in this paper has been funded by the German Research Foundation (DFG MA 2504/1-1...1-3). The water analogon has been made available by Dr. Hentschel, EGNM/O, Volkswagen AG.

References

1. Elsinga, G.E., Scarano, F., Wieneke, B., van Oudheusden, B.W.: Tomographic particle image velocimetry. Exp. Fluids 41, 947–999 (2006)
2. Herman, G.T., Lent, A.: Iterative reconstruction algorithms. Comput. Biol. and Med. 6, 273–294 (1976)
3. Kotowski, R.: Zur Brücksichtigung lichtbrechender Flächen im Strahlenbündel. Schriftreihe der DGK, Reihe C, Heft 330 (1987)
4. Maas, H.-G.: Complexity analysis for the establishment of image correspondences of dense spatial target fields. Int. Arch. Photogram. Rem. Sens. Spatial Inform. Sci. 29, Part B5, 102–107 (1992)

5. Maas, H.-G.: New developments in multimedia photogrammetry. Optical 3-D Measurement Techniques III, Wichmann (1995)
6. Maas, H.-G., Grün, A., Papantoniou, D.: Particle tracking velocimetry in three-dimensional flows, Part 1. Photogrammetric determination of particle coordinates. Exp. Fluids 15, 133–146 (1993)
7. Maas, H.-G., Stefanidis, A., Grün, A.: From pixels to voxels: tracking volume elements in sequences of 3-D digital images. Int. Arch. Photogram. Rem. Sens. Spatial Inform. Sci. 30, Part 3/2 (1994)
8. Netzsch, T., Jähne, B.: A high performance system for 3-dimensional particle tracking velocimetry in turbulent flow research using image sequences. Int. Arch. Photogram. Rem. Sens. Spatial Inform. Sci. 30, Part 5W1 (1995)
9. Malik, N., Dracos, T., Papantoniou, D.: Particle Tracking velocimetry in three-dimensional flows, Part 2. Particle tracking. Exp. Fluids 15, 279–294 (1993)
10. Putze, T.: Geometric modelling and calibration of a virtual four-headed high speed camera-mirror system for 3-D motion analysis. Optical 3-D Measurement Techniques VII II, 167–174 (2005)
11. Putze, T.: Quality analysis of flow field data determines by 3D PTV in gas flows. In: Proc. 12th Int. Symp. Flow Vis., Göttingen, Germany (2006)
12. Putze, T.: 3D flow analysis inside a plexiglass engine using 3D PTV. In: Proc. 13th Int. Symp. Flow Vis., Nice, France (2008)
13. Putze, T.: Novel reconstruction approach for tomographic PIV. In: Proc. 13th Int. Symp. Flow Vis., Nice, France (2008)
14. Putze, T., Hoyer, K.: Modellierung und Kalibrierung eines virtuellen Vierkamerasystems auf Basis eines verstellbaren Spiegelsystems. Beiträge der Oldenburger 3D-Tage 2005, Wichmann (2005)
15. Putze, T., Maas, H.-G.: 3D determination of very dense particle velocity fields by tomographic reconstruction from four camera views and voxel space tracking. Int. Arch. Photogram. Rem. Sens. Spatial Inform. Sci. 37, Part B5, 33–38 (2008)
16. Raguse, K.: Dreidimensionale photogrammerische Auswertung asynchron aufgenommener Bildsequenzen mittels Punktverfolgungsverfahren. Schriftreihe der DGK, Reihe C, Heft 602 (2007)
17. Scarano, F.: Iterative image deformation methods in PIV. In: Measurement Science and Technology, vol. 13, pp. R1–R19. IOP Publishing Ltd. (2002)
18. Willneff, J., Grün, A.: A new spatio-temporal matching algorithm for 3D particle tracking velocimetry. In: Proc. 9th Int. Symp. on Transport Phenomena and Dynamics of Rotating Machinery, Honolulu, Hawaii (2002)

3D Tomography from Few Projections in Experimental Fluid Dynamics

Stefania Petra, Andreas Schröder, and Christoph Schnörr

Abstract. We study the tomographic problem of reconstructing particle volume functions in experimental fluid dynamics from the general viewpoint of compressed sensing, which is a central theme of current research in applied mathematics. The probability of exact reconstructions from few projections is studied empirically and shown to resemble provable results for idealized mathematical measurement setups. Application of our reconstruction algorithm to noisy projections outperforms the state-of-the-art both with respect to accuracy and runtime.

1 Introduction

This paper summarizes results of our project that has started two years ago. Our research work is motivated by the work [10]. The authors introduced a new 3D technique, called *Tomographic Particle Image Velocimetry (TomoPIV)* for imaging turbulent fluids with high speed cameras. The technique is based on the instantaneous reconstructions of particle volume functions from few and simultaneous projections (2D images) of the tracer particles within the fluid. The reconstruction of the 3D image from 2D images employs a standard algebraic reconstruction algorithm [11].

Tomographical setups relevant for experimental fluid dynamics significantly differ from those of medical imaging, where projections of the object to be reconstructed are acquired under a large range of angles, i.e. the image to be reconstructed is highly oversampled, while reconstruction algorithms are based on the regularization of the inverse Radon transform [15]. TomoPIV, on the other hand, employs only

Stefania Petra · Christoph Schnörr
University of Heidelberg, Dept. Math. and Computer Science, Image and Pattern Analysis Group
petra,schnoerr@math.uni-heidelberg.de

Andreas Schröder
German Aerospace Center (DLR), Göttingen
andreas.schroeder@dlr.de

W. Nitsche and C. Dobriloff (Eds.): Imaging Measurement Methods, NNFM 106, pp. 63–72.
springerlink.com

few projections due to both limited optical access to wind and water tunnels and cost and complexity of the necessary measurement apparatus. As a consequence, the reconstruction problem becomes severely ill-posed, and both the mathematical analysis and the design of algorithms fundamentally differ from the standard scenarios of medical imaging.

Our research work addresses two major open problems:

1. A crucial parameter for 3D fluid flow estimation from image measurements is particle density. This parameter also largely influences the tomographical reconstruction problem. Higher densities ease subsequent flow estimation by means of a *cross correlation technique* [19] and increase the resolution and measurement accuracy. However, higher densities also aggravate ill-posedness of the reconstruction problem. A thorough investigation of this trade-off is lacking.
2. Another major issue concerns problem size and computation time. 3D problems and, in particular, time-dependent 3D problems require considerable computational resources. Yet, adopting some ad hoc iterative reconstruction algorithm and terminating after few, sometimes even after a single(!) iteration, cannot be regarded as a solid strategy without further analysis of the setup and its essential parameters. A study of the reconstruction problem – optimization criteria and algorithms – helps to underpin proper design of technical systems.

The objective of our project is to address these two problems taking into account relevant developments in applied mathematics.

2 Related Work

TomoPIV [10] adopts a simple discretized model for an image-reconstruction problem known as the *algebraic image reconstruction* model [6], which assumes that the image consists of an array of unknowns (voxels), and sets up algebraic equations for the unknowns in terms of measured projection data. The latter are the pixel entries in the recorded 2D images that represent the integration of the 3D light intensity distribution $I(z)$ along the pixels line-of-sight L_i obtained from a calibration procedure. We consider an alternative to the classical voxel discretization and assume that the image I to be reconstructed can be approximated by a linear combination of Gaussian-type *basis functions* $\mathscr{B}_j$,

$$I(z) \approx \sum_{j=1}^{n} x_j \mathscr{B}_j(z), \quad \forall z \in \Omega \subset \mathbb{R}^3, \quad \text{of the form} \tag{1}$$

$$\mathscr{B}_j(z) = e^{-\frac{\|z-p_j\|_2^2}{2\sigma^2}}, \quad \text{for } z \in \mathbb{R}^3 : \|z-p_j\|_2 \le r, \tag{2}$$

or value 0, if $\|z-p_j\|_2 > r$, located at a Cartesian equidistant 3D grid p_j, $j = 1,\ldots,n$ within the volume of interest Ω. The choice of a Gaussian-type basis function is justified in the TomoPIV setting, since a particle projection in all directions results in

a so-called *diffraction spot* of approximately 3 pixel diameter. The i-th measurement obeys

$$b_i :\approx \int_{L_i} I(z)dz \approx \sum_{j=1}^{n} x_j \int_{L_i} \mathscr{B}_j(z)dz = \sum_{j=1}^{n} x_j a_{ij}\,, \tag{3}$$

where a_{ij} is the value of the i-th pixel if the object to be reconstructed is the j-th basis function. The main task is to estimate the weights x_j from the recorded 2D images, corresponding to basis functions and solve $Ax \approx b$.

The matrix A has dimensions $(\#\,\text{pixel} =: m) \times (\#\,\text{basis functions} = n)$. Since each row indicates those basis functions whose support intersect with the corresponding projection ray the projection matrix A will be sparse. Unfortunately there is no sparsity pattern which can be exploited.

Compressed sensing is a new measurement paradigm [3, 8] which seeks to capture the "essential" aspects of a high-dimensional object using as few measurements as possible. The basic principle is that sparse or compressible signals (i.e. can be well approximated with a small number of active basis functions) can be reconstructed *exactly* from a surprisingly small number of linear measurements, provided that the measurements satisfy an *incoherence* property (see, e.g. [5] for an explanation of incoherence).

A further remarkable result of Candès and Tao [4] is that if, for example, the rows of A are randomly chosen Gaussian distributed vectors, there is a constant C such that for a signal x with at most k nonzero entries and $m \geq Ck\log(\frac{n}{k})$, the solution x^* of

$$\min \|x\|_1 \text{ s.t. } Ax = b \tag{4}$$

will be exactly the original signal x with overwhelming probability.

Donoho and Tanner [9] have computed sharp reconstruction thresholds for Gaussian measurements, such that for any choice of sparsity k and signal size n, the required number of measurements m to recover x can be determined precisely.

Within our particular TomoPIV setting the size of x can be chosen arbitrarily large depending on the number of gridpoints where the basis functions are located, e.g. $n = O(10^9)$. The current measurement apparatus employs 4-6 camera of 1024^2 pixels each. The particle density is 0.05pp (particle/pixel), thus the underlying signal should be well approximated by $O(k)$ Gaussian basis functions, where $k = 0.05 \cdot 1024^2$. For a perfectly k compressible signal $k\log(\frac{n}{k}) = 4.3609 \cdot 10^5$ pixels would suffice, which corresponds to half of the number of pixels in one camera. Why are then still 4-6 camera currently in use? One answer is that the signal is only approximately $27 \cdot 0.05 \cdot 1024^2$ sparse when the 3D image is discretized in voxels in view of one particle diameter of 3 voxels. This corresponds to at least $7.1089 \cdot 10^6$ measurements (7 cameras) to obtain perfect recovery of the 500000 particles within the volume. Moreover, the measurement matrix A lacks the nice properties as incoherence which would guarantee perfect recovery, see [17] for a discussion on both voxel- and blob-based discretization scenarios. However the blob-based projection matrix yields considerably better reconstruction of a k-sparse vector due

to the fact that each basis function is intersected by more pixel "rays", a property relevant for the deterministic measurement matrix construction from [12].

3 Reconstruction Algorithms

3.1 Algebraic Reconstruction Techniques

The state-of-the-art of TomoPIV [10] is the *Multiplicative Algebraic Reconstruction Technique (MART)*. It was first proposed in [11] and is a *maximum entropy* algorithm, with a solution satisfying

$$\min f_E(x) := \sum_i x_i \log(x_i) \;\text{ s.t. }\; Ax = b\,,\; x \geq 0\,. \tag{5}$$

It applies only to systems in which $b > 0$ and A has only nonnegative entries. This applies to our scenario since all $a_{ij} > 0$ and zero or negligible measurements can be eliminated by a procedure leading to an "equivalent" feasible set $\mathscr{F}_r$ of reduced dimensionality, see [17, Prop. 2.1]. The authors in [2] proposed a further noticeable preprocessing procedure called *multiplicative line-of-sight estimation* to fix possible particle positions and thus to reduce considerably the dimension of the original system. MART converges linearly to a solution in $\mathscr{F}_r$ provided that it is nonempty, compare [16] and the reference therein.

The closely related *Simultaneous Multiplicative Algebraic Reconstruction Technique (SMART)* minimizes the Kullback-Leibler cross entropy $KL(Ax,y)$ over the nonnegative orthant and converges, for consistent projection equations, to that member of $\mathscr{F}_r$ for which the cross-entropy distance to the initial vector $KL(x,x_0)$ is minimized.

The iterative method *SART (Simultaneous Algebraic Reconstruction Technique)* of Andersen and Kak, see [1], was successfully applied to tomographic particle image reconstruction in [2]. SART writes as

$$x^{k+1} = x^k + \lambda V A^T W (b - Ax^k)\,, \tag{6}$$

where $\lambda \in (0,2)$, V and W diagonal matrices defined by

$$V := \operatorname{diag}\Big(\frac{1}{A_{+1}},\ldots,\frac{1}{A_{+n}}\Big) \quad \text{and} \quad W := \operatorname{diag}\Big(\frac{1}{A_{1+}},\ldots,\frac{1}{A_{m+}}\Big) \tag{7}$$

with $A_{+j} := \sum_{i=1}^m a_{ij}$ and $A_{i+} := \sum_{j=1}^n a_{ij}$. SART was developed as a major refinement of the *Algebraic Reconstruction Technique (ART)* [11], a reincarnation of Kaczmarz's [14] method of alternating projections. The convergence of SART towards a solution of the weighted least squares problem $\min \|W^{\frac{1}{2}}(Ax-b)\|$ was established in [13]. The likewise parallelizable method due to Cimmino was recently reconsidered by the authors [18] in the context of TomoPIV.

All the methods above have the distinctive feature that they are *row action method* [6] and have demonstrated effectiveness on huge problem instances but suffer from the slow convergence rate.

They return a sufficiently good approximation x^k after few iterations [10, 2] for sufficiently small particle densities. In practice, subsequent iterations do not improve the quality of the computed solution, however, but actually result in increasingly worse approximations. This is because the iterates become completely dominated by the errors inevitably present in the data.

3.2 ℓ_1-Minimization and Linear Programming

The ℓ_1-minimization problem (4), known also as *basis pursuit* [7], can be recast as a linear program and then solved by conventional linear programming solvers. However, such solvers are not suited for large-scale matrices A arising in our application. Usually only matrix-vector operations involving A and A^T are feasible. A recent method motivated by the compressed sensing context is the *Bregman Iterative Algorithm* [20]. The name is due to the fact that it employs a Bregman iterative regularization, which gives an accurate solution after solving only a very small number of instances of the unconstrained problem

$$\min_x \|x\|_1 + \frac{1}{2}\|Ax - b^k\|_2^2 \tag{8}$$

by a fast *fixed-point continuation (FPC)* solver that is based solely on simple operations for solving the above unconstrained subproblem. The algorithm starts with the initialization $b^0 := 0$, $x^0 := 0$ and then for $k = 0, 1, \ldots$ writes

$$b^{k+1} := b^k + (b^k - Ax^k), \tag{9}$$

$$x^{k+1} := \text{argmin}_x \|x\|_1 + \frac{1}{2}\|Ax - b^{k+1}\|_2^2 \,. \tag{10}$$

It is equivalent to the well-known augmented Lagrangian method (also known as the method of multipliers), thus constraints can also be included. It is shown in [20] that the method yields a global optimum in a finite number of iterations.

4 Design and Evaluation Criteria

4.1 Design Criteria

Assuming there could be several possible solutions, the common practice is the definition of an optimization problem of the form

$$\min f(x) \text{ s.t. } Ax = b, \ [x \geq 0,] \tag{11}$$

where f measures the quality of the candidate solutions. Possible choices for this penalty could be:

- entropy measures as in the case of MART and SMART, respectively.
- ℓ_p-norms for various p in the range $[0,\infty)$. Popular choices are:
  - ℓ_2-minimization is the method of least squares. It finds out of all possible solutions the one of least energy and can be easy carried out (e.g. ART, Cimmino). Unfortunately, this minimizer is not guaranteed at all to be sparse. If we take nonnegativity into account this situation may change dramatically.
  - ℓ_1-minimization is convex and can be solved in reasonable time by convex programming techniques.The important question in this connection is whether the method actually can recover the original k-sparse signal x.
  - ℓ_0-minimization enforces sparsity and selects out of all possible solutions which match the given data selects the sparsest one. This regularization approach was considered by the authors in [18] in the context of TomoPIV, but appears to be less practical in the real TomoPIV setting because several(!) linear programs for one volume reconstruction have to be solved.

We discussed above (compressed sensing) that the choices $p = 0$ and $p = 1$ may lead to the same reconstruction provided it is sparse enough. This equivalence phenomenon depends on properties of the measurements matrix A. They are known for classes of matrices none of which covers our application area, however.

Clearly, if the set of feasible solutions $\mathscr{F} := \{x | Ax = b, x \geq 0\}$ contains only a single element, then all the above choices of f will lead to the same solution. This is exactly what happens when a sufficiently sparse solution exists. In this case we can apply any efficient method designed to find the element in $\mathscr{F}$.

4.2 Evaluation Criteria

We wish to inspect empirical bounds on the required sparsity that guarantee exact reconstruction and critical parameter values that yield a performance similar to the settings considered in compressed sensing (e.g. [9]).

These parameter values allow us to answer the question how sparse a vector should be (particle density) such that ℓ_0 can be solved by ℓ_1-minimization, linear programming or quadratic programming with constraints.

Consider a matrix $A \in \mathbb{R}^{m\times n}$, the undersampling ratio $\delta = \frac{m}{n} \in (0,1)$ and the sparsity as a fraction of m, $k = \rho m$, for $\rho \in (0,1)$. This phase transition $\rho(\delta)$ as function of δ indicates the necessary undersampling ratio δ to recover a k-sparse solution with overwhelming probability. More precisely, if $\|x\|_0 \leq \rho(\delta)\cdot m$, then with overwhelming probability the ℓ_0-problem of finding the k-sparsest solution can be solved by ℓ_1-minimization. For Gaussian matrices there are precise values of $\rho(\delta)$, see [9], which can be computed analytically.

Relevant for TomoPIV is the setting as $\delta \to 0$ and $n \to \infty$, that is severe undersampling. Then a *strong asymptotic threshold* $\rho_S(\delta) \approx |2e\log(\delta)|^{-1}$ and *weak asymptotic threshold* $\rho_W(\delta) \approx |2\log(\delta)|^{-1}$ holds for Gaussian matrices. The weak

thresholds says that ℓ_0/ℓ_1-equivalence typically holds while for the strong one equivalence holds for all $\rho_S(\delta)\cdot m$-sparse signals.

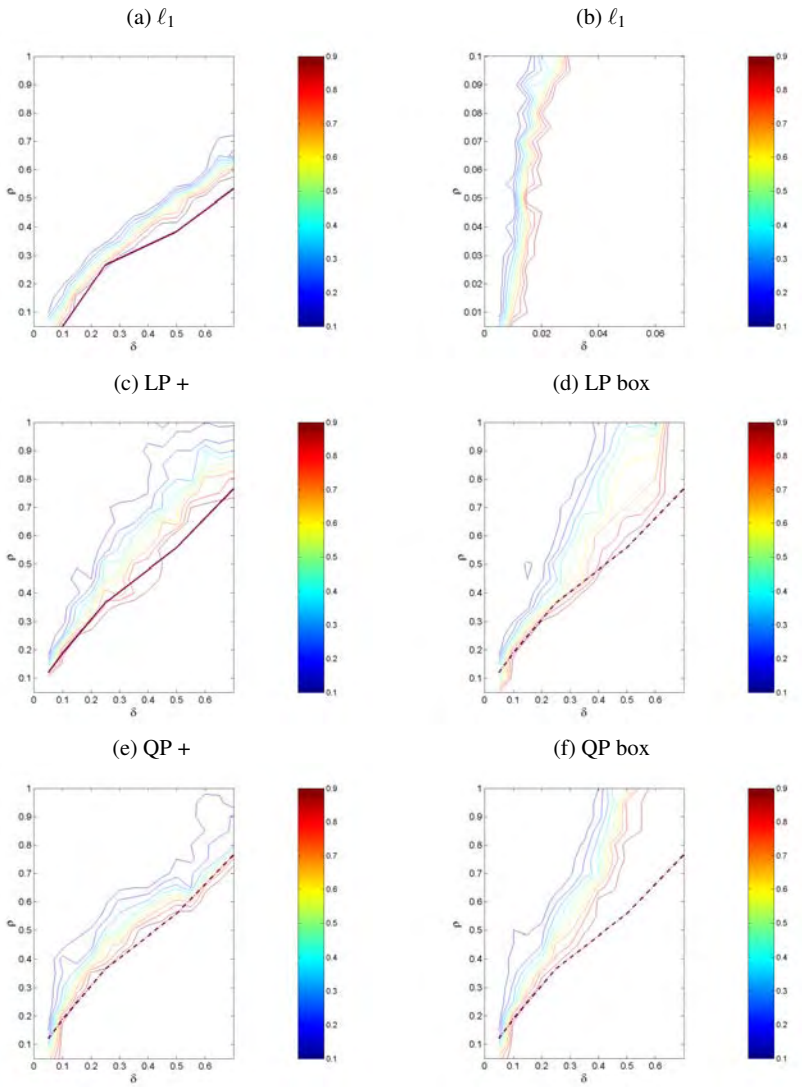

Fig. 1 Probability of correct recovery of a random particle distribution that can be expressed with exactly k basis functions as a function of $\delta = \frac{m}{n}$, $n = 2000$ and $k = \rho m$. The thick curve $\rho(\delta)$ depicts a phase transition of ℓ_1-minimization (a) and linear programming (c)-(f) to find the k-sparsest solution, but for Gaussian random matrices, see [9]. Figure (b) shows a "zoom in" of (a): here we have chosen $n = 200000$. We believe that $\rho(\delta) \approx |2\log(C\delta)|^{-1}$ as $\delta \to 0$ similar to the analytic curve for Gaussian matrices presented in [9]. The right n-dependent value of constant C is a subject of our current research

5 Numerical Results

Although the projection matrices within the TomoPIV setting do not satisfy the nice properties of Gaussian measurement matrices, we observed critical parameter values similar to those for Gaussian matrices. We generated a 100×20 grid at which we

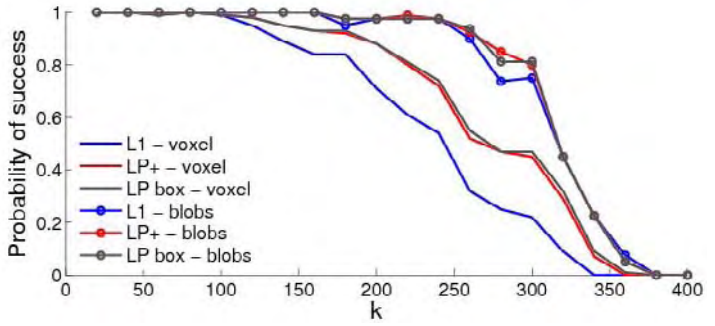

Fig. 2 Empirical probability of exact reconstruction of an increasing number k of "particles" by means of an $3 \cdot 32^2 \times 32^3$ projection matrix from 3 orthogonal projections for both voxel and blob scenarios. Substantially more particles are reconstructed for the blobs-based discretization matrix for all three methods of choice: ℓ_1-minimization (blue), linear programming with positivity constraints only (red), linear programming with box constraints (black)

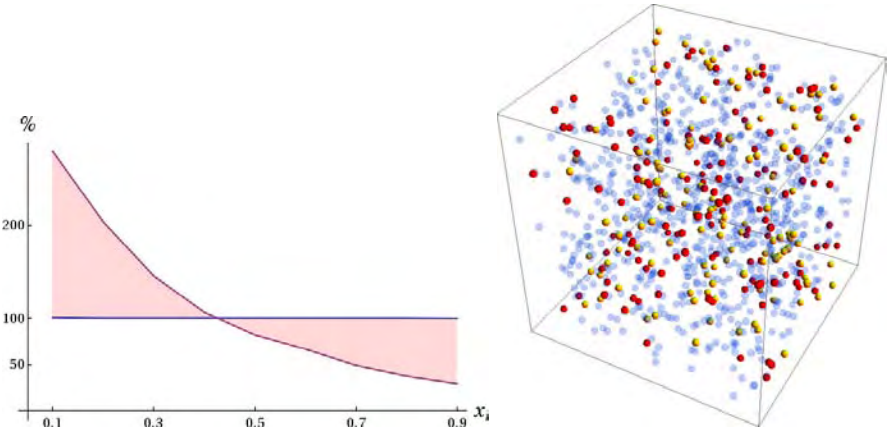

Fig. 3 Reconstruction experiment for 1000 particles in a small cube from 3 orthogonal projections, using SART reconstruction after reducing the system (cf. section 3.1) and the Bregman iterative algorithm (section 3.2). The iteration was terminated after convergence for the latter algorithm, and after a comparable runtime for SART. **Left panel.** Number of reconstructed particles corresponding to the coefficients x_i exceeding a threshold $\in [0.1, 0.9]$ for SART (red) and our approach (blue). SART may return far too many particles ($> 200\%$) or too less, whereas our approach always returned the exact reconstruction. **Right panel.** Choosing a threshold for which SART returns the correct number of particles yields both missing particles (yellow) and additional ghost particles (red)

located $n = 2000$ Gaussian basis functions. First a big projection matrix was generated resulting from parallel projections at angles $(-60^o, -55^o, \ldots, 0^o, 5, 10, \ldots, 60^0)$. Then $m = \delta n$ random rows were selected to compute the right hand side measurement vector. The plane $(\delta, \rho) = [0, 0.7] \times [0, 1]$ was divided in a 20×20 mesh, and for each point 50 random problem instances were generated. The empirical probability that the approaches presented above correctly recover a $k = \rho m$-sparse solution for each parameter combination is presented in Fig. 1 (a), (c)-(f). For the asymptotic scenario see Fig. 1 (b), computed for the bigger value $n = 200000$. A threshold-effect is clearly visible in all figures exhibiting parameter regions where the probability of exact reconstruction is close to one.

The advantage of using blob-based volume discretizations is demonstrated in Figure 2. Figure 3, finally, illustrates the comparison of our approach with the SART iteration used in [2].

6 Conclusions

The reconstruction of a relatively dense particle distribution in a volume from few projections can be modeled as finding the sparsest solution of an underdetermined linear system of equations, because the original particle distribution can be well approximated with only a very small number of active basis functions relative to the number of possible particle positions in a 3D domain. In general the search for the sparsest solution is intractable (NP-hard), however. The newly developed theory of Compressed Sensing showed that one can compute via ℓ_1-minimization or linear programming the sparsest solution for underdetermined systems of equations provided they satisfy certain properties, which unfortunately do not hold for our particular scenario. Still, we showed empirically in the present work that there are thresholds on sparsity (i.e. density of the particles) depending on the numbers of measurements (recording pixel in the CCD arrays), below which these methods will succeed and above which they fail with high probability. When they succeed they yield near perfect reconstructions (without any ghost-particles). Theoretically, constrained versions of several algebraic reconstructions techniques will also converge to the original solution for very sparse scenarios. Due to their slow convergence they are outperformed by an augmented Lagrangian method for ℓ_1-minimization, however, that provides considerably better particle reconstructions than the currently used methods.

Acknowledgements. The authors would like to thank the German Science Foundation (DFG) for supporting this work within the priority research program 1147, “Imaging Measurement Methods for Flow Analysis”, under grant SCHN 457/10-1. The authors enjoyed collaboration, fruitful discussions and data exchange with many partners of the priority program, including Volker Beushausen, Christoph Brücker, Octavian Frederich, Christoph Garbe, Rainer Hain, Bernd Jähne, Christian Kähler, Hans-Gerd Maas, Wolfgang Nitsche, Holger Nobach, Torsten Putze, Frank Thiele, Cam Tropea, and Rüdiger Westermann.

References

1. Andersen, A., Kak, A.: Simultaneous Algebraic Reconstruction Technique (SART): A Superior Implementation of ART. Ultrasonic Imaging 6, 81–94 (1984)
2. Atkinson, C.H., Dillon-Gibbons, C.J., Herpin, S., Soria, J.: Reconstruction Techniques for Tomographic PIV (Tomo-PIV) of a Turbulent Boundary Layer. In: 14th Int. Symp. on Applications of Laser Techniques to Fluid Mechanics, Lisbon (2008)
3. Candès, E., Romberg, J., Tao, T.: Robust uncertainty principles: Exact signal reconstruction from highly incomplete frequency information. IEEE Trans. on Information Theory 52, 489–509 (2006)
4. Candès, E., Tao, T.: Near optimal signal recovery from random projections: Universal encoding strategies? IEEE Trans. on Information Theory 52, 5406–5425 (2006)
5. Candès, E., Romberg, J.: Sparsity and incoherence in compressive sampling. Inverse Problems 23, 969–985 (2007)
6. Censor, Y., Zenios, S.A.: Parallel Optimization: Theory, Algorithms and Applications. Oxford University Press, New York (1997)
7. Chen, S.S., Donoho, D., Saunders, M.A.: Atomic decomposition by basis pursuit. SIAM J. Sci. Comput. 20, 33–61 (1998)
8. Donoho, D.: Compressed sensing. IEEE Trans. on Information Theory 52, 1289–1306 (2006)
9. Donoho, D., Tanner, J.: Thresholds for the recovery of sparse solutions via ell-1 minimization. In: Conf. on Information Sciences and Systems (2006)
10. Elsinga, G., Scarano, F., Wieneke, B., van Oudheusden, B.: Tomographic particle image velocimetry. Exp. Fluids 41, 933–947 (2006)
11. Gordon, R., Bender, R., Herman, G.T.: Algebraic reconstruction techniques (ART) for three-dimensional electron microscopy and X-ray photography. J. Theor. Biol. 29, 471–481 (1970)
12. Indyk, P.: Explicit constructions for compressed sensing of sparse signals. In: Symp. on Discrete Algorithms (2008)
13. Jiang, M., Wang, G.: Convergence of the simultaneous algebraic reconstruction technique (SART). IEEE Trans. on Image Processing 12, 957–961 (2001)
14. Kaczmarz, S.: Angenäherte Auflösung von Systemen linearer Gleichungen. Bull. Acad. Polonaise Sci. et Lettres A, 355–357 (1937)
15. Natterer, F., Wübbeling, F.: Mathematical Methods in Image Reconstruction. SIAM, Philadelphia (2001)
16. Petra, S., Schnörr, C., Schröder, A., Wieneke, B.: Tomographic Image Reconstruction in Experimental Fluid Dynamics: Synopsis and Problems. In: Romane, A., Bucuresti (eds.) Mathematical Modelling of Environmental and Life Sciences Problems (2007)
17. Petra, S., Schröder, A., Wieneke, B., Schnörr, C.: On sparsity maximization in tomographic particle image reconstruction. In: Rigoll, G. (ed.) DAGM 2008. LNCS, vol. 5096, pp. 294–303. Springer, Heidelberg (2008)
18. Petra, S., Popa, C., Schnörr, C.: Extended and Constrained Cimmino-type Algorithms with Applications in Tomographic Image Reconstruction. IWR preprint (2008), `http://www.ub.uni-heidelberg.de/archiv/8798/`
19. Scarano, F., Riethmüller, M.L.: Advances in iterative multigrid PIV image proccesing. Exp. Fluids 29, 51–60 (2000)
20. Yin, W., Osher, S., Goldfarb, D., Darbon, J.: Bregman Iterative Algorithms for l1-Minimization with Applications to Compressed Sensing. SIAM J. Imaging Sciences 1, 143–168 (2008)

Tomographic PIV for Investigation of Unsteady Flows with High Spatial and Temporal Resolution

Reinhard Geisler, Andreas Schröder, Karsten Staack, Jürgen Kompenhans, Gerrit E. Elsinga, Fulvio Scarano, Christian Poelma, Jerry Westerweel, Bernhard Wieneke, and Dirk Michaelis

Abstract. Particle Image Velocimetry (PIV) has been used for instantaneous recordings of velocity fields within a volume of a flow. The volume information was gained by multiple cameras and a tomographic approach based on the Multiplicative Algebraic Reconstruction Technique (MART). Volume cross-correlation enabled the calculation of instantaneous 3D-3C velocity vectors. The usability of this measurement tool has been proven in different applications including setups at wind and water tunnels.

1 Introduction

Particle Image Velocimetry (PIV) in a stereo setup is now a standard tool for flow field measurements in wind tunnels, capable of determining all three components of the velocity vectors within a plane. However, up until now, no universal measurement tool has been established for capturing the instantaneous velocity information within a whole volume. On the other hand, the requirement for such a tool for the investigation of unsteady three-dimensional flow phenomena such as turbulence or

Reinhard Geisler · Andreas Schröder · Karsten Staack · Jürgen Kompenhans
Institut für Aerodynamik und Strömungstechnik, Deutsches Zentrum für Luft- und Raumfahrt e.V. (DLR), Bunsenstraße 10, 37073 Göttingen, Germany
Reinhard.Geisler@dlr.de

Gerrit E. Elsinga · Fulvio Scarano
Department of Aerospace Engineering, Delft University of Technology, P.O. Box 5058, 2600 GB Delft, The Netherlands

Christian Poelma · Jerry Westerweel
Laboratory for Aero & Hydrodynamics, Delft University of Technology, Leeghwaterstraat 21, 2628 CA Delft, The Netherlands

Bernhard Wieneke · Dirk Michaelis
La Vision GmbH, Anna-Vandenhoeck-Ring 19, 37081 Göttingen, Germany

W. Nitsche and C. Dobriloff (Eds.): Imaging Measurement Methods, NNFM 106, pp. 73–82.
springerlink.com

flow separation is growing. Depending on the specific experimental conditions, different techniques can provide more or less satisfactory results.

Planar PIV can be extended to volume-resolving PIV by means of scanning systems [1]. Since the process of scanning the observation plane through the volume takes some time, this method can only be applied to steady, periodic or very slowly varying unsteady flows. For fast unsteady flows limited depth information can be obtained with multi-plane setups, where only a few parallel planes are recorded simultaneously, but are separable by, for example, the polarisation state or the wavelength of the light.

Holographic methods are able to capture the instantaneous velocity information within a whole volume [6]. Using high-resolution photochemical plates, a volume of medium size can be captured with high spatial resolution. However, temporal resolution is very limited and can be achieved only with complex optical setups [4]. On the other hand, electronic image sensors (CCD, CMOS) can provide temporal resolution, but such a recording setup is applicable only for small volumes and with a limited spatial resolution.

Photogrammetric methods such as particle tracking [7] [8] use setups similar to stereo-PIV extended to a larger number of cameras (typically 4). The depth information is gained from triangulation of each individual particle. Like planar PIV, photogrammetry is scalable both in space and time to match a wide range of requirements. However, the necessary particle matching process requires low seeding density and thus strictly limits the spatial resolution.

Using the same (or nearly the same) setup, data can also be processed in a three-dimensional PIV evaluation. This is possible using an algebraic reconstruction process known, for example, from medical x-ray tomography [5]. In its adaptation to PIV [2], the Multiplicative Algebraic Reconstruction Technique (MART) can reconstruct the intensity distribution within a volume from a number of camera images taken from different viewing directions.

2 Tomographic PIV — Fundamentals

Tomographic PIV is based on the simultaneous observation of particles in a measurement volume from different directions (typically 4). Using Scheimpflug correction optics and small camera apertures, the images are kept nearly in-focus within the measurement volume. To calibrate the imaging system, a calibration grid is recorded in different parallel planes throughout the volume. This calibration is used to calculate mapping functions from the real world space to the camera images and vice versa. A volume-self-calibration based on particle triangulation and statistical evaluation is used to improve the accuracy of these mapping functions to an order of 0.1 pixels [12].

For the recording of particles following the flow, a pulsed laser illuminates the complete observation volume. As in planar PIV, two laser pulses in fast succession deliver two images. Prior to further processing, the images undergo a pre-processing stage: Typically a minimum image is subtracted, the intensity is

normalised and a Gaussian filter may be applied to suppress noise. Using the mapping functions derived from the calibration, the images of the different cameras are numerically projected back into the three dimensional space by the MART algorithm [2]. The result of this iterative process is a three-dimensional image of the volume, where every voxel (3-dim. pixel) contains the light intensity calculated for its specific location. Since this is the exact three-dimensional analogue to the more usual two-dimensional PIV image, the velocity vectors can be determined with the well-established multi-grid cross correlation and image deformation algorithms extended to their three-dimensional formulation. Finally, in a post-processing step spurious vectors are detected and replaced by interpolated values.

Similar to the problem with ambiguity in photogrammetry, MART can reconstruct bright voxels where no real particles are present. However, in tomographic PIV these 'ghost'-particles do not severely affect the velocity vector result, as these particles are not correlated in time and thus will increase correlation noise only. Provided this noise stays within a certain limit the correct correlation peak can nevertheless be detected.

In the present studies the LaVision software DaVis 7.3 and 7.4 was used for data processing.

3 Application I: Time-Resolved Tomographic PIV in a Wind Tunnel

In a feasibility study, tomographic PIV has been applied to time-resolved recordings in a measurement performed at the 1 m wind tunnel at DLR Göttingen. The 'Leit-experiment', a finite cylinder on a flat plate, as well as a turbulent spot in a laminar boundary layer flow over a flat plate were investigated.

3.1 Setup

A flat glass plate with an elliptical leading edge is mounted horizontally in the open test section of the wind tunnel (Fig. 1a). On the upper side of the plate a boundary layer flow with a free stream velocity of $U_\infty = 7$ m/s is established. It is adjusted for a zero pressure gradient by a trailing flap at the end of the plate. Olive oil droplets of about 1.5 µm diameter are fed into the flow as tracer particles. The measurement volume of $40 \times 40 \times 20\,\text{mm}^3$ is located right above the surface of the plate 530 mm downstream of the leading edge. It is illuminated by a high repetition rate dual-cavity laser (Lee LDP-200 MQG, Nd:YAG SHG) at a pulse rate of 5 kHz and a total pulse energy of 21 mJ. After passing through a beam expander the laser beam enters an arrangement of nearly parallel mirrors on opposite ends of the plate. The mirrors reflect the beam back and forth throughout the measurement volume thus increasing the effective intensity by a factor of around 10 with respect to a single-pass system. Four Photron APX high-speed cameras equipped with Nikon $f = 100$ mm lenses at an aperture setting of $f_\# = 8$ are used to record the volume from below the plate (Fig. 1b). The cameras are set to a resolution of 768×768 pixels and to a frame rate of 5 kHz.

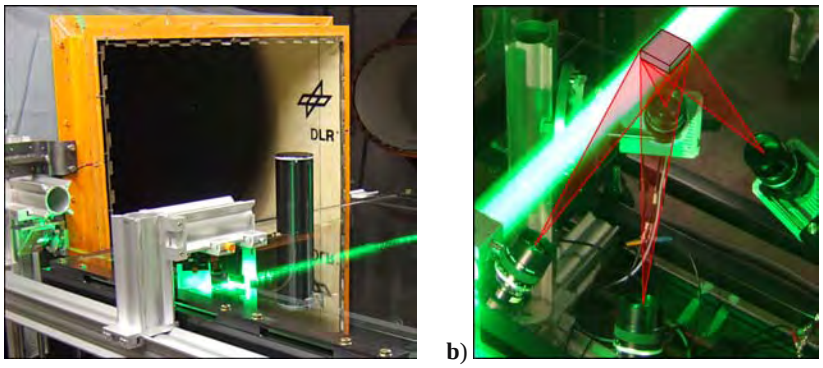

Fig. 1 Setup at the 1 m wind tunnel at DLR Göttingen: (**a**) Finite cylinder 'Leitexperiment' and volume light sheet on the flat glass plate in front of the wind tunnel nozzle; (**b**) View through the glass plate upon the arrangement of the cameras below and the alignment to the observation volume above the glass plate (*red sketch*)

3.2 Results

In a first experiment, a finite cylinder of 120 mm diameter and 240 mm height, the so-called 'Leitexperiment', is mounted 350 mm upstream of the observed volume and 180 mm downstream of the leading edge. The flow has been tripped just downstream of the leading edge to generate a turbulent boundary layer flow along the plate. An example evaluation of the captured time-resolved velocity vector field is depicted in Fig. 2. Although the flow structures here are large with respect to the measurement volume, their local temporal evolution is clearly observable.

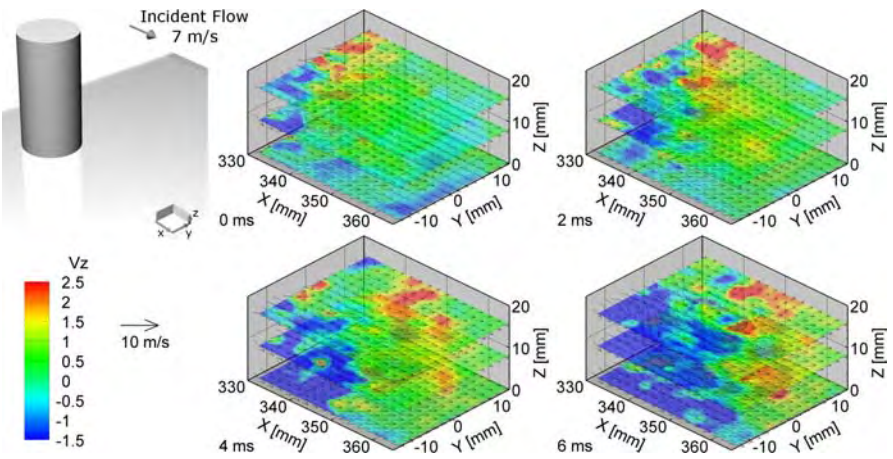

Fig. 2 Tomographic PIV results from the 'Leitexperiment' (finite cylinder at $x = 0$ mm, $y = 0$ mm) with a recording time resolution of 200 µs. Here: Four selected snapshots with a time separation of 2 ms are shown. Depicted are three selected planes from the velocity vector field

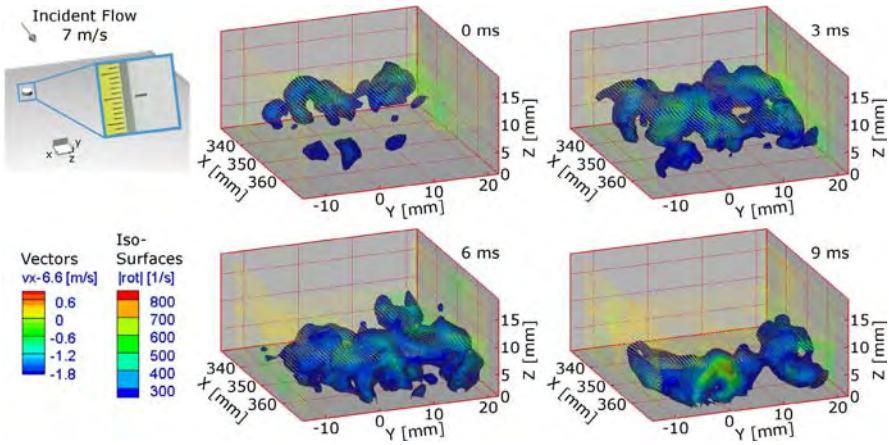

Fig. 3 Tomographic PIV results from a turbulent spot, 350 mm downstream of the injection slit with a recording time resolution of 200 µs. Here: Four selected snapshots with a time separation of 3 ms are shown. Depicted are selected planes of velocity vectors and the iso-surfaces of the vorticity

In a second experiment, a turbulent spot is investigated. At the former location of the cylinder, a slit of $2 \times 0.5\,\text{mm}^2$ is inserted into the flat plate. The plate is prepared to keep the boundary layer flow laminar. Through the slit a flow pulse of 1.5 ms duration is injected into the flow by a pressure chamber loudspeaker. A turbulent spot is formed which grows in stream- and span-wise directions while travelling downstream. Around 70 ms after injection, the spot is observed passing the measurement volume (Fig. 3). The measurement volume is well-adapted to the dimensions of the passing spot: Flow structures such as hairpin-like vortices can be identified and their time-dependent development can be traced through the measurement volume [9].

4 Application II: Investigation of a Free Turbulent Jet Air Flow

In time-resolved measurements the spatial resolution is limited due to the available sensor size and pixel clock of the cameras. Hence a measurement with high spatial resolution was carried out by capturing statistically independent double-exposure images using four cameras of 4 mega pixels resolution. A free turbulent jet air flow of a nozzle was investigated.

4.1 Setup

The tomographic setup consists of four pco.2000 Cameras (2048×2048 pixels) arranged in a pyramidal geometry below the observation volume (Fig. 4). Applying the Scheimpflug-condition, the cameras are equipped with $f = 135\,\text{mm}$ Zeiss lenses at an aperture setting of $f_\# = 16$. A quadruple Big Sky 200 laser is used for illumination. By triggering two of the oscillators at the same time, two exposures of each

Fig. 4 Arrangement of the four pco.2000 cameras mounted under Scheimpflug-condition below the nozzle. The Big Sky CFR 200 laser system on the left illuminates the measurement volume in front of the nozzle

about 350 mJ pulse energy are available. The laser beam is expanded asymmetrically by a factor of 7.5 in the horizontal and 3 in the vertical direction. Limited by an aperture to an area of 48×20 mm, the expanded beam passes through the measurement volume and is then reflected back by a slightly tilted mirror. After returning through the light-sheet optics, the beam is coupled out by a mirror and finally dumped. This optical layout not only nearly doubles the effective intensity, but also leads to a comparable brightness of all the particle images due to the scattering properties (forward / backward) for all four cameras being similar.

4.2 Results

The investigated flow is the free turbulent jet air flow of a nozzle (diameter $D = 15$ mm) mounted perpendicularly to the laser light sheet and operated at a Mach number of $M = 0.2$ and a Reynolds number of $Re = 70000$. Since the recordable volume can only cover 48 mm along the flow axis, the nozzle is translated in steps of 45 mm and the flow at different distance ranges from the nozzle is thus recorded, one after another. For each distance 10 runs of 75 double images were recorded. DEHS (Diethylhexyl Sebacate) droplets of around 1 µm diameter acting as tracer particles are fed into the settling chamber of the nozzle at the start of each run. The settling chamber pressure is kept constant to get a Mach number of 0.2 at the nozzle exit. For the tomographic reconstruction, the MART algorithm was used with 3 iterations. The multigrid cross correlation led to a final correlation window cube of 64^3 voxels, which at a voxel size of 41 µm corresponds to a size of 2.6 mm. At an overlap of 75%, the vector spacing is 0.66 mm (Fig. 5). Different aspects of the turbulent

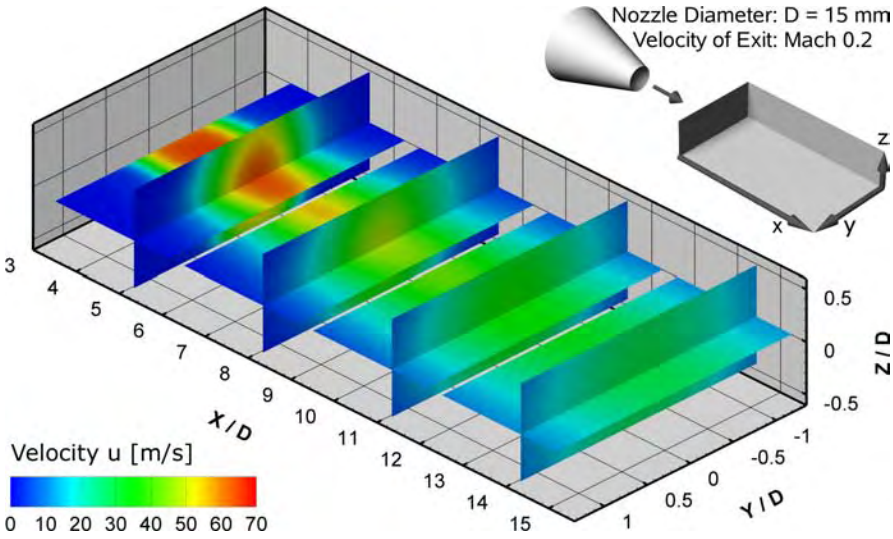

Fig. 5 Tomographic PIV results from a free turbulent jet air flow. Depicted is the velocity component in main flow direction (u) from selected planes of the averaged velocity vector field

flow have been investigated in the instantaneous and averaged results; momentum exchange, probability density functions, spatial correlations, vortex topology and self-similarity [11].

5 Application III: Investigation of a Turbulent Boundary Layer in a Water Tunnel

A joint test campaign was launched for the investigation of a turbulent boundary layer (TBL) flow in the water tunnel at TU Delft. Flow quality and boundary layer properties are verified by a 2D PIV measurement. The time-resolved tomographic PIV results give valuable insight into the complete flow topologies within the TBL.

5.1 Setup

In the $60 \times 60\,\text{cm}^2$ test section of the water tunnel at TU Delft a 2.5 cm thick acrylic glass plate of $80 \times 250\,\text{cm}^2$ was vertically mounted, dividing the test section at 25% of its width. At a downstream distance of 15 cm from the elliptical leading edge the flow was tripped by a span-wise zig-zag band. The measurement area is located a further 194 cm downstream inside the fully developed turbulent boundary layer (TBL). The TBL flow is adjusted for a stream-wise zero pressure gradient by a trailing edge flap. Polyamide tracer particles of 56 µm average diameter are fed into the water.

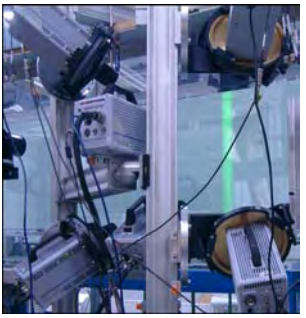

a)

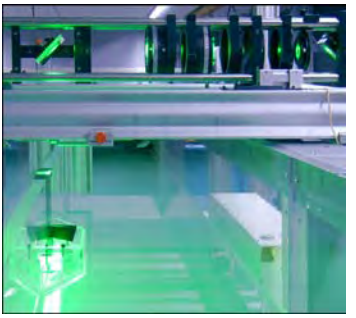

b)

Fig. 6 Setup at the water tunnel at TU Delft: (**a**) Arrangement of the six high-speed cameras imaging the laser light sheet; (**b**) Light sheet forming optics on top of the water tunnel and acrylic glass 'boat' on the surface of the plate for a smooth transition of the light sheet into the water

The time-resolved volumetric measurement was performed using six Photron high-speed cameras at a frame rate of 1000 Hz and a resolution of 1024×1024 pixels. From the side of the tunnel, looking through the tunnel wall, the water and the flat plate itself, they record the particles in the turbulent boundary layer over an area of $63 \times 68\,\mathrm{mm}^2$ and a thickness of 15 mm, starting at the surface of the flat plate (Fig. 6a). The camera lenses (four Zeiss $f = 100\,\mathrm{mm}$ and two Nikon $f = 105\,\mathrm{mm}$) are operated at an aperture setting of $f_\# = 11$ to ensure sufficiently sharp particle images throughout the volume. Where necessary, Scheimpflug correction was applied. An acrylic glass window 'boat' is attached to the plate above the measurement area to improve the optical access through the free water surface. Using this window, the volume is illuminated from the top of the water tunnel by the expanded beam of a Quantronix Darwin-Duo Nd:YLF laser with a maximum of 2×25 mJ/pulse at 1 kHz repetition rate (Fig. 6b). A programmable timing unit (LaVision PTU) generates the 1 kHz signal which triggers both oscillators at the same time. In phase with this, a frame synchronising signal is generated and fed in parallel to all cameras. An additional signal triggers the recording of all cameras at the same frame. Data is recorded in a time series of 2048 images at 1 kHz making a total observation time of 2 seconds.

The MART algorithm with 5 iterations is applied to gain a reconstructed volume of $734 \times 176 \times 793$ cubic voxels of 85.9 µm size. The subsequent PIV evaluation is done in steps of 2 ms with the multi-grid evaluation resulting in a final interrogation window size of 32^3 voxels (corresponding volume: $2.75 \times 2.75 \times 2.75\,\mathrm{mm}^3$). At an overlap of 75% the volume is thus represented by a total of 200376 ($92 \times 22 \times 99$) velocity vectors spaced at intervals of 0.687 mm.

5.2 Results

The test campaign is designed as a fundamental experiment for the characterisation of the turbulent boundary layer. Hence, a 2D-2C PIV measurement was performed

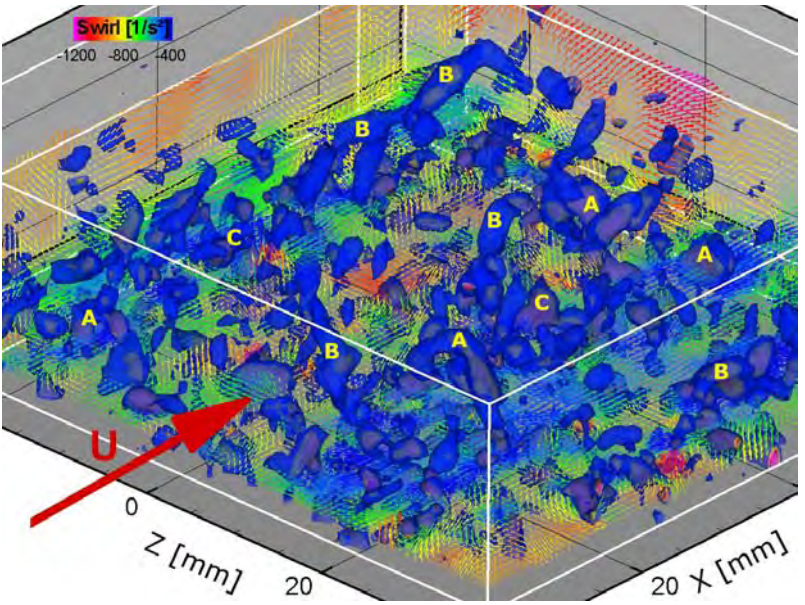

Fig. 7 Instantaneous 3D-velocity volume extracted from a time series depicting flow structures by iso-surfaces of swirl-strength (λ_2) and selected velocity planes ($u - u_{\mathrm{ref}}$ colour coded, $U = 0.53$ m/s). Hairpin-like (A), cane (B) or arbitrary (C) vortices can be identified

first to verify the flow quality and characterise the boundary layer (details in [10]). The free stream velocity is $U = 0.53$ m/s with a turbulence level below 0.5%. The thickness of the turbulent boundary layer is 38 mm corresponding to $Re_\Theta \sim 2460$ based on momentum thickness at the measurement volume.

Subsequently, the tomographic PIV measurement was performed. In the snapshots of the velocity vector volumes (Fig. 7) vortical structures such as hairpin-like (A), cane (B) or arbitrary (C) vortices can be identified from the iso-surfaces of the swirl-strength value λ_2. With the adopted colour coding of the vectors to represent the velocity $u - u_{\mathrm{ref}}$, where low and high values are represented by blue and red colours, respectively, speed streaks are visible. Further evaluation is carried out using space-time-correlations, conditional averaging and performing a comparison in Eulerian and Lagrangian reference frames [10].

6 Conclusion

Tomographic PIV measurements have been performed in different applications encompassing wind and water tunnel test campaigns. The possibility of instantaneous recordings within complete volumes allows the investigation of complex three-dimensional unsteady flows. From the first feasibility studies, tomographic PIV has been developed to a valuable tool, especially in turbulence research. Acquired data

provide a deep insight into turbulent processes and serve as a validation base for computational fluid dynamics.

Acknowledgements. The present work was supported by the German Science Foundation DFG [3], TU Delft, LaVision and DLR internal funding.

References

1. Brücker, C.: 3-D scanning-particle-image-velocimetry: Technique and application to a spherical cap wake flow. Applied Scientific Research 56(2–3), 157–179 (1996)
2. Elsinga, G.E., Scarano, F., Wieneke, B., van Oudheusden, B.W.: Tomographic particle image velocimetry. Exp. Fluids 41(6), 933–947 (2006)
3. Geisler, R.: Entwicklung und Anwendung von Messsystemen der PIV zur räumlich bzw. zeitlich hochauflösenden Erfassung von Geschwindigkeitsfeldern instationärer Strömungen in Windkanälen. Final report, DFG reference number Ko 1718/5-1 (2008)
4. Hentschel, W., Lauterborn, W.: New speed record in long series holographic cinematography. Appl. Opt. 23(19), 3263–3265 (1984)
5. Herman, G.T., Lent, A.: Iterative reconstruction algorithms. Comput. Biol. Med. 6, 273–294 (1976)
6. Hinsch, K.: Holographic particle image velocimetry. Meas. Sci. Technol. 13, R61–R72 (2002)
7. Maas, H.G., Gruen, A., Papantoniou, D.: Particle tracking velocimetry in three-dimensional flows. Exp. Fluids 15(2), 133–146 (1993)
8. Pereira, F., Gharib, M., Dabiri, D., Modarress, D.: Defocusing digital particle image velocimetry: a 3-component 3-dimensional dpiv measurement technique. application to bubbly flows. Exp. Fluids 29(7), S78–S84 (2000)
9. Schröder, A., Geisler, R., Elsinga, G.E., Scarano, F., Dierksheide, U.: Investigation of a turbulent spot and a tripped turbulent boundary layer flow using time-resolved tomographic PIV. Exp. Fluids 44(2), 305–316 (2008)
10. Schröder, A., Geisler, R., Wieneke, B., Elsinga, G.E., Scarano, F.: Lagrangian and eulerian views into a turbulent boundary layer flow using time-resolved tomographic PIV. In: Proc. of the 14th Int. Symposium on Applications of Laser Techniques to Fluid Mechanics, Lisbon, Session 7.1.5 (2008)
11. Staack, K.: Untersuchung von kohärenten Strukturen im turbulenten Freistrahl mit Hilfe der tomographischen Particle Image Velocimetry. Diploma thesis, Univ. Göttingen / DLR (2008)
12. Wieneke, B.: Volume self-calibration for stereo PIV and tomographic PIV. In: Proc. of PIV 2007, Rome (2007)

Time-Resolved Two- and Three-Dimensional Measurements of Transitional Separation Bubbles

Sebastian Burgmann and Wolfgang Schröder

Abstract. Advanced methods of the Particle-Image Velocimetry (PIV) technique such as Time-Resolved and Stereo-Scanning PIV have been applied to investigate the separation bubbles on top of a finite circular cylinder and on the suction side of an SD7003 airfoil. A kind of three-dimensional vortex-shedding mechanism associated with the inviscid Kelvin-Helmholtz-instability has been identified to govern the flow field in both cases. The time-averaged velocity distribution is strongly affected by these vortex cascades although the unsteadiness of the bubbles due to the band of frequencies in the spectra of the vortex-shedding mechanism is hidden. Several analyzing methods are used and/or developed and the capabilities of more sophisticated experimental investigations of the three-dimensional flow field associated with separation bubbles are outlined.

1 Introduction

Laminar flow separation may occur amongst others at sharp edges, e.g. at a forward facing step, or due to an adverse pressure gradient (APG). The separated shear layer is highly unstable in both cases and possesses a high receptivity of instabilities. A transition mechanism develops and the flow reattaches enclosing a recirculation region. A simple model of the time-averaged flow field associated with an APG-induced separation bubble is shown in figure 1. Usually the separated shear layer is governed by an inviscid Kelvin-Helmholtz instability mechanism, leading to a roll-up of the shear layer and a consecutive vortex shedding process at the downstream end of the separation bubble.

Such separation bubbles have been investigated by means of non-intrusive optical measurement techniques like the Particle-Image Velocimetry (PIV) technique. Exemplarily the separation bubble on top of a finite circular cylinder, which represents the ‘sharp edge’ separation type, has been investigated, whereas the separation bubble due to an adverse pressure gradient has been analysed on the suction side of an SD7003 airfoil. To investigate the temporal development of the

Sebastian Burgmann · Wolfgang Schröder
Institute of Aerodynamics, RWTH Aachen University, Wuellnerstrasse 5a, 52062 Aachen, Germany

W. Nitsche and C. Dobriloff (Eds.): Imaging Measurement Methods, NNFM 106, pp. 83–92.
springerlink.com

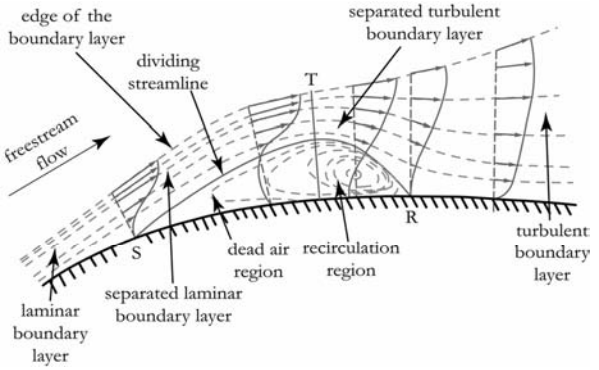

Fig. 1 Model of the time-averaged velocity distribution of an APG-induced separation bubble after Horton [6]

separation bubble induced flow field a time-resolved PIV (TR-PIV) technique has been applied using high-speed cameras and lasers. Since the transition related vortex shedding is supposed to be highly three-dimensional, additionally to a planar time-resolved analysis as provided by TR-PIV a three-dimensional velocity measurement technique is necessary. The Scanning-PIV technique, i.e., the consecutive illumination of parallel light-sheet planes such that a volume is 'scanned', is used to analyze the three-dimensionality of the flow. Two methods are demonstrated and described in the following sections. First, a single camera can be used and the 3D-velocity distribution is calculated assuming zero-divergence, and second, a combination of two cameras in a stereo setup can be applied. One of the drawbacks of Scanning-PIV is the necessary prerequisite of low flow speed like in water flows. Therefore, Holographic PIV offers another possibility to spatially highly resolve the instantaneous flow field even at higher speeds. This will be discussed in the final section.

2 Principle Description of Scanning PIV

A very simple way to spatially and temporally analyze the flow field is provided by a rotating-mirror drum technique, which has been applied to investigate the separation bubble on top of the cylinder. This technique uses a continuous wave Argon+-laser, a lens combination to generate a light sheet, and a cylindrical drum with mirrors which are stepwisely attached on the surface (see figure 2). The flow is illuminated at high speed in consecutive parallel planes. A camera whose optical axis is perpendicular to the planes is used to detect the particle movements within the planes.

The in-plane velocity distribution can simply be calculated by usual PIV-algorithms. Assuming vanishing divergence the third velocity component can be calculated by a form of the continuity equation given in equation 1 using the boundary condition of zero-velocity on the wall, i.e., the surface of the cylinder. In this equation ε_z denotes the accuracy of the light-sheet position with a maximum error of $\varepsilon_{z,max}=0.2$. The method has been successfully applied in Burgmann et al. [3].

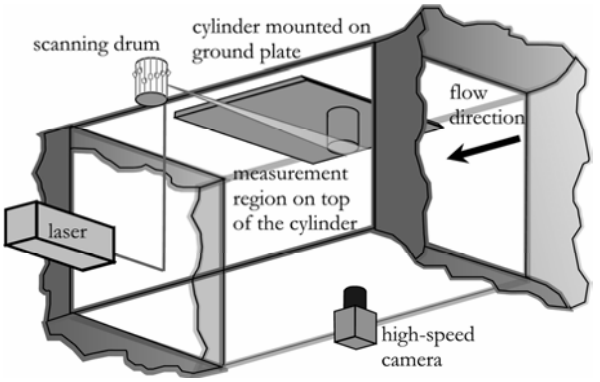

Fig. 2 Sketch of the Scanning-PIV setup for the investigation of the separation bubble on top of a finite circular cylinder

$$w(i) = \sum_{1}^{i} \frac{\Delta w}{\Delta z}(i) \cdot (1+\varepsilon_z) \cdot \Delta z(i) \quad , \quad i \in [1,k] \tag{1}$$

Since the depth of field may exceed the depth of focus of the lens at a necessary aperture, a dynamic focussing device may me used. Based on the system used by Angele et al. [1] such a system has been developed and tested which is based on a rotating disc placed between the lens and the camera. The possible defocusing of some measurement planes can be corrected by changing the optical path length inserting glass plates of different thickness in the disc.

A more adequate way than calculating the third velocity component would be to directly measure the off-plane component which has been done using a Stereo-Scanning PIV setup with two cameras. This measurement technique has been applied for the investigations of the separation bubble on the suction side of an SD7003 airfoil [4,5]. The angle between the two cameras and the measurement planes causes some optical distortions which can be almost completely avoided by simply attaching liquid filled prisms on the test-section walls of the water tunnel (see figure 3). Since in this case infrared laser diodes have been used to illuminate the measurement volume whose light emission is invisible for the human eye the misalignment of the light-sheet and the calibration grid becomes critical. A correction of this misalignment has been performed applying a disparity map calculation following Wieneke [13].

Special care has to be taken to perfectly parallelly align the light sheets with respect to each other and the airfoil surface such that the spatial structure of the vortices in the reattachment zone of the separation bubble can be regarded as sufficiently resolved. Using a double-slit device attached to the airfoil surface this prerequisite has been fulfilled in the measurements allowing to reliably visualize, e.g. streamlines, vorticity-contours, or λ_2-contours.

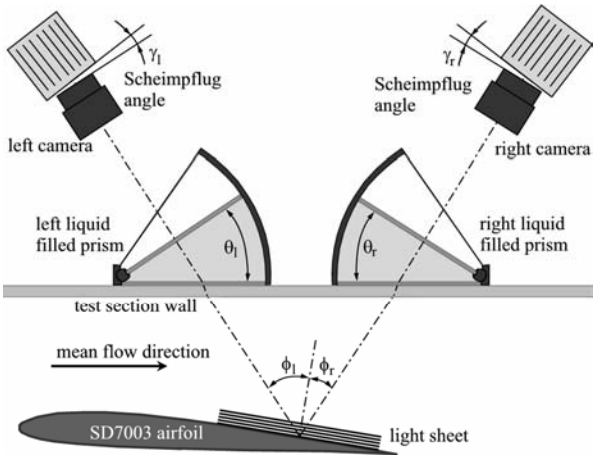

Fig. 3 Sketch of the optical setup for the Stereo-Scanning PIV measurements on the suction side of an SD7003 airfoil

3 The Three-Dimensional Flow Field on Top of a Finite Circular Cylinder

In the following, some results of the TR-PIV and Scanning-PIV measurements of the separation bubble on top of the circular cylinder are presented. The cylinder and the mount, i.e., the base-platform have been designed according to the lay-out published by Leder [8]. The two-dimensional results in a single light-sheet aligned with the flow direction and perpendicular to the top surface of the cylinder evidence a cascade of KH-like vortices to develop as a consequence of the geometry induced separation. The application of the optical flow technique which was performed by P. Ruhnau and C. Schnörr (IPA Group, Department of Mathematics and Computer Science, University Mannheim) was proven to give similar results as the classical cross-correlation method of PIV (see figure 4). The three-dimensional mean velocity field is exemplarily shown in figure 5 on the left for a

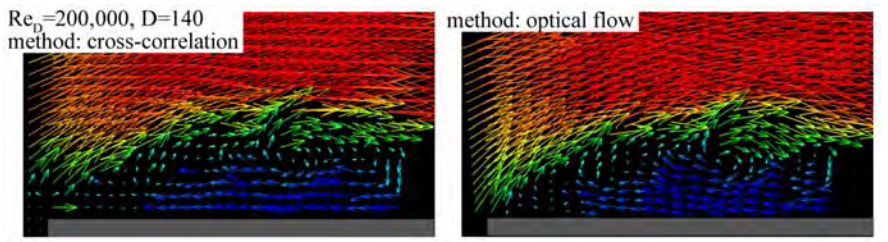

Fig. 4 KH-like vortex structures on top of a finite circular cylinder. Calculation of velocity vectors by cross-correlation (left) and optical flow technique (right)

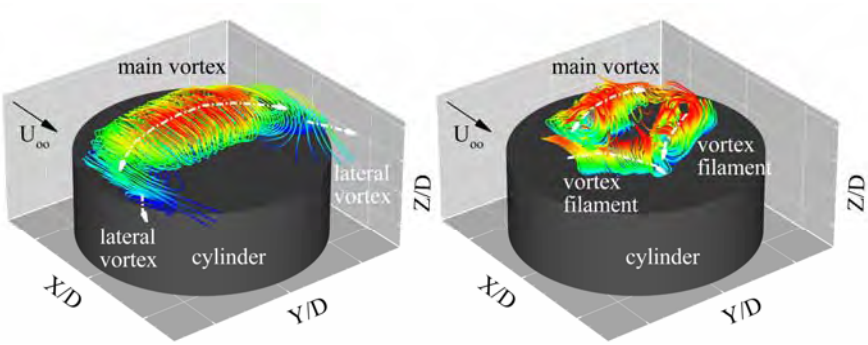

Fig. 5 Time-averaged velocity field (left) and instantaneous vortex field (right) on top of the cylinder at Re_D=65,000, visualized by streamlines

diameter based Reynolds number of Re_D=65,000 depicting the huge recirculation region on top of the cylinder as well as some parts of the side-vortices emerging at the 'edges' of the cylinder-hat. Nevertheless, this flow field is highly unsteady as can be seen in figure 5 on the right showing a snapshot of the flow field. Several vortical structures are evident which possess some kind of lateral oscillation motion. Note, one central vortex seems to exist. It is oriented perpendicular to the freestream direction and forms a slight bow. On the lateral areas of this vortex two additional vortices emerge pointing more in the streamwise direction. These vortices trigger some kind of fluttering motion, i.e., the orientation of the vortical axis alters in time, although they still point more or less in the downstream direction. These alternating vortices have also been found by Roh and Park [10] on top of a cylinder under similar conditions.

Note, in these cases the third, i.e., the off-plane velocity component, has been calculated assuming vanishing divergence of the flow field. The reliability and applicability of this method has been shown in [3] and in the corresponding presentation at the symposium 'Lasermethoden in der Strömungsmesstechnik', GALA06, for the case of vortical structures evolving on the suction side of an SD7003 airfoil. In the following section, these vortical structures will be further discussed.

4 Temporally and Spatially Resolved Vortical Structures on an SD7003 Airfoil

On the suction side of an SD7003 airfoil a separation bubble has been detected at angles of attack of α=4,6,8 and Reynolds numbers of Re_c=20,000, 40,000, 60,000 [2,4,5]. It has been shown in the last decade that Kelvin-Helmholtz-like vortical structures are associated with the occurrence of pressure-induced separation bubbles, e.g., by Watmuff [12] or McAuliffe & Yaras [8]. Using TR-PIV in a single light sheet these vortices have also been found for all investigated angles of attack and Reynolds numbers, an example of which is shown in figure 6 in a moving

reference frame exhibiting the typical cat-eye pattern associated with KH-instabilities [5]. The analysis of the vortex shedding frequencies has evidenced a dependence of the Strouhal number based on the momentum thickness and boundary layer velocity at separation $St_{KH} = U_s \theta_s / f$ on the angle of attack as well as on the Reynolds number as can be seen in figure 7. In other words, viscous phenomena seem to strongly affect the originally inviscid KH-instability mechanism. The range of the Strouhal numbers in this case coincides with experimental and numerical results of Talan & Hourmouziadis [11] and Yang & Voke [14].

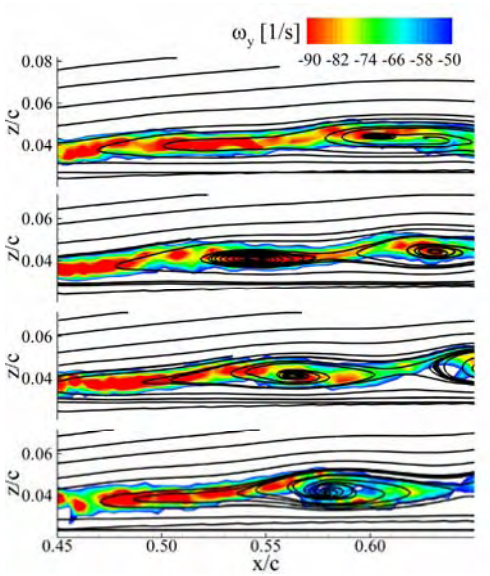

Fig. 6 (left) Cascade of vortices being shed from the main recirculation region exhibiting the cat-eye pattern, streamlines and vorticity contours are visualized in a moving reference frame

Fig. 7 (bottom) Strouhal number as a function of angle of attack and Reynolds number

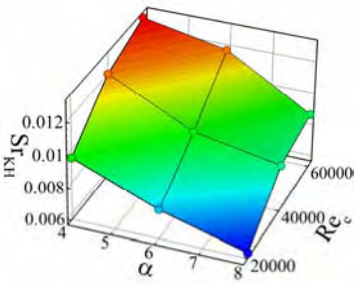

The characteristics of the separation bubble, i.e., separation point, transition onset, reattachment, etc. have been thoroughly investigated in [4,5]. Since the vortex-shedding procedure at the downstream end of the separation bubble yields several locally confined backflow regions it has been tried to assess the instantaneous reattachment and the standard deviation of this value, i.e., the range of vortex-size occurring in the reattachment region. By extracting the wall-normal velocity w on a line almost parallel to the airfoil surface and defining a threshold value of

$$w_{threshold}(t) = \overline{w}(\tilde{x},t) + 1.25 \cdot \sigma_w(\tilde{x},t) \tag{2}$$

with $\sigma_w(\tilde{x},t)$ being the standard deviation of w the instantaneous reattachment has been analyzed leading to significantly smaller mean-values than the reattachment lengths obtained from the time-averaged velocity field [5]. The bubble length calculated with the new method showed only a small dependence on angle of attack and a strong influence of the Reynolds number in contrast to the

separation which shows opposite behavior. Furthermore, it has been found that the bubble length may vary up to 20% of its mean length at angles of attack of 4° and may reach variations of up to 37.5% of the mean length at angles of attack of 8°. The standard deviation σ is approximately 13% at Re_c=20,000 and exceeds 20% at Re_c=60,000. That is, the vortices possess a size which is of the same order as the main recirculation region. Therefore, these vortices locally alter the pressure distribution by an amount which is not negligible and they strongly affect the aerodynamic performance and stability of small aircraft like micro-air vehicles (MAV's).

First measurements with light-sheet planes parallel to the airfoil surface and a single camera at Re_c=20,000 gave rise to the assumption of the existence of curved three-dimensional vortices at the downstream end of the separation bubble [2]. This assumption has been further substantiated by Stereo-Scanning PIV measurements. It has been evidenced that the vortex structures undergo a deformation process when moving downstream. Several typical vortical structures can be found in the flow field as can be seen in figure 8. Starting with spanwise oriented vortex filaments further downstream c-shaped vortices and arc-like vortices appear as well as downstream pointing vortex structures. Nevertheless, it has been shown that the c-shape vortex seems to be the initial stage of the vortex deformation process, since arc-like and downstream pointing vortices can be interpreted as results of a decomposition process of c-shape vortices. A typical temporal development process of a c-shape vortex is exemplarily presented in figure 9. Further details on the three-dimensional structures as well as on the coherence of Λ-like or arc-like structures with c-shape vortices can be found in [5]. Interestingly, the arc-like structures become more dominant at higher Reynolds numbers. However, since the separation bubble in these cases is relatively small in relation to the measurement area a larger region of the flow field downstream of the reattachment area has been recorded. At lower Reynolds numbers the possible further

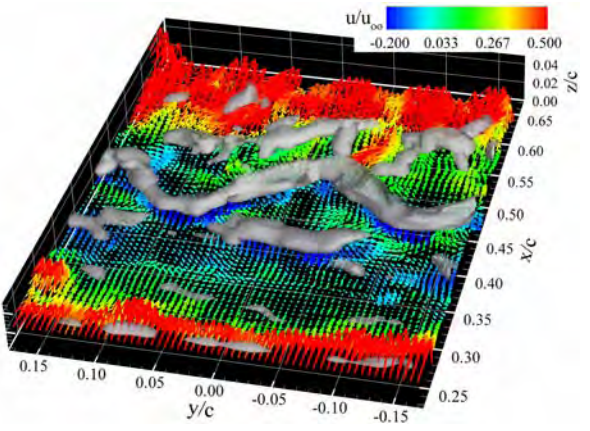

Fig. 8 Typical flow field evolving in the reattachment zone of the separation bubble on the suction side of an SD7003 airfoil (α=6, Re_c=40,000) showing c-shape vortices, Λ-vortices, and vortex filaments visualized by λ_2-contours

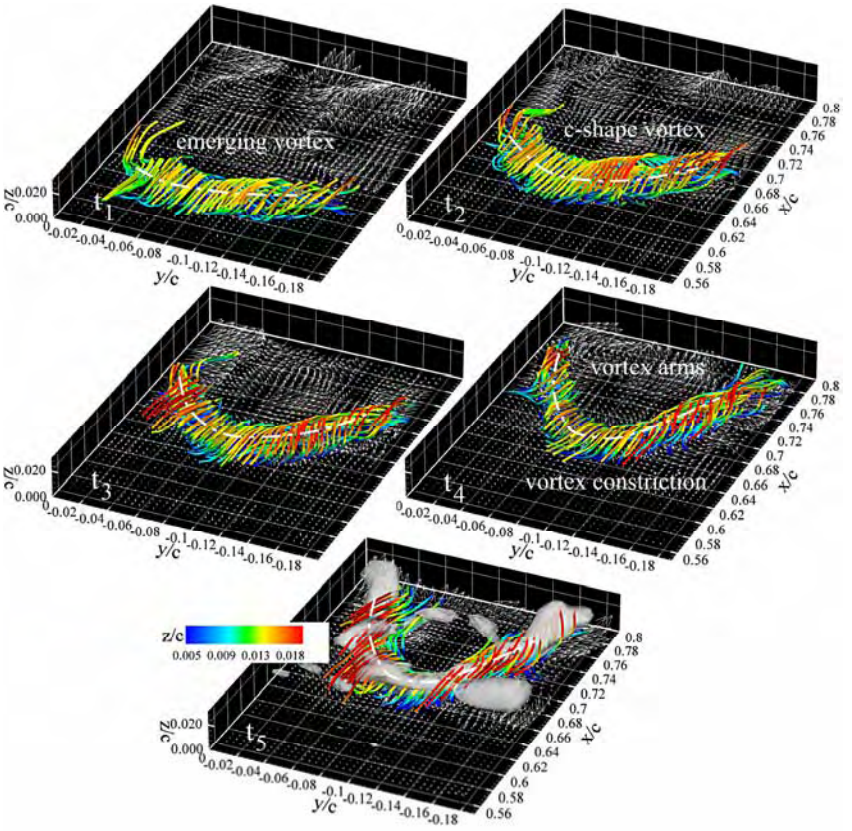

Fig. 9 Typical temporal development of a c-shape vortex on the way downstream, showing the turning-in of the vortex arms, the constriction of the vortex in the mid-section and the consequent formation of screwdriver-like vortex pairs, visualization by instantaneous streamlines color coded with the z-direction (α=4°, Re_c=40,000)

deformation into Λ-vortices is beyond the size of the measurement volume. Furthermore, the spatial resolution in terms of separation bubble length is reduced in these cases. Nevertheless, given the description in [5] the arc-like structures can be reconstructed as results of a deformation of a c-shape vortex even at higher Reynolds numbers.

The influence of the freestream turbulence level on the size and characteristics of the separation bubble has also been investigated, showing the bubble to decrease significantly in size at higher turbulence levels. Nevertheless, the same three-dimensional vortex structures emerge at the downstream end of the main recirculation zone [4,5]. This result also substantiates the assumption that the c-shape vortex is somehow typical for this kind of separation bubbles.

5 Conclusion and Outlook

Spatial velocity measurement techniques are essential to further and deeper understand many flow conditions, since most technical applications involve three-dimensional flow structures such as separation bubbles which may evolve due to sharp edges or adverse pressure gradients. Optical measurement techniques like PIV may serve as an adequate tool. Currently several PIV measurement techniques like Scanning-PIV, Tomographic PIV, and Holographic PIV have been shown to be applicable to investigate three-dimensional flows. In this study, Stereo-Scanning PIV or even 'Mono'-Scanning PIV have been successfully applied to investigate separation bubbles and the three-dimensional vortical structures that evolve as a consequence of these bubbles. Nevertheless, due to velocity limitations of the Scanning-PIV technique further investigations using analogue Holographic PIV are currently conducted which will allow the analysis of higher Reynolds number flows. This holographic system has been designed as an Off-Axis stereoscopic setup with complex conjugate reconstruction following the work of Konrath et al. [7]. Based on a modular concept, i.e., one module for a parallel projection of the particle field close to the hologram and one reference beam module that also provides the reconstruction beam system, the double images can be recorded on the same hologram simply using two reference beams.

Acknowledgements. This work was funded by the Deutsche Forschungsgemeinschaft within the priority research program SPP 1147 "Bildgebende Messverfahren für die Strömungsanalyse" (Imaging Measurement Methods for Flow Analysis) under the contract SCHR 309/25.

References

1. Angele, K.P., Suzuki, Y., Miwa, J., Kasagi, N., Yamaguchi, Y.: Development of a High-Speed Scanning Micro-PIV system. In: 6th Int. Symp. on Particle Image Velocimetry, Pasadena, September 21-23 (2005)
2. Burgmann, S., Schröder, W., Brücker, C.: Scanning PIV measurements of a laminar separation bubble. Exp. Fluids 41(2), 319–326 (2006); Special Issue PIV 2005
3. Burgmann, S., Klaas, M., Schröder, W.: Vortex Detection via Scanning PIV measurements. In: Symposium Lasermethoden in der Strömungsmesstechnik, GALA 2006, Braunschweig, paper 40.1, September 5-7 (2006)
4. Burgmann, S., Dannemann, J., Schröder, W.: Time resolved and volumetric PIV measurement of the transitional separation bubble of an SD7003 airfoil. Exp. Fluids 44(2), 609–622 (2007)
5. Burgmann, S., Schröder, W.: Investigation of the vortex induced unsteadiness of a separation bubble via time-resolved and scanning PIV. Exp. Fluids (2008), doi:10.1007/s00348-008-0548-7 (Special Issue PIV 2007)
6. Horton, H.P.: A semi-empirical theory for the growth and bursting of laminar separation bubbles. Aeronautical Research Council CP 1073 (1969)
7. Konrath, R., Schröder, W., Limberg, W.: Holographic particle-image velocimetry applied to the flow within the cylinder of a four-valve internal combustion engine. Exp. Fluids 33, 781–793 (2002)

8. Leder, A., Hüttmann, F.: Leitexperiment: Umströmung eines Zylinderstumpfes, Konfiguration des Leitexperiments (2003), http://www.spp1147.tu-berlin.de
9. McAuliffe, B.R., Yaras, M.I.: Separation-bubble-transition measurements on a low-Re airfoil using particle image velocimetry. In: Proceedings of GT 2005, ASME Turbo Expo. 2005, Reno, GT2005-68663, June 6-9 (2005)
10. Roh, S.C., Park, S.O.: Vortical flow over the free end surface of a finite circular cylinder mounted on a flat plate. Exp. Fluids 34, 63–67 (2003)
11. Talan, M., Hourmouziadis, J.: Characteristic Regimes of Transitional Separation Bubbles in Unsteady Flow. Flow, Turbulence and Combustion 69, 207–227 (2002)
12. Watmuff, J.H.: Evolution of a wave packet into vortex loops in a laminar separation bubble. J. Fluid Mech. (397), 119–170 (1999)
13. Wieneke, B.: Stereo-PIV using self-calibration on particle images. Exp. Fluids 39(2), 267–280 (2005)
14. Yang, Z., Voke, P.R.: Large-Eddy Simulation of Boundary-Layer Separation and Transition at a Change of Surface Curvature. J. Fluid Mech. (439), 305–333 (2001)

Coloured Tracer Particles Employed for 3-D Particle Tracking Velocimetry (PTV) in Gas Flows

Dominique Tarlet, Christian Bendicks, Robert Bordás, Bernd Wunderlich, Dominique Thévenin, and Bernd Michaelis

Abstract. This work describes an improved method for Particle Tracking Velocimetry in three dimensions (3-D PTV), applicable for gaseous flows and based on coloured tracer particles. This method allows a considerable increase of the tracer number density, while maintaining a constant rate of 3-D correspondence ambiguities from the different cameras. It is therefore perfectly suited for gas flows, where a high tracer density is requested to follow small-scale flow features. Furthermore, coloured tracer particles enable a longer next-step searching distance for the lagrangian reconstruction of trajectories. First, theoretical and numerical considerations are presented to check the ability of the employed coloured tracer particles to follow the considered flow. Then, 3-D PTV results obtained by the method described here are shown and appear to be very promising for later investigations of gas flows involving vortical structures and recirculation zones down to small scales, around 1 mm.

1 Introduction

Although relatively often used for liquid flows, Particle Tracking Velocimetry (PTV) is still considered as a major challenge in gaseous flows. The first difficulty is to find tracer particles with properties suitable for such gaseous conditions, which is a much more considerable challenge than in liquids [9]. The next major problem is the occurence of ambiguities concerning one tracer particle seen by the different cameras, especially considering the higher tracer densities necessary for gaseous measurements [11, 14], resulting from higher characteristic speeds and smaller

D. Thévenin · D. Tarlet · R. Bordás · B. Wunderlich
Institut für Strömungstechnik und Thermodynamik (ISUT), Otto-von-Guericke-Universität, Universitätsplatz 2, 39106 Magdeburg
thevenin@ovgu.de

B. Michaelis · C. Bendicks
Institut für Elektronik, Signalverarbeitung und Kommunikationstechnik (IESK), Otto-von-Guericke-Universität, Universitätsplatz 2, 39106 Magdeburg
bernd.michaelis@ovgu.de

W. Nitsche and C. Dobriloff (Eds.): Imaging Measurement Methods, NNFM 106, pp. 93–102.
springerlink.com

space- and time-scales of the important flow structures. Finally, technological limits of the available cameras come into play when considering high local velocities (beyond 10 m/s) in gaseous flows. Nevertheless, the widely recognized interest of lagrange-based measurements (such as PTV) for the investigation of turbulence and vortical structures in real flows [16] is a sufficient reason to face all these challenges.

The solution proposed in this work is to employ coloured particles and use the associated separation into different colour classes. Considering separately each resulting colour class, the apparent particle density is decreased without restrictions in the measurement accuracy, which simplifies the computational task for re-constructing trajectories. Due to the difference in the colour classes of two neighbour tracer particles the 3-D correspondence problem becomes immediately easier to solve. Colour recognition is realised in practice by means of an Artificial Neural Network (ANN), treating the raw information out of the Bayer-Pattern sensors of the cameras. The technique described in this paper for particle colouring is easily reproducible by other researchers, and a new training of the ANN would enable the recognition of different colour shades produced by different pigments.

First, the ability of coloured tracer particles to respond to a steep change in the velocity of a gaseous flow is quantified. The applied technique is then to locate the particles in 3-D and to recognize their colour (presently red, green or blue), then to re-build their trajectories by an algorithm treating 3-D spatial coordinates. Excepting colour recognition, a similar PTV strategy has already been employed by other authors, e.g. [17, 12, 18, 15, 6]. The obtained results demonstrate that the complete 3-D PTV procedure is working very well in the considered flow, involving organized structures, is able to reveal small-scale flow information (millimeter size) and simultaneously long uninterrupted trajectories, which constitutes an ideal complement to other measuring techniques, like Particle-Image Velocimetry. Present tests demonstrate the possibility of extending this method to a higher number of colours, and to apply it for gas flows at higher velocities.

2 Quantifying the Properties of Coloured Tracer Particles

In the course of this project, many different materials available on the commercial market have been tested. The EMS (Expanded Micro Spheres) have been clearly identified as being the best possible tracer for this purpose and are therefore retained for all presented measurements [2]. The physical properties of EMS are listed in Tab.1, together with a quantitative comparison of EMS with the best (non-coloured) PTV tracers available commercially (oil fog droplets). It has been shown [13] that oil droplets should have a diameter smaller than 3 μm to be employed as a tracer for laser optical measurements. Nevertheless, our own measurements based on Phase-Doppler Anemometry (PDA) show that the PEG droplets generated by a commercial system (Dantec Dynamics 10F03) have a mean diameter of almost 7 μm in the measurement section. For further comparisons both conditions (real system : 6.89 μm diameter denoted as PEG; ideal system from the litterature [13]: 3 μm diameter denoted as REF) have therefore been considered in Table 1. Note that for the results

Table 1 Properties of tracer particles

Name	**Density** (kg.m^{-3})		**Mean diameter** (μm)	
	available	used here	available	used here
Expancel ®(EMS)	24-70	70	20-120	70
Coloured EMS (r,g,b)		320		71-73
Polyethyleneglycol (PEG)	1130			6.89
Reference oil fog (REF)	1000		3	3

presented here, only EMS particles with a diameter of 70 μm are considered, while other sizes, down to 20 μm have also been tested [2].

Dying of the particles is realised according to a standardized protocol. A small quantity (70 mg) of EMS particles of diameter 70 μm is introduced into a polyethylene recipient of volume 4 cm^3. Then, 250 mg of a 50%-mix in mass of the dye (in the present case Edding T25 liquid ink of colour red, green or blue), and 50% of ethanol is added to the particles. Five minutes of careful mixing by means of a laboratory spatule ensures a homogeneous repartition of the dye by means of transport and diffusion through this porous medium. The dyed particles are then spread onto a cardboard layer for a day, during which they are turned three times. After drying the obtained colour particles are sieved through a metal filter of size 75 μm in order to remove possibly agglomerated particles. A microscope check demonstrates that the particle have kept their original structure and that the increase in diameter is negligible, at most equal to 3 μm. Only the three primary colours (red, green and blue) are used here, which is easiest for later recognition through a CMOS Bayer-Pattern sensor, detecting directly these 3 primary colours.

It is established [19] that suitable tracer particles are difficult to identify for gaseous flows, since the gas density is very low. This is particularly true at higher turbulence levels, where fast trajectory fluctuations are found. This issue can be quantified by computing three characteristic values describing the mechanical interaction between a tracer particle and the surrounding flow: settling velocity, relaxation time and Stokes number. Settling velocity v_t and relaxation time τ_p (Eq.1) have already been discussed in detail in [2, 3]. The relaxation time τ_p characterizes how fast the tracer particles react to a change in flow velocity [5]. In practice this time corresponds to the time needed by a particle to reach 63% of its final velocity after an instantaneous change in local flow velocity [8]. Results for τ_p are shown in Table 2. The Stokes number Stk (Eq.1) is a ratio of crucial importance for PTV. It quantifies the ability of tracer particles to adapt, quickly enough or not, their velocity to the instantaneous velocity of the surrounding gaseous flow. Equation (1) is obtained by considering a Stokes flow around the tracer particles [5], while τ_f is the characteristic time-scale of the gaseous flow, obtained by dividing a characteristic scale by a characteristic velocity:

$$\tau_p = \frac{1}{18}\frac{\rho_p d^2}{\rho_f \nu}\,, \quad \tau_f = \frac{l_{char}}{V_{char}}\,, \quad \mathrm{Stk} = \frac{\tau_p}{\tau_f} \tag{1}$$

Table 2 Stokes number Stk obtained with the different tracer particles for the present flow conditions

	coloured EMS	**PEG**	**REF**
d (μm)	73	6.89	3
τ_p (s)	39.8×10^{-4}	1.63×10^{-4}	2.74×10^{-5}
$\tau_{f,min}$ (s)	$4.75.10^{-2}$		
$\tau_{f,max}$ (s)	0.19		
Stk_{min}	2.1×10^{-2}	8.6×10^{-4}	1.4×10^{-4}
Stk_{max}	8.4×10^{-2}	3.4×10^{-3}	5.8×10^{-4}

Building on top of previous generic numerical simulations of large-scale flow instabilities [1], the real wind tunnel employed for the later measurements has been considered in the present computation. After a steady-state simulation (Fig.1) with inlet velocities between 0.5 and 0.8 m.s^{-1}, the Reynolds-Stress Model (RSM) is used in its low-Reynolds formulation for a further unsteady computation relying on Fluent. RSM is considered suitable to describe the flow patterns resulting from an anisotropy in the Reynolds stress, such as the recirculations found here around the curved winglets interacting with each other. These unsteady simulations reveal vortical structures with a perimeter l_{char} between 9.5 and 19 mm, with inside velocities V_{char} between 0.1 and 0.2 m.s^{-1}, leading to the characteristic flow time scale listed in Table 2. It is finally observed from Table 2 that the coloured EMS particles lead to a very low Stokes number (typically around 10^{-2}) for the considered flow conditions, and are therefore perfectly suitable for the considered investigation. First

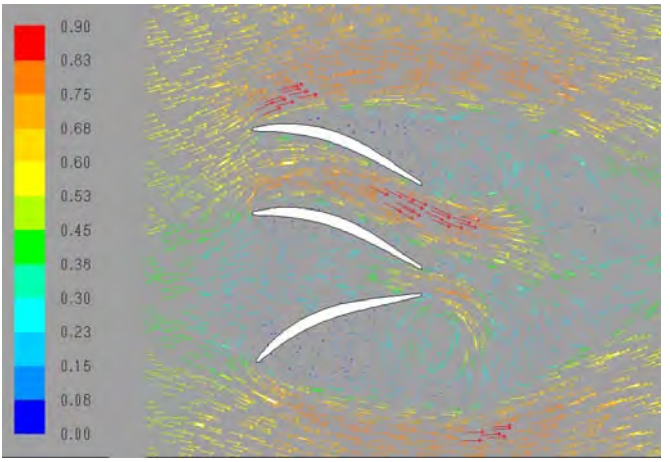

Fig. 1 Example of computational results employed to get an order of magnitude of the expected flow fluctuations. Here, the instantaneous velocity field (in m/s) is shown in the middle plane (zoom on the winglet region)

tests have demonstrated that EMS particles with a diameter down to 20 μm can be used to investigate flows with higher velocities or higher turbulence. At such scales the separation into colour classes is a real challenge and the ANN procedure is still being improved for that purpose [7]. Therefore, the results shown later employ only EMS particles of 70 μm diameter.

3 Colour Recognition by Artificial Neural Network

In the present application colour recognition is used to differentiate between colour classes and to separate between different colour shades. Consequently, the use of Artificial Neural Network (ANN) trained with user's data is an appropriate solution. Monochrome indexed images are used, with raw information from a G-R/B-G Bayer Pattern ("input data", see Fig.2) delivered to the entry layer of the ANN as a feature vector of 12 elements [7]: The 9 values of the pixels around the next green one, plus the 2-D coordinates on the image and one integer function of the location of the next green pixel on the Bayer pattern (0: there, 1: right, 2: left, 3: below, 4: above).

In order to train the ANN, the wind tunnel is first seeded exclusively with red or green or blue EMS-particles of 70 μm diameter, leading to a training file composed of 5000 feature vectors for each colour. This information is passed to an ANN composed of 4 layers with 12, 9, 5 and 3 neurons respectively. The training algorithm is based on back-propagation, activated through 5000 steps. The steepness coefficient of the activation functions of the neurons has been raised to 0.8 for the last layer, to 0.65 for the 2 intermediate layers, and left to 0.5 at the entry layer. The resulting ANN is then tested against a set of 100 feature vectors of each colour, randomly sampled among non-training data. For each colour, the percentage of effectively recognized vectors is called "Recognition rate". Excellent results are obtained, with a typical recognition rate exceeding 90% : 97% for red, 91% for green, 85% for blue.

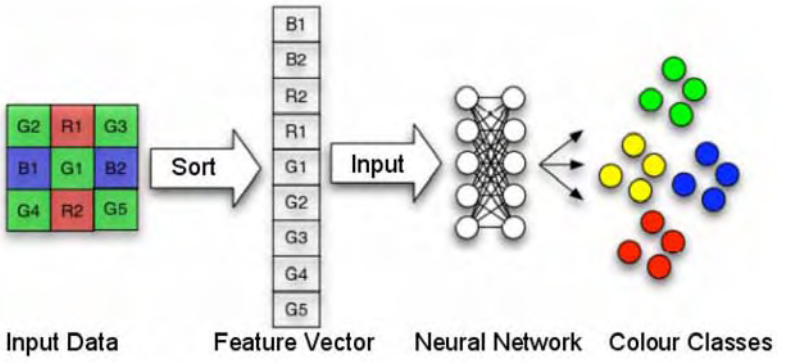

Fig. 2 ANN principle for colour classification

4 3-D Coordinates by Means of Photogrammetry

Besides solving the 3-D correspondence problem, calibration of each camera is required to compute 3-D coordinates. Calibration means determining the extrinsic and intrinsic parameters of the used camera model. Extrinsic parameters define the location and orientation of the camera reference frame with respect to a known world frame. The intrinsic parameters characterize the optical, geometric, and digital properties of the camera. The mathematical formulation of the camera model is expressed by the collinearity equations which describe the transformation of 3-D world coordinates to 2-D image coordinates [10]. To compute the unknown camera parameters a set of well-known 3-D coordinates is needed, which can be mapped to their corresponding positions in camera images. For this purpose the image of a calibration target (Fig.3, left) is captured for each camera. For each mark two colinearity equations are set up (one for each image coordinate). This leads to an over-determined equation system, solved by the least-squares method.

To search for tracer correspondences in camera image triples the epipolar geometry is utilized as described by Maas [11]. Imagine a line defined by the center of projection of a camera to a (tracer) position on the image plane of the same camera. Its projection to the image plane of another camera is called epipolar line. Candidates of corresponding tracers would only be located on a small band around this line. Although the search space is now quite restricted, there is still a large number of candidates at high particle densities. The number of ambiguities can be reduced by taking the third camera image into account. Here also the epipolar line of the selected position in the first camera image is created and furthermore all epipolar lines based on candidates of the second image. The number of candidates is now limited to tracer positions near to intersections of epipolar lines (Fig.3, right). Nevertheless there will be still a number of ambiguities [11]. For a further reduction of ambiguities, the colour information can now be used, as described in the previous

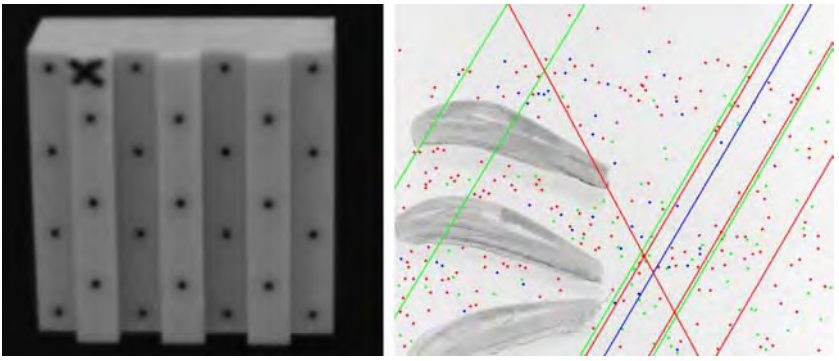

Fig. 3 Calibration target (left) and example of correspondence search using epipolar geometry and considering colour (right)

section. Finally the 3-D positions of the tracers are calculated by triangulation, in conjunction with the calibration data.

5 Re-building Trajectories

The presently employed PTV method uses the specific algorithm of Crocker and Grier [4] to link locations of the N particles present at a given step of time. Colour information is also taken into account. The principle of this algorithm relies on the squared displacement δ_i^2 between the point of ID i and its corresponding candidate at the next step of time. This algorithm actually minimizes the *sum* of these squared displacements, $\sum_{i=1}^{N} \delta_i^2$. More efficient algorithms are presently being tested.

6 Experimental Setup

For the present PTV measurements a suitable flow involving interesting structures has been generated within the focal depth of the cameras. It relies on a small Eiffel wind-tunnel (non-recirculating, roughly 1 m long) seeded on the suction side with dyed EMS-particles (Fig. 4). Three polyethylene winglets (as already shown in Fig.3 and in the computation in Fig.1) of length 17 mm are placed within the measurement region of size 25 mm $\times$ 30 mm $\times$ 6 mm (depth). Based on the previously presented simulations, these winglets are intended to create characteristic flow patterns involving recirculation (top), large streamline curvature (middle), and sudden acceleration (bottom). PTV and even more PTV based on colour recognition requests an excellent illumination. For this purpose four DEDOCOOL lamps are employed. They are equipped with daylight filters enabling to obtain a colour temperature between 5000 and 5300 K, which corresponds to a white light for the

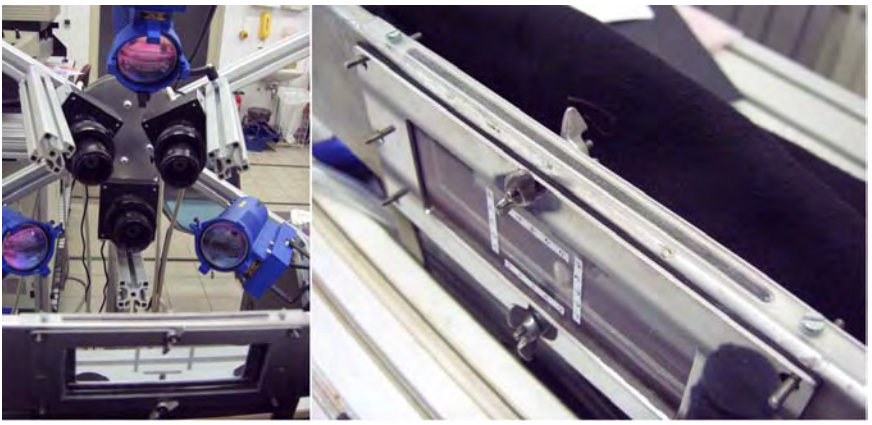

Fig. 4 Experimental setup, showing the rigid support for lamps and cameras (left) and the wind-tunnel measurement section (right)

human eye. This colour temperature is essential to obtain proper colour recognition. To capture the images 3 Basler A500kc cameras (1280 × 1024 pixels) are focused on the measurement section.

7 Results of 3D-PTV Involving Coloured Tracers

Due to lack of space, the two-dimensional validation of the developed PTV procedure by comparison with Particle-Image Velocimetry cannot be presented here. Full-scale 3-D PTV results relying on colour recognition as described in the previous sections are therefore presented directly. An exposure time of 1 ms has been used in the present case (Fig.5). The key observation is that the three flow features mentioned previously (corresponding to recirculation, strong deviation and rapid acceleration) appear very clearly in the PTV results. Although a detailed comparison is beyond the scope of this publication, the agreement with companion flow simulations, as introduced before (Fig.1) is already striking concerning the main flow features. The acceleration between the 2 bottom winglets and the evolution of the velocity field above the top winglet are fully resolved, leading to a smooth evolution of the measured velocities. Even small-scale flow structures (around 1 mm) are identified by the PTV measurements, especially in the recirculating zone at the top of the measurement section. For the present image, the flow was seeded with 40%

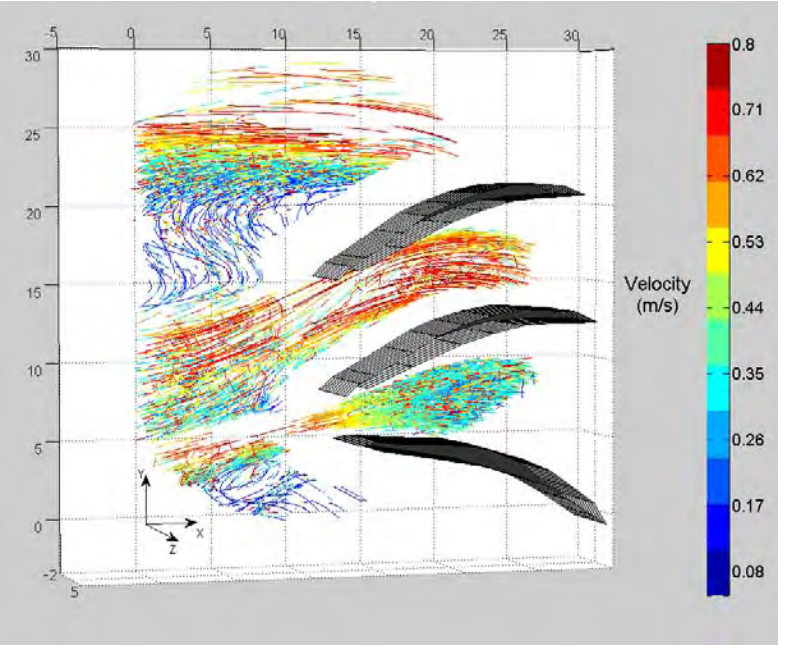

Fig. 5 3-D PTV results of velocities around the three winglets, using three different tracer particle colours (scale in mm)

of red particles, 35% of green and 25% of blue, which should lead globally to a maximum recognition rate when considering results of Section 3.

8 Conclusion

The results presented in this work demonstrate that colour recognition can effectively be employed for 3-D PTV measurements in gaseous flows. These very first results are already promising but major progress are still expected during the remaining 18 months of this project. The algorithms underlying colour recognition and 3-D PTV will be further improved, in order to enable use of more colours and of an even higher seeding density.

Acknowledgements. The authors would like to thank the DFG (Deutsche Forschunggemeinschaft, Schwerpunktprogramm 1147) for the financial support of this project. The help of R.V. Ayyagari is gratefully acknowledged.

References

1. Bordás, R., Janiga, G.: Numerical simulation of flow instabilities in an axial-flow compressor. In: MicroCAD International Scientific Conference 2007, Miskolc, Hungary, pp. 21–28 (2007)
2. Bordás, R., Fellegi, G., Wunderlich, B., Kuhn, R., Thévenin, D., Michaelis, B.: Appropriate tracers to measure velocities in particle-laden gas flows using optical techniques. In: Sommerfeld, M. (ed.) 6th International Conference on Multiphase Flows - ICMF 6, Leipzig, Germany (2007)
3. Bordás, R., Bendicks, C., Kuhn, R., Wunderlich, B., Thévenin, D., Michaelis, B.: Coloured tracer particles employed for 3-D PTV in gas flows. In: 13th International Symposium on Flow Visualization - ISFV 13, Nice, France (2008)
4. Crocker, J.C., Grier, D.G.: Methods of digital video microscopy for colloidal studies. Journal of Colloid and Interface Science 179, 298 (1996)
5. Crowe, C.T.: Multiphase flow handbook. Taylor & Francis, Abington (2006)
6. Kasagi, N., Nishino, K.: Probing turbulence with three-dimensional Particle Tracking Velocimetry. In: Proceedings of the International Symposium on Engineering Turbulence - Methods and Measurements (1990)
7. Kuhn, R., Bordás, R., Wunderlich, B., Michaelis, B., Thévenin, D.: Colour class identification of tracers using artificial neural networks. In: 10th International Conference on Engineering Applications of Neural Networks, Thessaloniki, Greece, pp. 387–394 (2007)
8. Kussin, J.: Experimentelle Studien zur Partikelbewegung und Turbulenzmodifikation in einem horizontalen Kanal bei unterschiedlichen Wandrauhigkeiten. In: Martin-Luther-Universität Halle-Wittenberg, Germany (2004)
9. Lobutova, E., Resagk, C., Rank, R., Müller, D., Putze, T., Maas, H.G.: 3-D Particle Tracking Velocimetry zur Untersuchung von gross-skaligen Strukturen in Rayleigh-Benard Konvektion. Fachachtung Lasermethoden in der Strömungsmesstechnik 1, 7–37 (2007)
10. Luhmann, T.: Nahbereichsphotogrammetrie. Wichmann-Verlag, Heidelberg (2000)

11. Maas, H.G.: Complexity analysis for the determination of image correspondences in dense spatial target fields. International Archives on Photogrammetry and Remote Sensing 24, 102–107 (1992)
12. Malik, N., Dracos, T., Papantoniou, D.: Particle Tracking in Three-dimensional Turbulent Flows - part II: Particle Tracking. Experiments in Fluids 15, 279–294 (1993)
13. Melling, A.: Tracer particles and seeding for Particle Image Velocimetry. Measurement Science and Technology 8, 1406–1416 (1997)
14. Netzsch, T., Jähne, B.: Ein schnelles Verfahren zur Lösung des Stereokorrespondenz-Problems bei der 3D-Particle Tracking Velocimety. In: Pöppl, J., Handels, H. (eds.). Springer, Heidelberg (1993)
15. Nishino, K., Kasagi, N., Hirata, M.: Three-dimensional Particle Tracking Velocimetry Based on Automated Digital Image Processing. Journal of Fluid Engineering 111, 384–391 (1989)
16. Ouelette, N.T., Xu, H., Bodenschatz, E.: A quantitative study of three-dimensional lagrangian Particle Tracking algorithms. Experiments in Fluids 40, 301–313 (2006)
17. Papantoniou, D., Dracos, T.: Analysing 3-Dimensional Turbulent Motions in Open Channel Flow by Use of Stereoscopy and Particle Tracking - Advances in turbulence 2. In: Hernholz, Fiedler (eds.). Springer, Heidelberg (1989)
18. Papantoniou, D., Maas, H.G.: Recent advances in 3-D Particle Tracking Velocimetry. In: Proceedings of the 5th International Symposium on the Application of Laser Techniques in Fluid Mechanics, Lisbon (1990)
19. Suzuki, Y., Kasagi, N.: Turbulent air-flow measurement with the aid of 3-D Particle Tracking Velocimetry in a curved square bend. Flow, Turbulence and Combustion 63, 415–442 (1999)

Two Scale Experiments via Particle Tracking Velocimetry: A Feasibility Study

Matthias Kinzel, Markus Holzner, Beat Lüthi, Alexander Liberzon, Cameron Tropea, and Wolfgang Kinzelbach

Abstract. In preparation of simultaneous large-scale / small-scale 3D Particle Tracking Velocimetry (3D-PTV) experiments in a developing turbulent flow we performed two types of measurements separately: (i) the velocity and coarse-grained velocity derivatives were measured in a large observation volume with focus on the large-scale flow features and (ii) spatially resolved velocity derivatives were measured in a small observation volume with the goal to obtain small-scale quantities associated with vorticity and strain. In this contribution we demonstrate that the characteristic flow structures were captured and velocity derivatives were accessed with sufficient accuracy. The problem of measuring velocity derivatives both in the Lagrangian and Eulerian frame of reference is also addressed. Although comparable accuracies in both settings could be achieved with our method, only statistics obtained from the spatially resolved measurement were found to be practically the same in both settings.

1 Introduction

Turbulent flows are intrinsically three-dimensional and characterized by a wide spectrum of scales, with eddy sizes ranging from the largest size, the integral scale L, down to the dissipative scale, the Kolmogorov length scale η. The Reynolds number

M. Kinzel · C. Tropea
Institute of Fluid Mechanics and Aerodynamics (SLA), Technische Universitaet Darmstadt, Darmstadt, Germany
Tel.: +49-6151-163354
Fax: +49-6151-164754
m.kinzel@sla.tu-darmstadt.de

M. Holzner · B. Lüthi · W. Kinzelbach
Institute of Environmental Engineering (IfU), Swiss Federal Institute of Technology, Zurich, Switzerland

A. Liberzon
School of Mechanical Engineering, Tel Aviv University, Israel

W. Nitsche and C. Dobriloff (Eds.): Imaging Measurement Methods, NNFM 106, pp. 103–111.
springerlink.com

of the flow determines the separation between the largest and smallest sizes, where $L/\eta \propto Re^{3/4}$, [13]. For the instantaneous measurement of the 3D flow field it is desirable to capture all relevant scales for a complete characterization of the turbulence at a given Reynolds number, which poses resolution requirements that are often difficult to meet. A second challenge concerns the measurement of flow information not only in a fixed frame of reference (the "Eulerian" frame), but also along the paths of fluid parcels (the "Lagrangian" frame), which is of great importance for example for the understanding of turbulent mixing processes, [14].

Modern non-intrusive whole field measurement techniques involve the use of high-speed cameras to image the motion of small neutrally buoyant tracer particles seeded into the flow within a given observation volume. Some of these techniques are further developments of the widely used planar Particle Image Velocimetry, where 2D velocity information is extracted via correlation techniques from the recorded images of two subsequent exposures and a laser light sheet is typically used for the illumination of the tracer particles, see [12] and references therein. The Scanning-PIV technique uses a light sheet scanning rapidly through the measurement volume, e.g. [1]. The volume is sliced by the laser sheet at sequential depth positions where the particle image pattern is recorded. The velocity information is then calculated for individual planes with the use of standard PIV methods. Alternatively, Tomographic-PIV uses a multi-camera setup to image an illuminated volume and reconstructs the 3D particle positions as a light intensity distribution by means of optical tomography, [2]. The reconstructed tomogram is then analyzed by means of 3D cross-correlation of two subsequent exposures. The so-called Defocusing-PIV relies on the defocusing principle to extract depth information from the recorded image of an observed volume and in principle one single camera with multiple apertures can be used, but higher seeding densities can be achieved with more than one sensor, e.g. [11]. Presently, the techniques mentioned up to now have a potential to reconstruct the three components of a number of velocity vectors of the order of $10^3 - 5 \cdot 10^4$, but so far this information is essentially restricted to the Eulerian frame of reference.

Particle tracking velocimetry (3D-PTV) instead is an intrinsically Lagrangian measurement technique that has been established in an automated form as a valuable tool for 3D flow measurements over the last two decades or so, e.g. [10] and references therein. The method relies on the stereoscopic recognition and subsequent tracking in time of tracer particles in an illuminated volume by using a multi-camera setup. A bottleneck of this technique lies in the maximum seeding density of tracer particles. In order to keep a low probability of false particle detection and of overlapping particle images the number of particles detected per frame is restricted to the order of 10^3. Using a scanning light sheet the maximum seeding density could be increased to an order of 10^4, see [6]. At this point, for a given flow problem to be analyzed there is a tradeoff between the use of a larger volume to capture the larger flow scales at the expense of spatial resolution at the smaller scales or, alternatively, it is possible to focus on a small observation volume and resolve the viscous scales but then one has to compromise on the larger scales. In a recent further development, [9] succeeded to obtain a resolution that is high enough to allow the full tensor of

velocity derivatives to be measured for the first time along particle trajectories. Due to the limitation on the seeding density, the Reynolds number was kept low and the observation volume small ($\sim 1cm^3$).

The motivation of the present study is to perform preliminary experiments in preparation for a new method that will yield Lagrangian small-scale information, but at the same time also relevant information on the large-scale structures of the flow. The method will be based on 3D-PTV measurements simultaneously in a small and a large observation volume. The feasibility of the method was tested by performing the two types of experiments separately. In the next section we describe the method and thereafter show the results in Section 3, followed by a summary and outlook.

2 Method

The measurements have been carried out in a $200\times200\times300$ mm^3 water tank in which the flow is mechanically forced from the top by an oscillating grid, see Fig. 1. The apparatus is the same as the one described in [4] except for the geometry of the grid. The simple woven screen was replaced by a fractal grid so that turbulence could be excited more effectively and over a larger range of scales. Following [7] a fractal grid with the simplest cross-type fractal pattern, a maximum grid bar width of 4mm and three fractal iterations was installed. The grid was driven with a frequency of 9 Hz and a stroke of 8 mm. The particle tracking velocimetry (3D-PTV) system consists of a Photron APX high-speed camera (1024×1024 pixels) in combination with an image splitter that mimics a four-camera setup, see [6] for details. In a first experiment the light beam of a continuous 20 Watt Argon-Ion laser is expanded through spherical lenses to illuminate a large volume of size $50\times50\times40$ mm^3 (thereafter referred to as Exp I) and in a second experiment a smaller volume of size $15\times15\times15$ mm^3 is illuminated (Exp II), see Fig. 1. The velocity and velocity derivatives along particle trajectories were measured for the two types of experiments in the same way as described in [9]. For Exp II the filtering scale was of the order of the integral scale of the flow. The postprocessing

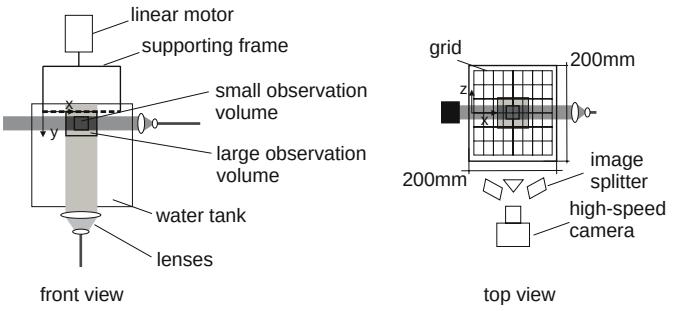

Fig. 1 Schematic of the experimental setup

was extended to allow for interpolation of the measurements on an Eulerian grid, similar to [5]. The Eulerian data was filtered in time by using binomial coefficients to realize a compact but Gaussian weighting function. The applied filter width was about $0.1\tau_\eta$, where τ_η is the Kolmogorov time scale. The measured r.m.s. velocity of the flow was about 10 mm/s and we estimated η=0.4 mm using $\eta = (\varepsilon/\nu)^{1/4}$, where $\varepsilon = 2\nu s^2$ is the measured dissipation ($s^2 = s_{ij}s_{ij}$ is the rate of strain and s_{ij} are the components of the rate of strain tensor). The Taylor microscale, λ, was about 6 mm and τ_η was estimated as 0.3 s. The Taylor-microscale Reynolds number is Re_λ=60.

3 Results

Similar to [4], in the present experiments the grid is started from rest and generates a turbulent flow region that spreads through the region of interest in time via entrainment of surrounding irrotational fluid. The results are based on a statistical analysis of velocity derivatives measured in experiments I and II. First we assess the accuracy of the measurements and after that we discuss the results related to the small and large scale structure of the flow, separately.

3.1 Checks

Coarse-grained velocity derivatives were obtained from Exp I, while spatially resolved velocity derivatives are available from Exp II. First, following the approach of [9], statistical checks based on precise kinematic relations are presented to validate our methodology and to assess the accuracy of the measurements in the Lagrangian and Eulerian frame.

The first check involves the Lagrangian acceleration obtained directly through differentiation along particle paths and independently obtained spatial derivatives of the velocity. The Lagrangian acceleration $a_i = Du_i/Dt$, is related to the local acceleration, $a_{l,i} = \partial u_i/\partial t$, and convective acceleration, $a_{c,i} = u_j \partial u_i/\partial x_j$, through the following equation:

$$\frac{Du_i}{Dt} = \frac{\partial u_i}{\partial t} + u_j \frac{\partial u_i}{\partial x_j} \tag{1}$$

Joint PDFs of a_i versus $a_{l,i} + a_{c,i}$ are shown in Fig. 2 for Exp I (top) and Exp II (bottom). It can be seen clearly that most points fall onto the diagonal and the aspect ratios of the iso-probability contours are very close to the ones shown in [9]. Interestingly, the result looks very similar for both types of experiments indicating that coarse-graining might affect Lagrangian acceleration and spatial derivatives of the velocity in a similar fashion so that the balance of Eq. 1 is maintained. For the above check, the Lagrangian data set was used, but the results obtained from the Eulerian data set (not shown) look practically the same. This indicates that the accuracy of the measured velocity derivatives is comparable for the two settings.

Another good resolution check involves the two invariants of the velocity gradient tensor, the first one relates to the relative strength of enstrophy and strain, $Q =$

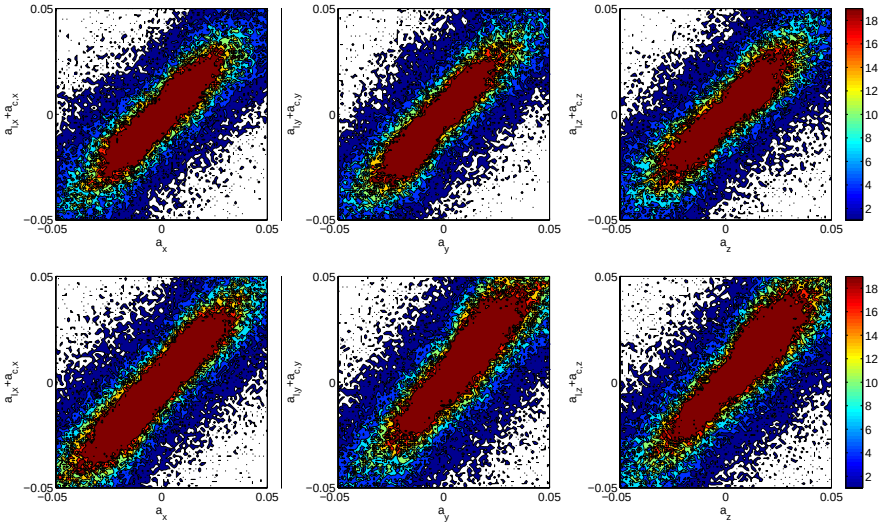

Fig. 2 Joint pdf of $a_{l,i}$+$a_{c,i}$ versus a_i for i=x, y, z for Exp I (top) and II (bottom)

$1/4(\omega^2 - 2s^2)$, and the second one to their production terms, $R = -1/3(s_{ij}s_{jk}s_{ki} + 3/4\omega_i\omega_j s_{ij})$. In homogeneous, statistically stationary turbulence the dominance of strain production for $Q < 0$ leads to the well known 'tear drop' shape of the iso-probability contours, while for coarse grained gradients the plots are symmetric. Fig. 3 shows Joint PDFs of R versus Q for Exp I (top) and Exp II (bottom) obtained from the Lagrangian (left) and Eulerian (right) data set. While the iso-contours from Exp I are symmetric and follow a Gaussian behavior (Fig 3 (top)), the results obtained from the well resolved data set yield the tear-drop shape (Fig 3 (bottom)). We note that for Exp I the variances of R and Q of the Eulerian data set are higher compared to the Lagrangian data set (Fig 3 (top)).

3.2 Small Scale Results

To further assess the effect of interpolation of the Lagrangian data onto the Eulerian frame we compare PDF's of the invariants R and Q.

The PDF's of R and Q are depicted in Fig 4 for Exp I (top) and Exp II (bottom). Again for Exp I there is a considerable difference between the PDF's obtained from the Lagrangian and the Eulerian data set. From similarity arguments we expect a general decrease of the values of R and Q through coarse graining and indeed the shape of the PDF from the Lagrangian data set follows this trend (Fig. 3 (top, left), Fig. 4 (top)), whereas the PDF from the Eulerian data set remains broader (Fig. 3 (top, right), Fig. 4 (top)). The reason for the difference between Eulerian and Lagrangian results in Exp I is persently not clear and will be subject to future

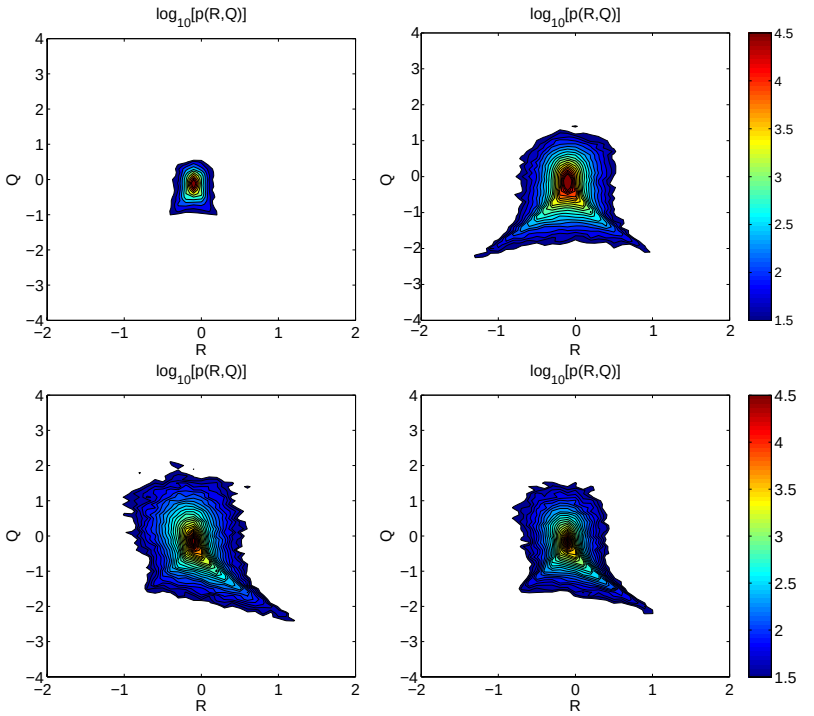

Fig. 3 Joint PDF of R versus Q for Exp I (top) and II (bottom) obtained from the Lagrangian (left) and Eulerian (right) data set

inverstigations. The PDF's obtained from the Exp II collapse, suggesting that both vorticity, strain and their production terms are well resolved.

3.3 Large Scale Results

The animation of enstrophy magnitude iso-surfaces in time is well suited for the visualization of the propagation of the turbulent region of the flow through the region of interest. Fig. 5 (left) and (middle) show two snapshots of these iso-surfaces at time t=1 and 2 s. In Fig. 5 (left) one can clearly distinguish between the turbulent region of the flow and the irrotational ambient fluid below. At the beginning of the experiment the turbulent eddies are concentrated in the upper half of the domain (Fig. 5 (left)) and after some time they are visible in the whole domain (Fig. 5 (middle)). In Fig. 5 (right) a contour plot of the ω_z magnitude in the mid-plane of the observation volume is shown together with the velocity vectors for t=2s. We can track the boundary of the turbulent region in time by using a simple level based method like in [4]. For each time instance t, and for each x and z the turbulent boundary is the lowest point, $y^*(x,z,t)$, in which the magnitude of the signal exceeds a fixed (for all times and x,z locations) threshold on vorticity. For each time the mean position

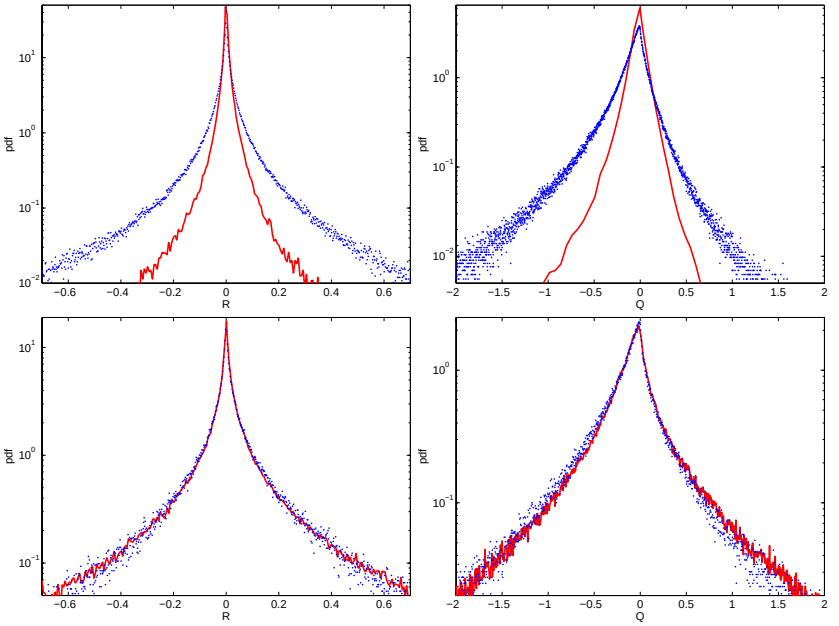

Fig. 4 PDF of R and Q for the Lagrangian (−) and the filtered Eulerian (···) from Exp I (top) and II (bottom)

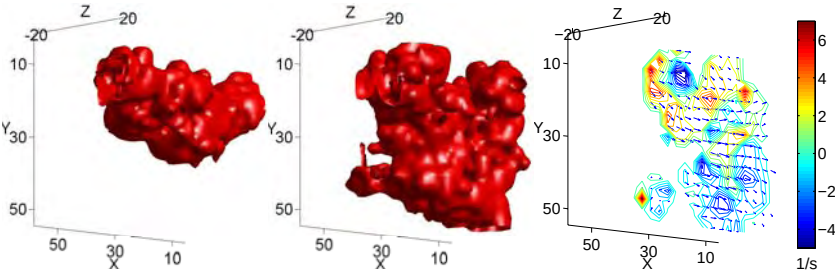

Fig. 5 Instantaneous enstrophy isosurfaces form Exp I at t=1s (left) and t=2s (middle) and center plane velocity distribution with overlayed vorticity iso-contours at t=2s

of the turbulence boundary is the average in the (x,z)-plane of the detected points, i.e., $H(t) = \langle y^*(x,z,t)\rangle_{x,z}$. The propagation of the turbulence boundary is depicted in Fig. 6 where $H(t)$ is plotted over time in linear (left) and logarithmic (right) coordinates. The solid line is a best fit taken from the Particle Image Velocimetry (PIV) measurements in [8] (the error bars represent the experimental scatter) and the circles are the present experiment. We note that our measurements are in agreement (within the experimental uncertainty) with [8]. This demonstrates also quantitatively that the relevant large-scale flow features could be successfully measured.

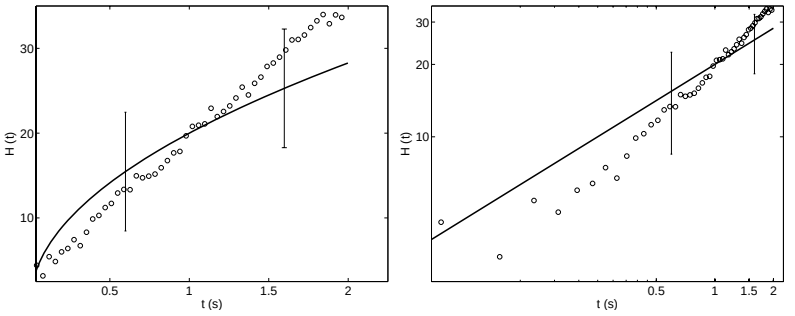

Fig. 6 propagation of $H(t)$ over time in linear (left) and logarithmic (right) coordinates where (-) stands for the best fit from [8] and (o) for the PTV data

4 Summary

In summary, we performed measurements of a developing turbulent flow by using 3D-PTV, a measurement technique that captures the velocity and velocity derivatives in a Lagrangian setting. In the experiments the turbulence is driven by an oscillating grid and spreads in time through the observation volume. A first experiment was performed with an observation volume large enough to access the dynamics associated with the energy containing eddies of the flow. From this experiment, the fields of coarse-grained velocity derivatives were calculated and with the use of these fields, first, the flow structure was visualized and, secondly, the spreading of the turbulent region was measured. The measurements were shown to be in close agreement with the results in [8]. In a second experiment a small observation volume was used so that the small intermediate range of scales of the flow could be discussed. While accuracy checks based on kinematic relations were shown to yield satisfactory results for both types of experiments, only from the small-scale experiment could genuine features of turbulence, like the tear-drop shape of the iso-probability contours of the R-Q plot, be recovered. Velocity derivatives were obtained in both the Lagrangian and Eulerian frame of reference. Although the accuracies were found to be comparable in both frames of reference, only statistics based on the spatially resolved measurement coincide in the two settings. Statistics of coarse-grained velocity derivatives were found to be somewhat different when obtained from the Eulerian or Lagrangian data set. We conclude that coarse-grained derivatives are useful, for example, for a qualitative characterization of the larger scales of the flow field, but they have to be used with caution. Subtle issues related to genuine properties of turbulence might not be recovered and the statistics might depend on specific filtering. However, this is precisely a reason why simultaneous two-scale measurements are needed.

The future step is to do both experiments, the recording in the large and in the small volume, simultaneously. This will allow for the coupling of the information on the large and the small scales and will shed more light on the interaction between eddies of different sizes, for example. For the future simultaneous measurements

some additional technical amendments will be necessary: two cameras (one with focus on the small, the other with focus on the large volume) will be synchronized and cross-calibrated as it was done in a previous study by the authors, [3]. To allow for different seeding densities in the two volumes, two different types of particles will be used, namely Rhodamine labelled particles for the large volume and conventional Polystyrene particles for the small volume. The first camera will be equipped with a dichroic red filter and the second camera with a dichroic green filter.

Acknowledgements. M. Kinzel gratefully acknowledges the support of the DFG within the SPP1147 program. A. Liberzon's visit at ETH was supported by ERCOFTAC and ETH visitor programs. Furthermore the authors would like to thank A. Tsinober and K. Hoyer for their contributions.

References

1. Burgmann, S., Brücker, C., Schröder, W.: Scanning PIV measurements of a laminar separation bubble. Exp. Fluids 41, 319–326 (2006)
2. Elsinga, G., Scarano, F., Wieneke, B., van Oudheusden, B.: Tomographic particle image velocimetry. Exp. Fluids 41, 933–947 (2006)
3. Guala, M., Liberzon, A., Hoyer, K., Tsinober, A., Kinzelbach, W.: Experimental study of clustering of large particles in homogeneous turbulent flow. J. of Turbulence 9(34), 1–20 (2008)
4. Holzner, M., Guala, M., Tsinober, A., Kinzelbach, W.: Generalized detection of a turbulent front generated by an oscillation grid. Exp. Fluids 41, 711–719 (2006)
5. Holzner, M., Liberzon, A., Nikitin, N., Kinzelbach, W., Tsinober, A.: Small scale aspects of flow in proximity of the turbulent/nonturbulent interface. Phys. Fluids 19, 071702 (2007)
6. Hoyer, K., Holzner, M., Lüthi, B., Guala, M., Liberzon, A., Kinzelbach, W.: 3D scanning particle tracking. Exp. Fluids 39, 923–934 (2005)
7. Hurst, D., Vassilicos, J.: Scaling and decay of fractal-generated turbulence. Phys. Fluids 19, 035103 (2007)
8. Kinzel, M., Holzner, M., Lüthi, B., Tropea, C., Kinzelbach, W., Oberlack, M.: Scaling laws of turbulent diffusion - an experimental validation. Exp. Fluids (2008) (in review)
9. Lüthi, B., Tsinober, A., Kinzelbach, W.: Lagrangian measurement of vorticity dynamics in turbulent flow. J. Fluid Mech. 528, 87–118 (2005)
10. Maas, H., Gruen, D., Papantoniou, D.: Particle tracking velocimetry in three-dimensional flows. Exp. Fluids 15, 133–146 (1993)
11. Pereira, F., Lu, J., Graff, E., Gharib, M.: Microscale 3d flow mapping with μDDPIV. Exp. Fluids 42, 589–599 (2007)
12. Raffel, M., Willert, C., Kompenhans, J.: Particle Image Velocimetry: A Practical Guide. Springer, Heidelberg (1998)
13. Tennekes, H., Lumley, J.: A First Course in Turbulence. MIT Press, Cambridge (1972)
14. Tsinober, A.: An informal introduction to turbulence. Springer, Berlin (2001)

Extended Three Dimensional Particle Tracking Velocimetry for Large Enclosures

Elka Lobutova, Christian Resagk, Robert Rank, and Dirk Müller

Abstract. An extended three-dimensional particle tracking velocimetry (3D PTV) technique for the determination of trajectories, velocity vectors and flow pattern within a large cylindrical observation volume was developed and applied in a Rayleigh-Bénard (RB) cell. The 3D PTV system consists of four CMOS cameras, two flash lamps, an image recording and data processing system. Helium filled soap bubbles and latex balloons have been used as tracer particles. The spatial resolution and accuracy have been investigated in a test cell with the dimensions of $4 \times 3 \times 4m^3$ by means of a given trajectory of a small glass sphere. A first application of the developed 3D PTV system in the large RB cell with a diameter of $7.15m$ and a height of $3.5m$ showed different characteristic flow patterns of the mean flow outside the boundary layers. The proposed technique has a wide range of potential application for the analysis of indoor air flows.

1 Introduction

Characterization of the large scale flow structures in ventilated rooms [3] is a largely unresolved problem of experimental fluid mechanics. The present work is an attempt to solve this problem using an optical technique, namely 3D PTV.

There are many well-known flow measurements techniques such as hot-wire anemometry (HWA), laser Doppler anemometry (LDA), particle image velocimetry (PIV) and particle tracking velocimetry (PTV). Each of them provides appropriate measured data for the derivation of defined flow properties. But none of them is

Elka Lobutova · Christian Resagk
Faculty of Mechanical Engineering, Ilmenau University of Technology, P.O. Box 100565, 98684 Ilmenau, Germany
elka.lobutova@tu-ilmenau.de

Robert Rank · Dirk Müller
E.ON Energy Research Center, RWTH Aachen University, Jägerstrasse 17–19, 52066 Aachen, Germany
Robert.Rank@eonerc.rwth-aachen.de

W. Nitsche and C. Dobriloff (Eds.): Imaging Measurement Methods, NNFM 106, pp. 113–124.
springerlink.com

appropriate to deliver all the parameters of the flow. HWA and LDA, e.g. [13] provide high spatial and temporal resolution for up to three components of the velocity but are limited to point measurements. They are unable to capture the instantaneous flow pattern, also known as coherent flow structures. PIV, e.g. [11] allows the determination of the flow field simultaneously at many points in the observation volume but it is limited to a two-dimensional analysis due to the light sheet illumination. An additional option of the PIV technique is the stereoscopic PIV. Thus we have the ability to measure the third velocity component but only in the given 2D light sheet. For the investigations of the Lagrangian trajectories, their statistics and the capture of the coherent large scale flow structures a full three-dimensional flow measurement technique like 3D PTV is suitable. The history of PTV is not new, it is one of the oldest flow measurement techniques. But until now there is no application of the 3D PTV technique suited for the determination of velocity fields and particle trajectories in very large measurement volumes. But why is the development of large scale 3D PTV so important?

For example, it is a great challenge to ensure good thermal comfort in rooms with a great many humans or heat generating devices e.g. in large office rooms or in passenger compartments of aircrafts, railway carriages, and cars. The airflow in these confined, or sometimes partly open, rooms is influenced by the geometry, the size of openings, the distribution of thermal loads, and the existence of any forced ventilation. Because of the superposition of all these influences, the structure of indoor flows is always very complex, highly turbulent and distinctly three-dimensional, and is therefore very hard to predict. Hence it is useful to study first the natural convection apart from the forced convection. A common model experiment for natural convection is the Rayleigh-Bénard (RB) cell. This is an adiabatic enclosure heated from below and cooled from the top. As a result the density at the bottom layer becomes lower than at the top, the fluid becomes lighter and vertical convective motion ensues. Beside the investigations of the boundary layers over the hot plate and under the cold plate the coherent large scale flow structures in the bulk are of special interest, because they occur in different modes at different aspect ratios ($\Gamma = D/H$) and Rayleigh (Ra) numbers.

From previous experimental investigations at high Ra and aspect ratio $\Gamma = 1$ we know about the existence of one large convective roll [12]. Compared to this case the flow in RB cells with aspect ratio $\Gamma \neq 1$ was investigated very rarely and the knowledge about the turbulent flow structure in the bulk (wind) is limited. Xia et al. [14] published for the first time the investigation of the large scale velocity structures in a rectangular water cell. First systematical study of the wind properties and the hypothetic flow patterns in a cylindrical air cell that would match observations for a continuously varying aspect ratio were published by du Puits et al. [10]. They report about direct measurements of both horizontal velocity components using a 2D LDV as well as measurements of temperature profiles using very small and fast microthermistor probes on the central axis of the RB cell. They analyze the autocorrelation functions of velocity and temperature time series and infer indirectly the global flow structure.

A qualitative study of the flow indicated the existence of different and particulary new flow structures. As deduced from earlier stereoscopic PIV measurements [1] there are mainly two states namely large single roll (LSR) and small single roll (SSR). But the stereoscopic PIV could not capture the small tornados, arising downwards from the cooling plate and upwards from the heating plate.

The development of the 3D PTV system started in 1990 [7, 8, 9]. It is based on methods of digital photogrammetry and recording particle image sequences by more than one synchronized camera. In early works this system was applied in test volumes from $120 \times 120 \times 15mm^3$ to $200 \times 200 \times 40mm^3$.

In this paper we will describe the application of the 3D PTV system in an observation volume of about $130m^3$ for the determination of long term particle trajectories and large scale flow patterns.

2 Experiment

2.1 The Barrel of Ilmenau

The experiments are performed in a large Rayleigh-Bénard experiment called "Barrel of Ilmenau" (BOI) (figure 1). It is a cylindrical container with a diameter $D = 7.15m$ and a height H, which can be varied between $0.05m$ and $6.30m$. For our measurements we have chosen a constant height $H = 3.57m$, corresponding to an aspect ratio $\Gamma = D/H = 2$. The working fluid is air. The temperature of the heating plate can be adjusted between $20°C$ and $80°C$ whereas the temperature of the cooling plate is kept at $20°C$. For the measurements described in this paper we set up a temperature difference $\Delta T = 40°C$. In this context, the Rayleigh number,

$$Ra = \frac{\alpha g H^3 \Delta T}{\nu \kappa} \tag{1}$$

is $1,3 \times 10^{11}$, where α is the thermal expansion coefficient, g is the gravitational acceleration, ν is the kinematic viscosity and κ is the thermal diffusivity.

As figure 1 shows, camera and illumination units are mounted on the wall inside the cell, the rest of the supporting equipment is placed on the cooling plate. As tracer particles we use helium filled soap bubbles, which are delivered from a bubble generator via flexible tubes. They are inserted in the measurement volume through conical diffusors which reduce the outlet velocity of the bubbles. In addition, for long term trajectory measurements we use latex balloons, which are also filled with helium and which can be added to the flow manually.

2.2 3D PTV System

A detailed description of the 3D PTV technique is given in papers by Maas [4] and Malik [6]. Therefore we will only give a short overview of the basic principles and

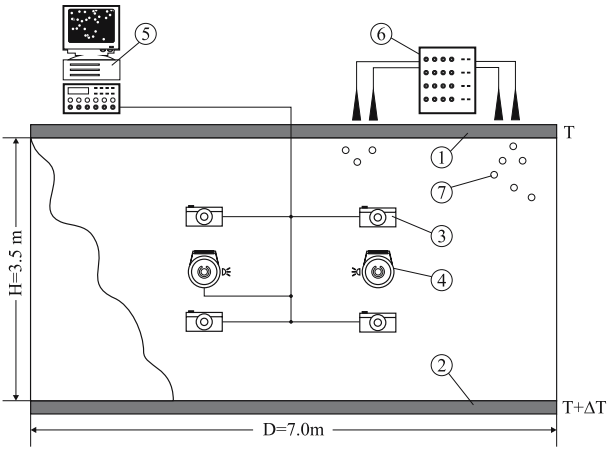

Fig. 1 Schematic diagram of the experimental facility ”Barrel of Ilmenau” and the setup of the 3D PTV system. 1 and 2 illustrate respectively the cooling and the heating plate of the Rayleigh-Bénard cell; 3 is the camera system, consisting of four Canon CMOS SLR cameras; 4 is the illumination unit, consisting of two Elinchrom high power flashes; 5 is the control and storage unit and 6 illustrates the bubble generator. Cameras and flashes are mounted on the wall, the rest of the supporting equipment is placed on the cooling plate. The bubbles are transported from the generator via flexible tubes and inserted in the measurement volume through conical diffusors which reduce the outlet velocity of the bubbles

will describe in detail the special requirements imposed for measurements in a large observation volume.

Before starting the measurements a camera calibration is necessary. For this purpose calibration targets are placed into the object space (wall and heating plate) to be imaged by the cameras. After a user supported preorientation the processing of the calibration images is performed automatically with the result that all parameters describing exterior and interior orientation and lens distortion for each camera are known.

Then the procedure of the 3D PTV application is as follows. The convectively driven flow is seeded with appropriate particles. The observation volume is illuminated uniformly using lamps with continuous emission or pulsed light sources. The particles are imaged by at least two synchronized cameras, but to reduce ambiguities it is advisable to use three or four cameras.

The pre-processing of the images begins with the elimination of the static background and after that the particle images can be segmented by using a region growing algorithm. The image coordinates of the particles are determined in each frame with sub-pixel accuracy by estimation of the gray value weighted center of gravity.

Now, knowing the orientation parameters of the cameras from the calibration procedure, the correspondent particles are computed by epipolar geometry. This means that proceeding from a specific point in one image an epipolar line in another image can be calculated, so that the corresponding point can be found.

After the establishment of the stereoscopic correspondences, the computation of the 3D coordinates of the particles is performed using the strict solution via least squares adjustment, called intersection. These results are passed on the tracking module to establish correspondences in time [6].

2.3 Tracer Particles

To make the flow visible it has to be seeded with small, neutrally buoyant tracer particles. This is relatively easy if the working fluid is water or another liquid, but it is a real challenge to find flow markers for air in a large volume. The reason for this is on one hand the physical density of the particles should correspond to the density of the flow medium and their size should be as small as possible to guarantee appropriate response behavior. On the other hand, the particles should be large enough to be visible for the cameras by suitable illumination.

We have chosen to use two types of tracer particles, namely helium filled soap bubbles with a diameter of 4*mm* and helium filled latex balloons with a diameter of about 15*cm*. The principle of helium filled particles is that a lighter-than-air gas inside a hollow sphere is used to compensate the sphere's mass. Both of the tracer particles have advantages and disadvantages. The use of soap bubbles allows us the reconstruction of the instantaneous three-dimensional velocity field, but we are limited in the case of Lagrangian measurements because of the relatively short lifetime of the bubbles of about four minutes. In the Lagrangian type of flow specification the fluid element quantities are defined as function of time and describe the dynamical history of this selected fluid element. The use of latex balloons as tracer opens up the possibility for the measurement of long term single trajectories, the calculation of the velocity and acceleration derivation and thereby the investigation of the statistical and structural properties of the turbulent flow.

For the production of the density neutral soap bubbles a high performance bubble generator has been developed [2]. The generator consists of four injection tubes, four cyclones and a high pressure fan. All the components are built into a rack with castors on the bottom. The dosing system for controlling the bubble fluid, the helium and air flow rate is integrated in the front side of the rack.

The bubbles are generated in an injection nozzle (figure 2). The injection nozzle consists of two concentric tubes for helium and bubble solution and an outer reservoir to supply air to the contraction zone in the cyclones (not shown). All tube design parameter as length and diameter have been optimized for a stable bubble generation process using specially developed bubble solution fluid (BSF) with a lifetime of about 4 minutes. The bubble generator is able to provide a high number of density neutral bubbles. The operation time of the bubble generator is approximately two hours before the internal bubble solution tank is empty. The fluid and gas quantities can be adjusted separately for all four cyclones to guarantee reasonable narrow distribution for the bubble diameters. The cyclones are connected to diffusers by flexible plastic tubes. The diffuser minimizes the momentum of the particles entering the experimental set-up.

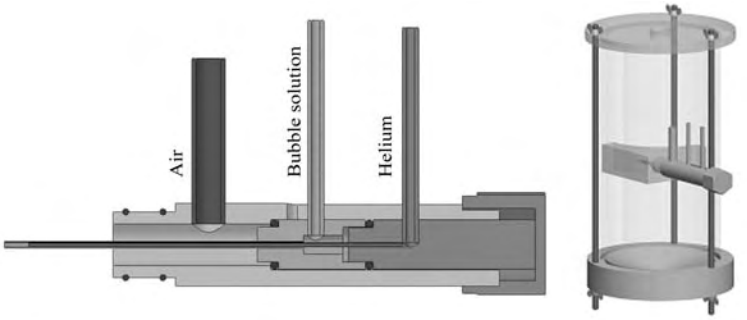

Fig. 2 Scheme of the injection tube (left) and cyclone (right) of the bubble generator

Alternatively to the standard system, the injection nozzle has been modified to realize an increased bubble diameter. The helium filling of the soap bubbles is replaced by a helium-air-mixture which is produced by an additional air connection and a mixing zone. The enlarged bubble volume allows a better detection of the bubble movements and it will also enhance the possibilities adjusting the bubble film color through nanoparticles.

The next step is a new nozzle generation with an active bubble size control device. A reconstruction of the injection tube will enable a more precise production of bigger bubbles. The bubble generation process will be forced by an alternation air volume flow rate caused by pressure waves from a loudspeaker system. Figure 3 shows the schematic diagram of the new injection tube. The air injection tube is built into a loudspeaker. By controlling the loudspeaker by a frequency synthesizer which pulses the airflow for the bubble separation. The bubble generation frequency can be adjusted and thus leading to a very narrow size distribution of the helium filled soap bubbles.

In the ongoing development the lifetime of the bubble film shall be enhanced at higher temperatures reducing the evaporation of the bubble film through an addition of a biopolymer matrix.

An important point are the specific optical properties of the bubbles. Due to the fact that the bubble is made of a very thin shell of a transparent medium it reflects less than 5% of the incident light. We tested two possibilities to increase the bubble

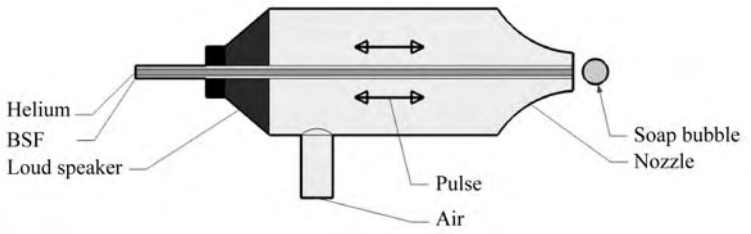

Fig. 3 Bubble generator nozzle with active bubble size control device

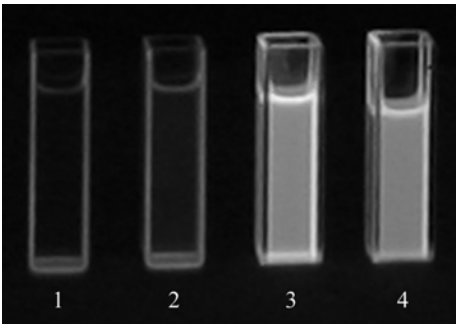

Fig. 4 Comparison picture for the luminescent BSF. From left to right the probes are water, non-luminescent solution and two luminescent solution. They are illuminated by UV light source and the picture is made with exposure of 30 seconds

Table 1 Comparison of the grey value level for four different BSF. ”0” corresponds to black and ”256” corresponds to white. The average was struck by about 900 pixels

Water (1)	Non-luminescent BSF (2)	Luminescent BSF ”1” (3)	Luminescent BSF ”2” (4)
5	10.5	87.6	82.7

visibility - indirectly by changing the surrounding optical appearance and directly by changing the bubble optical properties.

There are several ways to improve the optical properties of the bubbles [5]. One of them is to increase the scattered light intensity from the bubble film by adding dyes to the BSF. A second way is to fill the bubble inside with smoke particles in order to make this part visible. But we tested an alternative approach by using luminescent BSF and illuminated the measurement volume with UV light. To quantify our test with luminescent BSF, we compared four different solutions - two luminescent, one non-luminescent BSF and pure water. To keep it near the real segmentation procedure based on region growing algorithm, we took pictures of the UV-illuminated solutions (figure 4) and compared the grey level values over a given area. The result is listed in table 1.

The principle aim of the indirect method is to shine as much light as possible on the bubble while keeping the background dark. So we illuminated the bubbles by high-power flash lamps and painted our inner cell walls with low-reflecting black paint. This test gave sufficient results, we could detect the bubbles even at long distance ($< 7m$), and we decided to use this illumination method for our 3D PTV measurements.

2.4 Camera System

When choosing the cameras two requirements should be met. First, due to the very large observation volume and the small particles, only cameras with a high spatial

resolution are considered. And second, a high temporal resolution provides more detailed information about the occurring time dependent flow structures. Unfortunately today's best imaging technology cannot be offered in an all-in-one camera that would comprise high resolution and high speed at the same time. The high resolution cameras are limited in the repetition rate and vice versa high speed cameras have low spatial resolution. After having gone through all pros and cons we decided to put the focus on the detection of small tracer particles and therefore we have chosen a high resolution camera.

The resulting camera system consists of four CANON EOS 20D SLR cameras with a spatial resolution of 8 megapixels. The frame rate is however limited to 3 fps, which was deemed sufficient to resolve the large scale flow in the BOI. The cameras are equipped with wide-angle lenses and mounted on the wall as sketched in figure 1. In this arrangement the covered volume is about 70% of the convection cell.

2.5 Validation Measurement

To proof the accuracy of the new 3D PTV technique for a very large volume a validation measurement was made in a rectangular cell with the dimensions of $4 \times 3 \times 4m^3$. A $13mm$ sized glass sphere was suspended by a $1.5m$ long wire on a step motor fixed on the top of the cell. The angular velocity was preset and the turning radius was measured. Over fifty sequences of the sphere's track were taken, which corresponds to more than five turns of the sphere. The comparison of the reconstructed trajectory and the real paths shows an error in the x-y plane of $\sigma_{xy} = 2.4mm$ which is about only $0,4\%$ of the turning diameter and an error in z direction of $\sigma_z = 0.8mm$. The measured velocity coincides with the calculated value. That the velocity determination is more accurate than the determination of the diameter is caused by the correlation between neighbourhoods in the image space. Two 3D points with a short distance are affected by the same bias. So the first derivation of the difference vector, the velocity, is not affected by bias. This is an advantage of the 3D PTV system.

3 Results

We performed two series of 3D PTV measurements, the first one using helium filled soap bubbles and the second one using helium filled latex balloons. The soap bubble sequences were taken with $2.5fps$ whereas the balloon sequences were taken with $1fps$. Both were done at aspect ratio $\Gamma = 2$ and temperature difference between cooling and heating plate at $\Delta T = 40°C$.

During the soap bubble measurement we met a problem with fixing cameras on the wall. Because of the thermal expansion of the wall segments during the convection experiment the orientation of the camera axes had changed exiguously. This led to a partly impossibility to establish correspondences between the related particles. We are in the process to solve this problem using alternative calibration procedures. Nevertheless the simple correlation between two captures from one camera shows that the particle concentration and visibility in the large observation volume is

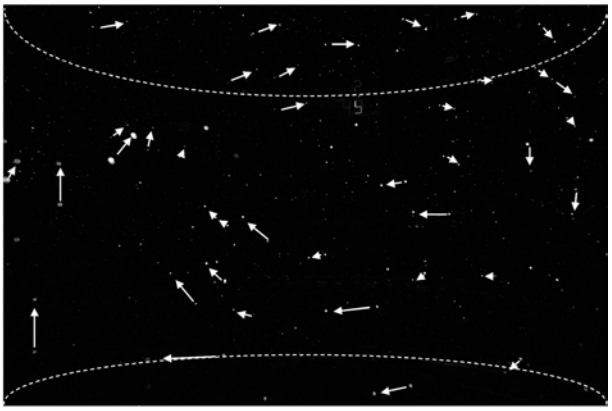

Fig. 5 Example of the visualization of the large scale flow structure in the BOI using helium filled soap bubbles. The correlation between the snapshots from one camera shows clearly the most occurring mode: large single roll

sufficient for the detection of the most occurring flow structure in the form of a large single roll (figure 5).

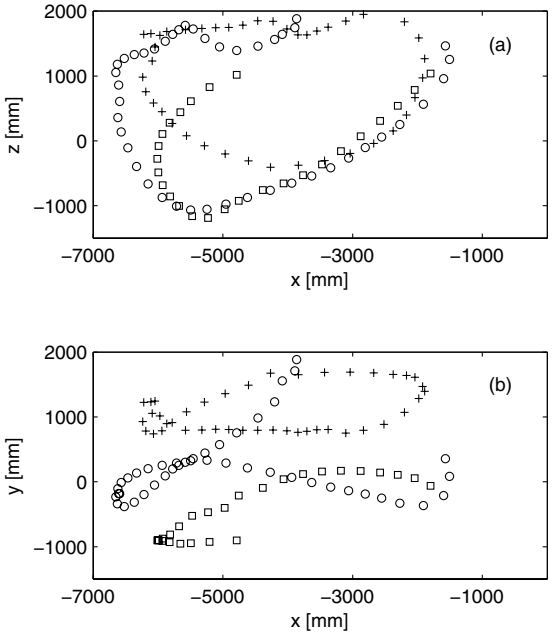

Fig. 6 Reconstructed long term trajectories representing large single roll in the whole cross section of the convective cell (a) and the same trajectories viewed from the top (b); $\Gamma = 2$ and $Ra = 1,3 \times 10^{11}$. Each point corresponds to one time step of 1s

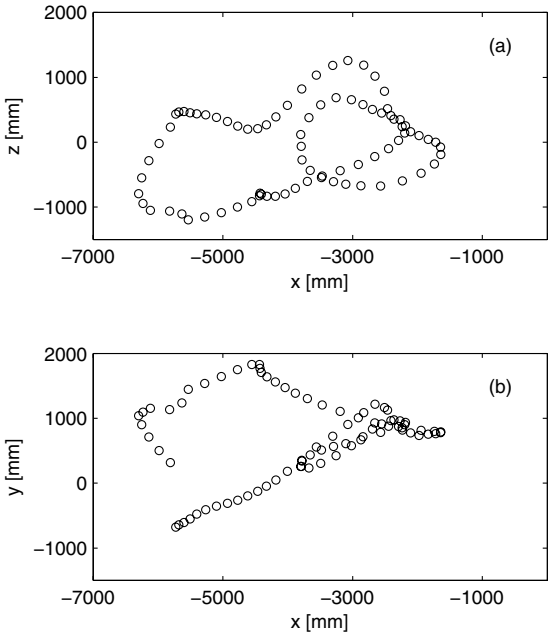

Fig. 7 Reconstructed long term trajectory representing transition between large single roll and small single roll in the whole cross section of the convective cell (a) and the same trajectory viewed from the top (b); $\Gamma = 2$ and $Ra = 1,3 \times 10^{11}$ each point corresponds to one time step of 1s

The helium filled latex balloons were primarily used to observe single long term trajectories. Representative results for Lagrangian trajectories in the BOI are shown in figure 6 and figure 7. Figure 6 (top) depicts a projection of a LSR in the x-z plane. The movement of three balloons was followed for 60 time steps, which corresponds to 60*s*. The measured velocity varies between $0.06m.s^{-1}$ and $0.6m.s^{-1}$. One could believe that this structure is two dimensional, but if we take a look at figure 6 (bottom), which is a top view (x-y plane), we see in fact a distinctive third flow direction. This result confirms our assumption that the flow structures are fully three dimensional. Further more we can clearly see in figure 7 a transition from LSR to SSR along one trajectory, which shows us the unstable character of the bulk flow at $\Gamma = 2$.

From these results we can not only get information about the structural modes of the wind but also calculate velocity and acceleration derivation, which will be subject of future publication.

4 Conclusion

We report about the development and application of a novel 3D PTV technique which is especially suitable to investigate coherent large scale flow structures in very large volumes. It is based on a four camera image recording system, a full

volume illumination with two flash lamps and helium filled soap bubbles or Latex balloons as tracer particles. Validation measurements with a known trajectory of a glass sphere show a high spatial and a sufficient temporal resolution of the method in order to characterize the large scale flow pattern modes with dimensions between $0.5m$ and $10m$. The helium filled soap bubbles used are suited refering to lifetime and concentration to seed the flow in a very large measurement volume with a typical length of 10m. But until now long term observation of single particle tracks fail on the limited life time at temperatures higher than $25°C$. For that task one should rather use the larger helium filled latex balloons with a lifetime of several hours as well at ambient temperatures up to $60°C$. The first application of the developed 3D PTV systems in the large scale convection cell BOI confirms the existence of three different coherent flow structure modes in the bulk region and its strong unstable behavior. The goals of further developments and investigations are the extension of the bubble lifetime at higher temperatures and the use of latex balloons, in order to record long time trajectories. That will give us the possibility for a detailed statistical analysis of Lagrangian trajectories caused by the coherent large scale flow pattern in the bulk region of the convection cell.

Acknowledgements. The work was financially supported by the Deutsche Forschungsgemeinschaft under grant no. RE 1066/5-1 and MU 2315/2-2. The PTV data processing was performed at Dresden University of Technology in the group of H-G Maas.

References

1. Bosbach, J., Wagner, C., Resagk, C., du Puits, R., Thess, A.: Large scale Rayleigh-Bénard convecion. In: Raffel, M., Willert, C., Wereley, S., Kompenhans, J. (eds.) Particle Image Velocimetry. Springer, Heidelberg (2007)
2. Dahms, A., Rank, R., Müller, D.: Enhanced particle streak tracking system (PST) for two dimensional airflow pattern measurements in large planes. In: Proc. of Roomvent 2007, Helsinki (2007)
3. Linden, P.F.: The fluid mechanics of natural ventilation. Annu. Rev. Fluid Mech. 31, 201–238 (1999)
4. Maas, H.G., Gruen, A., Papantoniou, D.: Particle tracking velocimetry in three-dimensional flows. Part I. Exp. Fluids 15, 133–146 (1993)
5. Machacek, M.: A quantitative visualization tool for large wind tunnel experiments. PhD Thesis, ETH Zürich (2003)
6. Malik, N.A., Dracos, T., Papantoniou, D.: Particle tracking velocimetry in three-dimensional flows. Part II. Exp. Fluids 15, 279–294 (1993)
7. Papantoniou, D., Dracos, T.: Analyzing 3D turbulent motion in open channel flow by use of stereoscopy and particle tracking. Advances in Turbulence 2 (1990) (Proc. of the Second European Turbulence Conference, Berlin)
8. Papantoniou, D., Dracos, T.: Lagrangian statistics in open chanel flow by 3D particle tracking velocimetry. In: Proc. Int. Symp. on Engineering Turbulence - Methods and Measurements, Dubrovnik (1990)

9. Papantoniou, D., Maas, H.G.: Digital photogrammetry for determination of tracer particle coordinates in turbulent flow research. In: ISPRS Com.V Symp., Zurich, published in SPIE Proc. Series, vol. 1395, Part I (1990)
10. du Puits, R., Resagk, C., Thess, A.: Breakdown of wind in turbulent thermal convection. Phys. Rev. E 75, 016302 (2007)
11. Raffel, M., Willert, C., Werely, S., Kompenhans, J.: Particle Image Velocimetry: A practical Guide. Springer, Heidelberg (2007)
12. Sun, C., Xia, K.Q., Tong, P.: Three-dimensional flow structures and dynamics of turbulent thermal convection in a cylindrical cell. Phys. Rev. E 72, 026302 (2005)
13. Tropea, C., Yarin, A., Foss, J.: Handbook of Experimental Fluid Mechanics. Springer, Heidelberg (2007)
14. Xia, K.Q., Sun, C., Cheung, Y.H.: Large scale velocity structures in turbulent thermal convection with widely variyng aspect ratio. In: Proc. 14th Int. Symp. on Applications of Laser Techniques to Fluid Mechanics 2008, Lisbon (2008)

High Density, Long-Term 3D PTV Using 3D Scanning Illumination and Telecentric Imaging

Jens Kitzhofer, Clemens Kirmse, and Christoph Brücker

Abstract. This article discusses the application of 3D SPTV (3D Scanning Particle Tracking Velocimetry) to the high-density reconstruction of Lagrangian trajectories using telecentric imaging and a homogenous 3D illumination. A cubic volume in the order of roughly 10 x 10 x 10 cm³ is illuminated by a 3D beam scanning device and is recorded by three high speed digital cameras equipped with telecentric lenses. A vortex ring in a water tank is used as a model flow. The advantages of this setup are small particle displacements relative to the distances between the particles due to the high speed recording and a large depth of field without distortions due to the telecentric lenses. The scanning laser beam generates a homogenous and efficient illumination of the particles over the whole volume and a precise parallel shift of the scanned planes. The quality and precision of illumination and the telecentric imaging yield a more simplified particle matching and 3D reconstruction. This results in a robust, accurate and easy detection of time resolved particle trajectories with a high spatial resolution within the measured volume.

1 Introduction

The investigation of flow fields is usually performed within an Eulerian framework. For the analysis of turbulent flows the Lagrangian frame gives additional important information about turbulent mixing, dispersion etc. This requires the reconstruction of long Lagrangian trajectories with a high spatial resolution. Therefore it is necessary to develop methods for processing a high number of particles in the measured volume and to track particles for long periods of time. These aims are not feasible by standard photogrammetric methods like those used for classical 3D PTV. With increasing number density of particles the problem of stereo-matching and overlapping particle images rise exponentially. Therefore, in classical 3D PTV the maximum number of trajectories is limited to the order of 10^3 in a typical cubic volume, which is recorded by 4 CCD cameras [4]. The expansion to 3D SPTV can solve these problems by dividing the observed volume into several

Jens Kitzhofer · Clemens Kirmse · Christoph Brücker
TU Bergakademie Freiberg, Institut für Mechanik und Fluiddynamik
Jens.Kitzhofer@imfd.tu-freiberg.de

W. Nitsche and C. Dobriloff (Eds.): Imaging Measurement Methods, NNFM 106, pp. 125–134.
springerlink.com

smaller volumes with fewer particles. The method of 3D Scanning PIV has already been proven to be a successful and practicable solution for the extension of classical PIV to 3D spatial resolution [1, 2]. Hoyer et al. implemented the method of a scanning light sheet for 3D PTV with one single high speed camera [4]. This, compared to classical PTV, nearly doubled the observation volume and the spatial resolution with a fourfold higher number density of reconstructed trajectories. The use of telecentric lenses and three high speed digital cameras promise a further enlargement of the observation volume and an increase of the number density of reconstructed trajectories. The advantages of the telecentric lenses are an approximately constant magnification, a large depth of focus and negligible image distortions. The 3D beam scanning system additionally yields a very homogenous particle image quality and a precise spacing of the light sheets. Therefore, it highly simplifies the matching algorithm and allows to implement a linear reconstruction method.

2 Experimental Set-Up

The experimental set-up is shown in figure 1. The laser beam of a continuous Argon-Ion laser (a) Coherent Innova 70 (2 W) passes an optical lens system (b) to adjust the desired thickness of the light sheets. The rotating mirror drum (c) reflects the laser beam into the direction of the observed volume and generates successively 10 parallel light sheet planes (f). The studied flow is a vortex ring travelling in an octagonal glass tank (e) filled with water. The vortex is generated at the exit of a piston tube with a diameter of 50 mm (g). The neutrally buoyant seeding particles (100 microns) are injected into the center of the vortex generator. The particle images are recorded with a three camera system consisting of digital high speed cameras Photron APX RS with a resolution of 1024 x 1024 Pixel² and an angular displacement of 45°, -45° and 90°. The side of the octagon opposite to the entrance side for the laser is covered with a light absorbing mat that reduces stray reflections. This is also valid for the faces opposite the cameras, thus giving a perfectly black background. The experiments are performed with a recording rate of 1000 frames/s. Using 10 scanning planes results in a separation time of 10 ms for each subsequent illumination of one scan plane.

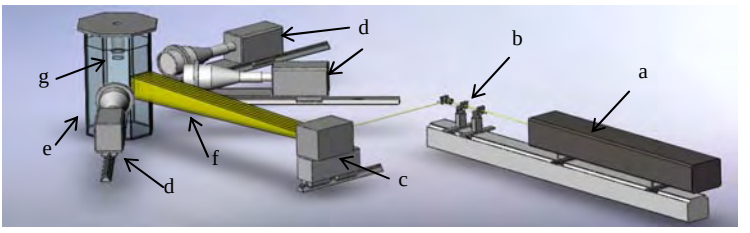

Fig. 1 Experimental Set-up (a Ar-Ion-laser, b lens system, c rotating mirror drum, d high speed camera, e octagon, f light sheets, g vortex generator)

2.1 Mirror Drum Scanner

The 3D beam scanning system consists of a rotating drum with 10 surface mirrors distributed on a helix around its circumference as shown in figure 2 on the left. An optical decoder on the drum axis provides the master clock for the synchronization of the cameras. During the rotation of the drum, the beam forms a vertical light sheet (figure 2 middle). Cinematic 3D beam scanning generates an efficient and homogenous illumination [1], which is important for the quality of the present 3D SPTV application. The thickness of each light sheet is 10 mm and the total spacing is 90 mm. The lateral overlap of the planes corresponds to 10 % of the sheet thickness. The constant overlap in depth is generated with the light sheet's parallel shift and shape. The accurate positioning of the light sheets in the observed volume is verified with a plane target.

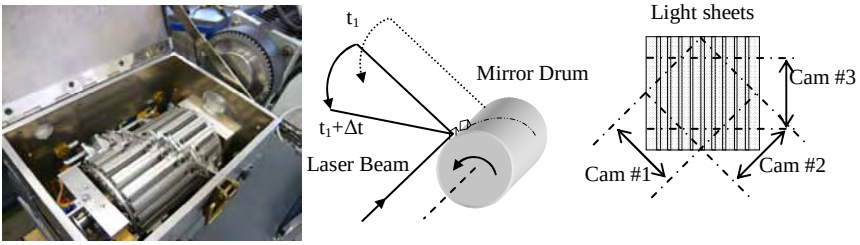

Fig. 2 Mirror drum (left), schematic sketch of the rotating mirror drum (middle) and observed plane from the top view (right)

2.2 Telecentric Lenses

The telecentric lenses used in this application are telecentric in object space. Therefore the focus point in the object space is at infinity resulting in a parallel projection. The advantages of using telecentric lenses consist of a long depth of field, a constant magnification over the whole depth of field, high accuracy and negligible distortions. The measured distortions are less than 0.1 % of the image diagonal in the outer image areas. The telecentric range with deviations of less than 0.1% has been evaluated to be about 90 mm with a scaling factor of 11.4 ± 0.02 Pix/mm at an f-number of f16. This is equivalent to a magnification M = 0.2. The cameras are adjusted perpendicular to the walls of the glass tank. Because of the parallel projection the observable measuring volume is limited by the image dimensions (figure 2 on the right) and corresponds to the inner hexagon that is imaged by all cameras simultaneously.

3 Reconstruction Methods

The following chapter describes the new algorithm for 3D reconstruction of Lagrangian trajectories and the simplification of the implementation due to beam scanning and telecentricity.

3.1 Camera Model

The transformation of a 3D-object scene onto a 2D-image scene is called projection, which mathematically means the formulation of a transformation matrix (camera model). A common model is the pinhole model [7], which assumes a perspective projection. The use of the telecentric lenses converts the perspective projection into a parallel projection at least within the telecentric range [7]. In general the global transformation from a 3D-point to a 2D-point is the product of an external, an internal and a perspective transformation. The external transformation matrix D specifies the orientation and the placement of the image plane related to a world coordinate system. Thus it describes the transformation of a 3D object point to a 3D camera point. The perspective transformation matrix P' describes the transformation of a 3D camera point to a 2D point in sensor coordinates of the camera. In case of the parallel projection the 3D camera point in x- and y-direction is the same as the sensor point in x- and y-direction. The internal transformation matrix A finally describes the relation between the 2D sensor points in pixel to a 2D point in mm. Therefore the matrices are:

$$D = \begin{bmatrix} R & \vec{t} \\ 0_3^T & 1 \end{bmatrix}, P' = \begin{bmatrix} 1 & 0 & 0 & 0 \\ 0 & 1 & 0 & 0 \\ 0 & 0 & 0 & 1 \end{bmatrix}, A = \begin{bmatrix} k & 0 & 0 \\ 0 & k & 0 \\ 0 & 0 & 1 \end{bmatrix} \tag{3.1}$$

R describes the 3x3 rotational matrix with entries r_i, which include the three Euler angles, and **t** a 3x1 translation vector in x-,y- and z-direction. The approximation for the telecentric projection consists in a zero translation in z-direction. The factor k describes the scaling factor in Pix/mm, which is proportional to the magnification. The projection matrix P for telecentric lenses then reads:

$$P = A \cdot P' \cdot D = \begin{pmatrix} k \cdot r_1 & k \cdot r_2 & k \cdot r_3 & k \cdot t_x \\ k \cdot r_4 & k \cdot r_5 & k \cdot r_6 & k \cdot t_y \\ 0 & 0 & 0 & 1 \end{pmatrix} \tag{3.2}$$

The projection matrix of the parallel projection includes six degrees of freedom. Compared with the ten degrees of freedom in the perspective projection, this is a simplification by four degrees of freedom [7]. For the 3D reconstruction it is important to determine the three unknown Euler angles, the two displacements of the cameras and the scaling factor by calibration.

3.2 Epipolar Geometry

For reconstruction of a Lagrangian trajectory in 3D it is necessary to find homologue trajectories in both camera views of camera #1 (C#1) and camera #2 (C#2). A mathematical model for a stereoscopic camera setup is given by the epipolar geometry [7]. It describes, that a point, which is found in C#1, has to be along a line in C#2. Mathematically the relation between both cameras is described by the fundamental matrix F. The relation of a 2D particle image position (x_1, y_1) in C#1

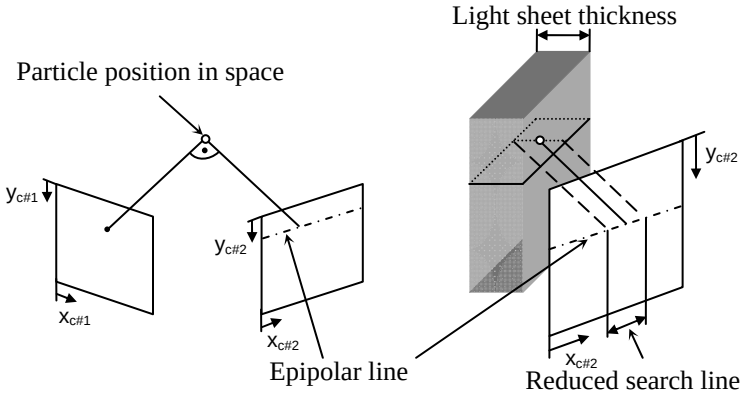

Fig. 3 Reducing of the search line for homologue points in camera two

to the position of the same particle in C#2 (x_2, y_2) is called epipolar equation and the line l_2 is called epipolar line:

$$(x_2 \quad y_2 \quad 1) \cdot F \cdot \begin{pmatrix} x_1 \\ y_1 \\ 1 \end{pmatrix} = 0 \text{ ' } l_2 = F \cdot \begin{pmatrix} x_1 \\ y_1 \\ 1 \end{pmatrix} \tag{3.3}$$

The evaluation of F is made within the calibration of the two projection matrices. An advantage of the scanning light sheets in combination with the epipolar line is shown in figure 3. The search range for a homologue point in C#2 along the epipolar line in C#2 is largely reduced by the small light sheet thickness. In this case the length of the line is reduced to 1/10 in comparison to the search line needed when all the volume is illuminated.

3.3 Calibration

The calibration of the three cameras includes the evaluation of the projection matrices of C#1, C#2 and C#3 and the evaluation of the fundamental matrices for each combination of the cameras. For a correct calibration an adequate calibration target is necessary. The target used in our calibration consists of 32 spherical steel balls with a diameter of 5 mm. The spheres are positioned in two planes with an equidistant spacing. In each image plane the centroids of the spheres were determined with sub pixel accuracy. A comparison with the known 3D object coordinates yields the projection matrix P and implicit the unknown 6 parameters of the cameras. The nonlinear distortion in the images is negligible because of the telecentry (0.1 %). Thus it is unnecessary to compute a nonlinear de-warping as in the case of using lenses with a defined focal length. The fundamental matrix is determined by comparing homologue centroid positions in the images. If the 2D positions of the spheres in the camera images have been localized, F can be evaluated with the so called 8-point algorithm expanded by the Frobenius-norm [7].

3.4 Particle Tracking

The particle tracking method in this investigation follows the 4-frame method developed by Malik et al [6]. In a first step the accurate particle positions in both cameras are determined using a circular 1D Gauss template. In a second step the 2D trajectories in C#1 are captured and in a third step for each trajectory of C#1 corresponding particles are searched in C#2 and C#3. For the 2D tracking in C#1 a hybrid PIV/PTV method has been implemented [3]. This method identifies the direction of movement of the particles by using a PIV correlation technique. In the method herein we do not identify the movement in small interrogation areas, but we try to find larger areas in the observed plane, where a direction of movement of the particles is dominant. In these areas the trajectories with the preferred direction are searched. If a trajectory could be observed for three time steps, the search area for the next time step is defined by the direction, the speed and the acceleration of the former trajectory. After the evaluation of the 2D trajectories, corresponding particles for each trajectory are searched in the second camera along the reduced epipolar line. If there is more than one possibility for a 2D trajectory, each possible 3D trajectory is constructed and compared. The trajectory with best fitting results is chosen. The fitting conditions are the length of a particle movement between two time steps, the preferred direction of movement and the difference in the direction of movement. If there is no possible candidate found in C#2, a candidate is searched along the epipolar line in C#3. If a reconstructed 3D trajectory is taken as a true particle path, the corresponding particle locations in the single frame data set of C#2 or C#3 are deleted. In the next iteration step the algorithm tries to find corresponding particles in the images of C#2 or C#3, in which the information is reduced because of the deleted particle positions. In classical 3D PTV the 3D coordinates of particles are successively determined by using the information of four different fields of view [4]. In case of various materials with different refractive indices within the object space, e.g. fluid and window, 3D coordinates are calculated using ray-tracing through a multimedia geometry [5]. This is necessary, because an optical beam is refracted when passing through different media with an angle of incidence unequal to 90°. The parallel projection of the telecentric lenses avoids this problem, because they are placed orthogonal to the surfaces of the tank. The 3D reconstruction of corresponding particles is carried out by a linear parallel projection algorithm including the orientations of the cameras. This is a tomographic reconstruction algorithm using the centroids of particles. The 3D tracking is applied for each light sheet. The last computational step is the search of corresponding trajectories between the light sheets. This means to connect the ends of trajectories in one light sheet with possible ends of a trajectory in the adjacent light sheet. The light sheets are oriented with an overlap of 1mm. Therefore a part of the same 3D trajectory is recorded in two light sheets. This results in a nearest neighbour comparison of the 3D-coordinates of the trajectories in the participating light sheets.

4 Results

The 3D SPTV with telecentric lenses is used for the investigation of a vortex ring as an approximately axis symmetric test object. Figure 4 shows a flow visualisation

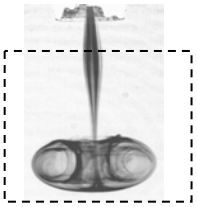

Fig. 4 Developed ring vortex and image section of the high speed cameras for the tracking region (dashed line)

picture of the vortex. At the top of figure 4 the lower edge of the vortex generator is visible. The image section of the three high speed cameras is indicated with dashed lines.

In figure 5 the particle images of the three cameras are presented for a light sheet in the middle of the ring vortex for a period of 204 scans. These pictures are created by summing up the single particle images for all the 204 time steps. The number of possible recorded time steps is limited by the maximum capacity of the camera memory (2 gigabyte). This conforms to a recording time of 2.04 s for a frame rate of 1000 frames/s. C#1 records the observed light sheet from the left side with an angle of 45°, while C#2 records the sheet from the right side with an angle of 45°. This means, that for trajectories in C#1 the corresponding particle images in C#2 have to be searched on the mirrored side. In C#3 the vortex image

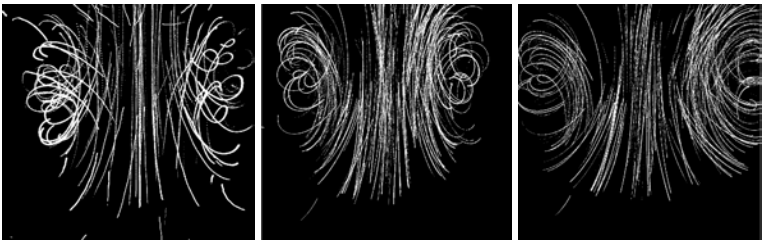

Fig. 5 Particle images summed up for all 204 time steps for C#1 (left), C#2 (middle) and C#3 (right) in a plane in the middle of the vortex

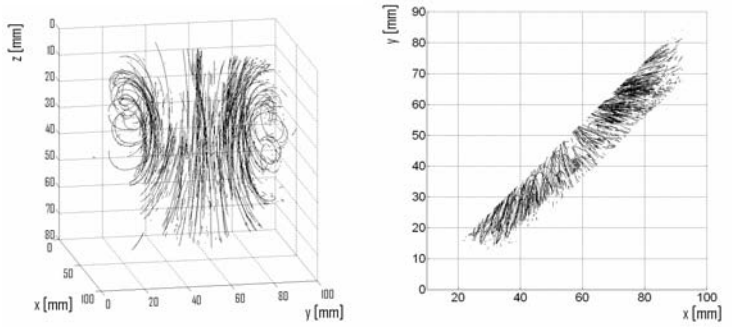

Fig. 6 Selected 3D trajectories for the light sheet in the middle of the ring vortex in isometric view (left) and in top view (right)

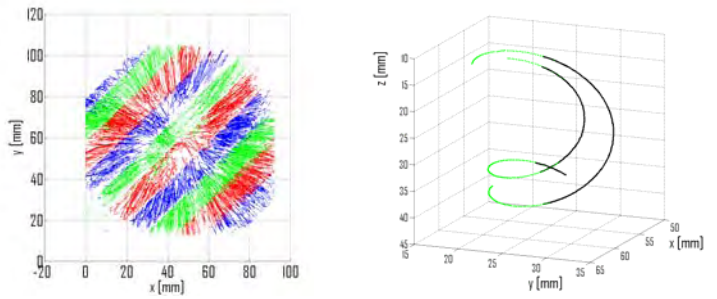

Fig. 7 Reconstructed trajectories of the particles in different light sheets (left). Connection of trajectories from one light sheet to another (right)

appears expanded. The reason is the orthogonal line of sight onto the light sheet plane. Moreover one can see the regions, which we distinguish for the 2D tracking algorithm. In the centre of the vortex is a preferred vertical movement and in the outer regions a preferred bias movement.

Figure 6 shows selected reconstructions of 3D trajectories in one single light sheet volume in an isometric view and in the top view. It is recognizable, that the reconstructed trajectories have the expected preferred movement and that the diameter of the vortex ring grows with the length of movement. In the top view in figure 6 the trajectories are cut at the lateral end of the light sheet. This is the area, where the trajectories in the next light sheet should continue.

The continuation of the trajectories is shown in figure 7, where the ten light sheets are connected. The circular envelope of the vortex ring and the connection of the trajectories appear precisely. Examples of such connected trajectories are shown on the right side of figure 7. The analyzed trajectory starts in the green coloured plane. The continuation of the trajectories in the next light sheet is coloured black. In this light sheet the trajectory describes a circular movement and moves back in the green light sheet. This means, that the same particle can be measured in both light sheets. The accuracy of the connections is about 1/10 pixel in the x-, y- and z-direction. This is equivalent to a distance of 9 microns and shows a rough measure of the total accuracy achieved with this technique.

Table 1 describes the parameters and the results for the 3D SPTV measurements by using high speed digital cameras and telecentric lenses. The seeded volume is about 365 cm³. This volume is approximately the half of the observed volume, because the injection of the particles is performed directly into the vortex generator. The maximum number of trajectories, which could be reconstructed in the light sheet in the middle of the vortex ring, is 560. For 10 light sheets the maximum number of trajectories are therefore 5600 for the seeded volume. If the whole observed volume is seeded with particles of the same number density, it is possible to reconstruct about 11000 trajectories. This is roughly by the factor of the number of light sheets higher than that achievable with standard photogrammetric PTV methods used in the same volume.

Table 1 Parameters of the 3D Scanning PTV method by using telecentric lenses

Maximum velocity	5cm/s
Observed volume (W x H x D)	9 x 9 x 9 ≈ 730cm³
Seeded volume	365 cm³
Median distance between particles	0.3 cm
Particles per pixel	0.003
Light sheet thickness	1 cm
Number of light sheets	10
Frame rate	1000 frames/s
Recording time	2.04s
Number trajectories (1LS) for seeded volume	560 (>13 time steps)
Number trajectories (10 LS) for seeded volume	5600
Number of possible trajectories for observed volume	11000

5 Conclusions

3D SPTV by using telecentric lenses increases the number and the length of analyzed trajectories and largely simplifies the algorithms of the 3D reconstruction. The increased number of analyzed trajectories is the result of the enlarged number density of particles in the observed volume. The reason is the separation of a defined volume in smaller volumes, which are defined by the number and the width of the light sheets. The length of the trajectories is raised, because of using high speed cameras and scanning illumination. The displacement of the particles is much smaller than the median particle distance. Moreover, the length of the trajectories extends further by the scanning light sheets: If a particle has left one light sheet, it is easy to find the particle in the next light sheet because of the overlapping areas of the light sheets. The accuracy of connected trajectories is about 1/10 pixel. Besides the large field of depth of the telecentric lenses, which magnifies the observable volume, advantages could be pointed out in the implementation of the 3D reconstruction of trajectories. The simplifications are the reduction of degrees of freedom in the projection matrix, the minimal nonlinear distortion and the parallel reconstruction of the 3D particle coordinates without the need to perform ray-tracing. The high potential of the 3D SPTV in combination with telecentric lenses and high speed cameras is pointed out by the 11000 possible reconstructed trajectories and by the possibility of observing the trajectories for all the 204 time steps in the observed volume.

Acknowledgments. The authors thank the German Research Foundation (DFG) for its financial support of the work presented here under number 1494/11-1.

References

1. Brücker, C.: 3D scanning PIV applied to an air flow in a motored engine using digital high-speed video. Meas. Sci. Techn. 8, 1480–1492 (1997)
2. Brücker, et al.: Scanning PIV measurements of a laminar separation bubble. In: Proc. 6th Int. Symp. Particle Image Velocimetry, paper 008, Pasadena, September 21-23 (2005)

3. Cowen, E.A., Monismith, S.G.: A hybrid digital particle tracking velocimetry technique. Exp. Fluids 22, 199–211 (1997)
4. Hoyer, K., Holzner, M., Lüthi, B., Guala, M., Liberzon, A., Kinzelbach, W.: 3D scanning particle tracking Velocimetry. Exp. Fluids 39, 923–934 (2005)
5. Maas, H.G.: Digitale Photogrammetrie in der dreidimensionalen Strömungsmesstechnik, Dissertation, ETH Zürich (1992)
6. Malik, N.A., Dracos, T., Papantoniou, D.A.: Particle tracking velocimetry in three-dimensional flows, Part II: Particle tracking. Exp. Fluids 15, 279–294 (1993)
7. Schreer, O.: Stereoanalyse und Bildsynthese. Springer, Berlin (2005)

Quantitative Measurements of Three-Dimensional Density Fields Using the Background Oriented Schlieren Technique

Erik Goldhahn, Olga Alhaj, Florian Herbst, and Jörg Seume

Abstract. Developments of the background oriented schlieren technique (BOS) towards a three-dimensional measurement technique for 3D density fields are presented. The projections of the density are tomographically reconstructed using filtered back-projection. Theoretical investigations show that the sensitivity of the BOS method depends on the geometric setup, the resolution of the camera, the focal length of the lens and the evaluation algorithm whereas the resolution of the method is described by its transfer function. Applications of the method at an under-expanded free jet of air and to the wake of wind tunnel cascade showed good results - qualitatively as well as quantitatively.

1 Introduction

The BOS method as patented by Meier [8] belongs to the schlieren techniques and detects the projection of the index of refraction gradient. It offers the ability to investigate unsteady density fields in compressible flows. A comparison of this method with holographic filters can be found in the paper of Augenstein et al. [1]. Its applicability to different flow problems and even full scale testing was demonstrated by Richard et al.[13]. Nafz et al. [10] applied BOS to measure the density of a transonic airflow around a turbine blade in a wind tunnel.

Due to the integrating character of the schlieren technique measurement methods, local values of density cannot be determined directly. For phase objects with axial symmetry, quantitative results can be derived from one projection using the Abel inversion technique. Klinge et al. [7] used a single projection recorded with the BOS method and a simple recursion formula to determine the density field of a wing tip vortex. For objects with higher complexity more projections are needed and accordingly a more advanced tomographic reconstruction algorithm must be employed. The number of required projections depends on the complexity of the object. There are several studies regarding optical tomography in combination

Erik Goldhahn · Olga Alhaj · Florian Herbst · Jörg Seume
Institute of Turbomachinery and Fluid Dynamics, Leibniz University Hannover, Germany,
Seume@tfd.uni-hannover.de

W. Nitsche and C. Dobriloff (Eds.): Imaging Measurement Methods, NNFM 106, pp. 135–144.
springerlink.com

with classical density measurement methods such as schlieren and interferometry. Rotteveel [14] applied an interferometric method to the flow inside a combustion engine model, Blinkov et al. [2] used multi-directional speckle photography to obtain the temperature distribution inside a candle flame and Faris et al. [3] used beam-deflection optical tomography on a supersonic jet. The experimental complexity as well as the effort required to evaluate the measurements is very high for these methods. In contrast, the BOS method offers the possibility to record and evaluate projections from different viewing directions easily. It is also possible to capture different projection directions simultaneously using one camera for each direction. So far BOS was mostly used as a simple means for flow visualization. Some quantitative investigations of 2D flows and flows with rotational symmetry have been carried out by Venkatakrishnan [15] and Venkatakrishnan and Meier [16]. In both cases the authors used a Poisson equation to determine the projected (line-of-sight integrated) density field. This field was then used as the input data for a tomographic reconstruction algorithm (filtered back projection). In this paper the gradient information is used directly to reconstruct 3D density fields.

2 Properties of BOS

Measurement Principle. A typical BOS setup contains of three main components:

1. a random dot pattern in the background of a flow of interest,
2. a digital camera and
3. a computer to record and evaluate the pictures taken by the camera.

Two pictures of the dot pattern are recorded - one in absence of the flow field and one when there is flow between the dot pattern and the camera.

Fig. 1 Schematic BOS-Setup

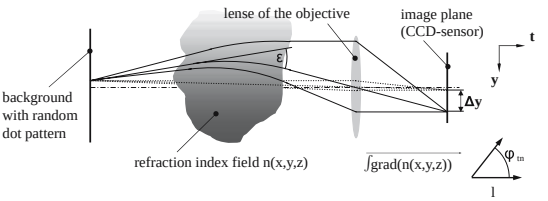

As all schlieren techniques BOS is sensitive to those components of the first spatial derivative of the refraction index *n*, which are perpendicular to the line of sight *t*. The integral of those components along *t* can be determined for gases with $n \approx 1$ using equation (1)

$$\varepsilon \approx \tan(\varepsilon) = \sin(\varphi_{\ln}) \cdot \int_l grad\{n(x, y, z)\} dt \ . \tag{1}$$

Here φ_{tn} is the angle between the line of sight and the direction of the refraction index' gradient vector. As equation (1) illustrates a variation of *n*, which is connected to the fluid density ρ by the Gladstone-Dale relation

$$n - 1 = K \cdot \rho \,. \tag{2}$$

where K is the Gladstone-Dale constant, causes a deflection ε of a light ray passing through the density field which leads to an apparent shift Δy of the background dot pattern in the image plane. Using cross-correlation algorithms, like the ones developed for the evaluation of particle image velocimetry (PIV) images, Δy can be determined by comparing the reference picture without flow with the picture with flow. Assuming the angle α in Fig. 2 to be small the deflection angle ε can be calculated using the geometric proportions of the BOS setup from that shift.

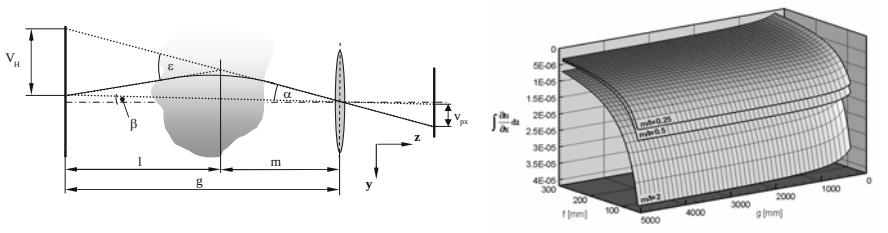

Fig. 2 Geometric setup for sensitivity estimation (left); sensitivity for three different m/l with v_{px} = 0.1 px (right) (Goldhahn and Seume [5])

Sensitivity. Since BOS is an integral measurement technique the sensitivity of the BOS method in detecting apparent shifts of the dots on the background V_H is directly linked to the question of the smallest detectable integral in equation (1). Goldhahn and Seume [5] showed that by simplifying the setup and concentrating the deflection of light onto one plane in space (Fig. 2 left) one can derive information of the smallest detectable integral resulting in

$$\varepsilon \approx \left(1 + \frac{m}{l}\right) \cdot v_{px} \cdot \left(\frac{g - f}{g \cdot f}\right) \cdot \cos^2(\beta). \tag{3}$$

Equation (3) shows that the sensitivity can be expressed just in terms of the geometric proportions g, m, l, the focal length of the lens f, the corresponding pixel shift on the CCD-chip of the camera v_{px} and the deviation angle β. The latter is typically small so that $\cos^2(\beta)$ tends to 1 and therefore may be omitted in most cases. Using a pixel shift of 0.1 pixels which is detectable with available cross-correlation algorithms, Fig. 2 (right) illustrates the smallest detectable line of sight integral value for three positions of the density object between camera and background. It can be seen that the sensitivity increases with a larger focal length of the lens f and with a smaller relative distance between camera and density object m/l, whereas the overall setup length g plays a minor. Additionally the sensitivity would benefit from a higher resolution of the camera.

Resolution. The apparent shift of the background dot pattern compared to the reference image contains 2D projections of the 3D refraction index gradient field. As

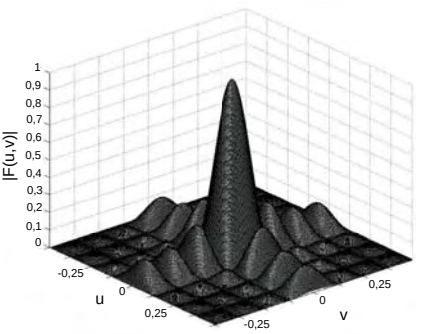

Fig. 3 2D amplitude spectrum of quadratic interrogation window

these projections are continues functions of the projection coordinates it is not possible to distinguish single objects in order to prescribe the resolution of a measurement. Nevertheless it is possible to obtain a definition of the resolution by decomposing a projection in its harmonic components so that the highest spatial frequency which can still be observed is the resolution of the BOS system. As Goldhahn and Seume [5] showed it is therefore necessary to know the transfer function of the system. Considering that the pixel shift determined by the cross correlation algorithm is an intensity weighted mean shift per interrogation area and assuming that it is overlaid with an certain amount of noise in each interrogation window Goldhahn and Seume [5] proposed equation (4) as a description of the evaluation process in one direction as a function of the auxiliary variables *x'*, *y'* and the size of the interrogation window *h*:

$$\left(\frac{\partial n}{\partial x}(x,y)\right)_{mean} = \frac{1}{h^2}\int_{-\infty}^{\infty}\int_{-\infty}^{\infty}\frac{\partial n}{\partial x}(x',y')\cdot\prod(x-x',y-y')\,dx'\,dy' \tag{4}$$

$$\prod(x,y) = \begin{cases} 1 \; for \; |x| \le \frac{h}{2} \wedge |y| \le \frac{h}{2} \\ 0 \; for \; |x| > \frac{h}{2} \wedge |y| > \frac{h}{2} \end{cases} \tag{5}$$

It is the 2D convolution of a window function (5) with the projections of the refraction index gradients divided by the window area (4). Hence the transfer function is given by the Fourier spectrum of the window function.

By means of the amplitude spectrum of a quadratic interrogation window, Fig. 3 illustrates that only the mean value of the shift is measured correctly. For all the other frequencies a decrease of the measured value is observed. If the integer multiplies of the spatial wavelength of the density gradients is equal to the interrogation window size, the values of the transfer function will become zero. Although this seems to be a disadvantage of the method, it is possible to reconstruct the true values of the projection with an inverse filter since the transfer function is known. The only exceptions are the values where the transfer function is zero.

3 Tomographic Reconstruction

The 3D density field is reconstructed out of the measured projections of the refraction index gradients using the tomographic filtered back-projection (e.g. Fomin [4]). Fig. 4 illustrates the relationship between the density gradient field and the projection under the angle θ. From the center slice theorem and the derivative theorem it is known that the Fourier transform of the derivative of the projected values of a physical parameter – here the refraction index n – corresponds to the Fourier transform of the object itself in a slice through the Fourier plane. In order to obtain the reconstruction of the whole spatial domain the projections are convoluted with a filter function $Q(k)$ and the results are back projected into the reconstruction area (6)

$$q(s) = \int_{-\infty}^{\infty} Q(k) e^{i 2\pi k s} dk \quad \text{and} \quad n(x,y) = \int_{0}^{\pi} q(s) * \varepsilon_s(s,\theta) d\theta \tag{6}$$

where k is the polar coordinate in the Fourier plane. The density may now be calculated using the Gladstone-Dale relation and the ambient density using the refraction index of Eq. (6). Stacking the reconstructed planes on top of each other one obtains a complete 3D distribution of the density field.

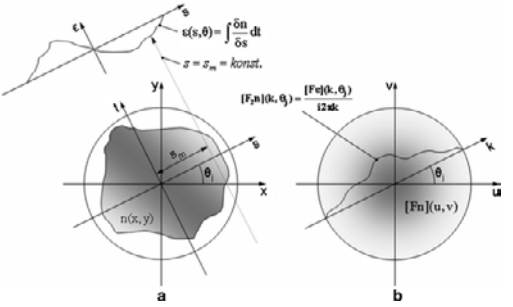

Fig. 4 Projection parallel to the geometry and the relationship between position and frequency domain (Goldhahn and Seume [5])

4 Measurements at a Double Free Jet of Air

Experimental Setup. The density of an under-expanded free jet of air is investigated. To create the jet, a simple double-hole orifice is used as shown in Fig. 5 a. The orifice is mounted on a settling chamber equipped with rectifier screens for flow quality enhancement.

The settling chamber is equipped with a port for total pressure readings and a sensor for total temperature. Both values are recorded together with the BOS measurements. Both, the camera and the background are supported by a stiff aluminium structure (Fig. 5a). The background is illuminated by a flash lamp, which is triggered together with the camera.

The total pressure in the pre-chamber is held constant at 1.5 bar (±0.02 bar) above ambient pressure. With that set-up, 36 measurement directions are captured

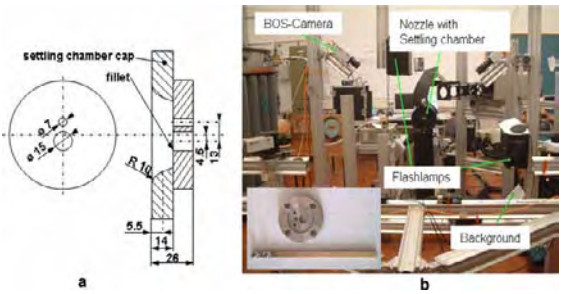

Fig. 5 Sketch of the double hole orifice (a); experimental setup (b) (Goldhahn and Seume [5])

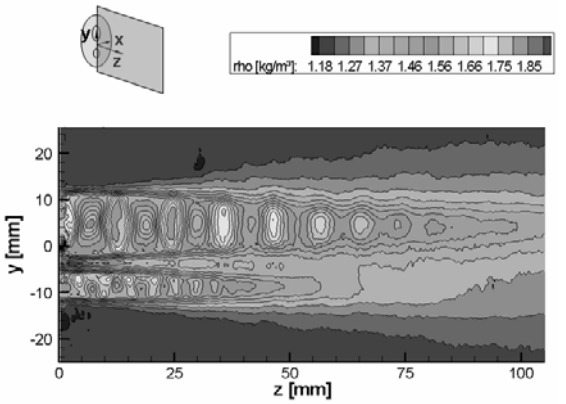

Fig. 6 Density distribution in the centre slice at x = 0 mm (Goldhahn and Seume [5])

in succession with one camera. In each direction, 60 measurement images are taken. The images where evaluated using interrogation windows of the size 8 px by 8 px with 50% overlap. In every viewing direction the mean values of the shift data were calculated by averaging the correlation maps for each image as it is done in PIV-processing (Meinhart et al. [9]). The 3D density field is determined using tomographic reconstruction with the averaged shift values in planes perpendicular to the jet axis. Parallel projection was assumed since the maximum opening angle of the used camera-lens combination was ±4° and the free jet extended only over approximately ±2°.

Results. The result of the reconstruction of the double free jet is shown in Fig. 6 which shows a slice along the jet axis at a position of $x = 0$ mm. The distance between data points is 0.3 mm. The jet is under-expanded and shows the density fluctuation which is typical for this type of flow.

Assuming isentropic conditions, it is possible to calculate the density at the nozzle exit to be 1.90 kg/m³. In Fig. 6 the measured density at the Nozzle exit amounts to a maximum of 1.85 kg/m³ which is 2.6% lower than from the isentropic calculation expected. However it should be pointed out, that the values directly adjacent to the nozzle exit are disturbed by the shadow which the nozzle casts on the images. This disturbance can be seen in Fig. 6.

5 Density Measurement behind Straight Blades

Experimental Setup. The experimental investigations were carried out in the linear cascade wind tunnel of the TFD (Fig. 7). The cascade box on the top of the wind tunnel carries three straight blades with a cross section of 240 mm x 120 mm and a pitch of 60 mm. The test blade is situated in the middle. The inlet flow conditions are measured with a Prandtl tube and a temperature sensor.

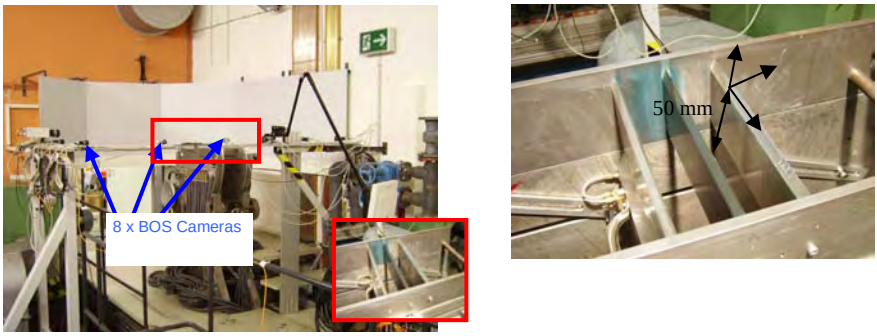

Fig. 7 Wind tunnel with blade cascade and dot pattern in the background (left); coordinate system (right)

Eight BOS cameras are placed around the cascade. All cameras are triggered together, which enables them to make photos at the same moment. The lines of sight of all cameras intersect in the middle of the test blade and compose between each other an angle of 22.5°. The background is situated on the opposite side of the cascade and is illuminated with normal lamps. The Mach number of the inlet flow obtained form the measurement equipments in the inlet was 0.56. For this Mach number 50 images were made with a frequency of 2 Hz for each camera. The images were evaluated using interrogation window of the size 16 px x 16 px with 50% overlap. The 3D density field was determined using the reconstruction mentioned above.

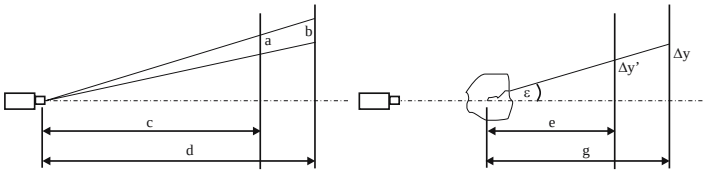

Fig. 8 Relationship between the original and the adjusted displacement due to a different location of the camera and the related distances to the background (left) and because of the different distance from the middle of the cascade to the background (right)

In order to apply the reconstruction the distances from the background to the camera and to the cascade have to be equal for all eight cameras. In this measurement this condition was not fulfilled. Therefore the images were adjusted according to their distances using the equations

$$a = b\frac{c}{d} \text{ and } \Delta y' = \Delta y\frac{e}{g}. \tag{7}$$

Figure 8 shows the relationship between the original image and the adjusted one.

Results. The result of the reconstruction of the flow behind the blades is shown in a slice in the middle of the cascade along the flow Fig. 9 (left). The contour plot shows a decrease of the density downstream the blade due to mixing effects as it analytically could be expected.

Figure 9 (right) compares the density distribution 50 mm downstream the middle blade in the centre of the cascade of the BOS-measurements with former measurements with five-hole wedge-probes by Oehlert and Seume [12]. Although the error of the density's average in the same position directly downstream the middle blade is only 1.6% (probe: 1.26 kg/m^3; BOS: 1.24 kg/m^3) which proves the potential of the BOS method for quantitative investigations, the distribution in Fig. 9 (right) shows a deviation of the results of 3.8% in maximum. This deviation is due to a blockage of the turbulence grid in the inlet of the wind tunnel during the BOS measurements which lead to an inhomogeneous flow distribution.

In a next step of the BOS development the density field between cascade blades will be investigated. This demands further development of the tomographic algorithm and is currently work in progress. Figure 10 illustrates the problematic sectors for the reconstruction algorithm: sector 2 for example does not contain any information due to blockage effects whereas inhomogeneous boundary conditions occur in sector 3 due to the blade surface and in sector 4 due to the flow directly striking camera 2.

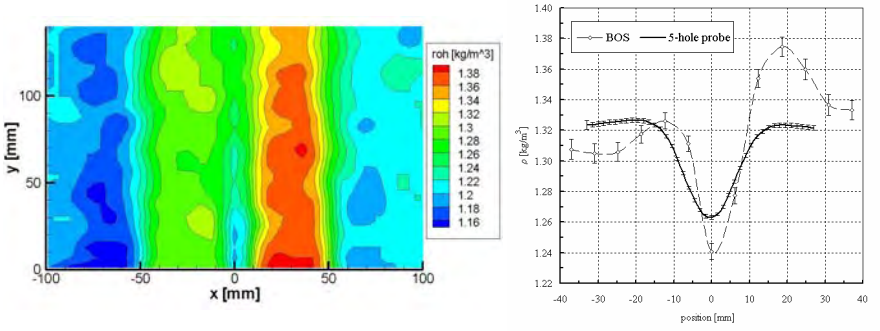

Fig. 9 BOS-measured density distributions in the middle of the cascade along the flow (left) and compared to probe measurements in a cutting plane y = 50 mm downstream the trailing edge of the blade (right)

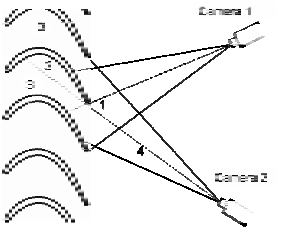

Fig. 10 Problematic sectors of BOS between cascade blades

6 Conclusions

The present work describes the development of the background oriented schlieren technique into a quantitative method for measuring 3D density fields or properties of a fluid which are deduced.

The fundamentals of the BOS method are presented including investigations of its sensitivity and its resolution. It could be shown that the sensitivity mainly depends on the geometry of the setup, the camera resolution, the focal length of the lens, and the evaluation algorithm. The resolution, on the other hand, is determined by the transfer function. Analysis shows that only the mean value of the pixel shift is measured correctly.

Together with the back-filtered projection as a tomographic reconstruction algorithm, BOS was successfully applied to an under-expanded free jet of air. The reconstructed 3D density field shows the typical diamond structure of an under-expanded jet with a good resolution.

In a second experiment, the BOS method was used to measure quantitatively the density field downstream of a cascade wind tunnel. The results are compared with the 2D distribution of pneumatic probe measurements which had been performed earlier. Major deviations between both measurements resulted from an unintended change of the inflow to the cascade. This had been caused by fouling of the turbulence grid, as it turned out. The good agreement of the average density, however, confirmed the applicability of the BOS method for quantitative investigations of complex external 3D flows.

Acknowledgments. Funding from Deutsche Forschungsgemeinschaft under grant Se 1023/3-3 is gratefully acknowledged. The authors would like to thank Dr. Kompenhans of DLR in Göttingen for his critical advice during the first half of the project and the initiators and coordinators of SPP1147, Professors Nitsche, Leder, and Tropea.

References

1. Augenstein, E., Leopold, F., Richard, H., Raffel, M.: Schlieren Techniques in comparison: The background oriented schlieren method versus visualization with holographic filters. In: 4th international symposium on particle image velocimetry, Göttingen, Germany (2001)
2. Blinkov, G.N., Fomin, N.A., Soloukhin, M.N., Vitkin, D.E., Yadrevskaya, N.L.: Specle tomography of a gas flame. J. Exp. Fluids 8, 72 (1989)
3. Faris, G., Byer, R.: Three-dimensional beam-deflection optical tomography of a supersonic jet. Appl. Optics 27(24), 5202–5212 (1988)

4. Formin, N.A.: Speckle photography for fluid mechanics, pp. 195–197. Springer, Germany (1997)
5. Goldhahn, E., Seume, J.: The background oriented schlieren technique: sensitivity, accuracy, resolution and application to a three-dimensional density field. J. Exp. Fluids 43, 241–249 (2007)
6. Kak, A.C., Slaney, M.: Principles of computerized tomographic imaging. IEEE Press, New York (1988)
7. Klinge, F., Kirmse, T., Kompenhans, J.: Application of quantitative background orientend schlieren (BOS): investigation of a wing tip vortex in a transonic windtunnel. In: Proceedings of PSFVIP-4, F4097, Charmonix, France (1998)
8. Meier, G.E.A.: Hintergrundschlierenverfahren. Deutsche Patentanmeldung, DE19942856A1 (1999)
9. Meinhart, C.D., Wereley, S.T., Santiago, J.G.: A PIV algorithm for estimating time-averaged velocity fields. ASME J. Fluids Eng. 122(2), 285–289 (2000)
10. Nafz, T., Ochs, M., Bauer, H.J.: Background Oriented Schlieren Möglichkeiten und Grenzen des optischen Verfahrens. In: 1st CEAS European Air and Space Conference, Berlin, Germany (2007)
11. Natterer, F.: The mathematics of computerized tomography. Wiley, USA (1986)
12. Oehlert, K., Seume, J.: Exploratory experiments on machined Riblets on compressor blades. In: European Fluids Engineering Summer Meeting, Miami U.S. (2006)
13. Richard, H., Raffel, M., Rein, M., Kompenhans, J., Meier, G.E.A.: Demonstration of the applicability of a background oriented schlieren (BOS) method. In: Proceedings 9th international symposium on applied laser techniques to Fluid Mechanics, Lisbon, Portugal (2000)
14. Rotteveel, S.R.: Optische Tomographie zur Untersuchung von Zylinderinnenströmungen. VDI Reihe 6 Nr. 278, p. 50. VDI Verlag, Düsseldorf (1992)
15. Venkatakrishnan, L.: Density measurements in an axis symmetric underexpandet jet using background oriented schlieren technique. In: 24 AIAA aerodynamic measurement technology and ground testing conference, paper AIAA 2004–2603, Portland, Oregon (2004)
16. Venkatakrishnan, L., Meier, G.E.A.: Density measurements using background oriented schlieren technique. J. Exp. Fluids 37, 237–247 (2004), doi:10.1007/soo348-004-0807-1

Tomographic Reconstruction and Efficient Rendering of Refractive Gas Flows

Ivo Ihrke, Kai Berger, Bradley Atcheson, Marcus Magnor, and Wolfgang Heidrich

Abstract. This chapter introduces techniques for the capture and efficient display of dynamic three-dimensional non-stationary gas flows. We describe a flexible Schlieren-tomographic system consisting of multiple consumer camcorders. A special choice of background pattern for Background Oriented Schlieren (BOS) imaging provides for flexibility in the experimental setup. Optical flow techniques are used to measure image space deflections due to heated air flows from arbitrary camera positions. A specially tailored sparse-view algebraic reconstruction algorithm is employed to tomographically recover a refractive index gradient field. After robust integration of these gradient fields, time-varying, fully three-dimensional refractive index fields are obtained. These can be rendered efficiently using a ray-casting style algorithm that is suitable for graphics hardware acceleration. Additional optical properties can be rendered within the same computational framework.

Ivo Ihrke
Imager Lab, University of British Columbia, Vancouver, BC, Canada
ivoihrke@cs.ubc.ca

Kai Berger
Computer Graphics Lab, TU Braunschweig, Braunschweig, Germany
berger@cg.cs.tu-bs.de

Bradley Atcheson
Imager Lab, University of British Columbia, Vancouver, BC, Canada
atcheson@cs.ubc.ca

Marcus Magnor
Computer Graphics Lab, TU Braunschweig, Braunschweig, Germany
magnor@cg.cs.tu-bs.de

Wolfgang Heidrich
Imager Lab, University of British Columbia, Vancouver, BC, Canada
heidrich@cs.ubc.ca

W. Nitsche and C. Dobriloff (Eds.): Imaging Measurement Methods, NNFM 106, pp. 145–154.
springerlink.com

1 Overview

Schlieren imaging techniques have long been used as a means to detect minute variations in refractive index. They convert angular deflections of light rays into intensity variations upon a surface, which can be more easily observed. Early systems placed a refractive medium (often a candle plume) inside a setup comprised of precision lenses and/or mirrors. A beam of collimated light, when shone through the medium, would pass by a filter before being focused onto an imaging plane. Any ray deflected from its original parallel path would be attenuated by this filter, resulting in a correspondingly darker spot on the imaging plane. Further details can be found in Settles' book [18], the most complete reference on Schlieren topics available today.

Classic Schlieren setups suffer from their high cost and difficulty of calibration. Recently, a different approach based on digital image processing has been proposed. The "Background Oriented Schlieren" (BOS) method [10, 15, 16] requires only a high frequency background pattern, positioned behind the refracting volume, and a camera to observe the pattern. Deflections of light rays passing through the medium cause apparent distortion of the background, which can be accurately measured using computer vision techniques.

While the projected refractive index variations can usually be interpreted by a trained user, they do not describe the full three-dimensional structure of the medium. For this, we need to perform a tomographic reconstruction of it, using Schlieren images captured from multiple viewpoints. Previous Schlieren-tomographic systems were made possible with only a single camera by operating on rotationally symmetric media [4] (in which views from any angle would be equivalent) or else on stationary flows [17] (in which the apparatus could be rotated to obtain more viewpoints). In our work, we present the first method to capture and reconstruct non-symmetric, non-stationary, time-varying refractive index variations [6]. We also develop a method to efficiently render the effects produced by inhomogeneous refractive index fields.

The chapter is structured as follows: we introduce the measurement setup for "Background Oriented Schlieren" capture of gas flows in Section 2 and describe their tomographic reconstruction in Section 3. In Section 4 we describe a light ray model which is used for the rendering of continuously varying refractive index fields such as the recovered gas flows. We conclude the chapter with our results and a discussion thereof in Section 5.

2 Background Oriented Schlieren Imaging

Any medium of inhomogeneous refractive index will cause light rays to bend as they traverse through it, leading to a characteristic *jittering* distortion of the background. BOS uses digital image processing techniques to convert this distortion directly into a measurement of the ray's total amount of deflection along its path.

Unlike with traditional Schlieren configurations, the BOS method has very moderate hardware requirements, which in turn makes multiple-viewpoint acquisition

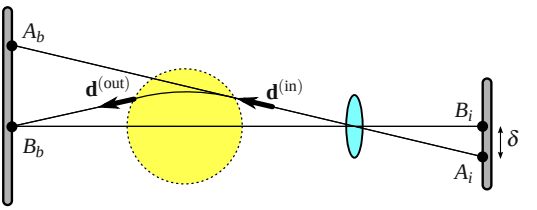

Fig. 1 Virtual displacement caused by ray deflection. Under normal circumstances, points A_b and B_b on the background are imaged at A_i and B_i respectively. However, when refraction takes place, B_b appears at A_i and we see a virtual displacement of δ

quite feasible. The basic principle, assuming a simple geometric optics model, is illustrated in Figure 1. A high frequency background pattern is viewed through a lens (implying that depth of field is of concern). Under normal circumstances, the ray travels straight, leading to point A_b being imaged at A_i. However, introducing a refractive medium into the scan volume causes the ray to bend, according to the well-known laws of optics. This causes an apparent distortion of the background pattern, with B_b now being imaged at A_i. *Optical flow* algorithms can be used to compare this distorted image with a known reference image in order to obtain the displacement vector field [8, 11, 14].

Note that the amount of distortion is proportional to the distance between the background and the scan volume, which should be maximised in order to ease the optical flow computation. However, to remain in focus, the scan volume should also be positioned as close to the background as possible. We compromise by placing it half-way between the camera and background (which are 5m apart). The camera array consists of 16 synchronised Sony HDR-SR7 camcorders, equipped with 400mm (35mm equivalent) lenses, positioned in an arc of almost 180° around the measurement volume.

Optical flow algorithms perform best when the image contains high frequency texture throughout. A random noise pattern will suffice, but could cause problems when its resolution differs greatly from that of the camera. For example, a noise pattern drawn from a Gaussian distribution will have an intensity histogram like that in the bottom left of Figure 2. Moving the pattern further away from the camera causes large patches of it to be imaged to each pixel in the camera, in effect blurring the whole image. The intensity histogram therefore becomes much narrower (see bottom right of Figure 2), which makes distinguishing between bright and dark spots more difficult, and hence the optical flow performance degrades considerably.

We solve this problem by using a multi-scale noise pattern, such as Wavelet Noise [9]. It is a sum of multiple independent noise functions with non-overlapping frequency spectra. This guarantees that the image will contain sufficient high-contrast detail at any scale. Histograms for the multi-scale noise pattern before and after scaling are shown in Figure 2, demonstrating the difference when compared to Gaussian noise.

We evaluated four different optical flow algorithms using a synthetically-warped noise pattern. For each algorithm we identified the single key parameter that most affects its results, and varied it across an empirically determined range. Figure 3

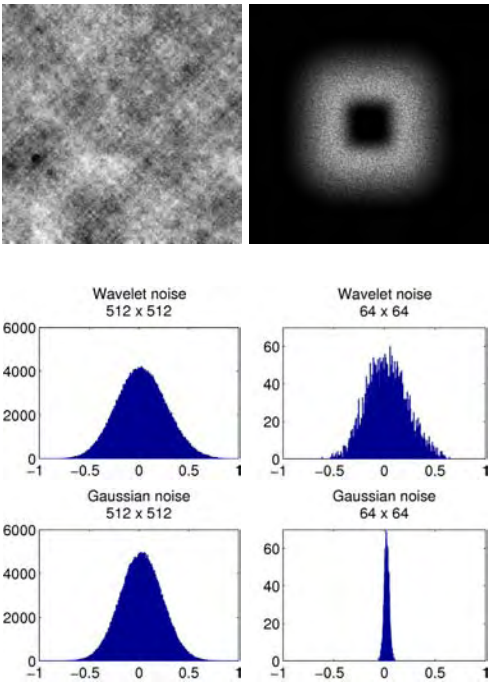

Fig. 2 **Top left**: final wavelet noise image; **Top right**: frequency spectrum of one of the noise bands; **Middle row**: the intensity histogram of a wavelet noise pattern remains Gaussian-shaped, even if the pattern is downsampled; **Bottom row**: if a Gaussian noise pattern is downsampled, its dynamic range decreases considerably. Figures reproduced from [5]

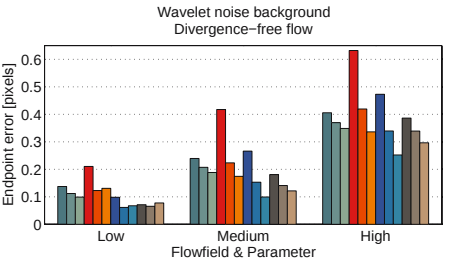

Fig. 3 The endpoint errors of different optical flow algorithms for a synthetic flow on a wavelet noise pattern. Figure reproduced from [5]

shows the average vector difference (endpoint) errors for the resulting vector fields, divided into three groups representing low, medium and high amounts of distortion. Within each group, the bars are grouped into four sets of three bars, representing the four algorithms and three of the selected parameter values. The green bars represent a variational algorithm by Brox et. al. [8] which produces good optical flow results in general, but tends to oversmooth this high frequency data. The MatPIV [19] toolbox (red) has been extensively used in earlier BOS work, but we found that significantly better results could be obtained with either the Horn-Schunck [11] (blue) or Lucas-Kanade [14] (brown) algorithms. The latter's lower sensitivity to parameter choice led to us choosing it for our later experiments.

When performing tomographic reconstruction, the intersection of the view frusta from all the cameras defines the reconstruction volume. However, the refractive medium may only occupy a small region inside this volume, and so we detect the visual hull [13] of the medium and exclude all the empty space around it from the equation system. This both speeds up the solution, and improves on the quality of the results.

To obtain a 3D visual hull we first require a binary mask for each 2D optical flow vector field, classifying pixels as either in- or outside the medium. To see why such a mask cannot be obtained by simply thresholding the vector field, consider the trivial case of a ray propagating parallel to the refractive index gradient. Such a ray will not be deflected at all, yet it should clearly be classified as inside the medium. A solution to this problem is to first integrate the optical flow vector field by solving the associated Poisson equation, and then thresholding the resultant heightfield.

As input to the tomography algorithm we require 3D deflection vectors, but are only able to capture 2D projections of these via optical flow. These can be transformed into 3D worldspace via the camera calibration matrices to obtain $\mathbf{d}^{(\text{in})}$ and an approximation $\hat{\mathbf{d}}^{(\text{out})}$ to $\mathbf{d}^{(\text{out})}$.

3 Tomographic Reconstruction

The 2D displacement vectors that have been computed by the optical flow algorithm are projections of 3D ray deflections, which are related to line integrals of the 3D refractive index gradients. We derive the relation between ray deflections and the refractive index field from the *ray equation of geometric optics*, which describes light propagation in optically inhomogeneous media as

$$\frac{d}{ds}\left(n\frac{d\mathbf{x}}{ds}\right) = \nabla n \tag{1}$$

where n denotes the refractive index field, $\mathbf{x}$ is the position of a mass-less particle travelling along the ray, and ds is the differential path along the curved ray. Reformulating Equation 1 as a first-order ODE system and integrating leads to the following equation, which relates 3D ray deflections to the gradient of the index field:

$$\mathbf{d}^{(\text{out})} - \mathbf{d}^{(\text{in})} = \int_c \nabla n \, ds. \tag{2}$$

Here $\mathbf{d}^{(\text{in})}$ denotes the incoming ray direction and $\mathbf{d}^{(\text{out})}$ denotes the outgoing ray direction with respect to the measurement volume for a ray path c.

We discretise the vector-valued function ∇n using normalised scalar basis functions ϕ_i. Insertion in Equation 2 yields

$$\sum_i \mathbf{n}_i \int_c \phi_i ds = \mathbf{d}^{(\text{out})} - \mathbf{d}^{(\text{in})} \tag{3}$$

where the vector-valued coefficients $\mathbf{n}_i$ parametrise the components of the unknown gradient. Reformulating Equation 3 as three linear systems of equations in each of the vector components leads to

$$\mathbf{S}\,\mathbf{n}_{(x,y,z)} = \mathbf{d}^{(\mathrm{out})}{}_{(x,y,z)} - \mathbf{d}^{(\mathrm{in})}{}_{(x,y,z)}\,. \tag{4}$$

Here (x,y,z) denote the individual linear systems, and $\mathbf{S}$ is the system matrix having the following structure:

$$\mathbf{S} = \begin{pmatrix} \int_{c_1} \phi_1 ds & \cdots & \int_{c_1} \phi_{n_b} ds \\ \vdots & \ddots & \vdots \\ \int_{c_{n_p}} \phi_1 ds & \cdots & \int_{c_{n_p}} \phi_{n_b} ds \end{pmatrix} \tag{5}$$

where n_b denotes the number of basis functions ϕ_i and n_p expresses the total number of deflection measurements in all cameras. We approximate the integrals of the individual matrix entries by Riemann sums over the single basis functions. The curved rays are approximated by straight rays. This is known as paraxial approximation, and is justified by the fact that the deviation between straight and curved rays is small. Simulations of our measurement setup have shown that the difference does not exceed 0.1 mm for measurement volumes of about 20 cm^3.

We employ localised radially symmetric basis functions to obtain a sparse linear system that can be solved by standard numerical algebra techniques. For the actual computation we only use the basis functions inside the visual hull [13] of the refractive index fields. The visual hull serves as a regularizer on the shape of the volume and minimizes projection artifacts [12].

The tomographic reconstruction results in a three-dimensional gradient field $\widehat{\nabla n}$ of the refractive index. It is then integrated by solving a Poisson equation. Note however, that the set of gradient vectors is not consistent in general. To deal with gradient inconsistency we resort to anisotropically weighted Poisson integration [3]

$$\nabla \cdot (\mathbf{D} \nabla n) = \nabla \cdot (\mathbf{D} \widehat{\nabla n}) \tag{6}$$

where $\mathbf{D}$ is a gradient-weighting diffusion tensor. For standard Poisson integration the tensor can be chosen as $\mathbf{D} = 1$. In our case we employ a tensor which prefers gradients from similar iso-surfaces of the underlying refractive index field, while weakening the influence of gradients orthogonal to them. For details on the definition and use of diffusion tensors refer to [2, 6, 20].

Equation 6 is again discretised within the visual hull, only. The boundary values are set to the refractive index of air, resulting in a sparse and positive definite linear system which is solved using a Jacobi-preconditioned Conjugate Gradient method [7].

4 Continous Refraction Rendering

Once three-dimensional models of gas flows have been obtained by the techniques described above, they can be placed into virtual environments. Their optical parameters can also be changed. For example, it is possible to add scattering and absorbing smoke

particles even though smoke has not been present during the capture. To achieve this, we first derive a mathematical description of the underlying image formation model, which is suitable for rendering continuously refracting objects, including advanced optical properties like scattering, emission and absorption. We then discretize and simplify the model to map it efficiently onto modern graphics hardware.

The radiance recorded by a camera is accumulated along a curved ray passing through the pixel and the refracting volume. The image formation process can be described by the following equation:

$$L(c) = \int_c L_c(\mathbf{x},\mathbf{d})\,\alpha(s,c)\,ds + L_{bg}\,\alpha(s_\infty,c) \tag{7}$$

where L_c expresses the radiance at a particular point in space $\mathbf{x}$, in a particular direction $\mathbf{d}$ due to the combined effect of emission and scattering, $\alpha(s,c) = \exp\left(-\int_0^s \sigma_t \circ c(t)\,dt\right)$ denotes the absorption of light along the ray at a certain distance s and L_{bg} denotes background radiance. The radiance $L_c(\mathbf{x},\mathbf{d})$ can be written in more detail by summing the out-scattered and emitted radiance:

$$L_c(\mathbf{x},\mathbf{d}) = \hat{\omega}\,L_s(\mathbf{x},\mathbf{d}) + L_e(\mathbf{x},\mathbf{d}). \tag{8}$$

Here L_s is the out-scattered and L_e the locally emitted radiance, while $\hat{\omega}$ expresses the albedo of the material. Introducing the scattering phase function p, the scattering term L_s can be formulated as an integral over the sphere Ω of incoming light directions

$$L_s(\mathbf{x},\mathbf{d}) = \int_\Omega p(\mathbf{x},\mathbf{d},\omega)L(\mathbf{x},\omega)\,d\omega = \int_\Omega p(\mathbf{x},\mathbf{d},\omega)\,dE_\omega. \tag{9}$$

This general formulation is clearly too involved to be computed quickly on graphics hardware. Therefore we simplify it by assuming that the scene is illuminated by a finite number of light sources, and that each point in the scene receives light by a finite number of incoming rays only. Applying these assumptions to our continuous model, $L_s(\mathbf{x},\mathbf{d})$ can be discretised and expressed as a sum over the incoming light rays:

$$L_s(\mathbf{x},\mathbf{d}) = \sum_j p(\mathbf{x},\mathbf{d},\mathbf{l}_j)\,\triangle E_{\omega_j}\,. \tag{10}$$

This allows us to precompute the irradiance values for all incoming light directions. Afterwards, Equation 7 can be computed on the fly by performing irradiance lookups into an additional three-dimensional texture.

Applying this discussion to our acquired gas flows, we see that we do not acquire emission, absorption or scattering properties. Thus, L_c is simply zero. Because the attenuation coefficient σ_t is zero throughout the volume, the absorption factor $\alpha(s_\infty,c)$ equals one and we obtain

$$L(c) = \int_c 0\,ds + L_{bg}\alpha(s_\infty,c) = L_{bg}\,. \tag{11}$$

The volume rendering of continuous refraction is a simple lookup of the background radiance. Additional optical properties like emission, absorption and scattering coefficients can be synthetically added to increase the visual appeal of the renderings. Since Equation 7 describes the forward model of volumetric light transport it could also serve as a basis for more advanced reconstruction schemes.

5 Results

We evaluated the accuracy of our reconstruction algorithm using simulated data experiments. We started by assessing the numerical error of the integration step, adding complexity to the synthetic experiments until the full system error as well as the errors introduced by the single processing steps could be determined.

Using a static, three-dimensional fuel injection data set [1], we first computed ground truth gradient vectors. By performing anisotropically weighted Poisson integration on the synthetic gradients we established a lower bound on the expected error of 42.15 dB peak signal-to-noise ratio (PSNR), or 0.78% root mean square (RMS) error.

In a second experiment we simulated the 3D deflection vectors $\mathbf{d}^{(\mathrm{out})} - \mathbf{d}^{(\mathrm{in})}$ by tracing curved rays according to Equation 1. A tomographic reconstruction was then performed on the simulated measurement data. The results of this experiment are shown in the first row of Table 1. In reality, only projections of this 3D deflection vector into the image planes of the cameras can be measured. The influence of this approximation was assessed in a third experiment (second row, Table 1). Finally, we distorted a wavelet background noise pattern using the projected, simulated deflection vectors. We applied optical flow computation to the distorted images to assess the influence of the optical flow on overall reconstruction accuracy (third row, Table 1). As can be seen from the results, optical flow computation introduces the largest error, followed by the approximation of the 3D deflection vector. However, using only 16 cameras, detailed reconstructions with only $\approx 1\%$ RMS error can be achieved.

We performed a number of measurements on real-world gas flows. Figure 4 (left) shows the resulting deflections from an air jet dispersing a candle plume measured

Table 1 Measured simulation errors for the tomographic reconstruction. The root mean square (RMS) error and the peak signal-to-noise ratio (PSNR) are compared for camera different setups

Simulation errors for tomographic reconstruction						
Experiment	8 Cameras		16 Cameras		32 Cameras	
	PSNR	RMS	PSNR	RMS	PSNR	RMS
Ground truth $\mathbf{d}^{(\mathrm{out})}$	40.55	0.94%	41.29	0.86%	41.39	0.85%
Approximate $\hat{\mathbf{d}}^{(\mathrm{out})}$	40.01	1.00%	40.69	0.92%	40.76	0.92%
Optical flow	39.29	1.09%	39.84	1.02%	39.88	1.01%

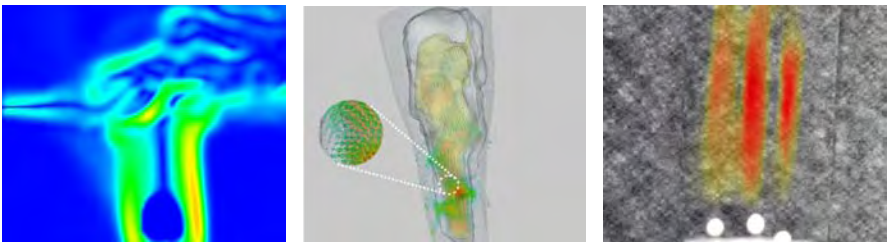

Fig. 4 Left: the displacement magnitude of a candle plume's interaction with a jet of compressed air; **Middle:** the 3D refractive index gradients of a flow from a gas burner and their integrated refractive index field; **Right:** the reconstructed plumes of 3 tea lights rendered into one of the input camera's view. Figures reproduced from [6]

Fig. 5 The reconstructed gas volume is placed into a virtual scene. The volume is attached to an oil lamp and distorts the relief on the wall

with the BOS technique, and (middle) visualizes the 3D gradients of a flow caused by a gas burner. The gradient vectors where recovered using approximately 150,000 basis functions and 700,000 pixel measurements for each time frame. Another experiment shows that our system is able to clearly separate spatially distinct features. The reconstructed plumes of three tea lights are overlaid onto one of the input images in Figure 4 (right).

We also modified the optical properties of the measured gas flows, adding absorption and scattering properties in regions of high refractive index gradient. In Figure 5, the refractive index volume of the gas burner flow is attached to an oil lamp and a candle data set is placed above a virtual candle. The light rays passing through the volume are distorted and cause the typical deflections of heated air flows. The wall relief is distorted as well as the content of the image on the opposite wall.

Acknowledgements. Ivo Ihrke was supported by a Feodor-Lynen Fellowship of the Humboldt Foundation, Germany. Part of this work was supported by the National Sciences and Engineering Research Council of Canada (NSERC), and the German Research Foundation (DFG) under grant MA2555/5-1.

References

1. Fuel injection volumetric data set. dFG SFB 382 (2000), http://www.volvis.org
2. Agrawal, A., Chellappa, R., Raskar, R.: An Algebraic Approach to Surface Reconstruction from Gradient Fields. In: Proceedings of ICCV, vol. 1, pp. 174–181 (2005)
3. Agrawal, A., Raskar, R., Chellappa, R.: What Is the Range of Surface Reconstructions from a Gradient Field? In: Leonardis, A., Bischof, H., Pinz, A. (eds.) ECCV 2006. LNCS, vol. 3951, pp. 578–591. Springer, Heidelberg (2006)
4. Agrawal, A.K., Albers, B.W., Griffin, D.W.: Abel Inversion of Deflectometric Measurements in Dynamic Flows. Applied Optics 38(15), 3394–3398 (1990)
5. Atcheson, B., Heidrich, W., Ihrke, I.: An Evaluation of Optical Flow Algorithms for Background Oriented Schlieren Imaging. Experiments in Fluids p in print (2008)
6. Atcheson, B., Ihrke, I., Heidrich, W., Tevs, A., Bradley, D., Magnor, M., Seidel, H.P.: Time-resolved 3D capture of non-stationary gas flows. ACM Transactions on Graphics (Proc. of SIGGRAPH Asia) 27(5), article 132 (2008)
7. Barrett, R., Berry, M., Chan, T., Demmel, J., Donato, J., Dongarra, J., Eijkhout, V., Pozo, R., Romine, C., van der Vorst, H.: Templates for the Solution of Linear Systems: Building Blocks for Iterative Methods. Society for Industrial and Applied Mathematics (1994)
8. Brox, T., Bruhn, A., Papenberg, N.: High Accuracy Optical Flow Estimation Based on a Theory for Warping. In: Pajdla, T., Matas, J(G.) (eds.) ECCV 2004. LNCS, vol. 3024, pp. 25–36. Springer, Heidelberg (2004)
9. Cook, R., DeRose, T.: Wavelet Noise. Proceedings of ACM SIGGRAPH 24(3), 803–811 (2005)
10. Dalziel, S., Hughes, G., Sutherland, B.: Whole-field Density Measurements by Synthetic Schlieren. Experiments in Fluids 28(4), 322–335 (2000)
11. Horn, B., Schunck, B.: Determining Optical Flow. Artificial Intelligence 17(1-3), 185–203 (1981)
12. Ihrke, I., Magnor, M.: Image-Based Tomographic Reconstruction of Flames. In: ACM Siggraph / Eurographics Symposium Proceedings, Symposium on Computer Animation, pp. 367–375 (2004)
13. Laurentini, A.: The Visual Hull Concept for Silhouette-based Image Understanding. IEEE Transactions on Pattern Analysis and Machine Intelligence 16(2), 150–162 (1994)
14. Lucas, B., Kanade, T.: An Iterative Image Registration Technique with an Application to Stereo Vision. In: International Joint Conference on Artificial Intelligence, vol. 3, pp. 674–679 (1981)
15. Meier, G.: Computerized Background-Oriented Schlieren. Experiments in Fluids 33(1), 181–187 (2002)
16. Richard, H., Raffel, M.: Principle and Applications of the Background Oriented Schlieren (BOS) Method. Measurement Science and Technology 12(9), 1576–1585 (2001)
17. Schwarz, A.: Multi-tomographic Flame Analysis With a Schlieren Apparatus. Measurement Science and Technology 7(3), 406–413 (1996)
18. Settles, G.: Schlieren and Shadowgraph Techniques: Visualizing Phenomena in Transparent Media. Springer, Heidelberg (2001)
19. Sveen, J.K.: An introduction to matpiv v.1.6.1. Eprint no. 2, Dept. of Mathematics, University of Oslo (2004) ISSN 0809-4403, http://www.math.uio.no/~jks/matpiv
20. Weickert, J.: Anisotropic Diffusion in Image Processing. Teubner (1998)

2D-Measurement Technique for Simultaneous Quantitative Determination of Mixing Ratio and Velocity Field in Microfluidic Applications

Volker Beushausen, Karsten Roetmann, Waldemar Schmunk, Mike Wellhausen, Christoph Garbe, and Bernd Jähne

Abstract. Two-dimensional Molecular-Tagging-Velocimetry (2D-MTV) has been used to investigate velocity fields of liquid flow in a micro mixer. Optical tagging was realized by using caged dye. For the first time patterns were generated by structured laser illumination using optical masks. This allows the generation of nearly any imaginable pattern. The flow induced deformation of the optically written pattern is tracked by imaging of laser induced fluorescence. Quantitative analysis of raw image series is carried out by novel "optical flow" based techniques. A comparison to the standard technique of µPIV has also been conducted. Additionally Planar Spontaneous Raman Scattering (PSRS) was applied in order to determine concentration fields for mixtures of ethanol and water.

1 Introduction

Over the past few years, microfluidic systems have experienced rapid development [1-4]. Due to the strongly increasing interest in microfluidic devices there is a growing demand for new diagnostic tools for the analysis of flow structures, mixture formation and reaction behaviour directly inside the micro channels. In particular non-intrusive measurement techniques which do not influence the flow and reaction processes in the channels are indispensable. Several reviews are concerned with miscellaneous detection techniques [5-7]. The present work covers the development of laser based imaging techniques, which can provide comprehensive information about microfluidic mixture formation and flow fields.

2 Flow Field Analysis by 2D-Molecular Tagging Velocimetry

In contrast to flow visualization techniques such as PIV or PTV, no seeding particles are needed for Molecular Tagging Velocimetry (MTV) [8-10]. Instead, the

Volker Beushausen · Karsten Roetmann · Waldemar Schmunk · Mike Wellhausen
Department of Photonic Sensor Technology, Laser-Laboratorium Goettingen e.V.,
Hans-Adolf-Krebs-Weg 1, D-37077 Goettingen, Germany
Volker.Beushausen@llg-ev.de

Christoph Garbe · Bernd Jähne
Interdisciplinary Center for Scientific Computing, University of Heidelberg,
Heidelberg, Germany

W. Nitsche and C. Dobriloff (Eds.): Imaging Measurement Methods, NNFM 106, pp. 155–164.
springerlink.com

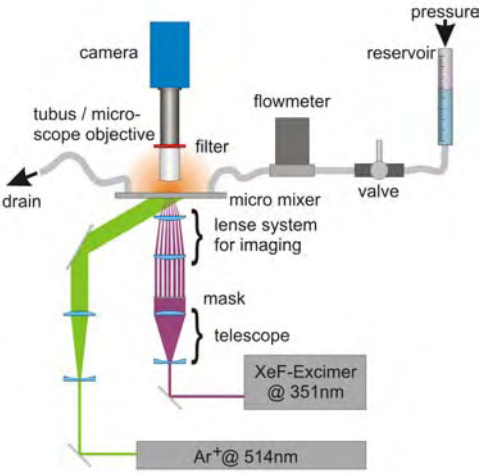

Fig. 1 Experimental setup for 2D-MTVrecordings

flow is tagged by structured illumination of a fluorescence dye and the pattern written this way is visualized temporally resolved by a CCD-camera. Tagging is made possible by using a so called "caged dye" [11] which initially does not fluoresce – only after photochemically cracking the bond of a functional group by a UV-Laser pulse the ability to fluoresce is activated. If the UV laser pulse is structured spatially by imaging a mask into the fluid, a well defined pattern of activated dye can be generated within the caged dye loaded flow. The fluorescence of the activated dye structures can now excited continuously by another laser and image series of the deforming fluorescing structures inside the flow can be captured by a fast camera.

Since diffusion occurs in the fluid and therefore the written patterns are spreading with progressing time classical correlation algorithms as used for PIV are only suitable to a limited extent. For this reason a specially adapted intensity gradient based optical flow (OF) estimation technique was further developed [12-14]. Detailed information about this technique can be found elsewhere [15-18].

The experimental setup is shown in figure 1. As the fluid demineralised water with a "caged dye"-concentration of 500 mg/l (caged Carboxy-Q-Rhodamine, Molecular Probes) was used. For generating the tagging-pattern in the fluid a pulsed XeF-Excimerlaser (COM-PEX 150, Lambda Physik AG) at 351 nm and a pulse energy of 200 mJ and for excitation of the fluorescence the expanded beam of an Argon-Ion laser (Innova 310, Coherent) at a wavelength of 514 nm have been applied. The image of the illuminated mask is demagnified and imaged into the fluid which flows inside the planar micro mixer. A CCD-camera (Imager Compact QE, LaVision) images the fluorescence of the dye patterns deformed by the flow at well defined points in time after the writing process. The camera is triggered with a frequency of 10Hz by a delay generator to guarantee a fixed time delay of 100ms between successive images. Depending on the dimensions of the evaluated flow either a microscope objective (5×, Zeiss) or a macro-objective (50mm, Nikon) is used. Interfering excitation light is suppressed by an optical bandpass

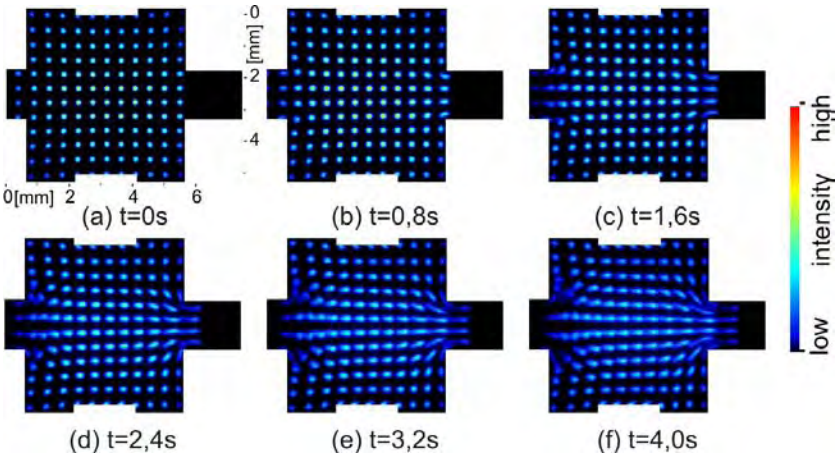

Fig. 2 2D-MTV image series of a laminar micro flow. The original sequence was taken with 10Hz, fewer images are shown here for a better visualization of the flow

filter (OG570, Schott). The measurement procedure has been presented previously in [19-22]. Figure 2 shows an image sequence generated by the described procedure. This is a typical example for the microfluidic flows investigated so far. The mixing chamber (5 mm × 5mm × 200 µm) is streamed from the left to the right while the four side channels that are intended to create periodically fluctuating flows for mixing purposes remain unused for these investigations.

The mixing chamber generates a widening of the cross section of the flow. In this case a regular dot pattern was used to tag the flow. The dots have a diameter of about 160 µm after the imaging process and their period is three times the diameter. A result of the flow analysis with OF is shown in Figure 3.

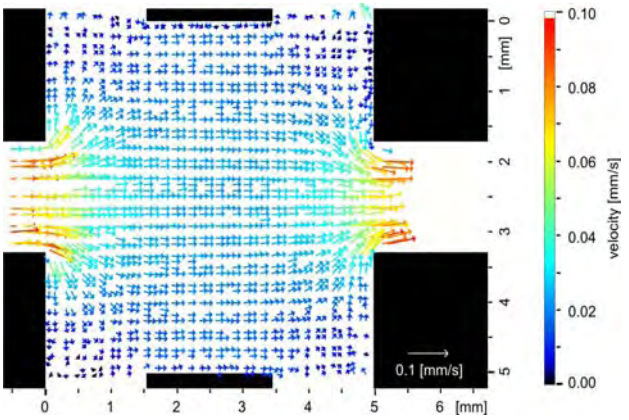

Fig. 3 Temporally averaged velocity vector field calculated from the image series in Figure 2

The illustrated vector field of a stationary flow as it most often appears in micro fluidics is time averaged over ten single vector fields. The vector fields were calculated from the same image sequence. A single vector field contains vectors only at positions were a dot was written into the flow like image 5 shows. Since the dots are moving during the sequence, as shown in Figure 2, the calculation of velocities is possible in almost the whole chamber. The gaps between the vectors are closing by the averaging process and nearly the entire field becomes visible. The resulting vector field reproduces the anticipated flow field very well.

3 Reference Measurements and Taylor Dispersion

A disturbing effect which is particularly distinct in micro flows is the so called Taylor dispersion. It is caused by the parabolic velocity profile that is formed between top and bottom plates in a flat channel. By means of this effect the fluorescing patterns blur increasingly during the progressing flow. This issue is drafted in Figure 6. The kind of detection, which integrates over the depth of the channel, leads to the deformation of the initially punctual pattern to a kind of “comet tail” that can be found for example in Figure 2. The evaluation results in lower velocities in the front of the moving pattern. Due to the region of the “tail” and higher ones at the fact that the velocity values in the vector field need to be allocated to different levels in the channel it is necessary to modify the evaluation algorithms in order to calculate velocities in a certain depth level. The necessary adjustments to the algorithms could be done provided that the flow is strictly laminar and two dimensional. A parabolic flow profile as shown in Figure 4 leads to assumptions about the resulting velocities after the two dimensional projection when the camera view integrates through the channel depth. The parabolic flow profile is based on a laminar Poiseuille flow. This allows to extend the differential equation for the optical flow calculations to take the Taylor dispersion into account. The concrete arrangements that were used can be found in [5,7,8]. The improvements presented there allowed to correct the errors that would result from Taylor dispersion and calculate velocity vector fields that match the conditions in the middle level (apex of the Taylor dispersion parabola). This enables a quantitative comparison of the calculated values with reference values taken by a flowmeter. Therefore tagging measurements in a straight channel with a rectangular profile of 1.12 mm × 200 µm were carried out. Figure 5 shows a result of these measurements. The underlying dot pattern is clearly visible because a velocity calculation is only possible if intensity structures are visible as mentioned previously. The dots measure about 80 µm in diameter and the period is two times the diameter. The mean flow velocity was calculated from the measured velocity vector fields by a local average determination. Because of the correction of the Taylor dispersion the mean flow velocity of this vector field corresponds to the maximum velocity in the middle level of the channel. The flow meter simultaneously detected the volume flow

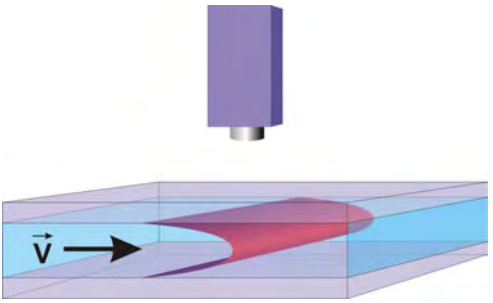

Fig. 4 Schematic diagram of the pressure driven flow between top and ground plate

of the fluid. These values are convertible to mean flow velocities by the known geometry of the cross section of the channel.

Mean flow velocities again can be converted to the maximum flow velocities in the middle level of the channel because of the parabolic flow profile. Both maximum flow velocities, of the OF calculations on the one hand and the measurements of the flow meter on the other, should match. Measurements in a wide range of flow velocities were used to create the comparison shown in Figure 6. The bisecting line is plotted to show the perfect accordance of both values. This means a very good qualitative match with the expected fluid flow and good quantitative accordance with standard µPIV measurements which are also performed in the same microchannel. The development of the measurement technique and the evaluation algorithms is at the beginning anyway and further improvements are possible. Fluctuations of the beam profile of the lasers caused problems with the basic assumptions of the algorithms. Thus a more stable laser or a more robust evaluation could lead to much better results. Further work should help to improve the measurement technique.

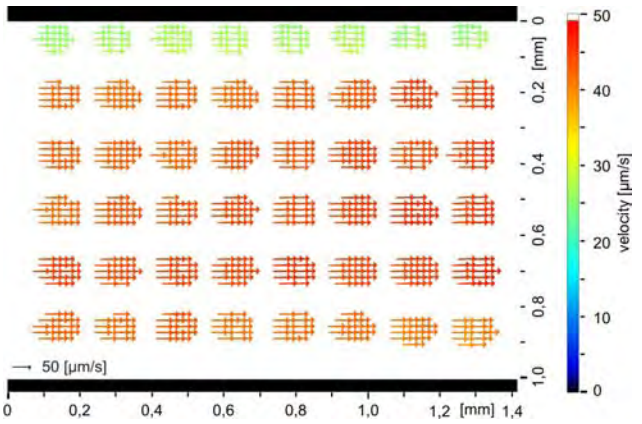

Fig. 5 Result of a tagging measurement with evaluation by a modified optical flow algorithm in a straight channel

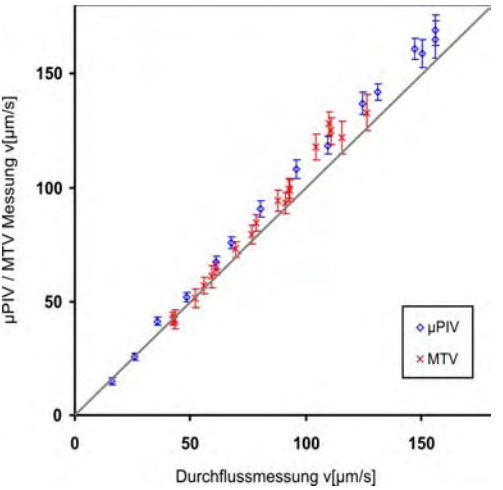

Fig. 6 Quantitative comparison between the velocity values determined by µPIV/MTV measurements and measurements by a flow meter

4 Determination of Species Concentrations by Planar Raman Scattering

The determination of density distribution of molecular species in microfluidic systems is realized by planar spontaneous Raman scattering. Due to its extremely low signal yield the application of spontaneous Raman scattering as measurement technique is challenging [23,24]. Existing approaches only used ether the spectral information or their temporal evolutions. Modern Raman microscopes apply pointwise scanning techniques in order to image species distributions inside or on the surface of microscopic objects. Also direct imaging of a specific Raman band was demonstrated in [25]. Due to the long exposure times necessary the recording of snapshot images of density distributions in instationary mixing processes was not possible yet. Lately single shot Raman measurements were carried out to characterize fuel sprays [26].

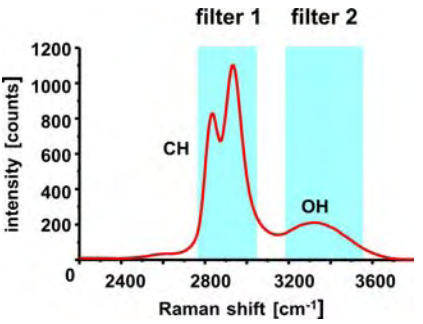

Fig. 7 Typical Raman spectrum of ethanol with examples of two narrow band filters

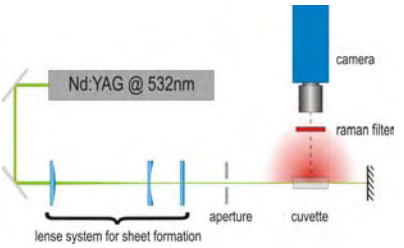

Fig. 8 Sketch of the experimental setup for the two dimensional determination of concentration fields by planar Raman scattering

In this contribution, instantaneous spatially resolved measurements with an outstanding time resolution are presented. The technique is used to acquire quantitative species distributions of specific species in microfluidic systems for the first time. The procedure has the ability to quantitatively visualize density distributions of certain species by using the characteristic spectral emissions of the participating fluids. The two dimensional measurement procedure uses the fact that different molecular species are clearly distinguishable from each other by means of their characteristic Raman spectra. This "spectral fingerprint" allows to detect features specific to an individual molecular species. Narrow bandpass-filters allow the spectral separation of the Raman scattered light of the relevant band without or with only minor interferences from other species. The local Raman scattered light intensities obtained this way are a direct measure of the density distributions of the examined species since the measured intensities are proportional to the number of molecules of the selected species in the measurement volume. Figure 7 is a draft of the described principle. This example shows a part of the Raman spectrum of ethanol with the characteristic band of the fundamental CH-vibration at 3000 cm^{-1}. A second band at 3300cm^{-1} corresponds to the OH-vibration. If ethanol is mixed with pure water it could be spectrally selected by filter 1. At the spectral position of filter 2 both species emit Raman scattered light. The experimental setup is drafted in Figure8.

Raman measurements were carried out either in a planar micromixer as well as in the three-dimensional mixing chamber of a multi-lamination mixer produced by Forschungszentrum Karlsruhe (http://www.fzk.de/fzk/idcplg?IdcService=FZK-&node=0899& lang=en) with water and ethanol as two distinct chemical features. For lack of space only results of the investigations in the three dimensional mixing chamber are presented here.

For excitation a pulsed Nd:YAG-laser at 532 nm (Brilliant B, Quantel) was used. The laser beam is formed to a small light sheet (approximately 800 µm thick and 12 mm high) by a lens system and a beam homogenizer. The light sheet selects a plane in the mixing chamber (quartz-cuvette, 10mm x 10mm x 40mm) that is imaged by an image intensified camera (Flamestar III, LaVision) through the Raman filter (633FS1025, LOT-Oriel). The spectral transmission of the Raman filter is chosen so that only the strong ethanol- band at 3000cm^{-1} is imaged. Both fluids exhibit an OH-band but the one of water is much stronger. Therefore a small amount of light from the OH-band of water is transmitted by the filter as well. For a mixture of two components this unwanted light can easily be removed by a "black-and white"-image correction. In this case the black-image contains the

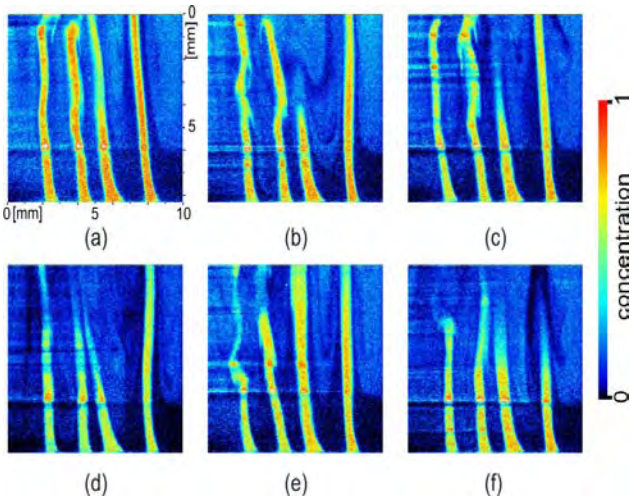

Fig. 9 Planar concentration distribution of ethanol in water during an instationary mixing process in a three-dimensional micro mixer

intensities measured of pure water and the "white-image" is taken from pure ethanol. Through a calibration procedure [22], the measured intensity values are converted to concentration values. Figure 9 exemplary shows a sequence of images acquired during the mixing process of ethanol and water in the mixing chamber. Here the laser sheet selects a plane directly above the inlet channels of ethanol which flows into pure water. The distribution of ethanol is clearly distinguishable from that of water and some interesting features are recognizable.

5 Conclusions

Two-dimensional Molecular Tagging Velocimetry was successfully applied to determine velocity vector fields in two dimensional micro flows. Comparison with micro-flow measurements showed very good agreement. New evaluation algorithms for inclusion of flow effects resulting from Taylor dispersion were developed by C. Garbe from University of Heidelberg and applied to the experimental data.

Single shot planar spontaneous Raman scattering was successfully applied to micro-mixing devices for the first time and quantitative planar mixing ratios could be extracted. In ongoing work both techniques are coupled in order to enable simultaneous measurements of local flow field and mixing ratio in microfluidic systems.

Acknowledgments. The authors thank the German Research Community (Deutsche Forschungsgemeinschaft-DFG) for funding of the project in the framework of the DFG-program "Imaging Measurement Methods for Flow Analysis" ("Bildgebende Messverfahren für die Strömungsanalyse", SPP 1147).

References

1. Erickson, D., Li, D.: Integrated microfluidic devices. Analytica Chimica Acta 507, 11–26 (2004), doi:10.1016/j.aca.2003.09.019
2. Lai, S., Wang, S., Luo, J., Lee, L.J., Yang, S.T., Madou, M.J.: Design of a compact disk-like microfluidic platform for enzyme-linked immunosorbent assay. Anal. Chem. 76(7), 1832–1837 (2004), doi:10.1021/ac0348322
3. Nguyen, N.T., Wu, Z.: Micromixers - a review. Journal of Micromechanics and Microengineering 15, R1–R16 (2005), doi:10.1088/0960-1317/15/2/R01
4. Srinivasan, V., Pamula, V.K., Fair, R.B.: An integrated digital microfluidic lab-on-a-chip for clinical diagnostics on human physiological fluids. Lab Chip 4, 310–315 (2004)
5. Mogensen, K.B., Klank, H., Kutter, J.P.: Recent developments in detection for microfluidic systems. Electrophoresis 25, 3498–3512 (2004), doi:10.1002/elps.200406108
6. Sinton, D.: Microscale flow visualization. Microfluid Nanofluid 1, 2–21 (2004), doi:10.1007/s10404-004-0009-4
7. Viskari, P.J., Landers, J.P.: Unconventional detection methods for microfluidic devices. Electrophoresis 27, 1797–1810 (2006), doi:10.1002/elps.200500565
8. Koochesfahani, M.M., Nocera, D.G.: Molecular tagging velocimetry maps fluid flows. Laser Focus World 37(6), 103–108 (2001)
9. Lempert, W.R., Harris, S.R.: Flow tagging velocimetry using caged dye photoactivated fluorophores. Measurement Science and Technology 11, 1251–1258 (2000)
10. Maynes, D., Webb, A.R.: Velocity profile characterization in sub-millimeter diameter tubes using molecular tagging velocimetry. Experiments in Fluids 32, 3–15 (2002), doi:10.1007/s003480100290
11. Gee, K.R., Weinberg, E.S., Kozlowski, D.J.: Caged q-rhodamine dextran: a new photoactivated fluorescent tracer. Bioorg. Med. Chem. Lett. 11(16), 2181–2183 (2001)
12. Garbe, C.S.: Measuring and modelling fluid dynamic processes using digital image sequence analysis. Habil. Ruprecht-Karls-Universität Heidelberg (2006)
13. Garbe, C.S., Roetmann, K., Beushausen, V., Jähne, B.: An optical flow MTV based technique for measuring micro fluidic flow in the presence of diffusion and Taylor dispersion. Experiments in Fluids 44(3), 350–439 (2008), doi:10.1007/s00348-007-0435-7
14. Garbe, C.S., Roetmann, K., Jähne, B.: An optical flow based technique for the non-invasive measurement of microfluidic flows. In: 12th International Symposium on Flow Visualization, Goettingen, Germany, pp. 1–10 (2006)
15. Barron, J.L., Fleet, D., Beauchemin, S.: Performance of optical flow techniques. International Journal of ComputerVision 12(1), 43–77 (1994)
16. Garbe, C.S., Spies, H., Jähne, B.: Estimation of surface flow and net heat flux from infrared image sequences. Journal of Mathematical Imaging and Vision 19, 159–174 (2003)
17. Haußecker, H., Fleet, D.: Computing optical flow with physical models of brightness variation. IEEE Transactions on Pattern Analysis and Machine Intelligence 23(6), 661–673 (2001)
18. Jähne, B.: Digitale Bildverarbeitung, 6th edn. Springer, Heidelberg (2005)
19. Roetmann, K., Garbe, C., Beushausen, V.: 2D-molecular tagging velocimetry zur Analyse mikrofluidischer Stömungen. In: Proceedings Lasermethoden in der Strömungsmesstechnik, pp. 26/1–26/10 (2005)

20. Roetmann, K., Garbe, C., Schmunk, W., Beushausen, V.: Microflow analysis by molecular tagging velocimetry and planar ramanscattering. In: 12th International Symposium on FlowVisualization (2006)
21. Roetmann, K., Schmunk, W., Garbe, C., Beushausen, V.: Analyse mikrofluidischer Strömungen mit molecular tagging velocimetry und planarer Ramanstreuung. In: Proceedings Lasermethoden in der Strömungsmesstechnik, pp. 31/1–31/8 (2006)
22. Roetmann, K., Schmunk, W., Garbe, C.S., Beushausen, V.: Micro-flow analysis by molecular tagging velocimetry and planar Raman-scattering. Exp. Fluids 44, 419–430 (2008), doi:10.1007/s00348-007-0420-1
23. Lee, M., Lee, J.P., Rhee, H., Choo, J., Chai, Y.G., Lee, E.K.: Applicability of laser-induced raman microscopy for in situ monitoring of imine formation in a glass microfluidic chip. Journal of Raman Spectroscopy 34, 737–742 (2003), doi:10.1002/jrs.1038
24. Leung, S.A., Winkle, R.F., Wootton, R.C.R., de Mello, A.J.: A method for rapid reaction optimisation in continuous-flow microfluidic reactors using online raman spectroscopic detection. The Analyst 130, 46–51 (2004), doi:10.1039/b412069h
25. Wood, B.R., Langford, S.J., Cooke, B.M., Glenister, F.K., Lim, J., McNaughton, D.: Raman imaging of hemozoin within the food vacuole of plasmodium falciparum trophozoites. FEBS Letters 554, 247–252 (2003), doi:10.1016/S0014-5793(03)00975-X
26. Malarski, A., Egermann, J., Zehnder, J., Leipertz, A.: Simultaneous application of single-shot ramanography and particle image velocimetry. Optics letters 31, 1005–1007 (2006)

Simultaneous, Planar Determination of Fuel/Air Ratio and Velocity Field in Single Phase Mixture Formation Processes

Frank Rotter, Jochen Scholz, Jens Müller, Tim Wiersbinski, Markus Röhl, Paul Ruhnau, Daniel Kondermann, Christoph S. Garbe, and Volker Beushausen

Abstract. Laser induced fluorescence is used to develop a 2D measurement technique for mixture formation analysis of fuel and air in a broad temperature regime from 398 K up to 548 K. The measurement principle is called FARLIF (*f*uel-*a*ir *r*atio by *l*aser-*i*nduced *f*luorescence). Its application is tested on the tracer toluene in the non-fluorescent model fuel isooctane as well as on an auto-fluorescing near-standard gasoline. A frequency quadrupled double-pulse Nd:YAG laser at 266 nm is used for excitation while the fluorescence is detected by an intensified double-frame CCD camera. The double-frame images are used for analysis of the mixture motion. For elevated temperatures the FARLIF signal shows a temperature dependence. Therefore, a correction mechanism is suggested.

1 Introduction

The mixing of gases is essential in many technical applications. For example, the controlled and well defined formation of ignitable hydrocarbon-air mixtures for energy generation in power plants, turbines, burners or internal combustion engines is a central point of interest for process improvements. New engine concepts are strongly needed in order to face limited fossil oil supply, rising demand and continuously increasing fuel prices. Furthermore, progressive environmental degradation results in more and more restrictive emission constraints. Therefore, many different optical diagnostic techniques have been developed during the past decades with the aim to get insight into and a better understanding of the processes governing the mixture formation [1].

Frank Rotter · Jochen Scholz · Jens Müller · Tim Wiersbinski · Markus Röhl · Volker Beushausen
Department of Photonic Sensor Technology, Laser-Laboratorium Göttingen e.V., Göttingen, Germany
frank.rotter@llg-ev.de

Paul Ruhnau
Computer Vision, Graphics and Pattern Recognition Group, University of Mannheim, Mannheim, Germany

Daniel Kondermann · Christoph S. Garbe
Interdisciplinary Center for Scientific Computing, University of Heidelberg, Heidelberg, Germany

W. Nitsche and C. Dobriloff (Eds.): Imaging Measurement Methods, NNFM 106, pp. 165–174.
springerlink.com

Today's measurement techniques allow a qualitative prediction of planar mixture distributions but a direct quantitative and time resolved determination is not accessible. However, without the exact knowledge of the mixture processes a further improvement of combustion processes only based on empirical optimization is no longer possible. Therefore, the aim of this project is the development of a technique to determine the spatial distribution, the temporal evolution and the velocity field of turbulent gas streams with a single measuring procedure. Within this project a cooperation with other workgroups was entered who develop new image processing techniques for flow-dynamics analysis.

As a promising approach the measurement of the *f*uel-*a*ir *r*atio by *l*aser-*i*nduced *f*luorescence (FARLIF) was chosen, which was proposed by Reboux et al. more then 10 years ago [2]. They used toluene as a tracer in the model-fuel isooctane and took advantage of the strong fluorescence-quenching of oxygen. It was shown that the fluorescence intensity grows linearly with the fuel-air ratio and that the fluorescence intensity is pressure-independent for a fixed fuel-air ratio at higher pressures (FARLIF concept). These experiments were conducted at ambient temperature and with an excitation wavelength of 248 nm. In the following years, many research groups have used this technique even at elevated temperatures without testing its applicability under these conditions. Schulz and Sick [3] showed that the situation for FARLIF applicability gets better for longer wavelength (266 nm) excitation.

In this project the application of the FARLIF concept on the tracer toluene in the non-fluorescent model fuel isooctane was tested as well as on a auto-fluorescing multi-component fuel ("Shell Euro Super colorless"). The latter has the advantage to be very similar to standard fuel and therefore is more realistic in evaporation and combustion behavior. In the following the applicability of FARLIF is evaluated for a broad temperature regime. The fluorescence is detected by image intensified CCD-cameras to obtain two-dimensional spatial resolution. In order to capture mixing dynamics, a FARLIF double-pulse technique is developed. It is used to calculate maps of the temporal derivative of the fuel-air ratio. Furthermore, with appropriate image processing these FARLIF double images can be used for the analysis of the motion of mixture clouds and structures (fluorescence motion analysis, FMA). During the FARLIF examination at higher temperatures (up to 548 K) temperature dependencies of the LIF intensity became obvious. Therefore, a correction mechanism is suggested.

2 The FARLIF Concept and Experimental Setup

Reboux et al. [2] proposed a concept to measure the *f*uel-*a*ir *r*atio by *l*aser-*i*nduced *f*luorescence called FARLIF. In the case of linear LIF (weak excitation) the fluorescence intensity I_f is proportional to the number density of the fluorophor n_f and the fluorescence quantum yield q_f. In the case of collisional quenching by oxygen as dominant fluorescence deactivation process I_f can be described by

$$I_f \propto n_{fl} \frac{k_{rad}}{k_f + k_{qO_2}\, n_{O_2}} \tag{1}$$

Here, the fraction represents q_f. It depends on the coefficient for spontaneous emission k_{rad}, the assembled coefficient for intra-molecular deactivation processes k_f, the oxygen quenching coefficient k_{qO_2} and the number density of oxygen n_{O_2}. If the oxygen quenching dominates the intra-molecular deactivations, i.e. if $k_f << k_{qO_2} \cdot n_{O_2}$, k_f can be neglected and the fluorescence intensity becomes proportional to the ratio of fluorophor and oxygen:

$$I_f \propto \frac{k_{rad}}{k_{qO_2}} \frac{n_{fl}}{n_{O_2}} \tag{2}$$

This means, with rising pressure the FARLIF signal becomes pressure independent and proportional to the equivalence ratio $\phi = 1/\lambda$, where the λ-value denotes the stoichiometric air-fuel ratio (for stoichiometric mixtures $\lambda = 1$, ignitable mixtures have $0.5 < \lambda < 1.3$).

In order to verify the FARLIF concept under controlled mixing situations and a broad temperature regime a heated pressure chamber was developed. A modular concept was used to provide the ability for future extensions. Initially, the chamber was designed to support a temperature range from room temperature up to 433 K and pressures between 1 mbar and 10 bar. During the progress of the project the temperature range of the setup could be extended to a maximum of 700 K. The chamber was equipped with three quartz windows – two, to let the laser sheet pass the test section and the third to observe the fluorescence perpendicular to the laser sheet. To generate a homogenous laser sheet, the light of a frequency quadrupled Nd:YAG laser with 266 nm emission was lead through a light sheet optic with homogenizer. At the entrance and the exit of the chamber a few percent of the beam was coupled out to monitor the laser energy. For mixture motion analysis a double-pulse LIF setup similar to standard PIV setups was developed by adding a second laser, identical to the first, to generate double pulses with a short temporal delay. In all cases, the fluorescence was detected by an intensified CCD-camera, which has the ability to record the fluorescence excited by the two lasers separately in two different frames. To scrutinize this setup the test chamber was extended by a coaxial nozzle which allowed the controlled simultaneous inlet of two gas compounds to generate mixing situations. Fuel-air mixtures were prepared in a heated 3.5-l pressure tank. For details please refer to [4-12].

3 FARLIF Verification with Toluene

Investigations were carried out in order to test the FARLIF concept for 5% or 10% toluene as fluorescence tracer in the commonly used non-fluorescent model fuel isooctane. Before studying the applicability of the FARLIF concept some preliminary investigations were done. In this aim the linearity of the LIF signal with

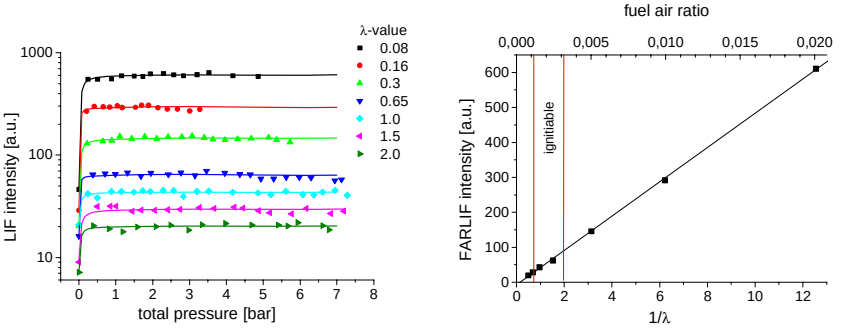

Fig. 1 FARLIF validation at 398 K with 266 nm excitation of toluene-isooctane-air mixture

excitation energy was successfully tested [5]. Another main precondition for FARLIF is the dominance of oxygen as collisional quencher, which could be confirmed as well [5]. For FARLIF verification several different gas mixtures of toluene in isooctane and synthetic air (80% nitrogen and 20% oxygen) were prepared in the heated pressure tank and the fluorescence was measured in the test chamber at different pressures (few mbar up to 10 bar) and temperatures between 398 K and 433 K. In the left part of figure 1 the fluorescence intensities versus total pressure are shown. The intensity rises with a very steep slope for low pressure and then forms a plateau with increasing pressure. This demonstrates the pressure independence of the LIF signal intensity for high pressures. The right part of figure 1 shows the plateau intensity versus equivalence ratio 1/λ. The values are located on a line through origin. Therefore, the FARLIF concept is directly validated far beyond the technical important region of ignitable mixtures ($0.5 < \lambda < 1.3$) and temperatures up to 433K.

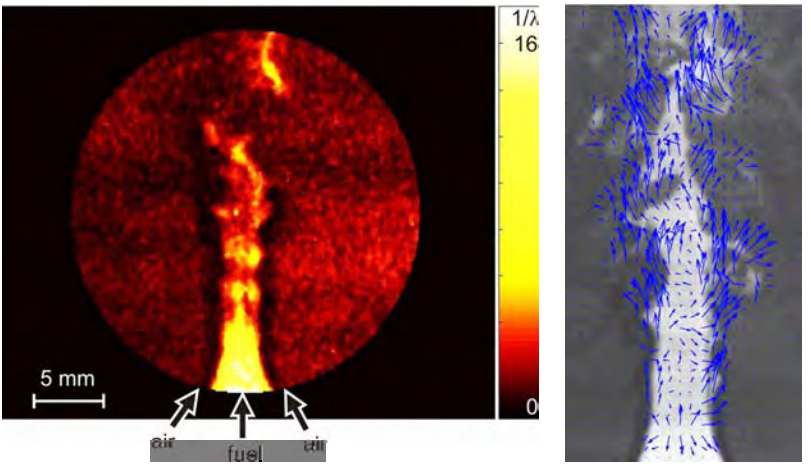

Fig. 2 Left image: Calibrated single shot FARLIF measurement at T = 398 K, p = 3 bar of the mixing of 10% toluene in isooctane as model fuel and air in the wake of a coaxial nozzle. Right image: FARLIF image with analysis of the mixture motion (please refer to text)

The left image of figure 2 shows an example for planar FARLIF measurement. The image shows a mixture situation in the wake of a two component coaxial nozzle. A premixed rich fuel-air mixture (ratio 1:3) was lead through the inner aperture of the nozzle while pure air streamed out of the outer aperture. The pressure was 3 bar and the temperature was 398 K. The laser sheet was centered over the nozzle exit and the flow is directed from bottom to top. Left and right from the central bright fuel inlet the dark areas of the air can be clearly distinguished. Further outside the signal rises again according to the increasing fuel content of the surrounding, already mixed gas.

An additional application of planar FARLIF images is the analysis of motion in mixtures. Similar to common PIV technique a double pulse laser and a dual-frame camera are used to take two images with a short temporal delay. The difference to PIV is that no seeding particles are used. Instead the fluorescing fuel structures are used to extract motion information. The right image of figure 2 shows the result of such a fluorescence motion analysis (FMA). For this analysis two images with a temporal delay of 200 μs were taken. The arrows are the result of the analysis done with an "optical flow" algorithm. They indicate the motion field of the FARLIF structure. It has to be mentioned that this is not equivalent to the velocity field of the flow but it shows where and how mixture structures are moving. This technique may be used to follow the movement of ignitable mixture clouds in optically accessible engines for example. For more details please refer to [4, 5, 13, 14].

4 FARLIF Verification with Near-Standard Fuel

After the promising results with toluene the focus was set on FARLIF applications with more realistic auto-fluorescent multi-component fuel without any additional tracer. Model fuels with one or only a few components are disadvantageous because they differ from standard gasoline in volatility and in combustion behavior. Therefore, "Shell Euro Super colorless" (PR 1632) was used in further investigations. This is a near standard gasoline, in which only the yellow-brownish bitumen components are eliminated. The native fluorescing hydrocarbons of this gasoline can be electronically excited by laser light with a wavelength of 266 nm and show sufficient auto fluorescence without any additional tracer. For this fuel the same preliminary investigations as for toluene in isooctane (linearity of LIF, dominance of oxygen quenching) were done with positive results [5]. The fluorescence intensity was even brighter than that of the toluene-isooctane mixtures. Also in this case the LIF signal of several mixture conditions was measured. The left image of figure 3 exemplifies the FARLIF intensities versus pressure of several mixtures near the ignitable regime at 398 K. Like toluene in isooctane the standard fuel shows steeply rising fluorescence for low pressures and forming of plateaus for elevated pressures. The plateau intensity of the fuel again is proportional to the equivalence ratio $1/\lambda$ as can be seen in the right image of figure 3. Here, the intensity is linear far beyond the ignitable regime. The results were similar at different temperatures up to 548 K. In all cases a formation of plateaus with rising pressure could be observed with plateau intensities proportional to the equivalence value.

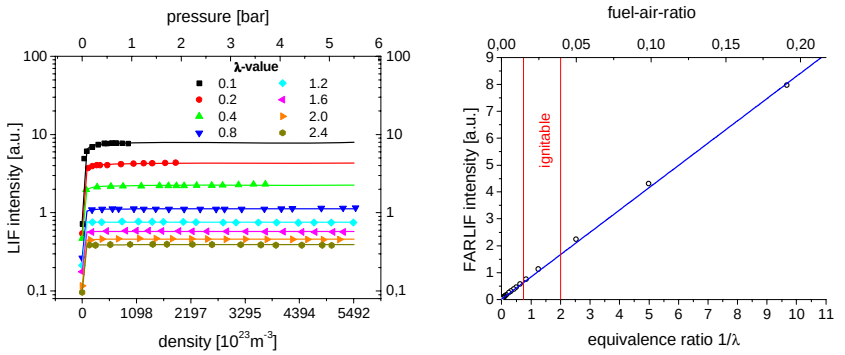

Fig. 3 FARLIF-validation at 398 K with 266nm excitation of gasoline-air mixtures

However, temperature dependencies became obvious. Figure 4 shows the normalized LIF signal versus pressure at different temperatures. The steep slope of the signal for low pressure flattens with rising temperature and the plateau is reached at higher pressures. This effect may be explained by additional intramolecular deactivation processes in the excited states of the fluorescing molecules which become accessible only at higher temperatures and compete with oxygen quenching.

Furthermore the slopes of the FARLIF calibration curves turned out to be temperature dependent. Therefore, FARLIF measurements are best suited for isothermal conditions. Otherwise the temperature has to be known for a correction. Therefore, a measurement concept for the temperature is introduced in the next section.

After validation of the FARLIF concept for standard gasoline the application of planar measurement was also tested. Analog to the toluene isooctane mixtures inhomogeneous mixture situations were generated by streaming fuel-rich air through a coaxial nozzle into air with lean air content. The left side of figure 5 shows an example of such a mixing situation at a temperature of 398 K under a pressure of 5 bar. Here, a cylinder of 0.9 mm diameter was introduced at the nozzle exit as a flow obstacle in order to increase mixing structures of the coaxial fuel-air flow. Again the flow is directed from the bottom to the top. The image was calibrated via the FARLIF calibration curve.

Fig. 4 Normalized pressure curves of LIF intensities for λ=1 mixtures at different temperatures

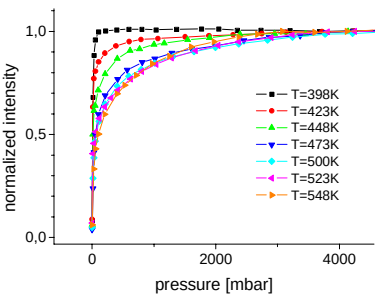

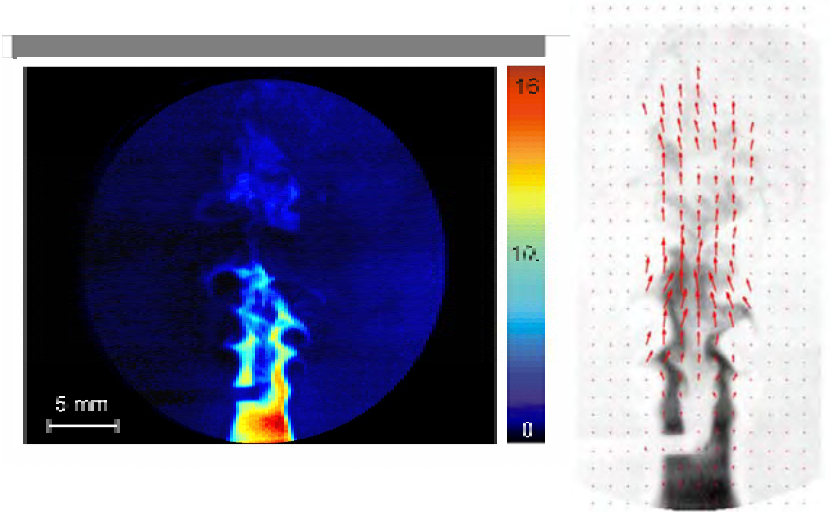

Fig. 5 Left image: Calibrated FARLIF measurement of gasoline and air mixing in a cylinder. Right image: Analysis of motion using double pulse planar FARLIF and FMA

With standard gasoline also double pulse FARLIF measurement was done and analysed with FMA. An example can be seen on the right side of figure 5. The background shows the calibrated FARLIF image. The mixture movement is well described by the arrows. The temporal deviation of these images provides additional information about the mixture motion. This is described in [7,9]. These articles also report the results of simultaneous PIV measurements, which were done in the context of this project to determine the velocity field for comparison with the mixture motion data. FMA was also tested with synthetic fluorescence images provided by Rainer Hain, Institute of Fluid Mechanics, Technical University Braunschweig [12]. For more details about FARLIF with near-standard gasoline please refer to [5-12].

5 Concept for Temperature Determination and Correction

In the progress of the experiments the FARLIF signal showed to be temperature dependent. Due to this it became necessary to find a correction strategy to enable FARLIF measurement under non-isothermal conditions and mixture situations with inhomogeneous temperature distributions. For this purpose preliminary investigations were done. Figure 6 shows in the left part two spectra of near-standard-fuel air mixtures which were recorded with a homebuilt spectrometer with a 1000 lines per mm grid. The upper spectrum is recorded at 375 K while the lower spectrum is recorded at 450 K. The spectra show two different fluorescence maxima: one in the short-wavelength region (S_1) and one in the long-wavelength region (S_2). The comparison of the two spectra shows that the ratio S_1/S_2 is

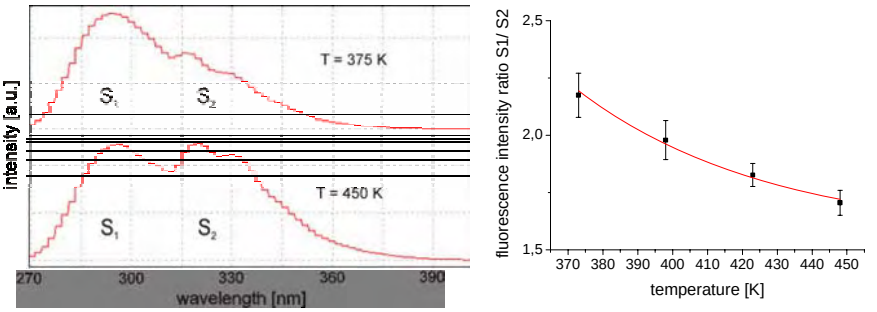

Fig. 6 Temperature dependence of LIF spectra of fuel-air mixtures

temperature dependent. These two spectral regions presumably can be associated to two different fluorescing component groups of the fuel: mono-aromatic and di-aromatic compounds. The right part of figure 6 shows the intensity ratio of S_1 and S_2 over the temperature. The curve shows a negative slope, which gives a correlation between temperature and fluorescence which can be used for temperature determination. This is in good agreement to investigations of the related kerosene fluorescence [15, 16].

6 Summary

In the conducted examination the FARLIF concept could be validated for toluene in isooctane (5 % and 10 %) as well as for almost-standard fuel “Shell Euro Super colorless”, both at an excitation wavelength of 266 nm. With toluene in isooctane as model fuel FARLIF could be validated for fuel-air mixtures with $\lambda \geq 0.2$ and temperatures up to 433 K in a pressure range from 1.5 bar to 10 bar. With almost standard fuel FARLIF could be validated for fuel-air mixtures with $\lambda \geq 0.4$ for temperatures up to 548 K and pressures above 2.5 bar. Unfortunately a temperature dependence has been observed. Thus FARLIF is best suited for measurements under isothermal conditions, otherwise a temperature correction has to be performed.

For both fuels the applicability of planar FARLIF imaging on isothermal transient fuel-air mixtures under engine relevant conditions was demonstrated. This technique could be used for example to identify ignitable mixture regions. In this connection the necessity of an absorption correction along the excitation path of the laser light has been taken into account. Investigations for an appropriate correction strategy of temperature effects and excitation light absorption are in progress.

Furthermore the application of double pulse FARLIF has been demonstrated. Two ways of analysis were mentioned. The calculation of temporal derivation fields shows qualitatively where and how fuel-air ratio maps are changing. Fluorescence motion analysis (FMA) using “optical flow” methods provides a vector field which describes the motion of fluorescence structures. This vector field does

not necessarily represent the flow field but it shows how and where mixture structures are moving. It could be used, for example, to determine when ignitable mixture structures reach the spark plug in an optically accessible engine.

To correct temperature effects of FARLIF measurement a concept for temperature determination was introduced. The work on this project is still in progress and will be accomplished in further examinations.

Acknowledgments. The authors gratefully acknowledge the financial support from the Deutsche Forschungsgemeinschaft DFG in the framework of the priority program SPP 1147.

References

1. Drake, M.C., Haworth, D.C.: Advanced gasoline engine development using optical diagnostics and numerical modeling. Proc. Combust. Inst. 31(1), 99–124 (2007)
2. Reboux, J., Puechberty, D., Dionnet, F.: A new approach of PLIF applied to fuel/air ratio measurement in the compression stroke of an optical SI engine. SAE technical paper series, No. 941988 (1994)
3. Schulz, C., Sick, V.: Tracer-LIF Diagnostics: Quantitative Measurement of fuel concentration, temperature and air/fuel ratio in practical combustion situations. Prog. Energy Combustion Sci. 31, 75–121 (2005)
4. Scholz, J., Röhl, M., Beushausen, V.: Mischungsfeldanalyse mit Fuel-Air-Ratio-LIF. Lasermethoden in der Strömungsmesstechnik, 13. Fachtagung der Deutschen Gesellschaft für Laser-Anemometrie GALA e.V., Cottbus, September 6-8 (2005)
5. Scholz, J., Röhl, M., Wiersbinski, T., Beushausen, V.: Verification and Application of Fuel-Air-Ratio-LIF. In: 13th International Symposium on Applications of Laser Techniques to Fluid Mechanics, Lisbon (2006)
6. Scholz, J., Wiersbinski, T., Beushausen, V.: Planare Fuel-Air-Ratio-LIF und PIV zur Gemischbildungsanalyse von Realkraftstoff. Lasermethoden in der Strömunsgsmesstechnik, 14. Fachtagung der Deuschen Gesellschaft für Laser-Anemometrie GALA e.V., Braunschweig, September 5-7 (2006).
7. Scholz, J., Röhl, M., Wiersbinski, T., Beushausen, V.: Planar Fuel-Air-Ratio-LIF with Gasoline. In: 12th International Symposium on Flow Visualization, Göttingen, September 10-14 (2006)
8. Scholz, J., Wiersbinski, T., Beushausen, V.: Kombination von FARLIF und PIV zur Gemischbildungsanalyse von Realkraftstoff. In: Leipertz, A. (ed.) Motorische Verbrennung – Aktuelle Probleme und moderne Lösungsansätze, Bericht zur Energie- und Verfahrenstechnik (BEV) 7.1, ESYTEC, Erlangen, pp. 291–302 (2007)
9. Scholz, J., Wiersbinski, T., Beushausen, V.: Planar Fuel-Air-Ratio-LIF with gasoline for dynamic mixture-formation investigations. SAE world congress, Detroit, USA (2007)
10. Scholz, J., Wiersbinski, T., Ruhnau, P., Kondermann, D., Hain, R., Beushausen, V.: Weiterentwicklung einer 2D Doppelpuls LIF Messtechnik mit Fluorescence Motion Analysis zur Untersuchung von Mischungsprozessen. Lasermethoden in der Strömungsmesstechnik, 15. Fachtagung der Deutschen Gesellschaft für Laser-Anemometrie GALA e.V., Rostock, September 4-6 (2007)
11. Scholz, J., Wiersbinski, T., Ruhnau, P., Kondermann, D., Garbe, C.S., Hain, R., Beushausen, V.: Double-Pulse Planar-LIF Investigations using Fluorescence Motion Analysis for Mixture Formation Investigation. In: Proc. 7th International Symposium Particle Image Velocimetry, PIV 2007, Rome, Italy, September 11-14 (2007)

12. Scholz, J., Wierbinski, T., Beushausen, V.: Double-Pulse Planar Fuel/Air-Ratio Measurement by Laser-Induced Fluorescence. Journal of Visualization 10(3), 248 (2007)
13. Garbe, C., Spies, H., Jähne, B.: Estimation of Surface Flow and Net Heat Flux from Infrared Image Sequences. Journal of Mathematical Imaging and Vision 19, 159–174 (2003)
14. Ruhnau, P., Schnörr, C.: Optical stokes flow estimation: An imaging based control approach. Exp. in Fluids 42(1), 61–78 (2007)
15. Baranger, P., Orain, M., Grisch, F.: Fluorescence spectroscopy of kerosene vapour: application to gas turbines. In: 43rd AIAA Aerospace Sciences Meeting and Exhebit, Reno, Nevada, paper N^{o} 2005-828 (2005)
16. Rossow, B., Orain, M., Grisch: Eqivalence ratio measurement in kerosene-fuelled LPP injectors using kerosene planar laser-induced fluorescence. In: 12th International Symposium on Flow Visualisation, Göttingen, September 10-14 (2006)

Development of Imaging Laser Diagnostics for the Validation of LE-Simulations of Flows with Heat and Mass Transfer

Andreas Braeuer, Anna Malarski, and Alfred Leipertz

Abstract. Imaging laser diagnostic techniques were developed and combined to simultaneously measure concentration and velocity fields in turbulent mixing processes. Raman imaging (Ramanography) was used to probe the concentrationfield while particle image velocimetry (PIV) was applied to gain information on the velocity field. Due to the inherent characteristics of both techniques, our work covers both, mixing processes with liquids and pressurized gases. In Hydrogen flows, a simultaneous detection of concentration and temperature fields is possible.

1 Introduction

Mixing processes are widely used, e.g. in combustion or in chemical, biotechnological and pharmaceutical industry. The numerical simulation of such processes is in progress during the last years. Especially the implementation of numerical methods like Direct Numerical Solution (DNS) and Large Eddy Simulation (LES) instead of statistical methods such as Reynolds Averaged Navier Stokes Method (RANS) offers the potential of more accurate results. For the validation of the LES or DNS results the time-resolved simultaneous measurement of the velocity and concentration or temperature fields is mandatory.

The already well established laser based Particle image velocimetry (PIV) was applied for all velocity measurements comprising this report. This technique is based on the multiple exposure of a particle-seeded flow [24] with calculation of mean velocity vectors from the displacement of the particles and the time interval between the exposures. This standard technique (commercially available, therefore we will forego a detailed explanation of the PIV technique) had to be combined with an additional laser diagnostics technique for concentration measurements. During this research project besides concentration in liquids, even composition and temperature was measured simultaneously in hydrogen flows using only one laser and three cameras.

Andreas Braeuer · Anna Malarski · Alfred Leipertz
Lehrstuhl für Technische Thermodynamik and Erlangen Graduate School in Advanced Optical Technologies (SAOT), Universität Erlangen-Nürnberg, Am Weichselgarten 8, 91058 Erlangen, Germany
andreas.braeuer@aot.uni-erlangen.de

W. Nitsche and C. Dobriloff (Eds.): Imaging Measurement Methods, NNFM 106, pp. 175–184.
springerlink.com

In the past a variety of laser diagnostic techniques was developed [10, 16, 25–27, 31], which qualify for locally and temporally resolved analysis of mixture generation (concentration, mole fraction, composition). Among all these techniques, only very few provide two-dimensional (2-D) information about the temperature and the mole fraction distribution simultaneously. Usually the respective techniques are laser-induced fluorescence (LIF) techniques which rely on composition and temperature dependent absorption and emission processes of a molecule [1, 13, 29, 30] and for measurements along one line or at one point as Raman scattering. Compared to Raman scattering, LIF has the advantage of a larger signal level but is only applicable in either fluorescent media or fluids which are seeded with a fluorescent tracer whereas nearly all media are Raman-active. For LIF flow analysis, usually a tracer molecule, which is known to indicate composition and temperature is added to a non-fluorescing carrier fluid. In this case the detected LIF-signals can definitely be ascribed to the tracer molecules. Thus, signal evaluation is straight forward if the photo physical properties of the tracer are known.

Special problems arise, if LIF composition and temperature analysis should be carried out in hydrogen flows, which due to energy policy and combustion applications become increasingly important. Hydrogen cannot be excited to fluorescence with available laser sources via single photon absorption. Thus tracer molecules have to be added to the hydrogen. But there are no tracer molecules available with hydrogen like properties regarding size and mass. Hence diffusion and transport properties of the hydrogen and the tracer are quite different. Additionally, which may be the essential drawback of all quantitative LIF tracer techniques, they suffer from a complex tracer calibration, complex experimental setups and data evaluation procedures. Apparently a 2-D measurement technique which has the potential to probe temperature and concentration directly from the hydrogen molecules itself and could be combined with a velocity field measuring technique would be an advanced tool for hydrogen energy conversion development.

Unfortunately Raman scattering suffers from very weak signal strengths. Thus, in a first step we started to develop the laser diagnostics technique consisting of PIV and Ramanography in a process where liquid ethanol was injected into liquid water at room temperature and ambient pressure. In this system the high molecular density of liquids contribute to sufficient Raman signal strengths. To the best of our knowledge, the simultaneous implementation of Ramanography and PIV in liquid mixing processes was realized within this research project for the first time [20]. In former approaches combined velocity and concentration field measurements were carried out by the detection of the particle Mie scattering and the fluorescence of the seed [11] which is easier due to the abovementioned reasons. Quasi simultaneous, point wise measurements of concentration and velocity were realised by other researchers using Raman spectroscopy and laser Doppler velocimetry (LDV) [5, 6, 8]. The LDV event triggered the Raman set-up with a 3 time delay to guarantee a particle free measurement volume for the Raman measurement. This is unsatisfying in turbulent and therefore strongly time dependent processes, because a direct relation between the concentration and the velocity is not given in such an approach.

Having optimized the experimental system in the liquid-liquid system, we switched over to a gaseous mixing process, which is of outmost importance for energy conversion processes dealing with hydrogen. For safety reasons hydrogen was injected into pure nitrogen at 11 MPa (abs) instead of air, which would be the usual oxidizer in common combustion applications. Again the experiment had to be optimized for the challenges of gaseous mixing systems, which arise due to the low molecular densities of gases in comparison to liquids. Therefore we will distinguish between the liquid and the gaseous systems in this report.

Different attempts to measure the distribution of one certain species molecule using 2-D Raman scattering are known since 1973 [12] when Hartley introduced the name "Ramanography". Since then Ramanography was applied for jet behaviour and turbulence investigations in reacting and non reacting flows under ambient pressure and in pressurized chambers at ambient temperature and under cryogenic conditions [4, 7, 17, 19, 21, 22].

In the second part of this report we describe the development of a Ramanography technique which simultaneously provides hydrogen mole fraction and temperature information. This is realized by directly probing the hydrogen and nitrogen molecular number densities in different rotational and vibrational energy levels. In addition to the benefit that no tracers are needed this technique profits from a simple experimental setup and a straight forward data evaluation procedure. A prior non-extensive calibration is necessary. The combination of this measurement technique with PIV and with optical flow techniques to simultaneously probe the velocity field is in progress and will be finalized before the DFG priority research programme 1147 will be completed in 2009.

2 Raman Scattering

Upon irradiating a sample of molecules with a monochromatic laser beam, besides elastic Rayleigh scattering, frequency shifted Raman scattering can be detected. The frequency shift corresponds to the energy difference $\nu_{\text{Raman-shift}}$ of two Raman active rotational and/or vibrational energy levels of the irradiated molecules [9, 14, 23, 28]. The Raman signal intensity is proportional to the population of the probed energy level. The Raman signal intensities of the energy levels of different species can easily be separated as the Raman shifts $\nu_{\text{Raman-shift}}$ of a molecule are species specific and thus different for different molecules. The Raman scattering working equation for signal detection perpendicular to the polarization of the irradiated laser beam is [18]

$$I(i) = \frac{I_{\text{Laser}}}{h\upsilon_{\text{Laser}}} \cdot \left(\frac{d\sigma}{d\Omega}\right) \cdot \Omega \cdot N(i)_{v,J} \cdot K \tag{1}$$

where the Raman signal intensity of species i I(i) [-] reflects the number of detected Raman scattered photons, I_{Laser} [Jm^{-2}] is the excitation laser energy fluence, $h\upsilon_{\text{Laser}}$ [J] is the photon energy of the laser frequency υ_{Laser}, $d\sigma/d\Omega$ [m^2sr^{-1}] is the integral Raman scattering cross section with Ω [sr^{-1}] the signal detection solid angle and K is a constant, which comprises all influencing factors of the

experimental setup. $N(i)_{v,J}$ is the number of species i molecules, which populate the vibrational v and rotational J energy level probed. The population distribution across the rotational and vibrational energy levels follows Boltzmann statistics.

3 PIV and Ramanography in Liquid Mixing Processes

A sketch of the used experimental set-up to analyze the injection of liquid ethanol into water is shown in Fig. 1. Both scattering processes were excited with a frequency-doubled Nd:YAG laser (532nm). The double-pulse option of the laser offers the observation of the particle seeded flow with a pulse delay of 80 µs for the PIV measurements. The Raman scattered light of the first pulse was detected for the concentration measurements. A detailed description of the experimental setup can be found elsewhere [20].

As the resolution of the Raman imaging system (each pixel covers a section of 72 x 72µm) is much better than that of the PIV system, the Raman data can be filtered by a 3 x 3 pixel median filter routine enhancing the SNR to 13.5 which was determined experimentally. A median filter was used as it conserves the sharp edges of the spray.

As an example for the simultaneous measurements, Fig. 2 shows the evaluated data of a spray 20 ms after injection with an injection pressure of 2.4 bar. In the background the ethanol concentration field is shown with the 3 x 3 5 median filter routine applied. As the nozzle generates a jet of two components that were already mixed inside the mixing pipe, the maximum ethanol concentration at the exit is only 45 % per unit volume. The simultaneously measured velocity field shows a very good agreement with the turbulent structure of the concentration field if the limited resolution of the PIV measurements is taken into account. The main flow direction follows the injection direction. In the outer regions of the jet nearly no flow can be observed.

Summarizing the first half of this report, we have demonstrated that it is possible to simultaneously apply a strong and a very weak scattering process for imaging purposes. Raman scattering provides a tremendous amount of information and is therefore the best method for concentration measurement. Until now the application of Raman imaging in particle laden environments caused a lot of disturbances due to the elastically scattered light. Here an optimised filter system

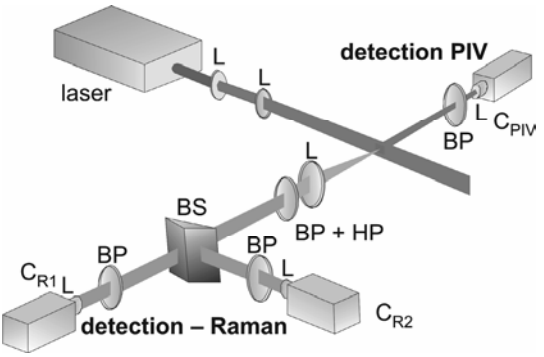

Fig. 1 Schematic of the experimental set-up (CPIV, double-shutter CCD camera for PIV measurements; C_{R1}, ICCD camera for Raman imaging of component 1; C_{R2}, ICCD camera for Raman imaging of component 2; L, lens; BP, band pass filter; HP, high pass filter; BS, beam splitter), from [20]

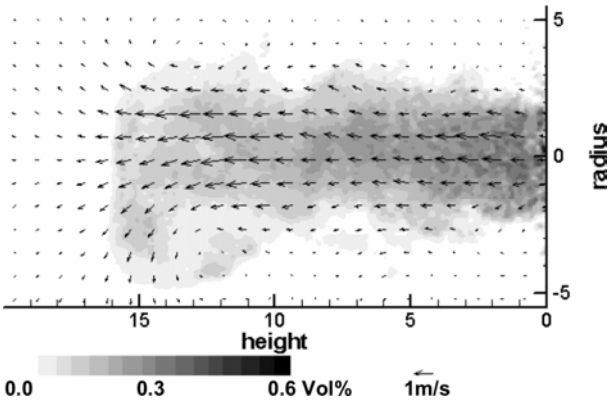

Fig. 2 Velocity and ethanol concentration field , p = 2.4bar, t = 20ms, T = 25°C, from [20]

with an optical density larger than 16 at the excitation wavelength was used to separate the Raman signal from the Mie (PIV) signal.

4 Mole Fraction and Temperature Analysis in Hydrogen Flows

Fig. 3 shows the experimental setup with only one laser source and three cameras to be used for the simultaneous detection of the H_2 mole fraction $x(H_2)$ and the H_2 temperature $T(H_2)$. A frequency doubled Nd:YAG-Laser at 532 nm with a FWHM pulse-length of 10 ns and a single-shot pulse energy of 650 mJ was used for the excitation of the Raman process. A detailed description of the setup used can be found elsewhere [3]. To prevent the pulse intensities from exceeding the injection chamber window damage threshold a single loop pulse-stretcher was used [15,2]. Three electron multiplying charge coupled device (EMCCD) cameras allowed the simultaneous detection of three different Raman signals. In contrast to EMCCD cameras, intensified cameras suffer from rather low quantum efficiencies of the Multi-Chanel-Plate. Fig. 4 shows a sketch of the injection chamber together with exemplary acquired Raman images of the H_2 and N_2 distribution.

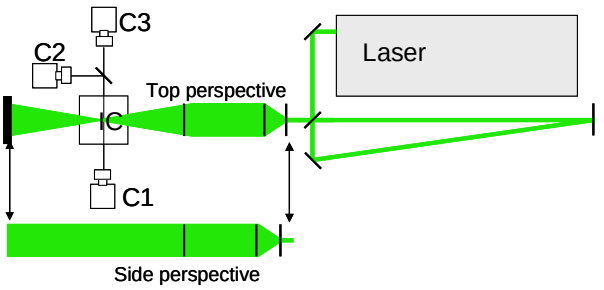

Fig. 3 Sketch of the experimental Raman setup used for the simultaneous 2-D detection of hydrogen mole fraction $x(H_2)$ and hydrogen temperature $T(H_2)$. C1-C3: EMCCD-Cameras; IC: injection chamber [3]

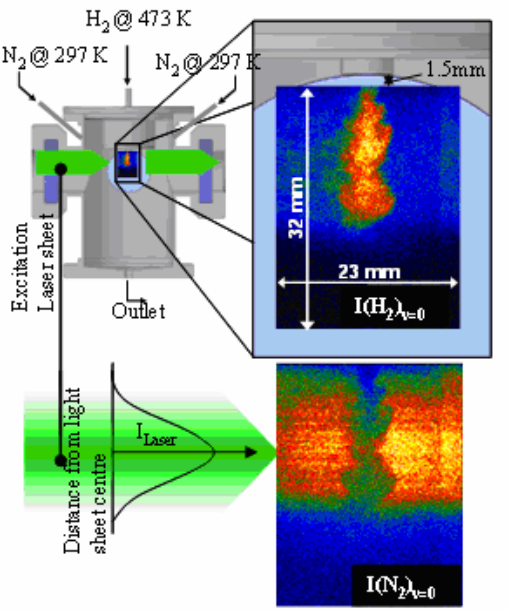

Fig. 4 Sketch of the injection flow sheet with illustration of the evaluated regimes inside the injection chamber. The jet image and its complement give the vibrational ground state v = 0 Raman signal intensities of hydrogen $I(H_2)_{v=0}$ and nitrogen $I(N_2)_{v=0}$, respectively. The intensity distribution inside the laser excitation light sheet is qualitatively illustrated [3]

Two-dimensional hydrogen mole fraction and temperature measurements were carried out inside a field of 32 x 23 mm with a local resolution of 200 µm x 200 µm and a temporal resolution of a few nanoseconds. Hot hydrogen (473 K) was injected into cold pressurized nitrogen (473 K, 1.1 MPa abs.).

Having carried out different experiments detecting different Raman signals one strategy was identified as the most suitable for the temperature range apparent in hydrogen combustion systems. Here the vibrational ground state signal of nitrogen, and the pure rotational Raman signals of the level J = 1 and J = 3 were detected. Temperature evaluation follows Boltzmann statistics, whereas mole fraction analysis follows the introduction of a virtual energy level as described in Braeuer and Leipertz [3]. The single-shot accuracy and precision were evaluated in a series of experiments also described elsewhere [3].

Exemplary single-shot and mean H_2 mole fraction $x(H_2)$ and H_2 temperature $T(H_2)$ images are displayed in Fig. 5. The mean images were calculated from 100 single-shot images. Close to the injector's nozzle some significant irregularities can be seen in Fig. 5. They must be attributed to the laser sheet excitation profile, which has a maximum in the middle of the light sheet and decreases to the upper and lower border. As the upper border was adjusted 1.5 mm underneath the injector's nozzle exit the excitation laser energy in this region is minor than in a certain distance from the injector's nozzle exit. Thus, in regions close to the injector's nozzle, noise dominates the detected Raman signals, which results in implausible results. For example, the H_2 mole fraction $x(H_2)$ at the top border in Fig. 5 must never be smaller than in a short distance downstream. Because of noise dominating the detected signals not only the mole fraction results but also the

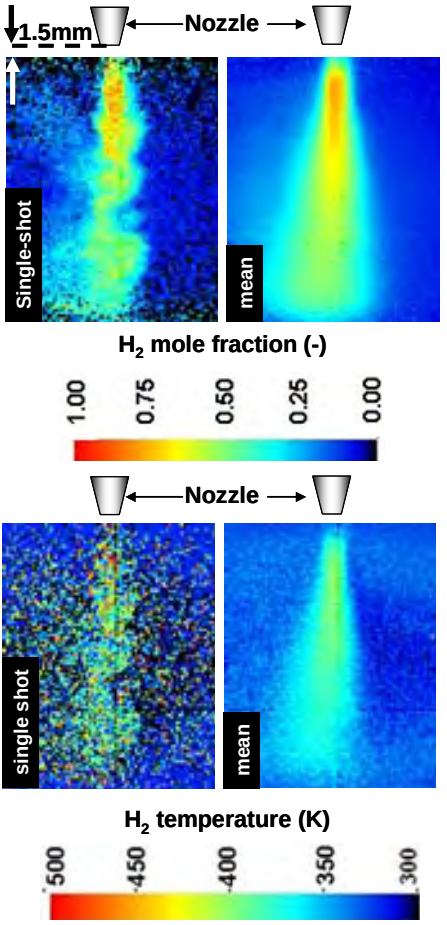

Fig. 5 Mean and single-shot hydrogen mole fraction $x(H_2)$ and hydrogen temperature $T(H_2)$ images of a hot (473 K) hydrogen jet which is injected into room temperature (297 K) nitrogen at an absolute pressure of 1.1 MPa [3]

temperature results show irregularities close to the injector's nozzle. A beam homogenizer to be used will help to eliminate these irregularities.

Raman scattering has been proven to be in general a promising tool for hydrogen mixture formation processes. Until now similar two-dimensional applications are known for either temperature or number density analysis of one species but not for composition analysis of a mixture. Time-resolved Ramanography applications with commercially available lasers in free jets had to be ascribed to either pressurized or cryogenic processes. Still some challenges remain. High laser energy may induce ignition of the hydrogen air mixture. This may especially become a problem if particles (dust or oil droplets) cause a breakdown. To circumvent this, a multi-loop pulse stretcher would be helpful to further decrease the laser pulse intensity. Alternatively a Nd:YAG laser cluster could be applied to excite the Raman process with temporally shifted multi laser pulses within 1 μs. Consequently high excitation energies could be realized with rather low intensity pulses.

Considering costs, the multi-loop pulse stretcher is superior to the laser cluster but more complex to adjust and to handle.

5 Conclusion

Combining the Raman technique introduced here with an optical flow field probing technique, what was already successfully accomplished within liquid systems, will yield temperature, mole fraction and velocity information all at once. This can be realized for example by measuring the optical flow during hydrogen injection. In this case a double pulse laser is required. For optical flow analysis the cameras must have a double shutter option.

In general the precisions and the accuracy of both, temperature and mole fraction analysis, can be significantly improved, if higher energy laser sources are available. In this case a comparison between heat and mass transfer will provide deeper insight in more fundamental approaches of thermodynamics. This is especially interesting for hydrogen, which is known to be characterized by Lewisnumbers different than 1.

Acknowledgments. The authors gratefully acknowledge funding of parts of this work by the German National Science Foundation (DFG) and funding of the Erlangen Graduate School in Advanced Optical Technologies (SAOT) by the DFG in the framework of the excellence initiative.

References

1. Braeuer, A., Beyrau, F., Leipertz, A.: Laser-induced fluorescence of ketones at elevated temperatures for pressures up to 20 bars by using a 248 nm excitation laser wavelength: ex-periments and model improvements. Appl. Opt. 20, 4982–4989 (2006)
2. Braeuer, A., Beyrau, F., Weikl, M.C., Seeger, T., Kiefer, J., Leipertz, A., Holzwarth, A., Soika, A.: Investigation of the combustion process in an auxiliary heating system using dual-pump CARS. J. Raman Spectrosc. 37, 633–640 (2006)
3. Braeuer, A., Leipertz, A.: Two-dimensional Raman mole-fraction and temperature measurements for hydrogen–nitrogen mixture analysis. Appl. Opt. 48, B57–B64 (2009)
4. Decker, M., Schik, A., Meier, U.E., Stricker, W.: Quantitative Raman imaging investiga-tions of mixing phenomena in high-pressure cryogenic jets. Appl. Opt. 37, 5620–5627 (1998)
5. Dibble, R.W., Kollmann, W., Schefer, R.W.: Conserved Scalar Fluxes Measured in a Tur-bulent Nonpremixed Flame by Laser Doppler Velocimetry and Laser Raman Scattering. Combust Flame 55, 307–321 (1984)
6. Dibble, R.W., Hartmann, V., Schefer, R.W., Kollmann, W.: Conditional sampling of velocity and scalars in turbulent flames using simultaneous LDV-Raman scattering. Exp. Fluids 5, 103–113 (1987)
7. Dowy, S., Braeuer, A., Schatz, R., Schluecker, E., Leipertz, A.: CO2 partial density distribution during high-pressure mixing with ethanol in the supercritical antisolvent process. The Journal of Supercritical Fluids (2008), doi:10.1016/j.supflu.2008.10.017

8. Duan, X.R., Meier, W., Weigand, P., Lehmann, B.: Phase-resolved laser Raman scattering and laser Doppler velocimetry applied to periodic instabilities in a gas turbine model combustor. Appl. Phys. B 80, 389–396 (2005)
9. Eckbreth, A.C.: Laser diagnostics for combustion temperature and species. Gordon and Breach, Amsterdam (1996)
10. Einecke, S., Schulz, C., Sick, V.: Measurement of temperature, fuel concentration and equivalence ratio fields using tracer LIF in IC engine combustion. Appl. Phys. B 71, 717–723 (2000)
11. Frank, J.H., Lyons, K.M., Long, M.B.: Simultaneous Scalar/Velocity Field Measurements in Turbulent Gas-Phase Flows. Combust. Flame 107, 1–12 (1996)
12. Hartley, D.L.: In: Lapp, M., Penney, C.M. (eds.) Laser Raman gas diagnostics, pp. 1151–1157. Plenum, New York (1974)
13. Koch, J.D., Hanson, R.K.: Temperature and excitation wavelength dependencies of 3-pentanone absorption and fluorescence for PLIF applications. Appl. Phys. B 76, 319–324 (2003)
14. Kohse-Höinghaus, K., Jeffries, J.B.: Applied combustion diagnostics. Taylor and Francis, New York (2002)
15. Kojima, J., Nguyen, Q.V.: Laser pulse-stretching with multiple optical ring cavities. Appl. Opt. 41, 6360–6370 (2002)
16. Kronemayer, H., Omerbegovic, K., Schulz, C.: Quantification of the evaporative cooling in an ethanol spray created by a gasoline direct-injection system measured by multiline NO-LIF gas-temperature imaging. Appl. Opt. 46, 8322–8327 (2007)
17. Kyritsis, D.C., Felton, P.G., Huang, Y., Bracco, F.V.: Quantitative two-dimensional instan-taneous Raman concentration measurements in a laminar methane jet. Appl. Opt. 39, 6771–6780 (2000)
18. Leipertz, A., Fiebig, M.: Using Raman intensity dependence on laser polarization for low gas concentration measurements with giant pulse lasers. Appl. Opt. 19, 2272–2274 (1980)
19. Long, M.B., Levin, P.S., Fourguette, D.C.: Simultaneous two-dimensional mapping of species concentration and temperature in turbulent flames. Opt. Lett. 10, 267–269 (1985)
20. Malarski, A., Egermann, J., Zehnder, J., Leipertz, A.: Simultaneous application of single-shot Ramanography and particle image velocimetry. Opt. Lett. 31, 1005–1007 (2006)
21. Masri, A.R., Dibble, R.W., Barlow, R.S.: Raman-Rayleigh Scattering measurements in re-acting and non-reacting dilute two-phase flows. J. Raman Spectrosc. 24, 83–89 (1993)
22. Mayer, W., Telaar, J., Branam, R., Schneider, G., Hussong, J.: Raman measurements of cryogenic injection at supercritical pressure. Heat and Mass Transfer 39, 709–719 (2003)
23. Miles, P.C.: Raman line imaging for spatially and temporally resolved mole fraction measurements in internal combustion engines. Appl. Opt. 38, 1714–1732 (2007)
24. Raffel, M., Willert, C., Kompenhans, J.: Particle Image Velocimetry. Springer, Heidelberg (1998)
25. Schulz, C., Sick, V.: Tracer-LIF diagnostics: quantitative measurement of fuel concentration, temperature and fuel/air ratio in practical combustion systems. Prog. Energy Combust. Sci. 31, 75–121 (2005)

26. Schütte, M., Finke, H., Grünefeld, G., Krüger, S., Andresen, P., Stiebels, B., Block, B., Meyer, H., Hentschel, W.: Spatially resolved Air-Fuel Ratio and residual gas measurements by spontaneous Raman scattering in a firing direct injection gasoline engine. SAE-paper 2000-01-1795 (2000)
27. Schütte, M., Grünefeld, G., Andresen, P., Hentschel, W., Homburg, A., Nassif-Pugsley, D.: Fuel/Air-Ratio measurements in direct injection gasoline sprays using 1D Raman scatter-ing. SAE-paper 2000-01-0244 (2000)
28. Taschek, M., Egermann, J., Schwarz, S., Leipertz, A.: Quantitative analysis of the near-wall mixture formation process in a passenger car direct-injection Diesel engine by using linear Raman spectroscopy. Appl. Opt. 44, 6606–6615 (2005)
29. Thurber, M.C., Grisch, F., Kirby, B.J., Votsmeier, M., Hanson, R.K.: Measurements and modeling of acetone laser-induced fluorescence with implications for temperature-imaging diagnostics. Appl. Opt. 37, 4963–4978 (1998)
30. Wieske, P., Wissel, S., Grünefeld, G., Pischinger, S.: Improvement of LIEF by wavelength-resolved acquisition of multiple images using a single CCD detector- Simultaneous 2D measurement of air/fuel ratio, temperature distribution of the liquid phase and qualitative distribution of the liquid phase with the multi-2D technique. Appl. Phys. B 83, 323–329 (2006)
31. Zhao, H., Ladommmatos, N.: Optical diagnostics for in-cylinder mixture formation measurements in IC engines. Prog. Energy Combust. Sci. 24, 297–336 (1998)

Optical Measurements in the Wake of a Circular Cylinder of Finite Length at a High Reynoldsnumber

Mario Jensch, Frank Hüttmann, Martin Brede, and Alfred Leder

Abstract. The flow around a cylinder of finite length with one end bound on a large end plate defines a challenging problem for both, the numerical simulation and the experiment. In the following article, some of the results are described which were obtained experimentally on this "Leitexperiment" during the DFG research priority program 1147. The emphasis is placed on the observation of the highly unsteady wake using time resolved particle image velocimetry. Here a large amount of data was inferred, resolving both, the spatial domain on a volume of 2D planes as well as the temporal domain by measuring fields of the 3D velocity vector at a rate of 1000 Hz. After a short introduction into the features of the time average flow field, a new approach is taken, using the POD as an instrument to reconstruct the unsteady 3D flow field from ensembles of instantaneous 2D TR-PIV fields containing the complete velocity vector. The POD modes from this were compared successfully with the results of the numerical simulation, performed simultaneously in the same research priority program [2].

1 Introduction

The three dimensional flow around a bluff body is a standard topic in fluid mechanics. Regarding the wake of a cylinder with low aspect ratio the list of previous experiments is very limited and mostly contains steady state results. A detailed review of the research on low aspect ratio cylinders has been given by Pattenden [11]. Results of LDA experiments have been discussed by Leder [7] and Richter [12]. With the introduction of the time resolved PIV measurement technique, new measurement capabilities are available. The unsteady flow can now be obtained, covering an entire 2D flow field. From this the problem arises that a large amount of data has to be analyzed. A good method to achieve a better understanding of the phenomena in unsteady flows is to reduce the data using the proper orthogonal decomposition technique [8] based on the work of Karhunen [10] and Loéve [9]. A given flow will be decomposed into orthogonal eigenmodes using the snapshot method of Sirovich [14], which not only contains information of basic flow structures but also of the energy content.

Experimental investigations were performed in the turbulent separated flow around a circular cylinder of finite length with one end fitted to an end plate at a

Mario Jensch · Frank Hüttmann · Martin Brede · Alfred Leder
University of Rostock, Chair of Fluid Mechanics, Albert-Einstein-Straße 2

W. Nitsche and C. Dobriloff (Eds.): Imaging Measurement Methods, NNFM 106, pp. 185–195.
springerlink.com

Reynolds number of $Re_D = \frac{U_\infty D}{\nu} = 200000$, D being the diameter of the cylinder. For this Reynolds number the onset of transition can be assumed at the separation point. The flow was investigated using the time-resolved stereo Particle Image Velocimetry (TR-PIV). The proper orthogonal decomposition method for experimental data reveals valuable new information about the coherent structures of the unsteady flow and opens a wide field for new data postprocessing.

2 Experimental Setup

The stereo TR-PIV system consists of two high speed CMOS cameras with Scheimpflug optic and a frequency doubled Neodym-YAG laser. The system allows a frame rate of 2000 Hz over 2.7 s, with a camera resolution of 1024 x 768 pixels², details see [4]. For the generation of the flow a Göttingen type wind tunnel with a 0.65 x 0.65 m² open test section has been used. It is operated at a flow speed of U_∞ = 26 m/s. The geometry setup is depicted in Figures 1 and 2. The Reynolds number value of 200000 was selected because it can be regarded subcritical for the boundary layer flow but supercritical for the separated shear layer. Hence the transition point can be expected to be directly at the location of the separation point. Additionally, the transition of the boundary layer of the plate is fixed by a trip wire close to the rounded leading edge.

The measurement series discussed here was performed in 16 x-z planes parallel to the mean flow with a spacing between the planes of 0.1 *D* in the lateral direction. The field of view of each plane covers 444 x 276 mm² with interrogation areas of 32 x 32 pixels² and an overlap of 50 %. Other measurement series which can not be discussed here due to space limitations contain a similar dataset measured in horizontal x-y planes, volume TR-PIV measurements of the flow on the free end of the cylinder and an 3D-LDA measurements of the entire flow field including the upstream part of the horseshoe vortex.

Cylinder geometry
diameter D = 120mm
length L = 2D
trip wire position x0 = -1.5D

End plate geometry
b = 5.833 D
l = 10.833 D
d = 0.15 D

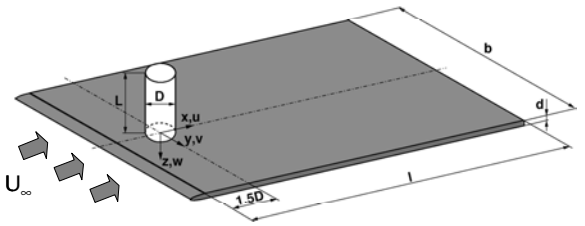

Flow parameter
Re_D = 200000
flow speed U_∞ = 26m/s
turbulence intensity
Tu = 0.5%
T =297K ±1K

Fig. 1 Configuration of the experimental setup

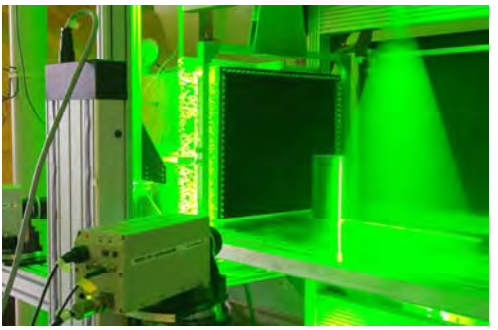

Fig. 2 Experimental setup in the windtunnel

3 Time Averaged Flow

To illustrate the flow features figure 3 depicts the time averaged flow topology in the wake using red and silver streamlines and blue isosurfaces of the λ_2-criterion of Jeong & Hussain [6]. Several vortices can be identified. A pair of counter rotating tip vortices can be found on the free end of cylinder. Because of the interactions of the lateral flow (red streamlines) and the recirculation arch vortex (silver streamlines) a pair of trailing vortices is induced at a stable position downstream at mid span of the cylinder. The recirculation arch vortex is induced by the flow over the free end. Additionally one half of the horseshoe vortex system is visualised, which can be found near the endplate. The corresponding counter rotating vortex is not represented due to the limited measurement area. These findings agree very well with the measurements of Leder [7] and Pattenden [11] and also to the simulations of Frederich [1] [3].

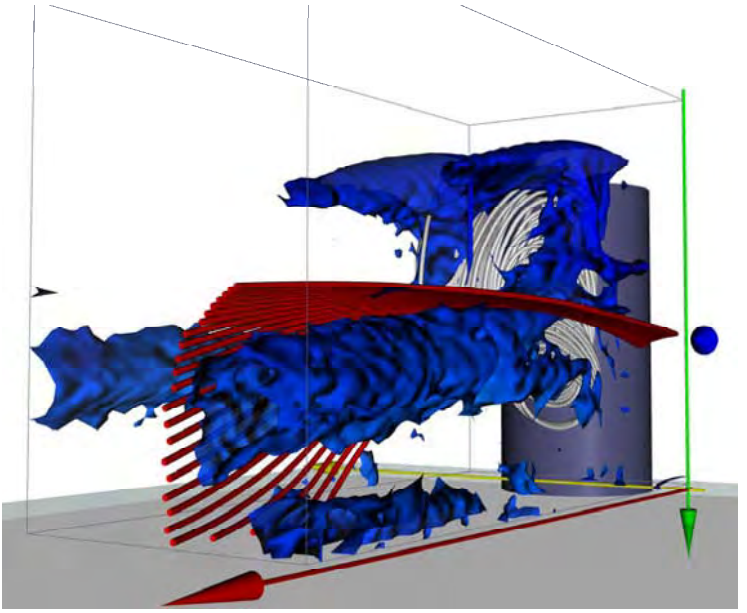

Fig. 3 Time averaged flow topology in the wake of finite circular cylinder

4 Spectral Analysis

Figure 4 illustrates the frequency versus the amplitude of the cross stream velocity fluctuation (v') over increasing x positions. The line is situated at y/D = -0.7 and z/D = -0.5. The dominant frequency is approx. 35 Hz which corresponds to a Strouhal number $Sr = f \frac{D}{U_\infty}$ of 0.16. This Strouhal number agree very well with measurements for one side bounded finite length cylinder [15], but is lower than values given in the literature of about Sr = 0.2 for circular cylinders between two plates [13]. Clearly the dominant frequency becomes more significant downstream and the spectral intensities have a maximum of 0.07 at x/D = 2. This point in the flow is located shortly downstream the recirculation arch vortex. The streamwise velocity fluctuation (u') shows the same dominant frequency and a similar spectrum. However the maximum of the spectral intensity is situated closer to the cylinder at x/D = 1.4 to x/D = 1.6 and with a value of about 0.082 a little bit higher. At the Position of x/D = 2 the spectral intensity at a frequency of 35 Hz is equal to that from the cross stream velocity v'. Furthermore the spectrum of the vertical velocity fluctuations (w') is not so pronounced like the others although 35 Hz is also the significant frequency. The spectral intensity is also increasing with increasing x position and has a maximum of 0.035 at x/D = 2 to x/D = 2.2.

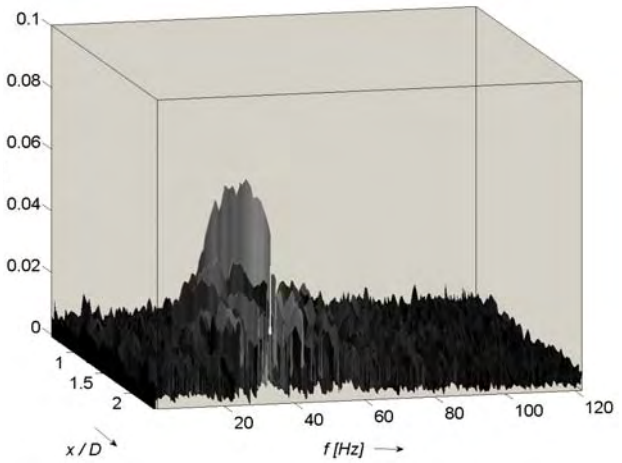

Fig. 4 Spectral analysis of the cross stream velocity component

5 Proper Orthogonal Decomposition

The starting point for the proper orthogonal decomposition is the snapshot ensemble $\mathbf{u}^m(\mathbf{x}) := \mathbf{u}(\mathbf{x}, t_m)$ of a velocity field $\{\mathbf{u}^m(\mathbf{x})\}_{m=1}^M$ at M discrete time steps

t_m. The key is to find an orthonormal system of modes $\{\mathbf{u}_i(\mathbf{x})\}_{i=0}^{N}$ $(N \le M)$ that describes the field with the Galerkin approximation

$$\mathbf{u}^{[N]}(\mathbf{x},t_m) \coloneqq \sum_{i=0}^{N} a_i(t_m)\mathbf{u}_i(\mathbf{x}) \tag{1}$$

in an energetic optimal sense, where $a_0 = 1$ and $\mathbf{u}_0 = \overline{\mathbf{u}}$ describe the time average flow. The two main elements in the POD snapshot method are the inner product of the velocity variation around the time average

$$(\mathrm{u}_i,\mathrm{v}_i)_\Omega \coloneqq \int_\Omega \mathrm{u}_i \mathrm{v}_i d\Omega \tag{2}$$

and the correlation matrix

$$C_{jm} = \frac{1}{M}\int_\Omega \mathbf{u}^j(\mathbf{x})\mathbf{u}^m(\mathbf{x})d\mathbf{x} \tag{3}$$

which comprises the second order structural information of the unsteady flow [14].

The plots tabulated in Figure 5 show the out-of-plane velocity component of the first POD mode at different TR-PIV measurement planes, starting at the tangential plane to the cylinder *y/D* = -0.5 down to *y/D* = -0.3. In each plane 2730 snapshots were used to calculate the POD. The left column shows the results obtained from POD, containing the maximum energy of the unsteady flow. It can be recognized, that the plane *y/D* = -0.5 (top left position) does not contain the same structures as the other planes (remainder of the left column). The reason for this is that every plane is decomposed on its own and the modes are sorted by the energy content of the measured plane and not of the entire velocity field volume of the wake. In this case a different mode is found with the maximum energy content. As a matter of fact in the decomposition here in the plane *y/D* = -0.5 a structure similar to that of mode number one in the adjacent plane *y/D* = -0.4 can be found in mode number two. Furthermore, the first POD modes calculated in the planes *y/D* = -0.4 and *y/D* = -0.3 look similar, but have the opposite sign because of their time coefficients.

For investigating the modes in space now the approach is made that parallel planes that contain the same coherent structures ought to share non orthogonal modes even if they do not have the same mode number or sign. For synchronizing the modes of parallel measurement planes a linear mapping is introduced between the modes of the vector velocity fields of two neighboring planes.

$$\mathbf{u}_i^1(\mathbf{x}) = C_{ij}^{1,2}\mathbf{u}_j^2(\mathbf{x}) \tag{4}$$

Where $\mathbf{u}_i^1(\mathbf{x})$ represents the calculated POD modes of one plane and $\mathbf{u}_j^2(\mathbf{x})$ the modes of the parallel neighboring plane. The operator C gives the degree of linearity between the different modes of both planes. On the one hand it is now possible to calculate the modes of plane one through convolution of C with the modes of plane two, or by convolving its inverse C^- with modes from field one

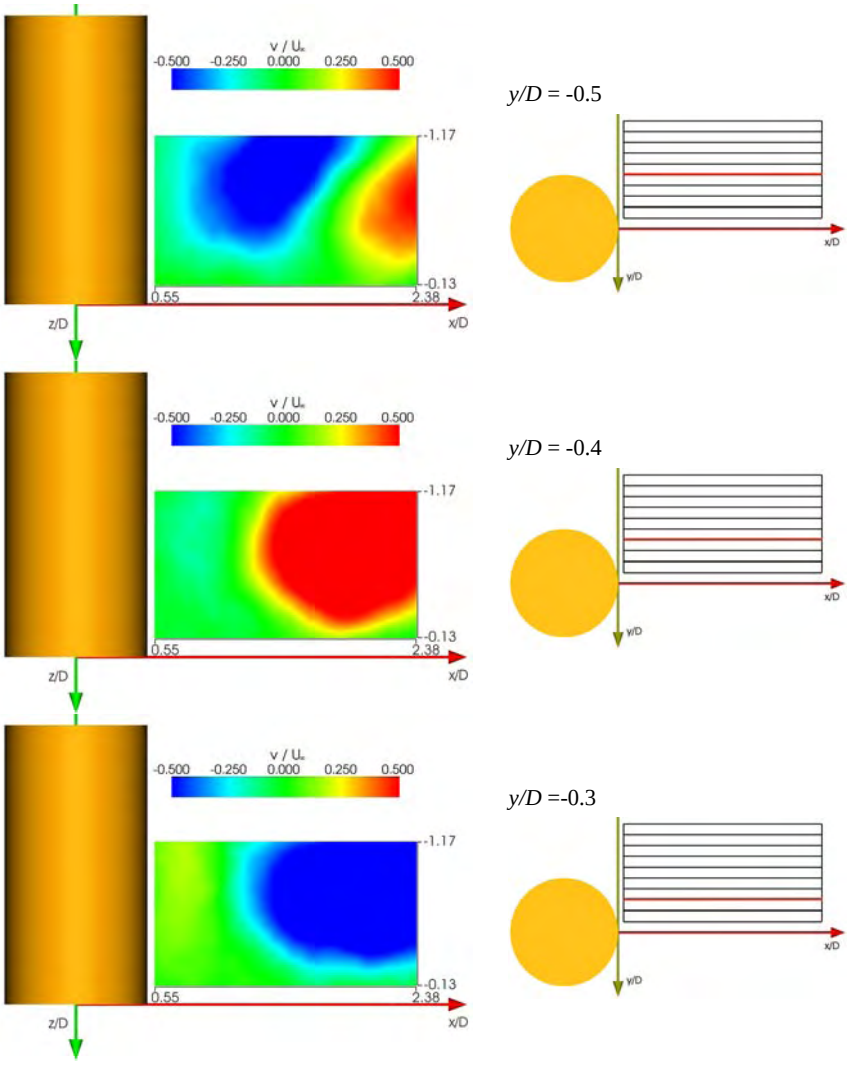

Fig. 5 Contour plot of the out-of-plane velocity component of the first POD mode before mapping (left) in different lateral planes (right)

giving the modes of plane two. On the other hand it is a filter which identifies the same structures in different planes even if they have a different mode number or sign. By analyzing the matrix elements of C, coherent modes and their sign can be identified.

Table 1 shows the rounded matrix elements of C obtained from the first six POD modes, which belong to the planes y/D = -0.3 and y/D = -0.4. A value of 1 denotes that in both planes the same structure exists with the same alignment, whereas

Table 1 Rounded coefficients *C* from plane y/D=-0.3, y/D=-0.4

	Mode number j →					
i ↓	-1	0	0	0	0	0
	0	-1	0	0	0	0
	0	0	0	0	-1	0
	0	0	0	-1	0	0
	0	0	0	0	0	1
	0	0	0	0	0	0

a value of -1 identifies the same structures with opposite alignment. This connection is pointed out by the first element in Table 1 and the corresponding contour plots in Figure 5 (left). Furthermore the element $C_{3,5}$ describes that mode 3 in plane y/D = -0.3 corresponds to mode 5 in plane y/D = -0.4. A value of zero implies no coherence.

Starting at a reference plane it is now possible to map the corresponding modes by filtering all planes. The resulting set of modes is not necessarily sorted by the energy content of each measured plane but sorted by the energy content of the reference plane.

The plots on the left side in Figure 6 depict the out-of-plane velocity component from the mapped first modes for different measured planes from y/D = -0.5 down to y/D = -0.3 with the reference plane chosen at y/D = -0.4. It is clear that the same structure is identified in all measured planes with the same alignment. Because of a very complex flow topology the method requires small distances between measured planes.

The plots tabulated in Figure 7 show the results from the mapped POD modes from the experimental PIV data connected to a 3D volume. The plots show isosurfaces representing a value of $u_i / U_\infty = \pm 0.3$ whereas red indicates positive and blue indicates negative values. Clearly the rearranged modes compose a smooth ensemble that allows the calculation of isosurfaces. A detailed comparison of these results to the numerical data was made in [5] and [11].

Because it is difficult to understand the physics of the flow by analyzing the POD-Modes, it is useful to recombine the time independent modes to a time dependent flow field. From this the problem arises that every decomposed plane implies its own Fourier coefficients. Additionally the coefficients are not very smooth. For this reason a phase averaging technique based on the Fourier coefficients was introduced. The Coefficients which represents the projection of the snapshots on the modes can be used to calculate a phase angle for every snapshot. Figure 8 demonstrate the principle connection.

After determining the phase angle for every snapshot an ensemble averaging on the recombined POD modes is possible. For this reason the method is a strong filter on the time dependence of a coherent structure. It is now possible to investigate

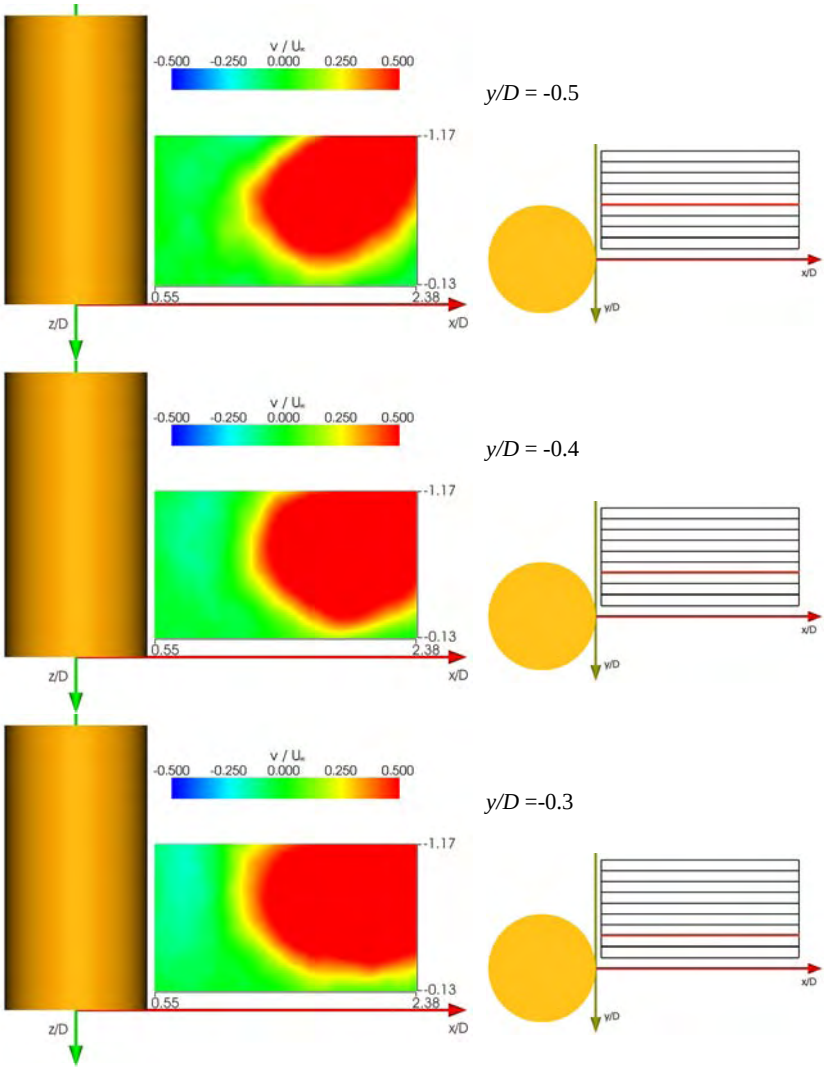

Fig. 6 Contour plot of the out-of-plane velocity component of the first POD mode after mapping (left) in different lateral planes (right)

the temporal behavior of one structure which is described by two POD modes. It should be noted that this method of structural averaging is particularly valuable because it works for time resolved data as well as for randomly sampled snapshots

Figure 9 illustrates the structure averaged results at phase angle φ (left) and a half period $\varphi+\pi$ later (right). The horizontal plane situated z/D = -0.8 represents a cut through several vertical measurement planes, which POD modes where

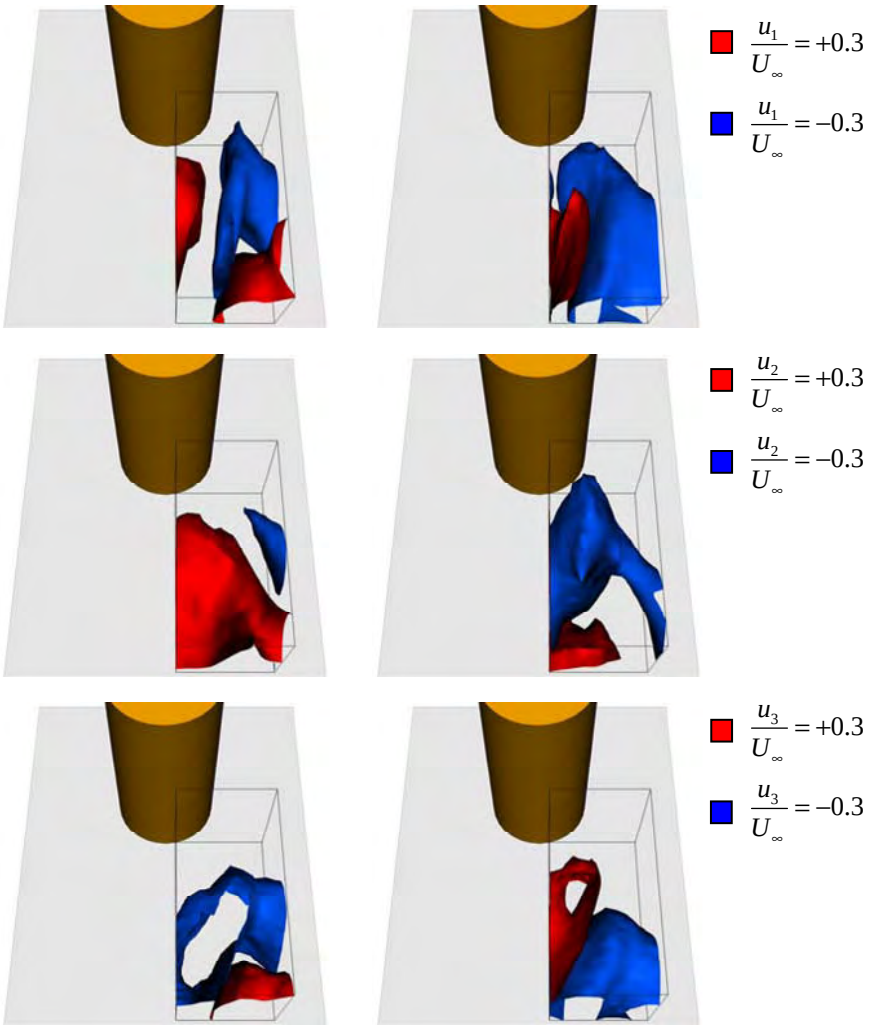

Fig. 7 First (column left) and second (column right) POD mode of the velocity vector components rearranged from TR-PIV data with incident Flow from the top

linear mapped. For phase averaging the first two Fourier coefficients where chosen, therefore the time dependence of the most energy containing structure in this area is presented. The in plane velocity components are given by vectors whereas the out-of-plane component is colored. On the side of the cylinder a periodical breakdown of the vertical velocity component towards the free end can be seen. Furthermore a vortex based on instability of the shear layer rolls up and swims down with a deformation of the vertical velocity component towards the endplate in the wake.

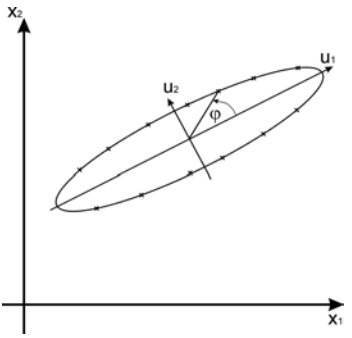

Fig. 8 Determining the phase angle from the Fourier Coefficients

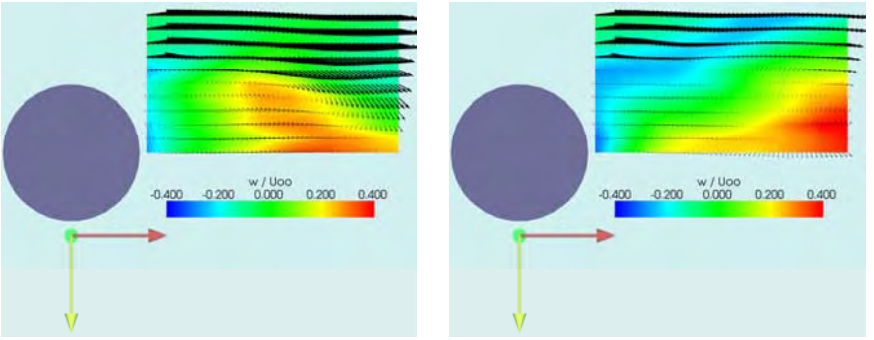

Fig. 9 Phase averaged flow field based on the first two time coefficients from POD at $t = \varphi$ (left) and $t = \varphi + \pi$ (right)

6 Conclusion and Outlook

We have performed 3C LDA and time resolved stereo PIV measurements in the wake, at the free end and at the base of the cylinder near the endplate. The time resolved stereo PIV measurements were arranged in vertical and horizontal planes. The topology of the time averaged flow was analysed and the results resemble the flow structure known previously from flow visualisation and LDA-experiments. Additionally, the proper orthogonal decomposition was applied to the TR-PIV results and linear mapping was introduced, which gives 3D three component POD modes to characterize the unsteady flow behaviour.

A comparison of the POD modes, based on the experiment, to the numerical data was successfully made, provided the same field of view was used. Furthermore, a phase averaging algorithm was applied on the rearranged volumetric POD modes to aid a better understanding of the temporal devolvement of the coherent structures. The combination of the linear mapping and the phase averaging technique was introduced as “structure averaging”. It is most useful because it can be applied to time resolved data as well as randomly sampled snapshots.

Ongoing measurements combining the unsteady surface pressure field and the time resolved velocity vector field have been performed and are currently under analysis.

Acknowledgments. The authors would like to express their gratitude for the financial support by the German Research Foundation (DFG) in the priority program 1147 “Imaging Measurement Methods for Flow Analysis”.

References

1. Frederich, O., Scouten, J., Luchtenburg, M., Thiele, F., Jensch, M., Hüttmann, F., Brede, M., Leder, A.: Joint numerical and experimental investigation of the flow around a finite wall-mounted cylinder at a Reynolds number of 200000. In: Proceedings of the ERCOFTAC International Symposium on Engineering Turbulence Modelling and Measurements, ETMM 7, pp. 517–522 (2008)
2. Frederich, O., Scouten, J., Luchtenburg, M., Thiele, F.: Numerical simulation and analysis of the flow around a wall-mounted finite cylinder. In: Nitsche, W., Dobriloff, C. (eds.) Imaging Measurement Methods for Flow Analysis. Springer, Berlin (2009)
3. Frederich, O., Wassen, E., Thiele, F.: Prediction of the flow around a short wall-mounted cylinder using LES and DES. Journal of Numerical Analysis, Industrial and Applied Mathematics (JNAIAM) 3(3–4), 231–247 (2008)
4. Jensch, M., Brede, M., Richter, F., Leder, A.: Verwendung des Time-Resolved Stereo-PIV Messsystems zur Ermittlung zeitaufgelöster Geschwindigkeitsfelder im Nachlauf eines Kreiszylinders. In: Dopheide, D., Müller, H., Strunck, V., Ruck, B., Leder, A. (Hrsg.) Lasermethoden in der Strömungsmesstechnik - 14. Fachtagung der GALA e.V. 2006, PTB Braunschweig, pp. 39.1–39.8 (2006) ISBN 3-9805613-3-X
5. Jensch, M., Brede, M., Leder, A., Frederich, O., Thiele, F.: Use of pod to visualize coherent structures from time resolved PIV data. In: Proceedings of the 14th International Symposium on Applied Laser Techniques to Fluid Mechanics, Lisbon, Portugal (2008)
6. Jeong, J., Hussain, F.: On the identification of a vortex. Journal of Fluid Mechanics 285, 69–94 (1995)
7. Leder, A.: 3D-flow structures behind truncated circular cylinders. In: Proceedings of FEDSM 2003, Fourth ASME-JSME Joint Fluids Engineering Conference, Honolulu, USA (2003)
8. Lumley, J.L.: The structure of inhomogeneous turbulent flows. In: Yaglom, Tatarski (eds.) Atmospheric Turbulence and Radio Wave Propagation (1967)
9. Loéve, M.: Probability Theory. Van Nostrand, Princeton (1995)
10. Karhunen, K.: Zur Spektraltheorie stochastischer Prozesse. Annaleas Academiae Scientiarum Fennicae 34 (1946)
11. Pattenden, R.J., Turnock, S.R., Zhang, X.: Measurement of the flow over a low-aspect-ratio cylinder mounted on a ground plate. Exp. Fluids 39, 10–21 (2005)
12. Richter, F., Leder, A.: Wirbelstrukturen und Kraftwirkungen am Kreiszylinderstumpf in Scherströmungen. In: Egbers, C., Jehring, L., von Larcher, T., Ruck, B., Leder, A., Dopheide, D. (eds.) Lasermethoden in der Strömungsmesstechnik - 13. Fachtagung der GALA e.V. 2005, GALA e.V., BTU Cottbus, pp. 23.1–23.9 (2005) ISBN 3-9805613-2-1
13. Roshko, A.: On the development of turbulent wakes from vortex streets. NACA Report 1191 (1954)
14. Sirovich, L.: Turbulence and the dynamic of coherent structures part 1-3. Quarterly of Applied Mathematics 45(3), 516–590 (1987)
15. Sumner, D., Heseltine, J., Dansereau, O.: Wake structure of a finite circular cylinder of small aspect ratio. Exp. Fluids 37, 720–730 (2004)

Surface Pressure and Wall Shear Stress Measurements on a Wall Mounted Cylinder

Christoph Dobriloff and Wolfgang Nitsche

Abstract. The paper reports on steady and unsteady surface pressure as well as mean and fluctuating wall shear stress measurements of high spatial resolution on and in the vicinity of a wall mounted finite circular cylinder with an height to diameter ratio of H/D=2. All measurements were performed at a Reynolds number of $Re_D=2\cdot10^5$ based on the cylinder diameter. The pressure measurements were conducted using a total of up to 179 simultaneously operated pressure tappings with piezoresistive pressure transducers. As a result, the complete instantaneous pressure distribution in the cylinder wake could be obtained. For the wall shear stress measurements, newly developed delta surface hot-wire probes, an enhancement of the standard surface hot-wire, were used. The probe design, its calibration procedure and the measuring principle are discussed as well.

1 Introduction

The experimental analysis of flow fields including the resulting wall forces and the comparison to numerical simulations is common standard in modern fluid mechanics research. For such comparative investigations within the priority programme *Imaging Measurement Methods for Flow Analysis* a finite wall mounted circular cylinder more accurately specified in the next section is used as a benchmark test configuration for a number of newly developed state-of-the-art imaging measurement techniques. However, as a reliable reference, measurements with well established conventional techniques are also used, namely measurements by means of laser Doppler anemometry (LDA) and time resolved particle image velocimetry (TR-PIV) for the flow field [9, 15], as well as measurements by means of pressure tappings and surface hot-wires for the surface forces, accordingly. The surface measurements and their results are thoroughly discussed within the next sections of this paper. Together with numerical simulations presented in [5] and [6] a complete dataset for further comparisons within the priority programme and future investigations is obtained.

Christoph Dobriloff · Wolfgang Nitsche
TU Berlin, Institute of Aeronautics and Astronautics, Marchstr. 12, 10587 Berlin, Germany
christoph.dobriloff@tu-berlin.de,
wolfgang.nitsche@tu-berlin.de

W. Nitsche and C. Dobriloff (Eds.): Imaging Measurement Methods, NNFM 106, pp. 197–206.
springerlink.com

2 Experimental Setup

For reasons of better comparability to results of the other projects within the priority programme, the general experimental setup follows a reference design, which consists of a vertical wall mounted cylinder with a height to diameter ratio of H/D=2. The end wall is a flat plate whose main dimensions are shown in Fig. 1. A trip wire of diameter d=0.4 mm behind the leading edge ensures a defined turbulent boundary layer across the whole base plate's surface. At the trailing edge, a spoiler swept downwards at an angle of α=8° is used to achieve a zero pressure gradient over the flat plate in clean configuration, i.e. with no cylinder present. For the measurements introduced here, the cylinder is mounted onto a turntable, which itself is flush mounted into the end wall. This allows for the use of a single line array of sensors on the cylinder and the turntable to cover the complete cylinder surface and the annular area around the cylinder for the measurements. Additionally, in the wake area of the cylinder the end wall is prepared for the use of several modular inserts which can be easily exchanged by differently instrumented ones. The inserts cover an area of up to five cylinder diameters downstream the cylinder and are also represented in Fig. 1.

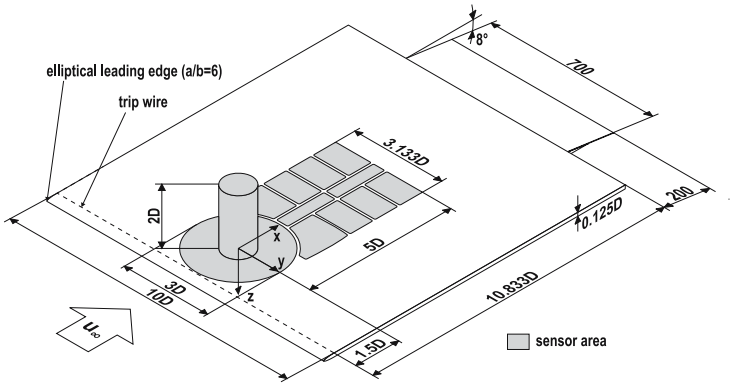

Fig. 1 Experimental setup (absolute values in mm, D=120 mm)

For all measurements, the entire assembly is mounted into the open test section of the closed-circuit low speed wind tunnel at the University of Rostock. Its nozzle cross-section is 0.65 m x 0.65 m and the test section is 1400 mm in length. A Reynolds number of $Re_D=2\cdot10^5$ based on the cylinder diameter is maintained during the measurements. At this Reynolds number, the flow around the cylinder starts to become critical, i.e. the region of laminar-turbulent transition within the cylinder boundary layer is approximately the same as the region at which flow separation occurs [20]. During all measurements the general flow parameters such as the free stream static and dynamic pressure as well as its temperature are continuously recorded.

2.1 Pressure Measurements

For the pressure measurements, a total of 179 pressure tappings is used, 63 of which are located on the cylinder and the turntable surface. The remaining tappings are located in the wake area of the cylinder. In Fig. 2, a detailed overview of the tapping positions is given. All tappings have a diameter of d=0.5 mm and are instrumented with piezoresistive miniature pressure transducers. Two kinds of transducers are used for the measurements. For all tappings within the end wall (including the turntable), Honeywell 24PCEFA6D transducers are used. With a height of only 8 mm, the sensors can be fully integrated into the end plate. For the tappings within the cylinder surface, Sensortechnics HCL12X5 transducers are used. Due to their even smaller size, all sensors can be placed within the cylinder directly behind each tapping. The integration of all sensors into the cylinder and the end wall permits the use of only very short plastic tubes for connecting the sensors to the tappings, thus, minimizing the damping behaviour of the tubes and actually enabling unsteady measurements at all.

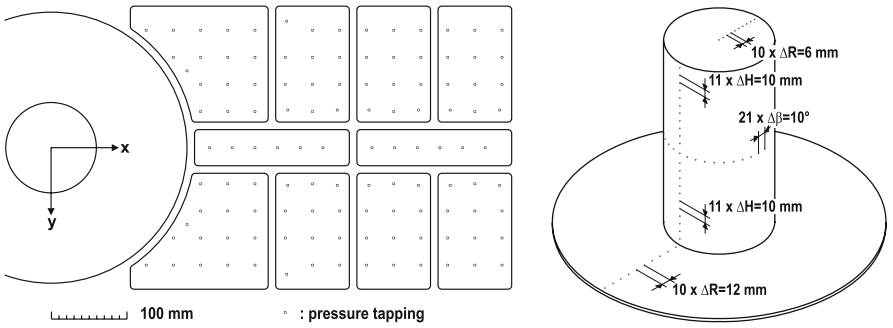

Fig. 2 Pressure tapping locations in the wake (left) and on cylinder and turntable (right)

All sensors are differential pressure transducers and are simultaneously calibrated directly before each measurement by connecting a KAL 84 static pressure calibrator to the interconnected reference pressure ports of all sensors. During the measurements, the free stream static pressure is used as reference pressure.

For the measurements, the transducer's output voltages are externally amplified by multi-channel low-noise operational amplifiers before being digitized by means of a 192-channel multiplexer connected to a Microstar DAP5400a data acquisition board with 8 A/D converters sampling with up to 1.25M samples per second each.

2.2 Wall Shear Stress Measurements

For the wall shear stress measurements, a new sensor design based on surface hot-wires was developed. The new sensor design is an enhancement of the standard surface hot-wire introduced in [18]. A first introduction of the enhanced sensor can be found in [19] and a slightly more comprehensive description in [4]. The

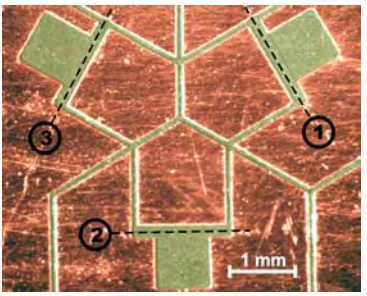

Fig. 3 Delta surface hot-wire probe

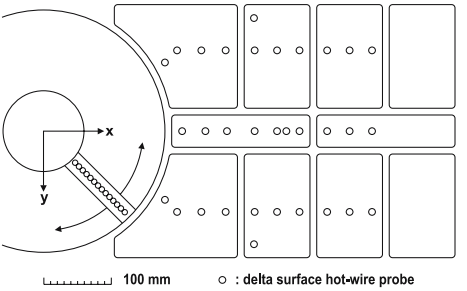

Fig. 4 Positions on the end wall

sensor is capable of determining the wall shear stress magnitude and direction at the same time. However, other than usual v-shaped surface hot-wires or hot-films, it is not limited to the range of about $\delta=\pm35°$ [11]. Instead, it can be used for arbitrary in-flow directions. This is achieved by combining three single surface hot-wires in a triangular arrangement, thus the name *delta probe*. The general layout is shown in Fig. 3. Herein, the hot-wires are highlighted as dashed lines. One important detail is the asymmetrical cavity beneath each wire, which is required to distinguish from which side of the wire the flow is approaching due to the different local flow condition within the cavity.

For measuring the wall shear stress distribution on the end wall, up to 32 individual delta probes are used to investigate the wake region of the cylinder, Fig. 4. Additionally, an array of 14 delta probes is used, which is flush mounted into a corresponding radial groove within the turntable, Fig. 4 and Fig. 5.

For the linear array, an in-situ calibration of all delta probes is done by exchanging the cylinder body by a highly sensitive flush mounted skin friction balance which directly measures the wall shear stress at the turntable centre. At different flow velocities, the turntable is then rotated in steps of $\Delta\varphi=5°$ while measuring the voltages of each surface hot-wire operated in constant temperature mode. Due to the turntable rotation, the delta probe positions are not fixed during the calibration. The probes therefore experience different wall shear stress levels than those measured with the skin friction balance, depending on whether the probe position lies up- or downstream relative to the balance position. This is compensated by a Reynolds number correction based on the distance of the balance and the probe to the

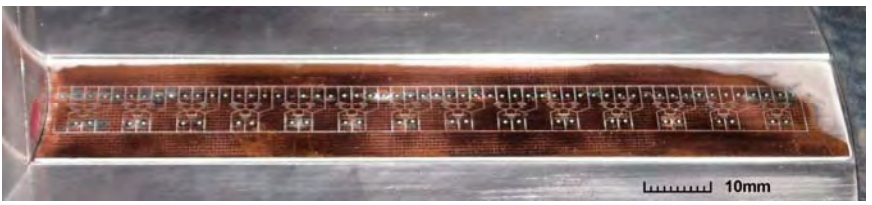

Fig. 5 Linear array of 14 delta surface hot-wire probes on the turntable

leading edge of the end wall. Two different boundary layer equations are used for the correction depending on whether the boundary layer flow is laminar (Blasius equation (1, left)), or turbulent (Prandtl equation (1, right), both from [17]), which can be influenced to some extent by or by not removing the trip wire during the calibration measurements. For the case of a transitional boundary layer over the turntable, no reliable correction can be done due to 3D-effects which are not accounted for in (1). However, the boundary layer condition itself (laminar/turbulent) can quite easily be checked by the measured surface hot-wire signal fluctuations [3]. In addition to that, preliminary hot-wire investigations showed the two-dimensionality of the boundary layer across the turntable, so no further correction in spanwise direction is necessary for the calibration.

$$c_{f,laminar} = \frac{0.664}{\sqrt{Re_x}} \qquad c_{f,turbulent} = \frac{0.0592}{\sqrt[5]{Re_x}} \tag{1}$$

For the individual delta probes used in the cylinder wake, a specific calibration setup is used, which is based on the same principle as for the linear array, however, here the probes are at fixed positions at the same x-coordinate like the skin friction balance and thus do not need to be Reynolds number corrected.

After the calibration, a surface is fitted through the measured voltages for each single hot-wire, as seen in Fig. 6. For an actual measurement, the hot-wire voltage is looked up in the calibration surface for each wire and results in a curve corresponding to the possible combinations of wall shear stress magnitudes and directions. Under the assumption that all three surface hot-wires of a delta probe are exposed to the same wall shear stress vector at the same time, this vector is obtained by searching the point of intersection between all three curves, Fig. 7. However, due to the overall sensor size, highly fluctuating smallest flow structures, e.g. in the size of only a few viscous or Kolmogorov scales, usually can not be resolved this way because the above assumption does not apply anymore. In fact, for an unsteady analysis, the signals have to be low-pass filtered such that only fluctuations with wavelengths above the sensor size are accounted for.

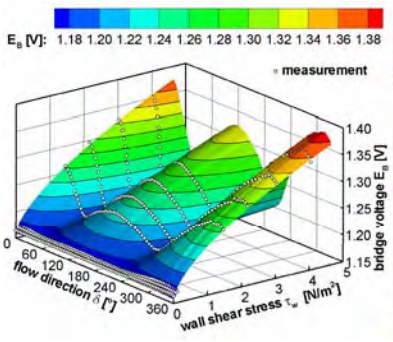

Fig. 6 Calibration surface

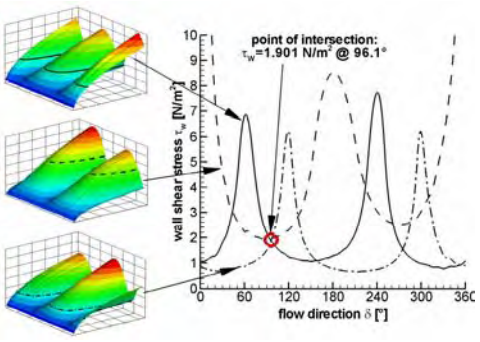

Fig. 7 Wall shear stress vector identification

During the calibration and the following measurements, all hot-wire voltages are temperature corrected using equation (2) (from [3]). Additional to the delta probes on the end wall a vertical linear array of 24 equidistant and vertically oriented standard surface hot-wires after [18] is applied to the cylinder wall to measure the wall shear stress fluctuations.

$$E_{eff}^2 = E_{meas}^2 \cdot \frac{T_{sensor} - T_{ref}}{T_{sensor} - T_{fluid}} \tag{2}$$

3 Results

Fig. 8 and Fig. 9 show the mean and fluctuating pressure distribution on the cylinder surface and the end wall. Typical flow structures of cylinder flows can be recognized. The stagnation region on the cylinder is characterized by pressure coefficients slightly below c_p=1. Due to the accelerating flow around the cylinder, the pressure decreases with minimum pressure coefficients of $c_{p,min}$=-0.53 to -0.74 at cylinder angles of φ=63° to 68° from the cylinder bottom to the top. Further downstream the flow separates at cylinder angles between φ=72° to 80° depending on the cylinder height. However, the region with positive pressure gradient is also the region with the highest fluctuations on the cylinder. These are especially high at the bottom caused by the interactions with the horseshoe vortex and the turbulent boundary layer of the end wall. Under consideration of partially different Reynolds numbers or cylinder aspect ratios, the results are in good agreement with measurements reported in [10, 12, 13, 14, 21] and with numerical simulations introduced in [5]. The cylinder top is characterised by two symmetrical regions of low pressure coefficients at about x/D=-0.15 corresponding to two vortex centres constraining a separation bubble on the free end and by a reattachment region at x/D>0.2 as also shown in [7, 10, 14, 16].

The cylinder flow is dominated by the alternating wake vortices whose time averaged footprints can be seen in Fig. 8 by the symmetrical low pressure region

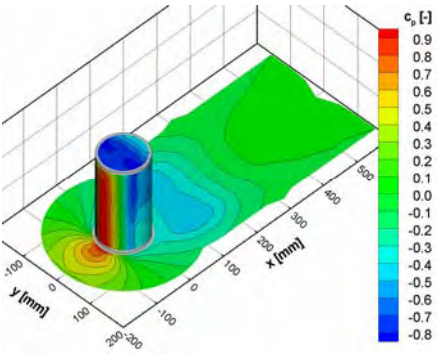

Fig. 8 Time averaged pressure distribution

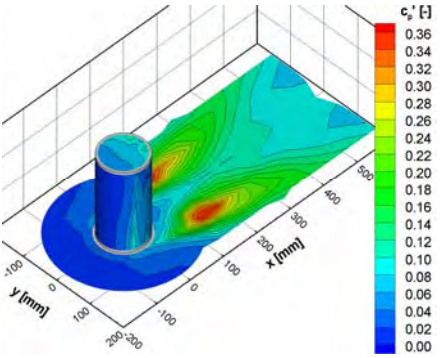

Fig. 9 Pressure standard deviation

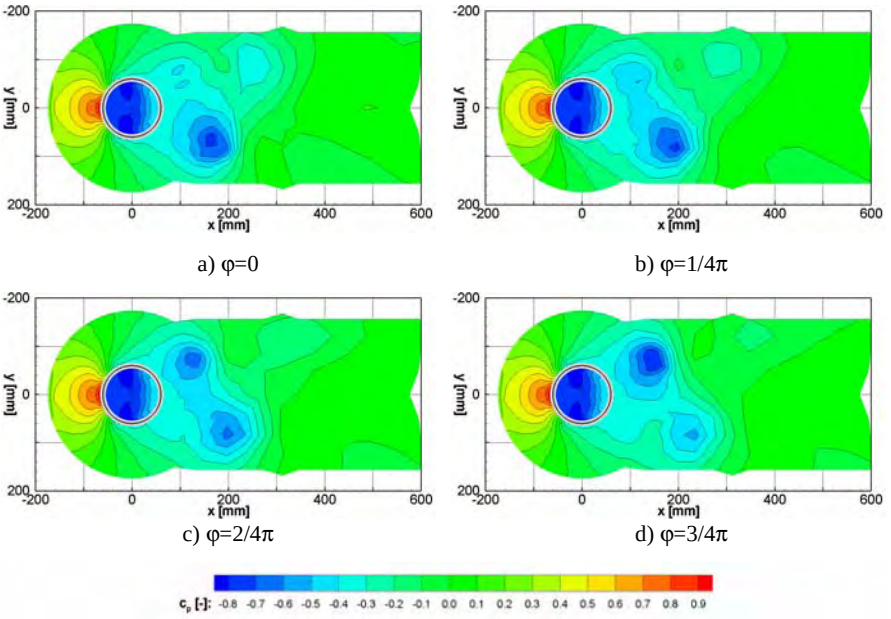

Fig. 10 a-d) Phase averaged pressure distribution on the end wall and the cylinder top for one half-cycle at four different phase-angles φ

behind the cylinder. In Fig. 9, the influence of the wake vortices can clearly be seen by the fluctuations, which are highest at a radius of about R=1.5D and quickly decrease with increasing distance to the cylinder. At about x/D=3, the vortices are drifting apart to the sides of the wake area, which is mainly caused by the downwash of the flow over the free end of the cylinder [1, 2, 8, 10]. The wake vortex formation and development can be seen in the phase averaged results shown in Fig. 10. a) to d), which are obtained using the pressure tapping positioned at x/D=1.5 and y/D=0.85 as reference. However, the vortex shedding is not as periodic as it might seem from Fig. 10. For instance, in Fig. 11 two series of consecutive snapshots of the pressure distribution in the cylinder wake are presented, which show the simultaneous formation of a vortex on both sides of the cylinder (a), and the formation of two weak vortices on the same side without one on the other side in between (b).

The time averaged results of the wall shear stress measurements on the turntable and the wake area are shown in Fig. 12 and illustrate the general flow topology including the horseshoe vortex formation, the wall shear stress increase due to the flow acceleration around the cylinder and a separation with the resulting shear layers. On the right side of Fig. 12, the wall shear stress distribution is compared to an oil flow visualization obtained from the same experimental setup and under the same boundary conditions. For a wide range, both are in very good agreement. However, the region of the flow over the cylinder top hitting the end wall can also be seen at about x/D=3 (x=360mm). Due to the highly unsteady character of the

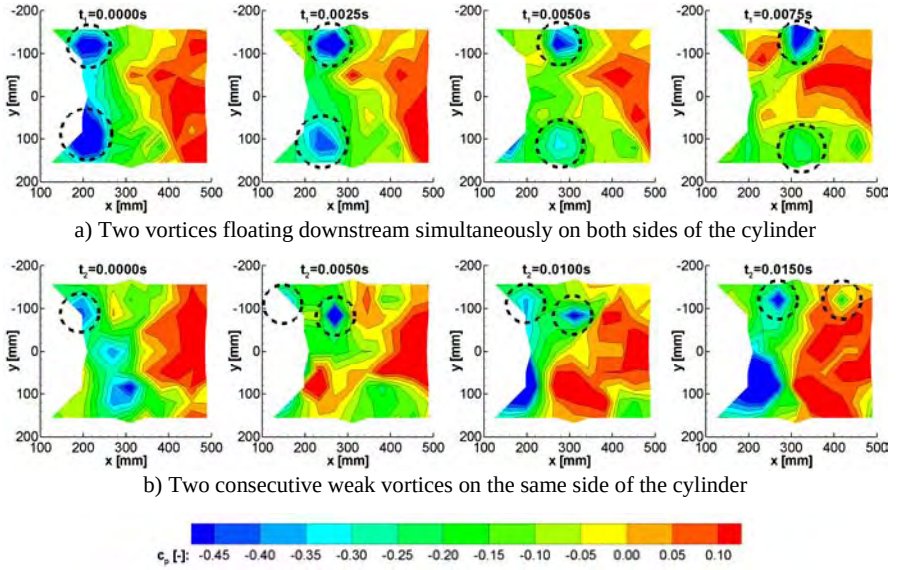

a) Two vortices floating downstream simultaneously on both sides of the cylinder

b) Two consecutive weak vortices on the same side of the cylinder

Fig. 11 Two time series of the unsteady pressure distribution in the cylinder wake

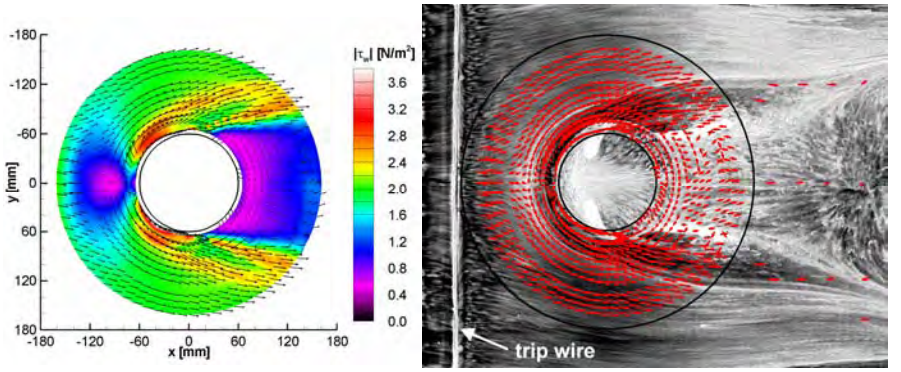

Fig. 12 Time averaged wall shear stress distribution (left) and comparison to oil flow visualization (right, the black circles represent the cylinder and turntable diameters)

flow, no preferred wall shear stress direction can be determined out of the time averaged hot-wire signals here, which is also the case for the near wake region directly behind the cylinder.

Results of the surface hot-wire measurements on the cylinder wall are presented in Fig. 13. In the left part, due to the lack of a wall shear stress calibration, the normalized voltages and their fluctuations are shown. Separately for each sensor the signals are linearly normalized such that the minimum voltage is set to 0 while

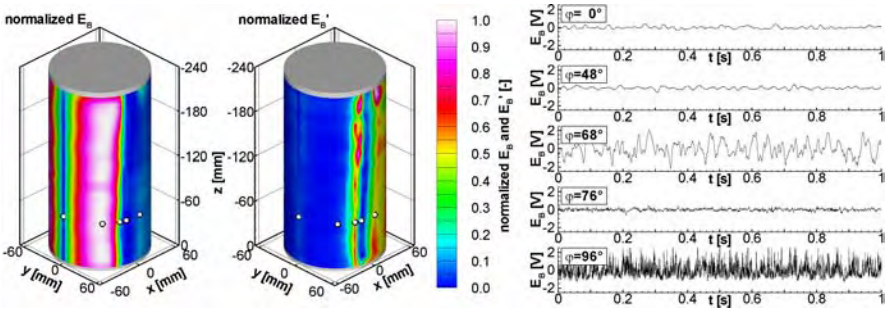

Fig. 13 Mean and fluctuating normalized surface hot-wire voltages on the cylinder (left) and selected time series of the fluctuating component of the signals (amplified) at z/D=0.53 (right)

the maximum is set to 1. Several phenomena exemplarily highlighted by five points of interest at z/D=0.53 can be seen. For each position, a time series of the bridge voltage fluctuations is plotted on the right side of Fig. 13. At φ=0° the stagnation line is identified by a very low wall shear stress and low fluctuations. At φ=48° the maximum wall shear stress due to flow acceleration is reached with still very low fluctuations, thus the boundary layer is completely laminar. Slightly downstream the wall shear stress decreases rapidly with the highest negative gradient and high fluctuations at φ=68°. However, the fluctuations are quite smooth and low in frequency and are not caused by boundary layer transition but by the unsteady behaviour of the separation line. A calm zone at φ=78° is observed, both, with a low overall wall shear stress and low fluctuations. Finally, at higher angles far within the separation, the turbulent boundary layer and the unsteady wake flow cause high fluctuations at a relatively low wall shear stress level.

4 Conclusion

Surface pressure and wall shear stress measurements were successfully conducted on a finite wall mounted circular cylinder and on the end wall in the vicinity and the wake of the cylinder by means of conventional and well established measurement techniques. Under consideration of partly different boundary conditions like the cylinder aspect ratio or the Reynolds number, the results are in very good agreement with many other measurements referenced in this paper. Together with the TR-PIV flow field measurements [9] and the numerical simulations [6] a complete dataset for further comparative investigations was generated.

Acknowledgments. The work was conducted within the framework of the priority programme 1147, *Imaging Measurement Methods for Flow Analysis*, funded by the German Research Foundation (DFG), whose financial support is highly appreciated.

References

1. Agui, J.H., Andreopoulos, J.: Experimental investigation of a three-dimensional boundary layer flow in the vicinity of an upright wall mounted cylinder. J. Fluids Eng. 114, 566–576 (1992)
2. Baban, F., So, R.M.C., Ötügen, M.V.: Unsteady forces on circular cylinders in a cross-flow. Exp. Fluids 7, 293–302 (1989)
3. Bruun, H.H.: Hot-Wire Anemometry. Oxford University Press Inc., New York (1995)
4. Dobriloff, C., Nitsche, W.: Delta surface hot-wires as a means of measuring wall shear stresses at arbitrary flow directions. In: Proceedings of the 22nd International Congress of Theoretical and Applied Mechanics, Adelaide, Australia, August 25-29 (2008) (CD-ROM)
5. Frederich, O., Wassen, E., Thiele, F.: Prediction of the flow around a short wall-mounted finite cylinder using LES and DES. JNAIAM 3(3–4), 231–247 (2008)
6. Frederich, O., Scouten, J., Luchtenburg, M., Thiele, F.: Numerical simulation and analysis of the flow around a wall-mounted finite cylinder. In: Nitsche, W., Dobriloff, C. (eds.) Imaging Measurement Methods for Flow Analysis. Springer, Berlin (2009)
7. Hain, R., Kähler, C.J., Michaelis, D.: Tomographic and time resolved PIV measurements on a finite cylinder mounted on a flat plate. Exp. Fluids 45(4), 715–724 (2008)
8. Hölscher, N., Niemann, H.J.: Turbulence and separation induced pressure fluctuations an a finite cylinder - application of a linear unsteady strip-theory. J. Wind Eng. Ind. Aerodyn. 65, 335–346 (1996)
9. Jensch, M., Hüttmann, F., Brede, M., Leder, A.: Optical measurements in the wake of a circular cylinder of finite length at a high Reynoldsnumber. In: Nitsche, W., Dobriloff, C. (eds.) Imaging Measurement Methods for Flow Analysis. Springer, Berlin (2009)
10. Kawamura, T., Hiwada, M., Hibino, T., Mabuchi, I., Kumad, M.: Flow around a Finite Circular Cylinder on a Flat Plate. B JSME 27(232), 2142–2151 (1984)
11. Nitsche, W., Brunn, A.: Strömungsmesstechnik. Springer, Berlin (2006)
12. Okamoto, S., Sunabashiri, Y.: Vortex shedding from a circular cylinder of finite length placed on a ground plane. J. Fluids Eng. 114, 512–521 (1992)
13. Okamoto, T., Yagita, M.: The experimental investigation on the flow past a circular cylinder of finite length placed normal to the plane surface in a uniform stream. B JSME 16(95), 805–814 (1973)
14. Pattenden, R.J., Turnock, S.R., Zhang, X.: Measurements of the flow over a low-aspect-ratio cylinder mounted on a ground plane. Exp. Fluids 39, 10–21 (2005)
15. Richter, F.: Experimentelle Untersuchungen zur Charakterisierung der Strömungs- und Turbulenzstrukturen im Nachlauf eines Kreiszylinderstumpfes unter Berücksichtigung der Zentrifugalbeschleunigung. PhD thesis, University of Rostock, Germany (2005) ISBN 3-86582-167-7
16. Roh, S.C., Park, S.O.: Vortical flow over the free end surface of a finite circular cylinder mounted on a flat plate. Exp. Fluids 34, 63–67 (2003)
17. Schlichting, H.: Boundary-Layer Theory. McGraw-Hill, New York (1979)
18. Sturzebecher, D., Anders, S., Nitsche, W.: The surface hot wire as a means of measuring mean and fluctuating wall shear stress. Exp. Fluids 31, 294–301 (2001)
19. Wolter, A., Berns, A., Dobriloff, C., Leder, A., Obermeier, E., Nitsche, W.: Surface measurement techniques for flow analysis on the Rostock Leitexperiment. Lasermethoden in der Strömungsmesstechnik 15, 21.1–21.10 (2007)
20. Zdravkovich, M.M.: Flow Around Circular Cylinders. Fundamentals, vol. I. Oxford University Press Inc., New York (1997)
21. Zdravkovich, M.M.: Flow Around Circular Cylinders. Applications, vol. II. Oxford University Press Inc., New York (2003)

Numerical Simulation and Analysis of the Flow Around a Wall-Mounted Finite Cylinder

Octavian Frederich, Jon Scouten, Dirk M. Luchtenburg, and Frank Thiele

Abstract. Numerical studies employing LES and DES are presented for the flow around a wall-mounted finite cylinder at a Reynolds number of $Re_D = 200,000$. Very good agreement between the numerical and experimental results is achieved for the steady mean motion, turbulence quantities and the motion of large coherent structures. The synergy between the joint studies within the research unit "Imaging Measurement Methods for Flow Analysis" and the application of POD, particle and structure tracking algorithms allow for a more complete description of the unsteady flow investigated. New insight to the coherent turbulent motion is obtained.

To investigate the flow field around the cylinder configuration several state-of-the-art technologies for simulation have been applied. The quality of the flow predictions and the resolved physics therein are examined employing both original and recent established post-processing methods.

1 Background and Objectives

The finite circular cylinder represents a very simple geometry, the flow around which is however highly complex, with three-dimensional and unsteady physical features typically observed. Especially for small aspect ratios, the flow regime rarely exhibits the typical vortex pattern of infinite cylinders, with the exception of alternate vortex shedding relicts in the lower half of the cylinder. Such flows featuring boundary layer separation, shear layer instability and the subsequent formation of complex vortices are typical for many technical applications. The detailed investigation of such a representative configuration (Fig. 1) with an aspect ratio of $L/D = 2$ at $\mathrm{Re}_D = 200,000$ benefits the understanding of mixing processes and the turbulent motion responsible for increased drag, noise or structural vibrations.

Octavian Frederich · Jon Scouten · Dirk M. Luchtenburg · Frank Thiele
Berlin Institute of Technology, Institute of Fluid Mechanics and Engineering Acoustics, Müller-Breslau-Str. 8, 10623 Berlin, Germany
octavian.frederich@tu-berlin.de

W. Nitsche and C. Dobriloff (Eds.): Imaging Measurement Methods, NNFM 106, pp. 207–216.
springerlink.com

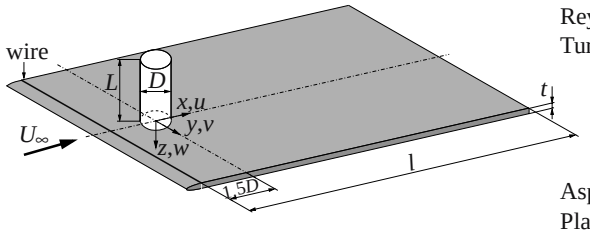

Reynolds number $\mathrm{Re}_D = 200,000$
Turbulence level $\mathrm{Tu} = 0.5\%$

Aspect ratio $L/D = 2$
Plate length $l/D = 10.83$

Fig. 1 Configuration investigated

The main objectives of the present investigation are the detailed cross-validation of the experiment with the simulation, and the analysis of both steady and unsteady physics giving a clear image of the flow dynamics. Therefore an extensive comparison of experimental and numerical results has been performed. Furthermore, established and self-developed examination methods have been applied in order to reduce the highly-resolved unsteady flow field to the relevant information content.

The results presented summarise the project state in the national German research unit "Imaging Measurement Methods for Flow Analysis" funded by the German Research Foundation (DFG). Thus, a short history of the numerical project is first given before the methods are described and selected results are presented. Finally, conclusions are drawn and the perspectives of the numerical database are shortly summarised. A comprehensive documentation of all investigations performed and the results obtained will be given in [6].

2 Approach and Project History

The numerical analysis of the highly-resolved spatio-temporal flow field around the finite cylinder configuration and the expected flow regime requires a numerical approach that is able to resolve turbulence at least partially. Because a Direct Numerical Simulation is not affordable for the present Reynolds number, Large-Eddy Simulation (LES) and the more recent Detached-Eddy Simulation (DES) are the most promising approaches. The application of different methodologies allows the examination of the predictive quality of these, whereas the combination of measurements and numerics provides a database for the validation and improvement of such numerical methods. In this context the simulations are able to deliver correlated surface and volume quantities and to identify regions of interest for additional measurements. Regarding the respective limitations of the numerical and experimental approaches (e.g. insufficient physical simulation time) such combined investigations allow a deepened understanding of flow phenomena and their interaction.

The work has been subdivided into three phases with various work packages. The first period comprises the complete pre-processing (discretisation, generation of boundary conditions, identification of influencing parameters, etc.), the first highly-resolved simulations as well as initial comparison with experiments. In the second

phase the time-averaging of the simulations, the examination of additional quantities, the investigation of model assumptions and detailed visualisations have been performed. The current third phase is used to analyse long physical time intervals, extract dynamic features of the flow and to compare the complementary experiments and numerics in-depth.

3 Numerical Setup and Methods

Based on precursor simulations with coarse discretisation the domain has been sized and the flow field has been highly resolved spatially. A block-structured grid with 12.3 million points employing hanging nodes close to the cylinder and in the wake was generated for this [2]. The adjusted temporal resolution uses a timestep of $\Delta t = 0.005 D/U_\infty$ determined by the grid spacing and the maximum local velocity. Using this discretisation, LES with the standard Smagorinsky subgrid scale model and $C_S = 0.1$ as well as DES with the LLR k-ω background model were performed. In the case of LES no wall modelling is employed, whereas for DES a hybrid adaptive boundary condition has been used, which allows seamless blending between high and low-Re formulations depending on the near wall resolution [10]. All simulations are carried out with the flow solver ELAN developed at the TU Berlin. This code uses a conservative finite-volume discretisation based on general curvilinear coordinates of the Navier-Stokes equations for compressible and incompressible flows and is of second order accuracy in time and space [14].

In order to simulate physical time intervals comparable to experimental measurements, which are of the order of seconds, the spatio-temporal resolution has had to be reduced considerably. This is realised by removing the local hanging-node refinement and adjusting the timestep to $\Delta t = 0.015 D/U_\infty$. To overcome the problem of log-layer mismatch when resolving the outer boundary layer fluctuations with LES, the very recent approach Improved Delayed DES (ID-DES, [12]) with the SA-E background model has been employed. This method extends the standard-DES with a capability for wall-modelled LES (WM-LES) and is able to resolve boundary layer fluctuations [9]. In addition, when using DES it is necessary to account for the expected laminar boundary layer separation explicitly, which has been carried out employing the trip-less approach proposed in [11]. This method is simply a two-stage simulation switching from a fully turbulent inlet to a quasi laminar thereby deactivating the turbulence production term in the attached boundary layer.

The dynamics of the flow are investigated using Proper Orthogonal Decomposition (POD, [8]), particle and coherent structure tracking (CST). The particle tracking is performed using an embedded Runge-Kutta-Fehlberg integration scheme with 4th-order accuracy and velocities taken from cubic interpolation in space and time. For the structure tracking, Lagrange-averaged velocity fields are used (described in [4]). The advantage of this approach is that it uses the Lagrangian velocity field itself to perform the smoothing away of small scales dynamically, while preserving coherent motion at the larger scales. Finally, a harmonic filtering approach has been applied to the predicted time series of the flow field utilising a two-step POD

procedure proposed by the authors of [13] as Temporal-Harmonic specific POD mode extraction (TH-POD).

4 Selected Results and Findings

A selection of highlight results from the numerical investigations are summarised in the following. The comparison with the accompanying experiments is included to validate the results obtained. For a more in-depth method description and detailed analyses the reader is referred to the relevant publications.

4.1 Time-Averaged Flow Topology

A detailed analysis of the time-averaged flow field predicted with LES has been used to provide a model of the flow topology [2]. A sketch of this steady flow topology, which is valid for both the experiments and numerics due to the very good agreement between these (see Sect. 4.2), is shown in Fig. 2.

The plate boundary layer impinges on the upstream cylinder face giving rise to a horseshoe vortex. On the cylinder top a complex recirculation region is surrounded by the oblique separation at the leading edge and the reattachment close to the trailing edge. Following the separation at around 80° on the cylinder shell, typical alternating vortex shedding occurs, which is however disturbed strongly by the flow over the free end. A recirculation arch vortex is formed by the combination of these phenomena and thus the main flow reattaches to the plate. Trailing vortices are generated near this reattachment region by superimposed velocity components. The analysis reveals that for this small aspect ratio no coherent longitudinal vortices exist throughout the whole wake, as typically stated in most investigations on finite cylinders [2].

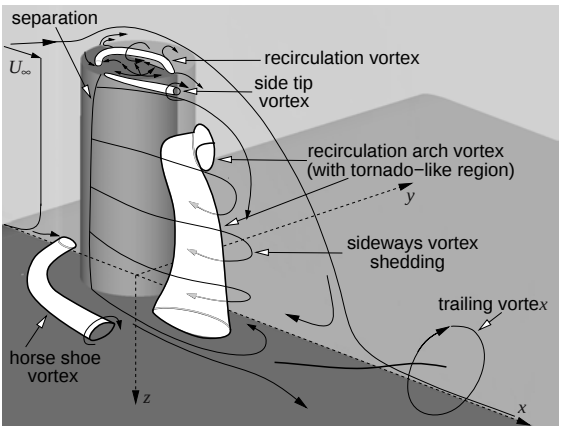

Fig. 2 Sketch of the time-averaged flow topology (first published in [2])

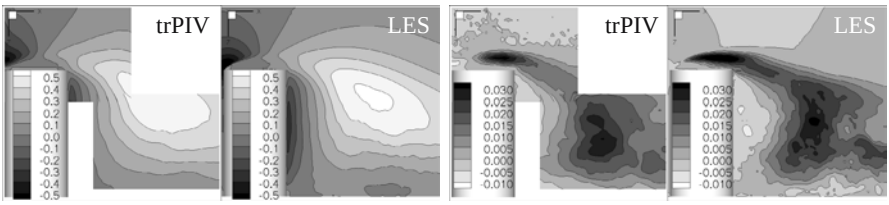

Fig. 3 Time-averaged vertical velocity $\overline{w}$ (left) and double correlation $\overline{u'w'}$ (right) for trPIV and LES in the plane $y/D = -0.1$

4.2 Comparison to Experiments and Different Approaches

The comparison of time-resolved PIV experiments (trPIV, [7]) and numerical results for the time-averaged flow reveals a very good agreement. The vertical velocity component $\overline{w}$ and the double correlation $\overline{u'w'}$ depicted in Fig. 3 outside of the symmetry plane demonstrate that this agreement is both qualitative and quantitative, although there are some common problems in the experiment close to the solid walls. Differences visible in the double correlation $\overline{u'w'}$ are attributed to the considerably higher spatial resolution of the numerical grid and slightly different inflow conditions. Further cross-comparisons and detailed validations between experiments and numerics including surface quantities have been published jointly in [2, 4] and [1].

The flow field has been predicted employing several turbulence approaches. LES and DES have been performed using the highly resolved discretisation, whereas the steady RANS and ID-DES used the reduced resolution. As reported in [5] LES provides an excellent reference solution and the DES encounters problems with laminar boundary layer treatment. Due to the artificial production of eddy viscosity in the laminar region the flow separates too late and thus the wake is too small for DES, although the flow characteristics are comparable to LES.

The steady RANS results have been obtained as initialisation for the ID-DES. With respect to the computational resources required the velocity field obtained would be acceptable in an industrial environment, while the resolved turbulent field is inaccessible to RANS. The ID-DES clearly represents an eligible compromise between loss of resolved physics and the resources required for long physical time intervals. At this stage this approach could not yet be finally judged, because the averaging is still in progress. The time-averaged velocity fields and RMS values depicted in Fig. 4 summarise the discussed findings.

4.3 Proper Orthogonal Decomposition - POD

POD offers a framework for the time correlation of experimental data gathered in different planes, simultaneously allowing for the extraction of the unsteady flow topology. The decomposition has been carried out on the time series obtained by LES (3d, [3]) as well as on planar datasets of time-resolved PIV (trPIV [7]) and

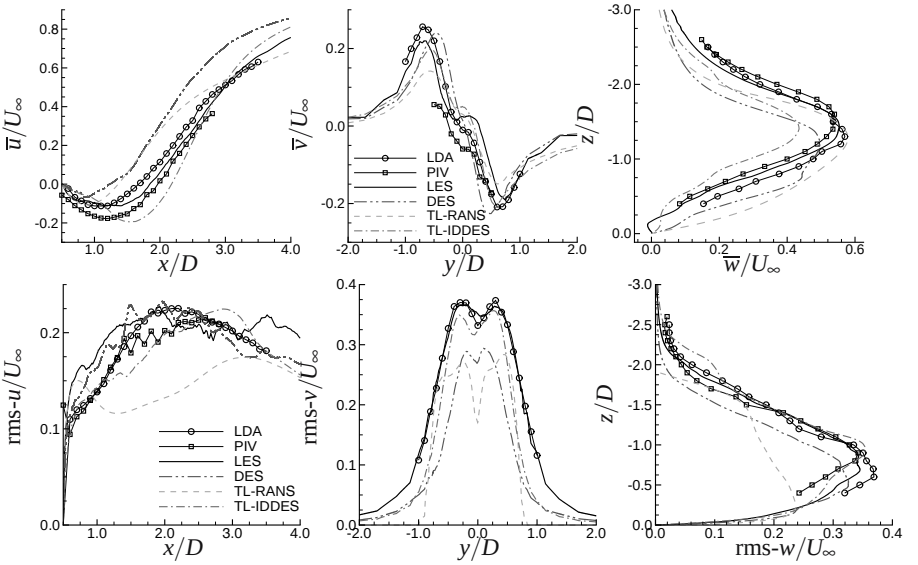

Fig. 4 Time-averaged velocities and RMS-values in different wake lines: y=0, z/D=−1 (left); x/D=2.2, z/D=−1 (middle); x/D=2.2, y=0 (right)

LES in the symmetry plane (2d3c). The databases available for POD comprise 2000 timesteps for trPIV covering 2.0 s and 2750 snapshots for LES within 0.32 s.

The dominant POD mode pair $(1,2)$ for the three-dimensional case is presented in Fig. 5 using isosurfaces of constant velocity components u, v, w. All components reveal travelling wave character, in which the combination of u and v describes typical alternate vortex shedding behind the cylinder swinging slightly up and down, described by the w component. These dynamics corresponds to a Strouhal number of St = 0.16 (cf. Fig. 6), which is the dominant frequency present in the flow field. Because the basic POD is not able to separate frequencies, a strict decomposition of frequencies is only found for the dominant mode pair. Despite this, further spatial modes have been associated to physical phenomena present in the flow field [3].

The POD results obtained from experimental and numerical databases in the symmetry plane agree well with each other with respect to mode shape, mode order and

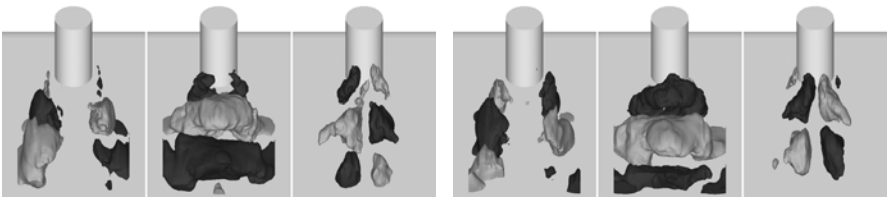

Fig. 5 Isosurfaces $u_i = \pm 0.18 U_\infty$ (light +, dark −) representing 3d POD modes 1 (left), 2 (right)

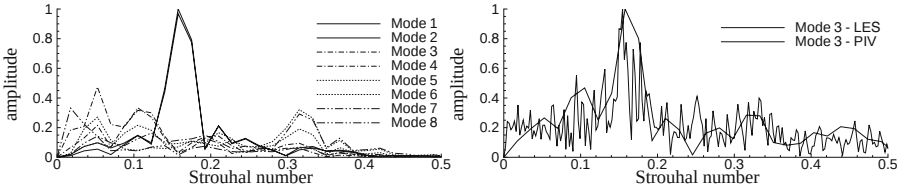

Fig. 6 Spectra of time coefficients: 3d POD (left); 2d3c POD of mode 3 for trPIV and LES (right)

time coefficients, as depicted in Fig. 6 (right) and Fig. 7. Both visualisations clearly demonstrate, that resolution of a POD frequency spectrum is easier for the experiment (Fig. 6) due to disk space limitations in the case of highly-resolved numerics, whereas the numerical results simply provide correlated information in an extensive domain not accessible by experiments (Fig. 7). This makes evident the necessity of a joint study.

4.4 Particle and Structure Tracking

A method used for studying the flow dynamics is particle tracking, where not only Lagrangian properties can be obtained but also turbulent motion can be visualised using streaklines and trajectories. In Fig. 8 (left) an exemplary streakline is shown revealing the instability of the separated shear layer. Moreover, the streakline changes the side of the cylinder it passes, an effect which happens periodically with the dominant frequency. The further turbulent spreading of the fluid is at least recognisable by the incoherently-distributed particles. The particle on the single trajectory shown in Fig. 8 (right) separates from the shell, evolves in a shear layer and enters the swirling region moving towards the plate. Due to recirculation it is moved upstream back to the cylinder and reattaches running upwards behind separation. After reaching the recirculation on the top, the particle moves downstream again on a spiral path reentering the recirculation, where close to the plate it is ejected after chaotic movement, becoming part of a trailing vortex (cf. Fig. 2).

The basic structure tracking method employed yields information about the spatial and temporal extent of individual vortex structures and their pathline with associated volume and convected velocity. The volumetric centroids of the structures found with the CST algorithm describe the structures' pathlines, shown in

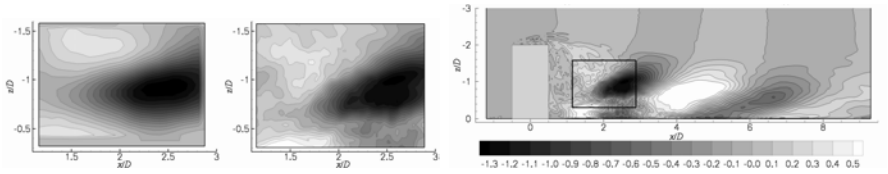

Fig. 7 Lateral velocity v_2 of 2d3c POD mode 2 for trPIV (left) and LES (middle and right)

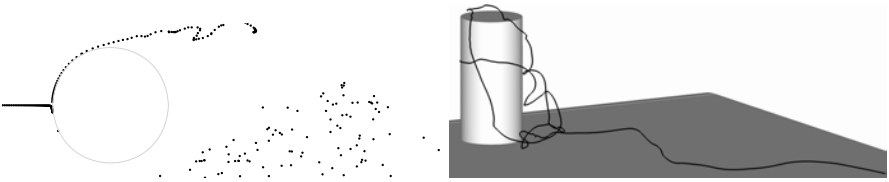

Fig. 8 Particles started at $(\text{-}1,0,\text{-}1)$: after a tracking time of 7 convective units D/U_∞ (left); single trajectory (right)

Fig. 9 (left). The longer-lived structures tend to be closer to the plate or farther behind the cylinder, whereas the shorter-lived ones are spread evenly throughout the domain. Examples of tracked structures in their temporal development are depicted in Fig. 9 (right) showing a tip vortex and a longitudinal vortex separating from the side of the cylinder.

The results obtained reveal that coherent structures can be tracked well by the CST method, whereas some sub-steps of the approach may fail in a highly turbulent region (details in [4]). Some improvement is however considered to be possible.

4.5 Harmonic Filtering

The POD approximation is statistically energetically optimal and not geared for and not optimised to extract modes based on their significance to the underlying system dynamics. Due to the association with temporal harmonics, the TH-POD method enforces physically meaningful modes and accommodates time variations in the harmonic frequency [13]. In a first step, the filtering has been performed using the varying harmonic determined by the phase angle of the dominant POD mode pair $(1,2)$. In Fig. 10 the first four TH-POD modes representing some of the decomposed most energetic structures with respect to the dominant harmonic are shown. The new dominant mode pair $(1,2)$ changes only slightly compared to this of the basic POD (cf. Fig. 5), and the modes 3, 4 are primarily constructed from the modes 5, 6 of the

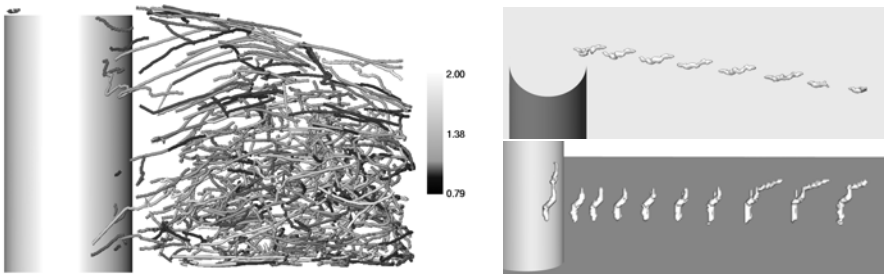

Fig. 9 Results of coherent structure tracking: structure paths coloured with lifetime w.r.t. D/U_∞ (left); tracked structures in successive timesteps with artificially magnified distance (right)

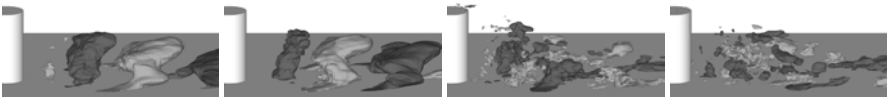

Fig. 10 First four TH-POD modes (left to right) of the filtered flow field represented by isosurfaces of the lateral velocity $v = \pm 0.18 U_\infty$ (light $+$, dark $-$)

unfiltered POD and characterise a higher harmonic. These and the further TH-POD modes generally form a non-orthogonal base. The reconstruction of the filtered flow field and the filtering with different signals (e.g. further frequencies or side force) are conducted presently.

5 Synthesis

The instantaneous vortex structures are much more complicated and detailed than could be represented by the averaged flow (Fig. 2). Thus, the aim is to provide a time-dependent topological model for the flow dynamics. Therefore the innumerable vortical structures resolved by LES must be clustered with respect to similar properties or reduced to the most relevant for a particular topology. The findings obtained so far justify optimism that a combination of all the methods presented (POD, CST, TH-POD, etc.) will lead to a detailed understanding of the flow in question.

The numerical simulations have been performed using several approaches of different complexity. While LES provides a reference solution, ID-DES in combination with coarsened resolution and an appropriate separation / transition treatment allows the investigation of long physical time intervals with acceptable quality.

This study comprises a constructive collaboration between numerics and experiment for a complex flow and delivers new insight on how to exploit this combined flow modelling effort. The numerical and experimental methods have been cross-validated and the flow statistics and the mode decomposition corroborate well.

6 Perspectives of the Numerical Database

The spatio-temporal flow field with correlated quantities has been provided to multiple concurrent projects focused on measurements, visualisation and image analysis. These cooperations have already resulted in a number of joint and project-specific publications (summarised by [6]) and further ones are planned. A combined numerical and experimental testcase database is intended to provide the potential for validation and development of numerical and experimental methods.

Acknowledgements. The work presented is supported by the German Research Foundation (DFG) within the research unit “Imaging Measurement Methods for Flow Analysis”. All

simulations were performed on the IBM pSeries 690 supercomputer of the North German Cooperation for High-Performance Computing (HLRN). We thank both organisations cordially for their support.

References

1. Berns, A., Buder, U., Obermeier, E., Wolter, A., Leder, A., Frederich, O., Thiele, F.: Aero-Micro-Electromechanical System Sensor Arrays for Time Resolved Wall Pressure Measurements. AIAA Journal (2008) (to be published)
2. Frederich, O., Wassen, E., Thiele, F., Jensch, M., Brede, M., Hüttmann, F., Leder, A.: Numerical simulation of the flow around a finite cylinder with ground plate in comparison to experimental measurements. In: Tropea, C., et al. (eds.) Notes Numer. Fluid Mech. Multidiscip. Des., vol. 96, pp. 348–355 (2007)
3. Frederich, O., Scouten, J., Luchtenburg, M., Thiele, F.: Database variation and structure identification via POD of the flow around a wall-mounted finite cylinder. In: Proc. BBVIV 5 (2007)
4. Frederich, O., Scouten, J., Luchtenburg, M., Thiele, F., Jensch, M., Hüttmann, F., Brede, M., Leder, A.: Joint numerical and experimental investigation of the flow around a finite wall-mounted cylinder at a Reynolds number of 200000. In: Proc. ETMM 7 (2008)
5. Frederich, O., Wassen, E., Thiele, F.: Prediction of the flow around a short wall-mounted cylinder using LES and DES. JNAIAM 3(3-4), 231–247 (2008)
6. Frederich, O.: Simulation und Analyse turbulenter Strömungen am Beispiel der Umströmung eines Zylinderstumpfes mit Endscheibe. PhD thesis, TU Berlin (under preparation) (2009)
7. Jensch, M., Brede, M., Leder, A., Frederich, O., Thiele, F.: Use of pod to visualize coherent structures from time resolved PIV data. In: Proc. 14th LxLaser (2008)
8. Lumley, J.L.: Stochastic Tools in Turbulence. Academic Press, New York (1970)
9. Mockett, C., Greschner, B., Knacke, T., Perrin, R., Yan, J., Thiele, F.: Demonstration of improved DES methods for generic and industrial applications. In: Peng, S.H., Haase, W. (eds.) Notes Numer. Fluid Mech. Multidiscip. Des., vol. 97, pp. 222–231 (2008)
10. Rung, T., Lübcke, H., Thiele, F.: Universal wall-boundary conditions for turbulence-transport models. ZAMM 81(1), 1756–1758 (2000)
11. Shur, M., Spalart, P., Strelets, M., Travin, A.: Navier-Stokes simulation of shedding turbulent flow past a circular cylinder and a cylinder with backward splitter plate. In: Désidéri, J.A., et al. (eds.) Computational Fluid Dynamics 1996, pp. 676–682 (1996)
12. Shur, M., Spalart, P., Strelets, M., Travin, A.: A hybrid RANS-LES approach with delayed DES and wall-modeled LES capabilities. J. Heat Fluid Flow 29(6), 1638–1649 (2008)
13. Tadmor, G., Bissex, D., Noack, B.R., Morzyński, M., Colonius, T., Taira, K.: Temporal-Harmonic specific POD mode extraction. AIAA Paper 2008-4190 (2008)
14. Xue, L.: Entwicklung eines effizienten parallelen Lösungsalgorithmus zur dreidimensionalen Simulation komplexer turbulenter Strömungen. PhD thesis, TU Berlin (1998)

Measurement of Distributed Unsteady Surface Pressures by Means of Piezoelectric Copolymer Coating

Jan Domhardt, Inken Peltzer, and Wolfgang Nitsche

Abstract. This paper describes applications of a newly developed pressure measurement technique, which is based on Pressure Sensitive Copolymer Coating. PSC provides a bridge between surface measurement methods with pressure-sensitive liquid crystal polymers (PSP) and conventional sensor technologies, e.g. arrays of pressure transducers or MEMS pressure sensors. It combines the advantages of both methods: measurements with a high spatial resolution and optimised model integration as well as high temporal resolution due to the active capacitive measuring principle.

The set-up and the application of linear and planar as well as flat and curved PSC coatings are described below. Investigations of the flow around and in the wake of a wall-mounted cylinder yielded results with a high spatial and temporal resolution, which are presented in this paper.

1 Introduction

Investigating complex unsteady flows requires surface measurement techniques providing a high temporal and spatial resolution. The direct measurement of surface forces using pressure transducers or MEMS sensor arrays is constrained, particularly in terms of the installation on curved surfaces and the spatial resolution. Indirect measurement techniques, such as surface hot-wire arrays or surface hot-films, are therefore generally used to obtain the required surface information.

The newly developed pressure-sensitive copolymer coating technique is based on the same physical principle as PVDF foils, so that the expertise derived from measurements with these foils can be applied. In the past, foil-sensors were successfully used for unsteady pressure measurements on moderately two-dimensionally curved structures in experiments carried out both in wind tunnels

Jan Domhardt · Inken Peltzer · Wolfgang Nitsche
TU-Berlin, Institut für Luft- und Raumfahrt, Marchstr. 12, 10587 Berlin
jan.domhardt@ilr.tu-berlin.de

W. Nitsche and C. Dobriloff (Eds.): Imaging Measurement Methods, NNFM 106, pp. 217–226.
springerlink.com

[1] and in free flight [2]. Dynamic calibrations by means of wall-integrated microphones and investigations of the piezoelectrical material properties were also successfully accomplished using PVDF-foil sensors [3, 6].

PSC was already introduced as a new surface measurement technique by Domhardt et al. [4]. With this method, the linear correlation between the mechanical pressure and the electric voltage, caused by the piezoelectric effect, is established by calibration measurements (Fig. 1(b)).

The aim of the first funding period for this project, was to investigate the capabilities of the PSC-technology by developing close-mesh, planar PSC coatings. Subsequently, calibration and wind tunnel experiments were carried out to gain insights into important design parameters for the instrumentation of the cylinder for the reference experiment with curved PSC areas. In addition to the assembly of the PSC inserts for the reference experiment, the existing multi-channel measurement system was extended, implementing spatial data acquisition and -analysis for the wind tunnel experiments. Sequential measurements of the reference experiment‘s cylinder with PSC line segments concluded the first funding period.

During the second funding period, the cylinder‘s surface and the wake region were equipped with further PSC areas. These PSC areas, made up of close-mesh sensing elements, allowed for surface measurements with a high temporal and spatial resolution, thus providing further insights into the flow topology of the reference experiment.

2 Measuring Principle of the PSC Technique

The basic element of PSC is the initially dissolved copolymer polyvinyliden fluoride-trifluoroethylene (PVDF-TrFE) that hardens in a multi-stage tempering process after it is sprayed onto a surface. Subsequently, the coating obtains ferroelectrical properties by concentrated treatment with a high voltage corona. This orients the polymer chains at the sensing elements in such a way that fluoride and hydrogen ions in the coating are rearranged to form a dipole moment [5].

The copolymer coating exploits the direct piezoelectric effect and responds to a mechanical displacement perpendicular to its surface, e.g. mean pressure fluctuations $p‘$ with a local charge displacement Q that can be amplified and detected. The charge displacement depends on the material-related piezo electric constant d_{33} and the area A of the sensing element.

$$Q = d_{33} \cdot p‘ \cdot A \tag{1}$$

Corresponding to the piezo-capacitive measuring principle of PSC, the surface to be investigated has to be equipped with sensing elements suitable for the measuring problem in hand. For this purpose, a pattern of capacitor electrodes is applied to the surface, which is subsequently sprayed with a 20μm PSC coating. Finally, the whole surface of the PSC coating is metallised with a 200nm metal layer, which acts as a counter electrode and electric mass shielding. Additional protection against

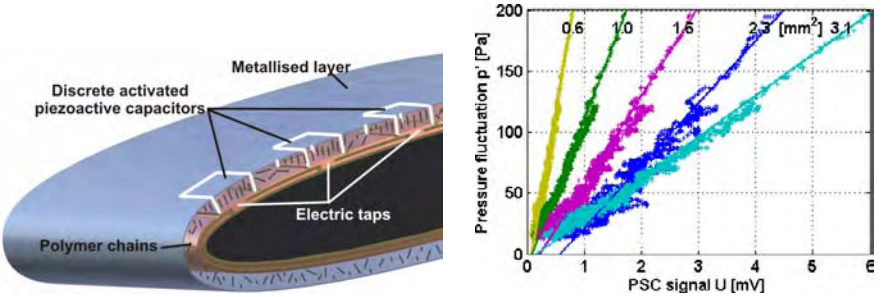

Fig. 1 Sketch of PSC's measuring set-up (a) and calibration results (b)

electromagnetic noise is provided by a further copper layer between the electric taps and the surface (Fig. 1(a)).

For the reference experiment measurements, the PSC areas were designed as a four-layer copper circuit board, to enable short signal paths between the signal amplifier and the electric taps. The charge amplification involved interchangeable 24 channel amplifiers with a lower threshold frequency of $f_u = 1.6Hz$ integrated into the PSC inserts. The measurements were carried out using a multi-channel system with a high temporal resolution, capable of scanning 320 channels simultaneously with a 14bit resolution and a sampling rate of 10 mega samples per second.

3 Flow Measurements Around a Wall-Mounted Cylinder

Within the framework of the DFG priority programme "Imaging measurement methods for flow analysis", a wall-mounted cylinder was defined as a reference experimental set-up. A number of research units applied their respective measurement techniques to the cylinder arrangements and could hence compare their results, e.g. [7, 8, 9].

3.1 Experimental Set-Up

The reference experimental set-up is represented by a short wall-mounted cylinder exposed to a transverse incident flow. The sharp-edged cylinder has a diameter of $D = 120mm$ and a height to diameter ratio of $H/D = 2$. The flat ground plate has the following dimensions: length $L = 10.8\overline{3} \cdot D$, width $W = 5.8\overline{3} \cdot D$ and thickness $T = 0.125 \cdot D$. The elliptical leading edge of the flat plate ends at a distance of $x = -1.5 \cdot D$ upstream of the cylinder's midpoint. The laminar-turbulent transition of the boundary layer is fixed in this position by means of a thin wire ($\varnothing\ 0.00\overline{3} \cdot D$). The diameter-related Reynolds number of $Re_D = 2 \cdot 10^5$ represents a flow condition where the laminar-turbulent transition in the free shear layer coincides with the

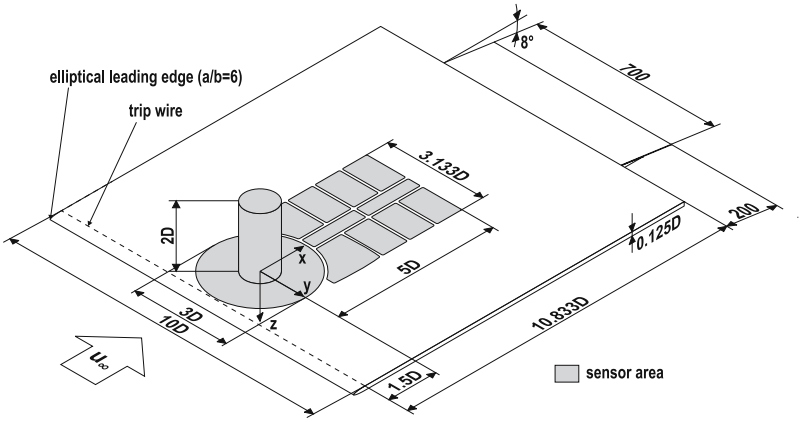

Fig. 2 Definition of experimental set-up

separation at the cylinder's circumference and results in an incident flow velocity of $u_\infty = 26.0 m/s$.

Furthermore, the project partners involved defined reference points at the cylinder's circumference and cap as well as in the wake region, which allowed a direct comparison of several measuring methods on the basis of time signals. For a comparison of planar measurements, the various groups participating in the project also coordinated their investigations on the distribution of sensors at the cylinder's circumference.

In the experiments presented in this paper, the cylinder was mounted on a turntable ($\varnothing\, 3 \cdot D$). The cylinder, the turntable and the wake inserts were exchangeable (Fig. 4). This set-up permits simultaneous measurements using measuring techniques designed by the associated working groups. The PSC inserts are flush mounted onto the surface of the test set-up, containing the exchangeable multi-channel charge amplifiers. To permit measurements with variable incident flow directions, circular sensing elements were used [2]. Based on preliminary investigations, the diameter of the various sensing areas was defined as $\varnothing\, 0.0125 \cdot D$ ensuring sufficient sensitivity [4, 10].

3.2 Phase-Averaged Measurements

As a first step, the flow around a wall-mounted cylinder was investigated by means of linearly arranged PSC arrays. To achieve a spatial measurement, the arrays were sequentially turned in steps of 4° and the results were phase-corrected afterwards by means of a low-pass filtered signal of a hot-wire in the wake of the cylinder.

The measurements in the near-wake region of the cylinder were performed by means of a revolvable radial PSC array consisting of 24 sensing elements. The image sequence in Fig. 3(a)-3(c) shows the appearance and the propagation of the

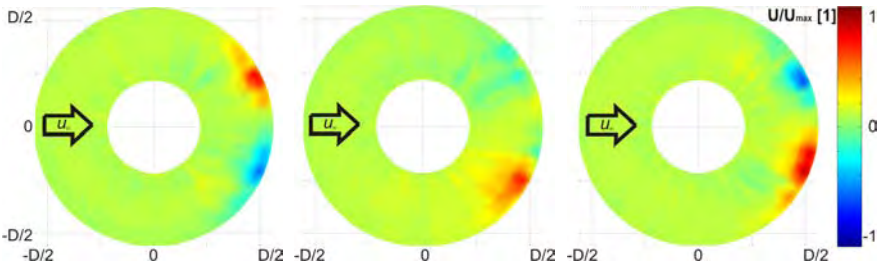

(a) $\phi = 0°$ (b) $\phi = 90°$ (c) $\phi = 180°$

Fig. 3 Phase-averaged and normalised PSC data at the turntable, $(Re_D = 2 \cdot 10^5)$

characteristic alternating vortex centres in the cylinder's wake. The normalised time signal U/U_{max} is displayed here at selected significant phase angles ϕ.

3.3 Investigations with High Spatial and Temporal Resolution

3.3.1 Measurements at the Cylinder's Circumference

For the investigation of the cylinder's circumference, an array of 288 extensively distributed PSC elements was used. A region of $\alpha = 120°$ was fitted with PSC elements staggered at $\alpha = 10°$ radially and $\Delta_z = 10mm$ vertically. In addition, radially staggered PSC line segments were placed at the height of $z = -0.06 \cdot D$, $z = -1 \cdot D$ and $z = -1.97 \cdot D$ over a range of $\alpha = 200°$. In the middle section, a PSC array with a close-mesh sensing matrix of $\alpha = 5°$ and $\Delta_z = 10mm$, distributed over five vertical rows is located (Fig. 4(a)).

In the incident flow region of the cylinder, the colours in Fig. 5(a) depict low normalised RMS values, indicating an attached laminar flow. In the wake region, the signal amplitudes increase strongly, signifying the separated flow. The intermediate range from attached to separated flow is clearly visible at $\alpha \leq 90°$. This result

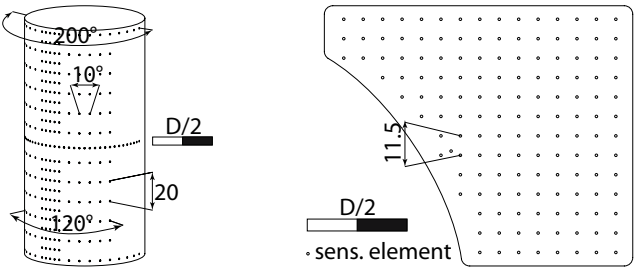

(a) (b)

Fig. 4 Distribution of sensing elements on the cylinder surface (a) and wake insert (b)

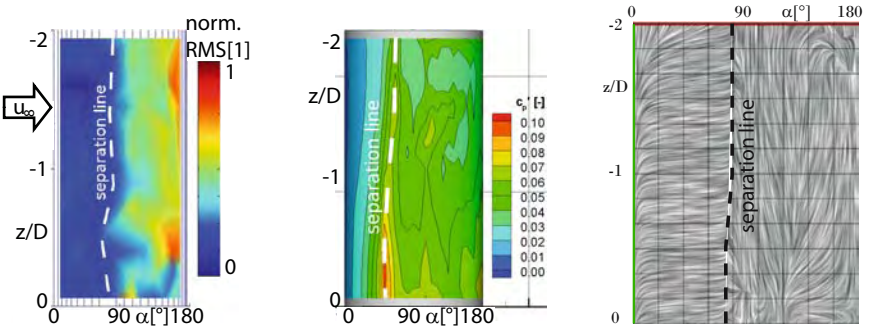

Fig. 5 Location of the separation line in measurement ($Re_D = 2 \cdot 10^5$) (a) PSC, (b) conv. pressure transducers and (c) CFD simulation (LES, time-averaged [11])

corresponds to reference pressure investigations (Fig. 5(b)[1]) and CFD simulation results (large eddy simulation [11], Fig. 5(c)). Both methods also indicate that the separation line is curved against the flow direction in the bottom region.

The results obtained show that the flow around a wall-mounted finite cylinder is highly unsteady. For the presentation of the unsteady data, a comb filter was used as part of the signal evaluation unit sequentially averaging the data over a range of $t = 0.1s$. This range, which was rather large compared to the sampling rate of $f = 4kHz$, are attributable to the frequency spectra (Fig. 6), where low frequencies occur at $f \leq 10Hz$.

Furthermore, the frequency spectrum allows a clear distinction between attached flow ($\alpha = 5°, 40°, 75°$) and separated flow ($\alpha = 95° - 180°$). A broadband increase in the spectra can also be observed in the transition region from attached to separated flow ($\alpha = 80° - 85°$), though with significantly lower amplitudes.

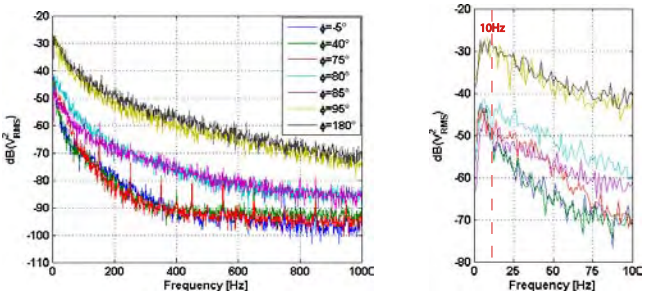

Fig. 6 Frequency spectrum at z=-D (a) and detail (b) ($Re_D = 2 \cdot 10^5$)

[1] The reference investigation displayed in Fig. 5(b) was performed by means of conventional pressure transducers by C. Dobriloff (SPP1147-sub-project "NI 282/16").

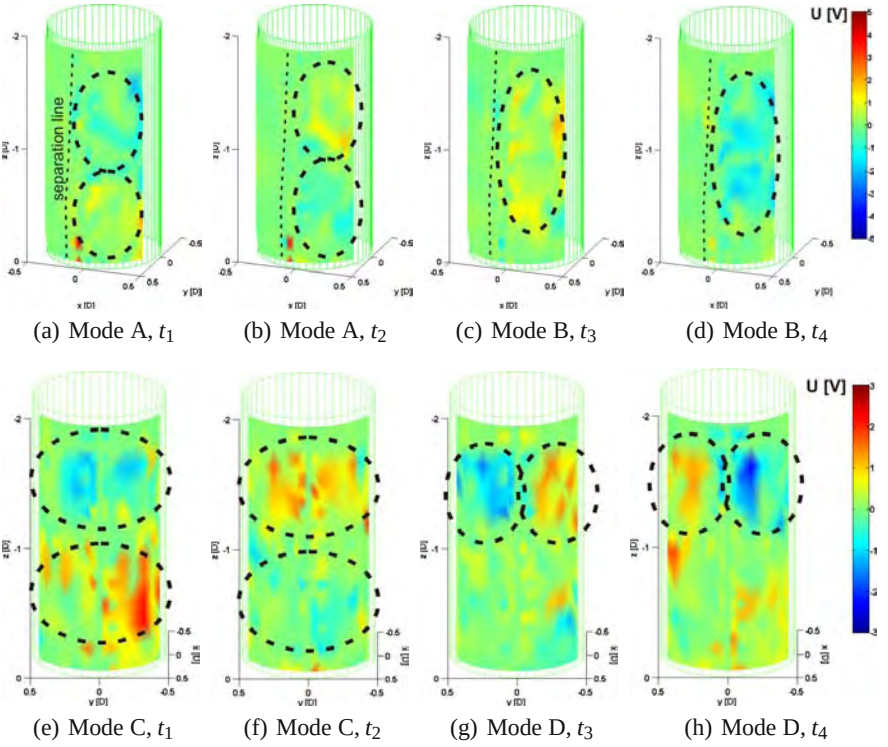

(a) Mode A, t_1 (b) Mode A, t_2 (c) Mode B, t_3 (d) Mode B, t_4

(e) Mode C, t_1 (f) Mode C, t_2 (g) Mode D, t_3 (h) Mode D, t_4

Fig. 7 Footprints of coherent structures on the side (a-d) and in the wake (e-h) of the cylinder's circumference, incident flow from the left (a-d) respectively from the top (rear view, e-h) $(Re_D = 2 \cdot 10^5)$

Initially, the image sequence Fig. 7(a)-7(d) shows the substantially undisturbed incident flow of the cylinder at low signal amplitudes. However, the wake region exhibits strongly increased amplitudes downstream of the separation line. At the same time, two horizontal regions with positive and negative pressure fluctuations respectively stand out switching their signs in the subsequent time step (Mode A, 7(a)-7(b)). In contrast, two time steps later large scale positive and negative fields of pressure fluctuations can be found across the whole height of the cylinder (see 7(c)-7(d), Mode B).

These structures can also be found in the subsequent time steps in the wake of the cylinder (Fig. 7(e)-7(h)). In addition, it is possible to distinguish between a symmetrical, horizontally separated flow state (Fig. 7(e)-7(f), Mode C), and an asymmetrical, vertically separated (Fig. 7(g)-7(h), Mode D) one. Comparing these measurements in the wake region with the measurements on the cylinder's circumference previously shown, it is obvious that modes A and C as well as modes B and D represent the same flow phenomena. The large-scale structures observed alternate asymmetrically and suggest an alternation between modes dominated by

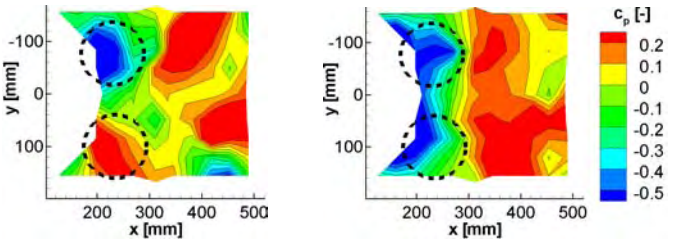

(a) asymmetric mode, t_1 (b) symmetric mode, t_2

Fig. 8 Investigations by means of conventional pressure transducers in the wake of the cylinder showing asymmetric (a) and symmetric (b) modes of vortex propagation in selected time increments, ($Re_D = 2 \cdot 10^5$)

the side tip vortices and those dominated by the Kármán vortices. These results show a resemblance to experimental data[2] (Fig. 8(a)-8(b)) and numerical results of the same configuration by Frederich and Thiele [12], where proper orthogonal decomposition (POD) was used to find and visualize coherent structures in the velocity field of the cylinder wake.

3.3.2 Measurements in the Wake of the Cylinder

The investigations in the cylinder's wake region were performed by means of a PSC insert, with 144 equidistantly distributed sensing elements $\Delta x,y = 11.5mm$ (Fig. 4(b)). As a result of preliminary investigations in the wake region, a characteristic Strouhal number of $St = 0.16$ was determined. To resolve the corresponding frequency of about $f = 34.\overline{6}Hz$, the image-based analysis of the time signals was performed by means of a comb filter setting of $f = 100Hz$.

Fig. 9(a)-9(b) shows the maxima of the propagating vortices in consecutive time increments. In keeping with the investigations at the cylinder's circumference, the alternating appearance of positive and negative pressure fluctuation amplitudes becomes obvious. In comparison to the results of the reference investigations[3] by means of conventional pressure transducers (Fig. 9(c)-9(d)) the vortex centre is located marginally closer to the axis of symmetry of the cylinder plate arrangement ($y = 0$).

The frequency spectra displayed in Fig. 10 were achieved in the region of maximum pressure fluctuation and show a dominant increase in the amplitudes in the frequency range of $f = 38 - 40Hz$. This closely corresponds with the results of the reference hot-wire probe measurements in the wake of the cylinder, represented by the black curve.

[2] The reference investigation displayed in Fig. 8 was performed by means of conventional pressure transducers by C. Dobriloff (SPP1147-sub-project "NI 282/16").

[3] The reference investigations displayed in Fig. 9(c)-9(d) were performed by means of conventional pressure transducers by C. Dobriloff (SPP1147-sub-project "NI 282/16").

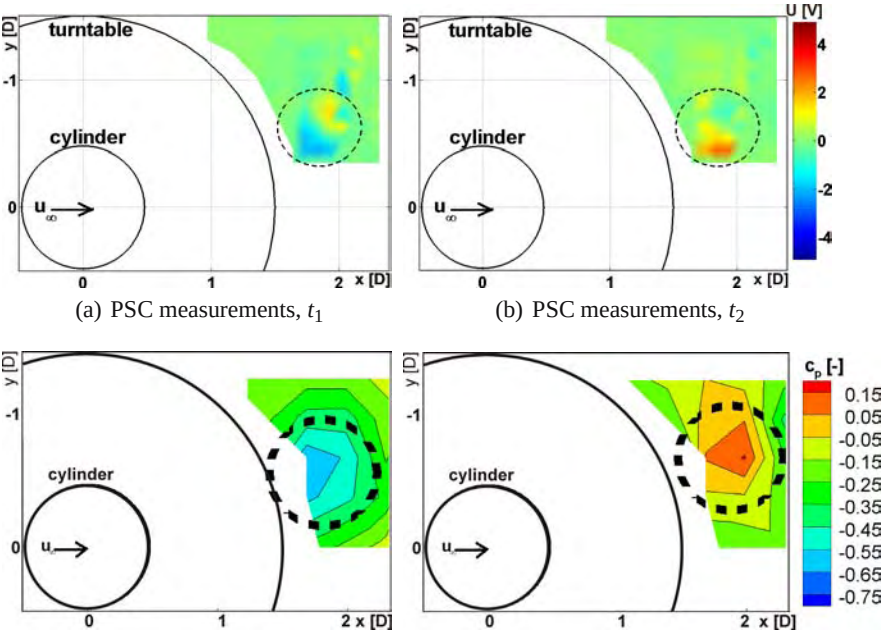

(a) PSC measurements, t_1 (b) PSC measurements, t_2

(c) Conventional pressure measurements, t_1 (d) Conventional pressure measurements, t_2

Fig. 9 Footprints of vortex structures in the far wake of the cylinder, investigated by PSC (time increments a-b) in comparison to reference investigations (c-d), ($Re_D = 2 \cdot 10^5$)

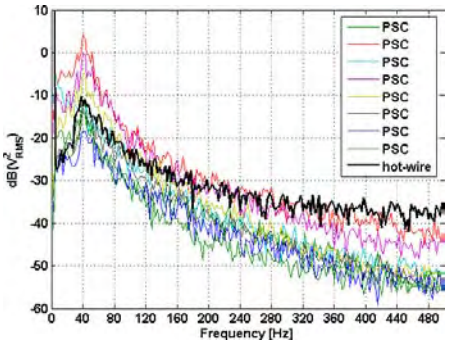

Fig. 10 Frequency spectrum in the wake of the cylinder ($Re_D = 2 \cdot 10^5$)

4 Conclusion

A new pressure measuring technique based on a piezoelectric copolymer coating has been developed which makes it possible to measure distributed surface pressures with a high spatial and temporal resolution under transient flow conditions on arbitrarily formed surfaces. Using the example of the reference experimental set-up, different flow states could be determined and characteristic coherent structures could be found

in the separated boundary layer. Due to the large-scale distribution of sensing areas and the simultaneous sampling, valuable additional findings could be obtained, completing the sequentially measured and phase-averaged results.

Acknowledgements. The research project on the Pressure Sensitive Copolymer coating technique is funded by the DFG (Deutsche Forschungsgemeinschaft - German Research Foundation) and was part of the priority research programme “Imaging measurement methods for flow analysis”.

References

1. Lee, I., Sung, H.J.: Development of an array of pressure sensors with pvdf film. Experiments in Fluids 26, 27–35 (1999)
2. Nitsche, W., Suttan, J., Becker, S., Erb, P., Kloker, M., Stemmer, C.: Experimental and numerical investigations of controlled transition in low-speed free flight. Aeropace Science Technologies 5, 245–255 (2001)
3. Sturzebecher, D., Nitsche, W.: Visualization of the Spatial-Temporal Instability Wave Development in a Laminar Boundary Layer by Means of a Heated PVDF Sensor Array. New Results in Numerical and Experimental Fluid Mechanics 60, 335–342 (1997)
4. Domhardt, J., Leuckert, J., Peltzer, I., Nitsche, W.: Measurement of Unsteady Surface Forces by Means of Piezoelectrical Copolymer Coatings. New Results in Numerical and Experimental Fluid Mechanics 96, 96–103 (2007)
5. Schellin, R., Hess, G., Kressman, R., Wassmuth, P.: Corona-poled piezoelectric polymer layers of P(VDF/TrFE) for micromachined silicon microphones. Journal of Micromechanics and Microengineering 5, 106–108 (1995)
6. Sullivan, C.J., Mueller, T.J.: Polyvinylidene fluoride film sensors for measurement of unsteady pressures on aerodynamic surfaces, Part I: Design, fabrication, calibration and demonstration. Experiments in Fluids 27, 79–84 (1999)
7. Rudolph, I., Reyer, M., Nitsche, W.: Investigations into the visualization of wall shear stress distributions using infrared thermography and analysis of the transient data. In: Proc. of the 45th AIAA Aerospace Sciences Meeting and Exhibit, AIAA-2007-375 (2007)
8. Dobriloff, C., Nitsche, W.: Delta surface hot-wires as a means of measuring wall shear stresses at arbitrary flow directions. In: Proceedings of the 22nd International Congress of Theoretical and Applied Mechanics, Adelaide, Australia, August 25-29, 2008 (2009)
9. Frederich, O., Luchtenburg, M., Wassen, E., Thiele, F.: Analysis of the unsteady flow around a wall mounted finite cylinder at Re=200 000. In: Advances in Turbulence XI, pp. 85–87 (2007)
10. Domhardt, J., Leuckert, J., Peltzer, I., Nitsche, W.: Bildgebende Erfassung instationärer Wanddruckfelder mit Hilfe von drucksensitiven Copolymerbeschichtungen. VDI-Bericht Nr. 2011, pp. 125–134 (2008)
11. Frederich, O., Wassen, E., Thiele, F.: Prediction of the Flow Around a Short Wall-Mounted Finite Cylinder using LES and DES. Journal of Numerical Analysis, Industrial and Applied Mathematics (JNAIAM) 3(3-4), 231–247 (2008)
12. Jensch, M., Brede, M., Leder, A., Frederich, O., Thiele, F.: Use of proper orthogonal decomposition to visualize coherent structures from time resolved PIV data. In: 14. International Symposium on Applications of Laser Techniques to Fluid Mechanics, Lisbon (2008)

AeroMEMS Sensor Arrays for Time Resolved Wall Pressure and Wall Shear Stress Measurements

Andreas Berns and Ernst Obermeier

Abstract. Novel highly sensitive AeroMEMS sensor arrays for transient wall pressure and wall shear stress measurements in fluid flows are presented. Sealed through silicon vias (TSV) and the employment of an elaborate mounting technique enable to electrically contact the sensor chips from the back side. Hence, flow disturbing bond wires on the front side are avoided when chips are mounted flush with the measured surface. The integration of a pressure and a wall hot-wire sensor on a single chip makes simultaneous pressure and wall shear stress measurements possible. The sensors suitability for measurements of fluctuations up to at least 19 kHz is demonstrated in a high-frequency laminar to turbulent transition experiment in a transonic wind tunnel. A complex 3D multi-sensor array has been developed employing 154 pressure sensors to gain extensive, precise and transient data about the surface pressure on a cylinder. Wind tunnel experiments are conducted at a Reynolds number of $2 \cdot 10^5$.

1 Introduction

One of the fundamental problems in fluid mechanics is the flow separation from solid surfaces, which occurs in various technical applications, such as airfoil wings, turbine blades, car bodies, and trains. But also environmental flows are subject to this phenomenon, for instance flows behind mountains, islands, and buildings. In most cases separation is undesired due to the initiation of complex eddies and vortices, mostly resulting in increased drag and noise [1]. Hence, the development of systems for active flow control is most desirable [2]. Provision of such systems would contribute to drag reduction and thus make nowadays transportation systems more efficient and safe [3]. However, precise monitoring of the boundary layer condition is essential to the development of systems for active flow control and also of great importance for the understanding of flow phenomena such as transition, separation, and reattachment. Crucial parameters for the

Andreas Berns · Ernst Obermeier
Microsensor & Actuator Technology Center (MAT), Technical University of Berlin, Gustav-Meyer-Allee 25, 13355 Berlin, Germany

W. Nitsche and C. Dobriloff (Eds.): Imaging Measurement Methods, NNFM 106, pp. 227–236.
springerlink.com

characterization of wall-bound flows are wall pressure and wall shear stress as well as their fluctuations. The use of appropriate measurement techniques capable of providing high sensitivity, high spatial resolution, excellent dynamic properties, and featuring minimum flow disturbance are required to detect and quantify the flow phenomena mentioned above. So called AeroMEMS sensors are well suited to meet these requirements [4, 5].Wall pressure measurements performed by employing single sensors connected to the surface by pin-holes [6] and tubes suffer from damping and thus dynamic resolution is reduced tremendously [7]. Flush mounted sensor arrays consisting of piezoresistive pressure sensors have proven to be the most promising measurement approach [8, 9]. However, sensors with bond wires on the front side exhibit an unavoidable influence on the flow to be measured. The sensors presented herein feature minimum flow disturbance due to through silicon vias and back side bond wires [10]. The on chip integration of a pressure and a wall hot-wire sensor makes simultaneous pressure and wall shear stress measurements possible. To prove the sensors' outstanding dynamic resolution a linear array consisting of 24 AeroMEMS pressure sensors with on chip wall hot-wires is mounted on a wing profile and is utilized for high-frequency laminar to turbulent transition measurements in a transonic wind tunnel [11].

To gain extensive data about the wall pressure distribution and the wall pressure fluctuation, as well as transient pressure data on the surface of a wall mounted cylinder, a 3D multi-sensor array was developed. A total number of 154 single pressure sensors is mounted flush with the surface of a cylinder, using especial mounting and contacting techniques. The experiment described in this work exemplifies the complex and unsteady flow around blunt bodies [12, 13].

2 AeroMEMS Sensors

The first generation of piezoresistive AeroMEMS pressure sensors were developed as prototypes for high accuracy wall pressure measurements in experimental fluid mechanics. Design optimization, fabrication, characterization, array assembly, and verification measurements are described in detail in [9] and [14]. These sensors have been improved and redesigned in order to be more suitable for flow measurements. In this chapter, the development of novel AeroMEMS sensors featuring through silicon vias and back side bond pads, as well as sensors with on chip wall hot-wires for simultaneous wall pressure and wall shear stress measurements are presented.

2.1 Sensor Design

The designs of two AeroMEMS sensors developed are depicted in Fig. 1. A pressure sensor with on chip pn diode for temperature measurements is shown in Fig. 1a (presented at MEMS conference 2008 [10]) and a design with on chip wall hot-wire for wall shear stress measurements (presented at SENSORS conference 2008 [15]) is shown in Fig. 1b. Chip size is 2×3 mm². Both, front and back side metallizations consist of AlSiCu and are connected using sealed through silicon vias. Thus, contacting the chip from the back side employing wire bonding is possible and ensures minimum flow disturbance. The back side bond pads are located near the center of the chip making them easily accessible for wire bonding during

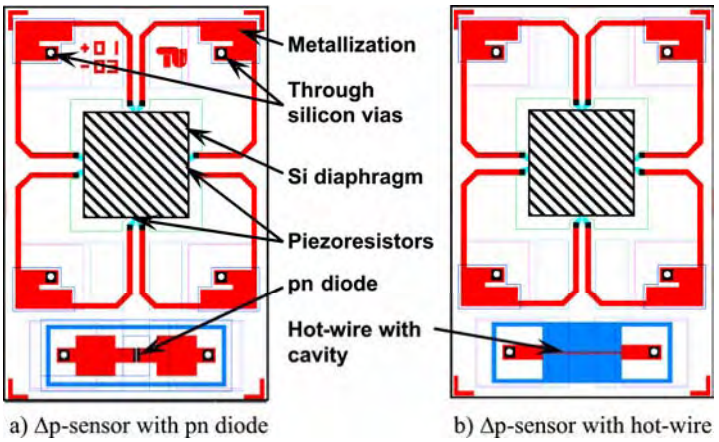

Fig. 1 Layouts of two piezoresistive AeroMEMS pressure sensor chips including sealed through silicon vias, on chip pn diode, and on chip wall hot-wire, respectively

array assembling. The diaphragm of the piezoresistive pressure sensor has a size of 800×800 µm² and a thickness of 4 µm. Piezoresistors are implanted into the silicon device layer forming a Wheatstone bridge. On the lower part of the chip either an on chip pn diode for surface temperature measurement (a) or an on chip wall hot-wire (b) is placed. The hot-wire which is thermally insulated by a 4 µm deep air-filled cavity serves as highly dynamic wall shear stress sensor. A third sensor design without implanted diode or hot-wire has also been realized in order to be used for exclusive surface pressure measurements.

2.2 Fabrication of the AeroMEMS Sensor Chips

Silicon-On-Insulator (SOI) wafers are used to obtain a uniform diaphragm thickness and are processed employing silicon micromachining technology [10]. Piezoresistors, heavily doped contact areas, and pn diodes are realized by ion implantation and rapid thermal annealing. Through silicon vias are wet chemically structured using both KOH and TMAH etching. Sidewall passivation of the vias is performed by various deposition process steps employing silicon dioxide and nitride layers in order to electrically insulate the metallization (AlSiCu) from the silicon substrate. The hot-wire, which also consists of AlSiCu, is structured by wet chemical etching and has a thickness of 2 µm, a width of 3 µm, and a length of 600 µm. The resistance R_{wire} is approximately 3.8 Ohm. The silicon diaphragm is structured by deep silicon etching using a Bosch process [16].

Photos of fabricated sensor dies are depicted in Fig. 2 showing the sensors with and without pn diode (Fig. 2a) as well as the chips with integrated hot-wire sensor (Fig. 2b). Due to the missing diode the chip on the right side of Fig. 2a has only four bond pads and thus facilitates complex array assembling. The sensitivity of the pressure sensors range from 3.5 µV/(V·Pa) to 4.5 µV/(V·Pa), depending on the diaphragm thickness. Detailed calibration data is published in [10].

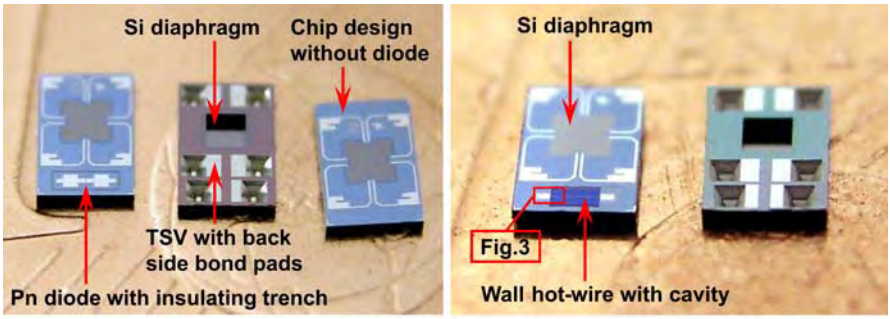

Fig. 2 Photos of fabricated sensor chips on an EURO cent coin. Chip size is 2×3 mm². Pressure sensors with and without diode (a) as well as sensors with hot-wire (b) are shown

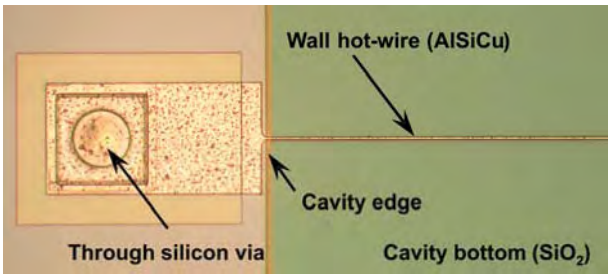

Fig. 3 Photo of one half of the wall hot-wire showing the cavity and the through silicon via

Figure 3 shows a close-up of one half of the wall hot-wire (red box in Fig. 2b). The cavity freeing the hot-wire is structured by dry plasma etching employing a nearly isotropic etch process. Due to the undercut the silicon below the wire is removed completely. The buried oxide (BOX) serves as etch stop layer.

3 Wind Tunnel Experiments

In this chapter two wind tunnel experiments utilizing different AeroMEMS sensor arrays are described. Pressure sensors with on chip wall hot-wire are employed for high-frequency laminar to turbulent transition measurements (Chapter 3.1). An elaborate 3D multi-sensor array has been developed to gain extensive, precise, and transient data about the wall pressure on the surface of a cylinder (Chapter 3.2).

3.1 High-Frequency Transition Measurements

A linear sensor array, consisting of 24 sensor chips with on chip hot-wire (5 mm spacing), is mounted on a wing profile (Fig. 4) and placed inside a transonic wind tunnel. Top and bottom side of the wing are symmetric resulting in a laminar to turbulent transition in the region of the array. Depending on the flow velocity the position of the transition moves across the surface of the wing profile.

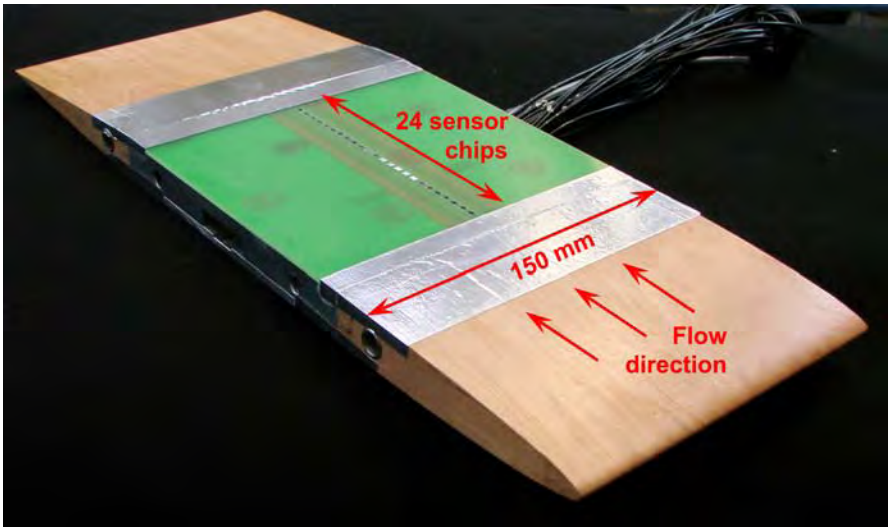

Fig. 4 A wing profile, equipped with 24 flush mounted pressure/wall shear stress sensor chips, used for laminar-turbulent transition measurements in a transonic wind tunnel [11]

Employing the novel AeroMEMS sensors described before simultaneous measurements of wall pressure and wall shear stress, as well as their fluctuations are performed. Analysis of the fluctuation signals provides detailed information about the boundary layer condition, which is laminar, turbulent, or transitional. Further information about the experimental setup and measurements can be found in [11].

The following plots show the FFTs of pressure signals and of the AC signal of a selected hot-wire at a Mach number of 0.32. Figure 5a shows the power spectra against frequency of different pressure sensor output signals. P-sensor position 1 refers to the first pressure sensor on the array. Output signals of sensors 1 to 5 indicate a transitional boundary layer condition showing a significant frequency peak at approximately 9.5 kHz. Sensors 6 and 7 exhibit a raised power spectrum and no significant frequency peak, indicating a turbulent boundary layer condition. Figure 5b depicts the FFTs of the output signals of sensor 1. The blue line corresponds to the pressure signal and the green line to the wall hot-wire sensor on this chip. The excellent correlation of both curves proves the sensors' suitability for high-frequency laminar to turbulent transition measurements. Even the first harmonic, featuring a frequency of 19 kHz can be detected with both measurement principles.

3.2 Surface Pressure Measurements on a Wall Mounted Cylinder Employing a 3D Multi-sensor Array

Experiments are conducted in a closed loop low-turbulence wind tunnel "Göttingen-type" at the University of Rostock. The circular cylinder model is mounted on a ground plate (Fig. 6) in the open test section of the wind tunnel. The circular

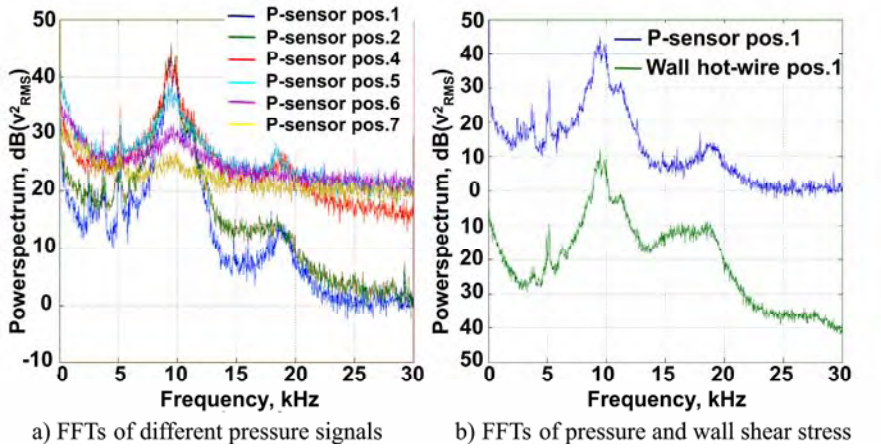

Fig. 5 FFTs of the pressure sensor output signals and the hot-wire output signal [11]

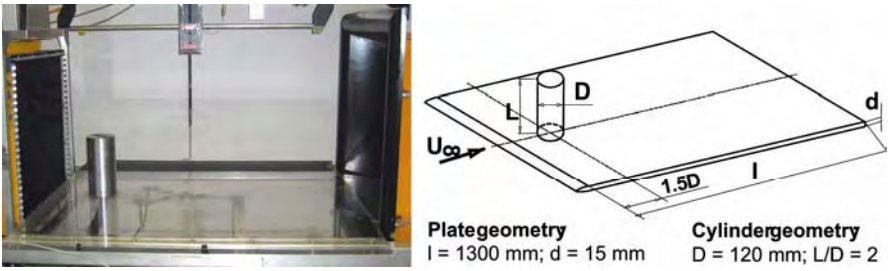

Fig. 6 Photo (left) and sketch (right) of the experimental setup called the "Leitexperiment"

cylinder has a diameter of D = 120 mm and an aspect ratio of L/D = 2.0. Measurements are performed at a Reynolds number $2 \cdot 10^5$ related to the diameter (u_∞ = 26 m/s). This setup was chosen to investigate the developing unsteady flow field and corresponding wall pressure distribution at the cylinder model. Previous measurements on this experimental configuration using an AeroMEMS sensor array consisting of 48 pressure sensors with front side bond wires (first sensor generation) were conducted in 2006 [13, 17].

Figure 7 shows the improved cylinder model equipped with a total number of 154 pressure sensors arranged in 10 different arrays. To ensure excellent surface quality the whole aluminum cylinder is finished by a turning fabrication step.

All openings for placement of the sensors are fabricated by a high accuracy CNC milling tool. Flexible printed circuit boards (PCB) glued to the back sides of the array segments form the electrical interface between sensors and measurement equipment. Pressure calibration is possible due to the use of reference pressure chambers, which are also glued to the back sides of the segments. A sensor array based on a PCB is mounted flush with the cap of the cylinder. An integrated ball

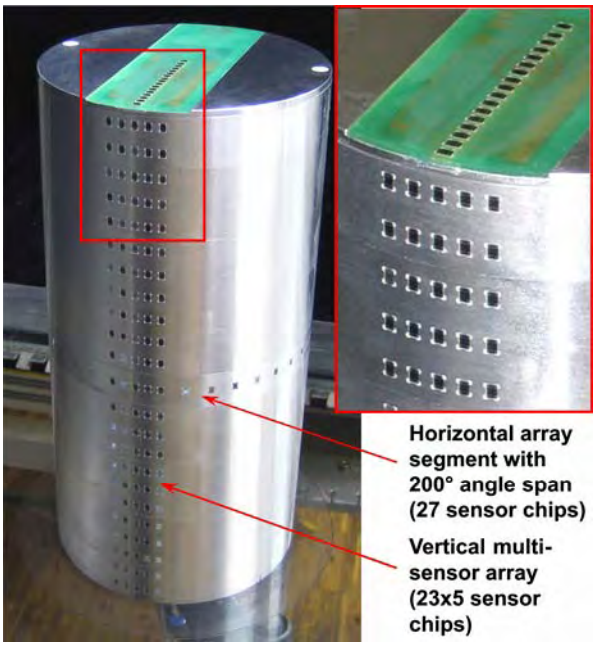

Fig. 7 Cylinder model with horizontal and vertical sensor arrays. Sensors are fixed in position by silicone rubber visible in the detailed picture on the right side

bearing ensures rotation of the cylinder during measurements and thus makes monitoring of the complete cylinder surface possible.

Figures 8 and 9 show selected results of the surface pressure measurements employing the novel multi-sensor array. The averaged wall pressure distribution P and the standard deviation ΔP of the wall pressure on the top of the cylinder are

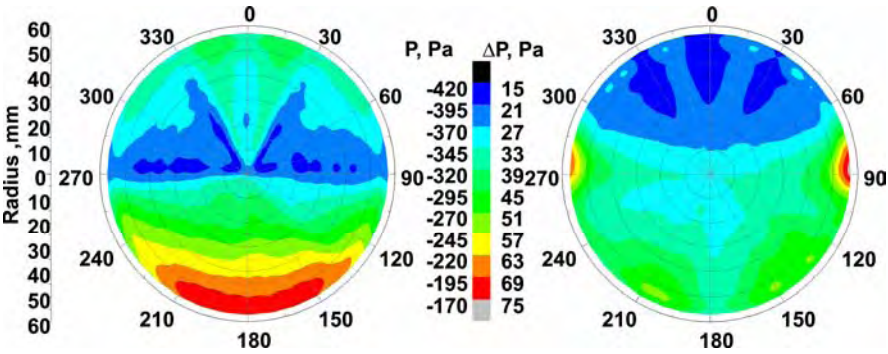

Fig. 8 Measured averaged wall pressure distribution (left) and standard deviation of the wall pressure (right) on the top of the cylinder is plotted in polar coordinates. The angle of flow impact is 0°

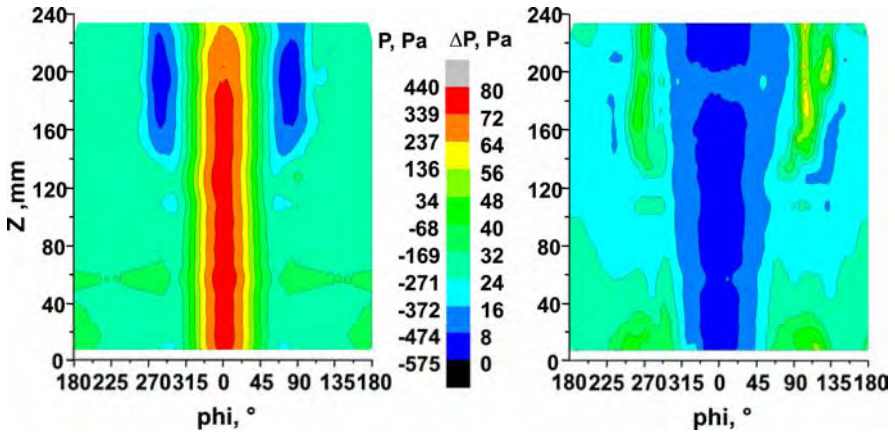

Fig. 9 Averaged surface pressure (left) and standard deviation of the pressure (right) on the surface of the cylinder. The angle of flow impact is 0°

depicted in Fig. 8. The radial coordinate is plotted on the left side and the color bar in the middle provides quantitative information about P and ΔP. The differential pressure on the top side has only negative values between -170 Pa and -420 Pa. The reason for this pressure distribution is the separation bubble on the top of the cylinder [17]. The highest pressure fluctuations occur at 90° and 270° where the side tip vortices separate from the top of the cylinder. Figure 9 shows the averaged wall pressure P and the standard deviation ΔP of the wall pressure on the surface of the cylinder. Z-position (ranging from bottom to top) is plotted against the angle phi (flow impact is located at 0°). The area of high differential impact pressure extends from 0° to 30°. In the region of the laminar boundary layer between 30° and 70°, where the pressure fluctuation is extremely low, the differential pressure decreases to a negative value. The pressure gradient increases until separation occurs between 80° and 100°. The pressure fluctuation has its maximum in the area of the separation. Between 120° and 180° the pressure and its fluctuation remain nearly constant. Due to the unsteadiness of the boundary layer condition in the region of flow separation the measured data are not perfectly symmetric. Eventually, only synchronous and transient wall pressure data can provide further information about the complex separation phenomena occurring in this experiment.

Extensive data processing and analysis of the transient pressure signals are currently under progress at the University of Rostock.

4 Conclusion

Novel AeroMEMS sensors were developed and arranged to form different flush mounted surface sensor arrays for wall pressure and wall shear stress measurements in fluid flows. Wind tunnel experiments have proven the suitability of the sensors to accurately measure both high-frequency fluctuations up to at least 19 kHz and high-resolution wall pressure distributions on 3D surfaces. Even though complexity and cost of sensor arrays and of the required measurement

equipment rapidly increase with the number of sensors, utilization of such sensor systems assure superior measurement quality. The arrays presented exhibit a fairly high sensor density and can be employed to precisely monitor wall pressure, wall shear stress, and their fluctuations with high temporal and spatial resolution. Furthermore, they can be used for real-time measurements in transient fluid flows. Thus, new insights into flow transition, separation and other near-wall flow phenomena can be achieved.

Acknowledgments. Financial support by the *Deutsche Forschungsgemeinschaft (DFG SPP 1147)* is gratefully acknowledged. Measurements have been conducted at the Institute of Aeronautics and Astronautics (Technical University of Berlin) and at the Department of Fluid Mechanics (University of Rostock).

References

1. Blake, M.K.: Mechanics of Flow-Induced Sound and Vibration. Academic Press, New York (1986)
2. Löfdahl, L., Gad-el-Hak, M.: MEMS applications in turbulence and flow control. Progress in Aerospace Sciences (1999), doi:10.1016/S0376-0421(98)00012-8
3. Tsao, T., Jiang, F., Liu, C., Miller, R., Tung, S., Huang, J.B., Gupta, B., Babcock, D., Lee, C., Tai, Y.C., Ho, C.M., Kim, J., Goodman, R.: MEMS based Active Drag Reduction in Turbulent Boundary Layers. In: Helvajian, H. (ed.) Microengineering Aerospace Systems. The Aerospace Press, El Segundo (1999)
4. Löfdahl, L., Gad-el-Hak, M.: MEMS-based pressure and shear stress sensors for turbulent flows. Measurement Science and Technology (1999), doi:10.1088/0957-0233/10/8/302
5. Tung, S., Maines, B., Jiang, F., Tsao, T.: Development of a MEMS-Based Control System for Compressible Flow Separation. Journal of Microelectromechanical Systems (2004), doi:10.1109/JMEMS.2003.823228
6. Willmarth, W.W., Wooldridge, C.E.: Measurements of the fluctuating pressure at the wall beneath a thick turbulent boundary layer. Journal of Fluid Mechanics (1962), doi:10.1017/S0022112062001160
7. Bull, M.K., Thomas, A.S.W.: High frequency wall-pressure fluctuations in turbulent boundary layers. Physics of Fluids (1976), doi:10.1063/1.861496
8. Leger, T.J., Johnston, D.A., Wolff, J.M.: Flex Circuit Sensor Array for Surface Unsteady Pressure Measurements. Journal of Propulsion and Power, ID: 0748-4658 20, 754–758 (2004)
9. Berns, A., Buder, U., Wolter, A., Leder, A., Obermeier, E.: AeroMEMS sensor array for high-resolution wall pressure measurements. Sensors and Actuators A (2006), doi:10.1016/j.sna.2006.04.056
10. Berns, A., Ngo, H.-D., Buder, U., Obermeier, E.: AeroMEMS Pressure sensor Array Featuring Through-Wafer Vias for High-Resolution Wall Pressure Measurements. In: 21st IEEE MEMS Conference (2008), doi:10.1109/MEMSYS.2008.4443801
11. Berns, A., Buder, U., Obermeier, E., Wang, X.H., Domhardt, J., Leuckert, J., Nitsche, W.: AeroMEMS Sensor with Integrated Pressure and Hot-Wire Sensor for High-Frequency Transition Detection. In: 47th AIAA Aerospace Sciences Meetings and Exhibit, AIAA 2009-318 (2009)

12. Leder, A.: 3D-Flow Structures behind Truncated Circular Cylinders. In: 4th ASME/JSME Joint Fluids Engineering Conference, FEDSM 2003-45083 (2003)
13. Berns, A., Buder, U., Obermeier, E., Wolter, A., Leder, A.: Application of AeroMEMS Surface Pressure Sensor Arrays in Experimental Fluid Mechanics. In: 46th AIAA Aerospace Sciences Meetings and Exhibit, AIAA-2008-0271 (2008)
14. Berns, A., Metzen, R.v., Mukhopadhyay, B., Obermeier, E., Wolter, A., Leder, A.: Ultra Sensitive AeroMEMS Sensor Array for High-Resolution Wall Pressure Measurements. In: 19th Eurosensors Conference, ID: MB 2007 (2005)
15. Berns, A., Buder, U., Wang, X.H., Nitsche, W., Obermeier, E.: AeroMEMS Pressure Sensor with Integrated Wall Hot-wire. In: 7th IEEE Conference on Sensors (2008), doi:10.1109/ICSENS.2008.4716746
16. Laermer, F., Schilp, A., Funk, K., Offenberg, M.: Bosch Deep Si Etching: Improving Uniformity and Etch Rate for Advanced MEMS Applications. In: 12th IEEE MEMS Conference (1999), doi:10.1109/MEMSYS.1999.746812
17. Berns, A., Buder, U., Obermeier, E., Wolter, A., Leder, A., Frederich, O., Thiele, F.: Aero-Micro-Electromechanical System Sensor Arrays for Time Resolved Wall Pressure Measurements. AIAA Journal (2009) (to be published)

Infrared-Based Visualization of Wall Shear Stress Distributions

Ilka Rudolph, Matthias Reyer, and Wolfgang Nitsche

Abstract. The wall shear stress is an important quantity in fluid mechanics and aerodynamics, especially when the fact that about 50% of an airplane's drag is due to viscous forces is considered. The goal of this project was the development of a novel, spatial measurement technique that is able to provide qualitative visualizations as well as quantitative information about the wall shear distribution. Like other visualizing methods, this technique exploits that changes in the surface temperature distribution of a heated structure are dependent on the near wall flow. The two main components of this new technique are a heatable structure and an infrared camera system to non-intrusively measure the surface temperature distribution. For the shear stress quantification, a turbulent flow across a flat plate was investigated experimentally and numerically. Wall shear stress visualizations were carried out for the flow around a finite, wall mounted cylinder and the results were compared to oilflow visualizations and surface hot-wire measurements.

1 Introduction

A variety of aerodynamically relevant phenomena, like flow separation, reattachment or transition from laminar to turbulent flow, can be detected from the wall shear stress distribution. For this reason, a variety of sensor-based wall shear stress measurement techniques were developed and tested in the last decades, [1], [2]. However, skin friction sensors only provide local shear stress information. This can be overcome by grouping sensors and forming sensor arrays, but this usually requires elaborate, complex instrumentation, [3]. Techniques like oilflow visualization are a frequently used tool for spatial visualizations of the shear stress distribution, but are restricted to time averaged visualizations. Quantitative as well as qualitative wall shear stress information can be obtained with liquid crystals, [4], [5], [6].

Ilka Rudolph · Matthias Reyer · Wolfgang Nitsche
TU Berlin, Institute of Aeronautics and Astronautics, Marchstr. 12, 10587 Berlin
ilka.rudolph@ilr.tu-berlin.de

W. Nitsche and C. Dobriloff (Eds.): Imaging Measurement Methods, NNFM 106, pp. 237–246.
springerlink.com

However, there are some drawbacks to liquid crystals. The results strongly depend on the viewing angle and the crystals have a limited durability. Infrared thermography is a frequently used tool for non-intrusive temperature detection and flow visualization, [7], [8], [9], but existing techniques for quantitative shear stress measurements using infrared thermography are restricted to local information, [10].

For this reason, the goal of this project was to develop a novel, infrared-based measurement technique that is able to provide qualitative visualizations as well as spatial, quantitative information about the wall shear stress distribution. The technique is based on the analogy between momentum and heat transfer in the boundary layer. If a heated structure is subjected to a flow, locations of high shear stress are also characterized by a high convective heat flux and are therefore cooled down more than locations of lower shear stress. Therefore, the resulting inhomogeneous surface temperature distribution correlates with the wall shear stress distribution.

2 Experimental Setup

Within the framework of the DFG priority program 1147, a reference experiment was defined to allow for a comparison of various measurement techniques. The flow past a finite, circular, wall mounted cylinder with a height to diameter ratio of $H/D = 2$ at a diameter based Reynolds number of $Re_D = 200.000$ was chosen. The visualization of wall shear stress distributions were performed for this reference experiment. The investigations were carried out in cooperation with Prof. Leder's group in Rostock at a closed loop windtunnel with an open test section. The spatial quantification of wall shear stress distributions was investigated for the turbulent flow on a flat plate with an elliptical nose. These experiments were conducted at an open windtunnel at the TU Berlin and a skin friction balance was used for reference measurements.

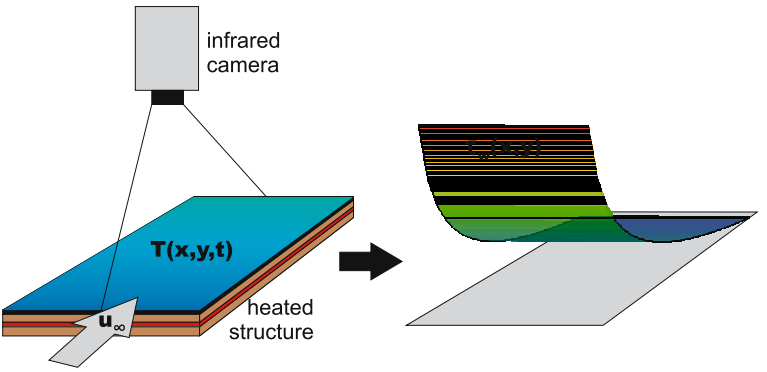

Fig. 1 Fundamental principle of the visualization and quantification technique that links the surface temperature distribution to the wall shear stress

Momentum transport and heat transfer in the boundary layer are closely linked. For this reason, the inhomogeneous surface temperature distribution of a heated structure that is subjected to a flow correlates with the wall shear stress. Therefore, one of the essential parts of the technique is a heatable structure. The setup of our structure consists of a copper layer that is heated by a heating mat. The copper layer is coated with a matte, black pvc layer to minimize reflections in the infrared spectrum, to ensure a high radiation emission, to minimize lateral heat conduction within the structure and to enable a fast response to changes in the flow field. Underneath the heating mat is another copper layer for added stability and to further homogenize the heating of the mat. The heating mat is produced in a chemical etching process and consists of a $25\,\mu m$ capton base with an $18\,\mu m$ copper coating. The surface temperature distribution on this structure is then detected with an infrared camera (Flir Systems, SC3000) and the infrared data can be used to visualize and quantify shear stress distributions. The fundamental principle of this technique is sketched in figure 1.

For the wall shear stress visualizations, the top of the cylinder and a circular area with a diameter of $d = 3D$ ($D = 120\,mm$) around the cylinder were equipped with heated structures. For the quantification experiments, a part of the flat plate with an area of $140mm \times 320\,mm$ was designed as a heated structure.

3 Visualization of Wall Shear Stress Distributions

One of the project's objectives was the application of the newly developed wall shear stress visualization technique to the reference experiment's flow around a circular cylinder. However, before this was achieved, preliminary investigations on a similar, smaller setup were carried out. These preliminary visualizations were performed at an open wind tunnel at the TU Berlin.

The temporal temperature gradient $\partial T/\partial t$ of the surface temperature field produced the best and most reliable shear stress visualizations, where the time step Δt corresponds to the inverse of the frame rate ($50\,Hz$ and $150Hz$ for the results presented here). Within the framework of the priority program, we had a cooperation with Prof. Jähne's group at the University of Heidelberg, who aided us in the image processing. A cylinder with a diameter of $D = 30\,mm$ and a height to diameter

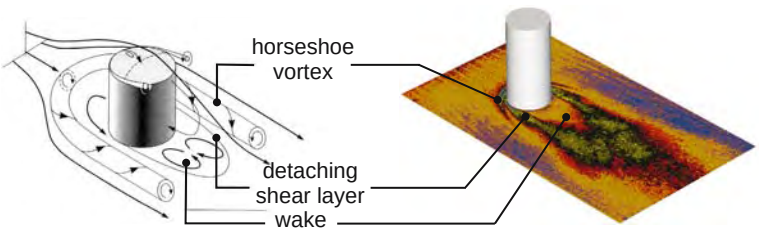

Fig. 2 Theoretical flow topology of the flow around a wall mounted cylinder and infrared visualization of the same topology

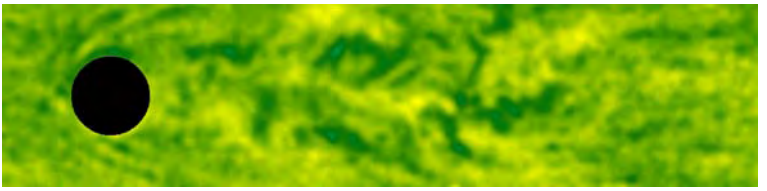

Fig. 3 Infrared visualization of the cylinder wake using a framerate of $150\,Hz$

ratio of $H/D = 2$ was used for these preliminary investigations. Figure 2 shows an infrared visualization for a diameter based Reynolds number of $Re_D = 30000$. The results agree very well with the theoretical flow topology shown on the left side. In figure 3, a visualization that was recorded at a framerate of $150\,Hz$ is depicted. The vortex street in the wake of the cylinder stands out very well in this image.

After the successful completion of the preliminary investigations, the wall shear stress visualizations of the reference experiment were carried out at the University of Rostock. The experiments were conducted in a close-loop wind tunnel with an open test section. The results presented here are for a diameter-based Reynolds

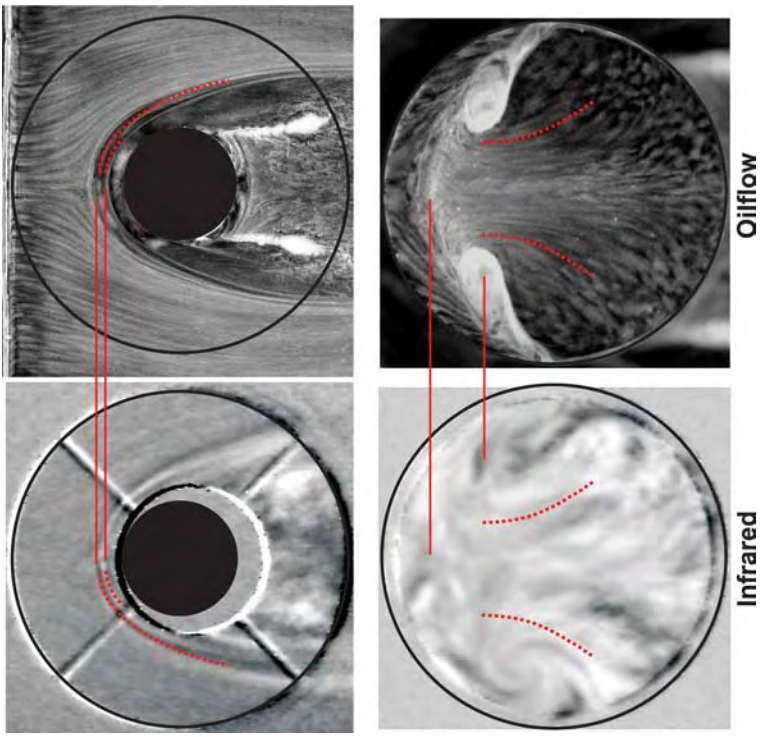

Fig. 4 Comparison of infrared images (bottom) and oilflow visualizations (top) for the base (left side) and top of the cylinder (right side)

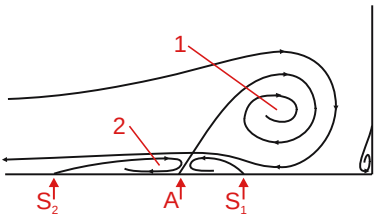

(a) Flow topology directly upstream of the cylinder with vortices (1,2), separation (S) and attachment points (A)

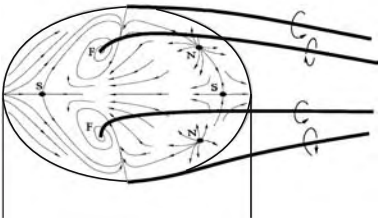

(b) Flow topology on the cylinder top [11] with tornado and side tip vortices

Fig. 5 Flow topology of the flow around a finite wall mounted cylinder

number of $Re_D = 200.000$. Figure 4 shows a direct comparison of oilflow and infrared visualizations for the base flow surrounding the cylinder (left side) and the top of the cylinder (right side). The black lines mark the heated areas (the circular area around the cylinder for the base flow and the top of the cylinder). In the oilflow visualizations, the cylinder was removed when taking the pictures, so that no part of the base flow is obscured. The infrared images were taken with the cylinder. That is why part of the base flow close to the cylinder cannot be seen. The results compare very well and the typical flow structures for this type of flow (horseshoe vortex, separating shear layers, separation on the top, foci of the top vortices etc.) are clearly visible in the oilflow as well as the infrared visualizations. The location of the horseshoe vortex system is identical in both visualizations, as is the shape of the vortices. According to [12], the horseshoe vortex system consists of a primary and a secondary vortex, as illustrated in figure 5(a). There are two dominating separation lines (S_1, S_2) and the vortices are separated by an attachment line (A). The two separation lines, the footprints of the vortices, are clearly visible in the visualizations and their location matches. The typical flow topology on the cylinder top (according to [11]) is illustrated in figure 5(b). The flow separates near the leading edge and forms a separation bubble. There are two vortex systems that dominate the flow topology: a pair of side tip vortices and a pair of tornado-like vortices evolving from the two foci. These vortex systems induce a downwash flow in the trailing edge region of the cylinder top. The two foci and the distortion of the streamlines

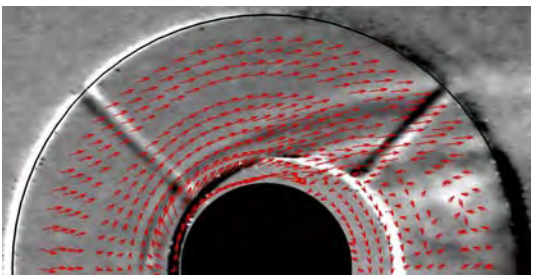

Fig. 6 Comparison of an infrared visualization of the base flow and shear stress vectors obtained from hot-wire measurements with delta probes [13]

are clearly visible in the visualizations and their shape and position matches. The separation line is easily discernible in the oilflow visualizations but harder to make out in the infrared image.

Figure 6 shows a direct comparison of surface hot-wire measurements (red arrows) and infrared visualization for the base flow. The hot-wire measurements were carried out by C. Dobriloff using a novel delta surface hot-wire sensor that is capable of measuring shear stress magnitude and direction, [13]. The results agree very well. All flow features that are visible in the infrared images also show up in the measurements and their location matches. Furthermore, the direction and the shape of the features (for example the horseshoe vortex) also coincide. More information on the visualization technique and further results and discussion can be found in the following publications, [14], [15], [16], [17].

4 Spatial Quantification of Wall Shear Stress Distributions

The correlation between momentum and heat transfer, which is the basis for the quantification, only holds for simple flow configurations. Therefore, the quantification can only be expected to produce reliable results for those types of flows. For this reason, the investigations into the spatial quantification of wall shear stress distributions were carried out for the flow across a flat plate without pressure gradients. To find a suitable correlation parameter that links the surface temperature distribution to the shear stress, the temporal temperature evolution of the surface temperature field was studied. There are two different ways in which such a quantification can be carried out. Either the heated structure is uniformly heated until it reaches steady state before the wind tunnel is turned on, or the structure is heated while the wind tunnel is running and after the surface temperature distribution reaches steady state the heating is reduced. Both methods result in a cooling of the surface temperature distribution. Figure 7 shows the cooling curves of four points on the heated structure with varying streamwise position. Here, the first method was used. It can be seen that the larger wall shear stress values towards the leading edge of the plate not only result in a cooler surface temperature at steady state (which is to be expected, since larger shear stress means higher convection), but also causes a faster cooling. Furthermore, the spatial gradients in the transient state are much higher than in the steady state, making it easier to resolve the temperature differences. The second method produces similar results, however the order of the curves is reversed.

To correlate the temperature distribution to the shear stress, the area ratio of the area underneath a cooling curve and a reference area was used. The area ratio is defined by

$$f = \frac{\int_{t_0}^{t_{max}} T(t)\,dt - T_{min}\,(t_{max} - t_0)}{(T_{max} - T_{min})\,(t_{max} - t_0)} \tag{1}$$

where the reference area is a rectangle defined by T_{max}, T_{min}, t_{max}, t_0.

Using this correlation parameter, a calibration was found and applied to calculate the spatial shear stress distribution from the infrared data. The result is displayed

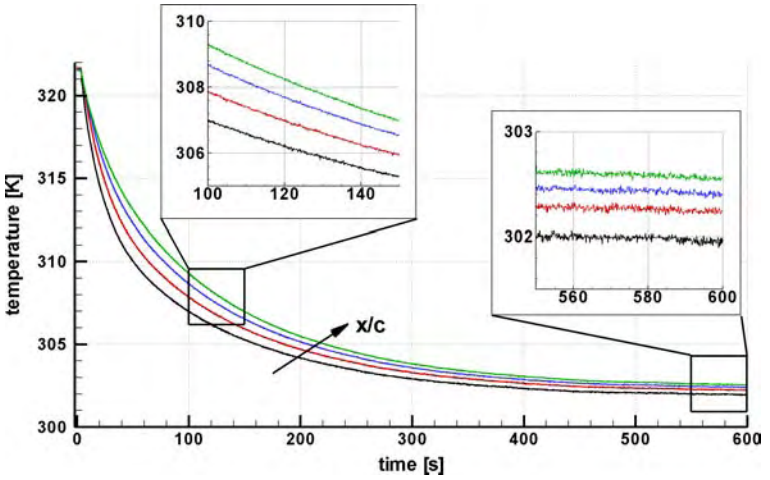

Fig. 7 Temporal surface temperature evolution at varying streamwise positions on a heated structure that was uniformly heated before the flow was turned on

in figure 8. The gray areas correspond to the reference measurements that were conducted using a skin friction balance. There is a very good agreement between the reference data and the data from the infrared measurements. The largest deviations occur toward the boundary of the heated structure, where convection is no longer the dominating heat transport mechanism and conduction into the surrounding structure occurs.

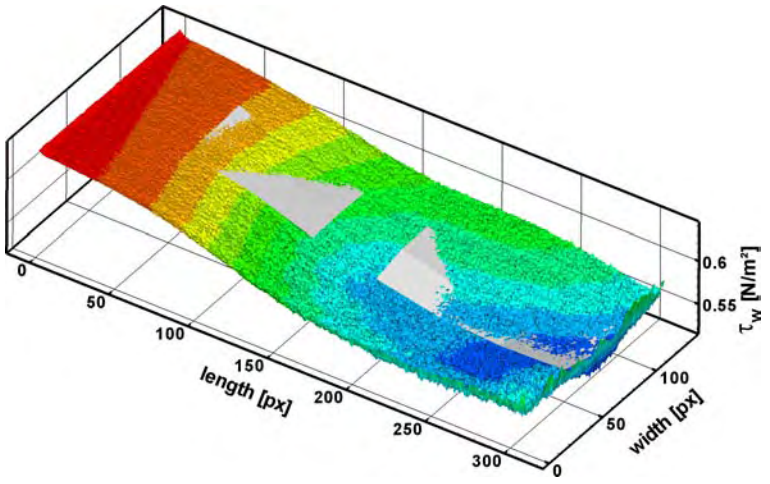

Fig. 8 Comparison of the spatial wall shear stress distribution from an infrared analysis on a flat plate with reference measurements using a skin friction balance (gray areas)

The spatial resolution of this technique is limited by the resolution of the infrared camera, which in turn is dependent on the optics and distance from the object. The investigations were conducted with a camera distance of $0.9\,m$, corresponding to a field of view of $0.32\,m \times 0.14\,m$ and a resolution of $1\,mm$ per pixel. Preliminary numerical simulations yielded that the maximum temperature gradient that can be expected for moderate velocities up to $20\,m/s$ is about $50\,K/m$ or $0.05\,K/mm$. This shows that the infrared camera's spatial resolution is more than sufficient to capture these temperature gradients.

During the investigation of the area ratio correlation, the resulting calibration was found to depend on the Reynolds number and therefore applicable only to constant free stream velocities. The reason for this was found to be the varying temperature boundary layer thickness. With increasing streamwise position, the thickness of the boundary layer increases, leading to different boundary conditions for the convective heat transfer. When a calibration is carried out for one free stream velocity, this effect is not fully accounted for. To further study the influence of the thermal boundary layer thickness and to find a suitable correction method, unsteady numerical simulations of a laminar flat plate where carried out using the ANSYS CFX software package. A two-dimensional flat plate with a length of $40\,mm$ that was heated by a constant temperature boundary condition ($T = 330\,K$) was simulated. The structure of the plate was similar to the heated structure and consisted of a $1\,mm$ copper layer with a $0.1mm$ PVC coating. The simulations were carried out for velocities ranging from $10\,m/s - 22.5\,m/s$ using the second method described above. The structure is heated while the wind tunnel is turned on. After the surface temperature distribution reaches steady state, the temperature boundary condition is reduced by $15\,K$, leading to a cooling of the surface temperature. Figure 9(a) shows the resulting area ratios for six different Reynolds numbers. It is easily discernible that the slope of the calibration, which for a laminar flow is a linear function of τ_w, varies with the velocity and the Reynolds number. However, a correction was found, adjusting the slope with respect to the free stream velocity

$$m = \frac{0.97}{u_\infty} \tag{2}$$

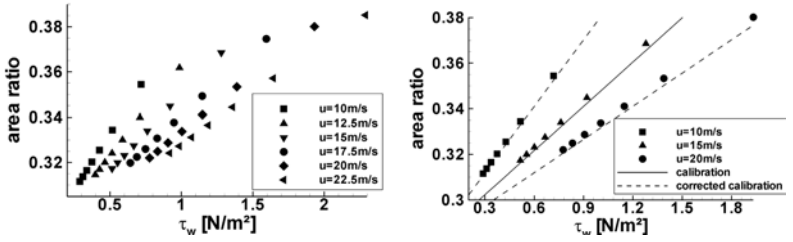

(a) Area ratios for varying Reynolds numbers and wall shear stress values

(b) Area ratio calibration and corrected calibration curves

Fig. 9 Numerical results of the area ratio for a laminar plate flow without pressure gradients

where m is the slope. With this slope correction, the structure has to be calibrated only once for one velocity and the calibration curves for all other Reynolds numbers can be deduced from that first calibration, see Figure 9(b). A correction method for turbulent boundary layers and the application to experimental data is currently researched. The following publications provide further results and discussion of the spatial quantification method, [14], [15].

5 Conclusion

A new infrared-based method for the spatial visualization and quantification of wall shear stress distributions was developed and investigated. The technique is based on the close relationship between heat and momentum transfer in the boundary layer and exploits that changes in surface temperature of a heated structure are dependent on the near wall flow and thus the skin friction. Therefore, the two main components of the method are a heatable structure and an infrared thermography system to measure the surface temperature field.

The visualization technique was applied to the priority program's reference experiment and compared to other techniques. The reference experiment was defined as the flow around a finite, circular wall mounted cylinder with a height to diameter ratio of $H/D = 2$ and a diameter-based Reynolds number of $Re_D = 200.000$. The visualizations were carried out in cooperation with Prof. Leder's group at a closed loop wind tunnel with an open test section at the University of Rostock. Temporal temperature gradients $\partial T/\partial t$ were found to provide the best shear stress visualizations and the image processing of the infrared data was aided by Prof. Jähne's group at the University of Heidelberg. The results were compared with oilflow visualizations and surface hot-wire measurements. A very good agreement can be seen for those three techniques. The flow topology at the cylinder base and the top also agrees well with existing literature.

Investigations into the spatial quantification of wall shear stress distributions were carried out for the turbulent flow across a flat plate at an open wind tunnel facility at the TU Berlin. The temporal temperature evolution was found to correlate with the wall shear stress and the ratio of the area underneath such a temperature curve to a reference area was used as correlation parameter. The resulting calibration was applied to the infrared data of the flat plate flow and the results agreed very well with reference measurements that were carried out with a skin friction balance. Further investigations showed that the calibration is Reynolds number dependent, since it does not account for the varying thermal boundary layer thickness and therefore the varying heat transport boundary conditions. However, a correction method was found that adjusts the calibration with respect to the Reynolds number.

Acknowledgements. This project was funded by the German Research Foundation (DFG) within the framework of the priority program 1147.

References

1. Nitsche, W., Haberland, C., Thuenker, R.: Comparative investigations on friction drag measuring techniques in experimental aerodynamics. In: Proc. of the 14th ICAS Congress, ICAS-2.4.1 (1984)
2. Naughton, J., Sheplak, M.: Modern developments in shear-stress measurement. Progress in Aerospace Sciences 38, 515–570 (2002)
3. Nitsche, W., Suttan, J., Haselbach, F., Sturzebecher, D.: Surface force measurements with high spatial and temporal resolution by means of liquid crystal foils, piezofoils and surface hot film arrays. In: Advanced Aerodynamic Measurement Technology, AGARD CP-601 (1997)
4. Reda, D.C., Wilder, M.C.: The shear-sensitive liquid crystal coating method: Visualization of continuous surface shear stress vector distributions. In: Advanced Measurement Techniques. VKI Lecture-Series, vol. 1 (2001)
5. Ireland, P.T., Jones, T.V.: Liquid crystal measurements of heat transfer and surface shear stress. Measurement Science and Technology 11, 969–986 (2000)
6. Fujisawa, N., Funatani, S., Kosaka, S.: Measurement of shear-stress distributions by liquid-crystal coating. In: Optical Technology and Image Processing for Fluids and Solids Diagnostics SPIE (2002)
7. Carlomagno, G.M., Cardone, G., Meola, A., Astarita, T.: Infrared thermography as a tool for thermal surface flow visualization. Journal of Visualization 1, 37–50 (1998)
8. Dariabeigi, K., Aldafer, D.W.: Aerodynamic applications of infrared thermography. In: Proceedings of Infrared Technology XV (1989)
9. LeSant, Y., Marchano, M., Millan, P., Fontaine, J.: An overview of infrared thermography techniques used in large wind tunnels. Aerospace Science and Technology 6, 355–366 (2002)
10. Mayer, R., Henkes, R.A.W.M., Van Ingen, J.L.: Quantitative infrared-thermography for wall-shear stress measurement in laminar flow. International Journal of Heat and Mass Transfer 41, 2347–2360 (1997)
11. Roh, S.C., Park, S.O.: Vortical flow over the free end surface of a finite circular cylinder mounted on a flat plate. Experiments in Fluids 34, 63–67 (2003)
12. Pattenden, R.J., Turnock, S.R., Zhang, X.: Measurements of the flow over a low-aspect-ratio cylinder mounted on a ground plane. Experiments in Fluids 39, 10–21 (2005)
13. Dobriloff, C., Nitsche, W.: Surface pressure and wall shear stress measurements on a wall mounted cylinder. In: Nitsche, W., Dobriloff, C. (eds.) Imaging Measurement Methods for Flow Analysis. Springer, Berlin (2009)
14. Reyer, M., Rudolph, I., Nitsche, W.: Investigations into the visualization and quantification of wall shear stress distributions using infrared thermography. In: Proc. of the 25th AIAA Aerodynamic Measurement Technology and Ground Testing Conference, AIAA-2006-3840 (2006)
15. Rudolph, I., Reyer, M., Nitsche, W.: Investigations into the visualization of wall shear stress distributions using infrared thermography and analysis of the transient data. In: Proc. of the 45th AIAA Aerospace Sciences Meeting and Exhibit, AIAA-2007-375 (2007)
16. Rudolph, I., Reyer, M., Nitsche, W.: Visualization of time-dependent wall shear stress distributions using infrared thermography. In: Proc. of the 12th International Symposium on Flow Visualization, ISFV12-30.3 (2006)
17. Rudolph, I., Reyer, M., Nitsche, W.: Infrared based visualization of wall shear stress distributions with a high temporal and spatial resolution. Journal of Visualization 10, 8 (2007)

Variational Approaches to Image Fluid Flow Estimation with Physical Priors

Andrey Vlasenko and Christoph Schnörr

Abstract. We present several variational approaches for fluid flow estimation from image sequences in experimental fluid dynamics. These approaches enable the contextual data analysis of particle images based on physical constraints, including bounds on the variation of divergence and vorticity of flow patterns, vanishing divergence for incompressible flows, and iterative estimation-prediction schemes based on vorticity transport for spatiotemporal regularization. All approaches amount to solving convex optimization problems that have unique solutions. They can be computed by standard numerical algorithms exploiting sparsity even for large-scale problems. We also present recent results on the physically consistent denoising of corrupted three-dimensional fluid flow estimates.

1 Introduction

Particle Image Velocimetry (PIV) has been the prevailing image measurement technique for estimating turbulent flows in experimental fluid dynamics for more than two decades [1, 11]. Local flow estimates are obtained by correlating local interrogation windows in subsequent image frames. Window parameters (size, shape) are adapted to local flow variation in order to optimize the trade-off between accuracy and resolution of flow estimation, and noise suppression.

A remarkable fact concerning correlation-based PIV is that prior knowledge, often available in terms of the physics of the underlying problem [16], is not taken into account. Furthermore, estimates at different locations do not explicitly depend on each other, and an overall optimization criterion with respect to all estimates in the whole image domain is lacking. This appears unnatural in view of the interaction over

Andrey Vlasenko · Christoph Schnörr
University of Heidelberg, Dept. Mathematics and Computer Science, Image and Pattern Analysis Group
{vlasenko,schnoerr}@math.uni-heidelberg.de
http://ipa.iwr.uni-heidelberg.de/

W. Nitsche and C. Dobriloff (Eds.): Imaging Measurement Methods, NNFM 106, pp. 247–256.
springerlink.com

a large range of scales in turbulent flows. Accordingly, correlation methods bear little resemblance to the Navier-Stokes equations that govern fluid flows.

Methods for combining prior knowledge and data processing have a long history in other fields of image processing. Variational methods, in particular, are amenable to incorporate physical constraints through additional variational terms. In constrast to correlation methods, even the simplest variational method gives rise to algorithms for flow estimation where estimates at different locations explicitly depend on each other. Likewise, the corresponding Euler-Lagrange systems bear some resemblance to the constitutive equations of fluid dynamics. In our opinion, this indicates an important long-term research direction enabling synergy between experimental fluid dynamics and numerical flow simulation.

In the remainder of this paper, we present past and ongoing own work within the DFG priority program 1147[1] on the design of variational methods for fluid flow estimation that incorporate physical prior knowledge [12, 13, 14, 15, 17, 18], along with related work of our group developed in a European project[2] [19, 20, 21, 2]. For related work, we refer to [3, 4, 5, 8, 10] and [7] and references therein.

The focus of our work is on variational methods

- that effectively steer algorithms for image sequence processing towards physically plausible fluid flow estimates, and
- that are mathematically well-posed and have unique solutions which can be computed even for large-scale problems with numerically stable algorithms.

The paper is organized as follows. We discuss unconstrained variational approaches in section 2 and constrained ones in section 3. Recent work on efficient variational techniques for denoising fluid flow estimates both in 2D and 3D is discussed in section 4. We conclude and indicate promising directions for future research in section 5.

Due to lack of space, we only present experimental results for our most recent work. Detailed presentations of all approaches sketched below, including thorough discussions of related work, can be found in the papers referenced above and downloaded from the IPA homepage.

2 Unconstrained Variational Fluid Flow Estimation

Given the intensity function $I\colon \Omega \to \mathbb{R}_+$ (particle image) defined over a 2D or 3D domain $\Omega \subset \mathbb{R}^d$, $d = 2,3$, the prototypical variational approach for estimating flow $u\colon \Omega \to \mathbb{R}^d$ for a fixed image frame (point of time) reads

$$\inf_u J(u)\,, \quad J(u) = \int_\Omega \Big\{ (\nabla I \cdot u + \partial_t I)^2 + \lambda\, r(Du, D^2u) \Big\} dx\,, \quad \lambda > 0\,. \tag{1}$$

[1] http://www.spp1147.tu-berlin.de/

[2] http://fluid.irisa.fr/

Minimizing the functional J entails minimizing the squared residuals of the continuity equation $\frac{d}{dt}I(x,t) = 0$ valid for incompressible flows, and a regularizing term $r(\cdot)$ depending on the first- or second-order spatial derivatives of the flow. The latter enforces spatially coherent flow estimates by bounding flow variation depending on a weighting parameter λ.

Basic and advanced examples for regularizers include (formulated for 2D problems $d = 2$) [9, 19]

$$r(Du) = \|\nabla u_1\|^2 + \|\nabla u_2\|^2 , \qquad r(D^2u) = \|\nabla \mathrm{div}(u)\|^2 + \|\nabla \mathrm{curl}(u)\|^2 . \tag{2}$$

The former term leads to reasonable estimates of low-turbulent flows [12] whereas the latter provides much more accurate estimates for highly turbulent flows. We point out that this second-order regularizer requires a careful discretization along with an additional term defined on the boundary $\partial\Omega$, in order to obtain unique and stable flow estimates from noisy image data [19]. By choosing a large weight for the term penalizing the divergence, nearly incompressible flows that are typical for 2D scenarios can be conveniently estimated, whereas strictly incompressible flows are better estimated by constrained variational methods as described next.

An extension of the first-order regularization approach to particle *tracking* velocimetry was studied in [13]. Unlike all other approaches discussed in this paper, however, this extension inherently leads to a *non*convex variational problem.

3 Constrained Variational Fluid Flow Estimation

Incompressible flows satisfy the constraint $\mathrm{div}(u) = 0$ approximately in 2D settings and strictly so in upcoming 3D scenarios. This section presents two variational approaches for estimating incompressible flows from image sequences.

3.1 Flow Estimation by Flow Control

The basic idea for constrained image flow estimation is to decouple data continuity term and regularization in (1) into an objective function and constraints. This enables regularization by enforcing flow properties strictly. A basic formulation reads [14]

$$\inf_{u,p,f,g} J(u,p,f,g)$$

with

$$J(u,p,f,g) = \int_\Omega \left\{ (\nabla I \cdot u + \partial_t I)^2 + \lambda \|f\|^2 \right\} dx + \gamma \int_{\partial\Omega} \|\partial_{\partial\Omega} g\|^2 ds \tag{3}$$

and subject to

$$\mu\Delta u + \nabla p = f \ \text{ in } \Omega , \quad \mathrm{div}(u) = 0 \ \text{ in } \Omega , \quad u = g \ \text{ on } \partial\Omega . \tag{4}$$

The functional (3) is minimized over all flows satisfying the Stokes equation (4). In comparison to (1), functional (3) additionally includes a multiplier function p related to the incompressibility constraint and control functions f, g as unknowns. These additional degrees of freedom can be determined because the set of admissible flows is constrained, and because control variables steer the constrained flow so as to fit as much as possible the observed optical flow in terms of the time-varying intensity function $I(x,t)$.

Additional regularization and numerical stability is achieved by slightly smoothing the control variables. The constraints reveal $f \propto \Delta u$, i.e. second-order regularization as in (2), but in a physically more strict way.

For scenarios with low Reynold numbers, this method yields physically consistent and accurate flow estimates. In such cases, p and f indeed may be interpreted as pressure and force field, estimated *from image data*. For higher Reynold numbers, these quantities become physically insignificant, yet still ensure highly accurate estimates of turbulent fluid flows through weakly constrained control functions f, g.

3.2 Enforcing Temporal Coherency

A computationally more expensive but still feasible method for additionally enforcing temporal coherency has been suggested in [15]. Flow estimation through constrained variational optimization

$$\inf_u J(u)\,, \quad J(u) = \int_\Omega \Big\{ (\nabla I \cdot u + \partial_t I)^2 + \lambda\,(\omega - \omega_T)^2 + \kappa \|\nabla \omega\|^2 \Big\} dx \tag{5}$$

subject to the linear constraints

$$\operatorname{div}(u) = 0\,, \quad \operatorname{curl}(u) = \omega\,, \tag{6}$$

is iterated with flow prediction through the vorticity transport equation

$$\partial_t \omega + u \cdot \nabla \omega = \nu \Delta \omega \quad \text{in } \Omega \times [0,T]\,, \quad \omega(x,0) = \omega_0\,. \tag{7}$$

Each flow estimate u by (5), (6) obtained for some image frame (point of time) defines the initial value $\omega_0 = \operatorname{curl}(u)$ in (7). A prediction ω_T of the flow for the period $[0,T]$ is then computed by (7). This curl field, in turn, is used to regularize the next flow estimate u in (5).

Numerical experiments show that although the implementation of this approach just needs two subsequent frames of an image sequence for estimating u at a specified point of time, the variational estimation-prediction framework effectively encodes a short-time memory over *many* frames that leads to physically consistent flow regularization both in space and time.

4 Constrained Fluid Flow Denoising in 3D

Our current work is focusing on a variational method for denoising fluid flow estimates in a physically consistent way. On the one hand, this task is more involved because we assume to be given as input data just a noisy vector field, *without* having access to the image data from which this fluid flow estimate was computed. On the other hand, our method is widely applicable, because vector fields produced by *any* method can be processed.

A second prominent feature of our method is that no explicit noise model is involved. Rather, the approach relies on modeling the class of physically admissible vector fields and regards anything else as noise. By this a broad range of both random and systematic errors can be removed by the very same approach, including white noise and local bursts of outliers, automatic completion of fluid estimates in local regions whose location is unknown, increasing the spatial resolution of fluid flow estimates, etc. A thorough study of the 2D case is reported in [17, 18]. The method equally applies in 3D, and we report preliminary results for the first time below.

4.1 Variational Approach

The method comprises four steps:

1. **Solenoidal Projection**
   As a first step, the given corrupted vector field d is projected onto the subspace of vector fields with vanishing divergence by solving

$$\Delta q = \operatorname{div}(d) \,, \quad q = 0 \ \text{ on } \partial\Omega \,, \tag{8}$$

   for q and removing the divergence from d,

$$v = d - \nabla q \,.$$

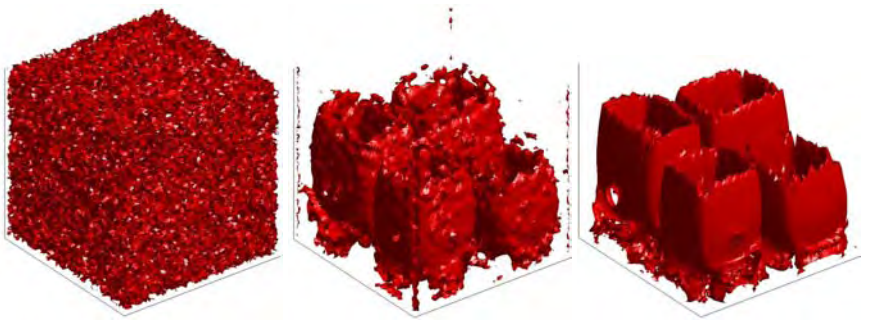

Fig. 1 Instantaneous snapshot of the vorticity of a four-cell vertical convection in three dimensions: noisy input (left), denoised result (center), ground truth (right)

2. **Lowpass Filtering**
   Next we remove high-frequency noise by filtering each component function of v with a Gaussian lowpass filter g_σ,

$$v_g = g_\sigma * v\,. \tag{9}$$

   The cutoff frequency is chosen large enough so as to preserve any relevant signal structure.
3. **Vorticity Rectification**
   The third step of the approach enhances the physical structures of v_g. To this end, we approximate its vorticity field

$$\omega_g = \nabla \times v_g\,, \tag{10}$$

   by solving the optimization problem

$$\inf_{\omega} J(\omega)\,, \qquad J(\omega) = \int_\Omega \Big\{ \|\omega - \omega_g\|^2 + \alpha\Big(\nu\|\nabla\times\omega\|^2 + 2\big\langle e(v_g), \omega\big\rangle\Big)\Big\} dx\,, \tag{11}$$

   where $e(v_g)$ is a shorthand for the left hand side of the vorticity transport equation

$$e(v) := \partial_t \omega + (v\cdot\nabla)\omega + (\omega\cdot\nabla)v = \nu\Delta\omega\,, \tag{12}$$

   whose 3D-formulation differs from the 2D case (7) by an additional term. The criterion (11) embodies a compromise between the approximation of ω_g in (10) and satisfying the vorticity transport equation (12).

   Note that $e(\cdot)$ is evaluated in (11) for the vector field v_g computed in the *previous* step. Furthermore, we omitted the time derivative $\partial_t\omega$ in order to restrict the computations to each individual image frame. This turned out to be a reasonable approximation in the cases considered so far. As a result, ω can be computed by just solving a large sparse linear system.
4. **Velocity Restoration**
   The final step of our approach recovers an incompressible, denoised vector field

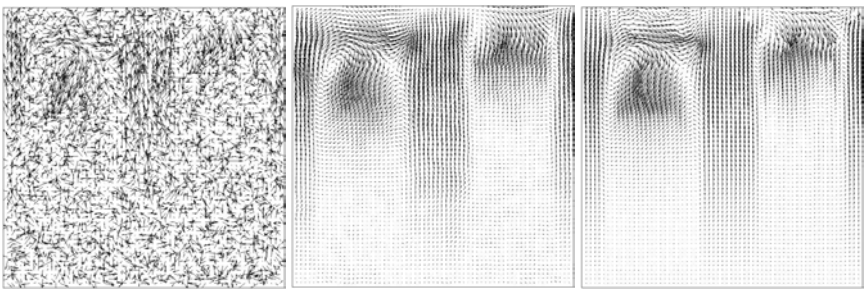

Fig. 2 Vertical cross-sections of the velocity fields through the centers of convective cells. These vector fields correspond to the vorticities shown in Figure 1: noisy input (left), denoised result (center), ground truth (right)

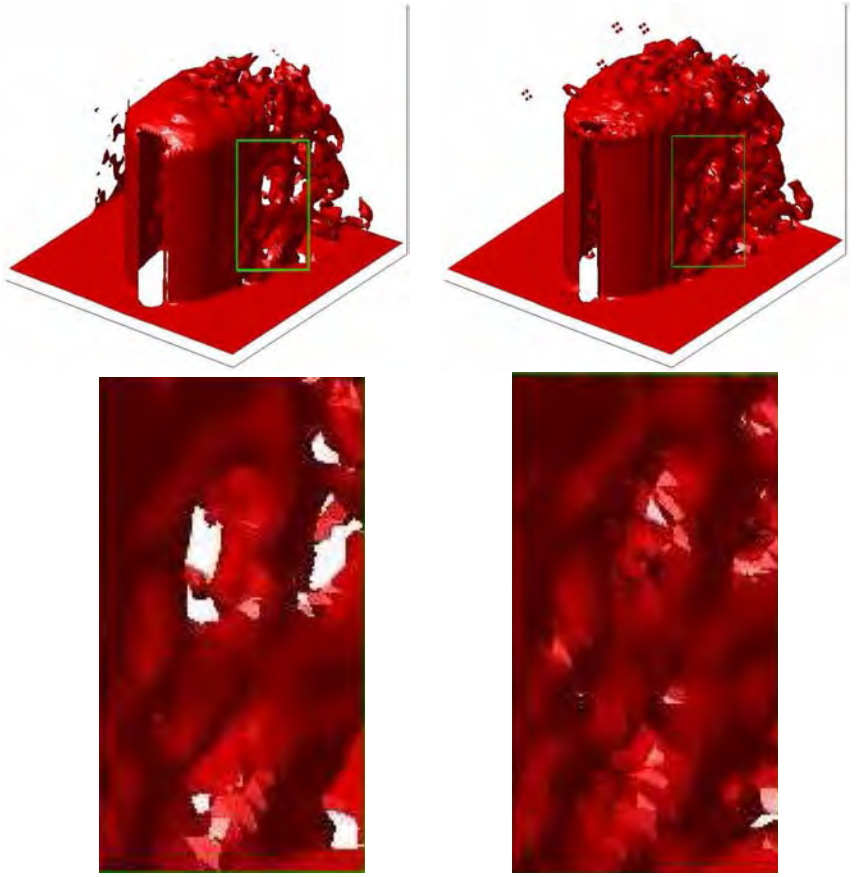

Fig. 3 Top: Instantaneous snapshot of the vorticity of a flow around a cylinder in three dimensions: denoised result (left) and ground truth (right). **Bottom:** the corresponding close-up views

from ω by minimizing

$$\inf_u J(u)\,, \quad J(u) = \int_\Omega \left\{ \|u - v_g\|^2 + \beta \|\nabla \times u - \omega_g\|^2 \right\} dx\,, \tag{13}$$

subject to

$$\operatorname{div}(u) = 0\,. \tag{14}$$

The minimizer u approximates both the velocity fields (9) and the rectified vorticity field (11).

Problem (13), (14) leads to a simple version of the saddle-point problem corresponding to (3), (4). For a consistent discretization with mixed finite elements, we refer to [14].

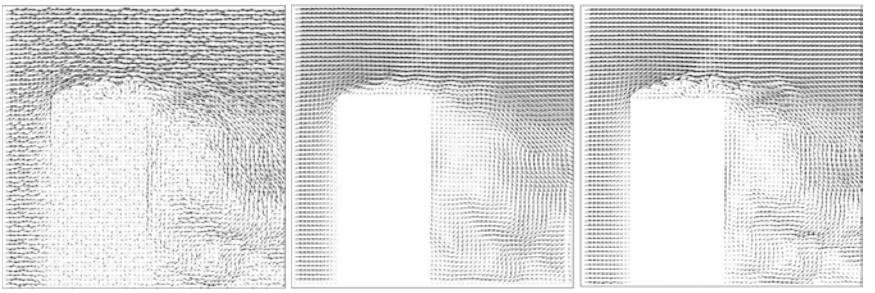

Fig. 4 Vertical cross-sections of the velocity fields through the centers of convective cells. These vector fields correspond to the vorticities shown in Figure 3: noisy input (left), denoised result (center), ground truth (right)

4.2 Numerical Experiments

We illustrate the performance of our method by visualizing input and output data of two experiments. In both cases, vector fields resulting from a direct numerical simulation [6] served both as ground truth and as input data after corrupting them with white noise.

The first experiment concerns a vertical convection process in 3D with a large noise level. Figure 1 shows, from left to right, the vorticity of the input data, the denoised vector field u from (13), (14), and ground truth. Figure 2 depicts corresponding cross-sections to illustrate the signal-to-noise level.

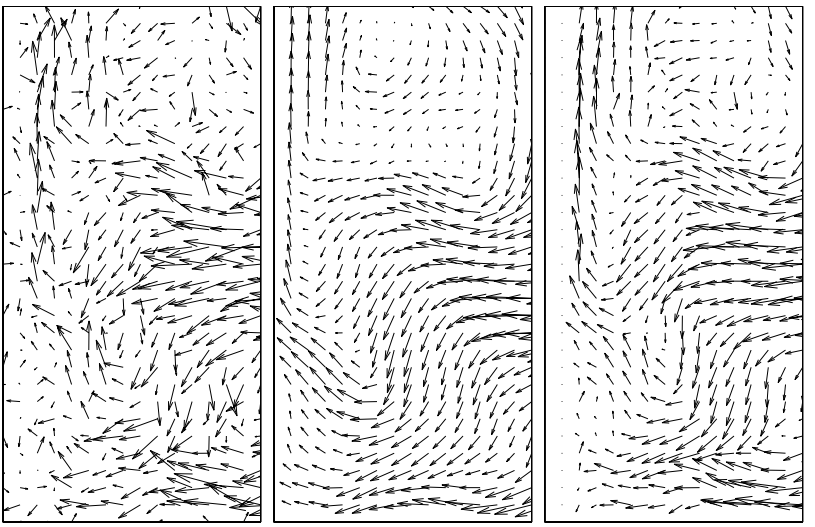

Fig. 5 Close-up views of the vector fields depicted in Figure 4 corresponding to the sections marked in Figure 3: noisy input (left), denoised result (center), ground truth (right)

The second experiment concerns a turbulent flow around a cylinder with smaller noise level. Figure 3 shows the vorticity of the input data (left panel) and the denoised output (right panel), respectively, together with two close-up views. Cross-sections analogously to Figure 2 are shown in Figure 4. Close-up views of these vector fields corresponding to the sections shown on the right in Figure 3, are depicted in Figure 5.

5 Conclusion and Further Work

We presented a range of variational methods for physically consistent image processing in experimental fluid dynamics. Our results demonstrate the ability of variational approaches to seamlessly integrate physical prior knowledge. This is particularly relevant for upcoming 3D scenarios in connection with tomographical methods in experimental fluid dyamics.

Another important points is that the mathematical aspects of variational methods and corresponding algorithms are similar to those used in numerical simulations. This may help to tie together in the long run approaches of experimental fluid dynamics and numerical simulation in order to bring to bear the synergy between these complementary fields of research.

This paper mainly focused on aspects of regularization and their physical consistency. The data terms in all approaches above are based on the continuity equation $\frac{d}{dt}I(x,t) = 0$, which is known to be less robust than correlation-based PIV-approaches in very noisy scenarios. Hybrid variational approaches that combine adaptive correlation-based schemes [2] or alternative more advanced local estimation schemes [7] with nonlocal physical priors as presented in this paper (cf. also [8]), is a promising direction for future research.

Acknowledgements. The authors would like to thank the German Science Foundation (DFG) for supporting this work within the priority research program 1147, "Imaging Measurement Methods for Flow Analysis", under grant SCHN 457/9-1,3. The authors enjoyed collaboration, fruitful discussions and data exchange with many partners of the priority program, including Volker Beushausen, Christoph Brücker, Cornelia Denz, Octavian Frederich, Christoph Garbe, Rainer Hain, Bernd Jähne, Christian Kähler, Hans-Gerd Maas, Wolfgang Nitsche, Holger Nobach, Torsten Putze, Frank Thiele, Cam Tropea, and Rüdiger Westermann.

References

1. Adrian, R.J.: Twenty years of particle velocimetry. Exp. Fluids 39(2), 159–169 (2005)
2. Becker, F., Wieneke, B., Yuan, J., Schnörr, C.: A variational approach to adaptive correlation for motion estimation in particle image velocimetry. In: Rigoll, G. (ed.) DAGM 2008. LNCS, vol. 5096, pp. 335–344. Springer, Heidelberg (2008)
3. Corpetti, T., Mémin, É., Pérez, P.: Dense Estimation of Fluid Flows. IEEE Trans. Patt. Anal. Mach. Intell. 24(3), 365–380 (2002)

4. Corpetti, T., Heitz, D., Arroyo, D., Mémin, É., Santa-Cruz, A.: Fluid experimental flow estimation based on an optical-flow scheme. Exp. Fluids 40(1), 80–97 (2006)
5. Cuzol, A., Hellier, P., Mémin, É.: A Low Dimensional Fluid Motion Estimator. Int. J. Computer Vision 75(3), 329–349 (2007)
6. Frederich, O., Wassen, E., Thiele, F.: Prediction of the flow around a short wall-mounted cylinder using LES and DES. J. Numer. Analysis, Industrial and Appl. Mathematics 3(3-4), 231–247 (2008)
7. Garbe, C., Kondermann, D., Jähne, B.: Spatiotemporal image analysis for fluid flow measurements. In: Nitsche, W., Dobriloff, C. (eds.) Imaging Measurement Methods. NNFM, vol. 106. Springer, Heidelberg (2009)
8. Heitz, D., Héas, P., Mémin, É., Carlier, J.: Dynamics consistent correlation-variational approach for robust optical flow estimation. Exp. Fluids 45, 595–608 (2008)
9. Horn, B.K.P., Schunck, B.G.: Determining Optical Flow. Artif. Intelligence 17, 185–203 (1981)
10. Papadakis, N., Mémin, É.: Variational Assimilation of Fluid Motion from Image Sequence. SIAM J. Imag. Sci. 1(4), 343–363 (2008)
11. Raffel, M., Willert, C.E., Wereley, S.T., Kompenhans, J.: Particle Image Velocimery – A Practical Guide. Springer, Heidelberg (2007)
12. Ruhnau, P., Kohlberger, T., Nobach, H., Schnörr, C.: Variational optical flow estimation for particle image velocimetry. Exp. Fluids 38, 21–32 (2005)
13. Ruhnau, P., Gütter, C., Putze, T., Schnörr, C.: A variational approach for particle tracking velocimetry. Meas. Science and Techn. 16, 1449–1458 (2005)
14. Ruhnau, P., Schnörr, C.: Optical stokes flow estimation: An imaging-based control approach. Exp. in Fluids 42, 61–78 (2007)
15. Ruhnau, P., Stahl, A., Schnörr, C.: Variational estimation of experimental fluid flows with physics-based spatio-temporal regularization. Meas. Science and Techn. 18, 755–763 (2007)
16. Tropea, C., Yarin, A.L., Foss, J.F. (eds.): Springer Handbook of Experimental Fluid Mechanics. Springer, Heidelberg (2007)
17. Vlasenko, A., Schnörr, C.: Physically consistent variational denoising of image fluid flow estimates. In: Rigoll, G. (ed.) DAGM 2008. LNCS, vol. 5096, pp. 406–415. Springer, Heidelberg (2008)
18. Vlasenko, A., Schnörr, C.: Physically consistent and efficient variational denoising of image fluid flow estimates. IEEE Trans. Image Processing (2008) (submitted)
19. Yuan, J., Schnörr, C., Mémin, E.: Discrete orthogonal decomposition and variational fluid flow estimation. J. Math. Imag. Vision 28, 67–80 (2007)
20. Yuan, J., Schnörr, C., Steidl, G.: Simultaneous optical flow estimation and decomposition. SIAM J. Scientific Computing 29(6), 2283–2304 (2007)
21. Yuan, J., Steidl, G., Schnörr, C.: Convex hodge decomposition and regularization of image flows. J. Math. Imaging and Vision (2008), doi:10.1007/s10851-008-0122-1

Real-Time Approaches for Model-Based PIV and Visual Fluid Analysis

Polina Kondratieva, Kai Bürger, Joachim Georgii, and Rüdiger Westermann

Abstract. In this research project, approaches for the reliable reconstruction of flow fields from captured particle images and their visualization have been developed. One aspect has been on developing techniques that can generate a velocity field that is consistent with a selected physical fluid model. Therefore, we have introduced a model-based approach that integrates a priori knowledge of this model into the reconstruction process. Another aspect has been on the design of techniques that are capable of dealing with real-time constraints, and which thus have the potential to be used in combination with high-speed camera systems to interactively steer the reconstruction process. Programmable graphics hardware has been exploited as a co-processor for numerical computations to achieve interactivity, both for the reconstruction and visualization of generated fields. All these techniques have been verified in an experiment on living microorganisms. In the last phase of the project we have focused on the extension of the techniques towards the processing of 3D particle images and the visualization of the reconstructed flow fields.

1 Introduction

Particle Image Velocimetry (PIV) has established as a powerful tool to experimentally determine flow structures in real fluids. Such systems provide image pairs of seeded particles at successive time steps, which are then registered on each other to reveal the unknown velocity field. Unfortunately, due to limitations of the seeding, imaging and registration processes, reliable reconstruction of velocity fields from captured images is greatly complicated. This is especially the case when experiments on living organisms are carried out, which implies that the illumination must not be too powerful and the density and size of seeded particles are limited. Due

Polina Kondratieva · Kai Bürger · Joachim Georgii · Rüdiger Westermann
Computer Graphics & Visualization Group, Technische Universität München, 85748 Garching bei München, Germany
{kondrati,buergerk,georgii,westermann}@in.tum.de

W. Nitsche and C. Dobriloff (Eds.): Imaging Measurement Methods, NNFM 106, pp. 257–267.
springerlink.com

to these restrictions the accurate reconstruction of velocity fields from such images are prone to artifacts and outliers, and the resulting fields, in general, do not comply with the physical model of the flow.

To address the aforementioned limitations, we have developed a model-based approach for the reconstruction of the motion of seeded particles from particle images. This technique exploits a priori knowledge about the physical flow model to make the motion consistent with the laws of physics. The reconstruction process has been combined with advanced visualization techniques to enable immediate visual analysis of the reconstructed fields, and it can thus be used to interactively control parameters of the experimental apparatus as well as the reconstruction process. The following specific contributions have been achieved in this project:

- FFT-based cross-correlation and multigrid optical flow have been implemented and used to predict an initial flow field from particle image pairs.
- The predicted field is corrected iteratively by a global filter operation that implements a numerical solver to the incompressible Navier-Stokes equations.
- To simulate the interaction between the fluid and organisms in the flow, boundaries and boundary conditions are considered in the correction step.
- Particle-based 2D and 3D flow visualization techniques including a set of importance measures like vorticity, helicity, lambda-2, or Lyapunov exponent have been developed.
- All stages of the reconstruction and visualization process have been implemented on programmable graphics hardware to achieve real-time performance.

The remainder of this paper is organized as follows. In Sect. 2 we briefly review previous work that is related to ours. In Sect. 3 we describe our novel approach for the model-based reconstruction of vector fields from particle images. The specific visualization options we have developed for the visual analysis of complex 2D and 3D flow fields are discussed in Sect. 4. In each section with present a detailed discussion and validation of the proposed techniques.

2 Related Work

Particle Image Velocimetry (PIV) is an optical technique used to measure the velocity of seeded particles in a real flow [27, 26, 21]. It is performed by capturing consecutive images of particles in the flow and then processing these images to determine particle displacements over time. Over the last years, a number of different approaches have been proposed for the reconstruction of these displacements from recorded images, which can roughly be classified into two categories: techniques based on *cross-correlation* (CC) analysis and *optical flow* (OF) computation.

CC-based techniques divide the image plane into small disjoint or overlapping interrogation windows and then compute the cross-correlation between corresponding window pairs in consecutive recordings. The spatial displacement that produces the maximum cross-correlation approximates statistically the average displacement of

particles in the interrogation window. For a thorough overview of these techniques we refer to [26, 21]. There is also a vast body of literature on the improvement of CC-based techniques that we will not attempt to overview here, however, [24, 16] provide many useful references on this subject and discuss some of the numerous approaches, including reduction of peak locking, predictor-corrector schemes, hierarchical methods as well as advanced post-processing techniques for outlier removal.

Whole-field methods based on the optical flow [7, 20, 23], on the other hand, can avoid the direct correlation between spatial resolution and probability of false estimates that is inherent to CC-based PIV-techniques. The optical flow estimates the motion of brightness patterns in two images by minimizing a global cost function, which represents the rate of change of image brightness. Since the original problem is ill-posed, a *regularizer* assuming smooth movements between adjacent pixels is typically used in the solution process.

To further improve OF-based reconstruction of flow fields from particle images, regularizers taking into account the physical model of the flow have been presented in [5, 3, 15, 4]. Recently, [22] proposed a variational approach using the Stokes equation as prior knowledge. By incorporating the motion characteristics of a viscous fluid in the optical flow estimation, the method computes a motion field that satisfies the prescribed flow model.

3 Model-Based Flow Reconstruction

Given a pair of particle images, both CC- and OF-based reconstruction methods aim at finding a non-parametric spatial transformation that deforms one image in such a way as to minimize the difference between the deformed and the second image. This non-parametric minimization problem can be solved using a regularization term according to the properties of the deformed materials. For instance, it can be based on the elastic potential (elastic registration) or the governing equations of fluid motion (fluid registration). A comprehensive survey and discussion of non-parametric motion models can be found in [14].

In this project we have proposed a model-based approach for the computation of a non-parametric transformation describing the motion of seeded particles in real flows [9, 18, 10]. In particular, our goal has been to determine the flow induced by living microorganisms, i.e., ciliates, and thus to gain insight into their feeding mechanisms and fluid exchange characteristics. The flows induced by these organisms are characterized by very low Reynolds numbers and they can thus be modeled by the Stokes flow equations. In regard to this observation, our method takes as input a predicted vector field and then corrects the field according to this specific flow model. The input field is computed from experimental image pairs using CC or OF estimation, and the correction is performed by applying a model-based global filter operation on it. This filter implements a numerical solver to the flow equations. An overview of the algorithm is presented in Fig. 1.

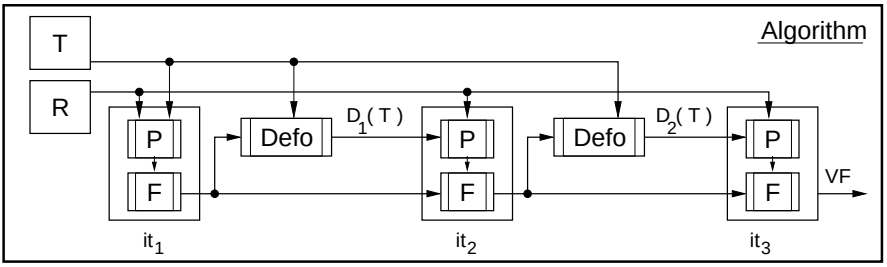

Fig. 1 Illustration of the model-based reconstruction process: Module `P` reads images `T` and `R` and computes the displacement field using CC or OF. Module `F` corrects the predicted field. Module `Defo` deforms `T` towards `R` using the corrected field. This process is repeated with the deformed image $D_i(T)$ until the average magnitude of the corrected field falls below a selected threshold

3.1 Flow Prediction and Correction

To predict an initial displacement field from a given pair of particle images, we have developed fast versions of both CC and OF on highly parallel graphics processing units (GPUs). Recent developments have shown, that the GPU can significantly outperform CPU implementations for both compute- and memory-intensive applications. A comprehensive collection of research papers in this particular area can be found in [17].

The direct cross-correlation between window pairs is computed by means of the discrete Fast-Fourier-Transform (FFT), i.e., by computing the cross-correlation between two signals in the frequency domain. Our GPU implementation of the FFT as proposed in [25] exploits the fact that the FFT can be written as a matrix-vector product, where the matrix can be further split into a chain of sparse matrices with a fixed structure for a particular window size. The multiplication of an input vector with these matrices can be carried out very efficiently on recent GPUs, and, in particular, due to the massively parallel nature of this architecture multiple window pairs can be cross-correlated in parallel.

For the implementation of OF-based flow prediction we have utilized a library for linear algebra on GPUs [11]. Our implementation takes advantage of the special structure of the OF system matrix, which is a sparse band-diagonal matrix for which special classes are available in this library. Standard iterative methods like the conjugate-gradient method can then be applied directly on the GPU to solve for the unknown velocity field. To further improve the efficiency of the OF computation, for the first time ever to our best knowledge we have developed a geometric multigrid scheme on the GPU. For a good introduction to the theory and applications of multigrid approaches let us refer to [6], and to [13, 8, 23] for the design of multigrid OF.

Table 1 compares the performance of CC- and OF-PIV on the GPU. For CC-PIV we have considered interrogation windows of different size. As can be seen, CC-PIV is significantly faster than its OF-based counterpart. On the other hand, a qualitative

Table 1 Performance of CC- and OF-PIV (in brackets) in ms. Since OF is a whole-field method, the size of the window pairs has no meaning

window/image	256^2	512^2	1024^2
8^2	0.8(37)	2.5(160)	8.3(760)
16^2	1.1(37)	3.3(160)	12.4(760)
32^2	1.4(37)	3.8(160)	15.7(760)

comparison of both approaches in the context of model-based flow reconstruction as given at the end of this section clearly reveals the strength of OF-based PIV.

3.2 Vector Field Correction

Vector field correction is performed by using the estimated field in a numerical solution of the incompressible Navier-Stokes equations (NSE), equipped with the Reynolds number of the fluid as well as appropriate boundary conditions and an external force field. The NSE are solved on the GPU by first solving explicitly for the velocity and then by solving implicitly for the pressure using a conjugate-gradient method. Pressure is finally used as a correction term to make the vector field free of divergence.

In all of our experiments, *outflow* boundary conditions have been enforced at the outer domain border. In the experiments involving living microorganisms, we have first extracted these organisms from the recorded template image using standard image segmentation techniques, and we have then considered them as obstacles in the numerical solution. Since the liquid surrounding the microorganisms is not penetrating the main body of the microorganism, *no-slip* boundary conditions have been assumed at the organism boundaries. In every iteration a force field is computed from the estimated displacement field disp_{esp} according to Stokes' law:

$$F_{Stokes} = 6\,\pi\,\mu\,r\,\cdot(\mathrm{disp}_{est}\cdot \mathrm{pxsize}/\Delta t)\,. \tag{1}$$

This yields at every pixel the external force that is required to move a spherical particle of radius r through the fluid of viscosity μ at a velocity that is equal to the displacement in the pixel grid over one time step Δt. We can thus derive an external force field, which ideally results in a velocity field equal to the estimated displacement field if considered in the NSE-solution. However, since the displacement field does not comply with the underlying flow model in general, the resulting velocity field will differ from this field in that it is corrected towards consistency with this model.

3.3 Results

In a first experiment we have generated two images by passively advecting dye in a swirl-like Navier-Stokes flow and by capturing the dye intensity at two different time

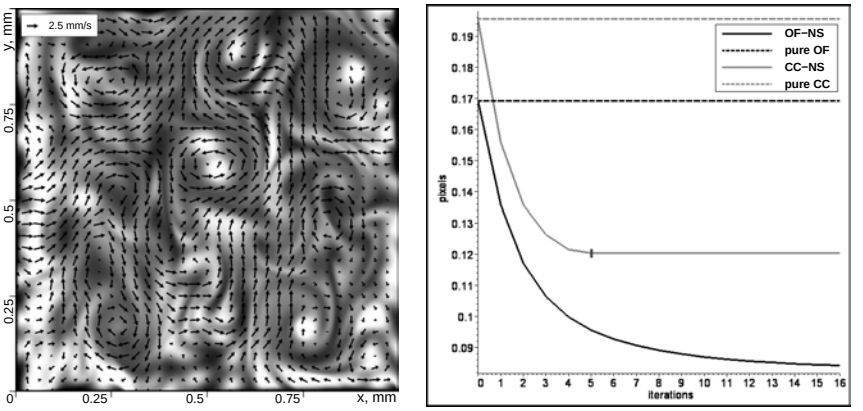

Fig. 2 (**a**) Ground-truth Navier-Stokes flow. (**b**) Average error of the velocity magnitude as a function of the number of iterations

steps. The flow was simulated using the following parameters: grid size of 256×256 pixels, Reynolds number Re = 10, density $\rho = 1000\ \mathrm{kg/m^3}$, dynamic viscosity $\mu = 0.001\ \mathrm{kg/(m \cdot s)}$, time between two exposures $dt = 0.775$ ms, and pixel size `pxsize` = 3.906 μm. The simulation yields a maximum and average displacement of 1.1 pixels and 0.2 pixels between two exposures, respectively. Fig. 2a shows the ground truth velocity profile overlaid on one of the synthetic images.

Fig. 2b shows the graph of the average error of the velocity magnitude as a function of the number of predictor-corrector iterations. Due to the highly non-uniform nature of the flow, including multiple small-scale structures, the CC approach has

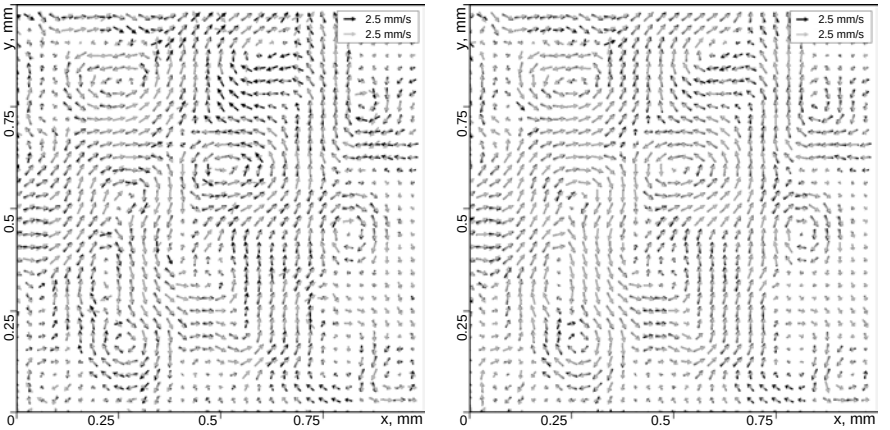

Fig. 3 Navier-Stokes flow: Ground truth vector field (black arrows) versus reconstructed vector field (light gray arrows) using CC-NS (left) and OF-NS (right). Visually, the less of the black arrows can be seen the more accurate is the reconstruction with respect to direction

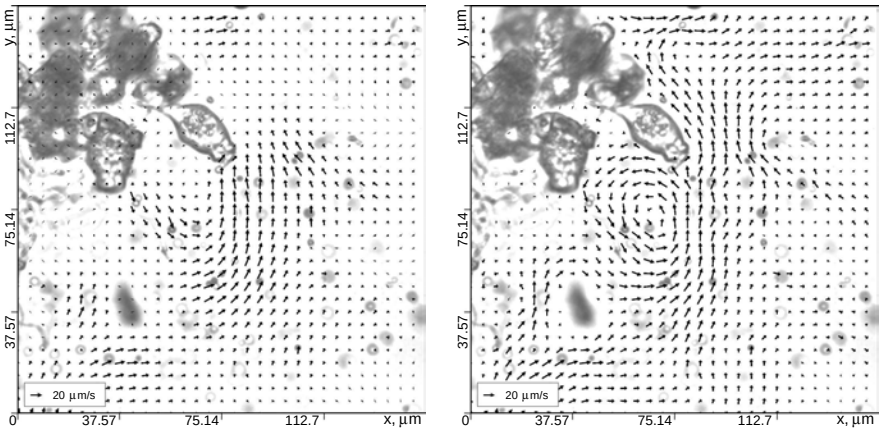

Fig. 4 Real-world experiment: Reconstructed velocity fields using OF and OF-NS. Only the model-based approach can reconstruct one of the vortices typically observed in nature

severe problems in reconstructing the velocity field. After the first iteration the model-based approaches (model-based correction with CC-based (CC-NS) and OF-based (OF-NS) prediction) already yield better fidelity than the CC and the OF method. With increasing number of iterations the predictor-corrector approaches can improve the reconstruction quality even further, with the OF-NS approach showing a much faster convergence than the CC-NS approach. Moreover, the CC-NS approach stops improving the results after the 5th iteration, because corrected displacements become too small and heterogeneous for the CC approach to be detected.

A comparative visualization of the reconstructed velocity fields using overlaid arrow plots is shown in Fig. 3. Black arrows correspond to the ground truth velocity field. Light gray arrows depict the vector fields reconstructed with CC-NS and OF-NS. While the CC-NS approach can reconstruct most of the main flow structures, it cannot compensate for the high rate of erroneous velocities introduced by the CC predictor. The OF-NS approach, in comparison, recovers the flow at extremely high accuracy. For a more thorough evaluation of our proposed model-based approach let us refer to [10].

In Fig. 4, for two bio-compatible measurements of the particle distribution in fluid flows induced by living ciliates the reconstructed velocity fields using OF and OF-NS are shown. In the OF-NS approach, 8 predictor-corrector iterations were performed. Both approaches are capable of recovering a flow that conforms to the characteristic flow pattern observed in nature. However, in regions with low particle density the OF approach reconstructs velocities close to zero, and it fails to recover a strong viscous eddy induced by the movement of the active ciliate. The predictor-corrector scheme, on the other hand, extracts a strong viscous vortex to the left of the ciliate and estimates an admissible velocity distribution in low density regions.

4 Particle-Based Flow Visualization

Besides the model-based reconstruction of vector fields from particle image pairs, we have developed a particle system for the interactive visualization of 2D and 3D vector fields as they are generated by PIV. For a thorough overview of particle-based and related integration-based techniques for flow visualization let us refer to [19]. In particular, we have exploited features of recent GPUs to numerically integrate particles along their trajectories and to immediately visualize these particles using specific geometric shapes and colors [1, 12]. Figure 5 shows a number of different particle shapes used for the interactive visualization of a 2D flow fields at fully interactive rates.

Since particle-based visualization, especially in 3D, quickly overextends the viewer due to the massive amount of visual information that is conveyed, we have also developed strategies to reduce this amount at the same time revealing important structures in the flow [2]. As an importance measure, we have introduced a new focus for particle tracing, so called anchor lines. Anchor lines are used to analyze local flow features by visualizing how much particles separate over time and how long it takes until they have separated to a fixed distance. It is of particular interest if

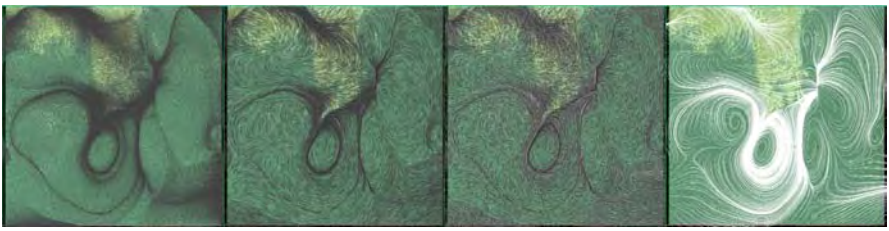

Fig. 5 Particle-based visualization of a 2D flow induced by micro-biological structures. From left to right, transparent ellipsoidal sprites, enlarged transparent ellipsoidal sprites, transparent arrows and stream lines are shown. For 1 million particles, 60 integration steps per second can be performed using an interpolation scheme of order 3 on a recent GPU

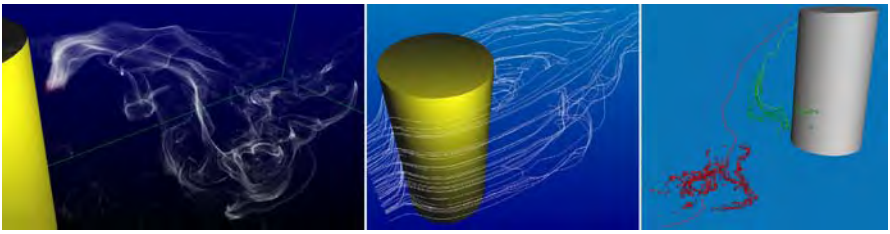

Fig. 6 Particle-based visualization of 3D instationary flows using semi-transparent sprites (left) and path lines (right). Anchor lines (path lines) and particles seeded close to the anchor lines starting points are shown on the right. Particle transparency is inversely proportional to the separation distance of particles from the anchor line

the finite time Lyapunov exponent - a scalar quantity that measures the rate of separation of infinitesimally close particles in the flow - is used to guide the placement of anchor lines. We employ this measure for the selection of characteristic trajectories in the flow. Specifically, we seed particles close to the starting points of these lines, and we only visualize those particles that leave the anchor. In this way, the amount of visual information can be reduced significantly (see Figure 6), and quantitative statements about particle movements over time and space can be derived.

5 Current and Future Work

In the last phase of the project we have put some efforts into the extension of the proposed model-based approach for vector field reconstruction towards 3D. Even though measured 3D particle distributions have not yet been available to us, we have started to develop a 3D simulation engine that is able to correct a given 3D displacement field in a model-based manner as described in Sect. 3. Therefore, we have a) extended our GPU-based NSE solver towards 3D and b) realized a novel 3D GPU-based Lattice-Boltzmann solver. Both solvers can handle free-moving obstacles and can thus be used to determine the flow induced by living organisms. Fig. 7 shows two 3D simulations that have been generated using these solvers, including obstacles and appropriate boundary conditions.

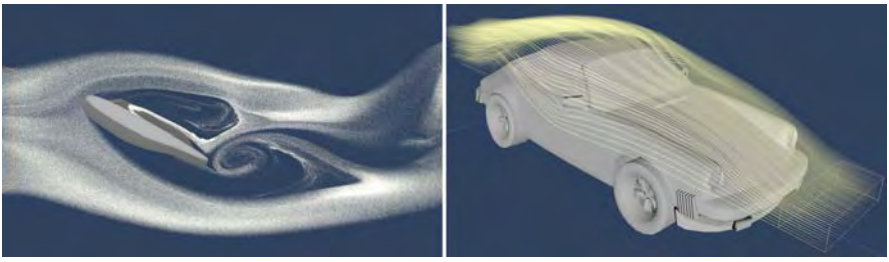

Fig. 7 3D fluid simulations on the GPU using 3D Navier-Stokes (left) and Lattice-Boltzmann (right) solvers are shown. For a $128^2 \times 256$ grid the numerical simulation runs at 8 and 35 simulation steps per second, respectively, including free-moving obstacles and inflow boundaries

Both solvers have been integrated into the particle engine to allow for an immediate visual feedback and analysis of the simulated fields. Thus, a general framework for the model-based reconstruction of flow fields from 3D particle distributions has been developed, which now has to be equipped with an appropriate method to estimate an initial displacement field from such measurements. In the future, we will thus focus our research on the realization of 3D-OF on GPUs and the integration of this approach into the proposed 3D simulation and visualization framework.

Acknowledgement. We would like to thank the German Research Foundation for supporting our project in the Priority Program 1147 ”Bildgebende Messverfahren für die

Strömungsanalyse". We would also like to thank our collaborators, Prof. C. Denz, University of Münster, and Prof. A. Delgado, University Erlangen-Nuremberg, for their valuable advices and support in this project.

References

1. Bürger, K., Schneider, J., Kondratieva, P., Krüger, J., Westermann, R.: Interactive visual exploration of instationary 3D-flows. In: Eurographics/IEEE VGTC Symposium on Visualization (EuroVis) (2007)
2. Bürger, K., Kondratieva, P., Krüger, J., Westermann, R.: Importance-driven particle techniques for flow visualization. In: Proceedings of IEEE VGTC Pacific Visualization Symposium (2008)
3. Corpetti, T., Mémin, E., Pérez, P.: Estimating fluid optical flow. In: 15th Int. Conf. Pattern Recognition, vol. 3, pp. 1045–1048 (2000)
4. Corpetti, T., Heitz, D., Arroyo, G., Mémin, E., Santa-Cruz, A.: Fluid experimental flow estimation based on an optical-flow scheme. Exp. Fluids 40(1), 80–97 (2005)
5. Gupta, S., Prince, J.: Stochastic models for div-curl optical flow methods. Signal Proc. Lett. 3(2), 32–34 (1996)
6. Hackbusch, W.: Iterative Solutions of Large Sparse Systems of Equations. Springer, New York (1994)
7. Horn, B., Schunck, B.: Determining optical flow. Artif. Intell. 17, 185–203 (1981)
8. Kalmoun, E.M., Rüde, U.: A variational multigrid for computing the optical flow. In: Vision, Modeling, and Visualization Conference, pp. 577–584 (2003)
9. Kondratieva, P., Georgii, J., Westermann, R.: Echtzeitverfahren zur modellbasierten rekonstruktion von strömungsfeldern aus experimentell bestimmten partikelsequenzen. In: 14. GALA Fachtagung, Lasermethoden in der Strömungsmesstechnik (2006)
10. Kondratieva, P., Georgii, J., Petermeier, H., Kowalczyk, W., Delgado, A., Westermann, R.: A real-time model-based approach for the reconstruction of fluid flows induced by microorganisms. Experiments in Fluids 45(2), 203–222 (2008)
11. Krüger, J., Westermann, R.: Linear algebra operators for GPU implementation of numerical algorithms. ACM Transactions on Graphics 22(3), 908–916 (2003)
12. Krüger, J., Kipfer, P., Kondratieva, P., Westermann, R.: A particle system for interactive visualization of 3D flows. IEEE Transactions on Visualization and Computer Graphics 11(6), 744–756 (2005)
13. Mémin, E., Pérez, P.: A multigrid approach for hierarchical motion estimation. In: International Conference on Computer Vision, pp. 933–938 (1998)
14. Modersitzki, J.: Numerical Methods for Image Registration. Oxford university press, New York (2004)
15. Nakajima, Y., Inomata, H., Nogawa, H., Sato, Y., Tamura, S., Okazaki, K., Torii, S.: Physics-based flow estimation of fluids. Pattern Recognition 36(5), 1203–1212 (2003)
16. Nobach, H., Ouellette, N.T., Bodenschatz, E., Tropea, C.: Full-field correlation-based image processing for PIV. In: 6th International Symposium on Particle Image Velocimetry (2005)
17. Owens, J.D., Luebke, D., Govindaraju, N., Harris, M., Krüger, J., Lefohn, A.E., Purcell, T.J.: A survey of general-purpose computation on graphics hardware. In: Computer Graphics Forum, vol. 26, pp. 80–113 (2007)

18. Petermeier, H., Delgado, A., Kondratieva, P., Westermann, R., Holtmann, F., Krishnamachari, V., Denz, C.: A hybrid approach between experiment and evaluation for artefact detection and flow field reconstruction. In: 12th International Symposium on Flow Visualization (2006)
19. Post, F.H., Vrolijk, B., Hauser, H., Laramee, R.S., Doleisch, H.: The state of the art in flow visualisation: Feature extraction and tracking. Computer Graphics Forum 22(4), 775–792 (2003)
20. Quenot, G.M., Pakleza, J.D., Kowalewski, T.A.: Particle image velocimetry with optical flow. Exp. Fluids 25(3), 177–189 (1998)
21. Raffel, M., Willert, C.E., Kompenhans, J.: Particle image velocimetry: A practical guide, 2nd edn. Springer, Heidelberg (2001)
22. Ruhnau, P., Schnörr, C.: Optical stokes flow estimation: An imaging-based control approach. Exp. Fluids 42(1), 61–78 (2007)
23. Ruhnau, P., Kohlberger, T., Schnörr, C., Nobach, H.: Variational optical flow estimation for particle image velocimetry. Exp. Fluids 38(1), 21–32 (2005)
24. Scarano, F.: Iterative image deformation methods in PIV. Meas. Sci. and Technol. 13(1), R1–R19 (2002)
25. Schiwietz, T., Westermann, R.: Gpu-piv. In: Vision, Modeling and Visualization 2004 (2004)
26. Westerweel, J.: Digital particle image velocimetry: Theory and application. PhD thesis, Delft University of Technology (1993)
27. Willert, C., Gharib, M.: Digital particle image velocimetry. Exp. Fluids 10(4), 181–193 (1991)

Biocompatible Visualization of Flow Fields Generated by Microorganisms

Bogumila Ewelina Zima-Kulisiewicz, Emanuela Botello-Payro, and Antonio Delgado

Abstract. Microflow induced by the ciliates called *Opercularia asymmetrica* is an interesting phenomenon in biofluidmechanics. Ciliates play an important role in the structural formation of microbial granules derived from activated sludge. Additionally, flow induced by protozoa (ciliates) is treated as an efficient mean of nutrient transport with minimum energy requirement. For the first time powerful digital imaging techniques are used for studying microorganismic convection. Investigations of the flow generated by *Opercularia asymmetrica* are carried out with help of digital micro Particle Image Velocimetry. Digital micro Particle Tracking Velocimetry is implemented to analyse cilia motion. In biological fluid mechanics flow visualization techniques must guarantee biocompatibility. Thus, in the present work appropriate light illumination and suitable seeding particles are used. Moreover, in order to predict artefacts and correct them novel neuronumerical hybrid is employed.

1 Introduction

Bioflow studies become an interesting field in microfluidcs. As an example flow induced by microorganisms living on Granular Activated Sludge (GAS) surface is given. Wastewater treatment based on growing GAS in a Sequencing Batch Reactor (SBR) is a multiscale phenomena in which macroscopic effects are controlled by microscopic causes. Several studies show that GAS consists of bacteria, fungi and protozoa connected together by extracellular polymeric substances (EPS) [5, 14, 16]. According to [16] and [20] protozoa (ciliates) are treated as backbone for the granulation process. The granules formation can be described as a three steps process [16]. Firstly ciliates settle on other organisms or particles and bulky growth of ciliates is recognized (e.g. *Epistylis* sp.). Stalks and zooids are colonized by bacteria. The cilia beats of the ciliates providing a continuous nutrient flux toward biofilm improve the colonization process. As a result, the granule grows and the core zone is developed. Here, many ciliates cells are completely overgrown by

Bogumila Ewelina Zima-Kulisiewicz · Emanuela Botello-Payro · Antonio Delgado
Institute of Fluid Mechanics, Technical Faculty, Friedrich-Alexander University Erlangen-Nuremberg, Cauerstrasse 4, 91058 Erlangen, Germany

W. Nitsche and C. Dobriloff (Eds.): Imaging Measurement Methods, NNFM 106, pp. 269–278.
springerlink.com

bacteria and die. A dense core of bacteria and remains of ciliate stalks is formed. Subsequently, a mature granule is developed. Finally, granules are composed of two zones (core zone and loose structured fringe zone) and serve as a new substrate for swarming ciliates. Investigations of [10] indicate that flow induced by the ciliates can be treated as efficient nutrient transport to the biofilm with minimum energy requirement.

However, microflow induced by *Opercularia asymmetrica* is poorly investigated in the literature and an intensive research is necessary for making progress towards better understanding of these natural phenomena which have been optimized in the course of evolution. In order to visualise fluid flow induced in biological systems powerful imaging methods for flow analysis are required. Flow induced by peritrichous ciliates was analysed for the first time by [13]. [15] studied flow field of marine peritrichous ciliates. First studies with *Opercularia asymmetrica* were carried out by [3, 6, 7, 10]. It is of crucial importance that the measuring and flow visualisation techniques employed must guarantee biocompatibility, i.e. they can not affect investigated biosystems. Unfortunately, this restricts possibilities for optimizing the image generation in comparison to other flow field visualisation problems in which no biological systems are present. In consequence, images of lower quality leading to erroneous artefacts are obtained. Thus, either novel detection techniques that are able to overcome these disadvantages or advanced evaluation methods enabling the sophisticated analysis and description of flow fields are requisite. In the present work detailed micro flow analysis with biotic seeding particles is done by using digital micro Particle Image Velocimetry (μPIV). As written above, ciliates induce a fluid flow through their cilia beat. In the present work motor activity of cilia is analysed with the help of digital micro Particle Tracking Velocimetry (μPTV) for the first time. Moreover, in order to predict artefacts and correct them, a novel so-called neuronumerical hybrid discovered by [10] is implemented.

2 Materials and Methods

Microorganisms are selected from GAS which grows in a laboratory scale SBR [19, 20]. Micro–fluid flow is observed by using an Axiotech 100 microscope (Carl Zeiss) with 10–, 20– and 50– fold optical magnification. In order to analyse cilia displacement 150– fold optical magnification is implemented. Granules removed from the SBR with a certain amount of seeding particles are placed on the glass plate. The prepared sample is covered with a cover–plate. Subsequently, the probe is analysed under a microscope. Experiments are repeated several times.

In the biological flow biocompatibility of the measurement technique belongs to the most important issues. Effective results can be obtained only with appropriate seeding particles and suitable light illumination technique. Artificial tracers (polystyrene particles of 4.8 μm from Microparticles GmbH, Germany) are instantaneously detected by microorganisms. While yeast cells (*Saccharomyces cerevisiae*, dimensions approx. 3–10 μm) and milk, being an emulsion with scattering particles (fat and proteins, dimensions 0.3–3 μm), are implemented as tracers for flow visualization. They are well recognized by ciliates as nutrients and do not

disturb the natural behaviour of zooids. Built in microscope white light with moderated intensity (upper light, light intensity level 1-10; lower light, level 1-7) is implemented as appropriate light source.

2.1 Digital Micro Particle Image Velocimetry

Micro flow induced by *Opercularia asymmetrica* is analysed with the help of digital micro Particle Image Velocimetry. Investigations are carried out with different aqueous solutions of yeast cells of 1:100, 1:200 and 1:300 (yeast to distilled water) and milk of 1:1, 1:2, 1:3, 1:4 (milk to distilled water).

The pictures are recorded by a high speed CCD camera (Mikrotron GmbH) with a maximum speed of 520 frames/s. In the present case, the images of flow patterns are taken with two different speeds, namely 25 and 65 frames/s. The pictures have a resolution of 860 x 1024 pixels, the interrogation window size is chosen as 32 x 32 pixels and the grid size as 20 x 20 pixels.

The calculation of the fluid velocity is carried out with the help of the software PIVview2C (PIVTEC GmbH), developed by [12]. The μPIV technique consists in comparing two images with known time spacing. The cross–correlation mode is used to extract the particle displacement [11]. The differences in position of the tracers in the first and second pictures represent the displacement. The knowledge of the time interval between two recordings permits computations of the liquid velocity u [8].

μPIV investigations are carried out by the multiple–pass interrogation algorithm which is built in the PIVview2C software. This method increases the data yield due to the higher number of matched particles and reduces the bias error [17]. Sub–pixel displacement of the correlation peak is obtained by a 3–point Gauss fit [18]. Subsequently, velocity data from PIVview2C are further processed with TECPLOT (Amtec Engineering).

2.2 Digital Micro Particle Tracking Velocimetry

Micro Particle Tracking Velocimetry investigations are performed in order to characterise the cilia movement of *Opercularia asymmetrica*. In order to improve the activity of the ciliates during the measurements, a mixture of milk and distilled water with a concentration of 1:3 is used. The pictures are recorded by a high speed CCD camera (PCO AG) with a maximum speed of 636 frames/s at a high resolution of 1280 x 1024 pixels. The images are acquired with a recording speed of 100 frames/s at the above mentioned resolution.

The motion analysis is carried out after calibration with OPTIMAS (Media Cybernetics, L. P.). Similarly to the μPIV case, μPTV is based on comparing two images with known time spacing. The points (cilia) for which the velocity is to be determined are marked manually on both images. The difference in position of the markers represents the displacement of cilia, which for the known time interval between images can be recalculated as cilia velocity u_C. The velocity vectors are visualised in TECPLOT (Amtec Engineering).

2.3 Novel Neuronumerical Hybrid with a Priori Knowledge

It is well known that biological flow investigations can be influenced by erroneous artefacts occurring during the processing of PIV data. Previous work of [1, 3, 4, 9] shows the powerful role of hybrid methods in modelling, diagnosing and predicting complex systems. In the present work, a novel neuronumerical hybrid being an efficient tool allowing to predict artefacts and correct them is implemented. It is based on the implementation of numerically expressed a priori knowledge on the flow field (Taylor's hypothesis) into an artificial neural network (ANN) as a functional node (see Fig. 1). Equation 1 expresses the Taylor's hypothesis

$$\left.\frac{\partial \tilde{u}}{\partial t}\right| + \left[\left(u+\varepsilon_u\right)\frac{\partial \tilde{u}}{\partial x} + \left(v+\varepsilon_v\right)\frac{\partial \tilde{u}}{\partial y} \right]_{(x_0,y_0)} = Ta\left(x_0, y_0\right) \cdot \tag{1}$$

Where ε_u, ε_v depict the velocity field corrections, $\left.\frac{\partial \tilde{u}}{\partial t}\right|_{(x_0,y_0)}$ the temporal derivative, $\left.\frac{\partial \tilde{u}}{\partial x}\right|_{(x_0,y_0)}$ and $\left.\frac{\partial \tilde{u}}{\partial y}\right|_{(x_0,y_0)}$ the spatial derivatives, $\left(\tilde{u},\tilde{v}\right)$ the velocity field obtained from PIV evaluation.

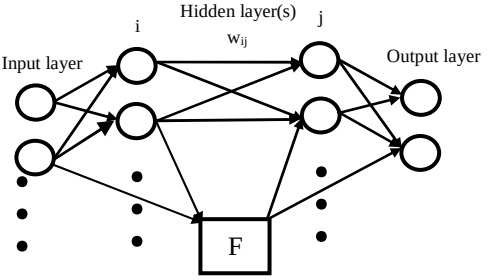

Fig. 1 Novel neuronumerical hybrid

The classical ANN is connected with the functional node part of the network using weights with the constant value of 1. This means that they are excluded from the training but propagate the error back to the classic ANN part to minimise the sum squared error. ANN consists of one input layer with seven nodes (x, y coordinates, two velocity components, one temporal and two spatial derivatives of velocity), three hidden layer with three nodes (two velocity components and Taylor value) and one functional node.

3 Results

3.1 Digital Micro Particle Image Velocimetry

Analysing µPIV investigations of the fluid flow in the vicinity of the granule surface, a characteristic micro flow pattern with two counter rotating vortices generated by cilia beats can be observed (see Fig. 2).

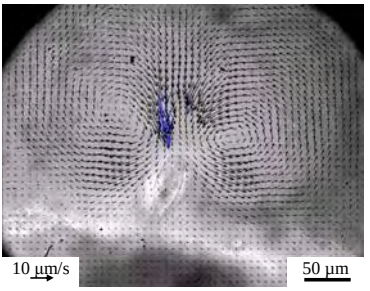

Fig. 2 Characteristic flow pattern generated by one ciliate observed at 50–fold magnification; seeding with milk (1:3)

Considering experiments with yeast cells as tracer particles, an aqueous solution of 1:100 (yeast to water) is required for the present investigations. In the case of the milk solution, the best results are obtained for several concentrations, 1:1, 1:2, 1:3 and 1:4 (milk to water). Higher concentrations of tracer substance can influence the investigated flow.

As shown by [10] experiments with yeast cells as seeding particles enable obtaining flow pattern for 10-fold optical magnification. However, more precise analysis is impeded in that case due to behaviour and size of tracer particles. In the present work, detailed investigations with higher optical magnifications (50-fold optical magnifications) are carried out. Exemplary experiments with yeast cells (1:100) and with milk (1:3) are compared. Fig. 3 proves that investigations with yeast cells at higher optical magnification are strongly limited. Calculated values of the velocity (maximal velocity amounts u_{max}= 10 µm/s) are underestimated and loaded with high error.

Moreover, it is impossible to obtain the flow field in a sufficient quality and quantify the velocity. Due to low density and large dimension of tracer particles many spurious vectors appear. However by using milk as seeding substance a detailed visualisation of the flow close to the body of ciliates is enabled. The maximal noted dimensionless velocity amounts u_{max}= 45 µm/s.

Since the ciliates in their natural habitat tend to live in colonies, detailed analysis and comparison of the action of a single *Opercularia asymmetrica* and a

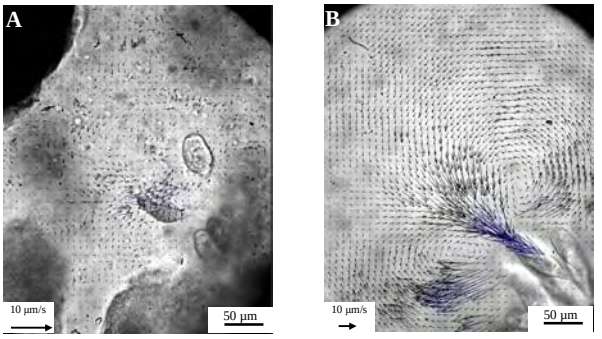

Fig. 3 Velocity field observed by 50-fold optical magnification for one ciliate; (A) seeding with yeast cells; (B) seeding with milk

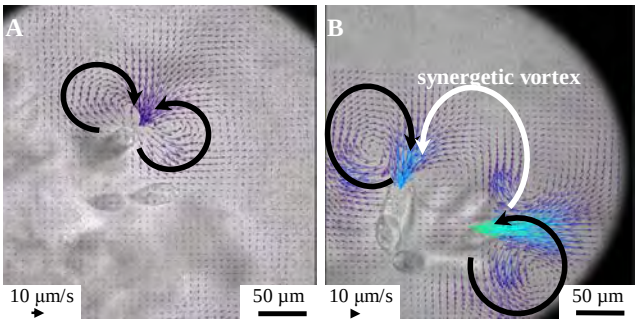

Fig. 4 Velocity distribution observed by 50–fold optical magnification for (A) one ciliate and (B) colony

colony will be shown below for 50-fold optical magnification with a milk to water ratio of 1:1 (see Fig. 4).

Here, an increasing tendency of velocity distribution with increasing ciliate number is observed. For the single ciliate the maximal velocity is equal to u_{max}= 26 µm/s while for the colony it is more than four times higher u_{max}= 113 µm/s. The above analysis clearly shows that cooperative colony work influences significantly the velocity distribution displaying a bio–synergetic effect. Moreover, comparing both situations, the characteristic two vortices can be seen in the case of a single organism. In the case of colony, instead of typical flow each ciliate produces one vortex. Additionally, a synergetic vortex belonging partially to two different ciliates appears.

Flow induced by ciliates on the micro–scale is in fact an efficient way of nutrient transport to the biofilm surface from the bulk liquid with minimum energy requirement. Presented above effective cooperative colony work can be confirmed by the investigations of the convective kinetic energy produced by living protozoa defined as

$$E_{kinconv} = u\frac{\partial E_{kin}}{\partial x} + v\frac{\partial E_{kin}}{\partial y} \tag{2}$$

where E_{kin} is the kinetic energy per unit volume

$$E_{kin} = \frac{1}{2}\rho\vec{u}^{\,2} \tag{3}$$

ρ represents liquid's density and $\vec{u} = (u, v)$ velocity vector. Fig. 5 presents the calculated two–dimensional spatial distribution of the kinetic energy generated by these microorganisms. Ciliates living in a colony produce more convective kinetic energy per single organism than a single ciliate. The synergy factor amounts to approximately 1.7. The analysed case concerns milk to water ratio of 1:3.

Additionally to investigations on living organisms a first attempt was made to mimic the flow pattern generated by ciliates. Bionic mechanism was designed employing active composite elements based on piezoelectric PZT ceramics and

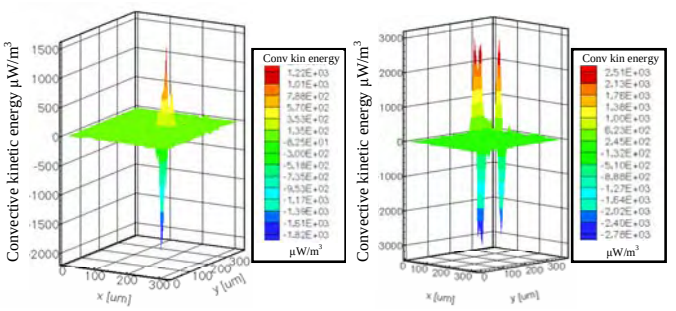

Fig. 5 Convective kinetic energy generated by one ciliate (left) and a colony (right)

Fig. 6 Flow pattern generated by "artificial ciliate"

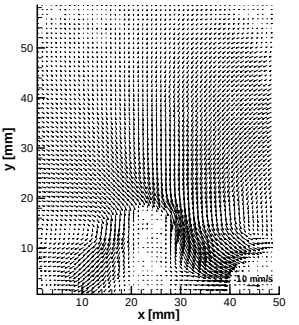

carbon fibres. The flow pattern induced by the developed "artificial ciliates" is shown in Fig. 6.

3.2 Digital Micro Particle Tracking Velocimetry

The oscillating motion of the cilia during 140 ms recording time is illustrated in Fig. 7, for three different exposures (A, B and C). It can be concluded that for one reciprocating beat, 140 ms are necessary. The time distance between each exposure is 70 ms and the beat frequency is 14,28 Hz. This value is within the frequency range of 10 to 80 Hz known from literature [6]. During one reciprocating

Fig. 7 Reciprocating cilia movement during 140 ms recording time

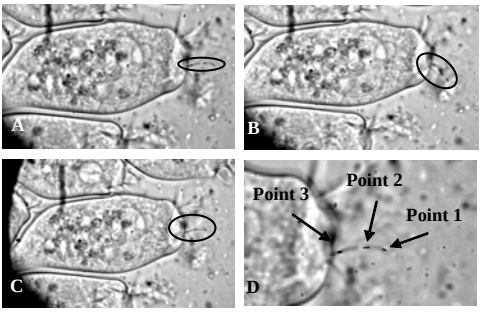

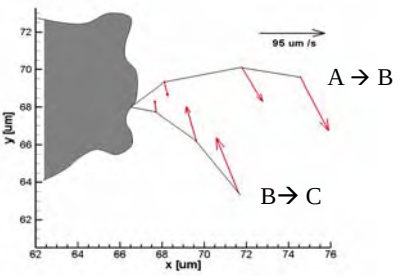

Fig. 8 Cilia velocity during one reciprocating cilia beat

beat the velocity of one good visible cilia was observed. Therefore three different points (Fig. 7 D) at the top, middle and bottom of the cilia were selected. Knowing the distance between the position A and B, respectively B and C at the selected points and the time interval (70 ms), the velocity can be easily computed.

In Fig. 8 it can be seen that the ascertained velocity range is between u_C=5 µm/s at the bottom and u_C=90 µm/s at the top of the cilia. It can be further observed that the cilia is displaced nearly with the same velocity sidewards (A → B) and backwards (B → C). The velocity magnitude is strongly dependent on the activity of the ciliates during the measurements.

3.3 Novel Neuronumerical Hybrid with a Priori Knowledge

In the biological flow artefacts can be caused by incorrect image evaluation or low image quality. As explained in the introduction part novel hybrid is implemented to prevent artefacts and correct them. Fig. 9 shows the effect of the Taylor hybrid applied on the PIV velocity field. It can be observed that the velocity field before application of the Taylor hybrid differs significantly from that processed by means of the neuronumerical hybrid method. Novel Taylor hybrid improves image quality reducing artefacts.

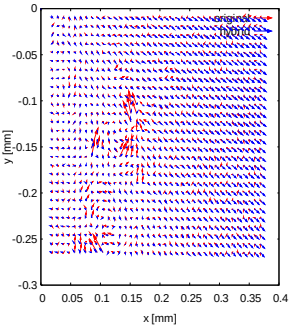

Fig. 9 Velocity field before (red arrows) and after (blue arrows) Taylor hybrid application

4 Summary

In the present work flow induced by microorganisms living on GAS surface is investigated. In order to analyse the fluid flow induced in biological systems

powerful imaging methods for flow analysis are required. Detailed fluid flow and cilia motion analysis is done by implementing two different digital imaging techniques namely μPIV and μPTV. Artefacts are corrected and predicted by means of a novel neuronumerical hybrid image analysis method. μPIV studies indicate the existence of two characteristic vortices generated by cilia beats. However, the flow structure induced by one ciliate differs considerably from that induced by a colony. Studies with two different tracer substances, yeast cells and milk, show that a more detailed representation of the fluid field is possible by using milk. Comparisons of the velocity distributions for one ciliate and a colony reveal efficient cooperative group work of more than one ciliate. Thereby, with increasing ciliate number, higher convective kinetic energy and velocities are seen. The synergy factor for convective kinetic energy amounts approximately 1.7 while the synergy factor for velocity is equal to 4.3. μPTV investigations show that the highest cilia velocity is observed on the top of cilia (u_C=90 μm/s) while the lowest values are seen close to the ciliates mouth (u_C=5 μm/s). Finally, it must be emphasized that the flow induced by ciliates is very interesting subject in biofluidmechanics. Thus, for better understanding of this phenomenon 3D μPIV and 3D μPTV should be done.

Acknowledgments. This study was supported by the German Research Fundation (DFG), projects DE 634/10-1, DE 634/10-2, DE 634/10-3.

References

1. Benning, R., Becker, T., Delgado, A.: Initial studies of predicting flow fields with an ANN hybrid. Adv. Eng. Softw. 32, 895–901 (2001)
2. Delgado, A., Nirchl, H., Becker, T.: First use of cognitive algorithms in investigations under compensated gravity. Micrograv. Sci. Technol. IX (3), 185–192 (1996)
3. Delgado, A., Petermeier, H., Kowalczyk, W.: Micro-PIV in Life Science, Particle Image Velocimetry. In: Raffel, M., Willert, C., Wereley, S., Kompenhans, J. (eds.), 2nd edn. Springer, Heidelberg (2007)
4. Díez, L., Zima, B.E., Kowalczyk, W., Delgado, A.: Investigation of multiphase flow in Sequencing Batch Reactor (SBR) by means of hybrid methods. Chem. Eng. Sci. 67, 1803–1813 (2006)
5. Etterer, T., Wilderer, P.A.: Generation and properties of aerobic granular sludge. Water Sci. Technol. 43, 19–26 (2001)
6. Hartmann, C., Özmutlu, Ö., Petermeier, H., Fried, J., Delgado, A.: Analysis of the flow field induced by the sessile peritrichous ciliate Opercularia asymmetrica. J. Biomech. 40, 137–148 (2007)
7. Kowalczyk, W., Zima, B.E., Delgado, A.: A biocompatible seeding particle approach for μ-PIV measurements of a fluid flow provoked by microorganisms. Exp. Fluids 43, 147–150 (2007)
8. Lindken, R., Gui, L., Merzkirch, W.: Velocity measurements in multiphase flow by means of Particle Image Velocimetry. Chem. Eng. Technol. 22, 202–206 (1999)
9. Petermeier, H., Benning, R., Delgado, A., Kulozik, U., Hinrichs, J., Becker, T.: Hybrid model of the fouling process in tubular heat exchangers for the dairy industry. J. Food Eng. 55, 9–17 (2002)

10. Petermeier, H., Kowalczyk, W., Delgado, A., Denz, C., Holtmann, F.: Detection of microorganismic flows by linear and nonlinear optical methods and automatic correction of erroneous images artefacts and moving boundaries in image generating methods by a neuronumerical hybrid implementing the Taylor's hypothesis as a priori knowledge. Exp. Fluids 42, 611–623 (2007)
11. Quenot, G.M., Pakleza, J., Kowalewski, T.A.: Particle Image Velocimetry with optical flow. Exp. Fluids 25, 177–189 (1998)
12. Raffel, M., Willert, C.E., Kompenhans, J.: Particle Image Velocimetry. A Practical Guide. Springer, Heidelberg (1998)
13. Sleigh, M.A., Barlow, D.: Collection of food by Vorticella. Trans. Am. Microsc. Soc. 95, 482–486 (1976)
14. Tay, J., Liu, Q., Liu, Y.: The role of cellular polysaccharides in the formation and stability of aerobic granules. Lett. Appl. Microbiol. 33, 222–226 (2001)
15. Vopel, K., Reick, C.H., Arlt, G., Pöhn, M., Ott, J.A.: Flow microenvironment of two marine ciliates with ectobiotic chemoautotrophic bacteria. Aquat. Microb. Ecol. 29, 19–28 (2002)
16. Weber, S., Ludwig, W., Schleifer, K.H., Fried, J.: Microbial composition and structure of aerobic granular sewage biofilms. Appl. Environ. Microbiol. 73, 6233–6240 (2007)
17. Westerweel, J., Dabiri, D., Gharib, M.: The effect of a discrete window offset on the accuracy of cross–correlation analysis of digital particle image velocimetry. Exp. Fluids 23, 20–28 (1997)
18. Willert, C., Gharib, M.: Digital Particle Image Velocimetry. Exp. Fluids 10, 181–193 (1991)
19. Zima, B.E., Diez, L., Kowalczyk, W., Delgado, A.: Sequencing Batch Reactor (SBR) as optimal method for production of Granular Activated Sludge (GAS) – fluid dynamic investigations. Water Sci. Technol. 55, 151–158 (2007)
20. Zima-Kulisiewicz, B.E., Díez, L., Kowalczyk, W., Hartmann, C., Delgado, A.: Biofluid mechanical investigations in Sequencing Batch Reactor (SBR). Chem. Eng. Sci. 63, 599–608 (2008)

Nonlinear Dynamic Phase Contrast Microscopy for Microflow Analysis

Frank Holtmann, Mike Woerdemann, and Cornelia Denz

Abstract. For the investigation and control of microfluidic systems innovative microscopy techniques are needed which can comply the requirements regarding to sensitivity and spatial as well as temporal resolution. A promising approach for this challenge is nonlinear dynamic phase contrast microscopy. It is an alternative full field approach that allows to detect motion as well as phase changes of unstained micro-objects in real-time without contact and non destructive, i.e. fully biocompatible. In this contribution we will present the dynamic phase contrast technique and its applications in micro flow velocimetry and micro-mixing analysis.

1 Introduction

Micro- and nanofluidic devices are of growing interest in the fields of micro scale chemical synthesis and medical diagnostics [25]. The ability to control small amounts of fluids (10^{-9} to 10^{-18} litres) has induced several promising strategies such as micro total analysis systems (μTAS) [15] or lab-on-a-chip devices (LOC) [7]. For an optimization of the chip design its flow characteristics have to be analyzed. Important parameters for this characterization are velocities occurring in the flow field and the mixing quality in reaction chambers.

Techniques for determining the velocity of fluid flows often rely on seeding the fluid with tracer particles [1]. Common velocimetry techniques are particle image velocimetry (PIV) and particle tracking velocimetry (PTV). In microfluidics the intensity of reflected light from tracer particles is usually too low for PIV evaluations [23], so that mainly fluorescent particles are employed [21].

The second important issue in microfluidics is mixing of reagents [23]. The desired control of quality and temporal behaviour of mixing requires a non-intrusive,

Frank Holtmann · Mike Woerdemann · Cornelia Denz
Westfälische Wilhelms-Universität Münster, Institut für Angewandte Physik, Corrensstraße 2, 48149 Münster, Germany
frank.holtmann@uni-muenster.de

W. Nitsche and C. Dobriloff (Eds.): Imaging Measurement Methods, NNFM 106, pp. 279–288.
springerlink.com

label-free analysis tool with high spatial and temporal resolution. Although fluorescence based techniques such as laser induced fluorescence have a great potential according to chemical sensitivity and spatial resolution [6] they can cause problems due to biotoxic implications [18, 23].

Here we present a different approach that can overcome the above mentioned challenges. A dynamic phase contrast (DynPC) microscope transfers temporally changing phase or amplitude information of an object into intensity information. This microscopy technique is a nonlinear optical filter, applied to the microscope image before its detection on the camera, thus allowing for real-time phase visualization [2] and measurement [11]. Hence the phase changes introduced by fluid flows or moving tracer particles can be visualized without using any fluorescent markers [13]. After an introduction of the working principle and the basic characteristics of nonlinear DynPC microscopy we will present applications in microfluidic velocimetry and quantification of micro-mixing processes.

2 Nonlinear Dynamic Phase Contrast Microscope

Nonlinear dynamic phase contrast microscopy is based on real-time holographic interferometry [8] by photorefractive two-beam coupling [28]. The image information transmitted by an optical system is used as the signal beam which is overlaid with a coherent reference beam within a photorefractive material. It is realized in a modular design, by mounting the photorefractive filter between a microscopes output and a camera (figure 1) [3]. In steady state the output equals zero intensity, due to an energy transfer from the signal to the reference beam. As a direct result of the interferometric nature of two-beam coupling, any novelty within the input signal instantaneously is detected as an intensity peak in the output signal. The novelty may be a change of amplitude or phase of any part of the input image [11]. After detecting an input change, the output falls towards zero intensity within a characteristic time τ which is determined by the grating time constant τ_g of the photorefractive material [29]. Although the decay of output intensity is known to be best described by an exponentially decaying term weighted by an infinite sum of Bessel functions [10], in most experimentally relevant situations it can be estimated very well by a purely exponential decay with an effective time constant τ [22].

In comparison to conventional phase contrast techniques the dynamic phase contrast is not a Fourier filter in the spatial domain, but a dynamic filter in the time domain with adjustable filter characteristics. Thus the method is often described as a temporal high pass filter, which detects temporally dynamic signals while suppressing the static background (novelty filter) [2, 4]. The particular features of this technique leads to several applications of the method, ranging from bio-compatible dynamic phase contrast microscopy [5, 20] and holographic phase contrast optical tweezers [27] to micro-flow velocity field analysis [26] and micro-mixing visualization [9, 13]. Detailed investigations of micro-organismic induced flow fields can be found in references [19, 30]. Here we will concentrate on the analysis of

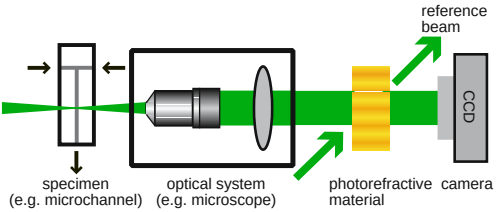

Fig. 1 The modularized DynPC microscope consists of an optical system (e.g. microscope), which images the object under investigation onto a camera and the photorefractive filter, where signal and reference beam interfere, which is mounted between the optical system and the camera

microfluidic velocity fields and the measurement of concentrations in micro-mixing devices.

3 Features of Nonlinear Dynamic Phase Contrast Microscopy

In the last section we described nonlinear DynPC microscopy as a temporal filtering system, sensitive for amplitude and phase changes. Therefore the temporal response of the system is of utmost importance. Figure 2 shows the intensity response for rectangular objects, moving with velocity v and length l from left to right through the field of view. The object velocity decreases from a) to c). If the ratio v/l is very large in relation to the inverse time constant of the system $1/\tau$ (figure 2 a)), the object shape is reproduced exactly, as in conventional microscopy, with a spatial resolution down to the diffraction limit. However, the contrast is enhanced significantly due to a suppression of any static background and phase information is transferred quantitatively in intensity information. Both features will be described in detail in the following sections. If, on the other hand, τ is chosen such that $v/l \approx 1/\tau$, *trail formation* is exhibited (figure 2 b)). Intensity and length of the trail depend on the velocity of the object [11, 13] and consequently can be utilized for measurement of the object velocity [26]. For ratios of v/l much smaller than $1/\tau$, contour formation is visible (figure 2 c)) . This feature can be used for optical edge enhancement for edges perpendicular to the direction of motion [22]. The three cases can be realized experimentally by changing the photorefractive time constant τ. This is possible from milliseconds to hours by adjusting the reference intensity [11, 13].

Fig. 2 Intensity response for rectangles, moving from left to right. Three cases are shown for different velocities v in relation to the system time constant τ for objects of length l. a) $v/l \gg 1/\tau$, b) $v/l \approx 1/\tau$, c) $v/l \ll 1/\tau$

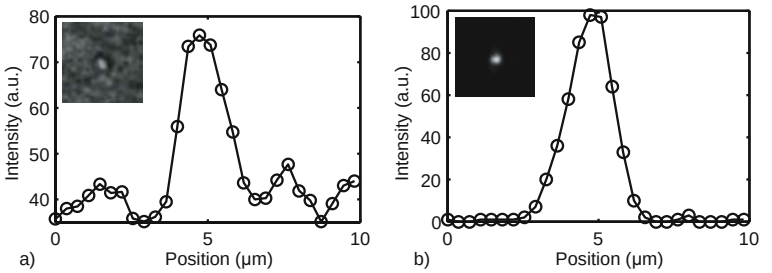

Fig. 3 Particle contrast for a polystyrene sphere with a diameter of 2 μm (images shown in the inset). Intensity profile under bright field illumination (left), and as observed with dynamic phase contrast (right). Lines are guides to the eye

3.1 Contrast Enhancement

The contrast enhancement feature of the dynamic phase contrast microscope can be demonstrated with a defined particle as used for PIV measurements. Figure 3 shows the intensity profile of a polystyrene particle (d = 2 μm) that is driven through the field of view by a laminar flow. In comparison with the conventional bright field image, a significant improvement (here by a factor of 3) of particle contrast is observed due to the phase sensitivity of the dynamic phase contrast microscope and the suppression of any background with slower dynamics than the particle velocity. The factor of contrast enhancement is depending on the phase shift by the particle and the ratio of signal and reference beam intensity. Optimization of contrast is achieved already at very low light intensity in the order of micro or even nano watts, due to the optical amplification by the reference beam which is not transmitted through the sample and thus does not contribute to the total light pollution.

3.2 Spatial Resolution

The spatial resolution of a microscopic technique is usually derived from the *point spread function* of the system. Therefore, a point source is imaged and the width of its airy disk is taken as a measure for the spatial resolution. For larger objects, e.g. μm thick tracer particles or biological cells, Mie scattering is getting relevant and has to be taken into account. For microfluidic applications this was investigated by Ovryn in detail [17]. Therefore here we concentrate on the system response for particles in the μm-range. The nonlinear dynamic phase contrast microscope detects moving objects or changes in phase and amplitude of an object. Static scenes are completely suppressed. Thus the definition of resolution is only well defined for moving objects. The lateral resolution of dynamic phase contrast microscopy, as can be seen in figures 2 and 3, is the same as in conventional microscopy. In contrast to conventional phase contrast microscopy we introduce no aperture in the Fourier plane and therefore we can utilize the full numerical aperture of the microscope

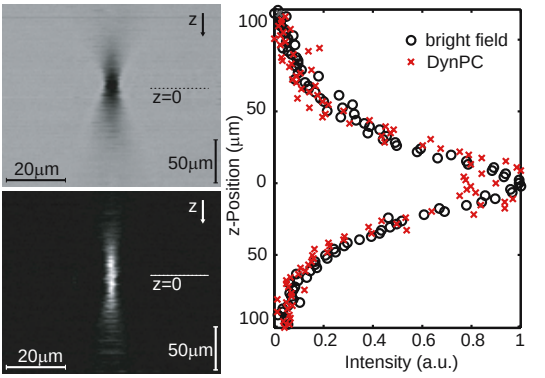

Fig. 4 Z-stack of a 5.6 μm thick, absorbing particle observed by conventional (top) and dynamic phase contrast microscopy (bottom). On the right the axial intensity profile is plotted. Intensities are normalized to the maximum

objective. For the axial resolution one can distinguish two different cases. The first one occurs when using completely absorbing tracer particles. A typical z-stack for a 5.6 μm thick completely absorbing particle is displayed in figure 4. For this measurement the particle is moved laterally and than an image is taken for every axial plane. Stacking the lateral intensity profile of the particle in one image yields the z-stack. Both systems show a symmetric response when focussing through the particle. For comparison of the z-stack intensity profile we normalized the intensity to its maximum. The intensity profile of the z-stack shows, that the axial width of the particle image is the same for both systems,which implies the same axial resolution.

The more interesting case is given when using transparent particles. Then Mie scattering and focussing effects by the particle come into account. In figure 5 it can be seen, that the maximum intensity is not congruent with the particle position. In μPIV or μPTV applications this effect can introduce an offset of several microns in the estimated axial position of the particle [17]. In DynPC microscopy this effect is suppressed and the phase shift of the particle is more important for the axial response of the system, yielding a symmetric response. This behaviour can be utilized for determining the correct axial position in scanning PIV or PTV measurements.

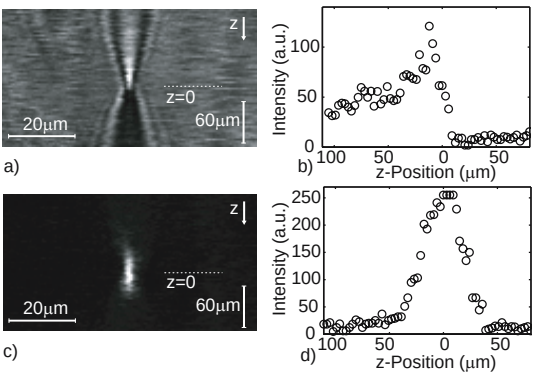

Fig. 5 Z-stack of a 4.4 μm thick, transparent particle observed by conventional coherent (a)) and dynamic phase contrast microscopy (b)). On the right the axial intensity profile is plotted

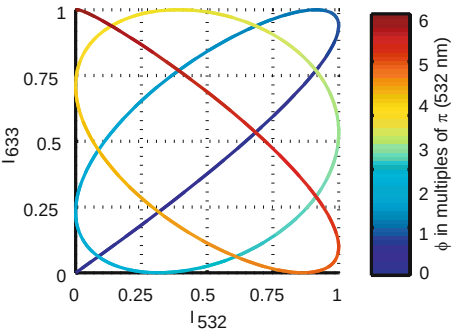

Fig. 6 Two-wavelength phase transferfunction of DynPC microscopy. The intensity tuple I_{532} and I_{633} is a direct measure of an introduced phase shift ϕ

3.3 Phase Sensitivity

The output intensity I_{out} of nonlinear DynPC microscopy is directly dependent on phase variations introduced to the signal beam. Based on theoretical and experimental investigations, the dependence of the dynamic phase contrast output on a phase shift ϕ can be described by $I_{out} = I_{max} \sin^2(\phi/2 + \chi - \pi/2)$ where I_{max} is the maximum signal intensity used in the system, which is fixed during the measurement process [13]. The extra phase term χ takes a possible grating phase shift into account, either introduced by the photorefractive material or an external phase shift applied to one of the two beams. For a measurement of phase shifts, the phase transfer function (PTF) of the system has to be determined experimentally by introducing known phase shifts onto either the signal or the reference beam. With this PTF a simple look-up table can be created to determine an unknown phase shift. The simplicity of this dependence allows real-time measurements of phase changes such as those introduced by density changes in fluids [13]. The output intensity I_{out} shows that the PTF has a quadratic sinusoidal dependence on the introduced phase shift ϕ. This causes a limited range of uniqueness within the interval from zero to π radians. For measurements of larger phase shifts in realistic liquid and gaseous fluid flows, this limitation has to be eliminated.

A phase triggering method can be employed to extend the phase measurement range to 2π radians [12]. For larger extensions of the phase measurement range a two-wavelength method can be used, because the PTF for a second wavelength is slightly different from the first one. The tuple of the two intensities I_{532} and I_{633} is than used as PTF for phase change evaluations (figure 6). With this technique phase changes of several π radians are possible [9].

4 Optimized Data Acquisition for Flow Field Analysis

Seeding a fluid with tracer particles to measure the velocity field has proven to be a reliable concept, but imaging the tracer particle field is a challenging task in microfluidics due to the usually poor signal to noise ratio on microscopic scales. DynPC microscopy is used to acquire high contrast images of tracer particle fields

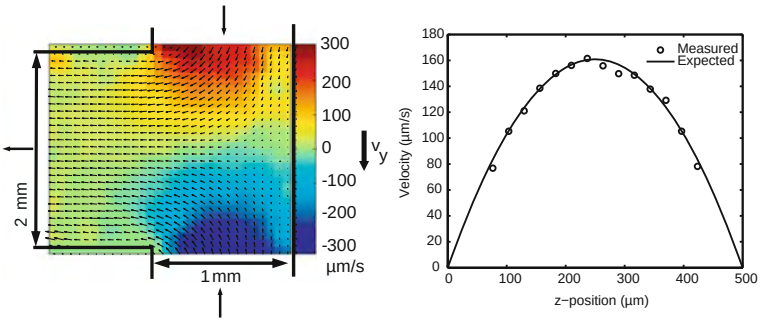

Fig. 7 PIV-measurement of a typical laminar flow field in a T-channel. The y-component of velocity is visualized by the colour coded background. On the right the maximum velocities of a 500 μm height rectangular channel are plotted for different z-levels

with a high signal to noise ratio (see section 3.1). For the demonstration of the capabilities of DynPC microscopy for μPIV measurements we determined the 2D velocity field of a micro-T-mixer, which will be described in section 6. In figure 7 the velocity in the middle layer of the channel with a heigth of 500 μm and width of 1 mm at the inlets and 2 mm at the outlet is shown.

Due of the particular axial response of dynamic phase contrast microscopy as described in 3 it is also possible to realize scanning-2D PIV evaluations. On the right side of figure 7 the maximum flow velocity for different z-positions of a 500 μm high rectangular channel is shown. Because the photorefractive filter unit is a modul mounted between the microscope and the camera all typical methods to obtain 3D velocity informations, like optical sectioning [16] or stereoscopic μ-PIV [14] can be realized with DynPC microscopy.

5 Photorefractive Velocimetry

The basic concept of photorefractive velocimetry is based on the unambiguous dependence of trail length and trail intensity on the object velocity (section 3). Trail length and object velocity correlate linearly and thus enable measurement of the object velocity by determination of its trail length [26]. Measurement of the trail intensity yields an additional, independent value for the object velocity and offers the opportunity of an instant validation of the measured velocity values.

As a first example of application we simulate a laminar tube flow on a spatial light modulator, taking dark amplitude objects as tracer particles. With the previously calibrated system the particle velocities are detected by analyzing their trail lengths. Figure 8 faces the measured particle velocities with the known velocity distribution. The measured values differ less than 1 px / s from the expected ones. A detailed discussion of photorefractive velocimetry, its velocity measurement range, and errors in velocity determination can be found in [26].

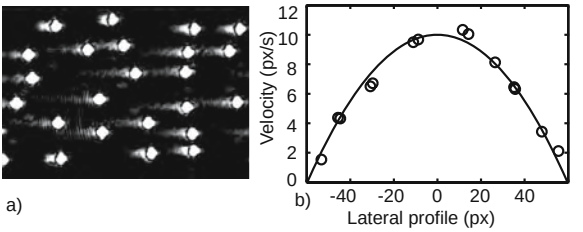

Fig. 8 Laminar tube flow (a) and corresponding velocity profile (b)). The parabolic curve shows the known velocity distribution and the dots indicate the velocities obtained by evaluating the trail lengths

6 Concentration Measurement in Microfluidic Mixing Processes

The phase transfer function of the dynamic phase contrast microscope can be used to quantitatively analyze phase and concentration distributions of mixing processes in fluids and gases [9, 13]. To study micro-mixing of liquids, we constructed a T-shaped mixing channel with a height of 500 μm and a channel width of 1 mm for the input channels and 2 mm for the outflow. After measuring the PTF, we started the phase change measurement and let a NaCl-solution in water (85.5 mmol/l) flow into the channel. These two liquids are barely distinguishable in colour and transparency and show an optical phase difference of approximately 1.5π radians. Because of this large phase difference we implemented a two-wavelength dynamic phase contrast to measure the concentration changes in this channel [9]. In this experiment the liquids were pumped into the channel with a syringe pump with an average flow rate of 36 ml/s, resulting in a laminar flow. Due to the laminar flow, the two liquids do not mix with each other. A diffusive mixing process was introduced by stopping the flow and was analysed by comparing the output intensities with the PTF. Owing to a linear relationship of the refractive index and the concentration C of an aqueous sodium chloride solution for the used wavelengths ($\lambda_1 = 532$ nm and $\lambda_2 = 633$ nm) [24] we can calculate the concentration change ΔC from the optical path length difference OPD. Figure 9 shows the result after the calibration has been applied to the images. The minimum change in the optical path length that we can currently detect with the system is related to $\lambda/40$ which corresponds to a concentration change of $4 \cdot 10^{-6}$

Fig. 9 Measurement of concentration changes due to diffusive mixing of a NaCl solution (85.5 mmol/l) in water. The inflow of the two fluids was stopped after taking the first image. Timespan between the three images is 30 seconds (framerate of the imaging system is 30 fps)

mol/cm^3 for a channel thickness of 500 μm. The maximal concentration change in the unique reconstruction range is up to 10^{-3} mol/cm^3 [9].

7 Summary

Nonlinear dynamic phase contrast microscopy is a phase sensitive method that enables real-time observation of dynamic processes on microscopic scales. In the wide field of microfluidic flow analysis the DynPC microscope can be profitable in three ways. Firstly, tracer particles are highlighted, while any static background is suppressed. This yields optimal image data for subsequent PIV/PTV evaluations. Secondly, if the system time constant is chosen appropriately, trail formation is exhibited and trail lengths and intensities allow for a direct access to flow velocities. Thirdly, micro-mixing processes can be observed without any labelling processes at all. The phase transfer function of the DynPC microscope enables a quantitative, spatially resolved analysis of concentration distributions in real time.

Acknowledgements. Our work was partially funded by the DFG in the frame of the priority program 1147 and the transregional research centre TRR61. Throughout the project period, several PhD and diploma students have contributed to the results and have advanced the field. Among them, we are especially thankful to Dr. V.V. Krishnamachari for starting most of the core issues and Dr. O. Grothe, H. Deitmar, M. Eversloh and M. Oevermann for their excellent experimental contribution to this project. We thank Prof. Dr. A. Delgado from the LSTM Erlangen, Prof. Dr. R. Westermann from the TU Munich and Dr. V. Beushausen from the LLG for the fruitful collaboration in the frame of the priority program 1147.

References

1. Adrian, R.: Twenty years of particle image velocimetry. Exp. Fluids 39, 159–169 (2004)
2. Anderson, D., Feinberg, J.: Optical novelty filters. IEEE J. Quantum Electron 25, 635–647 (1989)
3. Berger, G., Deitmar, H., Denz, C., Grothe, O., Holtmann, F., Krishnamachari, V.: Motion detection modular microscope system. PCT patent application WO002007128433 (2007)
4. Cudney, R.S., Pierce, R.M., Feinberg, J.: The transient detection microscope. Nature 332, 424–426 (1988)
5. Denz, C., Holtmann, F., Woerdemann, M., Oevermann, M.: Nonlinear dynamic phase contrast microscopy for microfluidic and microbiological applications. In: Proc. SPIE. Advanced Microscopy with Integrated Optical Traps, vol. 7038 (2008), doi:10.1117/12.801501
6. Dittrich, P., Manz, A.: Single-molecule fluorescence detection in microfluidic channels - the Holy Grail in muTAS? Anal. Bioanal. Chem. 382, 1771–1782 (2005)
7. Geschke, O., Klank, H., Tellman, P. (eds.): Microsystem Engineering of Lab-on-a-Chip Devices. Wiley, New York (2004)
8. Hariharan, P.: Optical Holography. Cambridge University Press, Cambridge (1996)

9. Holtmann, F., Eversloh, M., Denz, C.: Label-free analysis of microfluidic mixing processes by dynpc microscopy. J. Opt. A: Pure Appl. Opt. 11, 034014 (2009)
10. Horowitz, M., Kligler, D., Fischer, B.: Time-dependent behavior of photorefractive two- and four-wave mixing. J. Opt. Soc. Am. B 8, 2204–2217 (1991)
11. Krishnamachari, V.V., Denz, C.: Real-time phase measurement with a photorefractive novelty filter microscope. J. Opt. A: Pure Appl. Opt. 5, 239–243 (2003)
12. Krishnamachari, V.V., Denz, C.: A phase-triggering technique to extend the phase-measurement range of a photorefractive novelty filter microscope. Appl. Phys. B 79, 497–501 (2004)
13. Krishnamachari, V.V., Grothe, O., Deitmar, H., Denz, C.: Novelty filtering with a photorefractive lithium-niobate crystal. Appl. Phys. Lett. 87, 071105 (2005)
14. Lindken, R., Westerweel, J., Wieneke, B.: Stereoscopic micro particle image velocimetry. Exp. Fluids 41(2), 161–171 (2006)
15. Manz, A., Graber, N., Widmer, H.M.: Miniaturized total chemical analysis systems: A novel concept for chemical sensing. Sens Actuators, B 1, 244–248 (1990)
16. Meinhart, C.D., Wereley, S.T., Gray, H.B.: Volume illumination for two-dimensional particle image velocimetry. Meas. Sci. Technol. 11, 809–814 (2000)
17. Ovryn, B.: Three-dimensional forward scattering particle image velocimetry applied to a microscopic field-of-view. Exp. Fluids 29, 175–184 (2000)
18. Parak, W.J., Pellegrino, T., Plank, C.: Labelling of cells with quantum dots. Nanotechnology 16(2), R9–R25 (2005)
19. Petermeier, H., Delgado, A., Kondratieva, P., Westermann, R., Holtmann, F., Krishnamachari, V., Denz, C.: Hybrid approach between experiment and evaluation for artefact detection and flow field reconstruction - a novel approach exemplified on microorganismic induced fluid flows. In: Proc. 12th Intern. Symposium on Flow Visualization (2006)
20. Petermeier, H., Kowalczyk, W., Delgado, A., Denz, C., Holtmann, F.: Detection of microorganismic flows by linear and nonlinear optical methods and automatic correction of erroneous images artefacts and moving boundaries in image generating methods by a neuronumerical hybrid implementing the taylor's hypothesis as a priori knowledge. Exp. Fluids 42, 611–623 (2007)
21. Santiago, J., Wereley, S., Meinhart, C., Beebe, D., Adrian, R.: A particle image velocimetry system for microfluidics. Exp. Fluids 25, 316–319 (1998)
22. Sedlatschek, M., Rauch, T., Denz, C., Tschudi, T.: Generalized theory of the resolution of object tracking novelty filters. Opt. Commun. 116, 25–30 (1995)
23. Sinton, D.: Microscale flow visualization. Microfluid Nanofluid 1, 2–21 (2004)
24. Washburn, E. (ed.): International Critical Tables of Numerical Data, Physics, Chemistry and Technology. Knovel, New York (2003)
25. Whitesides, G.M.: The origins and the future of microfluidics. Nature 442, 368–373 (2006)
26. Woerdemann, M., Holtmann, F., Denz, C.: Full field particle velocimetry with a photorefractive optical novelty filter. Appl. Phys. Lett. 93, 021108 (2008)
27. Woerdemann, M., Holtmann, F., Denz, C.: Holographic phase contrast for dynamic multiple-beam optical tweezers. J. Opt. A: Pure Appl. Opt. 11, :034010 (2009)
28. Yeh, P.: Two-wave mixing in nonlinear media. IEEE J. Quantum Electron 25, 484–519 (1989)
29. Yeh, P.: Introduction to photorefractive nonlinear optics. Wiley, NY (1993)
30. Zima-Kulisiewicz, B.E., Botello-Payro, E., Delgado, A.: Biocompatible visualization of flow fields generated by microorganisms. In: Nitsche, W., Dobriloff, C. (eds.) Imaging Measurement Methods for Flow Analysis. Springer, Berlin (2009)

Spatiotemporal Image Analysis for Fluid Flow Measurements

Christoph S. Garbe, Daniel Kondermann, Markus Jehle, and Bernd Jähne

Abstract. In this chapter, a framework will be presented for measuring and modeling transport processes using novel visualization techniques and extended optical flow techniques for digital image sequence analysis. In this way, parameters besides the 2-D *xy* velocity components can be extracted concurrently from the acquired 2-D image sequences, such as wall shear rates and momentum transport close to boundaries, diffusion coefficients, and depth *z* in addition to the *z* velocity components. Depending on the application, particularly the temporal regularization can be enhanced, leading to stabilization of results and reduction of spatial regularization. This is frequently of high importance for flows close to boundaries. Results from applications will be presented from the fields of environmental and life sciences as well as from engineering.

1 Introduction

The standard techniques for measuring fluid flow optically in experimental fluid mechanics is based on *Particle Image Velocimetry* (PIV) or on *Particle Tracking Velocimetry* (PTV) [24]. Particularly PIV relies on tracer particles illuminated by a laser and a flavor of cross correlation for the subsequent estimation of motion from pairs of such images. For PTV, particles are usually segmented and tracked. This leads to a significantly lower density of seeding that can successfully be handled. Apart from algorithmic differences, both approaches have conceptual differences. While PIV measurements are linked to an Eulerian frame of reference, PTV measurements are Lagrangian in nature.

The proposed methods presented in this chapter open up novel possibilities of fluid flow measurement. This ranges from new techniques for fluid flow visualization to advanced digital image sequence analysis. Especially when trying to extract additional parameters of the flow, a strong linkage between visualization technique,

Christoph S. Garbe · Daniel Kondermann · Markus Jehle · Bernd Jähne
Interdisciplinary Center for Scientific Computing, University of Heidelberg
{Christoph.Garbe,Daniel.Kondermann,Markus.Jehle,
Bernd.Jaehne}@iwr.uni-heidelberg.de

W. Nitsche and C. Dobriloff (Eds.): Imaging Measurement Methods, NNFM 106, pp. 289–304.
springerlink.com

modeling and estimation technique are essential to success. This marks the main difference of our techniques to current state of the art PIV or PTV techniques, were usually only the motion of visualized particles is of interest. For our techniques, not only the velocity, but also velocity profile or constant of diffusivity are accessible through an adaptive modeling.

Techniques of flow visualization presented here include (i) thermographic techniques in which patches of water are heated up at the air-water interface and surface flow as well as shear rates from velocity gradient below the water surface can be measured, (ii) an approach of molecular tagging velocimetry (MTV) in which Taylor dispersion is modeled explicitly, (iii) fuel/air ratio measurement by laser induced fluorescence (FARLIF) and two particle based approaches where a dye is added to the water body and the depth of particles below the interface is reconstructed from the intensity change of the particle. This technique has been applied to a medical application for measuring wall shear rates in artificial heart pumps and at the free air-water interface. In addition, a thermographic technique is presented that makes wall shear rate measurements in wind tunnels feasible.

In Section 2 we will outline the extended optical flow models used for these applications and in Section 3 two techniques for estimating the model parameters are presented. Finally, in Section 4 a brief outline of the aforementioned applications will be given with references for in depth descriptions.

2 Extended Optical Flow Models

In this chapter, optical flow is computed in a gradient based approach, as opposed to correlation based techniques as found in PIV. The reason for relying on gradient based techniques is that they offer a much greater flexibility [24]. As we shall see in this section, gradient based approaches make it feasible to precisely model physical processes and experimental characteristics. This can be done both locally, relating image intensities to parameters of motion or globally by imposing spatial constraints on neighboring flow locations. In this section we will introduce local data terms, while [26] establishes techniques for imposing physical priors globally. We will show that local gradient based approaches are highly flexible and can be applied to a wide range of applications, extracting additional information than only flow fields from the image data.

Computing motion with gradient based approaches from image sequences is an inverse problem. As such, it is important to derive a correct model for relating the parameters of motion to image intensities or changes thereof. We regard $n-$dimensional signals, or image intensities, $I(\mathbf{x})$ defined over a region Ω, e.g., images and image sequences. Motions (translations) and orientations correspond to linear d-dimensional subspaces E of Ω with $1 \leq d < n$, such that

$$I(\mathbf{x}) = I(\mathbf{x} + k\mathbf{u}) \quad \forall k \in \mathbb{R} \text{ and } \forall \mathbf{x}, \mathbf{x} + k\mathbf{u} \in \Omega \text{ and } \mathbf{u} \in E. \tag{1}$$

In order to estimate motion in the regarded volume, one needs to detect the existence of such a subspace E and to estimate the parameter vector $k\mathbf{u}$, which corresponds.

The values of I can be scalar as in gray-level images or vector valued (denoted **I**) as in color or multi-spectral images. The estimation is often based on the fact that constancy of the signal in a certain direction in Ω can be relied upon. This constancy as is reflected in (1) implies linear differential constraints such as the classical *brightness constancy constraint equation (BCCE)*

$$\frac{\partial I}{\partial \mathbf{u}} = 0 \text{ for all } \mathbf{u} \in E\,. \tag{2}$$

This is the simplest special case of general partial differential equations which result from applying a suitable differential operator $\alpha(\mathbf{u})$ on the signal:

$$\alpha(\mathbf{u}) \circ I = 0 \tag{3}$$

in the following section we will introduce more elaborate operators $\alpha(\mathbf{u})$. Assuming the constancy of a moving brightness pattern, motions can be interpreted as local orientations in spatio-temporal signals. Many motion models are based on Taylor expansions of (1) (see e.g. [6]). Writing (1) with time t as individual parameter, we obtain

$$I(\mathbf{x}(t),t) = I(\mathbf{x}+\mathbf{u}(x,t)\Delta t, t+\Delta t)\,, \tag{4}$$

where I is interpreted as the constant brightness signal produced by a spatial point $\mathbf{x}(t)$ moving in time t. First order approximation of (4) yields

$$\frac{\mathbf{d}I}{\mathbf{d}t} = 0 \quad \Leftrightarrow \quad \nabla^T_{(\mathbf{x},t)} I \cdot (\mathbf{u}^T, 1)^T = 0\,, \tag{5}$$

where ∇ is the gradient operator with respect to parameters given as indices and the general differential operator $\alpha(\mathbf{u})$ from (3) takes the form $\alpha(\mathbf{u}) := \nabla^T_{(\mathbf{x})}\mathbf{u} + \frac{\partial}{\partial t}$. Being based on derivatives, such models are called *differential models*. One may further model the motion field $\mathbf{u}(x,t)$ locally by applying a Taylor expansion

$$\nabla^T_{\mathbf{x}} I(\mathbf{u} + \mathbf{A}\Delta\mathbf{x}) + \frac{\partial I}{\partial t} = 0 \tag{6}$$

where the matrix $\mathbf{A} = \nabla_{\mathbf{x}}\mathbf{u}^T$ contains the spatial derivatives of $\mathbf{u}$, and $\Delta\mathbf{x} = \mathbf{x}_0 - \mathbf{x}$ are local coordinates. This is called an *affine motion model*. These and other motion models, i.e. parametrizations of $\mathbf{u}$, can be found e.g. in [6]. Parametric motion models of high orders pose the problem of overfitting in the presence of noise. This problem can be resolved through model selection, such as by performing statistical tests on the residuals of the fit [1].

2.1 Diffusion of Brightness

In a number of applications, particulary in thermographic image sequence analysis, the simple BCCE does not hold, as conduction of heat (or more general diffusion

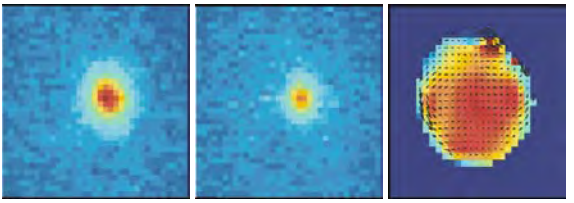

a) **b)** **c)**

Fig. 1 Isotropic diffusion of heat in a polymer heated with a laser. In **a** and **b** two frames of the sequence are shown and in **c** the computed diffusivity and optical flow field. The images were recorded with an infrared camera. Reproduced from [8]

of a substance) leads to a change of image intensities along motion trajectory. This change of image intensity has to be modeled accordingly.

Diffusion is the process by which matter is transported from one part of a system to another due to random molecular motions driven by a concentration gradient. In the transport of heat by conduction, energy is also transported by random molecular motions, where the transfer comes about due to a temperature gradient. As can be deducted by intuition there exists a strong analogy between the two processes. This was first recognized by [5], who derived diffusion on a quantitative basis by adopting the mathematical framework of heat conduction derived earlier by [7].

Fick's Second Law describes the non-steady state of a system subject to diffusion. The rate of change of a concentration in a given volume is given by the efflux through the volume's boundary. This results to

$$\frac{\partial C}{\partial t} = \nabla\left(D \nabla C\right) = D \Delta C, \tag{7}$$

where $\Delta I = (\partial^2 I/\partial x^2 + \partial^2 I/\partial y^2)$ is the Laplace operator. The last transform is valid only for a scalar, isotropic diffusivity D.

In digital image processing, the gray values correspond to the concentration C in Equation (7). The corresponding equation is then given by

$$\left[-\Delta I \; I_x \; I_y \; I_t\right] \cdot \left[D \; u_1 \; u_2 \; 1\right] = \mathbf{D} \cdot \mathbf{p} = 0, \tag{8}$$

where D is the constant of diffusivity. An example of such a process is the conduction of heat in an isotropic material. Results of such an image sequence recorded with an infrared camera are presented in Figure 1.

The case of a direction dependent diffusion, the constant of diffusivity is in fact a tensor $\mathbf{D}$. Therefore, the last simplification in Equation (7) is not valid. This yields

$$I_x \cdot u_1 + I_y \cdot u_2 + I_t - \nabla\left(\mathbf{D} \cdot \nabla\right) I = 0, \tag{9}$$

with the anisotropic diffusion tensor $\mathbf{D}$. This tensor is given by

$$\mathbf{D} = \begin{bmatrix} d_{00} & d_{01} \\ d_{10} & d_{11} \end{bmatrix} = \begin{bmatrix} d_{00} & d_{10} \\ d_{10} & d_{11} \end{bmatrix}, \tag{10}$$

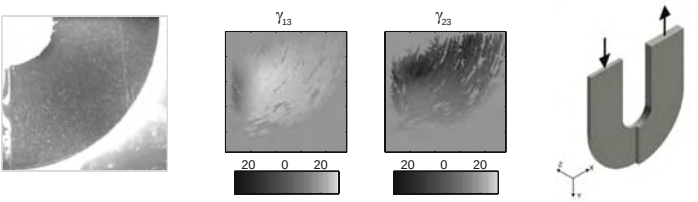

Fig. 2 Fluid flow in an U pipe. Depth is measured through exponential decay of Lambert-Beer's law. This allows to measure 3D velocity from Equation (13). Pictures from [15]

where use was made of the fact that the diffusion tensor **D** is a symmetric tensor, that is $d_{ij} = d_{ji}$. Inserting this expression in Equation (9) leads to the following vector equation

$$\left[I_x \; I_y \; -I_x x \; -I_y y \; -2I_x y \; I_t \right] \cdot \left[u_1 \; u_2 \; d_{00} \; d_{11} \; d_{10} \; 1 \right]^\top = 0. \tag{11}$$

2.2 Exponential Brightness Change

Apart from diffusive processes, which are dominant source of intensity change in thermal image sequences, exponentially decreasing intensities are often encountered. An important application of this type of model is the visualization of chemical reactions. On global scales, satellites can measure chemical species in our atmosphere, the motion of which has then to be estimated with an exponential decay model. On smaller scales, the exponential decay can be used when light is attenuated due to Lambert-Beer's law. One application will be presented in Section 4.1 and more detailed in [14]. Here, light of particles is attenuated by a special dye in the fluid. The attenuation follows again Lambert-Beer's law and can be directly correlated to the depths of particles inside the fluid. Similar applications is that of measuring shear rates close to a wall in medical applications as will be outlined in Section 4.2.

For this measurement technique, the intensity of a particle is given by $I(z) = I_0 \exp -2z/z_* = I_0 \exp -z/z_{2*}$, where I_0 is the incident monochromatic lights intensity before penetrating into the fluid, z is the distance of the particle below the surface, and z_* is the penetration depth of light inside the dyed water body and $z_{2*} = z_*/2$. The factor 2 is due to the fact that light has to traverse the distance of the particle below the surface once to it and once back. This technique can be extended to a measurement with incident light of two wavelengths with the benefit of independence of particle sizes, since only ratios of intensities are considered [14].

A particle moving below the surface thus leads to the differential equation

$$\frac{\mathbf{d}I}{\mathbf{d}t} = u_1 \frac{\partial I}{\partial x} + u_2 \frac{\partial I}{\partial y} + \frac{\partial I}{\partial t} = -I_0 \frac{1}{z_{2*}} \frac{\partial z}{\partial t} \exp\left(-\frac{z}{z_{2*}} \right) = -\frac{u_3}{z_{2*}} I, \tag{12}$$

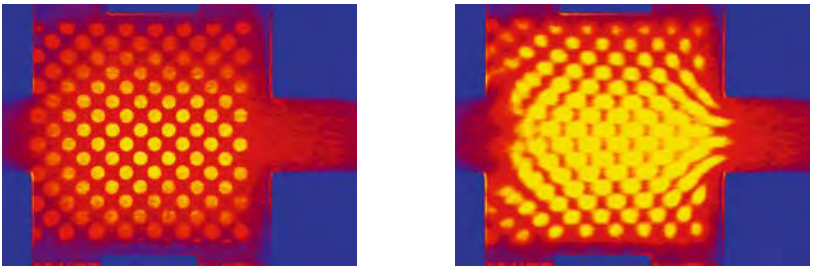

A **B**

Fig. 3 In **A** and **B** two frames of a microfluidic image sequences are shown. The implication of Taylor dispersion (Poiseuille flow, $n = 2$) can clearly be observed. Structures seem to diffuse in the direction of fluid flow. Reproduced from [11]

where u_3 is the velocity orthogonal to the interface. This equation can be expressed in vector notation, leading to

$$\mathbf{d}^\top \mathbf{p} = [I_x, I_y, I/z_{2*}, I_t] \cdot [u_1, u_2, u_3, 1]^\top = 0. \tag{13}$$

Again, partial derivatives are denoted by subscripts. By generalizing the concept of parametric affine motion models to 3D flow fields, it is possible to estimate the wall shear rate directly [15] as shown in Figure 2.

2.3 Integration across Flow Profiles

When visualizing fluid flow, often a tracer is visualized with digital cameras. Due to the projective nature of the imaging process, the tracer is integrated across a velocity profile. For a number of fluid flow configuration, the velocity profile can be approximated to leading order by

$$u(x_3) = A \cdot x_3^n,$$

where A is a term independent of the coordinate direction of integration x_3 and time t. Integration across such a profile leads to an intensity change, modeled by the differential equation [9]

$$\frac{\mathrm{d}s}{\mathrm{d}t} = u_1 \frac{\partial s}{\partial x} + u_2 \frac{\partial s}{\partial y} + \frac{\partial s}{\partial t} = -\frac{1}{n \cdot t} s. \tag{14}$$

This equation presents a generalization of the results obtained for Couette flow (shear driven flow, $n = 1$) and Poiseuille flow (pressure driven flow, $n = 2$). These brightness change models take into account effects such as Taylor dispersion and have been applied successfully to microfluidics in Section 4.4 (c.f. [11]) or in shear driven flows at the air-water interface 4.3 (c.f. [10]).

3 Solving the Flow Problem

Estimating motion from the previously proposed brightness constraint equations represents an ill posed problem. Generally, only one constraint equation is available and multiple parameters need to be solved (2D motion field and parameters of intensity change, i.e. constant of diffusivity or exponential decay). To overcome this problem, additional constraints have to be imposed. Different approaches have been proposed in literature. A distinction can be made between local approaches in which constancy of parameters is required in a small spatio-temporal neighborhood and global techniques in which global smoothness of parameters is assumed. Here we will confine ourselves to local approaches. The application of global approaches to fluid flow measurements can be found in [26].

3.1 Local Spatiotemporal Approach

A commonly made assumption is that of a locally smooth motion field. Therefore, the equations of motion can be pooled over a local neighborhood. This leads to one such equation for each pixel in the local neighborhood. In addition, we require a weighting for the resulting over-determined system of equations. This is introduced to weigh central pixels stronger than those at the border of the neighborhood. The resulting system of equations for the diffusion model (8) is given by

$$\mathbf{WD}\cdot\mathbf{p}=\mathbf{W}\begin{bmatrix} -\left(\frac{\partial^2 I_1}{\partial x^2}+\frac{\partial^2 I_1}{\partial y^2}\right) & \frac{\partial I_1}{\partial x} & \frac{\partial I_1}{\partial y} & \frac{\partial I_1}{\partial t} \\ -\left(\frac{\partial^2 I_2}{\partial x^2}+\frac{\partial^2 I_2}{\partial y^2}\right) & \frac{\partial I_2}{\partial x} & \frac{\partial I_2}{\partial y} & \frac{\partial I_2}{\partial t} \\ \vdots & \vdots & \vdots & \vdots \\ -\left(\frac{\partial^2 I_n}{\partial x^2}+\frac{\partial^2 I_n}{\partial y^2}\right) & \frac{\partial I_n}{\partial x} & \frac{\partial I_n}{\partial y} & \frac{\partial I_n}{\partial t} \end{bmatrix}\cdot\begin{bmatrix} D \\ u_1 \\ u_2 \\ 1 \end{bmatrix}=0, \tag{15}$$

where $\mathbf{W}$ is a $n\times n$ diagonal weighting matrix, $\mathbf{D}$ is the $n\times 4$ data matrix and $\mathbf{p}$ is the sought parameter vector. Naturally, this approach is readily adapted to the other motion models proposed previously or combinations of them. Subscripts I_i indicate the i-th pixel in the local neighborhood. Depending on the noise in the data, typical neighborhoods are chosen to be 11×11 pixel, leading to a system of $n=121$ equations. The entries of the weighting matrix $\mathbf{W}$ are set by a two dimensional Gaussian distribution, centered at the center pixel. The spatio-temporal image intensity gradients $\partial I/\partial x$, $\partial I/\partial y$ and $\partial I/\partial t$ are computed from optimized Sobel filters [13]. Efficient implementations are available, significantly speeding up the estimation process. For instance, the weighting with $\mathbf{W}$ can be performed by convolving the gradient images $\partial I/\partial k$, $k\in x,y,t$ with a separable Gaussian blurring filter [12].

The system of equations (15) can be solved for the parameter $\mathbf{p}$ using a weighted total least squares approach [25]. This boils down to an eigensystem analysis of the square matrix $\mathbf{J}=\mathbf{W}^\top\mathbf{D}^\top\mathbf{DW}$, where in this example $\mathbf{J}\in\mathbb{R}^{4\times 4}$, also known as the extended structure tensor. The parameter vector $\mathbf{p}$ is then given as the normalized eigenvector to the smallest eigenvalue. This parameter vector is found for the pixel

centered in the local neighborhood. The parameters for all pixels of the image sequence are computed by repeating this analysis for each pixel in a sliding window type fashion.

In this gradient based approach, parameters can only be retrieved at locations were an intensity structure due is present. To prevent wrong information (no motion) from areas without visible tracers diffuses into these regions, integration of the structure tensor is performed using a normalized convolution [17]. The normalized convolution weights the smoothing with a certainty, which can be set to zero for areas without any tracer.

In addition to performing a normalized convolution, confidences for the computed parameter fields are estimation in a post-processing step. Due to its adaptation to typical flow fields, the approach proposed by [19] was chosen for computing confidence values. For added accuracy, estimated parameter vectors can be discarded based on these values. This will naturally lead to sparse motion fields. For applications, in which dense fields are required, a subsequent parameter field interpolation can be conducted [18]. The required regularizer can be any of those presented by [26]. This leads to highly accurate dense flow fields.

3.2 Trajectory-Based Approach

Another approach was developed for highly turbulent, non-stationary flows with complex and often occluding motion of the tracers. Most optical flow estimators concentrate on spatial regularization techniques, ignoring the rich temporal structure of such long sequences. Therefore spatially nearby trajectories are bundled into

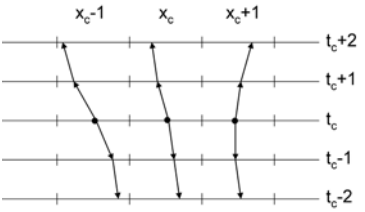

Fig. 4 A one-dimensional example for a trajectory ensemble in a three-neighborhood around $(x_c, 0, t_c)$. Each trajectory consists of four flow vectors relative to the position of the trajectory at time frame t. By the application of PCA to a large set of training ensembles, this representation can be described by just a few parameters

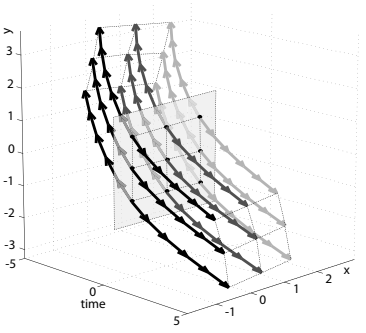

Fig. 5 Example for a trajectory ensemble with $l = 5$ and $w = 1$ of a diverging (c.f. black trajectories in front) and rotating flow

an ensemble, parameterized by linear subspace estimation. Thereby, an adaptable representation of the abundant temporal information is obtained which accounts for diverging and converging pixel neighborhoods. Using this model, accurate motion estimates can be extracted without requiring spatial smoothness or piecewise constancy.

A trajectory ensemble as a set of trajectories in a spatial neighborhood can be defined as follows. Let $\Omega \subset \mathbb{N}^3$ denote the domain of a given image sequence and $I : \Omega \to \mathbb{R}$ a map to the image intensities. Furthermore, let $\mathbf{x} = (x_c, y_c, t_c) \in \Omega$ be the location at which the flow is to be estimated. Then we define the (frame-independent) pixel-grid neighborhood of $\mathbf{x}$ of width and height $2w$ as:

$$\mathcal{N}_{\mathbf{x}} := [x_c - w, x_c + w] \times [y_c - w, y_c + w], w \in \mathbb{N} \tag{16}$$

A single trajectory of length $2l$ at this location can be defined as a parametric function:

$$T_{\mathbf{x}} : [t_c - l, t_c + l] \to \Omega,\ l \in \mathbb{N} \text{ with } T_{\mathbf{x}}(t_c) = (x_c, y_c, t_c) \tag{17}$$

This definition ensures that a trajectory always crosses the image plane in frame t_c at the predefined location (x_c, y_c, t_c). Furthermore, let $\mathbf{d} = (x_d, y_d, 0) \in \mathcal{N}_{\mathbf{x}}$ be a spatial displacement vector. Then we define a trajectory ensemble as:

$$T_{\mathcal{N}_{\mathbf{x}}} := \{T_{\mathbf{x}+\mathbf{d}}(t) | \mathbf{x} + \mathbf{d} \in \mathcal{N}_{\mathbf{x}}\} \tag{18}$$

A two-dimensional example for this description is given in Figure 4. The resulting trajectory ensemble model consists of a discrete set of flow vectors. Techniques from unsupervised learning can be used to parameterize the flow within a neighborhood of fixed size. Here we confine ourselves to the standard technique of principal component analysis [16]. Based on the training data, these subspace estimation methods yield a map from a set of k parameters to an actual trajectory ensemble: $M : \mathbb{R}^k \to T_{\mathcal{N}_{\mathbf{x}}}$. The inverse mapping $M^{-1}(T_{\mathcal{N}_{\mathbf{x}}})$ can be used to find the best matching parameters describing a given trajectory ensemble, e.g. in order to transform an initial guess flow field into parameter vectors p.

Several options for the choice of training data for learning M exist. Many physical fluid flows can be simulated by Computational Fluid Dynamics, which we successfully utilized as highly application specific training data.

For the optical flow estimation based on trajectories, we define an energy function based on the discrete set of flow vectors of $T_{N_{\mathbf{x}}}$ together with a similarity measure $\mathcal{S}(\mathbf{x}, \mathbf{d}, I)$:

$$E(p, \mathbf{x}) := \sum_{\mathbf{d} \in M(p) = T_{N_{\mathbf{x}}}} \mathcal{S}(\mathbf{x}, \mathbf{d}, I) \tag{19}$$

Here, squared differences (SD) was chosen as the similarity measure:

$$\mathcal{S}(\mathbf{x}, \mathbf{d}, I) := (I(\mathbf{x}) - I(\mathbf{x} + \mathbf{d}))^2 \tag{20}$$

A wide range of optimization techniques can be applied for minimizing the nonlinear energy functional $E(p, \mathbf{x}(t))$, such as line search and trust-region methods

[4]. As it turns out, the optimization problem can be regarded as continuous and bounded. Here, we choose a trivial gradient descent method with one minor modification: in order to increase the probability of finding a global energy minimum, similar to particle filtering, we seed a number of random parameters by adding noise to the initial guess.

4 Applications

4.1 3D-3C Measurements at the Free Air-Water Interface

Using the previously described approaches to motion estimation, a technique was developed that makes the three dimensional three component (3D-3C) measurement of fluid flow directly at the free water surface possible. A fluid volume was illuminated by light emitting diodes (LEDs) perpendicularly to the surface. The set-up can be seen in Figure 6. The fluid was seeded with small spherical tracer particles. A monochromatic camera pointing to the water surface from above recorded the image sequences. The distance of the spheres to the surface was coded by means of a dye in the water phase, which absorbs the light of the LEDs according to BeerLamberts law. By applying LEDs with two different wavelengths, it was possible to use particles variable in size. The velocity vectors were obtained by using an exponential brightness change model for the optical flow as presented in Section 2.2. The vertical velocity component was computed from the temporal brightness change. The set-up was validated with a laminar falling film, which served as a reference flow. The result of this measurement is presented in Figure 6. The method was also applied to buoyant convective turbulence as an example for a non stationary, inherently 3D flow. Details of this application and results can be found in [14].

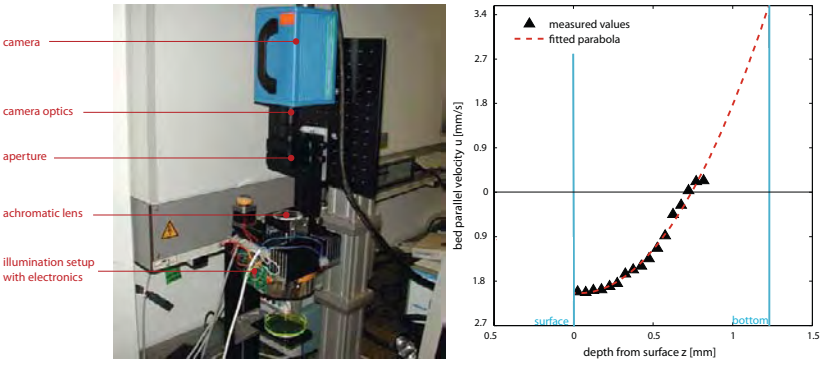

a) **b)**

Fig. 6 In **a** the set-up for the falling film experiment is shown, in **b** the velocity measurements are compared to the theoretically expected values

Fig. 7 In **a** the result of a CFD simulation is shown, in **b** the visualized particles integrated through time and in **c** the results of the motion estimation

4.2 Shear Flow at Moving Boundaries in Artificial Hearts

The time resolved measurement of three dimensional flow fields next to non-planar surfaces is of great interest in biofluidic mechanics. Many diseases, such as thrombotic events and atherosclerosis, directly depend on shear stresses and shear rates near vaulted walls in arteries or in artificial organs. The matter is further complicated by the fact that these walls often move due to non-constant blood pressure.

Here, a measurement technique termed Wall-PIV was developed, which is similar to the one described in section 4.1. The major difference between PIV and Wall-PIV is the used light: in most PIV set-ups, the flow is illuminated by a laser sheet, which cannot be aligned to a vaulted surface. Hence, in Wall-PIV, the transparent flow phantom is fully illuminated from the outside with a diffuse monochromatic light placed next to the camera. To limit the depth of view of particles to approx. 0.3 mm, a molecular dye with a high absorbance for the emitted wavelength of light is added to the fluid. Similar to PIV the fluid flow is visualized with tracer particles. Contrary to PIV, the 3D-3C flow estimation uses the motion estimation technique described in section 3.2. As training data, the CFD simulation of a blood pump similar to the one used in the experimental set-up was used in order to make use of as much prior knowledge as possible. Such a simulation in addition to real world data and fluid flow results are presented in Figure 7. More details concerning this application can be found in [2].

4.3 Viscous Shear at the Air-Water Interface

In small scale air-sea interactions, the friction velocity is an important parameter, indicating the momentum transport from the atmosphere to the ocean by wind forcing. This quantity is the driving force in a number of exchange processes that could previously not be measured directly. Here, a technique based on active thermography was used to measure this parameter directly at the air-water interface for the first time [10]. Measurements have been conducted by heating up patches of water with a CO_2 laser leading to linear patterns across the wind direction. From the

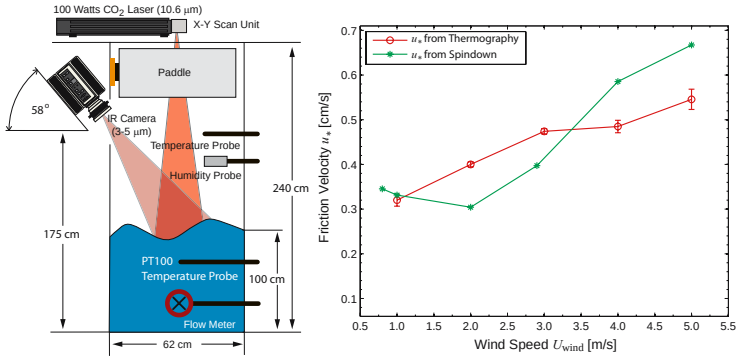

Fig. 8 In **a** the set-up for the active thermographic system in the laboratory is presented and in **b** results of a measure of $u_\star$ are shown [10]

velocity profile of Couette flow, the shear at the interface was computed leading to the friction velocity $u_\star$, an important parameter for air-water interactions. The analysis was based on a TLS approach (see Section 3.1) and Equation (14) was used as motion model. For comparison, $u_\star$ has also been measured with an alternative instrument for ground truth. The comparison of these measurements is presented in Figure 4.3. The difficulty of measuring the friction velocity is reflected in deviations to the standard measuring technique.

4.4 Molecular Tagging Velocimetry

A novel approach to Molecular Tagging Velocimetry (MTV) was developed for microfluidic flows [11]. Here, a pressure driven flow through a microfluidic mixer leads to Poiseuille type flow and Equation (14) for $n = 2$ was applied in a TLS framework (c.f. Section 3.1). To test the performance on microfluidic flows, a spatially homogeneous flow was set up in a microfluidic chamber [20]. Ground truth was derived from accurate measurements of the water flow through the chamber and by using

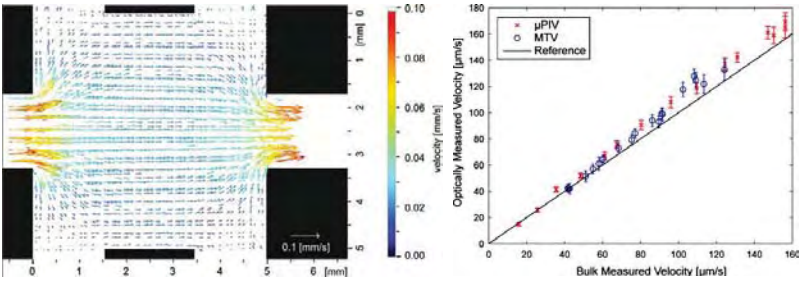

Fig. 9 In **a** the results of a MTV-based flow measurement inside the cuvette is shown and in **b** a comparison between our new approach and µPIV is presented

μPIV. Results are presented in [11] and recapitulated in Figure 9. The slight bias in some measurements can be attributed to calibration errors of the flow meter [11]. The data points were measured by integrating over the center part of three frames. The standard deviation was computed over the same area of the three frames. It can clearly be seen that there exists a good agreement between measurement and ground truth. For most data points, the ground truth value is well within the error bar. An in depth description of this application is presented in [3].

4.5 Mixture Formation Analysis with Fluorescence Motion Analysis

Double-pulse LIF imaging was used to gain insight into dynamic mixture formation processes. The set-up consists of a modified standard PIV assembly. The fuel/air ratio measurement by laser induced fluorescence (FARLIF) approach is used for a quantification of the LIF images and therefore to obtain pairs of 2D fuel/air ratio maps. Optical flow was used in order to estimate the motion of fluorescence (i.e. mixture) structures, and gives insight into the dynamics showing the distortion and the motion of the inhomogeneous mixture field. Results for this fluorescence motion analysis (FMA) are presented in Figure 10. For the validation of the approach, synthetic LIF image pairs with predefined motion field were generated and the results compared with the known original motion field. This validation shows that FMA yields reliable results even for image pairs with low signal/noise ratio. An image with deviations from the ground truth are shown in Figure 10. Also, the experimental combination of double-pulse FARLIF imaging with FMA and simultaneous PIV measurement was demonstrated. The comparison of the FMA motion field and the flow velocity field captured by PIV shows that both results basically reflect complementary information of the flow field. Details concerning these techniques and a discussion of the results have been published in [23] and are outlined in [21].

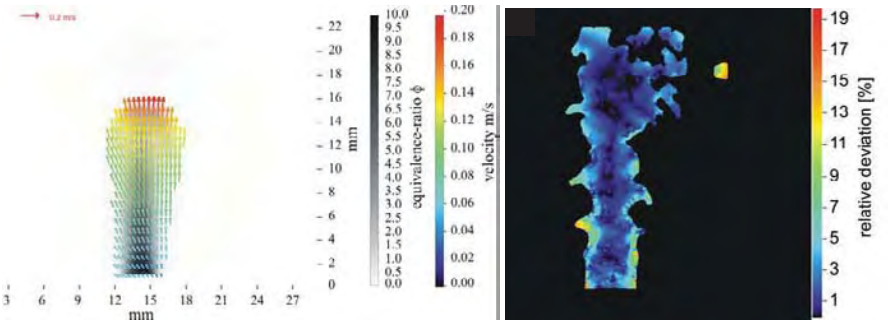

Fig. 10 In **a** the velocity estimation of the fluorescence motion analysis is presented and in **b** the comparison to a synthetic ground truth sequence [23]

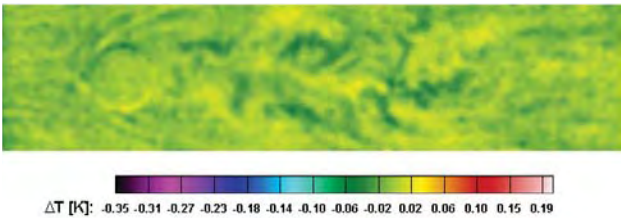

Fig. 11 The visualized temperature difference due to wall shear rate in an air flow around a cylinder [22]

4.6 Wall Shear Rates Using Thermography

The wall shear stress is a quantity of great importance in fluid mechanics, particularly in the analysis of flow processes close to walls. Optical flow measurements and orientation analysis was used to develop a technique to quantitatively measure shear rates and visualize the results. The physical principle of this technique is the analogy between momentum and heat transport at a heated surface. An airflow was blowing on top of the surface and different flow structures where placed on it to vary the wall shear rates. With the help of an infrared camera system, the temporal evolution of the surface temperature field was measured non-invasively. A result of such measurements is shown in Figure 11, where the airflow around a cylinder can be seen. The results were validated in a measurement combined with standard measurement techniques.

5 Conclusions

In this chapter, a framework has been presented that consists of (i) refined fluid flow visualization techniques, (ii) modeling of both the measurement process as well as the underlying physical principles and (iii) a subsequent image sequence analysis.

Only in encompassing these three vital steps, highly accurate fluid flow measurements where feasible while additional parameters of the flow could be estimated simultaneously. This makes it feasible to measure velocity gradients close to free surfaces in addition to the surface velocity fields. The novel techniques contrast current PIV or PTV techniques by measuring gradient fields directly and inherently modeling transport processes. Applications of these novel techniques were presented from medical and environmental sciences and from engineering.

Acknowledgements. The authors gratefully acknowledge the financial support of the German Science Foundation DFG within the priority program SPP 1147. We also thank our collaborators within the SPP 1147 for our interesting, successful and thoroughly enjoyable joint work.

References

1. Andres, B., Hamprecht, F.A., Garbe, C.S.: Selection of local optical flow models by means of residual analysis. In: Hamprecht, F.A., Schnörr, C., Jähne, B. (eds.) DAGM 2007. LNCS, vol. 4713, pp. 72–81. Springer, Heidelberg (2007)
2. Berthe, A., Kondermann, D., Jähne, B., Kertzscher, U.: The wall-piv measurement technique for near wall flow fields in biofluid mechanics. In: Nitsche, W., Dobriloff, C. (eds.) Imaging Measurement Methods for Flow Analysis. Springer, Heidelberg (2009)
3. Beushausen, V., Roetmann, K., Schmunk, W., Wellhausen, M., Garbe, C.: 2D-measurement technique for simultaneous quantitative determination of mixing ratio and velocity field in microfluidic applications. In: Nitsche, W., Dobriloff, C. (eds.) Imaging Measurement Methods for Flow Analysis. Springer, Heidelberg (2009)
4. Conn, A.R., Gould, N.I.M., Toint, P.L.: Trust-region methods. SIAM, Philadelphia (2000)
5. Fick, A.E.: Über Diffusion. Annalen der Physik 94(4), 59–86 (1855)
6. Fleet, D., Weiss, Y.: Optical flow estimation. In: Paragios, N., Chen, Y., Faugeras, O. (eds.) Mathematical Models in Computer Vision: The Handbook, ch. 15, pp. 239–258. Springer, Heidelberg (2005)
7. Fourier, J.B.: Théorie analytique de la chaleur. In: Ouvres de Fourier, Gauthier-Villars et Fils, Paris, France (1822)
8. Garbe, C., Spies, H., Jähne, B.: Estimation of complex motion from thermographic image sequences. In: Thermosense, pp. 303–317 (2003)
9. Garbe, C.S.: Fluid flow estimation through integration of physical flow configurations. In: Hamprecht, F.A., Schnörr, C., Jähne, B. (eds.) DAGM 2007. LNCS, vol. 4713, pp. 92–101. Springer, Heidelberg (2007)
10. Garbe, C.S., Degreif, K., Jähne, B.: Estimating the viscous shear stress at the water surface from active thermography. In: Garbe, C.S., Handler, R.A., Jähne, B. (eds.) Transport at the Air Sea Interface, pp. 223–239. Springer, Heidelberg (2007)
11. Garbe, C.S., Roetmann, K., Beushausen, V., Jähne, B.: An optical flow mtv based technique for measuring microfluidic flow in the presence of diffusion and taylor dispersion. Exp. in Fluids 44(3), 439–450 (2008)
12. Jähne, B.: Digital Image Processing. Springer, Heidelberg (2005)
13. Jähne, B., Scharr, H., Körkel, S., Jähne, B., Haußecker, H., Geißler, P.: Principles of filter design. In: Handbook of Computer Vision and Applications, pp. 125–151, 2. Academic Press, London (1999)
14. Jehle, M., Jähne, B.: A novel method for three-dimensional three-component analysis of flows close to free water surfaces. Experiments in Fluids 44(3), 469–480 (2008)
15. Jehle, M., Jähne, B., Kertzscher, U.: Direct estimation of the wall shear rate using parametric motion models in 3D. In: Franke, K., Müller, K.-R., Nickolay, B., Schäfer, R. (eds.) DAGM 2006. LNCS, vol. 4174, pp. 434–443. Springer, Heidelberg (2006)
16. Jolliffe, I.T.: Principal Component Analysis. Springer, Heidelberg (1986)
17. Knutsson, H., Westin, C.F.: Normalized and differential convolution: Methods for interpolation and filtering of incomplete and uncertain data. In: CVPR, New York City, pp. 515–516 (June 1993)
18. Kondermann, C., Kondermann, D., Garbe, C.: Postprocessing of optical flows via surface measures and motion inpainting. In: Rigoll, G. (ed.) DAGM 2008. LNCS, vol. 5096, pp. 355–364. Springer, Heidelberg (2008)

19. Kondermann, C., Mester, R., Garbe, C.: A statistical confidence measure for optical flows. In: Forsyth, D., Torr, P., Zisserman, A. (eds.) ECCV 2008, Part III. LNCS, vol. 5304, pp. 290–301. Springer, Heidelberg (2008)
20. Roetmann, K., Schmunk, W., Garbe, C.S., Beushausen, V.: Micro-flow analysis by molecular tagging velocimetry and planar raman-scattering. Experiments in Fluids 44(3), 419–430 (2008)
21. Rotter, F., Scholz, J., Müller, J., Wiersbinsky, T., Röhl, M., Ruhnau, P., Kondermann, D., Garbe, C., Hain, R., Beushausen, V.: Simultaneous, planar determination of fuel/air ratio and velocity field in single phase mixture formation processes. In: Nitsche, W., Dobriloff, C. (eds.) Imaging Measurement Methods for Flow Analysis. Springer, Heidelberg (2009)
22. Rudolph, I., Reyer, M., Nitsche, W.: Infrared-based visualization of wall shear stress distributions. In: Nitsche, W., Dobriloff, C. (eds.) Imaging Measurement Methods for Flow Analysis. Springer, Heidelberg (2009)
23. Scholz, J., Wiersbinski, T., Ruhnau, P., Kondermann, D., Garbe, C., Hain, R., Beushausen, V.: Double-pulse planar-lif investigations using fluorescence motion analysis for mixture formation investigation. Experiments in Fluids 45(4), 583–593 (2008)
24. Tropea, C., Yarin, A.L., Foss, J.F. (eds.): Springer Handbook of Experimental Fluid Mechanics. Springer, Heidelberg (2007)
25. Van Huffel, S., Vandewalle, J.: The Total Least Squares Problem: Computational Aspects and Analysis. SIAM, Philadelphia (1991)
26. Vlasenko, A., Schnörr, C.: Variational approaches to image fluid flow estimation with physical priors. In: Nitsche, W., Dobriloff, C. (eds.) Imaging Measurement Methods for Flow Analysis. Springer, Heidelberg (2009)

Extraction and Visualization of Flow Features

Kudret Baysal, Tobias Schafhitzel, Thomas Ertl, and Ulrich Rist

Abstract. This paper presents tools which allow an advanced investigation of spatial and temporal progress of segmented vortex structures in flow fields with the consideration of vortex dynamics. The work is based on the local and Eulerian detection and segmentation of vortex structures and the visualization of these structures with recent visualization methods, e.g. the application of LIC-textures on the surfaces of 3d structures. The second step is the tracking of vortex structures based on the time-dependent integration of vortex core lines. In the third step, according to the vortex dynamics, the individual degree of impact is determined by computation of induced velocities via the Biot-Savart equation for each vortex. The induced velocities are used to determine the induced kinetic energy and enstrophy, which allows the evaluation of a global value of influence for each vortex structure, that can be tracked in time.

1 Introduction

The physical understanding of boundary layers or mixing layers is of fundamental interest for fluid dynamical research. A principal method in the investigations of physical aspects of flow fields is the observation of characteristic features of the flow fields, which are coherent in space and time. Although the so-called coherent structures or vortex structures are well-known in the analysis of flow fields, e.g. laminar-turbulent transition or effects of flow control mechanisms, the investigations of real-life flow fields based on coherent structures are not straightforward.

Kudret Baysal · Ulrich Rist
Institut für Aerodynamik und Gasdynamik, Universität Stuttgart, Pfaffenwaldring 21, 70569 Stuttgart, Germany
{baysal,rist}@iag.uni-stuttgart.de

Tobias Schafhitzel · Thomas Ertl
Institut für Visualisierung und Interaktive Systeme, Universität Stuttgart, Universitätsstrasse 38, 70569 Stuttgart
{schafhitzel,ertl}@vis.uni-stuttgart.de

W. Nitsche and C. Dobriloff (Eds.): Imaging Measurement Methods, NNFM 106, pp. 305–314.
springerlink.com

The aim of this paper is to present techniques for an advanced investigation of three-dimensional and time-dependent flow fields. The first goal of this work is the automatic identification and segmentation of vortex structures in order to find an appropriate visualization, which allows the engineer to investigate the extracted features in an interactive manner. For the visualization, recent algorithms have been applied, which exploit newest graphics hardware features. This is followed by vortex tracking, i.e., the time-dependent mapping of individual vortex structures to capture their temporal development. For this purpose, a framework has been developed, which provides, beside the investigation of vortices in a single snapshot, also the time-dependent visualization of these structures. This allows an advanced analysis of kinematic properties of the vortex structures, e.g. size, shape, and vorticity strength. The results of these studies allow the acquisition of quantitative information for flow fields, which are necessary in the development of flow field models or in the comparison and validation of experimental and numerical studies.

The second goal is the consideration of vortex dynamical effects, which allows the study of interactions between vortex structures, e.g. vortex merging, and self-excited effects, e.g. the autogeneration of hairpin vortices, which is a significant mechanism in the generation of turbulence. The strategy of this work is the determination of the velocity field induced by each vortex structure in a flow field and their influence in the time-dependent development of other vortex structures. In order to support the consideration of vortex dynamics within our framework, the engineer is able to select an arbitrary vortex structure, which is then used to determine the time as well as the vortex structure which perturbs the selected vortex strongest. The time-dependent dynamical investigation of interactions between structures enables the investigation of effectiveness of flow-control mechanisms.

2 Flow-Features Identification

The main vortex identification methods are based on the widely accepted definition of a vortex structure as a finite volume of fluid particles with a vortical motion around a center line. The complexity of the vortex structures and lacks in the understanding of these structures caused discussions of different aspects of vortex structures and their identification. This resulted in several approaches for vortex identification, whereby the focus was for the last few years on the influence of axial stretching and shearing [3] on vortex identification, as investigations of vortex regions with high shear had revealed a gap in the reliability of the widely used criteria, e.g. λ_2 [2] or the Okubo-Weiss criterion, also known as Q criterion.

Although the influence of high-shear regions in the identification of vortex structure regions is in the focus of discussions, the understanding of it is still not clear. Hence it is necessary to analyze the effects of shearing on vortex structure identification and vortex dynamics.

One of the latest approaches, which is considering the effects of shear in the vortex identification, is the approach of Kolář [3]. The triple decomposition method of Kolář is an extension of the classical decomposition of the velocity gradient tensor

$\nabla \mathbf{u}$ into a symmetric and an asymmetric part. The motivation of the new decomposition is the fact that the asymmetric tensor, which holds the vorticity, is not able to distinguish between pure shearing motion and vortical motion. Therefore, the decomposition of $\nabla \mathbf{u}$ into three tensors is desirable, where the third tensor describes pure shear motion and the new *corrected* vorticity tensor considers only vortical motion. Although the application of the new criterion for two-dimensional examples, e.g. mixing layers, is promising, the lack of an algorithm for three-dimensional flow fields makes a general application impossible, at present.

For the examples in the following sections the λ_2 criterion is used, which is, despite its inaccuracies in high-shear regions, the most reliable criterion for three-dimensional flow fields.

3 Visualization of Vortices

The goal of our project was to provide an interactive visual representation of vortex structures. Therefore, the following subgoals should be accomplished: (1) vortex segmentation. This step is crucial for separating arbitrarily connected vortex structures, like those resulting from conventional isosurface-generation algorithms; (2) vortex visualization. Based on the foregoing segmentation step, the vortices need to be visualized appropriately; (3) multi-field visualization, i.e., the visualization of vortices and additional quantities, e.g., the velocity field; (4) vortex tracking. Since most of the underlying velocity fields represent a time-dependent flow, an appropriate time-dependent visualization of vortex structures is needed.

3.1 Vortex Segmentation

The role of vortex segmentation can be illustrated by a simple scenario. Imagine we have a scalar field like the one that results from the λ_2 computation. Then, from the point of view of visualization there are various methods for drawing an isosurface of this input data, which represents, according to the theory of λ_2, the vortex boundaries if the isovalue is set to a small value below zero in order to avoid artifacts due to noisy data.

Our goal was to provide the engineer more interactivity in terms of selecting single vortex structures, fading them out, or simply to investigate them in more detail. Therefore, a criterion, which delivers a list of segmented vortices must be found–the vortex core line. We define a vortex core line as a connected set of *local* pressure (or λ_2) minima. The end points of a vortex core line are found by searching for discontinuities of the core line tangent or by checking if the function value of the core line becomes positive. A predictor-corrector method by Stegmaier et al. [8] is used for computing the vortex core lines: first a list of seed points is generated. Since 3D minima of λ_2 are a subclass of the local λ_2 minima discussed above, they must be part of the vortex core line and, therefore, can serve as seed points without any restrictions.

Once the list of seed points has been generated, the algorithm starts by processing them in a consecutive order. Each seed point is tested if it is inside the vortex boundaries, the $\lambda_2 = 0$ isosurface, of an already detected vortex. If this is the case, the seed point is discarded. Otherwise it serves as first point $\mathbf{p}_0$ on the growing vortex core line, where both a prediction and a correction step are performed. Since the vorticity can be regarded as the local axis of rotation and we assume that the vortex rotates around the vortex core line, it can be used for predicting the next position on the core line. However, an integration along the vorticity vector would involve a numerical error, which need to be corrected in a second step. Here, again the vorticity is computed, now at the predicted position. The corrected position $\mathbf{p}_{i+1}$ is finally found by searching for the λ_2 minimum on a plane perpendicular to the vorticity. Then the loop is repeated, using $\mathbf{p}_{i+1}$ as starting point until a discontinuity of the core line is detected or λ_2 becomes positive. In order to identify all vortex core lines, the algorithm is performed over all seed points. For a more detailed discussion we refer to [8].

In a last step, the isosurfaces are computed for each vortex individually by creating planes at the computed positions $\mathbf{p}_i$. The geometrical data is stored together with the points and the topology of the vortex core lines into appropriate data structures, which are discussed in Section 3.2.

3.2 Vortex Visualization

Once the vortices and their respective core lines are computed, they to need be stored into data structures which are appropriate for an interactive visualization. Here, the goal of vortex visualization exceeds a simple visualization of their λ_2 isosurfaces—apart from a good visual representation, the user should be able to interact with the visualized data. Therefore, the following features should be supported: (1) global transformation of all vortices; (2) selection and transformation of individual vortex structures; and (3) removal of uninteresting vortices.

Although the first condition could also be fulfilled when only λ_2 isosurfaces would be drawn, for (2) and (3) the vortex segmentation of Section 3.1 is absolutely crucial. Since (2) and (3) intend to perform any actions on individual vortex structures, the most appropriate data representation would consist of a scene graph, i.e., a data structure, which stores each element of the scene individually and where for each scene element a separate transformation matrix is attached. In this case, the vortex core lines and their related λ_2 isosurfaces build the leaves of the scene graph and drawing can be performed for each leaf individually.

Drawing the vortices in a consecutive order with one global transformation matrix fulfills condition (1); enabling the local transformation matrices additionally allows the transformation of single vortex structures and, therefore, fulfills condition (2); condition (3) exploits again the fact that the vortices are drawn in a consecutive order. If a vortex should not be drawn, a small quad is created at the upper part of the screen and represents the invisible vortex. Figure 1 shows the vortex visualization, where the colors represent the vortex strength according to the λ_2 values on

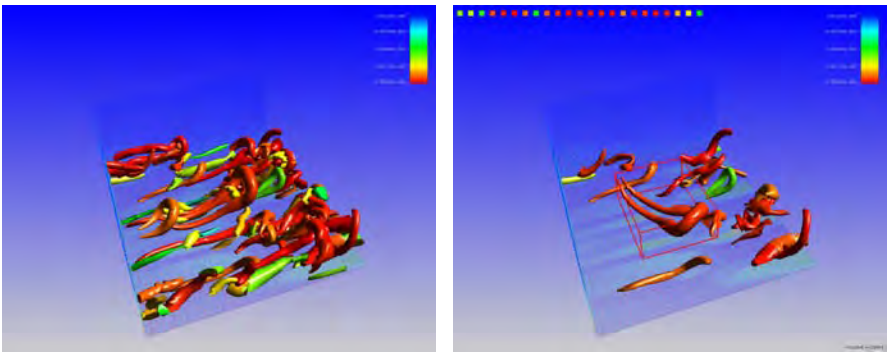

(a) (b)

Fig. 1 Visualization of a segmented vortex field: Figure (a) shows the λ_2 isosurfaces colored according to the vortex strength. Here, the gradient goes from green (= weak) to red (= strong); Figure (b) demonstrates the interactivity of our framework. Individual vortices can be selected and transformed while uninteresting vortices are blended out and drawn as small quadrilaterals at the top of the screen

the vortex core line. In Figure 1 (a), the segmented vortices of a transitional flow are shown. Figure 1 (b) illustrates how an individual vortex is picked, while uninteresting vortices are faded out and displayed as small quadrilaterals in the upper left corner of the window. Due to the underlying scene graph, the selected vortex can be transformed independently. Applying color coding to the isosurfaces (green = weak, red = strong) helps the user to identify stronger vortices at a glance.

3.3 Introducing Line Integral Convolution

So far, vortices have been extracted from a velocity field, vortex core lines were computed, and an appropriate visualization framework was developed in order to enable an interactive investigation of the extracted vortices. However, up to now, only the locations, the spatial extents, and the vortex strengths are perceptible for the user—there is no possibility to identify the direction of rotation of the individual vortices so far! This information, though, is quite important because it plays a crucial role in vortex dynamics, where the direction of rotation of a vortex is of special meaning considering the amplification of other vortices (see Section 5).

For this purpose, the flow feature visualization described above is combined with a real-time texture-based flow visualization technique–the line integral convolution (LIC) algorithm [1]–which is a common method in computer graphics. The major advantage of this algorithm is that it exploits the capabilities of modern graphics hardware and, therefore, is highly interactive. Without going into technical detail, LIC is actually used to draw stream lines by integrating along a given vector field, whereby stream lines appear as lines of low frequencies. A result of 2D LIC is shown in Figure 2 (a). Since the original LIC algorithm is not appropriate for drawing stream lines on curved surfaces as those which result from our vortex

(a) (b) (c)

Fig. 2 Line integral convolution (LIC)—a texture is smeared out in direction of the vector field. This results in low frequencies along the stream line and high frequencies perpendicular to its gradient: (a) shows LIC on a 2D planar surface with additional dye advection; (b) LIC has been applied on a curved surface, here the λ_2 isosurface representing a vortex region. The vector field is projected onto the isosurface to achieve long line-like patterns; (c) the shape of the particle traces are further emphasized by enabling illumination

visualization algorithm of section 3.2, an extended version by Weiskopf and Ertl [9] has been applied to the λ_2 isosurfaces. Based on the fact that the velocity field is almost tangential to the $\lambda_2 = 0$ isosurface, the vector field is projected onto the isosurface. This results in line-like patterns on the λ_2 isosurfaces and has the following advantages: (1) the motion of a particle close to a vortex region is perceptible at a glance; and (2) applying animated LIC, the direction of rotation is perceptible as well without loosing the information provided by the vortex visualization. Figure 2 (b) and (c) show LIC on vortex surfaces, whereby in (c) the particle traces are further emphasized by illumination. For a more detailed discussion we refer to the work of Schafhitzel et al. [5].

4 Vortex Tracking

Considering unsteady vector fields instead of individual snapshots, the temporal behavior of the extracted vortex structures are of special interest because this information can be used for detecting temporal events. The mapping of vortex structures, which have been extracted at time t to their counterparts at a later time step $t + \Delta t$ is called vortex tracking and builds the base of any temporal investigation of vortices.

The tracking algorithm we used is based on the work of Schafhitzel et al. [6], where the vortex core line at time t is sampled and particles are integrated along the vector field in order to estimate the new position of the vortex core line at time $t + \Delta t$. This method is simple and reliable, since the vortex core line is supposed to be the region inside a vortex which exceeds at least the upper boundary of λ_2 ($\lambda_2 = 0$) and, therefore, the particles seeded on the vortex core lines do not tend to leave the vortex from t to $t + \Delta t$.

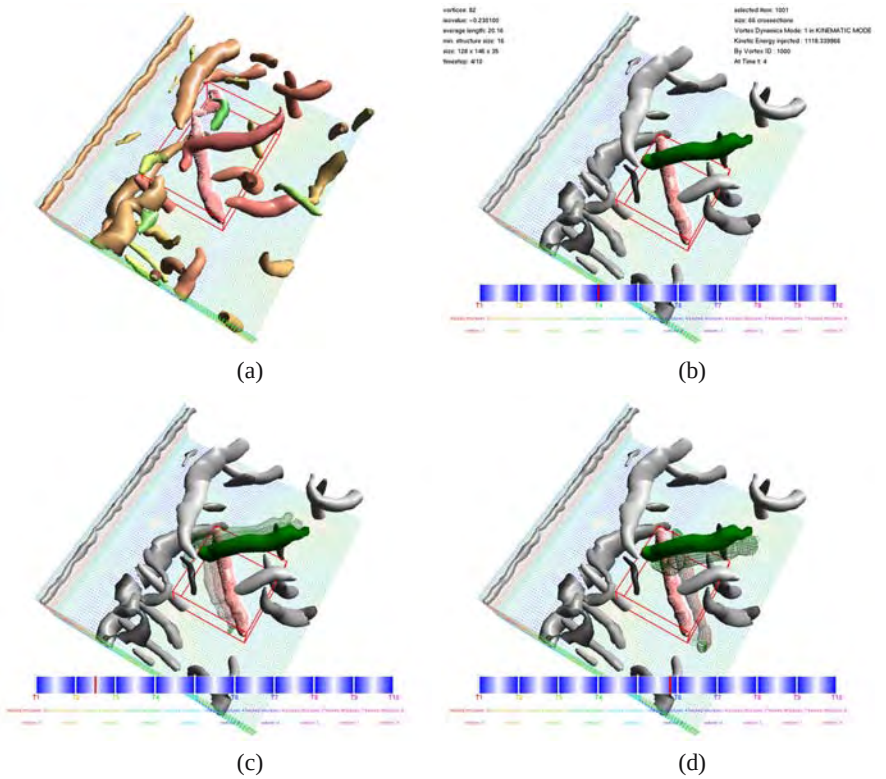

Fig. 3 The visualization of an experimental data set [4]. The data was measured using tomographic PIV and shows a circular cylinder wake at Reynolds $Re = 360$. The cylinder, which is located parallel to the left edge of the data set is not visualized. In this example, vortex dynamics are considered: (a) initial situation at $t = 0$. All vortices are color coded according to their strength. The red bounding box gives feedback about the vortex selected for tracking; (b) the moment of strongest perturbation at $t_p = 4$. The representation has changed to time t_p where the green vortex influences the selected structure (red); (c) backward tracking. The wire frame representation shows where the structures came from; (d) forward tracking. Here, the wire frame representation shows the further development of both structures [6].

Our framework, which is represented in Figure 3, supports user interactivity in the following manner: (1) the user is able to select a single vortex at an arbitrary time step in order to track it forward and backward along the time-dependent vector field. Here, all the relationships between the vortices at the different time steps are created; (2) a time line is provided, which can be used to manipulate the time at which the vortex should be visualized. By smoothly sliding the red bar along the time line, the transitions between the time steps are visualized; (3) topological changes are supported when a vortex core line hits more than one structure. Note that the detection of vortex reconnection events depends on the quality of the underlying vortex core line detection method. For a topology-preserving λ_2-based vortex core

line detection method we refer to the work of Schafhitzel et al. [7]. Altogether, this method provides a fast and interactive investigation of vortices inside a time-dependent flow because once a vortex has been selected and tracked, the user is able to switch between the different time steps very fast.

5 Considering Vortex Dynamics

The analysis of coherent structures is based on the purpose to gain physical understanding of the mechanisms in fluid dynamics, which is necessary for a reliable comparability of experimental and numerical studies, the reproducibility of these studies, or predictive modeling of flow field regions, e.g. separated flows and wakes. A method for the detection of vortex core lines is described in Section 3.1; the tracking of vortices is discussed in Section 4. These methods enable the spatial and temporal investigation of kinematic properties (e.g. size, vorticity, and energy) of vortex structures and, therefore, provide quantitative information for an advanced comparison of studies and physical models.

However, an analysis of coherent structures, which is limited to kinematic properties cannot be sufficient in the investigation of central questions in the development of flow fields. Hence, an additional investigation of the dynamic properties (e.g. emergence, growth, and stability) of the coherent structures is necessary to answer these questions.

A straightforward strategy for the consideration of vortex dynamics in the analysis of coherent structures is the observation of dynamical values, e.g., kinetic energy or enstrophy, which are defined by

$$E_{kin} = \frac{1}{2}\int_V (\mathbf{u}(\mathbf{x},t))^2\, d^3\mathbf{x} \text{ and } E_{rot} = \frac{1}{2}\int_V \omega(\mathbf{x},t)^2\, d^3\mathbf{x}\,, \tag{1}$$

respectively, where ω denotes vorticity. Thereby, several problems arise: the first is the lack of a proper definition of the region of integration. In test cases with two vortex structures like collision of vortex rings, it is sufficient to integrate over the whole domain. However, in real flow fields containing hundreds of structures of interest, each of them needs a more specified definition of the integrated volume. A reasonable choice are the spatial extents of the vortical regions.

The second problem addresses a major aspect in the investigation of dynamical properties–the interaction between coherent structures–like the merging of coherent structures or the self-excited effects of complex coherent structures (e.g. hairpin vortices). A technique which deals with these effects is the determination of the induced velocities of each coherent structure. The fundamental equation for this technique is the Biot-Savart equation, which computes the induced velocity field out of the vorticity field:

$$\mathbf{u}_{ind}(\mathbf{x},t) = \frac{1}{4\pi}\int_V \frac{\omega(\mathbf{x}',t)\times(\mathbf{x}-\mathbf{x}')}{|\mathbf{x}-\mathbf{x}'|^3} d^3\mathbf{x}'\,, \tag{2}$$

where the influence of $\mathbf{x}'$ on $\mathbf{x}$ is computed.

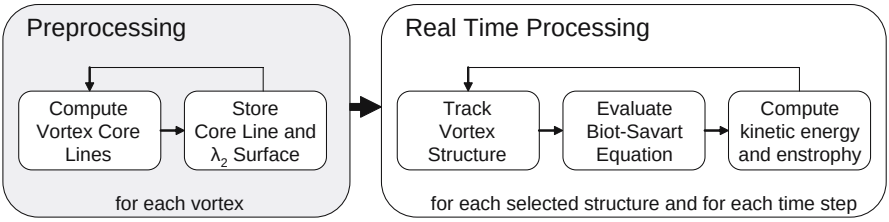

Fig. 4 Program flow of our framework: first, the vortex core lines are computed; second, the structures are tracked and computed for their influence on each other. This stage can be interactively manipulated by the selection of the structures to be tracked [6]. ©2008 by Schafhitzel et al.

A pure monitoring of the induced velocities has only a limited significance for a characterization of the interaction between coherent structures because the consideration of the influences on a vector field is not straightforward. Hence, an approach, which combines both methods described above is used to determine the interaction of coherent structures. For this purpose, the influence of one vortex structure on another is described by a characteristic integral value, e.g. the kinetic energy, which depends on the induced velocity field $\mathbf{u}_{ind}$. Figure 4 shows the overall program flow which is separated into two independent parts: (1) the preprocessing, where the core lines and the vortex segmentation are computed; and (2) the real-time processing, which consists of the tracking and the consideration of vortex dynamics. In contrast to the first stage, the second stage can be widely influenced by the user.

The example presented in Figure 3 shows results of the tracking method, which has been extended by taking into account vortex dynamics in order to find the time where the selected structure is perturbed strongest by another vortex. The computation results in a list containing the strongest perturbing vortices and the appropriate information in terms of kinetic energy and enstrophy.

The resulting time instant t_p defines the time of the strongest perturbation, and therefore, the visualization is set to t_p for both the focus and the context. In Figure 3, the detection and visualization of t_p is shown. By selecting a vortex at an arbitrary time (Figure 3(a)), the vortex with the strongest influence is computed, displayed as green vortex in Figure 3(b) at time t_p. Starting from here, both structures are tracked backward and forward to gain information about their origin and their further development (Figures 3(c) and (d)). Additionally, the detailed information about the detected and the selected vortex, e.g., the energy induced, IDs, length, etc. is displayed as text.

A detailed investigation of areas of interest inside a flow field or selected vortex structures as described in Figure 3 reveals additional temporal information about interactions between vortex structures and their effects on flow-field events. This helps the researcher to perform detailed studies of unsteady flow fields like, e.g. the wake of a circular cylinder, that has been selected as a reference configuration for this DFG priority research area. However, in absence of suitable experimental data

from other projects we had to work on data provided by Scarano et al. [4] for the present example.

6 Conclusions

Recent flow-field measurements techniques such as those considered within the present DFG priority research program are capable of producing several gigabytes of raw data within a short time. Without appropriate post-processing and visualization methods the physical insight hidden in these data would remain unexplored. The methods presented here allow the researcher an interactive exploration of such data on a higher abstraction level based on the concept of "vortices". As such, vortex identification, segmentation, quantification and tracking are a prerequisite for any detailed investigation of *unsteady* separated flows, which might be encountered after boundary layer separation, in mixing layers or in wakes. However, the present tool is not yet complete,. It still lacks more methods for an automatic tracking of events like vortex creation out of shear or vortex merging. According work is necessary and in progress.

Acknowledgements. We thank the DFG for financial support of this work under grants ER 272/4 and RI 680/14 and we are very grateful to Fulvio Scarano, TU Delft for providing the cylinder data set used in the present article.

References

1. Cabral, B., Leedom, L.C.: Imaging Vector Fields Using Line Integral Convolution. In: Proc. ACM SIGGRAPH, pp. 263–270 (1993)
2. Jeong, J., Hussain, F.: On the Identification of a Vortex. J. Fluid Mech. 285, 69–94 (1995)
3. Kolář, V.: Vortex Identification: New Requirements and Limitations. Int. J. of Heat and Fluid Flow 28, 638–652 (2007)
4. Scarano, F., Poelma, C., Westerweel, J.: Towards four-dimensional particle image velocimetry. In: 7th International Symposium on Particle Image Velocimetry (2007)
5. Schafhitzel, T., Weiskopf, D., Ertl, T.: Interactive Investigation and Visualization of 3D Vortex Structures. In: Electronic Proceedings International Symposium on Flow Visualization 2006 (2006)
6. Schafhitzel, T., Baysal, K., Rist, U., Weiskopf, D., Ertl, T.: Particle-based vortex core line tracking taking into account vortex dynamics. In: Proceedings International Symposium on Flow Visualization 2008 (2008)
7. Schafhitzel, T., Vollrath, J., Gois, J., Weiskopf, D., Castelo, A., Ertl, T.: Topology-Preserving $\lambda 2$-based Vortex Core Line Detection for Flow Visualization. In: Computer Graphics Forum (Eurovis 2008), vol. 27(3), pp. 1023–1030 (2008)
8. Stegmaier, S., Rist, U., Ertl, T.: Opening the Can of Worms: An Exploration Tool for Vortical Flows. In: Proceedings IEEE Visualization 2005 (2005)
9. Weiskopf, D., Ertl, T.: A Hybrid Physical/Device-Space Approach for Spatio-Temporally Coherent Interactive Texture Advection on Curved Surfaces. In: Proceedings of Graphics Interface 2004 (2004)

Author Index

Notes on Numerical Fluid Mechanics and Multidisciplinary Design

Available Volumes

Volume 106: Wolfgang Nitsche, Christoph Dobriloff (eds.): Imaging Measurement Methods for Flow Analysis - Results of the DFG Priority Programme 1147 “Imaging Measurement Methods for Flow Analysis” 2003–2009. ISBN 978-3-642-01105-4

Volume 105: Michel Deville, Thien-Hiep Lê, Pierre Sagaut (eds.): Turbulence and Interactions - Keynote Lectures of the TI 2006 Conference. ISBN 978-3-642-00261-8

Volume 104: Christophe Brun, Daniel Juvé, Michael Manhart, Claus-Dieter Munz: Numerical Simulation of Turbulent Flows and Noise Generation - Results of the DFG/CNRS Research Groups FOR 507 and FOR 508. ISBN 978-3-540-89955-6

Volume 103: Werner Haase, Marianna Braza, Alistair Revell (eds.): DESider – A European Effort on Hybrid RANS-LES Modelling - Results of the European-Union Funded Project, 2004–2007. ISBN 978-3-540-92772-3

Volume 102: Rolf Radespiel, Cord-Christian Rossow, Benjamin Winfried Brinkmann (eds.): Hermann Schlichting – 100 Years - Scientific Colloquium Celebrating the Anniversary of His Birthday, Braunschweig, Germany 2007. ISBN 978-3-540-95997-7

Volume 101: Egon Krause, Yurii I. Shokin, Michael Resch, Nina Shokina (eds.): Computational Science and High Performance Computing III - The 3rd Russian-German Advanced Research Workshop, Novosibirsk, Russia, 23–27 July 2007. ISBN 978-3-540-69008-5

Volume 100: Ernst Heinrich Hirschel, Egon Krause (eds.): 100 Volumes of ’Notes on Numerical Fluid Mechanics’ - 40 Years of Numerical Fluid Mechanics and Aerodynamics in Retrospect. ISBN 978-3-540-70804-9

Volume 99: Burkhard Schulte-Werning, David Thompson, Pierre-Etienne Gautier, Carl Hanson, Brian Hemsworth, James Nelson, Tatsuo Maeda, Paul de Vos (eds.): Noise and Vibration Mitigation for Rail Transportation Systems - Proceedings of the 9th International Workshop on Railway Noise, Munich, Germany, 4–8 September 2007. ISBN 978-3-540-74892-2

Volume 98: Ali Gülhan (ed.): RESPACE – Key Technologies for Reusable Space Systems - Results of a Virtual Institute Programme of the German Helmholtz-Association, 2003–2007. ISBN 978-3-540-77818-9

Volume 97: Shia-Hui Peng, Werner Haase (eds.): Advances in Hybrid RANS-LES Modelling - Papers contributed to the 2007 Symposium of Hybrid RANS-LES Methods, Corfu, Greece, 17–18 June 2007. ISBN 978-3-540-77813-4

Volume 96: C. Tropea, S. Jakirlic, H.-J. Heinemann, R. Henke, H. Hönlinger (eds.): New Results in Numerical and Experimental Fluid Mechanics VI - Contributions to the 15th STAB/DGLR Symposium Darmstadt, Germany, 2006. ISBN 978-3-540-74458-0

Volume 95: R. King (ed.): Active Flow Control - Papers contributed to the Conference “Active Flow Control 2006”, Berlin, Germany, September 27 to 29, 2006. ISBN 978-3-540-71438-5

Volume 94: W. Haase, B. Aupoix, U. Bunge, D. Schwamborn (eds.): FLOMANIA - A European Initiative on Flow Physics Modelling - Results of the European-Union funded project 2002 - 2004. ISBN 978-3-540-28786-5

Volume 93: Yu. Shokin, M. Resch, N. Danaev, M. Orunkhanov, N. Shokina (eds.): Advances in High Performance Computing and Computational Sciences - The Ith Khazakh-German Advanced Research Workshop, Almaty, Kazakhstan, September 25 to October 1, 2005. ISBN 978-3-540-33864-2

Volume 92: H.J. Rath, C. Holze, H.-J. Heinemann, R. Henke, H. Hönlinger (eds.): New Results in Numerical and Experimental Fluid Mechanics V - Contributions to the 14th STAB/DGLR Symposium Bremen, Germany 2004. ISBN 978-3-540-33286-2

Volume 91: E. Krause, Yu. Shokin, M. Resch, N. Shokina (eds.): Computational Science and High Performance Computing II - The 2nd Russian-German Advanced Research Workshop, Stuttgart, Germany, March 14 to 16, 2005. ISBN 978-3-540-31767-8

Volume 87: Ch. Breitsamter, B. Laschka, H.-J. Heinemann, R. Hilbig (eds.): New Results in Numerical and Experimental Fluid Mechanics IV. ISBN 978-3-540-20258-5

Volume 86: S. Wagner, M. Kloker, U. Rist (eds.): Recent Results in Laminar-Turbulent Transition - Selected numerical and experimental contributions from the DFG priority programme 'Transition' in Germany. ISBN 978-3-540-40490-3

Volume 85: N.G. Barton, J. Periaux (eds.): Coupling of Fluids, Structures and Waves in Aeronautics - Proceedings of a French-Australian Workshop in Melbourne, Australia 3-6 December 2001. ISBN 978-3-540-40222-0

Volume 83: L. Davidson, D. Cokljat, J. Fröhlich, M.A. Leschziner, C. Mellen, W. Rodi (eds.): LESFOIL: Large Eddy Simulation of Flow around a High Lift Airfoil - Results of the Project LESFOIL supported by the European Union 1998 - 2001. ISBN 978-3-540-00533-9

Volume 82: E.H. Hirschel (ed.): Numerical Flow Simulation III - CNRS-DFG Collaborative Research Programme, Results 2000-2002. ISBN 978-3-540-44130-4

Volume 81: W. Haase, V. Selmin, B. Winzell (eds.): Progress in Computational Flow Structure Interaction - Results of the Project UNSI, supported by the European Union 1998-2000. ISBN 978-3-540-43902-8

Volume 80: E. Stanewsky, J. Delery, J. Fulker, P. de Matteis (eds.): Drag Reduction by Shock and Boundary Layer Control - Results of the Project EUROSHOCK II, supported by the European Union 1996-1999. ISBN 978-3-540-43317-0

Volume 79: B. Schulte-Werning, R. Gregoire, A. Malfatti, G. Matschke (eds.): TRANSAERO - A European Initiative on Transient Aerodynamics for Railway System Optimisation. ISBN 978-3-540-43316-3

Volume 78: M. Hafez, K. Morinishi, J. Periaux (eds.): Computational Fluid Dynamics for the 21st Century. Proceedings of a Symposium Honoring Prof. Satofuka on the Occasion of his 60th Birthday, Kyoto, Japan, 15-17 July 2000. ISBN 978-3-540-42053-8

Volume 77: S. Wagner, U. Rist, H.-J. Heinemann, R. Hilbig (eds.): New Results in Numerical and Experimental Fluid Mechanics III. Contributions to the 12th STAB/DGLR Symposium, Stuttgart, Germany 2000. ISBN 978-3-540-42696-7

Volume 76: P. Thiede (ed.): Aerodynamic Drag Reduction Technologies. Proceedings of the CEAS/DragNet European Drag Reduction Conference, 19-21 June 2000, Potsdam, Germany. ISBN 978-3-540-41911-2

Volume 75: E.H. Hirschel (ed.): Numerical Flow Simulation II. CNRS-DFG Collaborative Research Programme, Results 1998-2000. ISBN 978-3-540-41608-1

Volume 66: E.H. Hirschel (ed.): Numerical Flow Simulation I. CNRS-DFG Collaborative Research Programme. Results 1996-1998. ISBN 978-3-540-41540-4